Sreevalsa Kolathayar · Chandan Ghosh ·
Basanta Raj Adhikari · Indrajit Pal ·
Arpita Mondal   *Editors*

Resilient Infrastructure

Select Proceedings of VCDRR 2021

Springer

Lecture Notes in Civil Engineering

Volume 202

Lecture Notes in Civil Engineering (LNCE) publishes the latest developments in Civil Engineering - quickly, informally and in top quality. Though original research reported in proceedings and post-proceedings represents the core of LNCE, edited volumes of exceptionally high quality and interest may also be considered for publication. Volumes published in LNCE embrace all aspects and subfields of, as well as new challenges in, Civil Engineering. Topics in the series include:

- Construction and Structural Mechanics
- Building Materials
- Concrete, Steel and Timber Structures
- Geotechnical Engineering
- Earthquake Engineering
- Coastal Engineering
- Ocean and Offshore Engineering; Ships and Floating Structures
- Hydraulics, Hydrology and Water Resources Engineering
- Environmental Engineering and Sustainability
- Structural Health and Monitoring
- Surveying and Geographical Information Systems
- Indoor Environments
- Transportation and Traffic
- Risk Analysis
- Safety and Security

To submit a proposal or request further information, please contact the appropriate Springer Editor:

– Pierpaolo Riva at pierpaolo.riva@springer.com (Europe and Americas);
– Swati Meherishi at swati.meherishi@springer.com (Asia - except China, and Australia, New Zealand);
– Wayne Hu at wayne.hu@springer.com (China).

All books in the series now indexed by Scopus and EI Compendex database!

More information about this series at http://www.springer.com/series/15087

Sreevalsa Kolathayar · Chandan Ghosh ·
Basanta Raj Adhikari · Indrajit Pal · Arpita Mondal
Editors

Resilient Infrastructure

Select Proceedings of VCDRR 2021

≗ Springer

Editors
Sreevalsa Kolathayar ⓘD
Department of Civil Engineering
National Institute of Technology Karnataka
Surathkal, Karnataka, India

Basanta Raj Adhikari ⓘD
Department of Civil Engineering, Institute
of Engineering (IoE)
Tribhuvan University
Lalitpur, Nepal

Arpita Mondal ⓘD
Department of Civil Engineering
Indian Institute of Technology (IIT)
Bombay
Mumbai, Maharashtra, India

Chandan Ghosh ⓘD
Ministry of Home Affairs Government
of India
National Institute of Disaster Management
New Delhi, India

Indrajit Pal ⓘD
Disaster Preparedness, Mitigation
and Management Program
Asian Institute of Technology
Khlong Luang, Pathum Thani, Thailand

Preface

Resilient infrastructures refer to the capacity of infrastructure systems to absorb the disruption and still retain their functionality and serviceability without failure. Research and innovations play a key role in creating infrastructures resilient to disaster risk in a sustainable and economical way. This book presents the select proceedings of the Virtual Conference on Disaster Risk Reduction (VCDRR 2021). All the papers in this volume are segregated in six clusters, e.g., disaster resilience and infrastructure, risk reduction and structural measures, evidence-based approach for DRR case studies, numerical modeling and constructions methods, prevention methods and safety engineering, and cross-cutting issue in DRR and infrastructure. The book is also a comprehensive volume on multi-hazards and their management for a sustainable built environment.

We thank all the staff of Springer for their full support and cooperation at all the stages of the publication of this book. We express our sincere thanks to the authors and reviewers for their contribution. We hope that this book will be beneficial to students, researchers, and professionals working in the areas of civil engineering and disaster management. The comments and suggestions from the readers are most welcome.

Surathkal, India   Sreevalsa Kolathayar
New Delhi, India   Chandan Ghosh
Lalitpur, Nepal   Basanta Raj Adhikari
Khlong Luang, Thailand   Indrajit Pal
Mumbai, India   Arpita Mondal

Contents

Risk Reduction and Structural Measures

Evidence Based Approach for DRR Case Studies

About the Editors

Dr. Sreevalsa Kolathayar pursued his M.Tech. from Indian Institute of Technology (IIT) Kanpur, Ph.D. from Indian Institute of Science (IISc) and served as International Research Staff at UPC BarcelonaTech Spain. He is presently Assistant Professor in the Department of Civil Engineering, National Institute of Technology (NIT), Karnataka. Dr. Kolathayar has authored six books and over 80 research articles. He is Associate Editor of two International Journals. His broad research areas are geotechnical earthquake engineering, geosynthetics and geonaturals, landslide, disaster risk reduction and water geotechnics. He is currently the Secretary of the Indian chapter of International Association for Coastal Reservoir Research (IACRR), and Executive Committee Member of Indian Society of Earthquake Technology. In 2017, The New Indian Express honored Dr. Kolathayar with 40 under 40—South India's Most Inspiring Young Teachers Award. He is the recipient of ISET DK Paul Research Award from Indian Society of Earthquake Technology, IIT Roorkee. He received "IEI Young Engineers Award" by The Institution of Engineers (India), in recognition of his contributions in the field of Civil Engineering. He was recently featured in *Geostrata Magazine* by American Society of Civil Engineers (ASCE). Dr Sreevalsa is the Organizing Chair of the Virtual Conference on Disaster Risk Reduction (VCDRR 2021).

Prof. Chandan Ghosh has devoted more than 30 years of his career in UG and PG teaching, research guidance, development of teaching tools and training modules for engineers, architects, and town planners. He has earned professional zeal in promoting Disaster Mitigation Technologies, including seismic base isolation, dampers, lightweight materials, etc. Besides developing some of the IEC materials such as "Snake and ladder game" for earthquake, flood, road safety, cyclone, DM plan for family, Prof. Ghosh has been deeply involved in conducting workshops/seminars on retrofitting, earthquake-induced damages, and landslides mitigation; taking pilot site-specific technical/experimental studies; developing/moderating of training modules; online training programs and curriculum for the self-study certificate program. He is always available for the community services and awareness campaign through experimental as well as field demonstration, social media,

and video documentaries. Prof. Ghosh is a prolific motivator in varied sustainable development activities, including bio-engineering measures for landslides/erosion controls, lake water cleaning by natural means, and urban flood mitigations. As a recognition of his seminal contributions, Prof. Ghosh received Prof. Leonard prize for the best doctoral thesis-1993, CIDC-Vishwakarma Awards-2013, IGS-Shri H. C. Verma Golden Jubilee Award-2013, and Lifetime achievement Award-2019 by IGS-Delhi Chapter.

Dr. Basanta Raj Adhikari is a geo-hazard expert and graduated from the University of Vienna, Austria. He is an assistant professor in the Department of Civil Engineering, Pulchowk Campus, Institute of Engineering, Tribhuvan University, Nepal. His main research focuses on tectonics of the Himalayas, climate change, hill-slope movement and human interaction, Himalayan sediment flux generation, community based disaster risk reduction. He is the author of more than 40 scientific research papers and book chapters and received various recognitions for his work in the field of earth science i.e. Young Scientist (Integrated Research on Disaster Risk) and "young affiliates" (The World Academy of Sciences). He has been transferring his scientific knowledge for disaster risk reduction at community level and has developed community based low-tech and low-cost landslide monitoring and early warning systems for sustainable livelihood in the Himalaya.

Dr. Indrajit Pal presently working as Assistant Professor and Chair at Disaster Preparedness, Mitigation, and Management program at the Asian Institute of Technology, Thailand. Prior to joining AIT, Dr. Pal served as a faculty member at Centre for Disaster Management at Lal Bahadur Shastri National Academy of Administration, Mussoorie, India (Premier National Institute for training Indian Administrative Services Officers). Dr. Pal has done extensive work on capacity development of decision-makers, risk assessment and disaster risk governance. Dr. Pal has written 6 books and more than 55 articles in international and national peer-reviewed journals apart from supervising masters and doctoral research. Dr. Pal has about 18 years of experience in research and capacity development on Disaster Risk Management and Governance and Disaster Risk Science and Education.

Dr. Arpita Mondal works as an Assistant Professor in the Department of Civil Engineering at the Indian Institute of Technology (IIT) Bombay. She is also an associate faculty member in the Interdisciplinary Program in Climate Studies at IIT Bombay. Arpita's research focuses on hydroclimatic extremes—how they can be characterized, what causes them, and how they are likely to evolve with climate change. She uses a combination of statistical analysis, physical understanding and computer model simulations. Arpita serves as an Associate Editor of the Springer journal *Regional Environmental Change*. She received the Early Career Research Award from the Science and Education Research Board (SERB), and the INSPIRE Faculty Award, both funded by the Department of Science and Technology, Government of India. She also received the Asian University Alliance (AUA) Scholars' Award. Arpita completed her Ph.D. at the Indian Institute of Science (IISc), Bangalore, M.Tech. at

IIT Bombay and Bachelors in Civil Engineering at Jadavpur University, Kolkata. As a Ph.D. student, Arpita had received the Endeavour Research Fellowship (Government of Australia), Fulbright-Nehru Research Fellowship (USIEF), and the Berkner Travel Grant of the American Geophysical Union (AGU). Arpita scored the first rank in the university in both her Bachelors and Masters.

Resilient Infrastructures and Disaster Risk Reduction—An Introduction

Indrajit Pal (ID)**, Satya Venkata Sai Aditya Bharadwaz Ganni, and Sreevalsa Kolathayar** (ID)

Abstract This chapter summarizes the contents of the book volume on resilient infrastructures which discusses various relevant topics such as disaster resilience and infrastructure, risk reduction and structural measures, evidence-based approach for DRR case studies, numerical modeling and constructions methods, prevention methods and safety engineering, and cross-cutting issue in DRR and infrastructure. Basic definitions and information on resilient infrastructure are also included in the chapter.

Keywords Resilience · Infrastructure · Disaster risk reduction

1 Introduction and Background

Resilience is the ability of a system, community or society exposed to hazards to resist, absorb, accommodate to and recover from the effects of a hazard in a timely and efficient manner, including through the preservation and restoration of its essential basic structures and functions [45]. The term "infrastructure" includes built environment consisting of buildings, roads, bridges, pipe networks, treatment facilities, etc. Resilient Infrastructures refer to the capacity of infrastructure systems to absorb the disruption and still retain their functionality and serviceability without failure. The World Bank Report [17] focuses on four infrastructure systems such as power; transport; telecommunications; and water and sanitation. The report suggests that making these systems more resilient can reduce the adverse effects of the disasters on livelihoods and minimize the cost of repairs. The Sendai Framework for Disaster Risk Reduction (SFDRR) thrust upon the importance of better disaster resilience of infrastructure as a foundation for sustainable development. Two of the four priorities of the SFDRR relate to resilient infrastructure development namely; "investing in

I. Pal (✉) · S. V. S. A. B. Ganni
Asian Institute of Technology, Khlong Luang, Thailand
e-mail: indrajit-pal@ait.ac.th

S. Kolathayar
National Institute of Technology Karnataka, Surathkal, India

DRR for resilience" through collaboration between public and private entities and "enhancing disaster preparedness for effective response and to "Build Back Better" in recovery, rehabilitation, and reconstruction". The SFDRR includes four specific targets related to loss reduction:

Reduce global disaster mortality;
Reduce the number of affected people;
Reduce direct disaster economic loss; and
Reduce disaster damage to critical infrastructure.

Target (4) is on infrastructure resilience which is an important prerequisite in accomplishing the other loss reduction targets in the framework.

The natural and anthropogenic hazards may lead to disasters, which might cause short- and long-term impacts on social and economic development of the country [38]. Disaster cost estimation is not only to arrive at compensation, relief or insurance purposes but also for making choice among alternative recovery projects or prior preventive actions. For designing any policy or a governance program, the functional need has to be translated into a functional requirement, a detailed quantitative and operational statement [32]. The stakeholders in the vulnerable areas may be subjective to the risk probability of an event. Experience and knowledge usually subject the people to perceive the risk. This article is an attempt to summarize the contents of the book volume on Resilient Infrastructures, [39]. All the papers in this volume are segregated in six clusters, e.g., disaster resilience and infrastructure, risk reduction and structural measures, evidence-based approach for DRR case studies, numerical modeling and constructions methods, prevention methods and safety engineering, and cross-cutting issue in DRR and infrastructure.

2 Disaster Resilience and Infrastructure

Das et al. in their paper *Disaster Resilience of Infrastructures—A Comprehensive Concept with Case Studies* reviewed the role of civil engineers from the planning stage to the implementation of civil engineering projects to ensure public safety in the event of a disaster. The development of engineering equipment, tools, and methods to reduce the effects of natural and technological hazards on the built environment is another way in which economic engineers can contribute significantly. It has been suggested that construction engineers need to play a more important role in policy and decision making [22]. The paper *Thickness optimization of RC jacket applied as a seismic retrofit measure on RC structural members to effectively resist earthquake loads* by Prasad et al. explained about how to strengthen constructed structures by different retrofitting techniques in order to resist lateral loads generated due to earthquakes. Retrofit of RC beams/RC columns present in a structure can be done by considering various thicknesses of the RC jackets that can effectively resist forces or stresses induced due to earthquakes [10]. Sen et al. [40] in Flood Resilience Quantification for Housing Infrastructure using Analytic Hierarchy Process describes that

a resilience quantification framework is developed after an extensive field survey on each parameter, the developed framework is implemented in a real case study area (Barak Valley) where a field survey is conducted. Using the AHP tool, the resilience of each surveyed area is evaluated. This framework can be applied to other critical infrastructure systems to assess that infrastructure's resiliency. The evaluated resilience values will help the stakeholders to strengthen the housing infrastructure against a future hazard and each parameter will help the decision-makers for informed decision making [40].

The paper *Feasibility of Post-Cyclone Portable Relief Shelter: Case of Odisha* by Das et al. aims to explore the viability of a portable post-cyclone relief shelter to normalize day-to-day operations and provide a better life. The research concludes with the proposed design of a prototype of a portable relief shelter, analyzing its feasibility in terms of cost, ease of fabrication, transportation services, and maintenance by using locally available material to achieve environmental sustainability [8]. *An explorative study on material feasibility for relief shelter for refugees* by Mohamed et al. aim of the paper is to suggest suitable materials that are competent in designing a viable shelter. Steel possesses great tensile strength and durability compared to other construction materials hence it can be utilized as an elementary construction material in geographical conditions like Bangalore. The shelters devised for the refugees are not just tarp tents or housings, but a shelter that is feasible in nature and durable for the comfort as well as the well-being of the users [5]. Dhanya et al. in the paper *Situational Analysis to understand the need to disseminate weather forewarnings and develop critical infrastructures for minimizing crop loss: Parambikulam Aliyar Basin, Tamil Nadu* presents study highlights the unusual weather phenomena happened during samba crop cultivation in Parambikulam Aliyar Basin, 2020–2021. In a survey, the majority of the farmers informed that they are unable to follow the weather advisories that they receive as SMS alerts. Majority of the farmers are not equipped with storage facilities or combined harvesters. Majority of the farmers told that farming faces constant risks from weather vagaries and climate change due to untimely rains. Their adaptation needs include availability of individual farm-based crop insurances as rainfall changes every 500 m [29]. The study by Singh and Samanta in their paper *Parametric study of cold-formed lipped channel flexural members under fire hazard presents a numerical parametric study on cold-formed steel flexural members exposed to fire hazards*. An increase in critical temperature was observed with an increase in slenderness value and span. The critical temperature of CFS members undergoing lateral torsional buckling having high slenderness was well above 450 °C. Based on the findings of this research, it can be concluded that Euro code recommended critical temperature for CFS members needs improvements for global buckling, whereas, for local or distortional buckling, there is a need for more investigation [26]. The paper *COVID'19 Future-Proof Infrastructure* by Vaidevi et al. describes that an effective infrastructure during this COVID-19 is framed with proper design, methods, and procedures in the construction and a plan focused on sustainable, future-proof infrastructure, access to no point of contact, and energy-saving. The cost of the construction may be increased, but as we all know, life is most important, and priority is given for healthy living. Future

research may be extended to bring out more solutions and ideas in the construction field with economics and a sustainable approach [34].

3   Risk Reduction and Structural Measures

The paper *Role of Cold Form Steel in COVID-19 Infrastructure* by Ranee and Srisanthi describes that the COVID-19 pandemic requires large-scale infrastructure facilities within a short span of time for quarantining the people, medical facilities like COVID triage center need to set up in many areas. Compared to traditional building materials, economics weighs in favor of Cold Form Steel (CFS). Compared to cement prices, steel has not increased steeply over the last decade while cement has increased by over 60%. CFS is also ideal for other infrastructures like low-cost housing, ware houses, etc. Government of India's plan to provide housing for all under Pradhan Mantri Awas Yojana (PMAY) uses CFS in large scale [27]. Phadnis in the paper Fragility Analysis for Frame with RC and Steel-Composite Shear Wall discussed that Chapter increase the overall rigidity and resistance against lateral loads Shear walls are structural members that are widely used in multi-storied buildings. The hinging pattern of the Frame-CM SW reveals that, the development of hinges at inferior damage levels as compared to the Frame-RC SW system. It is concluded that the performance behavior of a frame with the CM SW system is superior in terms of damage probability than a frame with RC SW [36]. Vijay Kumar Polimeru and Arghadeep Laskar in the paper development of VC++ Wrapper for structural modeling in Open SEES presents about development and implementation details of a simple yet elegant VC++ wrapper (vcpp wrapper). This wrapper can be used to efficiently debug the convergence errors encountered in complex NLFEA problems. Also, this wrapper helps in understanding the implementations and working mechanisms of materials, elements, solvers, etc., which is very essential in debugging the complex nonlinear finite element models built in OpenSEES [37]. Karthik Manoharan in the paper *A state-of-the-art review on Methods of retrofitting in structural members* discussed various advanced techniques adopted to practice retrofitting such as external plate bonding, section enlargement of structural elements, external post-tensioning, epoxy injections, grouting strategies, FRC bars in retrofitting and fiber reinforced polymer composites. This presented an article overview of strengthening of structural members using various retrofitting techniques. The article discussed the importance and purpose of retrofitting which contributes to the sustainability of existing buildings to enhance bearing capacity without demolishing or rebuilding. Based on the detailed discussion six significant techniques such as a fiber reinforced polymer composite (FRC), FRC bars in retrofitting, grouting strategies, section enlargement and external post-tensioning which serves the benefit of strengthening structural members [41]. The study by Nemaliga et al. in their paper Rehabilitation and retrofitting of structural elements using various fibers presents an analytical study of different parameters on concrete

columns wrapped with fiber reinforced polymer (FRP). Parameters like Wrap thickness (Layers) and type of fiber of them were altered and studied. It is found that Stress Carrying Capacity of CFRP, GFRP and AFRP wrapped elements have been increased. By looking at the trend of output it can be concluded that CFRP could be best among all FRP used for study in order to enhance overall strength of structural elements [42]. In the paper, *Evaluation of failure criteria in RC structural elements due to additional internal stresses developed in structural elements due to temperature exposure* by Y. K. Guru Prasad and Nisarga Ravi discussed reinforced concrete structural elements. The elements like beams, columns, slabs and shear walls, present in multi-storyed buildings, undergo damage in the form of stiffness and strength degradation, when exposed to high temperatures such as fire break out in buildings [43]. *The explorative study on Retrofitting of Distressed RC Structures using Near Surface Mounted Reinforcement* by Prasad et al. discussed a numerical study carried out on retrofitting of structural elements. From the point of structural performance in terms of restoring distressed structural members, the near surface mounted-reinforcement retrofit is effective, earlier to install and comparatively lesser in the overall cost of the retrofit when compared to RC jacketing [13].

4   Evidence-Based Approach for DRR Case Studies

Mugunth et al. in the paper *Analytical Investigation of Infilled frames with Openings under Static Loading* presented a view on the behavior of the infilled frame with different openings when cement mortar interface material is used under static loading through numerical analysis. It mentioned that to improve the structure performance against lateral loads like wind and seismic forces, reinforced concrete structures should have lateral rigidity to resist them [35]. Pandulu et al. in their paper *Behavior of doubly symmetric built-up cold-formed steel beams* had elaborated about the behavior of doubly built-up cold-formed beams under flexure. Load-carrying capacity and moment of inertia can be increased, by increasing depth of section, flange width and thickness. From this study, it is concluded that doubly symmetric built-up cold-formed sections are preferred for higher load-carrying capacity with less complicated buckling modes [7, 35]. Ain et al. in the paper *Behavior of Ordinary Load-bearing Structure under Distant Large Explosion, Beirut* scenario discussed nonlinear analyses of a load-bearing masonry structure subjected to a highly explosive material. Concrete-Damaged Plasticity (CDP) model for concrete and brick masonry available in the employed software has been utilized. From the results of analyses performed, it can be inferred that load-bearing structures cannot survive under the pressure generated by blast of such magnitude [3]. The study on *Determination method of the structural strength of deep reinforced concrete beams using ANSYS software* by Phan Van Phuc explained about the numerical method in determining the structural strength of reinforced concrete (RC) deep beams using ANSYS, a commercial finite element analysis software. Scientists, designers can use ANSYS Workbench to determine structural strength and instead for experiments or mechanical analysis

methods. Using simulation software to calculate the strength of the structural, load–displacement relationship, which was determined quite accurately, will shorten the time as well as save economic fees for the experiment [18]. A comparative study on Analytical Investigation on Progressive Collapse of 3-D Reinforced Concrete Frames under High-Temperature by Vishal Murugan and K. S. Satyanarayanan is done by considering the behavior of reinforced concrete key elements like beam, column and slab under high-temperature. To improve the structural performance of the frame structures by providing some alternate load path to the frame structure to prevent the progressive collapse [2]. Vadher et al. in the paper *Study on Fatigue Response of Concrete and its Effect on Lifecycle Behavior of Concrete Structures* discussed that the stress level at cyclic loading is inversely proportional to the number of cycles prior to fatigue failure. As stress level reduces, the failure is observed to be more sudden (brittle) in nature. The first segment represents slow and gradual increment in damage. The second stage damage propagation is stable propagation and varies linearly with the number of loading cycles. The final stage of damage propagation represents sudden increment in rate of damage propagation, creating instability in the material, leading to its failure [12]. The paper *Study on Behavior of Diagrid System on a G + 36 High Raised Building* by Nagendra V. S. and Sofi A. presents about the behavior of a diagrid structural system on a G + 36 high raised building, using CSI-ETABS software. The study deals with the performance characteristics of the building under seismic activity evaluated by response spectrum analysis and nonlinear static pushover analysis [25]. In the paper, *A Comparative Study of Flat Slab, Waffle Slab and Post-Tensioned Slab under the Action of Dynamic Loads* by Mahesh Kumar C. L. and Shwetha K. G. had discussed various slabs. The check of stability of the Flat slab, post-tensioned slab, and waffle slab has been carried out by considering the shear parameters and deflection parameters and their behavior under the seismic static and dynamic loads [20].

5   Numerical Modeling and Constructions Methods

In the paper, *Numerical Study of GFRP Strengthened Brick Masonry Wallette* by Hasim Ali Khan discussed to address questions about the seismic vulnerability of buildings with unreinforced masonry (URM). A research program was explored to examine the efficacy of glass fiber reinforced polymer (GFRP) schemes as a seismic retrofit involvement for out-of-plane loaded URM walls susceptible to shear mode failure during earthquakes. The unreinforced Wallette indicated brittle collapse. The performance constraints are expressively increased parallel and diagonal severally [44]. The present study on Numerical Analysis of Geotextile-Strengthened Shear Critical RC Beam by Subhrasmita Majumder and Showmen Saha has investigated the shear behavior of geotextile-strengthened RC beam by nonlinear finite element simulations. Shear deficit RC beam specimens strengthened with geotextile material modeled in finite element software, ANSYS. From the numerical results, the equivalent stress con-tour mode of the geotextile bonded beam is improved compared

to the control beam. The load-carrying capacity of GT is increased by 34.6% as compared to the CB. The energy dissipation capacity of the geotextile bonded beam is significantly increased by 78.2%, which shows better ductility behavior than the control beam. Hence, geogrid seems to be an alternative material with excellent ductile behavior to strengthen the RC beam (ICOVP 2017 n.d.).

6 Prevention Methods and Safety Engineering

This study on *Vulnerability of Railway Switches and Crossings Exposed to Flooding Conditions* by Hamarat et al. provides new insights into the understanding of the dynamic behavior of a turnout system during an unprecedented event of flooding. The outcomes of the study show that considering the effects of flooding on dynamic forces during operation and design phases could be a key to prevent undesired events. A further investigation is recommended to evaluate whether it is beneficial to increase the ballast stiffness under the left rail/stock rail or not [4]. In the study, *Stability assessment of a fire damaged retrofitted RC structure having vertical irregularity* by Mohammed Mazharuddin and Y. K. Guru ehavi described about the behavior of buildings under high temperatures. The RC jacket and steel plate bonding applied individually to retrofit slender RC columns that have undergone fire damage and are present in the portions of the building that have vertical irregularity are found to be equally effective in reducing the displacements due to gravity loads and also help in restoring the stability of such columns. It is observed from the results that, RC jacket and steel plate bonding retrofits reduce the displacements and averts the buckling effectively in the fire damaged slender RC columns due to gravity loads [9]. The paper *Computational Fluid Dynamic Analysis in Dam Spillway due to Sector Gate Opening* by Zawawi et al. presents an analyses fluid dynamic in dam spillway with 4.9 m of sector gate opening. The high velocity contributes to the large hydraulic jump may lead to damaging effect to the stilling basin surface downstream. It shows that the higher the velocity, the more damaging effect to the stilling basin surface [11]. The study on Integration of Building Information Modeling (BIM) and Artificial Intelligence (AI) to detect combined defects of infrastructure in the railway system by Jessada Sresakoolchai and Sak Kaewunruen applies BIM and AI together to detect combined defects in the railway infrastructure. The results of the study show that the developed models have the potential to detect defects with accuracies up to 99% and are beneficial for the asset management of the railway system in terms of risk management, passenger comfort, and cost-efficiency. The accuracies of the CNN models are almost 100%. At the same time, precisions and recalls of CNN models are about 90% or higher. This shows that CNN has the potential to detect combined defects in the railway infrastructure [21].

7 Cross-Cutting Issue in DRR and Infrastructure

In the paper *Blast Performance of RCC Slab and Influence of its Design Parameters* by Ahmadi et al. presents a finite element model of one-way reinforced cement concrete slab. They have been tested under blast loading for which experimental results/observations are available in the literature has been developed with respect to concrete cover, thickness, rebar diameter, spacing, and concrete strength via ABAQUS/Explicit. The damage resistance of the slabs is found to be increasing with higher concrete cover under the applied blast loading. A higher concrete strength slab with 15 and 20 mm concrete covers performs better with regard to maximum displacement as compared to normal strength concrete slab with a smaller concrete cover. A higher reinforcement ratio improves the damage resistance of the slab but does not influence the mid-span displacement [28]. In the paper, Self-Flowable Rich Cementitious Matrices for Ferrocement Jacketed Beam-Column Joint by Revathy et al. descried that Beam-column joints are considered as the weakest and vulnerable region in the structural system, as they are subjected to high shear forces under seismic action. This study focuses on the efficacy of employing the developed self-flowable cementitious mortar for ferrocement jacketed beam-column joints. A rich self-flowable and high strength nano-silica-based cementitious mortar is utilized for the ferrocement jacketing techniques. The exterior beam-column joints retrofitted with a ferrocement jacket were found to be very effective in load-carrying capacity, deflection, cracking behavior, and stiffness when compared to the control specimen. The test results indicated that the developed rich flowable matrices employed for ferrocement jacketed beam-column joints showed an appreciable increase in load-carrying capacity and attained maximum energy absorption capacity [30]. Onkar Chothe and Vinay Agarwal in the paper *An Experimental Investigation on Applications of Fiber Reinforced Composites for Rehabilitation of Concrete Beams* discussed that the present study focuses on rehabilitation of concrete beams with usage of composite fibers. In the present study, concrete beams were tested for strength capacities with glass fiber and carbon fiber reinforced polymer composite [6]. In the paper, *two-layered steel-fiber concrete beam with concrete grade change in layers* by Thi My Dung Do et al. had reviewed that after testing these two-layered reinforced concrete beams, the authors simulated the two-layered reinforced concrete beams with ANSYS software. In the case of two-layered concrete beams with above concrete layers of steel-fiber concrete the normal concrete layer, the values of compressive stress, tensile stress and vertical displacement of concrete beams in the middle span of case studies are no different. The below steel-fiber concrete layer has a lower value in the compressive stress area, the tensile stress region has a higher tensile stress value than the two-layer concrete beams with the above layer of steel-fiber concrete [24]. The paper Effective Peripheral Distribution of Base Isolators for Plan Asymmetric Buildings to Minimise Torsion by Rithuparna et al. described that this study focuses on the influence of base isolation techniques in mitigating the torsional effect on plan asymmetric buildings. L-shaped buildings with greater plan eccentricity in X-direction were chosen for the study. It can be concluded that base isolators effectively

reduced torsion in the buildings considered in this study. Cost-effectiveness is one of the major aspects considered while choosing a seismic protection system. Although isolators perform well compared to other systems, their application is limited owing to their high cost. Peripheral distribution acts as an economical option since they produced similar or better results than the uniform distribution of isolators (Wiley, n.d.). P. S. Prasad and Kishor Kumar in the paper Highways Upgradation in the Hilly areas and its Impact—An example of Uttarakhand described about the issues which had been addressed prior and during the highway upgradation/modernization. Also it will discuss the possible rectification in the future for risk free management of the highway. In many places, it was also observed that the debris dumped on downhill without any planning. This causes the downhill slopes more denudation and instability. The debris material should also not be dumped riverside. The selected dumping yards should be properly designed and the dumping methodology should be properly implemented at the site [23]. The explorative study on Out-of-plane Response of Clay Brick Unreinforced and Strengthened Masonry Walls under Explosive-induced Air-blast loading by Anas et al. explained about how the out-of-plane behavior of clay brick unreinforced masonry walls under air-blast loading has been investigated using commercial software, ABAQUS/CAE 2017. The application of the horizontal RC band in the target wall considered in this study improves its performance with regard to central displacement and damage dissipation energy, however, the band after every three courses in the wall is found to be more effectively improving the cracking resistance under the maximum explosive load of 8.40 kg TNT considered. The above conclusions may prove to be useful to not only design engineers but also to the sectional committee for developing the codal provisions of the masonry structures likely to take air-blast loads [16]. Zahari et al. in the paper Particle Image Velocimetry Dynamic Analysis on the Penstock Vortex Flow for the Dam Reliability Study presents the detailed the particle image velocimetry (PIV) experimental work in the study of vortex flow in the penstock section. The scaled down physical model for the penstock pipe and turbines were constructed for the PIV analysis. Particle image velocimetry (PIV) experimental analysis was applied on the dam reliability problem, to study the vortex flow in the penstock of the dam bottom outlet. Further comparison with numerical simulated flow in penstock revealed there is 12% discrepancy between the experimental and numerical maximal flow velocities, for which it indicated the findings were acceptable. Using the prescribed PIV setup, the flow visualization in dam structure is made possible and viable for the subsequent dam reliability study [1]. In the study, Performance of Base-Isolated RC Building under Surface Blast Loading by Tolani et al. described the usefulness of the base isolation technique in reducing the structural damage caused by the surface explosion is investigated. Base isolation technique is effective in reducing top floor displacement, inter-story drift and damage of the building under near blast condition. For distant blast, top floor displacement and the number of hinges formed are reduced due to base isolation, but there is not a considerable reduction in inter-story drift. For a base-isolated building under surface blast conditions, with the increase in the value of the post-yield stiffness ratio, the isolator displacement decreases but damage to the

structure increases [19]. The paper Influence of Charge Locations on Close-in Air-blast Response of Pre-tensioned Concrete U-Girder by Anas et al. presents that the finite element simulations of the pre-tensioned simply sup-ported concrete U-Girder subjected to air-blast pressures of 982, 3877, and 7004 Mpa. The simulations are conducted using the nonlinear finite element program, ABAQUS/CAE. The increase in the damage dissipation energy indicates that the girder suffers more damage and cracking. Damage in the form of concrete spalling led by flexural failure has been observed on the compression side of the deck slab and flanges. To improve the cracking resistance of the girder, an additional investigation needs to be conducted to study the effect of girder strengthening under close-in air-blast loading [15].

8   Summary

Outlook [31] estimated that the global infrastructure investment needs to be $94 trillion between 2016 and 2040. This estimate is 19% higher than that is delivered currently, and is an average of $3.7 trillion per year. To meet this investment need, the world will need to increase the proportion of GDP it dedicates to infrastructure to 3.5%, compared to the 3.0% expected under current trends. Thus, the globe is committed to ensure that all future infrastructure systems are resilient in the face of disasters in order to protect their investments as well as safeguard lives. Under-standing multi-hazard risk and resilient infrastructure development is paramount for the sustainable future development and greatly governed by the risk perception of the stakeholder [33].

This chapter summarized the contents of the book volume on resilient infrastruc-tures which discusses various relevant topics such as disaster resilience and infras-tructure, risk reduction and structural measures, evidence-based approach for DRR case studies, numerical modeling and constructions methods, prevention methods and safety engineering, and cross-cutting issue in DRR and infrastructure.

References

1. Abas A, Ng FC, Gan ZL, Ishak MHH, Abdullah MZ, Chong GY (2018) Effect of scale size, orientation type and dispensing method on void formation in the CUF encapsulation of BGA. Sadhana—Acad Proc Eng Sci 43(4). https://doi.org/10.1007/s12046-018-0849-3
2. Agarwal A, Varma AH (2014) Fire induced progressive collapse of steel building structures: the role of interior gravity columns. Eng Struct 58:129–140. https://doi.org/10.1016/j.engstruct.2013.09.020
3. Anas SM, Ansari MI, Alam M (2020) Performance of masonry heritage building under air-blast pressure without and with ground shock. Aust J Struct Eng 21(4):329–344. https://doi.org/10.1080/13287982.2020.1842581
4. Andersson C, Dahlberg T (1998) Wheel/rail impacts at a railway turnout crossing. Proc Inst Mech Eng Part F: J Rail Rapid Transit 212(2):123–134. https://doi.org/10.1243/0954409981530733

5. Apel S (2019) The role of sustainable design in the current refugee crisis. Sci Sustain J 3
6. Attari N, Amziane S, Chemrouk M (2012) Flexural strengthening of concrete beams using CFRP, GFRP and hybrid FRP sheets. Constr Build Mater 37:746–757. https://doi.org/10.1016/j.conbuildmat.2012.07.052
7. Basaglia C, Camotim D (2013) Buckling, postbuckling, strength, and DSM design of cold-formed steel continuous lipped channel beams. J Struct Eng 139(5):657–668. https://doi.org/10.1061/(ASCE)ST.1943-541X.0000651
8. Bashawri A, Garrity S, Moodley K (2014) An overview of the design of disaster relief shelters. Procedia Econ Finance 18:924–931. https://doi.org/10.1016/S2212-5671(14)01019-3
9. Behnam B (2020) Vulnerability assessment of irregular steel structures under traveling fires. Struct Des Tall Spec Build 29(11):e1745. https://doi.org/10.1002/tal.1745
10. Chandurkar PP, Pajgade DPS (2013) Seismic analysis of RCC building with and without shear wall. Int J Modern Eng Res 3(3):1805–1810
11. Chanel PG, Doering JC (2008) Assessment of spillway modeling using computational fluid dynamics. Can J Civ Eng 35(12):1481–1485. https://doi.org/10.1139/L08-094
12. Choo JF, Choi YC, Kwon SJ, Park KT, Yoo SW (2018) Low-cycle flexural fatigue behavior of concrete beam reinforced with hybrid FRP-Steel Rebar. Adv Civ Eng 2018. https://doi.org/10.1155/2018/6986047
13. De Lorenzis L, Nanni A (2001) Shear strengthening of reinforced concrete beams with near-surface mounted fiber-reinforced polymer rods. ACI Struct J 98(1):60–68. https://doi.org/10.14359/10147
14. Design of seismic isolated structures: from theory to practice | Wiley. (n.d.). Retrieved May 3, 2021 from https://www.wiley.com/en-us/Design+of+Seismic+Isolated+Structures%3A+From+Theory+to+Practice-p-9780471149217
15. Goel MD, Matsagar VA (2014) Blast-resistant design of structures. Pract Period Struct Des Constr 19(2):04014007. https://doi.org/10.1061/(ASCE)SC.1943-5576.0000188
16. Hafezolghorani M, Hejazi F, Vaghei R, Bin Jaafar MS, Karimzade K (2017) Simplified damage plasticity model for concrete. In: Structural engineering international, vol 27, pp 68–78. International Association for Bridge and Structural Engineering, Eth-Honggerberg. https://doi.org/10.2749/101686616X1081
17. Hallegatte S, Rentschler J, Rozenberg J (2019) Lifelines: the resilient infrastructure opportunity. The World Bank
18. Ismail KS, Guadagnini M, Pilakoutas K (2018) Strut-and-Tie modeling of reinforced concrete deep beams. J Struct Eng 144(2):04017216. https://doi.org/10.1061/(asce)st.1943-541x.0001974
19. Jayasooriya R, Thambiratnam DP, Perera NJ, Kosse V (2011) Blast and residual capacity analysis of reinforced concrete framed buildings. Eng Struct 33(12):3483–3495. https://doi.org/10.1016/j.engstruct.2011.07.011
20. Joshi DD, Murnal PB (n.d.) Performance of flat slab structure using pushover analysis. IOSR J Mech Civ Eng (IOSR-JMCE) 8. Retrieved from www.iosrjournals.orgwww.iosrjournals.org
21. Kaewunruen S, Rungskunroch P, Welsh J (2018) A digital-twin evaluation of net zero energy building for existing buildings. Sustainability 11(1):159. https://doi.org/10.3390/su11010159
22. Kameda H (2000) Engineering management of lifeline systems under earthquake risk. Bull N Z Soc Earthq Eng 33(3):248–264. https://doi.org/10.5459/bnzsee.33.3.248-264
23. Koti Marg K, Puram R (2018) Manual of specifications and standards for two laning of highways with paved shoulder Indian roads congress
24. Krishnaraja AR, Kandasamy S (2018) Flexural performance of hybrid engineered cementitious composite layered reinforced concrete beams. Periodica Polytechnica Civ Eng 62(4):921–929. https://doi.org/10.3311/PPci.11748
25. Lacidogna G, Nitti G, Scaramozzino D, Carpinteri A (2020) POLITECNICO DI TORINO Repository ISTITUZIONALE Diagrid systems coupled with closed-and open-section shear walls: optimization of geometrical characteristics in tall buildings Diagrid systems coupled with closed-and open-section shear walls: optimization of geometrical characteristics in tall buildings ScienceDirect Diagrid systems coupled with closed-and open-section shear walls:

optimization of geometrical characteristics in tall buildings, pp 402–409. https://doi.org/10.1016/j.promfg.2020.02.277

26. Lee JH (2004) Local buckling behavior and design of cold-formed steel compression members at elevated temperatures

27. Li LY, Chen JK (2008) An analytical model for analysing distortional buckling of cold-formed steel sections. Thin-Walled Struct 46(12):1430–1436. https://doi.org/10.1016/j.tws.2008.03.005

28. Low HY, Hao H (2002) Reliability analysis of direct shear and flexural failure modes of RC slabs under explosive loading. Eng Struct 24(2):189–198. https://doi.org/10.1016/S0141-0296(01)00087-6

29. Manandhar S, Vogt DS, Perret SR, Kazama F (2011) Adapting cropping systems to climate change in Nepal: a cross-regional study of farmers' perception and practices. Reg Environ Change 11(2):335–348. https://doi.org/10.1007/s10113-010-0137-1

30. Oltulu M, Şahin R (2013) Effect of nano-SiO_2, nano-Al_2O_3 and nano-Fe_2O_3 powders on compressive strengths and capillary water absorption of cement mortar containing fly ash: a comparative study. Energy Build 58:292–301. https://doi.org/10.1016/j.enbuild.2012.12.014

31. Outlook GI (2017) Infrastructure investment needs 50 countries, 7 sectors to 2040. July, A G20 Initiative. Global Infrastructure Hub, Sydney

32. Pal I, Bhatia S (2017) Disaster risk governance and city resilience in Asia-Pacific region. In: Science and technology in disaster risk reduction in Asia: potentials and challenges, pp 137–159. https://doi.org/10.1016/B978-0-12-812711-7.00009-2

33. Pal I, Karnjana J (2021) Factoring multi-hazard risk perception in risk assessment and reduction measures in landslide and flash flood prone areas—a case study of Sichon district, Nakhon Si Thammarat province, Thailand. J Disaster Res 16(4)

34. Pal S (2020) Braced for impact: architectural praxis in a post-Pandemic society. Advance. https://doi.org/10.31124/ADVANCE.12196959.V1

35. Penava D, Sarhosis V, Kožar I, Guljaš I (2018) Contribution of RC columns and masonry wall to the shear resistance of masonry infilled RC frames containing different in size window and door openings. Eng Struct 172(July):105–130. https://doi.org/10.1016/j.engstruct.2018.06.007

36. Phadnis PP, Kulkarni DK, Kulkarni AB, Karjinni VV (2018) Performance of composite steel-concrete shear walls with encased vertical steel sections. Indian Concr J 92(7):74–81

37. Polak MA, Vecchio FJ (1993) Nonlinear analysis of reinforced-concrete shells. J Struct Eng 119(12):3439–3462. https://doi.org/10.1061/(ASCE)0733-9445(1993)119:12(3439)

38. Rahman KF, Pal I, Parven A (2020) Energy security and disaster risk governance in energy sector of Bangladesh. Int Energy J 20(Special Issue 3A):523–534

39. Roy J, Islam ST, Pal I (2021) Implementation framework for sustainable development: what matters in the context of Bangladesh, Bangabandhu Chair special issue, energy, disaster, climate change: sustainability and just transitions in Bangladesh. Int Energy J 21(Special Issue 1A):1–8

40. Sen MK, Dutta S, Laskar JI (2021) A Hierarchical Bayesian Network Model for Flood Resilience Quantification of Housing Infrastructure Systems. ASCE-ASME J Risk Uncertainty Eng Syst Part A: Civ Eng 7(1):04020060. https://doi.org/10.1061/ajrua6.0001108

41. Shin DH, Kim HJ (2020) Cyclic response of rectangular RC columns retrofitted by hybrid FRP sheets. Structures 28:697–712. https://doi.org/10.1016/j.istruc.2020.09.016

42. Sridevi G, Shivaraj A, Sudarshan G, Biradar U (2020) Comparative study on dynamic behaviour of RC building with conventional and flat slab. In: Lecture notes in civil engineering, vol 38. Springer, pp 201–209. https://doi.org/10.1007/978-981-13-7615-3_18

43. Szumigała M, Polus Ł (2015) A comparison of the rise of the temperature of an unprotected steel column subjected to the standard fire curve ISO 834 and to a natural fire model in the office. Eng Trans 63. Retrieved from http://et.ippt.gov.pl/index.php/et/article/view/59

44. Umair S, Numada M, Amin M, Meguro K (2015) Fiber Reinforced polymer and polypropylene composite retrofitting technique for masonry structures. Polymers 7(5):963–984. https://doi.org/10.3390/polym7050963

45. UNISDR (2009) UNISDR Terminology on Disaster Risk Reduction

Disaster Resilience and Infrastructure

Disaster Resilience of Infrastructures—A Comprehensive Concept with Case Studies

Subhash Chandra Nigam, Atasi Das ⓘ, and Bhagwati Charan Shukla

Abstract Disaster resilience of infrastructures—a comprehensive concept with case studies disasters, either natural or man-made have severe impact on the individual to society to the whole nation. The frequency of disasters has alarmed the country. Capacity building in disaster risk management requires strategic planning, political support, and significant technical implementation. After the Latur earthquake in 1993, the rivers, which caused floods in the province, were Tapi, Wardha, and sometimes Pen-Ganga. The eastern parts of the empire are prone to severe flooding. Deccan harbor makes up 50% of the state's drought-prone areas. Twelve percent of the population live in drought-prone areas. Once every 5 years, insufficient rainfall is reported. Severe droughts occur once every 8–9 years. The state of Maharashtra, India, has taken an important step in preparing and implementing a disaster management plan for the government and all regions. This paper has reviewed the potential role of civil engineers in disaster risk management. It has been identified that civil engineers have been at the forefront of creating a safer environment, community policy, codes of practice based on globalization and a research program as a tool to reduce the impact of various disasters. It has also been recognized that despite the many challenges and obstacles, engineers can play a very important and varied role in disaster management activities. The full paper will detail upon the disaster resilient measures undertaken currently and that could be potentially undertaken to mitigate or reduce the risk and bring comfort to the disaster-prone areas.

Keywords Disaster management · Mitigation · Risk assessment · Civil engineering

S. C. Nigam · B. C. Shukla
Infrastructure Development Consultants, Bhopal, India
e-mail: subhash@idc-india.com

B. C. Shukla
e-mail: bhagwati@idc-india.com

A. Das (✉)
G R Infraprojects Limited, Gurugram 122015, India

1 Introduction

Disasters are catastrophic or unfortunate events or catastrophic events that have a profound effect on society and the nation. They may arise as a result of natural disasters such as earthquakes, tsunamis, floods, or hurricanes, or as a result of man-made disasters such as terrorist attacks, war, and industrial accidents. Disasters cause severe damage worldwide every year. India has always been at risk of natural disasters, and six million people are affected by disasters each year due to their unique climatic conditions [1, 2]. Often, during a major disaster, engineering structures such as buildings, bridges, dams, roads, water supply projects, coastal buildings, infrastructure, etc., are severely affected, causing severe disruption to human life and disrupt normal life. Natural disasters point to mistakes made in the development of engineering structures in the area and teach important lessons for the future. If learning is used in these unfortunate cases, the side effects can be reduced in the years to come.

Unexpected disaster response and rapid post-disaster rehabilitation (i.e., disaster resilience) for cities are much needed because of the dangers of urbanization. Reinforcement of the resilience could adequately demonstrate the city's resilience to disasters. Many existing studies have focused and raised several frameworks on estimates of the severity of a disaster, and related research items include different types of disasters (e.g., earthquakes, hurricanes, floods, and fires), various domains (e.g., engineering, social, and economic), and multiple levels (e.g., city, community, and construction). Among these research materials, seismic studies in the field of political engineering are completely inclusive [3].

1.1 Disaster Risk Management and Risk Reduction

Disaster risk management can be defined as a range of activities designed to maintain disaster and emergency management and to provide a framework to assist people at risk of preventing or recovering from the impact of a disaster. Disaster risk management is a cycle of activities that deal with situations that occur before, during, and after a disaster. The various stages of disaster management are: Mitigation, preparedness, response, and recovery tasks in one category may exceed those in the previous one. Starting with minimizing the risk and adverse effects of disasters, preparedness to respond, respond, and provide emergency services such as search and rescue, firefighting, etc., and assist in recovery that may include physical rehabilitation and rehabilitation in the post-disaster community. Interestingly, civil engineers can play an important role in all stages of the disaster risk management cycle [4] (Fig. 1).

Complete prevention of natural disasters is impossible or sometimes undesirable. Social risk in the event of a disaster is actually a function of high risk, public exposure to risks, and public vulnerability in a particular disaster. Therefore, reducing
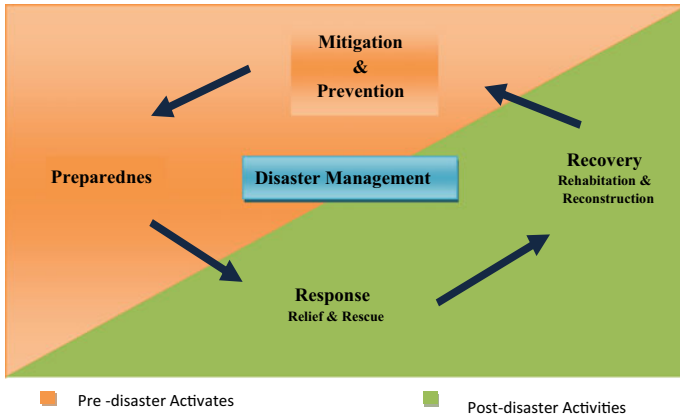
Fig. 1 Phases of disaster management cycle

the risk/undesirable effects of disasters can be a promising way to deal with those disasters.

Civil engineers are at the forefront of developing effective methods and procedures for managing and reducing risk. The primary role of civil engineers in reducing natural disasters is the development of infrastructure development technologies, such as soft soil improvement technologies, high-performance buildings, and warning and rescue systems. The second role is to build infrastructure that is highly resilient to natural disasters. The third role of civil engineers is to participate in the rescue and recovery work [5].

However, two of the most important contributions to economic engineering in disaster management have been the coding and standards, as well as the actual construction and construction of infrastructure used to prevent accidents and losses caused by accidents (Fig. 2).

2 Dedicated Engineering Offers—SWOT Analysis

A SWOT analysis was performed to review the advanced engineering information that could be used to reduce the effects of the disaster, the challenges in implementing public engineering practices, and future developments, and the potential of public engineering in mitigating various disasters. SWOT is a dictionary of strengths, weaknesses, opportunities, and threats.
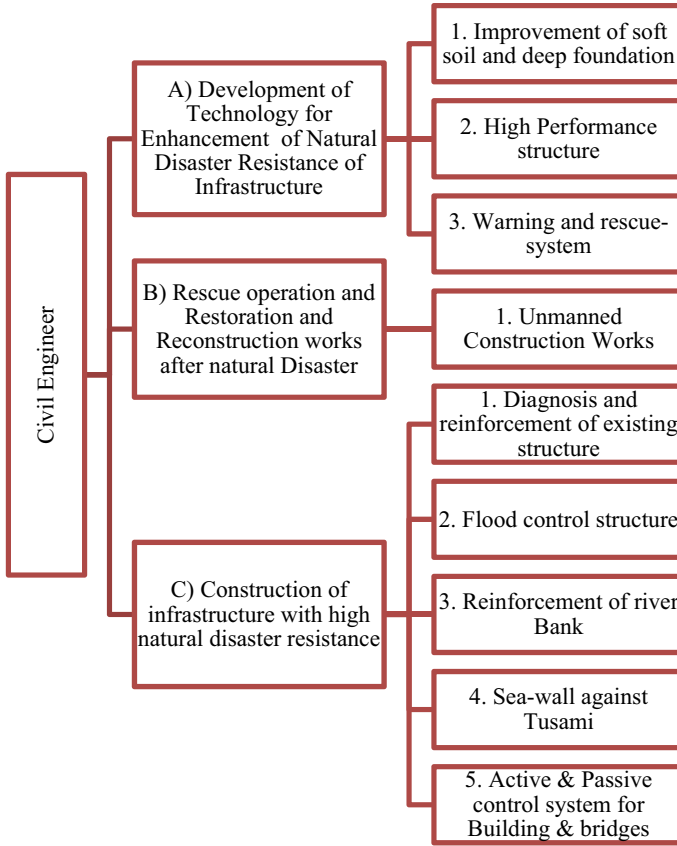
Fig. 2 Comprehensive role of civil engineers in disaster reduction

2.1 Strength

At this stage the engineering contribution to risk reduction is expressed in terms of risk. The role that civil engineers can play in reducing accidents as a result of a natural or man-made disaster is enormous and is presented in a summary in Table 1.

Civil engineering becomes the oldest branch, and among all, the engineering disciplines can play a role in increasingly specialized. In the role of the current category of engineers in disaster, risk reduction is discussed with reference to advanced public engineering technologies. The major contributions of experienced civil engineers are highlighted in Table 2.

Apart from the list, the building engineer (experienced or inexperienced) can vary greatly in various positions such as: Site managers or auxiliary engineers can perform various construction tasks. It is their responsibility to use the right materials and the right construction technology, and to get the job done according to the

Table 1 Potential catastrophic impact of civil engineers

Disaster type	Potential contribution of civil engineers
Earthquakes	Improving understanding of earthquakes and their effects. Improving seismic risk reduction strategies for areas and systems (e.g., adoption of recent building codes and best construction methods), and improving seismic hazard identification (e.g., development of earthquake maps), and risk assessment methods and their use, redevelopment of old buildings [4]
Floods	Flood reduction reduces structural and non-construction measures. A civil engineer can offer both options. Other ways to control floods where the role of civil engineers is to predict flooding through extreme imitation, water harvesting, etc.
Cyclone	Engineering's risk reduction measures can be taken to reduce the loss of life and property during storms. One of the biggest threats of a hurricane is the speed of strong winds. Engineering design codes are used to ensure that buildings and structures are constructed to withstand air pollution depending on the climatic conditions of each region
Landslides	Reduction of the risk of landslides includes engineering and non-engineering methods. The engineering mitigation methods used include the construction of groundwater structures, the construction of surface drainage systems, the protection of slopes such as hydro-seeding, reinforced concrete and reinforced concrete grids, and the reassembly of filling slopes
Drought	The need to reduce the risk of drought in a holistic manner involving the use of integrated water resources. Engineering methods include testing programs, upgrading of water supply and construction of new equipment, technical assistance in water conservation, and other water related activities, and water reduction / conservation programs [6]

detailed drawings and details. Risk assessment (pre-disaster) and risk assessment (post-disaster) are some of the areas where economic engineers can contribute the most.

Researcher and academician: Construction engineers provide critical guidelines for determining public policy and defining a research agenda. Civil engineers can develop new and disaster-proof technologies in building a safe environment built with all the essentials. To this end, civil engineers are required to keep themselves updated with the latest research and advances in construction technology, advances in building materials, and in analysis or construction programs. An easy way to achieve this goal is to attend meetings, workshops, training programs, and conferences. Also, a community engineer can be involved in training and teaching the basic and practical knowledge needed to reduce the various natural and man-made disasters [8].

Policymakers and planners should prepare a spatial development plan by considering the vulnerability of the area to various hazards. Details and guidelines for construction activities should be carefully placed, especially in high-risk areas. Before punishing any project, all details must be checked by the authorities. Third-party testing or peer review should be emphasized in the design and monitoring phase. Local authorities should assess project compliance with all requirements or definitions before approving building use (BU).

Table 2 Potential role of civil engineers in terms of technology

Discipline	A potential contribution
Civil Engineering	Construction engineers should be involved from the planning phase of the frameworks and must follow all the details set by the operational code. The building engineer needs to use the latest analytical methods and provide detailed structural drawings that include ductile details. Advanced methods such as performance-based design (PBD) should be followed by high-quality construction and unconventional construction rather than following simple coded methods
Geotechnical	The engineering geotechnical engineer should provide a detailed groundwater investigation, which can greatly assist in the construction of earthquake-resistant. The global response to location and drinking capacity should be assessed prior to project planning and implementation
Transportation engineering	Transport crisis such as earthquakes, landslides, and floods. Disrupts traffic, railway line, etc.
Geomatics	About 80% of daily decisions at national or local, economic, financial/tax, demographic, spatial planning, environment, hazardous areas, infrastructure, housing, etc. That clearly demonstrates the wide range of researcher skills including ground management, geodetic engineering, geo-informatics, satellite technology, and remote sensing can make a significant contribution to the development, simplification, and shortening of disaster risk management [7]
Environmental engineering	Environmental engineering can help reduce the emissions of greenhouse gases and other environmental pollutants; it can provide safe drinking water and help maintain good hygiene in the event of a disaster

Once construction work is completed, and it is up to the building users to ensure proper repairs. If any additions or alterations are required to the building or use of the building, the building engineer will be considered. Finally, civil engineers have also played a key role in post-disaster situations—in rescue operations, damage assessments, and reconstruction. Civil engineers should also take the support of other engineering departments in the better planning, implementation, and implementation of their construction and infrastructure projects [9].

2.2 Weakness

Many disasters occur regardless of their political affiliation and cause great damage to various social services and disrupt basic structures that are essential to daily life. However, due to the poor representation of civil engineers in the political, policy and decision-making structures pose a barrier to the development of appropriate

mitigation measures. In addition to the above, civil engineers face many obstacles in performing their functions in various roles [10]. Some of these obstacles are:

(a) Pressure from political or constructive campaigns
(b) Inadequate research and feasibility of research
(c) Delays in project restrictions and other management processes
(d) Pressure of time
(e) Builders who are not interested in quality
(f) Adequate time for investigation and design
(g) Controversial interests of stakeholders
(h) Tender and specification of tenders
(i) Insufficient resources and poor working conditions.

The above distractions can allow road engineers to follow common practices that lead to more corruption and accidents during a disaster [11]. Because of this, the popular saying that "CIVIL stands for corruption is very important in life." However, the construction engineer (in every role) must make every effort to overcome the above limitations and must do his or her job with the utmost care that can lead to a change in attitude to engineering practices and the term CIVIL should represent "courage is vital for health."

2.3 Opportunity

Despite a number of challenges ahead of civil engineers practices, there is still much to be done. Few joint, long-term actions are proposed by ASCE [12]. If those proposals are backed up emotionally and physically, then the opportunity for civil engineers can be increased.

(a) A strong community engineering education system that prepares leadership and provides non-technical skills to work on projects that affect the public interest.
(b) A clearly defined organizational structure, in which a licensed community engineer assumes the role of project planner/co-ordinator.
(c) Many civil engineers are involved in community policy organizations where future community indicators are developed and where civil engineers can gain public trust.
(d) More and more engineers are selected from public positions where they can directly influence infrastructure and sustainable development policy and legislation.
(e) High level of collaboration and communication between civil engineers and non-engineer stakeholders, who want to balance the sustainable environment with the required infrastructure.

Making all the above-mentioned proposals a daunting task will continue to challenge civil engineering in the future. However, a united civil engineering community

can begin the difficult task that will eventually fulfill that promise. Recent styles of community engineering work can also be a decision to maximize the potential of community engineering engineers in disaster risk management.

To address the shocking effects of the many natural and man-made disasters of the first decade of the twenty-first century, as well as the apparent shortage of information on design, maintenance, and lessons learned, an international commission was set up defining global investment strategies for research and development. As a result, civil engineers have led to a shift from refinement to defense. By 2025, the world will become a more dangerous place, with an ongoing threat of major natural disasters and acts of terrorism. Environmental engineers are at the forefront of developing and implementing appropriate risk management and mitigation methods, recognizing that higher rewards can come from high-risk solutions [13].

Risk is obviously a major driver of innovation, as engineers explore what innovations, processes, and designs can be used while measuring the potential for failure— measuring risk and reward. To facilitate this process, governments have established faster times to change new laws, allowing for faster acceleration of new inventions. Work-specific risk decisions are made at many levels as engineers become the leaders of business risk management, some holding the title of risk manager. Various communities of civil engineering have seen the heat of the future demand and have begun to work in this way. According to Parkash [14], further education and engineer training in ethics in international engineering jobs is needed to ensure engineers become role models. Recognizing the importance of both housing and roads, two key infrastructure needed for the country's growth, Central Building Research Institute, Roorkee (CBRI) and Central Road Research Institute, New Delhi (CRRI), laboratories two Scientific and Industrial Research Council (CSIR), India, has begun jointly to provide two-year PG courses in infrastructure engineering and disaster risk reduction with the aim of promoting disaster risk management in infrastructure such as buildings and roads. Recently, a certification and licensing program for a qualified building engineer is under way. Although the licensing process has not yet been implemented, it can still be considered a major step in improving the security of the built environment [15].

Despite the many challenges and obstacles, public engineering will continue to play a key role in reducing risks as future generations become more difficult and dependent, and as new threats emerge (e.g., effects of climate change, water scarcity, terrorism). Engineers will need to use new knowledge and skills to develop new and effective ways to prevent, prepare for, and respond to the future disasters [16]. In addressing the diversity of environmental risks, engineers also educate the public about the limitations of new technologies so that informed decisions can be made about how infrastructure is built while and controls expectations. Periodically, the codes and engineering standards that meet local requirements are also included in disaster risk reduction policies.

2.4 Threat

There are many threats identified in various ways that can pose a challenge to the community of civil engineers. The first threat is the allocation of resources and the allocation of resources during disaster management. The allocation of resources during disaster operations has been identified by various errors that hinder effective and efficient decision-making. These challenges include prioritization of limited resources, selection of vehicle routes, and location tracking of limited resources should be well-distributed to first responders to life-saving activities. However, the provision of resources such as construction equipment often cannot meet the need for major disasters. This can lead to further injuries and injuries. In addition, there are organizational and administrative challenges. Resources managed by various organizations need to be available, and the integration of resources into them is a major obstacle to disaster response. Lack of access, standard policy, coordination, and communication of sensitive information to inform status and decision-making are barriers that need to be addressed [17].

Currently, in large cities growing at high rates of human and material exposure, disaster management focuses on post-disaster response that poses major challenges to the implementation of pre-disaster mitigation strategies such as planning and construction of a new project [18]. Another obstacle exists in risk assessment which is an important component in the disaster risk management cycle. In developing and standardizing risk-taking approaches, public engineering work must address clients, politicians, the media, and the public (http://www.training.fema.gov). More recently, climate change has emerged as one of the biggest challenges ahead of a disaster management engineer. The likelihood of an environmental and wind disaster occurring at the highest risk of climate change [19] (Pittock 2009). The dangers associated with climate change are real, but their predictions are far from accurate which makes the work of civil engineers challenging and difficult.

Apart from the above, other potential threats to support the role of civil engineers in disaster risk reduction may arise as follows:

(a) Change of political climate, international policies leading to conflict, changing social policies.
(b) Lack of interest or insufficient interaction between the various stakeholders to share resources and information.
(c) Disasters are unpredictable, and in addition, their outcome and behavior are reversible.
(d) Lack of interest and/or awareness in the construction industry.
(e) The absence of an appropriate licensing authority to oversee the construction process and its approval, corruption, and management industry.
(f) Threats posed by the land reform process and subsequent degradation.

3 Case Study

3.1 End-to-end Early Warning System for Surat City

In the event of sudden emergencies such as floods, landslides, and hurricanes, timely and accurate warnings that help prepare and prevent losses. The earlier the warning, the better prepared. For example, in the event of Hurricane Pahilin in 2013, India's Ministry of Meteorology provided reliable information on the strength and impact of the site a few days before the event, which aided the preparation and response efforts. The development of the end-of-town warning system for the city of Surat (Gujarat) is presented here as a case study that can be repeated by the cities of Maharashtra.

Surat, located near the mouth of the Tapi River (where it meets the Arabian Sea) in Gujarat, India's eighth most populous city in the textile, diamond, and heavy industry industries. Since much of the area in Tapi is located in a high rainfall area, Surat used to experience frequent floods. Increased industrial exports in the 1980s required the capacity of the Ukai dam ponds to be increased to meet the growing demand. Over time, there have been other changes such as the texture of the air, and the overflow of the river that has reduced the amount of river transport within the city. As a result, at the end of the rainy season—when the dam is filled with its maximum capacity, any increase in intrusion due to unexpected/heavy rainfall within the catchment forces to evacuate large amounts of water shortly after the dam—leading to flooding in Surat city. Twenty years ago, the frequency of floods had increased due to increased rainfall variability (the worst cases), especially in the catchment area. Floods and the resulting damage also increase over time due to construction, landfill sites in floodplains, etc.

In an effort to reduce the impact of the floods and the damage caused by Surat, it was decided to suspend the warning system early for the end of monitoring and forecasting of extreme weather events in the Upper and Middle Tapi basins and the card (tidal rivers) floods. This is in line with the initial establishment of the Surat Climate Change Trust (SCCT) which includes efforts in three countries—Madhya Pradesh, Maharashrta, and Gujarat to cover the entire Tapi River. SCCT also provided platform participants and information managers at various institutions and levels (from national, state, regional, and city) to share information, learning, and communication before and after floods and to plan and implement integrated/integrated action.

The key features of Surat's end-to-end early warning system are:

(a) Increases linking and verbs
(b) Improved pool applications: Climate change has information on hydrological and hydraulic models to assist in the development of predictable models for the entry and flow of pools. This hydrological model provides advance information (5-day entry forecasts) to decision-makers
(c) All stakeholders responsible for flood information production, distribution, repairs, warnings, and management from the national level to the government, districts, and cities are presented on the same page

(d) Improvements in city flood warnings include the installation of weather systems, data transfer routes from pits to lakes to city levels, development of climate and mobility models, improved existing flood preparedness and construction plans

(e) Installation of ten automatic weather stations and two city water metering units, providing weather information, wave, and flow information

(f) Capacity management (GIS) data for flood management.

3.2 Groundwater Management in Drought-prone Areas: A Case of Pani Panchayat, Maharashtra

India is the world's largest consumer of groundwater accounting for 25% of the world's total water use. Groundwater mitigates the risks that a farmer faces in terms of climatic diversity manifested by drought and extended periods. In addition to the critical importance of the lives of millions of people, poor management of groundwater management has led to widespread corruption in many parts of the world. It has surpassed the stabilization rate in several Northern Indian states (such as Delhi, Punjab, Haryana, and Rajasthan), while it is on the verge of reaching unstable levels in countries such as Gujarat, Tamil Nadu, Karnataka, and Uttar Pradesh with more than 70% annual reimbursement. However, there are many packages available even in these unused areas where groundwater levels drop to several hundred feet. A key factor contributing to such catastrophic damage is the country's groundwater law that gives full rights to landowners to use groundwater. Reducing land and water rights is an hour's need for a systematic system of land water management and regulation in India. The Pani Panchayat case is a unique experiment that shows how land and water rights can be abolished in order to distribute equitably with groundwater conservation.

Pani Panchayat was a social movement started by Mr. Vilasrao Salunke in 1974 to encourage local farmers in the Naigaon region of the Purandhar taluka drought in Maharashtra. Due to the dangerous conditions of groundwater and the government's inability to manage it, he has taken over 40 ha of land by renting it from the local temple for the construction of a refilling pond, a borehole dug in the outlet, and an irrigation system. The encouraging results of the trial led to the establishment of Gram Gaurav Pratisthan (GGP) with the mandate to increase the combined management of surface water and groundwater in the village.

4 Conclusions

This paper has reviewed the critical contribution of civil engineering to disaster risk management. From the planning stage to the implementation of civil engineering projects, the focus is on all stakeholders to ensure public safety in the event of

a disaster. The contribution of civil engineering is very important in the setting of codes and engineering standards. The development of engineering equipment, tools, and methods to reduce the effects of natural and technological hazards on the built environment is another way in which economic engineers can contribute significantly. However, risk reduction options themselves do not guarantee protection from natural hazards and other hazards. Therefore, a holistic view of multiple risks covering social, economic, and environmental issues in risk reduction is preferred. Engineering professionals, who contribute to risk reduction, will be required to work in all fields, as well as more actors and participants. Professionalism, sensitivity to community needs, a multi-sectoral approach, and the integration of efforts focused on improving the built environment, construction, and infrastructure projects will lead to a safer society in the future. It has been suggested that construction engineers need to play a more important role in policy and decision-making. It has also been identified that construction engineers need to improve their knowledge in an area such as the impact of climate change on disaster situations through research activities. Finally, it can be said that as a civil engineer of any area, one can choose in the field of art, be it design, research, planning, teaching, or management, it is important to remember that there is no limit to the satisfaction a person will experience.

References

1. Patil P (2012) Disaster management in India. Indian Res J 2(1):1–6
2. Daya K, Ayaz Md, Lohit Kumar SSN (2011) Disaster management in India. Project term, Submitted to Department of State Engineering, IIT Kanpur, India
3. Aktan AE (1999) The civil engineer in the new millennium. In: Proceedings of the Uğur Ersoy symposium on structural engineering, METU, July, 1999, in Ankara
4. Heaney JP, Petarka J, Wright LT (2000) Requirements for research in natural disaster engineering materials. J Infrastruct Struct 6(1):4–14
5. Jigyasu R (2004) Sustainable post disaster reconstruction through integrated risk management. In Proceedings of 2nd international conference on post disaster reconstruction. Conventry University, UK
6. Hayes MJ, Wilhelmi OV, Knutson L (2004) Drought risk reduction: closing of vision and action. Environ Risk Rev 5(2):106–113
7. Spiker EC, Gori PL (2003) A strategy to reduce the risks of land degradation in seizures— framework for reducing losses. U.S. Geological Survey Circular 1244, p 56
8. Magel H (2005) Concerning researchers' commitment, role and organizational education and sustainable development. Keynote address at the opening ceremony of 8 SEASC 2005 on November 22, 2005 at Bandar Seri Begawan, Brunei Darussalam.
9. Haigh R, Amaratunga D, Kerimanginaye K (2006) Assessing the role of the construction sector in disaster preparedness, response and recovery
10. Patel PV (2010) The role of civil engineers in disaster risk reduction. Indian Concr J XVIII 11:29–31
11. Penny G (2005) Disaster by design corruption, construction and catastrophe. Br J Criminol 45(4):528–546
12. ASCE (American Society of Civil Engineers) (2006) The vision for civil engineering in 2025. Report prepared by the ASCE Steering Committee to Plan a Summit on the Future of the Civil Engineering Profession in 2025. American Society of Civil Engineers, Virginia, USA

13. Hamada M (2009) The role of economic engineers in disaster risk reduction under environmental and social changes and policies for the protection of a safe society. Tugrul Tankut A (Scheduled) Earthquakes and tsunamis: civil engineering disaster reduction activities: achieving millennium development goals. Springer Netherlands, pp 115–131. http://www.jsce-int.org/president/2006/ciche_lecture/HAMADA_CICHE_speech.pdf
14. Parkash S 2012. Ethics in disaster management. Ann Geophys 55(3). https://doi.org/10.4401/ag-5633
15. Kameda H (2000) Engineering management of living systems under earthquake risk. In: Progress of the 12th earthquake engineering conference held at IIT Kanpur, India, Paper ID: 2827. https://www.iitk.ac.in/nicee/wcee/article/2827.pdf
16. Pande RK (2006) Participation in disaster risk management and management: experience from Uttaranchal (India)
17. Chen AY, Peña-Mora F, Ouyang Y (2011) A collaborative GIS framework to support equipment distribution for civil engineering disaster response operations. Autom Constr 20:637–648
18. Wenzel F, Bendimerad F, Sinha R (2007) Megacities–megarisks. Nat Hazards 2:481–491
19. Fatima M, Safdar Q (2011) Analysis of the extreme events in Pakistan: creating links between climate change adaption and disaster management. Int Poster J Sci Technol 1(1):12–14
20. http://www.training.fema.gov/emiweb/edu/docs/EMT/Engineering%20Contribution.pdf

Thickness Optimization of RC Jacket Applied as a Seismic Retrofit Measure on RC Structural Members to Effectively Resist Earthquake Loads

Anup Anilkumar Shukle and Y. K. Guruprasad

Abstract The structures which are not designed for resisting seismic loads and are constructed in earthquake-prone zones, must be strengthened by adopting different retrofitting techniques in order to resist lateral loads generated due to earthquakes. The retrofitting of such structures enhances their seismic performance and helps in avoiding demolition of such structures. The objective of the present work is to identify the optimum thickness of the reinforced concrete (RC) jacket which is being applied as a retrofitting technique to retrofit RC beams/RC columns present in a structure by considering various thicknesses of the RC jackets that can effectively resist forces or stresses induced due to earthquakes. The optimization of the thickness of the RC Jacket is carried out considering lateral loads acting on the structure produced from an earthquake as well as gravity loads which are acting upon the structure. A numerical analysis is carried out to understand the behaviour of a retrofitted structure subjected to an earthquake, whose structural elements—RC beams/RC columns are strengthened adopting RC jackets having an optimum thickness.

Keywords RC structure · Retrofitting · RC jacket · Optimum thickness of RC jacket · Earthquake loads

1 Introduction

Reinforced concrete (RC) is a widely used building material in the construction of structures. Reinforced concrete structures undergo damage during their lifetime due to external agencies such as seismic loads, weathering, fire, due to erroneous design and use of low substandard construction materials [1]. When the damage taken place in the RC structure are within repairable limits, retrofitting/repair may be adopted to restore such distressed structures instead of demolishing the entire structure or part of the structure [2, 3]. Since, complete demolishing of the structure would pose a large financial burden on the owner of the building, and it will be certainly a waste of natural resources when retrofitting or strengthening is an

A. A. Shukle · Y. K. Guruprasad (✉)
Department of Civil Engineering, Ramaiah Institute of Technology, Bangalore, India

adoptable alternative. Strengthening of structures can be achieved by retrofitting [4, 5]. Retrofitting is also adopted when the structure requires to be upgraded in terms of load carrying capacity. Retrofitting may also be adopted to upgrade older structures in terms of enhancing their load carrying capacity and to improve their resistance towards external forces such as earthquake [6]. There are various methods available to adopt retrofitting according to the requirements such as external plate bonding, section enlargement/reinforced concrete jacketing, grouting, epoxy injection, external post tensioning, near surface mounted FRP bars or strips [7]. There are various factors governing the selection of retrofitting methods such as existing concrete strength, magnitude of concrete strength to be enhanced, enhancement in load carrying capacity, cost of construction and maintenance, seismic effect consideration, accessibility to work areas, time constraints in applying retrofitting, environmental clearance aspects. Kaliyaperumal and Sengupta [8] investigated the effect of RC jacketing on the flexural strength and performance of columns. The authors conducted slant shear tests to study the interface between the old and new concrete. Their work shows that the moment capacities of the retrofitted column specimens were more than those of the existing columns. The retrofitted beam-column-joint sub-assemblage specimens showed substantial increase in ductility lateral strength and energy dissipation. Badari Narayanan et al. [9] studied the effect of jacketing on the positive flexural capacity and performance of beams near an interior joint. Authors carried out the testing of beam-column joint sub-assemblage specimens along with the prediction of the behaviour and strength of the retrofitted beam specimens. The authors observed that there is increase in retention of ductility and strength after concrete jacketing. The results further showed that the retrofitted sub-assemblage which has been tested under the monotonic loading shows increase in the lateral strength and energy. Chisari and Bedon [10] explained multi-objective genetic algorithm (GA) optimization procedure for the seismic retrofitting of reinforced concrete building frames with fibre-reinforced polymer (FRP) jackets. Authors solved the optimization problem by finite element (FE) models which are able to take into account of parameters such as the strengthening and ductility increase contribution for the provided FRP jacketing configuration. The results of the study obtained by authors show that the potential of the approach will provide the Pareto front of multi-objective optimization problem and allows for general considerations about influence of design variables on the behaviour of a given reinforced concrete building. Ravala et al. [11] worked on the effectiveness of various methods of jacketing for RC beams. The authors considered ten beams of size $150 \times 300 \times 2100$ mm to study the effectiveness for various methods of jacketing. The authors compared effectiveness of each and every type of jacketing methodology on plane smooth surface with chipped surface for the RC beams. As an outcome of their investigation, for smooth surface RC beam, superior performance was observed for the beam jacketed using combined dowel connectors and bonding agent with micro-concrete. The authors found that implementation of various jacketing methods proved more beneficial for RC beams with chipped surface as compared to that for beams with smooth surface. Ju´lio et al. [12] worked on retrofitting technique called RC jacketing of reinforced concrete columns. The authors found that RC jacketing method leads to a uniformly

distributed increase in strength and stiffness of columns. The durability of the original column was also improved by adoption of RC jacketing method. Sotoud [13] studied the behaviour of the structures due to steel jacketing of columns. The author considered columns of moment resisting RC frame with two spans and two storeys were covered in steel jackets of different thicknesses and performed nonlinear static analysis. The results obtained by from the nonlinear static analysis of frame performed by the author show that the base shear of the structure increases about 23%. As the results obtained by authors, steel jacket method of retrofitting of columns increases the ductility of the structure in the range of 65–81% depending on the thickness of the jacket. The author found that while increasing the steel jacket thickness, increases the ductility of the studied structures, and it has no considerable effect on improving the base shear. Zou et al. [14] worked on various thicknesses of FRP jackets used for the confinement of columns that are taken as the design variables. In their work, the pushover drift of structure is expressed in terms of the FRP sizing variables applying the principle of virtual work and the approximation of Taylor series. The author employed optimality criteria (OC) approach for finding the solution of the nonlinear seismic drift design problem. The result of their analysis showed that the FRP confinement increases the strength of columns but has less effect on their stiffness, which is a crucial advantage in seismic retrofit as larger stiffnesses lead to larger seismic loads. The optimization technique is able to design FRP thicknesses in the columns so as to efficiently control and distribute the damage throughout the structure by changing the failure mode from a column side-sway mechanism to a mechanism which adopts an acceptable deformation in storey level and weak beam strong column behaviour. It is understood from the works carried out on retrofitting of structural elements adopting an RC jacket that study on optimum thickness of RC jacket that may be adopted for retrofitting purpose is limited. Therefore, the **objective of the present work** is to arrive at an optimum thickness of the RC jacket that is adopted to effectively retrofit and restore the damaged/distressed RC structural elements (RC beams and RC columns) that is present in the structure that have not been priorly designed for earthquake resistance. A reduced compressive strength of concrete present in the structural elements is the reason for the distress/damage in the structural elements (RC beams and RC columns).

2 Assessment of Optimum Thickness of the RC Jacket Applied to Retrofit Distressed RC Structural Members Having Varied Degrees of Damage

The structure considered in this study is a multistorey reinforced concrete structure having 11(G + 10) floors. The 11 storey structure in this study is a hospital building that has been modelled in ETABS considering irregularity in plan as shown in Fig. 1 and has been subjected to earthquake loading as per response spectrum method IS 1893 (Part 1) [15] RC beams and columns present in the structural
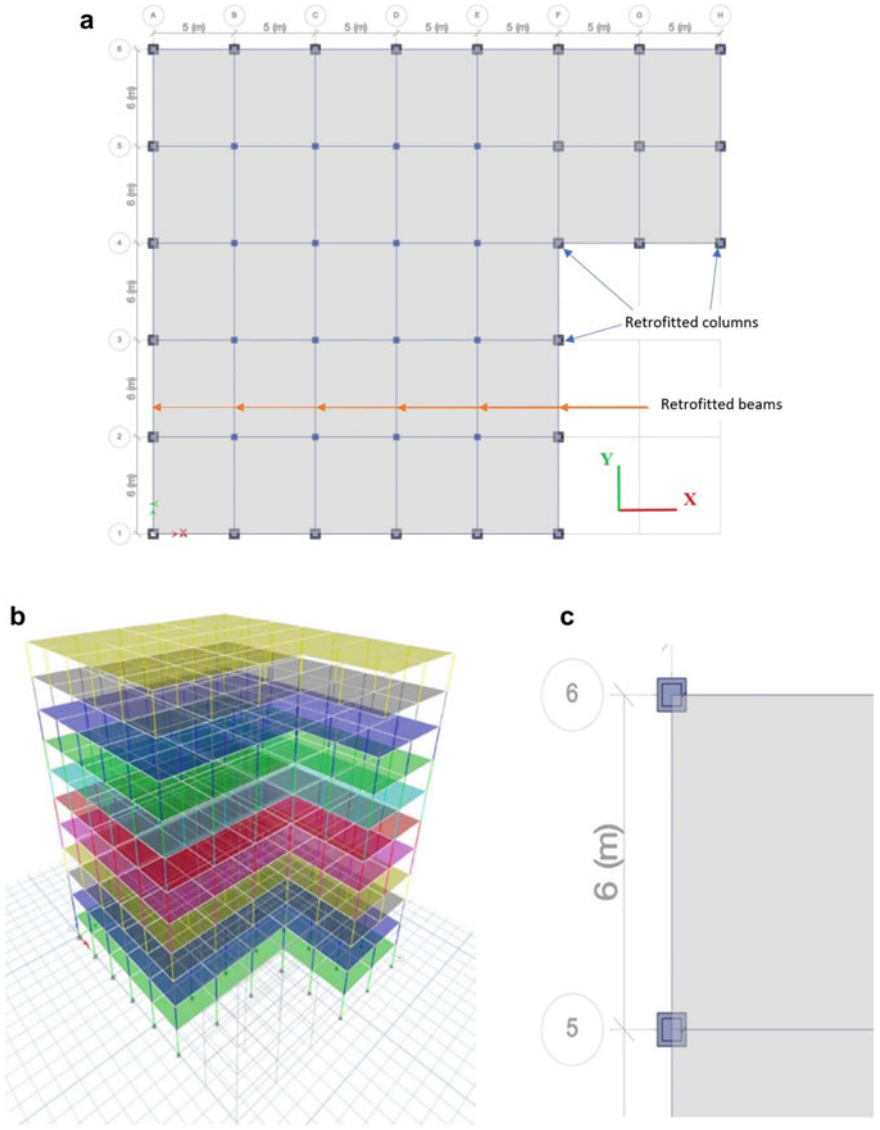
Fig. 1 **a** Plan view of the structure, **b** Isometric view of the structure, **c** Plan view of retrofitted columns

model have been retrofitted by the application of RC jacket for a particular degree of distress/damage(d) that has already taken place in the structural members on account of reduced compressive strength of concrete present in the structural members. The reason for the distress/damage in the structural members having a reduced compressive strength of concrete is due to erroneous mix design and placing of concrete

during the construction phase of the structure. Due to the reduced compressive strength of concrete, the load carrying capacity of the structural elements tends to come down. The damage (d) in the structural members is considered due to the reduced compressive strength of concrete present in the structural members that have not been designed for earthquake resistance. The undamaged or original compressive strength of concrete that had to be present actually in the structural members during the construction phase is 25 MPa. The reduced values of compressive strength of concrete present in the structural elements (RC beams and columns) considered in this study are: 20 MPa, 15 MPa, 9 MPa and 7 MPa, respectively. The reduced compressive strength in concrete in the structural elements is basically obtained from non-destructive evaluation/condition assessment studies (core test). All the peripheral beams, columns and beams along Y-direction were found to be having damage in them due to the reduced concrete strength. In this study, an attempt has been made by applying an RC jacket having different thicknesses, namely 100, 125, 150, 175 and 200 mm, on to the distressed/damaged RC elements (RC beams and columns) that have reduced values of compressive strength of concrete, so as to study the response of the same structure that may be subjected to a future earthquake after application of the retrofit. Response spectrum analysis is carried out to determine the effectiveness of the retrofit by arriving at an optimum thickness of the RC jacket. The typical retrofit sections of beams and columns that were modelled in ETABS are shown in Fig. 2 (Fig. 2a: retrofit section of column, Fig. 2b: retrofit section of beam). The effectiveness of RC jacket thickness is decided with respect to the maximum
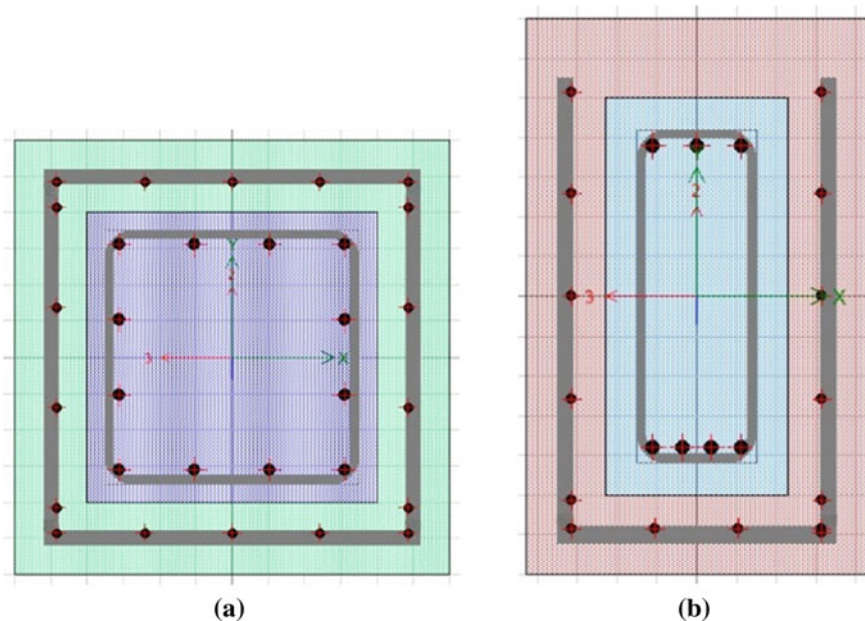
Fig. 2 Typical cross-sections of **a** Retrofitted column, **b** Retrofitted beam

storey displacement caused due to the gravity loads as well as seismic loads. Live loads were considered as per IS 875 (Part 2) [16]. All the load combinations are considered as per IS 1893 (Part 1) [15], and IS 15988 [17] is considered for seismic strengthening of the existing RC structure in this study.

2.1   Preliminary Data of the Structure

- Number of storeys: 11, storey height: 3.5 m, height of structure: 38.5 m, bay length: 5 m (X-direction), 6 m (Y-direction) plan area: 870 m^2
- Beam dimension: 230×500 mm in X-direction and 230×600 mm in Y-direction, column dimension: 400×400 mm, slab thickness: 150 mm
- Grade of concrete: M25 [18], grade of steel: Fe500
- Reinforcement details of columns: #12 rebars of 16 mm ϕ, lateral ties-8 mm ϕ @ 225 mm c/c
- Reinforcement details of beams: #4 rebars of 16 mm ϕ in tension zone, #3 bars of 16 mm ϕ in compression zone, strirrups-2L 8 mm ϕ @ 175 mm c/c
- Reinforcement details of RC jacket applied on distressed RC columns: #18 rebars of 12 mm ϕ main steel, lateral ties-10 mm ϕ @ 200 mm c/c
- Reinforcement details of RC jacket applied on distressed RC beams: #14 rebars of 12 mm ϕ main steel, lateral ties-10 mm ϕ @ 200 mm c/c
- Note: while applying the RC jacket to the distressed RC beams and columns during the retrofitting phase at site, 8 mm ϕ shear keys would be provided for bond between old and new concretes in the RC jacket. Bonding epoxy is applied on to the surface of old concrete before the new concrete is placed in the RC jacket.
- Live load: 4 KN/m^2
- Seismic zone: V, zone factor: 0.36, importance factor: 1.5, response reduction factor: 3, damping ratio: 0.05, soil type: II.

3   Results and Discussion

The results of the analysis that has been carried out in this study have been reported in this section. The results reported are for the structure that has been subjected to seismic loading on account of carrying out response spectrum analysis with application of RC jacket as a retrofit measure.

Table 1 shows the value of reduced compressive strength, reduced modulus of elasticity of concrete and the corresponding damage that has taken place in the concrete present in the structural members (RC beams and columns). Table 2 shows the maximum top storey displacement in X and Y directions (in plan) in the structure without the application of retrofit for various degree of damages that have taken place

Table 1 Reduced compressive strength, reduced modulus of elasticity of concrete and the corresponding damage taken place in concrete present in structural members

Reduced compressive strength of concrete (MPa)	Modulus of elasticity E_i of concrete (MPa)	Scalar damage $d = 1 - \frac{Ei}{Eo}$	Percentage of damage due to reduction in compressive strength of concrete in structural elements (beams and columns) (%)
7	13,228.75	0.471	47.1
9	15,000.00	0.400	40.0
15	19,364.92	0.225	22.5
20	22,360.67	0.105	10.5

Table 2 Maximum top storey displacements in the X and Y directions in the structure that is subjected to seismic loads without application of retrofit for various degree of damages taken place in concrete present in the structural members (RC beams and columns)

Percentage of damage due to reduction in compressive strength of concrete in structural elements (beams and columns) (%)	Maximum (top) storey displacements in X-direction (in mm)	Maximum (top) storey displacements in Y-direction (in mm)
0.00 (undamaged structure)	232.591	222.413
10.5	294.892	361.971
22.5	314.007	408.768
40.0	355.489	502.454
47.1	376.326	555.072

in the structural members. Tables 3 and 4 show the maximum top storey displacements that have taken place in the structure that was subjected to seismic loads with application of RC jacket as retrofit having different thicknesses for various degree of damages taken place in concrete present in the structural members (RC beams and columns).The damage that has taken place in the concrete present in the structural members (RC beams and columns) has been taken into account due to an already occurred earthquake, post-retrofit. The damage (d) has been assessed with the help of non-destructive evaluation techniques (the same has been explained in the previous section). The percentage reduction of top storey displacement with respect to the maximum top storey displacement of undamaged structure in X and Y directions has also been reported in Tables 3 and 4, respectively.

Figure 3a shows the relation between the reduced modulus of elasticity of concrete (E) and the corresponding scalar damage (d). Figure 3b shows the relation between the scalar damage (d) and the reduced compressive strength of concrete. Figures 4a, b, c and d show the percentage reduction in the maximum top storey displacement for 10.5, 22.5, 40.0 and 47.1% damage that has taken place in concrete present in structural elements (RC beams and columns), respectively.

Table 3 Maximum top storey displacement in the X-direction taken place in the structure that is subjected to seismic loads with application of RC jacket as retrofit having different thicknesses of RC jacket for various degree of damages taken place in concrete

| RC jacket thickness (in mm) | Percentage of damage due to reduction in compressive strength of concrete in structural elements (beams and columns) and top storey displacements (mm) for different thicknesses of RC Jacket | | | | | | | |
| | 10.5% | | 22.5% | | 40.0% | | 47.1% | |
	Top storey displacements	% reduction in displacement	Top storey displacements	% reduction in displacement	Top storey displacements	% reduction in displacement	Top storey displacements	% reduction in displacement
100	166.773	43.45	168.475	46.34	171.120	51.86	172.259	54.23
125	153.155	48.06	145.464	53.67	156.492	55.97	157.362	58.18
150	141.091	52.15	142.122	54.73	143.718	59.57	144.402	61.63
175	130.443	55.76	131.274	58.19	132.559	62.71	133.109	64.63
200	121.062	58.94	121.746	61.22	122.802	65.45	123.254	67.25

Table 4 Maximum top storey displacement in the Y-direction taken place in the structure that is subjected to seismic loads with application of RC jacket as retrofit having different thicknesses of RC jacket for various degree of damages taken place in concrete

RC jacket thickness (mm)	Percentage of damage due to reduction in compressive strength of concrete in structural elements (beams and columns) and top storey displacements (mm) for different thicknesses of RC Jacket							
	10.5%		22.5%		40.0%		47.1%	
	Top storey displacements	% reduction in displacement	Top storey displacements	% reduction in displacement	Top storey displacements	% reduction in displacement	Top storey displacements	% reduction in displacement
100	152.172	57.96	154.086	62.30	157.090	68.73	158.393	71.46
125	139.675	61.41	141.003	65.50	143.216	71.49	144.170	74.03
150	129.683	64.17	130.649	68.03	132.140	73.70	132.779	67.08
175	120.835	66.62	121.610	70.25	122.806	75.56	123.317	77.78
200	112.985	68.78	113.620	72.20	114.599	77.19	115.017	79.27
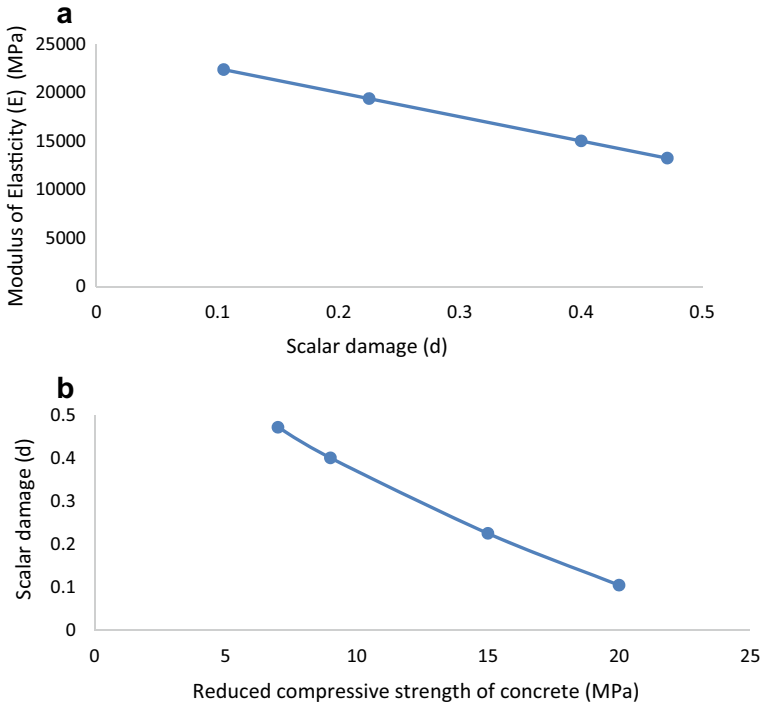
Fig. 3 **a** Variation of modulus of elasticity (E) with respect to the corresponding scalar damage (d), **b** Variation of scalar damage (d) with respect to the corresponding reduced compressive strength of the damaged concrete present in structural members

It is learnt from the results (Tables 3 and 4) that there is a comparatively minimum difference in the reduction of the maximum top storey displacement when the structural elements (RC beams and columns) present in the structure are retrofitted by an RC jacket having a thickness between the range of 175–200 mm when compared to an RC jacket having the thickness in the range of 125–150 mm.

Therefore, based on the previously mentioned observation of the results that has been obtained by carrying out the analysis in this work that by providing an RC jacket having a thickness in the range of 125–150 mm applied on to the structural elements (RC beams and columns), as a retrofit measure has been found to be an optimum range of thickness of the RC jacket. The optimum range of the RC jacket thickness (125–150 mm) has been arrived at based on the percentage of reduction in the maximum top storey displacement.

Since the dimensions of the structural elements become comparatively larger after providing 175 and 200 mm RC jacket thickness, the dead weight of the structure increases as well as there is an in cost of the retrofit, and the aesthetics of the structure also gets affected.
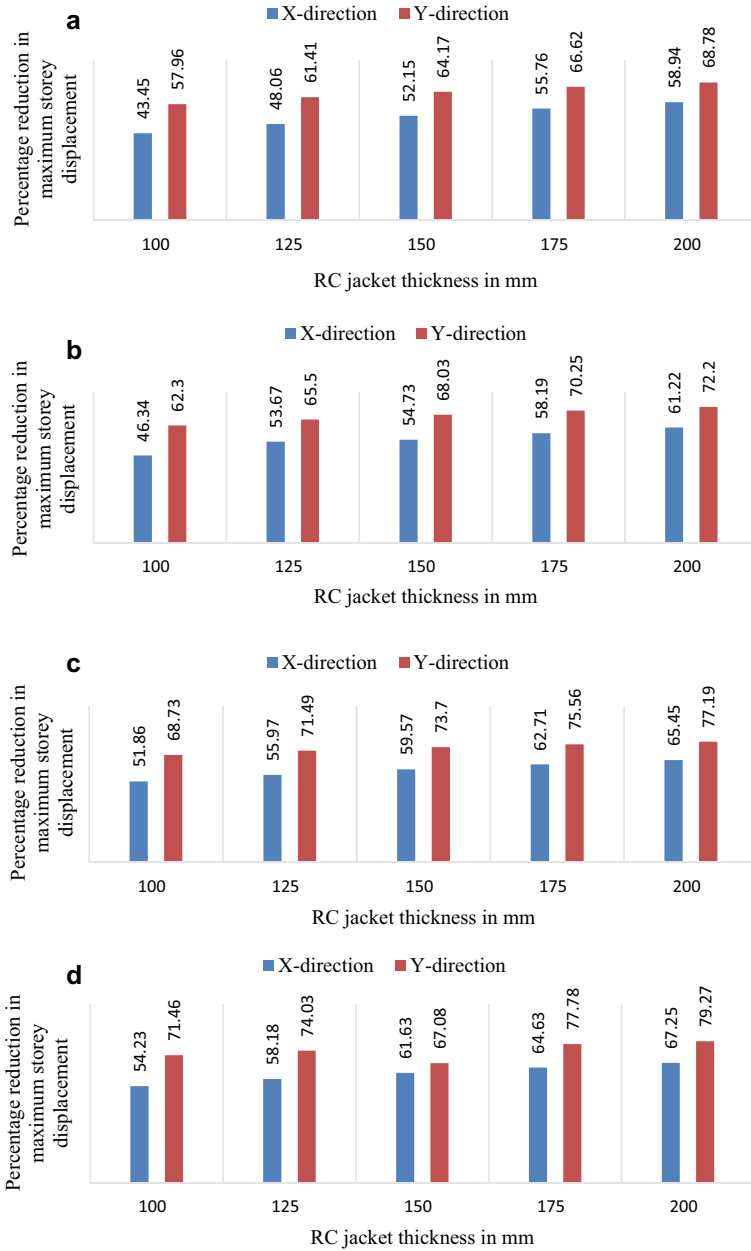
Fig. 4 **a** Percentage reduction in maximum storey displacement for 10.5% damage (d) taken place in concrete present in structural elements (RC beams and columns), **b** Percentage reduction in maximum storey displacement for 22.5% damage (d) taken place in concrete present in structural elements (RC beams and columns), **c** Percentage reduction in maximum storey displacement for 40.0% damage (d) taken place in concrete present in structural elements (RC beams and columns) and **d** Percentage reduction in maximum storey displacement for 47.1% damage (d) taken place in concrete present in structural elements (RC beams and columns)

4 Conclusion

- It is observed from this study that the damage/distress taken place in the concrete present in the structural members was evaluated on an account of a reduced compressive strength of concrete that is identified based on non-destructive evaluation/condition assessment (core test).
- The reduction in the compressive strength of concrete present in the structural members was due to erroneous mix design and placing of concrete during the construction phase of the structure. The non-destructive evaluation/condition assessment (core test) was performed in various structural members, when the structural members had shown signs of distress in the form of structural cracking.
- It is observed from the results in Tables 3 and 4 that there is a reduction of the maximum top storey displacement when the structural elements (RC beams and columns) were strengthened by the application of an RC jacket having a thickness between the range of 175 to 200 mm. The RC jacket thickness in the range of 175 to 200 mm comparatively tends to increase the dead weight in the structure and also results in an increase in the cost of the retrofit.
- It is inferred from the results obtained from this study that an RC jacket having a thickness in the range of 125 to 150 mm applied as retrofit on to the structural elements (RC beams and columns) present in the RC structure has been found to be an optimum range of thickness of the RC jacket.

References

1. Shrikhande M, Agarwal P (2006) Earthquake resistant design of structures by PHI Learning Pvt. Ltd
2. Karayannis CG, Chalioris CE, Sirkelis GM (2008) Local retrofit of exterior RC beam–column joints using thin RC jackets—an experimental study. Earthquake Eng Struct Dynam 37:727–746
3. Chandurkar PP, Pajgade PS (2013) Seismic analysis of RCC building with and without shear wall. Int J Modern Eng Res (IJMER) 3(3):1805–1810
4. Truong GT, Dinh NH, Kim J-C, Choi K-K (2017) Seismic performance of exterior RC beam–column joints retrofitted using various retrofit solutions. Int J Concr Struct Mater. https://doi.org/10.1007/s40069-017-0203-x
5. Menon D, Sengupta AK, Sarkar P (2004) Seismic evaluation and retrofit of existing multi-storied buildings. In: World congress on natural disaster mitigation, February 19–21, 2004. New Delhi, pp 370–378
6. Sengupta AK, Srinivasulu Reddy C, Badari Narayanan VT, Asokan (2004) Seismic analysis and retrofit of existing multi-storied buildings in India—an overview with a case study. In: 13th world conference on earthquake engineering. Vancouver B.C., Canada, August 1–6 2004, Paper no. 2571
7. Dubey R, Kumar P (2016) Experimental study of the effectiveness of retrofitting RC cylindrical columns using self-compacting concrete jackets. Constr Build Mater 124:104–117
8. Kaliyaperumal G, Sengupta AK (2009) Seismic retrofit of columns in buildings for flexure using concrete jacket. ISET J Earthq Technol 46(2):77–107. (Paper No. 505)

9. Badari Narayanan VT, Sengupta AK, Satish Kumar SR (2012) Seismic retrofit of beams in buildings for flexure using concrete jacket. SET J Earthq Technol 49(1–2):1–22. (Paper No. 518)

10. Chisari C, Bedon C (2016) Multi-objective optimization of FRP jackets for improving the seismic response of reinforced concrete frames. Am J Eng Appl Sci 9(3):669–679

11. Ravala SS, Daveb UV (2013) Effectiveness of various methods of jacketing for RC beams. Procedia Eng 51:230–239

12. Ju´lio ES, Branco F, Silva VD (2003) Structural rehabilitation of columns with reinforced concrete jacketing. Prog Struct Eng Mater 5:29–37

13. Sotoud S (2009) Seismic retrofit of reinforced concrete columns with steel jackets of different thicknesses. In: Proceedings of the 1st International conference on concrete technology, Tabriz, Iran, 6–7 November 2009

14. Zou XK, Teng JG, De Lorenzis L, Xia SH (2007) Optimal performance-based design of FRP jackets for seismic retrofit of reinforced concrete frames. Compos: Part B 38:584–597

15. IS 1893 (Part1) (2016) Criteria for earthquake resistant design of structures

16. IS 875 (Part 2): Code of practice for design loads (other than Earthquake) for building and structures—imposed loads

17. IS 15988 (2013) Seismic evaluation and strengthening of existing reinforced concrete buildings—guidelines [CED 39: Earthquake Engineering]

18. IS 456 (2000) Plain and reinforced concrete—code of practice [CED 2: cement and concrete]

Flood Resilience Quantification for Housing Infrastructure Using Analytic Hierarchy Process

Mrinal Kanti Sen, Subhrajit Dutta, and Golam Kabir

Abstract Natural hazards are severely damaging infrastructure systems, so it is essential to make the existing infrastructure more resilient to increase the considered infrastructure resisting ability. Resilience is the enduring capacity of an infrastructure system against natural disasters and quickly recover after the disaster. As the impact of any hazard cannot be stopped or reduced, and resilience depends on several parameters, it is essential to study the sensitivity of the resilience parameters. Additionally, a robust framework should be developed with the concept of resilience to enhance the resisting ability. The basic need of living is the housing infrastructure, so a practical resilience-based framework for housing infrastructure must be developed. In this work, a framework for quantification of resilience against flood hazard is developed by using a multi-criteria decision method (MCDM) tool, such as the analytic hierarchy process (AHP). Initially, several resilience parameters are considered based on literature and experts' knowledge. Then, a field survey is performed for the collection of required data. After getting the data needed, a flood resilience model is developed. Lastly, using AHP, the importance of each resilience parameter is identified, and also, the resilience is evaluated for all the surveyed places. The sensitivity of each parameter will help the decision-makers to focus on the most critical parameter/s to make the considered infrastructure more resilient for future hazards. Additionally, the evaluated resilience values will help the stakeholders by providing the surveyed places' real scenario against flood hazard.

Keywords Flood · Resilience quantification · Analytic hierarchy process · Housing infrastructure

M. K. Sen (✉) · S. Dutta
Department of Civil Engineering, National Institute of Technology Silchar, Silchar, India

G. Kabir
Industrial Systems Engineering, University of Regina, Regina, Canada

1 Introduction

The occurrence of hazards always interrupted the capability of any society or any infrastructure of a community, which also affects the functionality. Disasters types have been inspected, and it was discovered that natural, human-made, and a blend of both debacles spread a wide range of shocking occasions. Our discussion in the current context will be limited to flood only. The management of disaster is generally discussed after its occurrence, but practically, the preparation of disaster management should be effectively planned for future hazards. The concept of resilience has been applied in a broad scope of systems, including building, urban structure, financial matters, business, socio-biological, network, and psychological planning and preparation for future hazards [1–5]. Resilience is characterized as the capacity of a system to withstand peril and jump back to its ideal execution level after the event of any danger [6]. Infrastructure systems are broadly recognized as a lifesaver in the network and play a crucial job in continuing financial flourishing and urban versatility and manageability. For a practical, all-around sustainable development, the growing need of the hour is to invest importance in considering infrastructure resilience in the real-life community. However, little priority has been given to it in the past few decades since the inception of the concept of resilience. However, as of late, there is expanding acknowledgment that this individual-focused way to deal with resilience is full of limitations because it needs affectability to be social and the physical setting. Another assemblage of work is endeavoring to extend the emphasis on resilience as a trait of the individual to strength as a network and social process. This new spotlight on "community resilience" looks at how individuals conquer pressure, injury, and other life challenges by drawing from the cultural and social systems and rehearses that comprise networks.

Bruneau et al. [4] developed a framework to quantitatively resilience and enhance the seismic resilience of a community's infrastructure. Sen and Dutta [1] developed an integrated global information system (GIS) and the Bayesian belief network (BBN) framework and model for quantifying the resilience of roadway infrastructure. Further, the proposed framework is modified by performing interdependency among housing and roadway infrastructure using BBN [2]. Nan and Sansavini [7] developed a quantitative method for assessing the resilience of interdependent infrastructures. Sen et al. [3] studied the resilience of housing infrastructure in Barak Valley, Northeastern India. In that study, previous disaster data are collected by performing a field survey, and the resilience is quantified by using a variable elimination algorithm. The drawback of that study is that the weightage of parameters is not considered. Resilience depends on various parameters, so it is essential to study the importance of each resilience parameter.

Several multi-criteria decision-making (MCDM) tools are available for evaluating the importance, like analytic hierarchy process (AHP) [8], fault tree analysis (FTA) [9], and structural equation model (SEM) [10]. FTA cannot identify critical node/s of a network as the analysis is done without considering the nonlinear relationship among parameters. A considerable amount of questionnaires are needed for SEM to

identify sensitive parameter/s of a network. Therefore, AHP can reduce the above-mentioned difficulty. This tool is generally considered a structured technique and used to organize or analyze mathematics-based complex decisions. This tool is developed in 1990 by Thomas Saaty [11]. Forman and Gass [12] discussed the structuring complexity, measurement on a ratio scale, and the principles of AHP tools. Kabir and Hasin [13] used an analytical hierarchal process (AHP) tool for finding the importance of power substation parameters. Saaty [14] discussed the applications and steps used in the AHP tool. Ho and Ma [15] discussed various literatures of AHP and compared all the published papers between 1997 and 2016. In this study, the AHP tool is used to evaluate the importance of resilience parameters, and a framework is developed for quantifying the resilience of housing infrastructure. The developed framework is implemented in a real community. Based on the above discussion, the objectives of the work are as follows;

1. To develop a framework for quantifying the housing infrastructure resilience against flood hazard.
2. To find out the importance of all resilience parameters by using AHP.
3. To find out the housing infrastructure resilience of a real community.

The paper is arranged as follows, in Sect. 2, the developed framework and the implementation of the developed framework in a real community are discussed, and finally, the results and conclusion section is discussed.

2 Implementation of the Developed Framework

2.1 The Resilience Quantification Framework

The developed framework for resilience quantification is shown in Fig. 1. In the framework, initially, all the resilience-dependent parameters are selected based on literature and experts' knowledge. A resilience model is then developed, and the
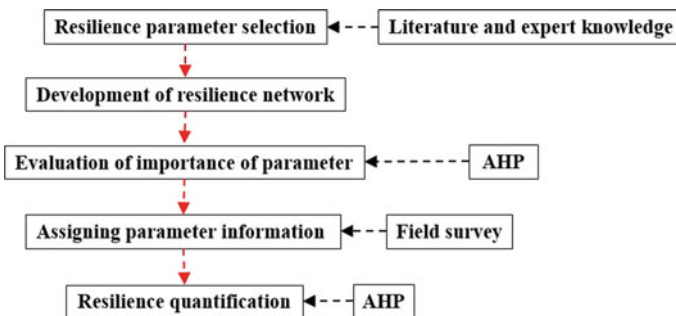
Fig. 1 Resilience quantification framework

importance of each resilience parameter is evaluated by using the AHP tool. The post-disaster information for each parameter is collected by performing a field survey. Then, the prior of each parent node is assigned based on collected data, and lastly, the housing infrastructure resilience is evaluated by using the AHP tool.

Analytic Hierarchy Process (AHP)

AHP is used to evaluate the importance of parameters or factors. It is an MCDM tool. The steps followed to study the significance of parameters in the AHP tool are as follows [16],

Step 1: Initially, a hierarchical network of an objective is developed with different levels (from top level to bottom level), where the objective is in top level, criteria are in intermediate levels, and alternatives are in the bottom level.

Step 2: Next, experts are asked to provide the score for relative importance between one parameter over another parameter to construct the initial pair-wise comparison matrix $A_{m \times n}$ of size $m \times n$ (shown in Eq. 1).

$$A_{m \times n} = \begin{pmatrix} a_{11} & \cdots & a_{1n} \\ \vdots & \ddots & \vdots \\ a_{m1} & \cdots & a_{mn} \end{pmatrix} \tag{1}$$

where $a_{11},\dots a_{1n},\dots,a_{m1},\dots a_{nm}$ are the elements of $A_{m \times n}$ matrix. The diagonal of this matrix is always one, which means that the importance of an element over the same element is one. The ranges for the score are given in Table 1.

Step 3: Next, the initial pair-wise matrix is normalized by dividing a normalized factor (N.F.), where N.F. is the summation of each element of a column. The normalized column is shown in Eq. 2.

$$\begin{pmatrix} \dfrac{a_{11}}{\sum\limits_{n=1}^{m} a_{n1}} & \cdots & \dfrac{a_{1n}}{\sum\limits_{m=1}^{m} a_{mn}} \\ & \ddots & \\ \dfrac{a_{m1}}{\sum\limits_{n=1}^{m} a_{n1}} & \cdots & \dfrac{a_{nm}}{\sum\limits_{m=1}^{m} a_{mn}} \end{pmatrix} \tag{2}$$

Table 1 Scores for pair-wise matrix

Scale	Importance
1	Equal
3	Moderate
5	Strong
7	Very strong
9	Extreme
2, 4, 6, 8	Intermediate
1/3, 1/5, 1/7, 1/9	For inverse

where $\sum_{n=1}^{m} a_{n1}$ and $\sum_{m=1}^{m} a_{nm}$ is the summation of each element for the first and nth column.

Step 4: Then, the importance of each parameter is calculated by averaging all the elements in the row of A_N matrix (shown in Eq. 3).

$$\begin{pmatrix} \frac{a_{11}}{\sum_{n=1}^{m} a_{n1}} & \cdots & \frac{a_{1n}}{\sum_{m=1}^{m} a_{mn}} \\ & \ddots & \\ \frac{a_{m1}}{\sum_{n=1}^{m} a_{n1}} & \cdots & \frac{a_{nm}}{\sum_{m=1}^{m} a_{mn}} \end{pmatrix} = \begin{pmatrix} \text{Average of all the element of row} = W_1 \\ \vdots \\ \vdots \\ \vdots \\ \vdots \\ \text{Average of all the element of row} = W_n \end{pmatrix} \quad (3)$$

Step 5: The consistency ratio is evaluated to check that the estimated importance is correct or not. Initially, each element in the column of $A_{m \times n}$ matrix is multiplied with its importance as shown in Eq. 4.

$$\begin{pmatrix} W_1 \times a_{11} & \cdots & W_n \times a_{1n} \\ \vdots & \ddots & \vdots \\ W_1 \times a_{m1} & \cdots & W_n \times a_{nm} \end{pmatrix} \quad (4)$$

Next, the weighted sum value for each row is calculated by adding each element in the row (shown in Eq. 5). Then, the ratio of weighted sum value with the importance of parameter (w_n/W_n, $n = 1, \ldots, n$) for each row is calculated, and λ_{max} is evaluated (shown in Eq. 6).

$$w_1 = \sum_{n=1}^{n} W_n \times a_{1n}$$

$$\vdots \quad (5)$$

$$w_m = \sum_{n=1}^{n} W_n \times a_{mn}$$

$$\lambda_{max} = \frac{\sum_{n=1}^{n} \frac{w_n}{W_n}}{n} \quad (6)$$

The consistency index (C.I.) is evaluated using Eq. 7, and the consistency ratio (C.R.) is assessed using Eq. 8.

Table 2 Random index

# of parameter	1	2	3	4	5	6	7	8	9	10
RI	0	0	0.58	0.9	1.12	1.24	1.32	1.41	1.45	1.49

$$\text{C.I.} = \frac{\lambda_{\max} - n}{n - 1} \tag{7}$$

$$\text{C.R.} = (\text{C.I.})/\text{Random Index}$$

where n is the number of parameters and random index (R.I.) is taken from Table 2. If the C.R. < 0.1, it means that the evaluated importance of the parameter is correct.

Step 6: The maximum probability value of a parameter is multiplied by the importance of that parameter to determine the weighted probability of that parameter. For example, parameter 1 having two states like "*yes*" or "*no,*" and probability of "*yes*" is 45% and "*no*" is 55%. Then, the weighted probability will be (shown in Eq. 8).

$$P_W(1) = W_1 \times P(\text{no}) \tag{8}$$

Finally, the probability of the objective is calculated by multiplying the importance of the parameters of the intermediate layer with the summation of the weighted probability of bottom layer parameters.

2.2 Implementation of the Framework

The developed framework is implemented in Barak Valley, Northeastern India. This region is selected because more than 30,000 houses get affected from 2015 to 2020 due to floods [17]. Initially, experts from the research-related domains are chosen. Here, a total of five experts is selected for construction of pair-wise matrix and selection of resilience parameter. Out of five experts, two are field officers in District Disaster Management Authority (DDMA), two are Assistant Professors from different institutions, and one is District Project Officer (DPO) of DDMA. Based on their knowledge and literature, a total of 12 resilience parameters is selected. The selected parameters are mainly based on two parameters: reliability and recoverability of housing infrastructure [1–3]. The selected resilience parameter for housing infrastructure for this work is as follows [3, 18], based on reliability, (R1) type of house, (R2) wall thickness, (R3) plinth level, (R4) flood depth, (R5) drainage, (R6) age of the building, and based on recoverability, (R7) income, (R8) insurance, (R9) resource availability, (R10) relief received, (R11) approachability, and (R12) education. Then, a resilience network model is developed based on selected parameters, as shown in Fig. 2.
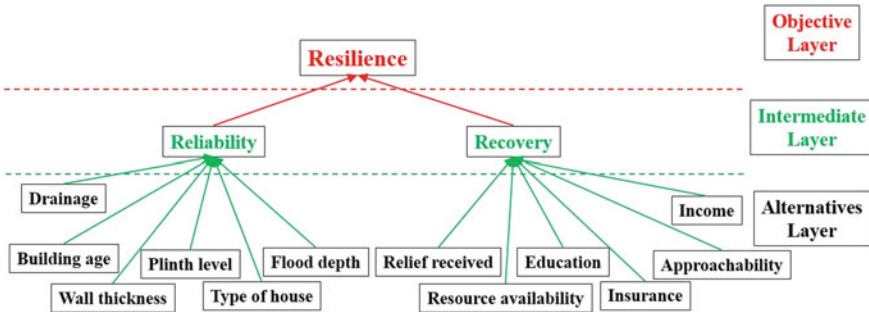
Fig. 2 Resilience network model

Experts are then asked to provide the scores for relative importance among parameters based on Table 1, and accordingly, an initial pair-wise comparison matrix $A_{m \times n}$ is developed using Eq. 1 (shown in Table 3).

After developing the matrix, using Eqs. 2 and 3, the importance of each parameter is evaluated, as shown in Fig. 3. It can be seen that R1 and R3 are the most sensitive against reliability, and R7 and R8 are the most sensitive against recovery of housing infrastructure.

After getting the weightage of all resilience parameters, a field survey is performed in the selected case study area. Total ten places are visited (all places are subdivided into various circle areas), in which a total of 212 houses are visited, and it took

Table 3 Initial pair-wise matrix for resilience parameters

Reliability parameters

	R1	R2	R3	R4	R5	R6
R1	1	4	5	6	5	8
R2	1/4	1	3	2	3	5
R3	1/5	1/3	1	3	2	5
R4	1/6	1/2	1/3	1	2	4
R5	1/5	1/3	1/2	1/2	1	2
R6	1/8	1/5	1/5	1/4	1/2	1

Recovery parameters

	R7	R8	R9	R10	R11	R12
R7	1	3	4	5	7	9
R8	1/3	1	2	3	5	7
R9	1/4	1/2	1	1	3	5
R10	1/5	1/3	1	1	2	4
R11	1/7	1/5	1/3	1/2	1	3
R12	1/9	1/7	1/5	1/4	1/3	1
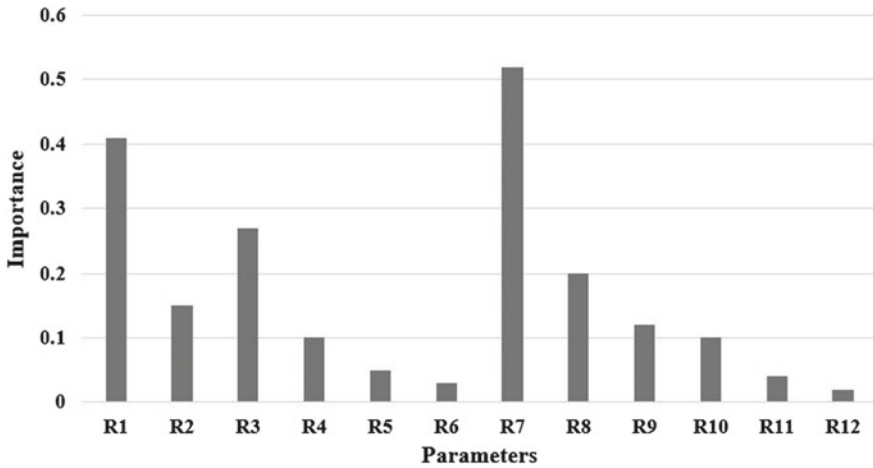
Fig. 3 Importance of resilience parameters

near about 25 min for each interview. Figure 4 shows the various surveyed places in Barak Valley, Northeastern India. All the required post-disaster data for resilience parameters are collected during the field survey, and the prior probability of all parent parameters is assigned accordingly. Using Eqs. 4–8 (Steps 5 to 6), resilience values for all surveyed places are quantified.

3   Results

In this study, all the parameters are assigned with two different probability states, such as resilient and non-resilient, based on experts' knowledge and field survey information. The quantified resilience values for all visited places are shown in Table 4. From the evaluated values, it can be observed that the housing infrastructure of areas like Dwabond, Algapur, Amjurghat, and Borbond of that valley is the most non-resilient, as 71.9, 68, 67.2, and 67% of housing infrastructure of those areas are non-resilient. It means that the stakeholders or decision-makers should give immediate attention to those places for strengthening the infrastructure to enhance the resilience against future hazards. All the surveyed areas are non-resilient, but Dullacherra is the least non-resilient compared to all other areas, as 60.3% of housing infrastructure are non-resilient. Non-resilient infrastructures surround the housing typology of this valley. Maximum of the houses of this valley are constructed with bamboo or wood with non-engineered construction. As the economic condition of maximum householders is weak, so they cannot build RCC houses or engineered houses. Every year, several homes get damaged, and due to which the government is paying a considerable amount for restoration. Nowadays, householders prefer RCC or Assam-type houses in rural areas by taking loans or help from various agenesis. Assam-type house is
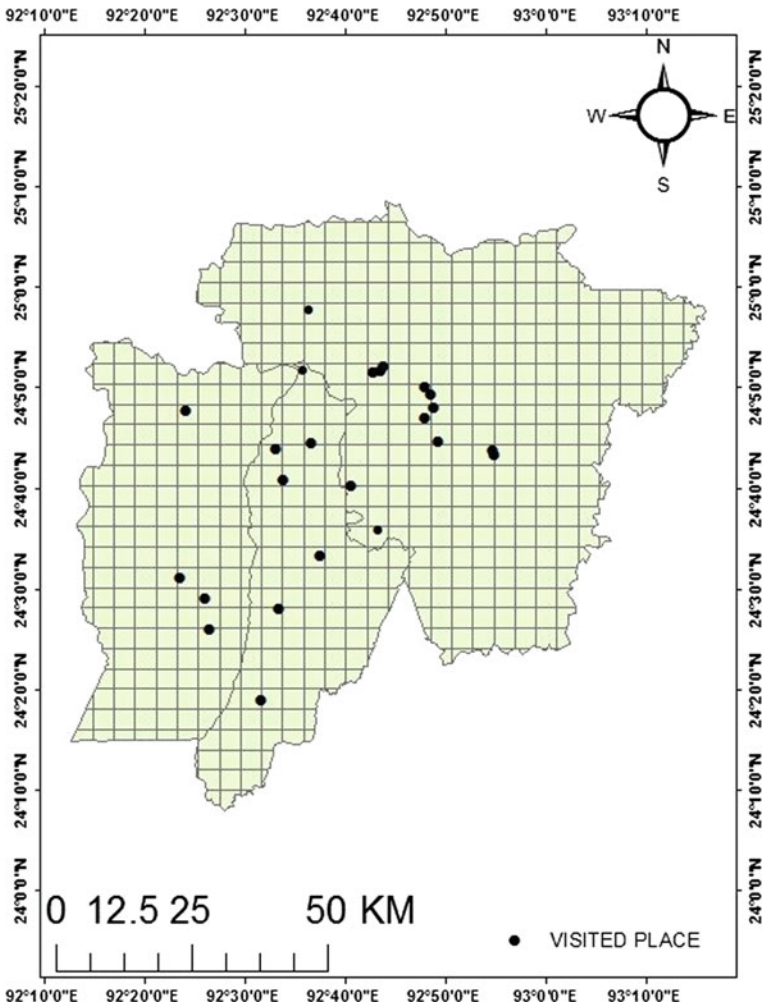
Fig. 4 Various surveyed areas in Barak Valley

also known as masonry house, which is more robust than bamboo or wooden house. There are two types of Assam-type house such as the half-wall house and full-wall house, where half-wall means the lower half is made up of the brickwork, and the upper half is made up of a mixture of bamboo-cement motor or bamboo-mud, and the full-wall means the whole wall is made up of brickwork.

Table 4 Visited places resilience values

Place name	Resilient	Non-resilient
Algapur	0.320	0.680
Amjurghat	0.328	0.672
Baleshwar	0.344	0.656
Bhatikupa	0.362	0.638
Borbond	0.330	0.670
Burunga	0.384	0.616
Dullacherra	0.397	0.603
Dwabond	0.281	0.719
Fanai cherra grant	0.392	0.608
Hailakandi town	0.374	0.626

4 Conclusion

In this work, a resilience quantification framework is developed, where various resilience parameters are selected. The importance of each parameter is evaluated. An extensive field survey is performed for the collection of information against each parameter. Then, the developed framework is implemented in a real case study area where a field survey is conducted. Using the AHP tool, the resilience of each surveyed area is evaluated. This framework can be applied to other critical infrastructure systems to assess that infrastructure's resiliency. The evaluated resilience values of Barak Valley will help the stakeholders to strengthen the housing infrastructure against a future hazard. The evaluated importance of each parameter will help the decision-makers to decide on giving attention to the sensitive parameters to make the considered infrastructure more resilient against a future hazard. In the future, more probability states will be considered for quantification of resilience value to get a more precise scenario. The developed framework can be updated by adding more information.

References

1. Sen MK, Dutta S (2020) An integrated GIS-BBN approach to quantify resilience of roadways network infrastructure system against flood hazard. ASCE-ASME J Risk Uncertainty Eng Syst Part A: Civ Eng 6(4):04020045
2. Sen MK, Dutta S, Gandomi AH, Putcha C (2021) Case study for quantifying flood resilience of interdependent building-roadway infrastructure systems. ASCE-ASME J Risk Uncertainty Eng Syst Part A: Civ Eng 7(2):04021005
3. Sen MK, Dutta S, Laskar JI (2021) Hierarchical Bayesian network model for flood resilience quantification of housing infrastructure systems. ASCE-ASME J Risk Uncertainty Eng Syst Part A: Civ Eng 7(1):04020060
4. Bruneau M, Chang SE, Eguchi RT, Lee GC, O'Rourke TD, Reinhorn AM, Von Winterfeldt D (2003) A framework to quantitatively assess and enhance the seismic resilience of communities.

Earthq Spectra 19(4):733–752

5. Youn BD, Hu C, Wang P (2011) Resilience-driven system design of complex engineered systems. J Mech Eng 133(10)

6. Pooley JA, Cohen L (2010) Resilience: a definition in context. Aust Commun Psychol 22(1):30–37

7. Nan C, Sansavini G (2017) A quantitative method for assessing resilience of interdependent infrastructures. Reliab Eng Syst Saf 157:35–53

8. Sambasivam VP, Thiyagarajan G, Kabir G, Ali SM, Khan SAR, Yu Z (2020) Selection of winter season crop pattern for environmental-friendly agricultural practices in India. Sustainability 12(11):4562

9. Lu L, Liang W, Zhang L, Zhang H, Lu Z, Shan J (2015) A comprehensive risk evaluation method for natural gas pipelines by combining a risk matrix with a bow-tie model. J Nat Gas Sci Eng 25:124–133

10. Fernández-Muñiz B, Montes-Peón JM, Vázquez-Ordás CJ (2017) The role of safety leadership and working conditions in safety performance in process industries. J Loss Prev Process Ind 50:403–415

11. Saaty TL (1988) What is the analytic hierarchy process? In: Mathematical models for decision support. Springer, Berlin, Heidelberg, pp 109–121

12. Forman EH, Gass SI (2001) The analytic hierarchy process—an exposition. Oper Res 49(4):469–486

13. Kabir G, Hasin MAA (2013) Integrating modified Delphi method with fuzzy AHP for optimal power substation location selection. Int J Multicriteria Decis Making 3(4):381–398

14. Saaty RW (1987) The analytic hierarchy process—what it is and how it is used. Math Model 9(3–5):161–176

15. Ho W, Ma X (2018) The state-of-the-art integrations and applications of the analytic hierarchy process. Eur J Oper Res 267(2):399–414

16. Bappy MM, Ali SM, Kabir G, Paul SK: Supply chain sustainability assessment with Dempster-Shafer evidence theory: implications in cleaner production. J Cleaner Prod 237:117771

17. ASDMA Homepage. http://sdmassam.nic.in/reports.html. Last accessed 26 Jul 2020

18. van de Lindt JW, Peacock WG, Mitrani-Reiser J, Rosenheim N, Deniz D, Dillard M, Harrison K (2020) Community resilience-focused technical investigation of the 2016 Lumberton, North Carolina, flood: an interdisciplinary approach. Nat Hazard Rev 21(3):04020029

Feasibility of Post-Cyclone Portable Relief Shelter: Case of Odisha

Ipsitaa Priyadarsini Das ⬤, Shanta Pragyan Dash ⬤, and Ramnath Nayak ⬤

Abstract Owing to its geographical location and topographical conditions, the Indian peninsula is vulnerable to tropical cyclones. According to previous research, it is observed that cyclones occur more frequently in the Bay of Bengal and affect the entire stretch of the eastern coast of the Indian subcontinent. The state of Odisha which lies in this region is the most affected and experiences severe destruction of property infrastructure and life. During such a disaster, multi-purpose cyclone shelters perform an important role in providing vital aid to the affected people. Depending on the severity of the disaster, these shelters provide individuals with protection during the disaster and necessary resources such as shelter, first-aid box, and food for the short term. Such shelters, however, do not provide post-cyclone facilities, especially when many families are without adequate shelter. The research aims to explore the viability of a portable post-cyclone relief shelter to normalize day-to-day operations and provide a better life. During the study, an analysis of the literature, case studies with surveys, and interviews of stakeholders and affected individuals was conducted, and it was concluded that there is a need to have such post-cyclone portable shelter during the post-cyclone period to address their basic needs. The research concludes with the proposed design of a prototype of a portable relief shelter, analyzing its feasibility in terms of cost, ease of fabrication, transportation services, and maintenance by using locally available material to achieve environmental sustainability.

Keywords Post-cyclone · Temporary shelter · Portable structure · Coastal · Odisha

I. P. Das (✉) · S. P. Dash
Manipal School of Architecture and Planning, MAHE, Manipal, Karnataka, India

S. P. Dash
e-mail: shanta.dash@manipal.edu

R. Nayak
Indian Design School, Mangalore University, Mangalore, Karnataka, India

1   Introduction

Over two decades, it has been noted that there has been a gradual increase in the incidence of natural disasters in both underdeveloped, developing, and developed countries. At present, the crisis has gotten much more severe with the bulk of the world's population at serious risk of natural disasters. [1]. If an account is taken of the observed and reported occurrences of natural disasters in the last two decades (1995–2005), the eastern part of India has undergone a greater number of hydrological disasters, such as floods, storm surges/coastal floods, cyclones, and ground-mass movements due to floods. Moreover, of India's 7516 km long coastline, about 5700 km was vulnerable to cyclones. [2].

The first part of the paper discusses the impact of cyclones in the Indian subcontinent considering the case of Odisha as a contextual study. It discusses the government mitigation strategies and plan of action during a post-cyclone scenario. The second part of the paper discusses the need for the post-cyclone shelter as an immediate relief and recovery aftermath of the disaster and the parameters to be considered for building a temporary portable shelter with a proposed structural system. The last phase of the paper concludes with the design of the prototype of a temporary portable shelter with its feasibility analysis and other related factors compared to the conventional type of post-relief shelter.

1.1   What is Cyclone?

In meteorological terms, cyclones can be described as an extensive volume of air in a rapid circular movement around a strong low-pressure zone at the center that can be the result of severe disturbances in the atmosphere. In the Northern Hemisphere, the air rotates in an anticlockwise movement, while in the Southern Hemisphere, it rotates in a clockwise movement. Cyclones are generally characterized by severe storms and adverse weather conditions [3]. The map (Fig. 1) is showing the wind direction and the formulation of a tropical cyclone concerning the equator. India is surrounded by two major water bodies like the Arabian Sea on the western side and the Bay of Bengal on the eastern side which is prone to cyclone formation. The majorly eastern part of the country hits the maximum number of cyclones due to the absence of large landmass like Western Ghats and Himalayas (Fig. 2). Also, India receives cyclone from The Pacific Ocean due to its geographical location. According to the "National Cyclone Risk Mitigation Project (NCRMP)," the records of the survey conducted from 1891 to 2002 indicate that the eastern coast of India has encountered nearly 308 cyclones out of which 98 were severely destructive [2]. However, the western coast has experienced 48 cyclones out of which only 24 were severe (Table 1).

Fig. 1 Spatial–temporal distribution of tropical cyclone [4]
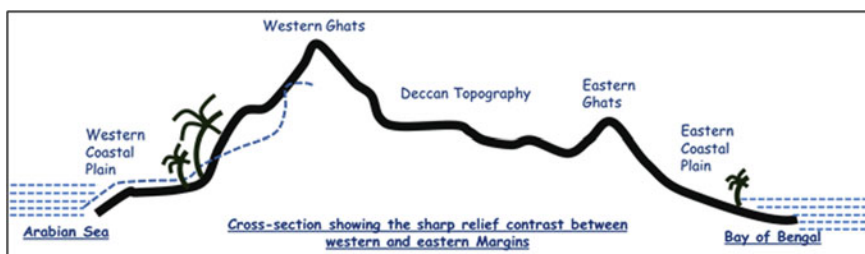
Fig. 2 Cross section through peninsular plateau showing sharp relief contrast between western and eastern margins [4]

West coast states	No. of cyclones	East coast states	No. of cyclones
Gujarat	28	Odisha	98
Maharashtra	13	Andhra Pradesh	79
Kerala	3	West Bengal	69
Karnataka	2	Tamil Nadu	54
Goa	2	Pondicherry	8

Table 1 Major tropical cyclone in India subcontinent from 1891 to 2002 [5]

1.2 The Context of Odisha

Odisha is highly vulnerable to natural disasters such as cyclones, flooding and flash floods, landslides, droughts, and earthquakes. (Fig. 3). This can be due to the distinctive geographical location and climatic environments. According to the SRC 2013 report, Odisha has experienced the highest number of cyclones consisting of all categories, especially with higher occurrences of category 3 to category 5 cyclones to date as a result of the subtropical coastal region. Along the coastline, adjacent to the Bay of Bengal, the majority of the cyclones in this region occur across the state of Odisha, followed by Andhra Pradesh, Tamil Nadu, and lastly West Bengal [6]. In Odisha, the coastal districts of Balasore, Puri, and Ganjam are slightly more vulnerable to landfall (cyclone-affected areas) than in the pre-monsoon (April to June) and post-monsoon cycles in general (October to December). Odisha also experiences cyclones of category 2 to category 5 intensity. However, the 1999 super-cyclone was the most catastrophic cyclone occurrence in its history.
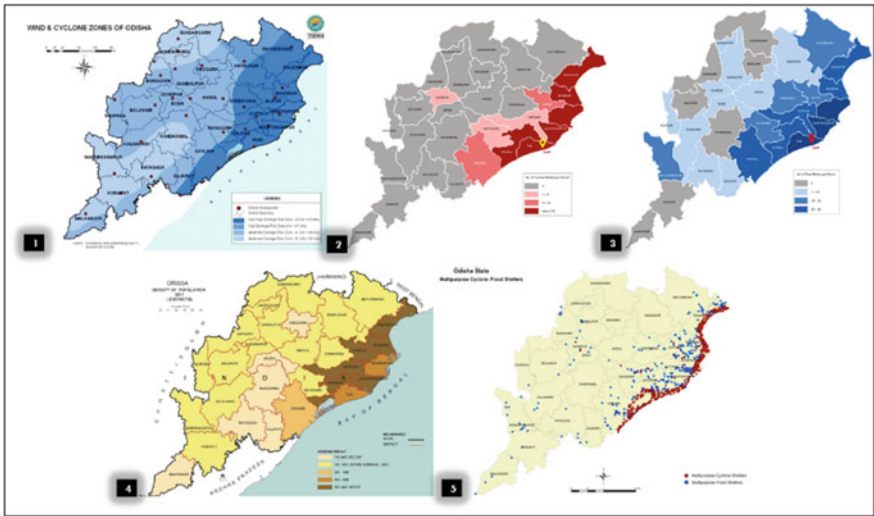
Fig. 3 (1) Map of Odisha showing the cyclone zone, (2) map of Odisha showing the maximum landfall area with the number of multi-purpose cyclone shelters available, (3) map of Odisha showing flooding zone, (4) map of Odisha showing the mapping of multi-purpose cyclone shelter near coastal region, and (5) map of Odisha showing the density of population [7]

1.3 The Government Mitigation Plan

Since the 1999 super-cyclone, the government gave thoughtful attention to flood recovery and prevention measures. The government has presented a four-stage tropical cyclone warning framework for disaster preparedness, recovery, and mitigation. The four steps are as follows:

I.   "**Pre-Cyclone Watch**" is followed with green alert and gives the early information about the cyclonic disturbance to the coastal belt followed with landfall to the areas.

II. "**Cyclone Alert**" comes with a yellow alert system, issued at least 48 h before the cyclone event.

III. "**Cyclone Warning**" comes with an orange alert system, and it is announced a minimum of 24 h before the cyclone event to warn the local population to evacuate the regions of the coastal belt which may be severely affected. It also provides the most recent position of the cyclone, its intensity, landfall area together with storm surge height, and expected type of damages [7].

IV. "**Post-Landfall Scenario**" comes after the disaster (cyclone), and it has the provisions to cover the overall damages caused to life and property. Once the cyclone starts dissipating, the final message on "de-warning" is issued.

Concerning the good disaster management scheme, the state government has made major progress in ensuring proper facilities and emergency operations through the Special Relief Commissioner (SRC). Each village, according to the panchayat, has a cyclone resilient R.C.C. shelter within a range of 5 km from the coastlines of the state. Each of such shelters has various necessary provisions such as food, first-aid box, clothes, fresh drinking water, and sanitary products that are essential during the event of a cyclone.

1.4 The Aftermath of Cyclone

The state of Odisha is most vulnerable to natural disasters. The geographical area, followed by a high population density and inefficient post-disaster recovery and mitigating efforts to address the adverse effects of the disaster, poses a condition of serious vulnerability to the state. As discussed earlier, the disaster relief and mitigation programs are involved in the event prior as well as during the disaster. As per the government report, Disaster Response, Management, and Mitigation Plan-2018, the goal has been set to ensure healthy living and promote well-being for all ages by the year 2030 [8]. The main objective of the report is:

- To reduce the cases of deaths during and in the aftermath of the disaster by adopting effective and timely medical response activities.
- To have a better life, one needs to stay in a better condition with a healthy environment.

"During the British era and post-independence years, disaster management was largely limited to post-disaster relief works, food-for-work programs, etc., under a Central Relief Commissioner who headed the State Relief Commissioners" [9]. If the 1999 Odisha super-cyclone occurrence is taken into account, the adverse impacts on the life, land, facilities, and livelihoods of the local population have been due to insufficient planning and preparedness by the state government. The death toll was more than 10,000 during the cyclone outbreak, and the post-disaster figures rose steadily due to lack of effective disaster recovery and mitigation programs.

2 The Need for the Temporary Shelter

Natural disasters such as cyclones are harmful to the life and resources of the local people. The adverse consequences of such disasters are found not only in the course of the incident but also in the aftermath of the event. The aftermath of a natural catastrophe poses a series of dangerous and unhealthful living circumstances for a long period. For a better understanding, the process of responding to a natural disaster and the comprehension of the sequence of events that occur before and post-disaster are required. This is illustrated by the flowchart as shown in Fig. 4.

The local government along with its subsidiaries and several other governmental and non-governmental agencies initiated several disaster relief and mitigation programs to reduce the negative impacts of the adverse conditions in the aftermath of cyclones. However, due to several tangible and intangible factors, not all the individuals of the local population gain access to the provision which leads to long-term delays in the rebuilding and resettlement efforts.

The research conducted by Haas, Kartez, Bowden (1977), and Geipel (1982) classifies the disaster relief and mitigation programs into four phases, which
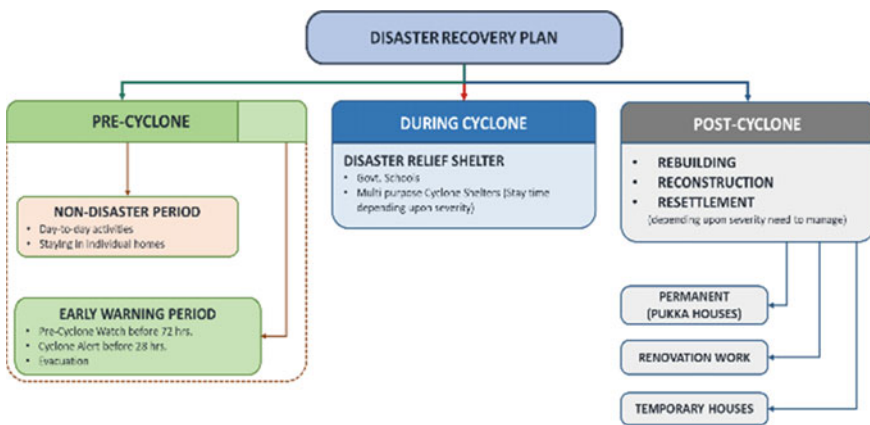
Fig. 4 Sequence of events occurring prior and post-disaster [4, 10]
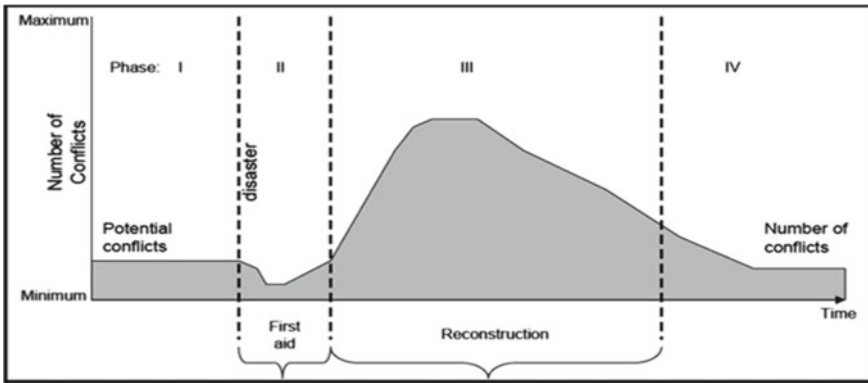
Fig. 5 Conflict model of recovery [11, 12]

are as follows: **Phase I**—period before the disaster, **Phase II**—period of emergency response immediately after the disaster, **Phase III**—period of post-disaster reconstruction, and **Phase IV**—period of resettlement.

In this research, it has been observed that the time required for the reconstruction is generally more than all the phases, prior or post-cyclonic condition. The graph for conflict model of recovery in Fig. 5 indicates that the extent of time required for the reconstruction of permanent structures in Phase III is maximum. This presents a particularly serious disadvantage since this is a very critical period in the normalization of the daily lives of the cyclone-affected local population. This is a critical indication that Phase III requires particularly high attention from the local government bodies for the provision of safe and healthy living conditions to those families who have lost their dwellings either partially or completely to the damaging effects of the cyclone. Such provisions must be provided for the entire duration of the reconstruction program until the affected families are completely resettled.

According to Enrico Quarantelli, the pioneer in the sociology of disasters and the general process of providing shelters in any disaster relief programs will essentially have four stages, which are *Emergency Shelter* (short-term—mostly tents), *Temporary Shelters* (mid-term—shelter/housing), *Temporary Housing* (extended durations), and *Permanent Housing* (long-term) [13]. Since it is of utmost importance to provide emergency shelters post-disaster and permanent housing as a part of the reconstruction and resettlement program, the local government accomplishes the first and the fourth stages of providing shelter effectively.

3 Literature Study

3.1 Development of the Parameters for Material

In the event of a cyclone, serious disruption to housing and other built infrastructure results in a substantial proportion of the urban population being homeless. The lack of a robust shelter that offers a stable and secure living environment leads to deplorable living conditions for the people affected by the cyclone. To have such a temporary and stable shelter, the materials for its manufacture must be identified and their ability to withstand the harsh environmental conditions that prevailed in the aftermath of the cyclone must be well understood. Also, for this, we should know what kind of structures is required that can be easily erected.

However, to consider the relationships between the manufacturing products and the adverse post-cyclone climate, certain conditions must be established based on the cyclone's effects and the environment. The following segment sets the pre-requisites for the identification of the parameters which are required for the formulation of the guidelines which will aid the selection of the fabrication materials. This is illustrated by the flowchart as shown in Table 2.

Hence, the following parameters have considered choosing materials to build a temporary portable shelter.

- Handling (easy to transport, light to weight ratio, and workability)
- Availability (abundance, locally available, and low cost)
- Endurance (weather condition, durability, pest attack, and termite/borer/fungus attack)
- Ecological sustainability (low environment impact on procurement and low impact on use).

The parameters have been taken into consideration to choose material for the frame structure of the shelter, for covering of the shelter, for the joist, for thermal protection, for waterproofing, for sealants, and for adhesives.

3.2 Development of Structural System

"The generic name deployable structures are used for a broad category of structures that can be transformed from a closed compact configuration to a predetermined expanded form, in which they are stable and can carry loads" [17]. These structural systems have the inherent ability to be converted from forms and shapes with small volumes or areas such that they can be stored and transported in small spaces and can be expanded to relatively larger volumes upon expansion depending upon the location in need. Hence, such structures are designed and fabricated to be structurally stable and maintain optimum performance even after undergoing a considerable

Table 2 Sequence of events occurring prior and post-disaster

Sl. no.	Post-cyclone conditions	About/key point	Inference
1	Debris: vegetative debris, infrastructure debris, construction debris	Due to cyclone wind damages happened to the different fields as follows and **can be reused** in a different sector. The cleaning of debris **needs immediate action** as it will affect other facilities to support victims [14, 15]	Easy to transport and lightweight
2	Liquid waste and vector control	Due to flood after cyclone, damage happened to the sewage system or due to overflow, the sewage water creates issue to marine life as well as urban or rural **health** by having **disease vector and pest** [14]	Endurance
3	Transportation conditions	Due to debris and flood issue, transportation of things will be difficult [14]	Easy to transport
4	Health/psychosocial support	Lack of privacy and security results in mental trauma and instills fear in the society as the properties are lost due to cyclone [16]	Safety, security, and privacy
5	Climatic risk	Change of weather and climatic conditions needs to be considered to account for decomposing, quick-drying, pest attack [15]	Endurance (termite attack)
6	Scarcity of raw materials and other resources (like construction materials, food, vegetation, etc.)	Difficult to get raw materials from outside and difficult to carry to the affected area due to debris [15]	Locally available materials, abundance, and easy to transport
7	Sanitation, solid waste management, and water supply system	Due to **surge height,** water logging is common in cyclone-affected areas which help to grow water-borne diseases	Material, scheme, and planning

transformation in form. "Deployable, foldable, expandable, portable, and reconfigurable structures can provide a change in the geometric morphology of the envelope by contributing to making it adaptable to changing external climate factors and to improve the indoor climate performance of the building" [18].

For use in deployable prefabricated systems, the **scissor linking** and **hinge structures** shall be taken into account. These systems fall into the category of "pantographic rigid links." These architectures incorporate rigid linkages and hinges in a configurable closed-loop mechanism, the primary extension factor being the "scissor linkage."

The scissor linkage (Fig. 6) is one of the most dominant types of deployable mechanisms that are used in the majority of the open–closed or extended–contracted morphological forms due to their versatility and distinct potential of extension and rotation.

Typically, the scissor linkage mechanism consists of folding support members that are connected at transitional points along their length such that the combination results in a crisscross "X" pattern. The transitional point at which two or more members are linked to each other is called a revolute joint or a scissor hinge. This hinge permits large geometric alterations (Fig. 7).
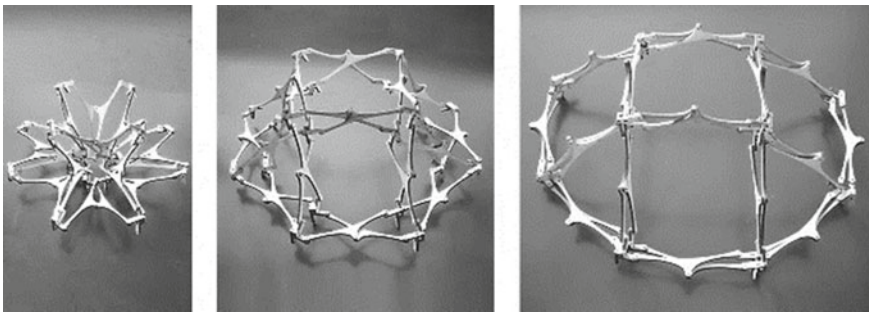
Fig. 6 Deployable structures using scissor mechanism for expandable dame-like structure [19]
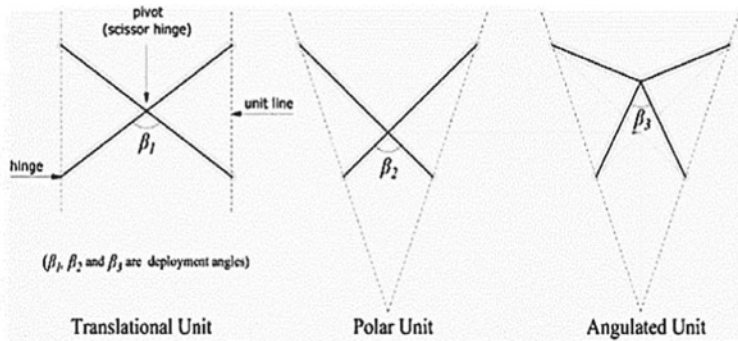
Fig. 7 Types of scissor linkage units by variation in the position of hinge [20]
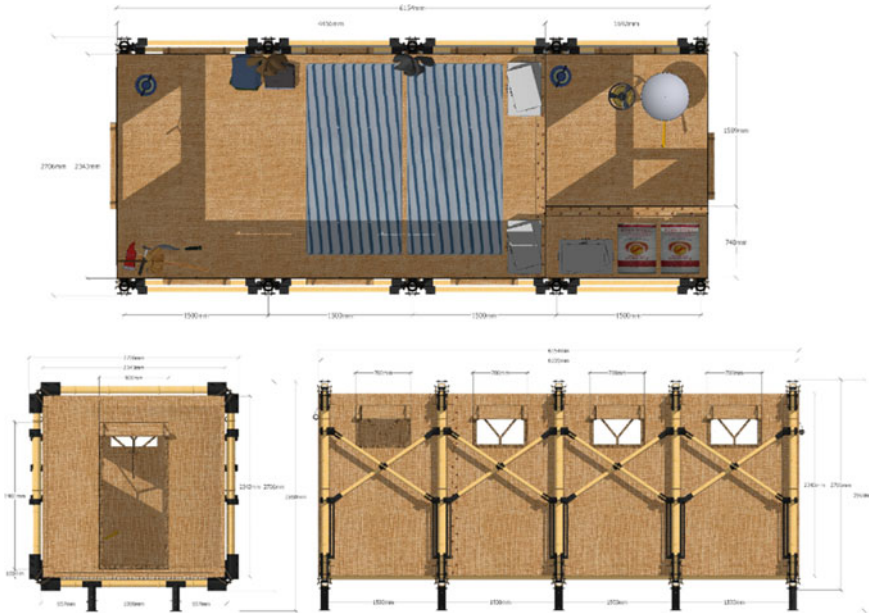
Fig. 8 Plan and elevation of prototype design [4]

4 Proposed Prototype Design

4.1 Description of Material

Materials have been selected based on affordability and durability. As it is available locally, the cost of the module has been minimized and can be reused. As the module is portable and foldable, each of the components or joints can be used if any other requirements arise and is biodegradable due to its sustainability design. The materials used are as follows (Fig. 8):

- For frame structure: bamboo.
- For covering: jute.
- For joining: jute and GI.

4.2 Description of Structural System

Scissor linkage and hinged units provide greater compression vs. expansion ratio, enabling efficient transportation of units as more number of modules can be transported in comparison with conventional prefabricated structures. However, such
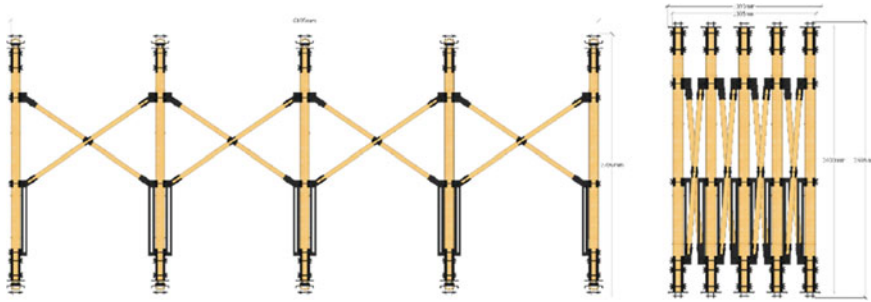
Fig. 9 Expanded and compressed elevation of structural frame, respectively [4]

deployable structures come with design challenges that are generally not experienced in the design and fabrication of conventional prefabricated modules. Certain volumes can have very limited number of iterations for compression and deployability while restricting the incorporation of certain design features. Such structures are best suited for the quick, easy, and convenient erection of livable modules in areas where conventional construction is hindered by the ambient conditions (Fig. 9).

4.3 Description of Transportation System

As the prototype is foldable and compact by nature, transport is feasible even under post-cyclone conditions. The regular truck (Tata 407) with a bed size of 2750 × 2170 mm can hold 6 units at a time. The compressed module size is 1390 × 2500 mm, while the extended/assembled module size is 6154 × 2500 mm (Fig. 10).
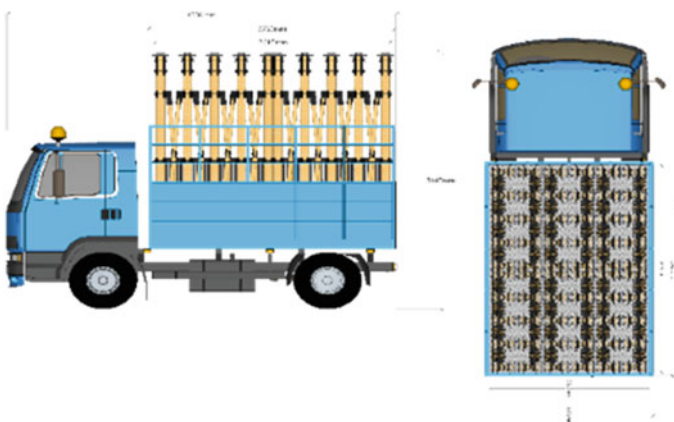
Fig. 10 Plan and elevation of 407 truck carrying the temporary portable module [4]

5   Feasibility Test of Prototype Design

The feasibility analysis of the prototype is carried out based on criteria such as structural system, material, infrastructure, facilities, and maintenance of traditional static frameworks such as concrete structures. The concrete foundation acts as a permanent structure that normally occurs during the post-cyclone rehabilitation phase (usually 2–3 months after the cyclone landfall). As per the District Disaster Management Plan (DDMP), polyethylene sheets are generally issued to affected persons, who are not appropriate for prolonged periods (as discussed earlier in this report). The following section (Table 3) indicates a feasibility analysis including a detailed comparison of post-cyclone shelters.

5.1   Structural System Factor

For easier assembly and dismantling, the shelter is required to be lighter in weight with many foldable units. The concept has come from temporary shelters like

Table 3   Feasibility test of prototype design with respect to post-cyclone shelter

Feasibility in terms of	Parameters	Conventional	Prototype (proposal)
Shelter	Type	Permanent	Temporary
Structural system	Volume	9.8 × 3.8 × 3.0 (Cmt.)	6.154 × 2.5 × 2.5 (Cmt.)
	Weight	NA	550.7 kg
	Assembly time	3 months	≈ 1 h
	Ease of assembly	Special tools and equipment required	No skilled labor, special tools, and equipment required for assembly
	Working mechanism	Rigid	Foldable
Material	Source	Locally available	Locally available
	Eco-friendly	No	Yes
Economy	Module cost	≈ Rs. 164,560/per structure	≈ Rs. 10,000.00/per module
	Transportation cost	Rs. 20.00/Km	Rs. 20.00/Km
Services	Toilet	With shelter	E-toilet units
	Drinking water	Well	BASUDHA water tank
Maintenance	Hygiene	Free from pest attack and climatic condition	Free from pest attack and climatic condition
	Repair	Possible by changing the parts of the structure but not the economy	Possible by changing the subunit

Table 4 Cost of material used for temporary portable shelter

Sl. no	Material name	Price/piece (a)	Requirement (in number)/unit (b)	Cost (a*b)
1	4″ dia bamboo	Rs. 100/piece	10 nos	Rs.1000/-
2	2″ dia bamboo	Rs. 50/piece	3 nos	Rs.150/-
3	2–5-mm thick GI flat bar	Rs. 488/kg	118 kg	Rs.5664/-
4	Jute	…	…	Rs.2500/-
5	Miscellaneous	…	…	Rs.686/-

camping tents and yurts, which are simple and easy to erect and dismantle [21]. The layout of the shelter is dependent on the post-cyclone climatic situation to shield its inhabitants from threats and unpleasant environmental conditions. The design would not apply to areas that endure water-logged conditions and strong winds for long periods, since it is mostly intended for temporary settlement. With few modifications in the materials, the shelter may serve as a permanent structure.

5.2 Material Factor

The material parameters for the shelter include the quality, cost, suitability, durability, local availability, local knowledge on the effective use of the materials, and the market value. The materials are also required to have a very low environmental impact [22].

5.3 Economy Factor

Money becomes a critical parameter during any disaster as these situations experience higher requirements of physical and monetary resources while there is an acute shortage of both. In the context of the material and fabrication, it is of utmost importance to ensure that the cost is minimum. Additionally, as transportation also adds to the module cost, these modules are required to be either locally produced or transported in larger numbers to maintain the costs to a minimum (Table 4).

Cost of one module type: Rs.(1000 + 150 + 5664 + 2500 + 686): Rs. 10,000/-
Transportation cost: Rs. 20/km.

5.4 Maintenance

The shelter shall be built in such a way as to ensure that all the structural systems/mechanisms and their corresponding materials perform properly under the

climatic conditions intended for use. The durability of the structure and expected life spans of the materials in the context of the subjected conditions must be taken into consideration before the design. This minimizes the occurrence and costs of repair and maintenance [23]. Furthermore, the parts that require frequent repair or change must be identified based on the nature of use as well as the climatic conditions they will be subjected to. Such parts must be made of readily available materials and require basic tools for servicing.

6 Conclusion

In the event of any disaster, shelters are necessary for normalizing the day-to-day lives of the impacted and displaced populace. Lack of adequate shelter during any disaster results in an increase in diseases and negativity. Moreover, loss of house implies loss of one's identity, safety, and privacy. The prototype presented in this paper helps in normalizing the lives of the victims after the landfall of cyclones by providing much-needed safety and privacy and resolving the looming depressive situation. The prototype design is quick to erect and dismantle as required by the situation. Furthermore, the prototype must be suitable to be used as a permanent structure for housing, tourist activities, and shops with few modifications upon requirement shops after the reconstruction phase of the disaster. This is exploratory research to identify the locally available materials and understand their respective physical properties for the suitability of structural requirements of the prototype. Also, it includes the possible structural systems and mechanisms to make it fit for assembly and dismantling. Further study is required for the practical application of the identified structural system/mechanism for the prototype along with the corresponding materials, such that it is suitable and effective for quick assembly and dismantling in the post-disaster and post-reconstruction phase uses.

References

1. Middle East Institute Homepage. https://www.mei.edu/publications/learning-deaths-disasters-case-odisha-india#_ftn2. 09 Jun 2016
2. National Cyclone Risk Mitigation Project (NCRMP) https://ncrmp.gov.in/
3. National Disaster Management Authority, Cyclone Page https://ndma.gov.in/en/2013-05-03-08-06-02/disaster/natural-disaster/cyclones.html. 03 May 2013
4. Source: Author: Ipsitaa Priyadarsini Das.
5. NCRMP Cyclone and their impact. https://ncrmp.gov.in/cyclones-their-impact-in-india/
6. Special Relief Commissioner (2013) Memorandum of very Sever cyclone. Government of Odisha, Bhubaneswar
7. Government of India (2017) Report: State disaster management plan, OSDMA Bhubaneswar
8. Government of Odisha (2018) Report: disaster response, management & mitigation plan-2018, Bhubaneswar

9. Thattai DV, Sathyanathan R, Dinesh R, Kumar LH (2017), Natural disaster management in India with focus on floods and cyclones. In: IOP conference series: Earth and environmental science 80: International conference on civil engineering & infrastructural issues in emerging economies, p 4
10. Mohapatra PR (OAS-I(SB)) Deputy Relief Commissioner of OSDMA, Odisha (Interview)
11. Joakim E Post-disaster recover and vulnerability. University of Waterloo, p 5
12. Geipel R (1982) Disaster and reconstruction: the Friuli (Italy) earthquakes of 1976. George Allen & Unwin Publishers Ltd., London
13. Peacock WG, Dash N, Zhang Y, Van Zandt S Post-disaster sheltering, temporary housing, and permanent housing recovery
14. Turton SM, Dale A (2007) An assessment of the environmental impacts of cyclone Larry on the forest landscapes of northeast Queensland, concerning responses to natural resource management issues in the aftermath report submitted to the Report by Bureau of Meteorology. http://rrrc.org.au/wp-content/uploads/2014/06/493-JCU-Turton-Dale-2007-An-assessment-of-the-environmental-impacts-of-Cyclone-Larry.pdf
15. Kell C (2019) Initial environmental issue—Cyclone Idai. Cyclone Idai initial environmental summary—Mozambique
16. Satapathy S (2009) Psychological care in disaster management: a training of Trainers (ToT) Module. NIDM Ministry of Home Affairs, New Delhi, Module 1.1, pp 9–32
17. Del Grosso AE (2012) Deployable structures. Adv Science and Technology, 122 (2012).
18. Doroftei I (2014) Deployable structures for architectural applications—a short review. Appl Mech Mater 233
19. Jermyn E Deployable structures. https://evajermyn.com/2012/05/28/deployable-structures/. 28 May 2012
20. Maden F, Korkmaz K, Akgun Y (2011) A review of planar scissor structural mechanisms: geometric principles and design methods. Arch Sci Rev 246
21. Agots (2007) Temporary demountable structures: guidance on procurement, design and use. London
22. Bashawria A, Garritya S, Moodleya K (2014) An overview of the design of disaster relief shelter. Elsevier
23. Johnson C (2007) Strategic planning for post-disaster temporary housing. Disasters
24. Cambridge Dictionary (2019) Disaster. https://dictionary.cambridge.org/dictionary/english/disaster
25. Government of Odisha (2013) Rapid damage & needs assessment report India cyclone Phailin in Odisha Bhubaneswar (December 2013)

An Explorative Study on Material Feasibility for Relief Shelter for Refugees

Ziya Sameer Mohamed and Shanta Pragyan Dash

Abstract There has been an unprecedented growth in the refugees' crisis due to humanitarian emergencies like countries' political situation, climate change, and related natural disasters. The report of United Nations High Commissioner for refugees 2018 stated that there has been a rapid increase in the displaced population from 43.3 million to 70.8 million between 2009 and 2018. In this regard, the role of refugee shelters plays a salient role in providing housing to these homeless. International discourse has increasingly focused on the unique way in which displaced people live in refugee shelters. The material for construction is the major challenge to accommodate the number of people with varied weather conditions. Hence, it is imperative to explore different kinds of materials that can be appropriate in the process of designing sustainable refugee shelters. The aim of the paper is to explore different kinds of materials that are competent in designing a viable shelter without compromising with the comfort and aspirations of the users. The various materials were selected based on diverse parameters; a model was developed utilizing the material which was simulated (using Sefaira software) to test how effectively the material would serve in the given region. The results aided in interpreting the optimum ranges within the dwelling for adequate thermal comfort of the users. This study, therefore, suggests recommendations to support the design of spatial and architectural solutions for shelter design for refugees with suitable material selection during the emergency approach.

Keywords Refugee shelters · Refugees' crisis · Viable shelter · Thermal comfort · Shelter design

1 Introduction

The unique form of human habitation faced by internally displaced persons in refugee camps has received growing attention from international discourse [5, 6, 21] (Alnsour and Meaton 2014). The exact conceptualization of the refugee camp space is not

Z. S. Mohamed (✉) · S. P. Dash
Manipal School of Architecture and Planning, MAHE, Manipal, Udupi, Karnataka, India

widely agreed upon. It has been defined as temporary, seasonal, city camps, semi-durable, "between conflict and city"-created spaces [5], which plays a formative role in the migration account of residents (Stevenson and Sutton 2011). In refugee camps, the living spaces are placed on a continuum between the two major claims. On the one hand, there is an argument that the refugee camp is a temporary place built for resettlement. International organizations and NGOs also make this claim. When looking at camp development guidelines and handbooks issued by the major international entities such as the UNHCR (UNHCR Innovation 2015), this role surfaces with transparency. The sense of a degree of constancy is on the other hand. The fundamental configuration and purpose of refugee shelters lacking alterations [62, 63] have been considered in UNHCR's solutions for the establishment of dwellings. This is not a deliberate policy; however, this could be an accidental outcome of a decision taken on strictly practical and economic grounds. There is a growing rhetoric, wherein refugee camps are established as places that steadily become indelible associations of daily life, social life, processes, and power systems [5, 6] (Stevenson and Sutton 2011). This research also discusses whether, as often caricatured by non-governmental organizations and humanitarian organizations, refugees living in camps are just momentarily transitional communities, or whether these refugee settlements congregate in a transitional intangible place that integrates the interim characteristics of an ecosystem and gradually grows into an irreversible gentrified and community infrastructure, an ambiguous community.

1.1 Objectives of Research

The significance of refugee camps in today's world cannot be under-emphasized [59]. Despite the resolutions carried out by the authorities of diverse regions, as of 2019, according to the United Nations High Commissioner for Refugees, there are over 79.5 million individuals who have been uprooted from their homes, amid which 26 million individuals are refugees [60] as shown in Fig. 1. These refugees require timely aid in terms of shelters. The main issue with these shelters is that they are unreliable in many cases. They are unable to cater to the users of all age groups and, hence, fail [20]. It is a renowned fact that the durability of the shelters depends on the materials used [27]. Hence, the objective of this research is to interpret materials and their properties relevant for modeling a viable refugee shelter such as the various grades of materials that can endure the given climatic condition without wearing out. It is also to understand the reason behind the perpetual failures of the shelters to accommodate the needs of the users. This study is an explorative analysis of feasibility of materials in the given context i.e., Bangalore, Karnataka, India. The outcome of this research is to explore different materials and select one which is feasible with respect to Bangalore and to understand its properties and behavior when it is used as a primary material in construction of a refugee shelter.
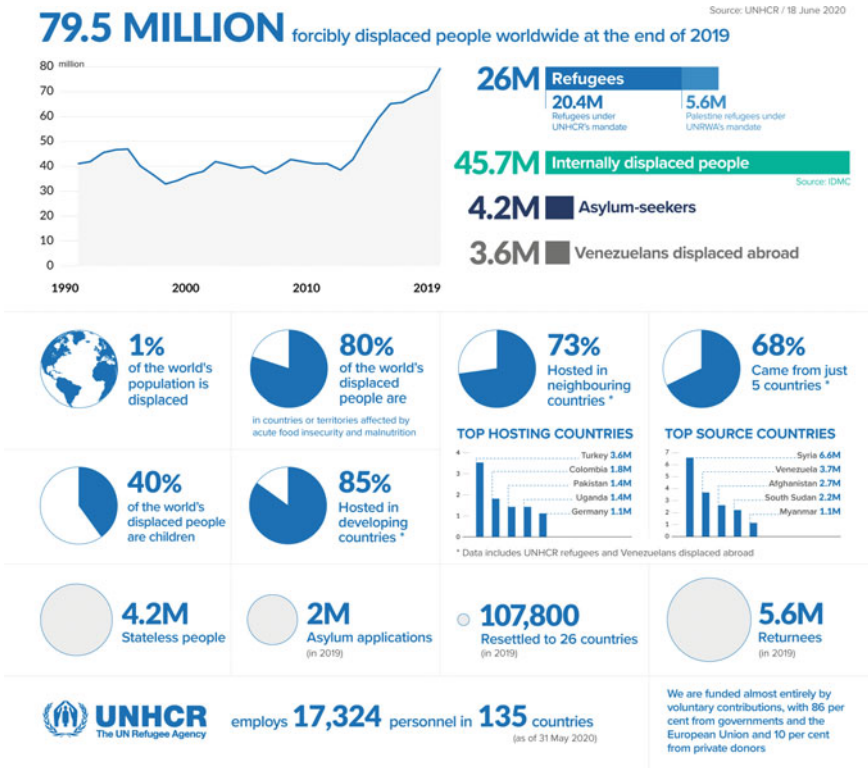
Fig. 1 Number of displaced people at a glance (unhcr.org)

1.2 Background Study

With respect to Indian context, refugees from Sri Lanka, Burma (now Myanmar), Bangladesh primarily live in Raichur, Northeast Karnataka [43]. Originally, the government did not help them when the refugees arrived [55]. But now, the government has agreed, after years of hardship, to provide them with necessities such as shelter and food [55]. Four camps, namely RH1, RH2, RH3, and RH4, which are an insulting acronym for rehabilitation camps, were provided to them. Every camp has its own school, supply shops, tea and snack shops, meat stalls, milk booths, and electricity. They lack public transportation in these camps. A two-wheeler is owned by any family [55]. A big concern in these camps is drinking water. Since there are no individual or public water connections, for everyday uses such as cooking, washing, and bathing, people have to get water from the nearest ponds [55]. In the summer, people have to compete for water as the pond water is allotted conforming to the household size. Initially, these refugees had been held in military tents for two years. Another big refugee settlement in Karnataka is in the Bylakuppe district, where many Tibetans have settled [55]. Refugee shelters have become entities that

range from the most transitory tent dwellings to constructing temporary settlements (UNHCR). These are developed as interim accommodation for refugees who have fled or lost their dwellings following a dispute or natural catastrophe. A refugee is anyone compelled by oppression, military conflict, or terrorism to leave his homeland. An individual who has been given the status of refugee on grounds of ethnicity, faith, allegiance, political viewpoints, or participation in a specific society association has a strong perception of tyranny (UNHCR).

1.3 Current Scenarios of Refugees

Prior to designing any shelter, the prevailing plight of the users always needs to be accounted for [30] (UNHCR). The present scenario of the refugee is such that most of these individuals have lost their identities and rights because of the constant destabilization [34]. Refugees are constantly treated as a hinder toward the host country, owing to which they experience dilemmas with equality [45]. The host country fails to provide vital shelter and necessities to the refugees since there are not laws in play that administer these situations, and hence, as a result, most of the refugees are stripped of essential shelter and food [14, 34, 35]. They generally criticize refugees for exhausting basic resources available and utilizing them for their demands [45]. They are regularly faulted for lesser job opportunities since most of the refugees resolve to move to the metropolis in pursuit of housing, which they have been stripped off for so long [27, 28]. This again contributes to some people believing that they should not host refugees, which prompts bigger issues like major displacement of an immense population [45]. In some instances, hosting refugees does impact the country in varied ways, such as culturally and environmentally [45]. Since they move in from diverse countries, it is pretty natural to have a socio-cultural conflict that alters people's equitably (UNHCR). So, it is imperative to make them feel welcomed and provide them with a sense of security. As far as humanity is been around, life has been about rebuilding, but as time passed, there were newer reasons for rebuilding; wars and political catastrophe being a few of them [22]. Since the image of refugees are tainted due to myths, designing for refugees should not be regarded as a task for their stature, but for them as humans, the design should cater to them as the user and not what they have turned into because of their transitory loss (Muggah and Abdenur 2018). The design should be such that people can continue their life as easily as they can post-trauma. As distant as flatback solutions go, they are economical and affordable but are not unquestionably viable or long-lasting. In some cases, like Dadaab refugee complex of Somalia, these shelters went from being a temporary one to a permanent dwelling [11]. Most of the refugees in the mentioned shelter have been residing there for almost 20 years (Figs. 2 and 3).

Fig. 2 Dadaab refugee complex, Somalia (archdaily.com)

Fig. 3 Mapping of refugees in India (hindustantimes.com)

THE ONES WHO FLED

Apart from these, who registered with the UNHCR, other refugee communities in India include Tibetans and Sri Lankans

59.5 million
individuals were forcibly displaced worldwide as a result of persecution, conflict, generalized violence, or human rights violations by 2014 end

8.3 million
persons more were displaced in 2014 than in 2013 (51.2 million). This is the highest annual increase in a single year

MAPPING REFUGEES
Figures courtesy UNHCR

Till end of August 2015
● Refugee ● Asylum seekers

SAUDI ARABIA • IRAQ • IRAN • AFGHANISTAN • PAKISTAN • CHINA • NEPAL • INDIA • MYANMAR • SOMALIA

SOMALIA	AFGHANISTAN		MYANMAR	
449 200	10,330	1,930	15,496	2,899
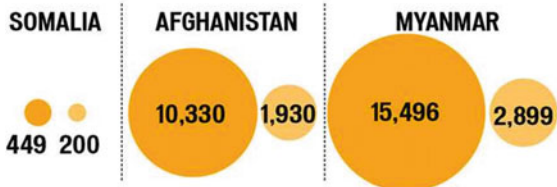
1.4   Material Consideration for Refugee Shelters

As far as flatback solutions go in terms of materials, most of the shelters are made out of tarps and PVC sheets. There is also been a lot of deliberation in terms of digitally fabricated materials [64], but it is not widely used in the contemporary world as it often tends to be expensive. Materials like recycled skis have been successfully used in designing and constructing shelters [32]. They generally made these shelters earthquake-resistant wherever demanded. In terms of materials, it can be considered that these shelters do not recognize the thermal point of view of the materials, neither the durability of the same. It should be mentioned that some of these shelters exceeded exceptionally in terms of catering to the thermal comfort of the users, but they did not come in economical, they were often very costly owing to which merely a selective few got shelters, and the others had to spiral back to the conventional tarp tents provided by the host country. Most of the materials used were not sustainable, fireproof, waterproof, or weather-resistant. The materials used were often lightweight [31]. Since not adequate recognition was committed to the materials in the design process, these shelters dealt with a pile of complexities such as over-heating, lack of thermal comfort, and enhanced solar gain. When plastic was adopted as a rudimentary material for refugee shelter, it lacked thermal protectivity as well as sustainability [19]. Even though conventional materials are utilized, alternative materials have invariably been around as an adversary which guarantees the users a longer durability and also confirms as a cost-effective approach of constructing shelters. In one of the refugee camps, the skin of the shelter was composed of lamented membranes, and the mere form of stability given was through enhancing pipes and straps [8]. Whereas the shelters that were constructed from cardboard tubes, corks and OSB boards proved to be much more stable than the other shelters [46]. The prime obstacles encountered during selection of materials are—high cost and delivery delay; hence, this just crystallizes the point that locally procured materials are the only way to cut the cost down and obtain instant material supply without any setback. In many instances, the shelters are not easy to assemble and, hence, call for technical assistance, which boosts the labor cost of the project, and hence, most of the projects end up being costly. Owing to this, many people have to degenerate back to tents for housing. There is an evident research gap in identifying the critical point of failure in refugee shelters with respect to materials which need to be paid attention to in order to create a viable/sustainable refugee shelter. There is a lack of understanding in terms of materials as none of the shelters provides both affordability and sustainability at the same time.

2   Methodology

The research beliefs of this study is based on understanding the properties of different materials with respect to the specified region and to select a material feasible in the

same provided that it complies with all the specifications required for an ideal refugee shelter. To understand this further, a comprehensive study has been carried by going through various literatures with respect to refugee shelter materials which helped in pinpointing the underlying issues and the research gaps present within them. They were compared on different parameters, both in terms of shelter design and materials. This suggested the materials that led to the failures of certain shelters, as well as the reason behind the failure. Once filtered thoroughly, the material that was presented was analyzed for further research. An extensive search was undertaken on these materials to evaluate if the selected material would thrive in the given region. They were compared on basis of different parameters with respect to the region. Once the material was selected based on diverse parameters, a model was developed utilizing the material which was simulated (using Sefaira) to test how effectively the material would serve in the given region. It was mainly simulated for thermal comfort, daylighting, and ventilation. Once the results were generated, they aided in interpreting the optimum ranges within the dwelling for adequate thermal comfort of the users. Based on the results, formulation of guidelines is done. These are a series of guidelines drafted for material selection and shelter designing. The conclusion is later drawn from the simulation and guideline, and it also suggests the scope for further research.

3 Literature Review

Refugee shelters in India are not unheard of. They have been around ever since the partition of India (Simbal Camp, Jammu) and indeed prior to that (UNHCR). Even though it is a well-known fact that most of the camps are established for people who are driven to surrender their countries/place of birth due to military conflicts and political warfare, there are a handful of camps that are set up for people who have lost their households due to natural calamities [27]. Regardless of the reason of displacement, these refugees are generally shunned aside when they require help. There are many problems faced by these refugees in terms of livelihood, land conflicts, social issues, and poverty [41]. In case of displacement due to natural disaster, the refugees are forced to face additional problems like debris removal, drainage, and land stabilization. Most of the shelter designs are monotonous and, hence, do not consider inclusivity as part of the design. The needs of pregnant women, elderly, and disabled people are often overlooked [20]. They are usually deprived of basic necessities like private latrines, provision of water, and safe disposal of excreta [20]. When the situation gets rough for the refugees, they go on hunger strikes. This clearly shows that there is no durable solution for refugees [35]. They will always be chained to dirty and over-crowded camps. New materials like compressed stabilized earth blocks are being used to fight the high cost and low-durability factors of refugee shelters. Since they are made of local soil, they cut down transportation cost as well [2]. The only back draw being that they are not necessary durable in certain weather conditions. They are sustainable in nature and, hence, good for the environment. They

are basically used to achieve resilience through sustainable technology [3]. Materials like galvanized steel and steel in general are also widely used for the construction of refugee shelters (Sphere 2018).

3.1 Case Studies

In the case of Gujarat earthquake that occurred in 2001, the shelters were constructed at a large scale. They were interim, transitional in nature. It was a low-cost design developed by using low walls as well as bamboo framed and grass-thatched roof [48]. One of the cons of such a construction is that the roof is not very stable and may collapse in case of another earthquake. Whereas in the case of the 1977 cyclone of India, the shelters were made of substantial materials such as cement, concrete, brick, and stone. Even though materials with higher tensile strength were used here, the shelter failed in terms of completion at time due to shortage of man supply for the intricate construction which led to delay in the completion [50]. In case of the *1971 conflict of refugees in India*, the Camp Barasat was designed after the civil war in Bangladesh (then East Pakistan) as it led to a displacement of almost 10,000,000 people. It was designed in phases. During the first stage of construction, shelters were made out of materials like thatch and bamboo [49]. In the later stages, materials like polythene sheets and corrugated tin roofing sheets were also used. Whereas in the *Ethiopia—2011—Sudanese conflict,* a preset shelter configuration (a tukul) was constructed. It was centered on the settlements the host community founded and resided in, distinct from the shelters, and the refugees were used to constructing. Construction training was undertaken as a result. The materials used in the construction of this shelter at Bambasi Camp were locally procured. Bamboo, grass, mud, and rope are few of the materials used [51]. The construction technique was such that the house was warm during the day time and cold during the night time. Grass was used for thatching the roof which led to an unstable roof [51]. The shelters created during the intercommunal wars in Myanmar are a great example of rapid construction which failed in terms of material selection. Materials that were locally accessible were used. The government tried to follow the guidelines laid down by Sphere handbook. Wooden bracings were used in most part of the construction [52]. Low-quality materials had to be utilized since bamboo was not in season during a certain period of construction which led to a very unstable shelter design. Due to the negligence in selection of materials, these shelters were not durable in nature [52]. Lastly, the shelter design at Azraq Camp was based on interlocking steel structures to protect against the severe weather conditions. The steel structures were easy to disassemble, transport, and then reassemble again. Since it was less technically complicated, it could be easily assembled by the refugee themselves. The roofing of the structure which was made out of inverted box rib corrugated sheets as it could not seal of rain or dust.

3.2 Case Study Analysis

The case study analysis in terms of shelter design and materials is done by comparing them against a set of different parameters as shown in Tables 1 and 2, respectively. When comparing the shelter designs, it was found that most of these shelters did not cater to the *privacy* needs of the users which led to problems. Most of these shelters used *locally procured materials* which led to a reduction in transportation costs. Due to lack of technical knowledge among the refugee population, some of these shelters took a *long time in terms of assembly* as people from the host country had to be hired for assembly. This added to the total sum of the shelter production. Shelters that did not include latrine facilities failed to cater to the user needs. Thermal comfort of the users was not paid attention to as some of the materials used in the shelters caused the interiors to overheat. Ventilation was always a problem in these camps as the materials would cause the shelter to overheat and without adequate ventilation, and the users always faced a tremendous amount of discomfort.

The comparative analysis in terms of materials discussed the various characteristics as shown in Table 2 of the following materials—bamboo, concrete, CGI sheets, grass, mud, nylon ropes, plastic ropes, plywood, PVC sheets, steel, timber.

According to the Sphere handbook 2018 and the UNHCR guidelines, the materials should be

1. Locally available.
2. Cost-effective.
3. Biodegradable.
4. Non-toxic
5. Energy-efficient.
6. Fire-resistant.

Table 1 Parameters for analysis in terms of shelter design

Assembly of shelter	Privacy
Cost	Size
Culture acceptability	Sustainability (pros)
Sanitation	Sustainability (cons)
Durability	Thermal comfort
Flexibility	Transportation cost
Material used	Ventilation

Table 2 Parameters for analysis in terms of materials

Conductivity	Insulation
Corrosion resistance	Strength
Cost	Thermal comfort
Durability	Water resistance
Fire resistance	Weathering resistance

7. Water-resistant.
8. Thermally efficient.
9. Durable.
10. Sustainable.
11. Recyclable.
12. Reusable.

The materials that satisfy the Sphere handbook 2018 and the UNHCR guidelines from the most to the least are as follows in accordance with Table 3 are.

1. Bamboo, steel—100%
2. Concrete, grass/thatch—75%
3. Mud, plywood, timber—67%
4. PVC sheets, CGI sheets—50%
5. Nylon ropes—42%
6. Plastic ropes—34%

4 Material Data Collection and Analysis

The primary data collection and analysis are done through designing prototype and simulating it based on different factors such as daylighting, ventilation, and energy efficiency. Simulation is a method of observational data gathering through the process of developing a model and then simulating them. Since the latter would be complex and costly, the experiments are conducted on prototypes rather than actual systems.

The secondary data for analysis are collected through various sources such as research papers, reports, archives, UNHCR books, and case studies. First, the required data are gathered and then codes are developed to classify the data by clustering them into relevant categories to analyze them conveniently. Next, coding of the relevant data is done by labeling specific groups with unique codes or labels to reduce the overlapping data. After tabulating them, observation of the data is done to review any similarities/differences in order to understand what each group is outlining. Finally, through abridging the data for a deductive approach, the data are summarized.

4.1 Material Feasibility

The following materials can be found in Bangalore for construction

1. Cement
2. Steel/TMT bars
3. Bricks
4. Concrete solid blocks
5. Sand
6. Ready mix concrete (RMC)

Table 3 Compatibility analysis of materials

	Bamboo	Concrete	CGI sheets	Grass/thatch	Mud	Nylon ropes	Plastic ropes	Plywood	PVC sheets	Steel	Timber
Locally available	✓	✓	✗	✓	✓	✗	✗	✓	✓	✓	✓
Cost-effective	✓	✗	✓	✓	✓	✓	✓	✗	✓	✓	✗
Biodegradable	✓	✗	✗	✓	✓	✗	✗	✗	✗	✓	✓
Non-toxic	✓	✗	✓	✓	✗	✓	✗	✗	✗	✓	✗
Energy-efficient	✓	✓	✓	✓	✓	✗	✗	✓	✗	✓	✓
Fire-resistant	✓	✓	✗	✗	✗	✗	✗	✓	✗	✓	✗
Water-resistant	✓	✓	✗	✗	✗	✗	✗	✓	✓	✓	✗
Thermal-efficient	✓	✓	✗	✓	✓	✗	✗	✓	✗	✓	✓
Durable	✓	✓	✗	✗	✗	✓	✓	✓	✓	✓	✓
Sustainable	✓	✓	✓	✓	✓	✗	✗	✓	✗	✓	✓
Recyclable	✓	✓	✓	✓	✓	✓	✓	✓	✓	✓	✓
Reusable	✓	✓	✓	✓	✓	✓	✓	✓	✓	✓	✓

7. Stone aggregate.

When talking about construction of refugee shelters, it needs to be noted that there are always children playing around contrary to the conventional building construction where only experts are present on site. Though concrete can be easily procured in Bangalore, concrete should be avoided for construction as it imparts harmful substances and also wears out the soil during the construction period. Steel construction does not require a lot of expertise, and it can be easily procured in Bangalore. It does not impart harmful substances into the environment and is sustainable in nature. In Bangalore's atmospheric conditions, both bricks and steel perform very well and are widely available. Steel construction is far more cost-effective, less labor-intensive to install, good for the environment, and more resistant to traditional shifts in humidity and temperature compared to brick structures. Once installed, compared with its brick equivalent, steel needs considerably less maintenance. In Bangalore, steel can be procured easily without much hustle. Ready mix concrete requires fast transportation as the concrete has a fixed workability time. While considering the traffic of Bangalore, it can be easily concluded that due the heavy traffic jams, the concrete will not reach the site on time. Comparing this inference to the literature case study inferences, it can be concluded that steel is the most suitable material for construction of refugee shelters in Bangalore.

The materials that satisfy the Sphere handbook 2018 and the UNHCR guidelines and are available in the region of Bangalore are stated below from the most to the least in accordance with Table 4 are.

1. Bricks, steel—100%
2. TMT bars—92%
3. RMC, concrete—75%

Table 4 Compatibility analysis of materials with respect to Bangalore

	Bricks	TMT bars	Steel	RMC	Concrete
Locally available	✓	×	✓	×	✓
Cost-effective	✓	✓	✓	✓	×
Biodegradable	✓	✓	✓	×	×
Non-toxic	✓	✓	✓	×	×
Energy-efficient	✓	✓	✓	✓	
Fire-resistant	✓	✓	✓	✓	✓
Water-resistant	✓	✓	✓	✓	✓
Thermal-efficient	✓	✓	✓	✓	✓
Durable	✓	✓	✓	✓	✓
Sustainable	✓	✓	✓	✓	✓
Recyclable	✓	✓	✓	✓	✓
Reusable	✓	✓	✓	✓	✓

Properties	Carbon Steels	Alloy Steels	Stainless Steels	Tool Steels
Density (1000 kg/m3)	7.85	7.85	7.75-8.1	7.72-8.0
Elastic Modulus (GPa)	190-210	190-210	190-210	190-210
Poisson's Ratio	0.27-0.3	0.27-0.3	0.27-0.3	0.27-0.3
Thermal Expansion (10-6/K)	11-16.6	9.0-15	9.0-20.7	9.4-15.1
Melting Point (°C)			1371-1454	
Thermal Conductivity (W/m-K)	24.3-65.2	26-48.6	11.2-36.7	19.9-48.3
Specific Heat (J/kg-K)	450-2081	452-1499	420-500	
Electrical Resistivity (10-9W-m)	130-1250	210-1251	75.7-1020	
Tensile Strength (MPa)	276-1882	758-1882	515-827	640-2000
Yield Strength (MPa)	186-758	366-1793	207-552	380-440
Percent Elongation (%)	10-32	4-31	12-40	5-25
Hardness (Brinell 3000kg)	86-388	149-627	137-595	210-620

Fig. 4 Mechanical properties of steel (efunda)

From the above, it can be concluded that *the materials that satisfy the guidelines and are easily available in Bangalore are steel.*

4.2 Properties of the Material—Steel

Overall, steel is tougher and stronger than its parent product, iron. Nevertheless, it is highly versatile and characterized by high tensile strength. Compared to other materials, the tensile strength of all grades of steel is high, but it varies greatly among steel types. The value at the low end is roughly 290 N/mm2; the tensile strength at the high end is as high as 870 N/mm2[1]. It is environment-friendly and would not decay into anything hazardous and contaminate the soil and other regions unknown. Renewable sources of energy (e.g., solar, wind, and hydro) make substantial use of stainless steel. The prevention of corrosion is another significant property.

Thermal energy of steel = 42.0 MJ/kg.

Energy in transportation of steel (tons) [production] = 42,000 MJ.

Energy in transportation of steel:

(a) 50 km = 50 MJ (b) 100 km = 100 MJ (Fig. 4).

---

[1] Sciencing.com/ properties and uses of steel.

4.3 Simulation

Basic requirements for a refugee shelter

1. Affordable, enabling certain necessary goods and services to be purchased by the family to live in comfort (Sphere 2018).
2. Livable, ensuring physical protection, secure and sufficient living quarters, accessibility to drinkable water, sufficient water, amenities for hygiene and sanitation (WASH), and preparation and storage of food (Sphere 2018).
3. Effective and functional, even for people experiencing limitations to mobility (Sphere, 2018).
4. Situated to provide access to possibilities for livelihoods and vital community services (Sphere 2018).
5. Standard living space of 3.5 m^2 per person, excluding kitchen space, washing area, and sanitation services. In cooler environments or dense urban areas where inbuilt kitchen space and washing and/or basic sanitation are included, 4.5–5.5 m^2 of living space per person (Sphere, 2018).
6. The internal floor-to-ceiling height at the highest point is at least 2 m (2.8 m in hot weather) (Sphere 2018).
7. ECBC requires buildings to maintain a degree of illuminance between 100 lx and 2000 lx for the minimum floor area percentage depending on the form of floor area (ECBC 2017).
8. Increased air flow on a specific plane is achieved by maintaining the opening sill height at 85% of the critical height (such as head level) for the following recommended occupancy levels: 0.75 m for sitting on a chair, 0.60 m for sitting on a bed, and 0.40 m for sitting on the floor (ECBC 2017).
9. The maximum air movement in the work area is when the height of the window is 1.1 m (ECBC 2017).

Framework for simulation.

The following factors affect the thermal comfort of the users [39]:

1. Temperature
2. Ventilation
3. Lighting
4. Humidity.

Hence, the simulation is being done to understand the efficiency of steel as a material and if it can provide optimum thermal comfort to the users as well as maintain other parameters such as indoor temperature, daylighting, humidity, sanitation which are the main problems/point of failures of refugee shelters.
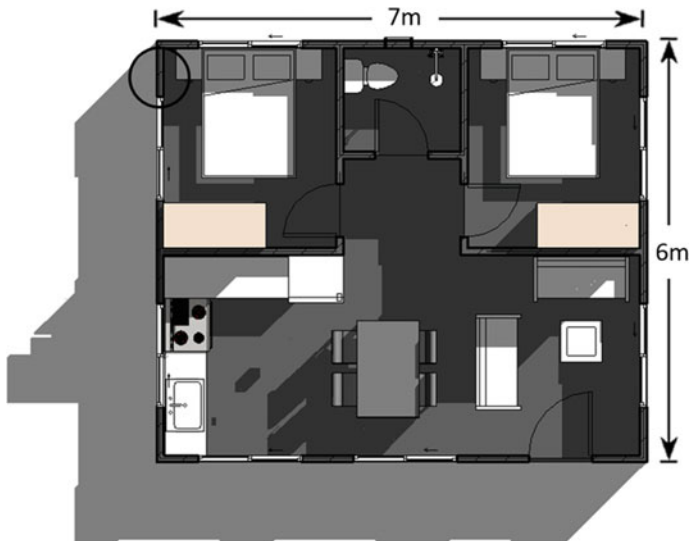
Prototype

Thermal comfort

The structure is well-insulated which allows the structure to use minimum heating and cooling energy to achieve thermal comfort. Overall, the house has achieved energy efficiency by incorporating various techniques such as natural ventilation, insulation of the structure, low-cost materials, and daylighting. As seen above, thermal comfort is achieved when the operative temperature is between 15 °C to 30 °C for more than 85% of the occupied hours (Figs. 5, 6, 7, 8, 9, and 10).

    i.All zones passed.

    ii.Worst zone: floor 1, P04 (1.4% over target).

Fig. 5 Framework for simulation

Fig. 6 Plan of the proposed prototype

Fig. 7 Material joinery
detail
(metalarchitecture.com)

Fig. 8 Metal panel joinery
(J.-H. Song et al./energy and
buildings 127 (2016)
138–158)
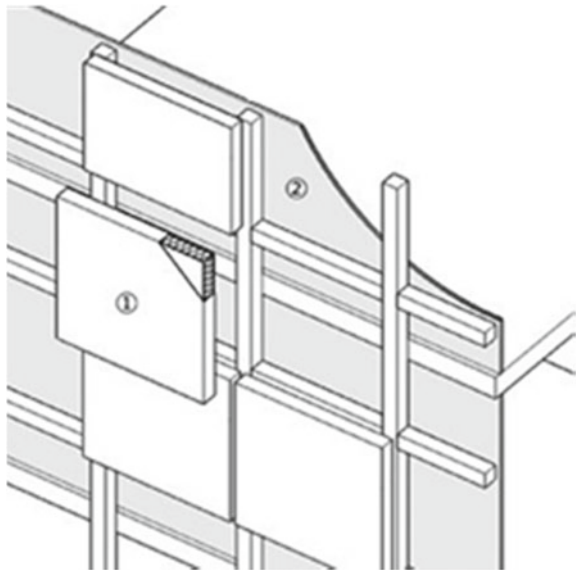
Ventilation/ wind

See Figs. 11, 12, 13, 14, 15, and 16

Maximum airflow is achieved by maintaining the sill height at 0.6 m, whereas the maximum air motion achieved by keeping the height of the windows is as 1.2 m. Methods like cross-ventilation have been used to increase natural ventilation in the house. The house receives ample ventilation when it is oriented in such a way that the front façade of the house faces the windward side as seen in Fig. 15.

Fig. 9 Metal panel joinery (J.-H. Song et al./energy and buildings 127 (2016) 138–158)

① Steel truss

② Metal panel

④ Steel truss fixing unit

③ Vertical and horizontal joints between metal panels
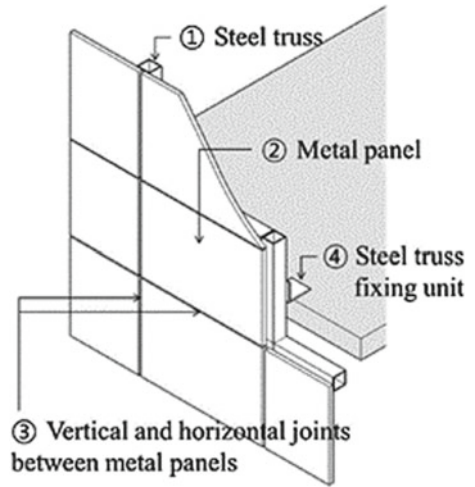
Fig. 10 Isometric view of the prototype
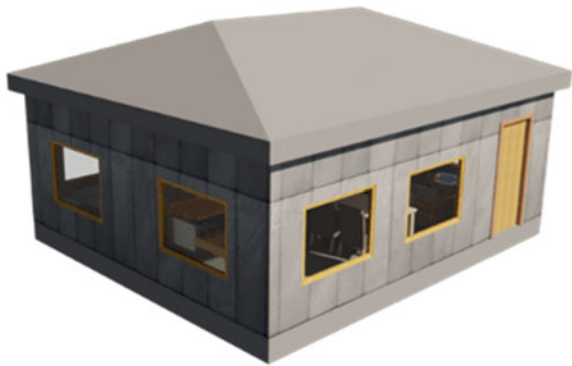
Fig. 11 Plan divided into different zones

P01

P04

P02

P03

Floor 1, Zone P01

Space Use Values: Residential (Plug...

Comfortable: 90.2% hrs

Too Hot: 9.8% hrs

Too Cold: 0.0% hrs

✓ Passed
5.2% over target

Floor 1, Zone P03

Space Use Values: Residential (Plug...

Comfortable: 88.2% hrs

Too Hot: 11.8% hrs

Too Cold: 0.0% hrs

✓ Passed
3.2% over target

Floor 1, Zone P02

Space Use Values: Residential (Plug...

Comfortable: 89.2% hrs

Too Hot: 10.8% hrs

Too Cold: 0.0% hrs

✓ Passed
4.2% over target

Floor 1, Zone P04

Space Use Values: Residential (Plug...

Comfortable: 86.4% hrs

Too Hot: 13.6% hrs

Too Cold: 0.0% hrs
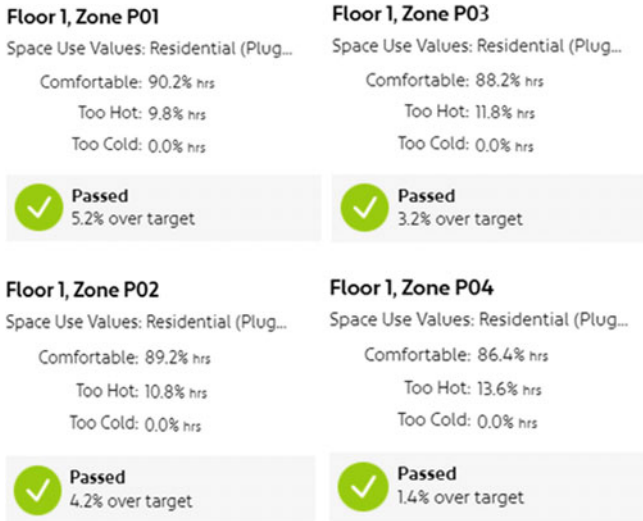
✓ Passed
1.4% over target
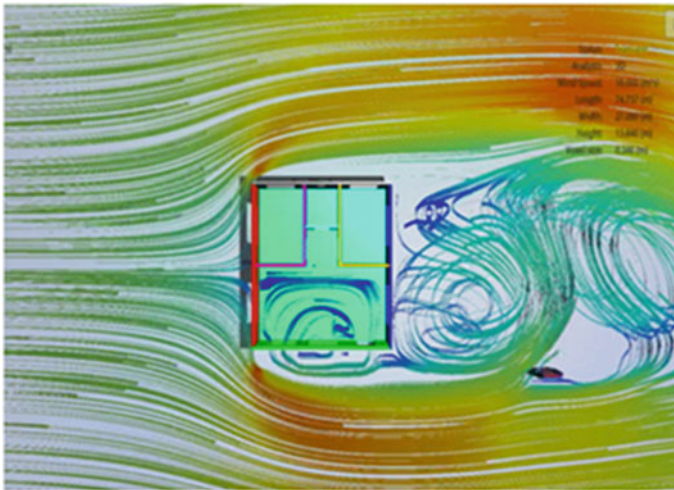
Fig. 12 Results of the simulation

Fig. 13 Orientation I

Daylight

The common areas and both the bedrooms receive an average of 300 lx of daylight. The house is well-lit during the day time which makes it energy as well as cost-efficient. Optimum daylight (200 lx—600 lx) is achieved by placing large openings throughout the house (Figs. 17 and 18).
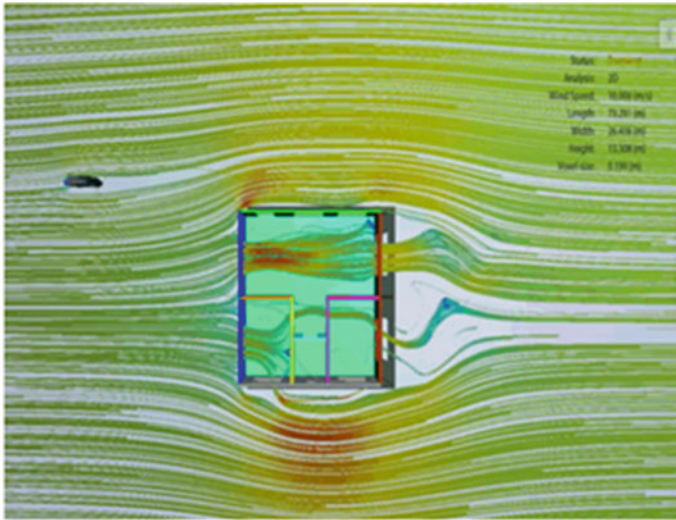
Fig. 14 Orientation II
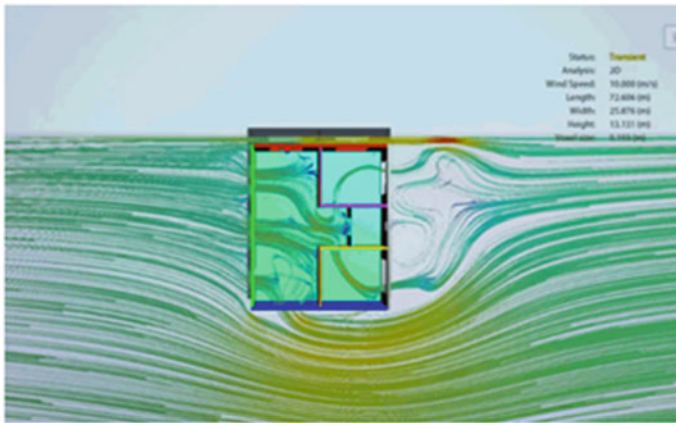
Fig. 15 Orientation III

Lux levels on the first of every month are measured at 0.55 m above the floor plate. Time does not take into account daylight savings time. Bedroom I achieves maximum daylight between June and August, whereas Bedroom II achieves optimum daylight throughout the year. The kitchen attains optimum daylight from November to February. The bathroom is underlit due to the absence of openings other than the vents.
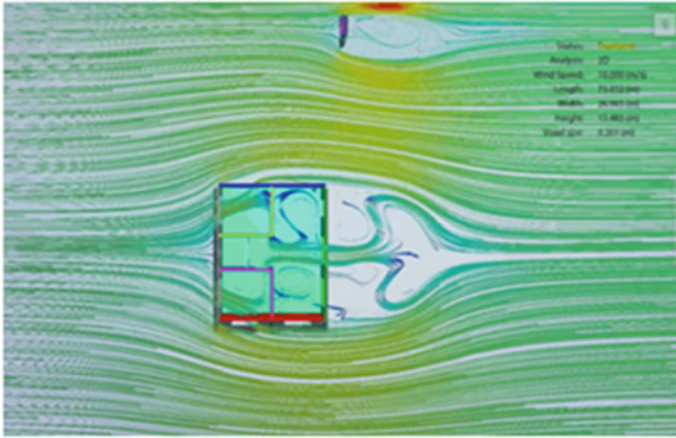
Fig. 16 Orientation IV
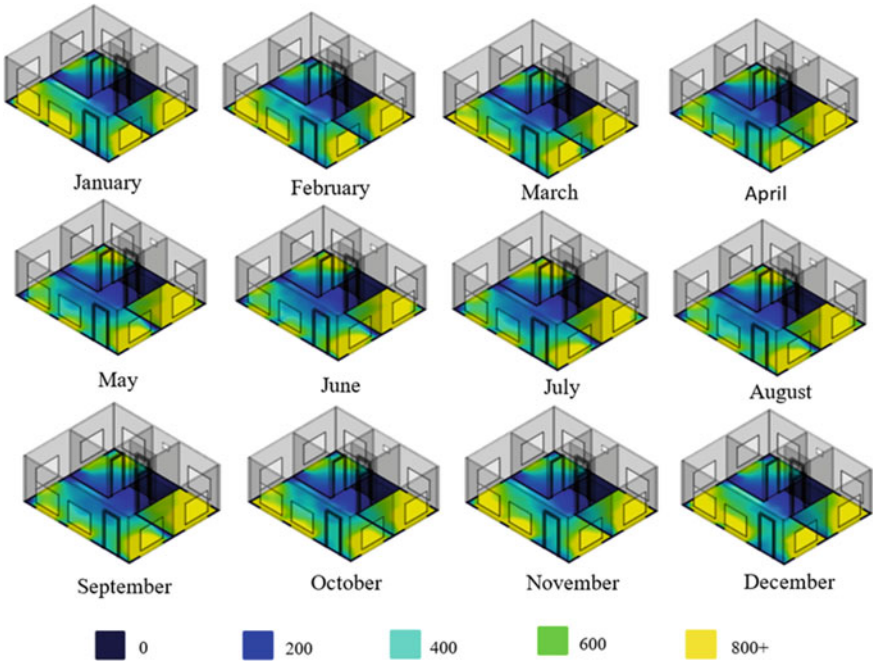
Fig. 17 Daylight received from January to December

Fig. 18 Daylight graph
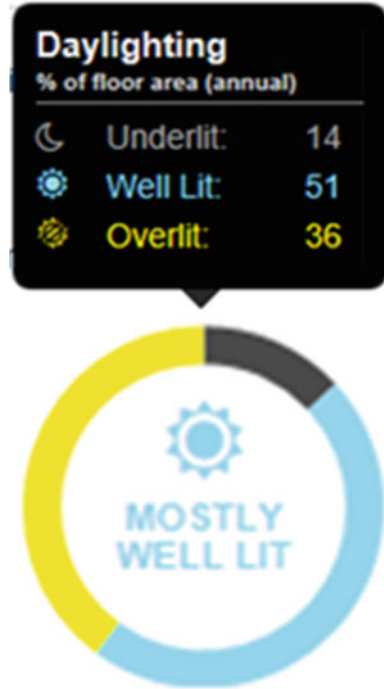
5 Formulation of Design Guidelines

The following guidelines have been formulated in order to create a viable refugee shelter. These guidelines include both technical and general information on as to how to create a durable shelter. The guidelines talk about the grade of material to be chosen, the material selection criteria in general as well as the technical details like the height of the sill, and the dimensions of different openings present in the house.

1. The optimum temperature within the house should be less than 32 °C for the comfort of the users.
2. Materials used should be locally procured in order for the shelter to be cost as well as energy-efficient.
3. The materials used for construction should be socially and culturally acceptable.
4. The material used should be lightweight for the ease of construction and transportation.
5. If the materials are locally procured, it helps in decreasing the transportation cost which in turn decreases the embodied energy making it energy-efficient as it would have a low impact on the environment.
6. The material used should be fire and weather-resistant.

7. The embodied energy of the material should be low so that it leads to less environmental impacts.
8. The material used should result in a higher durability of the shelter and should efficiently eliminate any problems such as water seeping through the walls and over-heating of the house.
9. The floor-to-ceiling height should be at least 2.8 m in hot climatic conditions.
10. Methods such as cross-ventilation help in bringing in natural wind which results in a reduced use of mechanical ventilation.
11. Large openings within the house are encouraged as it would result in an increased amount of natural ventilation.
12. The optimum temperature within the house should be less than 32 °C for the comfort of the users.
13. Materials used should be locally procured in order for the shelter to be cost as well as energy-efficient.
14. The materials used for construction should be socially and culturally acceptable.
15. The material used should be lightweight for the ease of construction and transportation.
16. If the materials are locally procured, it helps in decreasing the transportation cost which in turn decreases the embodied energy making it energy-efficient as it would have a low impact on the environment.
17. The material used should be fire and weather-resistant.
18. The embodied energy of the material should be low so that it leads to less environmental impacts.
19. The material used should result in a higher durability of the shelter and should efficiently eliminate any problems such as water seeping through the walls and over-heating of the house.
20. The floor-to-ceiling height should be at least 2.8 m in hot climatic conditions.
21. Methods such as cross-ventilation help in bringing in natural wind which results in a reduced use of mechanical ventilation.
22. Large openings within the house are encouraged as it would result in an increased amount of natural ventilation.
23. The shelters should ideally be accessible by all age groups; hence, the design should be inclusive in nature.

6 Conclusion

Most of the shelter designs in today's world lack the majority of the specifications which shape an ideal refugee shelter. However, because of the collapse of such camps and the demand for a more viable housing solution, these camps must be thought about as settlements rather than just temporary shelters. Once it gets identified as a makeshift shelter, it loses its essence and, hence, ends up being just another shelter constructed without any judgment or reasoning. As recognized in a majority

of the case studies, these shelters fail miserably when thermal comfort, sanitation, ventilation, and alternative specifications are taken into deliberation. These are the principal obstacles to be tackled while designing/constructing any refugee shelter.

Through the simulation, it can be established that steel as a construction material is feasible in the region of Bangalore, Karnataka, India, for the construction of refugee shelters. Steel can also be utilized as an elementary construction material for refugee shelters in regions which have similar geographical conditions like Bangalore. Steel in general is a remarkably potent material. It possesses great tensile strength and durability compared to other construction materials. It is sustainable in nature as well. The users desire a series of factors for viable housing. Through the simulation performed, it can be stated that the material in study–steel, satisfies the norms for all of these specifications, i.e., thermal comfort of the users, natural ventilation, and daylighting. The prototype used for simulation consisted of a living area, a dining area, a kitchen, two bedrooms, and one washroom. Due to the providence of a private unit of washroom for a family of 6–8 people, the model also complies with the need for sanitation of the users.

Hence, this research upholds the fact in general that refugee shelter designs should not be taken casually and that these shelters demand to be carefully thought about in terms of discrete criteria–material being one of the most prominent ones. The scarcity of exploration in the field of materials pertaining to refugee shelters with reference to their surroundings has contributed to the deterioration of several shelters in the contemporary world. Therefore, this research suggests radical advances toward the concept of refugee shelter study in terms of materials so that, henceforth, the shelters devised for the refugees are not just tarp tents or housings, but a shelter that is feasible in nature and durable for the comfort as well as the well-being of the users.

References

1. (n.d.)
2. (CRS), CR (2019) Developing locally affordable hazard resistant house
3. (CRS), CR (2019) Introducing sustainable technologies creating resilient shelters
4. Abdenur RM (Jul 2018) Refugees and the City the twenty-first-century Front Line. Carol Bonnett
5. Agier M (2002) Between war and city: towards an urban anthropology of refugee camps. SAGE Publications
6. Agier M (2008) On the margins of the world: the refugee experience today
7. Akcapar SK (2018) South Asian refugees in India
8. Alessandra Zanelli CM (2019) Innovative refugee shelter design with pneumatic sandwich structure. Maggioli Spa with License Creative Commons
9. Ali DSZ (2018) A study of affordable refugee housing solutions. Ain Shams University, Urban Design and Planning
10. Ali DSZ (N/A) A study of affordable refugee housing solutions
11. Alshoubaki H (2017) The temporary city: the transformation of refugee camps from fields of tents to permanent cities
12. Andini, S. R. (2017). *Analysis of socio economic conditions and migration patterns of migrant settlements in Bengaluru.*

13. Apel S (2019) The role of sustainable design in the current refugee crisis
14. Azizi S (2017) The legal regime on the protection of women refugee with special reference to India, U.K and US
15. B, D. B. (2018). *Labour Migration in Karnataka - Some Issues and Challenges.*
16. B, DB (2019) Migration of agricultural laborers in Karnataka—a study
17. Bartolacci J (2014) How refugee camp architecture is capturing the power of shade
18. Bradley M (Mar 2019) Resolving refugee situations seeking solutions worthy of the name. Carol Bonnett
19. Brownell E (2019) Better shelter
20. Bruijn Bd (2009) The living conditions and well-being of refugees
21. Brun C (2003) Reterritorilizing the relationship between people and place in refugee studies
22. Castillo Gd (2008) Rebuilding war-torn states: the challenge of post-conflict economic reconstruction
23. Chapter 4: Minimum Standards in Shelter, Settlement and Non-Food Items. (N/A)
24. Rowley D (2002) A social and demographic study of Tibetan refugees in India. Elsevier Science Ltd
25. (2014) Dadaab refugees: an uncertain tomorrow. Médecins Sans Frontières
26. Daniel Fosas DA (2018) Refugee housing through cyclic design. Taylor and Francis
27. Zea Escamilla E, GH (2015) Global or local construction materials for post-disaster reconstruction? Sustainability assessment of twenty post-disaster shelter designs
28. Francis Goyes ST (2017) Refugees, incremental housing, and shelter in the 21st century. Massachusetts Institute of Technology
29. Francis Goyes ST (2017) Refugees, incremental housing, and shelter in the 21st century
30. Freedman J (20199) Grand challenges: refugees and conflict
31. Ghandi M (2018) Designing affordable, portable, and flexible shelter for the homeless and the refugees
32. Graziano Salvalaia MI (2016) Architecture for refugees, resilience shelter project. Elsevier ltd.
33. Haddad E (2008) The refugee in international society. Cambridge University Press
34. Harrell-Bond B (1995) Refugees and the international system. Refugee Studies Centre
35. Holzer E (2012) A case study of political failure in a refugee camp. Oxford University Press
36. Jacobs K (2017) Rethinking the refugee camp
37. Jamal Alnsour JM (2014) Housing conditions in Palestinian refugee camps, Jordan
38. Kumin FN (2017) A guide to international refugee protection and building state asylum systems
39. Lala B (2017) Analysis of thermal comfort study in India
40. Lara Alshawawreh FP (2020) Qualifying the sustainability of novel designs and existing solutions for post-disaster and post-conflict sheltering
41. LeGrand LM (2012) A reflection on the importance of settlements in humanitarian shelter assistance
42. MacGregor M (2019) Design for refugees: when does a shelter become a home?
43. Marshilong D (2018) Refugees status in India: a special reference to rohingya refugees
44. Mihaela Robila PC (2018) Refugees and social integration in Europe. Human development and family studies
45. Miller SD (Aug 2018) Assessing the impacts of hosting refugees. Carol Bonnett
46. Oliveira NM (2019) Flexible refugee shelter. IOP Publishing Ltd
47. Post I (2019) Building refugee shelters under 24 hours
48. Projects S (2008) India–Gujarat—2001—Earthquake
49. Projects S (2008) Shelter projects—case study
50. Projects S (2009) India—1977—Cyclone
51. Projects, S. (2012). *Shelter Projects - Case Study.*
52. Projects S (2014) Shelter projects—case study
53. Rania Aburamadan CT (2020) Designing refugees' camps: temporary emergency solutions, or contemporary paradigms of incomplete urban citizenship? Insights from Al Za'atari
54. Rebecca Sutton AS (2011) There's no place like a refugee camp? urban planning and participation in the camp context

55. S, K. (2016). When Karnataka faced its own refugee crises and rose to occasion.
56. Team Ae (2014) The humanitarian works of Shigeru Ban
57. UNHCR. (2013). *UNHCR Global Trends 2012: Displacement The New 21st Century Challenge.*
58. UNHCR (2018) UNHCR global trends: forced displacement in 2018
59. UNHCR (2019) UNHCR global trends: forced displacement in 2019
60. UNHCR. (2019) Zaatari refugee camp: camp infrastructure and facilities—May 2019
61. UNHCR (N/A) Rupture in South Asia
62. Vitale TC (2005) Transitional settlemen—displaced populations
63. Vitale TC (2008) Transitional settlement and reconstruction after natural disasters
64. Vlietstra, W. (2015). *The Digitally Fabricated Transitional Shelter.*

Situational Analysis to Understand the Need to Disseminate Weather Forewarnings and Develop Critical Infrastructures for Minimizing Crop Loss: Parambikulam Aliyar Basin, Tamil Nadu

P. Dhanya and V. Geethalakshmi

Abstract The present study highlights a snapshot view of agrarian situation of Parambikulam Aliyar Basin (PAP), Tamil Nadu due to the unusual weather phenomena happened during samba crop cultivation, 2020–2021. Events like cyclonic storms and unexpected continuous rains during the margazhi month (December and January) in Tamil Nadu is highly unusual. Knowledge Attitude Practice (KAP) methodology as a Rapid Rural Appraisal tool (RRA) has been used in this paper to investigate farmers' perceptions and validate the existing scientific knowledge on the impacts of unexpected weather vagaries on Rabi crop cultivation in PAP basin. The survey was conducted among the groundnut, maize, sorghum, rice and coconut farmers of PAP basin. Majority of the farmers informed that they are unable to follow the weather advisories that they receive as sms alerts. The survey helped to understand that weather vagaries have impacted the harvest ready samba rice crops. Majority of the farmers are not equipped with storage facilities or combined harvesters. The farmers have an opinion that intermittent rainfall has increased the weeds and timely supply of herbicides and insecticides would help them in a better way. Majority of the farmers told that farming faces constant risks from weather vagaries and climate change due to untimely rains. Most of the farmers have an opinion that the weeds and pests are increasing each year. Their adaptation needs include availability of individual farm-based crop insurances as rainfall changes every 500 m. There is a popular demand from the famers to have community owned custom hiring centres in each villages in order to offset the adverse economies of scale due to high cost of individual ownership of farm machineries such as mini tractors, trailors, seed drillers, power tillers operated groundnut harvester., trans planters, portable groundnut pod stripper, groundnut thresher, maize husk cum sheller, fodder sorghum harvesters, coconut tree climbers, etc.

Keywords Weather forewarnings · Agro advisories · Automatic weather stations · Critical infrastructures · Crop loss · Crop insurance · Parambikulam Aliyar basin

P. Dhanya (✉) · V. Geethalakshmi
Directorate of Crop Management, Tamil Nadu Agriculture University, Coimbatore, India

1 Introduction

Weather information is an essential component of adaptation planning process when world is faced with an increasing compound nature of impacts and cascading risks posed by climate change (Tripathi, and Mishra 2017). Impacts of climate change can be seen as a rapidly evolving situation (IPCC 2015). Climatic and weather vagaries are creating record breaking events in tropical countries and aggravates the already existing problems with respect to the dependent sectors such as agriculture ecosystems, economy, employment, health care and protection of the environment [13]. It also called attention to the fact that hundreds of millions of people, especially in Africa and Asia are deprived of food or risk of hunger because of the lockdown in response to the corona virus pandemic, India is also facing the same. Apart from the pre-existing challenges of rise in air temperature, evapotranspiration, uncertain rainfall and increasing desertification, as mentioned by IPCC for dry land areas. All kinds of disasters including the pandemic COVID-19 may worsen the pre-challenges for agriculture & allied sectors and livelihood of people. More than a billion people currently live in water-scarce regions, and as many as 3.5 billion could experience water scarcity by 2025.

Food and Agricultural Organization of the United Nations reported that currently 800 million people suffer from chronic hunger and the demand for food is estimated to grow by 50 per cent during the year 2050 with reference to the base year 2010 [6]. Severe climate vagaries with pandemic disrupts food production and agriculture with severe consequences for small and marginal farmers [5]. For example, untimely rains during the Nisarga cyclone (in May 2020) that happened during the early pandemic period posed severe challenges to the poor farming communities in both coastal as well as interior parts of Tamil Nadu including the present study area. Recently, during November, 23–24, 2020, the Indian Meteorological Department (IMD) has issued a red alert for the many areas of Tamil Nadu and Kerala in view of the brewing storm, Nivar cyclone. Almost 1200 National Disaster Response Force (NDRF) rescue personnel have been deployed in Tamil Nadu, Andhra Pradesh and Puducherry as part of disaster preparedness. Disasters and sudden weather vagaries have impacted most vulnerable people and their livelihood irrespective of the country being developing or developed (Philips 2020). Disasters obstructs the farm production ecosystems, the food exports and imports in many countries and affect the critical supply chains [1, 8]. Being a semi-arid region, farming communities in Tamil Nadu have been struggling due to frequent droughts and dry spells. At the same time, socio-economic issues and conflicts persist and might get worse in future due to multiple environmental challenges in the state.

During any agrarian crisis situation, it is essential to alert local communities towards specific needs and adopt precautionary measures and even validate their impacts, preparedness and responses [20]. For this purpose, researchers and scientific communities conduct a baseline survey to capture the current socio-economic conditions and analyses resource availability and average production and income of the farmers [3]. This enables post impact assessment to gauge the benefits of the

interventions proposed by state governments, universities and district level authorities. However, collective, conscious and coordinated actions can play a vital role in finding timely resolutions for unprecedented challenges during disasters.

2 Materials and Methods

2.1 Study Area

The selected study area for the research is Pollachi south, north and Anaimalai blocks in the Parambikulam Aliyar Basin (PAP), in Tamil Nadu. It was conducted as part of the rapid rural assessment socio-economic community survey proposed under DST scheme entitled "Enhancing climate change adaptive capacity and agricultural productivity in Parambikulam Aliyar Basin areas through ICTs and other technological interventions." The main rivers flowing through this area is Aliyar and Palar. PAP has a geographical extension between 10.3617543°N and 77.0920165°E. Aliyar is one of the tributaries of the river Kannadipuzha, a main tributary of the river Bharathapuzha. The study area lies in the foothills of Valparai, in the Anamalai Hills of the Western Ghats. At present, the discharges are being let down through sets of sluices/ canals, viz., Pollachi Canal, Vettaikaranpudur Canal and the other small river sluices. The primary purpose of the dam is to support irrigation for Pollachi and nearby places for Agriculture purpose. The major crop cultivation in these areas are coconut, groundnuts, maize, sorghum and millets. Part of this area gets good rainfall during south west monsoon season; however, majority of the area comes under rain shadow regions.

3 Methodology

Knowledge Attitude Practice (KAP) methodology as a Rapid Rural Appraisal tool (RRA) has been used in this paper to investigate farmers' perceptions and validate the existing scientific knowledge on the impacts of unexpected weather vagaries on their Samba (Rabi) crop cultivation in PAP basin. It was a semi-structured, pre-validated questionnaire that was used to gather information regarding knowledge, attitude and practice related to crop cultivation impacts due to unprecedented weather vagaries. KAP methodology was used by many researchers around the world to study the knowledge, attitude, behaviour and practices (KABP) of the communities on infectious diseases [17, 20]. This way the first-hand information can be gathered on farmers' views, knowledge, attitude and practice existing coping capacities when there is weather vagaries through telephonic interactions and online survey.

Contact details of around 200 farmers were collected from Regional Coconut Research Station Aliyar, Agriculture offices of Anaimalai block, Pollachi north and

Pollachi south block of Coimbatore District. Key questions were prepared in vernacular language, 'Tamil.' Farmers were randomly selected from the list. In order to get good representative sample population of respondents, telephonic and mobile surveys were conducted for the selected 122 small and marginal farmers in PAP basin. It was an interactive community-based descriptive survey conducted during the period of January 8th and 9th, 2021. An attempt was also made to understand the technology adoption in these areas whether the farming communities are able to respond to the available agro advisories services. The survey results were compiled and analysed using SPSS version 16.0. Descriptive statistics, percentage frequency were calculated.

The present study highlights a snapshot view of agrarian situation and where things stand at a certain point in time during the unexpected weather phenomena's such as NIVAR cyclone and extended winter rainfall during the first week of January. Events like the continuous rains during the margazhi month (December and January) in Tamil Nadu is highly unusual which is due to active easterly wind means that there is abundant moisture brought-in over the land from the Bay of Bengal, offering favourable conditions for cloud formation that triggers thunderstorms. The survey was conducted among the groundnut, maize, sorghum, rice and coconut farmers of Parambikulam and Aliyar basin (Fig. 1).

4   Results and Discussion

The results of the RRA—KAP survey outcomes are analysed to understand and validate the impacts of weather vagaries. The analysed results indicated that (i) Nivar cyclone during the month of November-December has impacted 30.8% of the surveyed farmers in the Parambikulam Aliyar Basin. The unusual rains in the January month has impacted 38.5% of the surveyed farmers (Table 1 and Fig. 3). It shows that more than cyclonic storms, the unseasonal continuous rainfall is troubling the farmers in this region. During the event of cyclones, the wide spread dissemination of warning is already carried out by Indian Meteorological Department and state agricultural universities through TV, Radios, SMS, newspapers. However, during event of unusual rainfall, the effectiveness of the dissemination of weather advisories and warning should be more (Fig. 2).

Almost 53.8% of farmers perceived impacts and risks due to sudden weather changes;

(i)   Being a small and marginal farmers, majority of farmers around 92.3% of the farmers have not applied for any weather-based crop insurances (Fig. 4 and Table 2).

(ii)   Almost 61.5% of the farmers expressed that farm mechanization may reduce risks from crop loss.

The crops that are majorly affected by recent continuous rainfall was rice crop at its flowering and milking stage and harvest ready crops. Sugarcane and corn is also
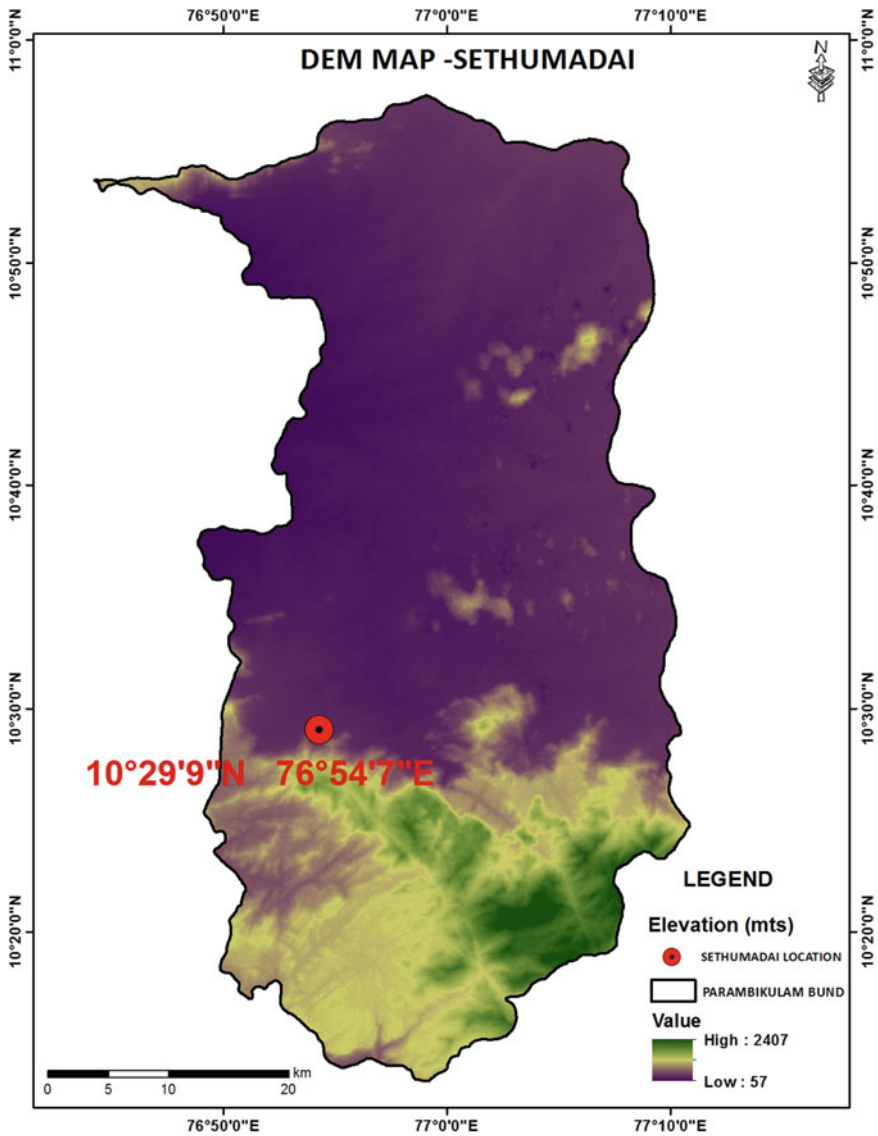
Fig. 1 Location map of the study area, Sethumadai village where Automatic Weather Station is fixed with Digital Elevation Model (DEM) of Parambikulam Aliyar Basin

impacted adversely by Margazhi rains. Land preparation, sowing, seedling, weeding and fertilization in the current rabi growing season was negatively influenced by the effect of non-cessation of north east monsoon rainfall even in the late December and early January months (iv) 76.9% of the farmers responded positively for farm

Table 1 Knowledge responses by the farmers

Knowledge responses		
Questions	No. of responses (%)	
Did Nivar cyclone impact your cultivation?	30.8 (Yes)	69.2(No)
Did you feel that the temperature or rainfall or wind created havoc to your crop ?	56 (Yes)	43(No)
Have you faced any farming difficulty due to the margazhi rains?	38.5 (Yes)	61.5(No)
Are you receiving Weather-based SMS alert	46.2(Yes)	53.8(No)

Fig. 2 Automatic Weather Station, Rain guage and soil moisture meter installed at the farmer's field in Sethumadai village as a critical infrastructure to minimize risks due to weather vagaries
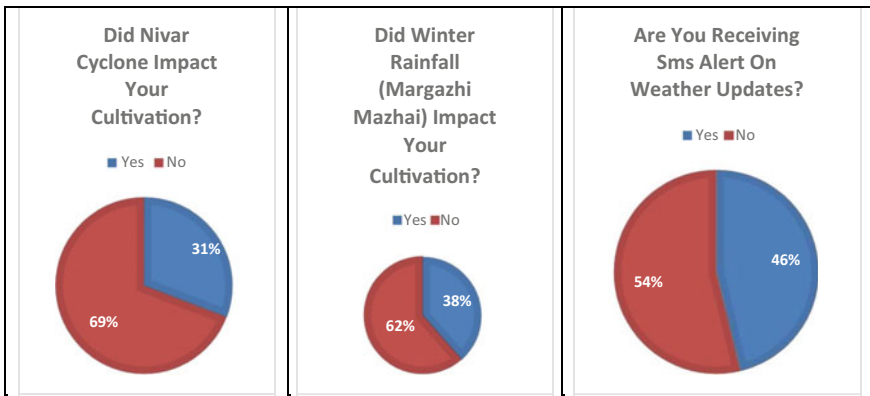
Fig. 3 Knowledge responses from KAP survey
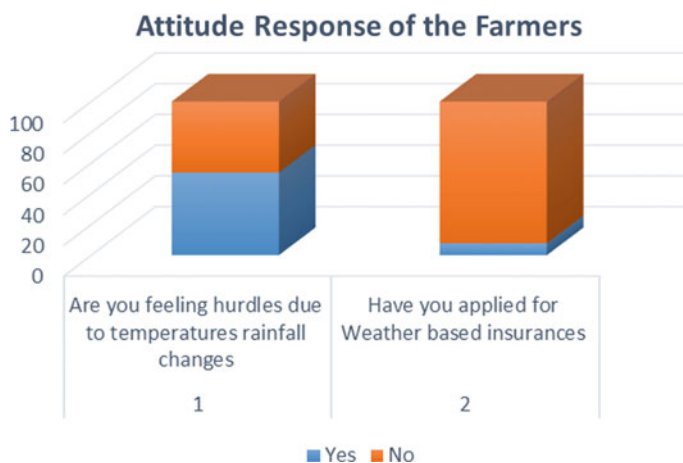
Fig. 4 Attitude response of the farmers from KAP survey

Table 2 Attitude responses

Questions	No of responses (%)	
Are you able to follow the weather Advisories received as sms alerts?:	37 (Yes)	63 (No)
Did the recent cyclones NIVAR and Margazhi rains double your already existing challenges?	26 (yes)	74 (No)
Do you think farm mechanization can reduce crop loss due to weather va garies	61.5 (Yes)	38.5 (No)

mechanization, especially by establishing community owned custom hiring centres (Table 3 and Fig. 5).

There were questions specifically aimed to understand the constraints of crop productions due to non-availability of farm labour during the pandemic. Majority (80.9%) faced shortages in farm labour. During this time, the farmers restricted their arable land only for their family consumptions and avoided commercial cultivation of crops. During the crises, the support from the family members, friends and villagers helped them to tide over the challenges, especially for large scale coconut farmers. The traditional farm workers are diverted into non-farm works MGNREGS (100 nal velai). This has also created farm labour shortages. Work restrictions on

Table 3 Practices and responses

Questions	No of responses (%)	
Are you availing canal irrigation from Aliyar Dam or Palar Dam?	29.2 (Yes)	71.8(No)
Are you availing any weather-based crop insurances ?	7.7(Yes)	92.3 (No)
Do you wish you have community	76.9 (Yes)	23.1(No)

Practice Response of the Farmers

Fig. 5 Practice responses of the farmers from KAP survey

masonry activities at construction sites has forced the younger workforce to take up MGNREGS works and leaving their traditional crop cultivation.

Risk perceptions on the impacts of weather vagaries on crop cultivation

The survey helped to understand that it has impacted the harvest ready samba rice crops. Majority of the farmers are not equipped with storage facilities or combined harvesters. The farmers have an opinion that intermittent and continuous rainfall during late December and early January months have increased the weeds and timely supply of herbicides and insecticides would help them in a better way. Majority of the farmers told that small holder farming systems faces constant risks from weather vagaries and climate change. Most of the farmers have an opinion that the weeds and pests are increasing each year. Their adaptation needs include availability of individual farm-based crop insurances as availability of rainfall changes every 500 metres. And therefore, it is significant that weather-based agro advisories and messages are location-specific and in vernacular language as weather varies within small distances and to enhance their worth and effectiveness. There is a popular demand from the famers to have community owned custom hiring centres in each panchayat in order to offset the adverse economies of scale due to high cost of individual ownership of farm machineries. The machineries that the farmers are in need in PAP including minitractors, trailors, seed drillers, power tillers operated groundnut harvester, trans planters, portable groundnut pod stripper, groundnut thresher, maize husk cum sheller, fodder sorghum harvesters, coconut tree climbers, etc.

Agriculture production systems across the world face multitudes of risks and challenges [6, 14], Jayasree 2020. The farmers who have grown greens, tomato, onions and tapioca have also confronted losses during weather vagaries as their produce has been destroyed due to incessant rainfall at their farms itself. Whole-sale buyers were not purchasing the produce as many hotels had closed down in the city.

Unusual rains, fogs, etc., have increased the risk and already existing burden on their income and livelihood. There may be a loss in season, difficulty in getting seeds for sowing, farm workers, machinery, etc. Policy interventions are required to recover the loss and damage due to weather fluctuations and reassume farm operations without much delay in the existing arable lands in our country.

The way forward

Farm risk has to be transferred and resilience has to be rebuilt in. The Gramin Krishi Mausam Seva (GKMS) of Earth System Science Organization (ESSO)-India Meteorological Department (IMD) is rendered on twice weekly basis in collaboration with State Agricultural Universities (SAUs), institutions of Indian Council of Agricultural Research (ICAR), IITs, etc. Active weather-based agro advisories at the farm level is provided by GKMS; however, more closed network of automated weather stations and effective dissemination and awareness has to be raised at village level. Periodical assessment of farmers adaptation needs is also highly warranted so as to cope with weather vagaries. The survey revealed that there is a need to disseminate weather forewarnings and develop critical infrastructures for minimizing crop loss at Parambikulam Aliyar Basin, Tamil Nadu. It is the need of the hour for the crop insurance sector also to evolve in a farmer friendly manner so as to enhance individual farm resilience from weather and climate vagaries.

Conflict of Interest The authors declare that they have no conflict of interest.

References

1. Adger WN (2003) Social capital, collective action, and adaptation to climate change. Econ Geogr 79:387–404. http://dx.doi.org/https://doi.org/10.1111/j.1944-8287.2003.tb00220.xde-velopmentgeography. Erdkunde 66:185–195. http://dx.doi.org/https://doi.org/10.3112/erd-kunde.2012.03.01

2. Arunachalam N, Tyagi BK, Samuel M et al (2012) Community-based control of Aedesaegypti by adoption of eco-health methods in Chennai city India. Pathog Glob Health 106(8):488–496. https://doi.org/10.1179/2047773212Y.0000000056

3. Ashok Kumar V, Rajendran R, Manavalan R et al (2010) Studies on community knowledge and behavior following a dengue epidemic in Chennai city, Tamil Nadu, India. Trop Biomed 27(2):330–336

4. FAO (2020) http://www.fao.org/news/story/en/item/1287515/icode/

5. FAO 2015, How to Feed the World in 2050, n.d

6. Fisher JA et al (2014) Understanding the relationships between ecosystem services and poverty alleviation: a conceptual framework. Ecosyst Serv 7:34–45

7. http://www.maplandia.com/india/tamil-nadu/coimbatore/anaimalai/downloaded the map

8. IFPRI Discussion Paper 01322 exploring local perceptions of climate change impact and adaptation in rural Bangladesh. In: Snigdha Ali PD (ed). Poverty Health and Nutrition Division (2014)
9. IPCC, Emergent Risks and Key Vulnerabilities, Final Draft, Chapter 19 ((2012). [online] http://ipccwg2.agov/AR5/images/uploads/WGIIAR5-Chap19_FGDall.pdf
10. IPCC, Summary for Policymakers. In: Climate Change and Land: an IPCC special report on climate change, desertification, land degradation, sustainable land management, food security, and greenhouse gas fluxes in terrestrial ecosystems (2019) [Shukla PR, Skea J, CalvoBuendia E, Masson-Delmotte V, Pörtner HO, Roberts DC, Zhai P, Slade R, Connors SR, van Diemen M, Ferrat E, Haughey S, Luz S. Neogi M. Pathak J. Petzold J, Portugal Pereira P, Vyas E. Huntley, Kissick K, Belkacemi M, Malley J (eds)]. In the press
11. IPCC. Special Report on Global Warming of 1.5 °C (Masson-Delmotte V et al (eds)) (WMO, 2018)
12. Jayashree B, Aram IA (2020) Conservation of millets: the role of community leaders in Kolli Hills South India. Indian J Traditional Knowl 19(1):101–110
13. Manandhar S, Schmidt V, Perret S, Kazama F (2011) Adapting cropping systems to climate change in nepal: a cross-regional study of farmers' perception and practices. Reg Environ Change 11:335–348. https://doi.org/10.1007/s10113-010-0137-1
14. Manaswi BH, Pramod K, Prakash P, Anbukkani P, Amit Kar, Jha GK, Rao DUM, Lenin V (2020) Impact of farmer producer organization on organic chilli production in Telangana, India. Indian J Traditional Knowl 19(1):33–43
15. Mataruka V (2009) Socio-economic influences on farming practices in the face of climatechange in inje county—a critical evaluation trabert, Susann (1); Müller-Mahn, Detlef (22011 TERRECO Science Conference October 2–7, 2011; Karlsruhe Institute of Technology, Garmisch-Partenkirchen, Germany Trabert—Climate Adaptation 57
16. Mc Gregor JA, Pouw N (2017) Towards an economics of well-being. Camb J Econ 41:1123–1142
17. Nambi AA, Bahinipati CS (2012) Adaptation to climate change and livelihoods: an integrated case study to assess the vulnerability and adaptation options of the fishing and farming communities of selected East Coast stretch of Tamil Nadu, India
18. Nivedita (2016) Knowledge, attitude, behaviour and practices (KABP) of the community and resultant IEC leading to behaviour change about dengue in Jodhpur City, Rajasthan. J Vector Borne Dis 53(3):279–282
19. Phillips CA, Caldas A, Cleetus R et al (2020) Compound climate risks in the COVID-19 pandemic. Nat Clim Chang. https://doi.org/10.1038/s41558-020-0804-2
20. Saravanan R. Karthikeyan S, Vincent A (2018) Extension and advisory services for climate smart agriculture. MANAGE Bulletin 3 (2018), National Institute of Agricultural Extension Management (MANAGE), Hyderabad, India

Parametric Study of Cold-Formed Lipped Channel Flexural Members Under Fire Hazard

Ravikant Singh and Avik Samanta

Abstract With the advancement in constructional materials and practices, cold-formed steel (*CFS*) has emerged as a leading material for a cost-effective and efficient alternative to their hot-rolled counterpart. *CFS* members are adopted widely in commercial, personal, and public spaces. Steel, in general, is considered safe at moderately elevated temperatures, but *CFS* members, due to their high section factors (perimeter to area ratio) are very prone to failure at elevated temperatures and may lead to catastrophic disasters in unfortunate fire events. Fire safety is a key consideration in designing and maintaining steel structures, yet there is very limited research in the field of *CFS* flexural members under fire. This paper reports numerical parametric study results on cold-formed lipped channel flexural members under simply supported boundary conditions. In this study, a finite element model was developed using commercially available software package *ABAQUS* and validated against experimental and numerical results available in the literature; then, the developed model was adopted for parametric study. Effects of loading on the *CFS*-lipped channel beams (*LCBs*) are studied considering non-uniform thermal profiles on the cross-section of members. In heat transfer analysis, ISO 834 fire-time curve was used in order to simulate the worst fire scenario. It was found that for *CFS LCBs*, the Eurocode 3, Part 1.2, prediction of 350°C is highly conservative for lateral torsional buckling at higher slenderness range, whereas in case of members having lower slenderness range and undergoing distortional or local buckling sometimes found to fail below the specified temperature range of 350°C. It was found that the slenderness plays a vital role in defining the critical temperature of a *CFS* flexural members.

Keywords Cold-formed steel · Fire safety · Flexural member

R. Singh (✉) · A. Samanta
Indian Institute of Technology, Patna 801106, India
e-mail: ravikant_1921ce01@iitp.ac.in

1   Introduction

Cold-formed steel (CFS) members are becoming popular at a very fast pace. In recent years, use of CFS members as the main load-bearing component has increased many folds. CFS structures are now being adopted in many South–East Asian countries in residential and commercial spaces [1]. High strength to weight ratio, fast construction, ease of fabrication, and installation makes it an attractive alternative to the hot-rolled steel or concrete. With numerous advantages comes some disadvantages too; due to high section factor (fire exposed area to volume ratio), these members are more vulnerable to failure at elevated temperatures [2]. Most of the past research focused majorly on CFS members at ambient temperature, and research in CFS members under fire is relatively new. Several past research in CFS flexural members under fire either considered either constant end moment [3, 4] or four point loading cases [5, 6]. Also, it was found that most of available research focused on uniformly elevated temperature only. None of the past research compared the effects of 3 point loading on the behavior of CFS members with thermal gradient; in this research, authors tried to fill this gap.

In this work, a detailed numerical parametric study was performed using the developed finite element (FE) model. All the simulations were performed using the commercially available software ABAQUS. Thermal and mechanical properties of steel were taken from available literature [7] and Eurocode [8]. 3 point loading patterns and simply supported boundary conditions were used in this study. In order to impose the worst fire scenario, fire action on members was defined using ISO-834 [9], fire-time relation.

2   Description of FE Model

2.1   Material, Geometric Imperfection, and Residual Stresses

In this study, high strength steel of grade G450 was selected. Nonlinear stress–strain relation based on the Ramberg–Osgood [10] model was used with recommendations based on Kankanamge and Mahendran [7]. Strain hardening material with gradual yielding type stress–strain curve was adopted in the model. Yield strength was taken as 514.5 MPa, whereas ultimate strength, and modulus of elasticity were taken as 542.5 MPa and 206.328GPa, respectively, from previous research [7].

Yield strength and modulus of elasticity of steel reduces with increase in temperature; therefore, an appropriate reduction factor was introduced in the material model. Reduction factor for yield stress is the ratio of the yield stress of steel at elevated temperature ($f_{y,T}$) to yield stress at ambient temperature (f_y); similarly, modulus of elasticity reduction factor is the ratio of elastic modulus of steel at elevated temperature (E_T) to elastic modulus at room temperature (E). For both reduction factors recommended value for class 4 section given in Eurocode 3, Part 1.2 [8] was taken in

this study. Other thermal parameters such as density, conductivity and specific heat, and coefficient of thermal expansion were also taken from Eurocode.

Geometric imperfections in CFS members refer to the deviation of member from desired geometry. CFS members due to their relatively slender section and thin profile are susceptible to damage. This geometric nonlinearity in the member can sometimes trigger the failure of the members. Thus, geometric imperfection in members cannot be ignored in the numerical model. The magnitude of initial geometric imperfection for local, distortional, and global (lateral torsional) buckling were taken from literature [11]. Coiling and uncoiling of CFS members introduces residual stress on these members [12]. Residual stresses are induced in CFS members due to plastic bending. It is evident from the literature [13] that the effects of residual stress diminish with an increase in temperature; thus in this study, the effects of residual stresses were ignored.

2.2 Analysis Type

Every simulation was performed in three stages. In the first stage, 2D heat transfer analysis was performed in order to know the thermal profile on different sections. In the second stage, Eigenvalue-buckling analysis was carried out in order to access the possible buckling mode and to get the shape of imperfection involved. In the third stage, a nonlinear thermo-mechanical simulation was performed with deflection pattern taken from the first eigenmode of eigenvalue analysis with appropriate imperfection. Further thermo-mechanical simulation was carried out in two steps; in first initial load was imposed on the member (50% of capacity), whereas in the second step, the fire was imposed on the member, and thermal effects were recorded for a total fire exposure time of 30 min.

2.3 Finite Element Meshing and Element Type

The finite element model was developed based on commercially available software ABAQUS. In 2D heat transfer analysis, model 4 noded diffusive heat transfer quadrilateral element with 11 degrees of freedom (DC2D4) was used. Whereas in thermo-mechanical simulation, 4 noded shell element with reduced integration approach, having three degrees of freedom per node was used (S4R). Hourglass control was activated in order to handle possible hourglass deformation arising during the simulation. Based on mesh sensitivity analysis, mesh density of 10 mm × 10 mm was found to provide the best results in reasonable computational time and accuracy.

2.4 Load and Boundary Condition

In order to simulate the fire action on member ISO-834 [9], the standard fire-time curve was used. 3 point loading was applied on member, with point load applied at center of the beam at mid of top flange. In order to avoid the concentration of load on a particular node, load was transferred through a plate attached to the loading and support faces of the member.

Load ratio is defined as the ratio of applied load to the ultimate load-bearing capacity of the member. In parametric study, magnitude of the applied load was equivalent to the load ratio of 0.5. The ultimate moment capacity of the member was evaluated from Eurocode 3, Part 1.1[14] using effective properties calculated from Eurocode 3, Part 1.3 [15] and Part 1.5 [16].

Simply supported boundary condition was applied on the member. In this study, warping free end conditions were used. An appropriate warping constant was introduced in the moment capacity equation in order to avoid any inconsistency in applied load. Load and boundary condition used in this study is illustrated in Fig. 1.
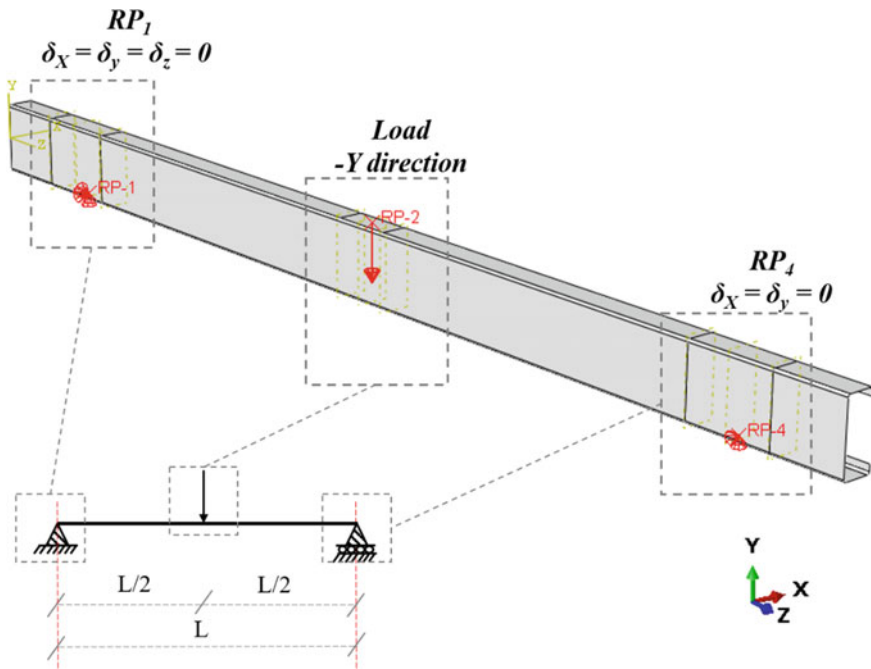

Fig. 1 Location of load and boundary conditions on 4-point loading model

3 Validation Study

In order to check the accuracy of the developed FE model, a validation study was performed. The developed model was validated against experimental [5] and numerical [6] results available in the literature. A separate validation study was performed for heat transfer model and thermo-mechanical model. Figure 2 represents the 2D heat transfer analysis result in terms of time–temperature curve at the web of lipped channel beam. The developed FE model was able to predict the thermal profile of the experimental and numerical study by Laim et al. [5, 6]. In Fig. 3, result of thermo-mechanical validation is presented. On the vertical axis of curve, downward displacement at the center of the beam is presented, whereas on the horizontal axis
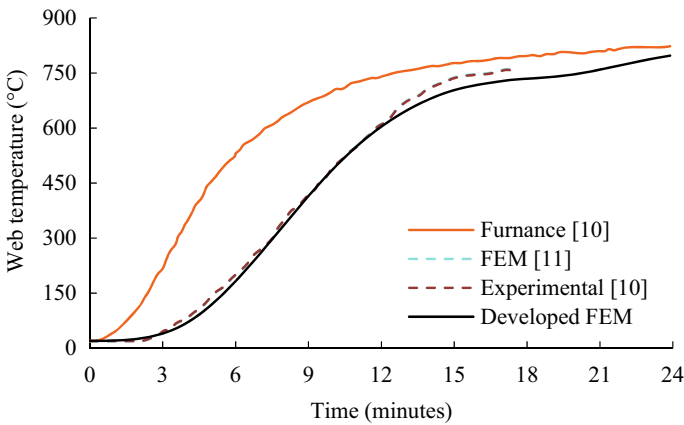

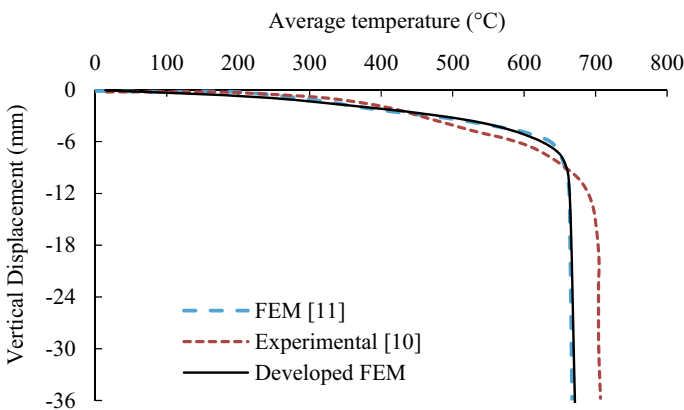**Fig. 2** 2D heat transfer analysis validation curve

Fig. 3 Comparison of experimental and numerical data with the developed FE model

average temperature recorded on the cross-section is plotted. A good agreement between experimental and numerical results was observed. From the results of the validation study, it was clear that the developed model was able to predict the critical temperature of the flexural member with adequate accuracy.

4 Parametric Study

From the developed model, a numerical parametric study was performed on a total of 20 members. 5 cross-section geometry was selected from Indian standard IS 811 [17]. To cover a wide slenderness range, four spans were selected. 3 point loading with simply supported boundary condition and warping free ends were used in this study. Table 1 contains details of sections considered in the parametric study. Different beams have assigned a particular beam number (B_x), and their corresponding geometric parameters are mentioned in Table 1.

The applied initial load was 50% of the load-bearing capacity of member at ambient temperature, calculated from Eurocode 3, Part 1.1 [14], using effective section properties from Part 1.3 [15] and Part 1.5 [16] of Eurocode 3.

Design buckling capacity ($M_{b,Rd}$) of Flexural member is calculated from the relation given in Eq. 1,

$$M_{b,Rd} = \chi_{LT}.W_y.f_y/\gamma_M \tag{1}$$

$$\text{for, } \bar{\lambda}_{LT}^2 \leq 0.4; \; \chi_{LT} = 1 \tag{2}$$

$$\text{For, } \bar{\lambda}_{LT}^2 > 0.4 \; \chi_{LT} = \frac{1}{\left[\phi_{LT} + \sqrt{(\phi_{LT}^2 - \bar{\lambda}_{LT}^2)} \right]} \tag{3}$$

$$\phi_{LT,\theta} = \frac{0.5}{[1 + \alpha(\bar{\lambda}_{LT} - 0.2) + \bar{\lambda}_{LT}^2]} \tag{4}$$

$$\bar{\lambda}_{LT} = \sqrt{W_y f_y/M_{cr}} \tag{5}$$

For buckling curve '*b*,' α in the above equation is taken as 0.34. f_y is the yield strength of the member, and W_y is the appropriate section modulus of the member; in our case effective section modulus (Class 4 or CFS member). M_{cr} can be calculated using the following relation,

$$M_{cr} = C_1 \frac{\pi^2 E I_y}{(k_y L)^2} \sqrt{\left(\left(\frac{k_y}{k_w} \right)^2 \frac{I_w}{I_y} + \frac{G J (k_y L)^2}{\pi^2 E I_y} \right)} \tag{6}$$

Table 1 Member geometry detail of selected section for parametric study

Beamsections	h (mm)	b (mm)	l (mm)	t (mm)	R_i (mm)	A (mm^2)	J ($10^3 \times$ mm^4)	I_x ($10^6 \times$ mm^4)	I_w ($10^9 \times$ mm^6)
B_1	90	50	10	1.60	2.40	314	0.26	0.418	0.158
B_2	120	50	15	2.00	3.00	467	0.61	1.030	0.453
B_3	150	50	20	3.15	4.73	828	2.68	2.660	1.240
B_4	180	80	20	3.15	4.73	1110	3.62	5.610	5.790
B_5	200	50	20	3.15	4.73	986	3.21	5.350	2.320

In Eq. 6, coefficient C_1 depends on the loading type, and in this study, its value was taken as 1.348 [18]. Factor k_w depends on the end warping condition of the beam. The value of k_w ranges from 0.5 to 1, as end condition in this study was warping free value of k_w was taken as 1. Results of parametric study is presented in Figs. 4 and 5. The factor k_y represents effective lateral buckling length factor, which in this study was taken as 0.8.
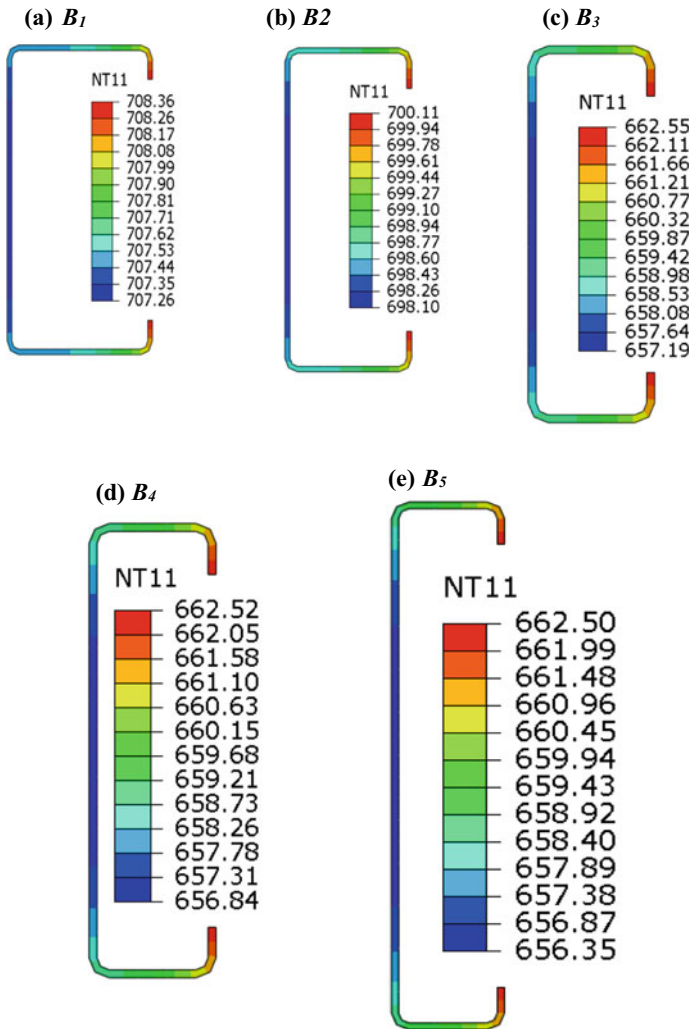
(a) B_1 **(b)** $B2$ **(c)** B_3

(d) B_4 **(e)** B_5

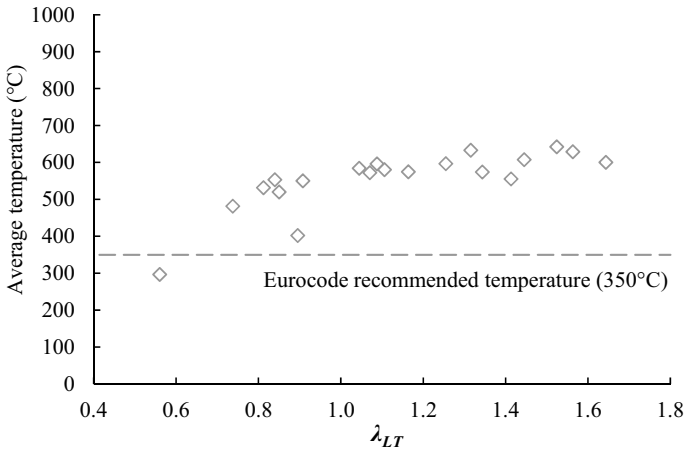**Fig. 4** Thermal profile of different members

Fig. 5 Representation of dimensionless slenderness vs average temperature of member

5 Results and Conclusion

The paper presents a numerical parametric study on cold-formed steel flexural members exposed to fire hazards. Effects of 3 point load pattern on critical temperature of CFS LCBs under simply supported boundary condition has been investigated. A total of 20 simulations were performed in three stages. Presented in Fig. 4a–e is member cross-sectional temperature at 15 min of the simulation run. In smaller sections such as B1 and B2, higher temperature was recorded than bigger sections such as B3-B5. Not much difference in the thermal profile was observed on smaller sections (B1and B2), whereas on the larger sections, a considerable difference in the thermal profile can be observed in the web and lips of channel sections. This is due to the fact that the rate of heat dissipation from the larger surface area of bigger members was much higher than their smaller section counterparts.

The results of this parametric study are presented in Table 2. Figure 5 contains all the simulation results in terms of the critical temperature of the member. On the horizontal axis, dimensionless slenderness, whereas on the vertical axis, the average temperature recorded on the member is presented. An increase in critical temperature

Table 2 Results of numerical parametric study

Critical temperature of members in °C					
Span	B_1	B_2	B_3	B_4	B_5
1.5 m	553.2	520.1	531.6	296.5	402.1
2.0 m	596.2	580.4	584.0	481.7	574.8
2.5 m	633.2	574.0	596.6	550.2	555.4
3.0 m	642.6	629.1	607.5	572.2	600.5

was observed with an increase in slenderness value and span. The critical temperature of CFS members undergoing lateral torsional buckling having high slenderness was well above 450 °C. Therefore, it may be concluded that at 50% load ratio, Eurocode prediction of critical temperature is highly over-conservative for members failing under lateral torsional buckling.

It is also worth mentioning that in very few cases (2 out of 20), for members undergoing distortional/local buckling at lower slenderness range, the critical temperature was close to 350 °C. In one member, the critical temperature was even below 350 °C. Thus, for members undergoing distortional/local buckling this thermal limit (350 °C) cannot be discarded as for members having low slenderness value, the critical temperature close to 350 °C was recorded. Based on the findings of this research, it can be concluded that Eurocode recommended critical temperature for CFS member needs improvements for global buckling, whereas, for local or distortional buckling, there is a need for more investigation with a large number of data set and members involved.

6   Notations

$M_{b,Rd}$	Design buckling capacity.
$\overline{\lambda}_{LT}$	Dimensionless slenderness.
I_W	Warping constant.
L	Member effective span.
EI_y	Minor axis flexural rigidity.
GJ	Torsional rigidity.
f_y	Yield strength.
I_y	Moment of inertia about minor axis.
I_x	Moment of inertia about major axis.
I_w	Warping constant.
W_y	Section modulus.
M_{cr}	Critical moment.
A	Cross sectional area.
H	Depth of section.
t	Thickness of member.
b	Width of section.
l	Lip depth.
R_i	Inner bent radius of section.

References

1. Roy K, Lim JBP, Lau HH, Yong PM, Clifton GC, Wrzesien A, Mei CC (2019) Collapse behaviour of a fire engineering designed single-storey cold- formed steel building in severe fires. Thin-Walled Struct 142:340–357

2. Javed MF, Hafizah N, Memon SA, Jameel M, Aslam M (2017) Recent research on cold-formed steel beams and columns subjected to elevated temperature: a review. Constr Build Mater 144:686–701

3. Dolamune Kankanamge N, Mahendran M (2012) Behaviour and design of cold-formed steel beams subject to lateral-torsional buckling at elevated temperatures. Thin-Walled Struct 61:213–228

4. Landesmann A, Camotim D (2016) Distortional failure and DSM design of cold-formed steel lipped channel beams under elevated temperatures. Thin-Walled Struct 98:75–93

5. Laím L, Rodrigues JPC, Da Silva LS (2014) Experimental analysis on cold-formed steel beams subjected to fire. Thin-Walled Struct 74:104–117

6. Laím L, Rodrigues JPC (2018) Fire design methodologies for cold-formed steel beams made with open and closed cross-sections. Eng Struct 171:759–778

7. Kankanamge ND, Mahendran M (2011) Mechanical properties of cold-formed steels at elevated temperatures. Thin-Walled Struct 49:26–44

8. EN1991–1–2: Design of steel structures (2004) General rules. Structural fire design, European Committee for Standardization, Brussels, Belgium

9. ISO 834–1: Fire resistance tests—elements of building construction, part 1: general requirements, International Organization for Standardization Geneva, Switzerland (1999)

10. Ramberg WR, Osgood W (1943) Description of stress–strain curves by three parameters. NACA technical note 902

11. Laím L, Rodrigues JPC (2016) On the applicability and accuracy of fire design methods for open cold-formed steel beams. J Build Eng 8:260–268

12. Quach WM, Teng JG, Chung KF (2004) Residual stresses in steel sheets due to coiling and uncoiling: a closed-form analytical solution. Eng Struct 26:1249–1259

13. Lee JH, Mahendran M (2004) "Local buckling behaviour and design of cold-formed steel compression members at elevated temperatures. In: Fourth international conference on thin-walled structures 315–22

14. EN1993–1.1: Design of Steel Structures, European Committee for Standardization Brussels, Belgium (2004)

15. EN1993–1.3: Design of Steel Structures. General Rules, European Committee for Standardization Brussels, Belgium (2004)

16. EN1993–1.5: Design of Steel Structures, Part 1–5: Plated Structural Elements, European Committee for Standardisation Brussels, Belgium (2006)

17. IS 811, Specification for cold formed light gauge structural steel sections, Bureau of Indian standards, New Delhi, India (1987)

18. Boissonnade N, Greiner R, Jaspart JP, Lindner J (2006) Rules for member stability in EN 1993–1–1, Background documentation and design guidelines, ECCS

COVID-19 Future Proof Infrastructure

C. Vaidevi , **D. S. Vijayan** , **C. Nivetha** , **and M. Kalpana**

Abstract The novel coronavirus (COVID-19) outbreak affected all sectors' development, especially infrastructure in the construction industry, which faces drastic changes and challenges of growth for further movement. So, engineering plays a vital role in constructing safe constructions with safety measures. The existing methods and ways in the construction industry do not give hands in this pandemic situation. Behind the safety, water use, and managing municipal solid waste are highly risk considering huge populations in the defense against the spread of COVID-19. In this paper, an effective infrastructure during this COVID-19 is framed with proper design, methods, and procedures in the construction and a plan focused on sustainable, future-proof infrastructure, access to no point of contact, and energy-saving. This new type of work increases economic and societal growth. Enhance the technologies, and productivity so obviously raises job opportunities for all sector people. An alternative model in the construction industry makes the work simple, faster, and more reliable. During these adverse effects, it gives solutions in concepts approach, services, and technology to solve the infrastructure challenges due to natural disasters.

Keywords Challenges · Infrastructure · Construction industry

1 Introduction

These days, it is very hard not to pay more attention to our physical realm about our sheltering place. Engineers and architect are more responsible for designing the post pandemic buildings during this situation. Because of air re-circulated within the

C. Vaidevi (✉) · C. Nivetha
Aarupadai Veedu Institute of Technology, Vinayaka Missions Research Foundation, Paiyanoor, Chennai 603104, India

D. S. Vijayan
Civil Engineering, Aarupadai Veedu Institute of Technology, Vinayaka Missions Research Foundation, Paiyanoor, Chennai 603104, India

M. Kalpana
Saveetha School of Engineering, Chennai, Tamil Nadu, India

building, which leads to contamination of all rooms causes infection during outbreaks higher risk case of public buildings [8].

From research conducted last year, it was noticed that warranting just a minimum of outdoor air and ventilation reduced influenza transmission when 50–60% of the people occupied the building got vaccinated [3]. In very hot or very cold seasons, in a classroom of a school or office room, the air passing out of the vent gets completely re-circulated.

Recent coronaviruses' last investigations showed that smaller particles that can be deeply inhaled caused the lower respiratory tract when the airborne transmission was occurring in the atmosphere [2].

Low humidity serves as a better platform for many viruses to survive well, literally what happens in summer (air-conditioned spaces) or winter. Few of the heating and ventilation systems are well equipped to maintain an optimum humidity range between 40 and 60%, but most of this fails to happen. In such cases, humidity can be increased at home by using portable humidifiers [1].

The speedy spread of coronavirus in the design community has resulted in the re-evaluation of regular works. It is essential and means a lot to design for a world that is not going to remain silent at the same, particularly when it comes to how we use a public place or public transport like airports, hospitals, gyms, hospitals, schools, and offices [9, 10].

There is a prediction that public spaces will be equipped with more automation to remove or reduce the contagion with the spreading of coronavirus [21]. All types of touch-less technologies such as voice-activated elevators, cell phone-controlled hotel room entry, automatic doors, hands-free light switches, temperature controls, advanced airport check-in, and security and automated luggage bag tags [1].

The construction practices of health care like reduction in the flat surfaces where a virus or germs can easily settle, provider of good ventilation systems that remove contaminated air from any given area can also be used in many other public spaces [5–7].

2 Precautions at the Construction Site

Already in construction, we have many safety measures like wearing a helmet, safety belt, gloves, shoes, etc., along with that now masks also included due to spreading of coronavirus, that affects the people involved during the work. To overcome this virus's spreading, safety measures play a vital role, like sanitizer, social distancing, and thermal detecting apart from this, it can provide a clean, virus-free environment by providing good ventilation and daylight shining inside the building [18, 19]. Research says that filtration, proper ventilation, etc., reduces the spreading of these pathogens COVID-19 virus [29].

Anyway, maintaining social distance is the only solution in this situation, so that can adapt using AI and innovative technology with no point of contact during
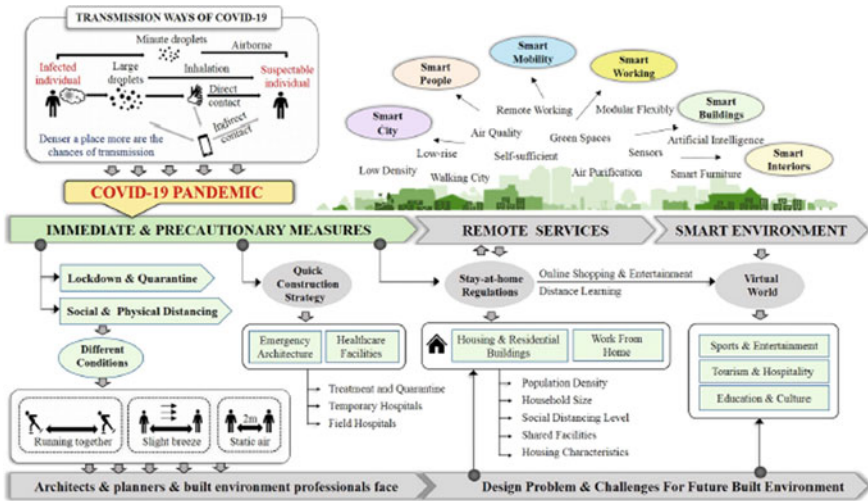
Fig. 1 COVID-19 pandemic research link variables. (*Source* Naglaa A. Megaheda, et. al, "Antivirus-built environment: Lessons learned from COVID-19 pandemic," Sustainable Cities and Society https://www.ncbi.nlm.nih.gov/pmc/articles/PMC7313520/)

construction work like sound system, mobile phones, automatic system, sensor system, etc., for communicating and give instruction to execute work [11, 12].

Most probably, if all components used in construction are pre-casted and assembled at the site will decrease the spreading of viruses [26]. Automated system in construction saves time and reduces the labors in the field.

This COVID-19 research shows the variables linked in the transmission of virus oriented to building and environment in this pandemic situation is shown in Fig. 1 [4].

The tabular column in Table 1 shows difference in pre and post-pandemic construction scenario.

3 Buildings Focused

Focusing on the design of components and structural elements creates proof for structure. The spacing between the buildings is the most important thing.

Provision of opening windows, heating, and ventilation systems in buildings is responsible for diluting airborne contaminants resulting in good indoor air quality and less infection. We usually provide the opposite, i.e., sealing our windows shut and recirculating the air [25]. This process leads to under ventilation of schools and office buildings. This condition impairs cognitive function as well leads to disease transmissions like coronavirus or the common flu.

Table 1 Pre and post pandemic building construction scenario

Pre pandemic	Post pandemic
Cast in-site	Preferred pre-cast components [26]
Manual operation	AI and Automation is used
Centralized in construction	Decentralization
Congested with no window system	Spacious with ventilation [13]
Closed scenario	Natural ventilation
No air circulation	Air recirculation
Limited humidity	Humidity level maintained
Materials used	Virus proof materials
Not much concentrated	Personal hygienic
Clean environment	Touchless environment [16]
Machines	Machines with technology

If not managed properly, they can spread disease. Nevertheless, it is necessary to get it right when enlisting homes, schools, offices, etc., in this fight [20]. In our country, maximum buildings are constructed with low-grade filters that can capture less than 20% of viral particles.

Buildings require mechanical ventilation systems in high-risk areas or at least portable air purifiers to control airborne particle concentrations. The quality portable air purifiers capture 99.97% of particles by HEPA filters [1].

4 The Structural Elements that Are Discussed Are Follows with the Plan, Section and Technology Adopted

The coronavirus spreads by touching the contaminated surfaces like countertops, door handles, elevator buttons, cell phones, etc. Frequent cleaning or sanitizing such contaminated surfaces can help in controlling the spread of disease. Green cleaning products could be used for home or any other low-risk environment. For Example, use of E.P.A. registered disinfectants in hospitals. Usually, when infected persons are present, it is recommended to clean frequently the home or the office [15].

The focus on public buildings is entirely different from residential buildings because the spreading starts from outside through then to peoples inside the house. In the house, a separate room with ventilation to re-circulate the air with proper cleaning is enough for home quarantine [14]. Nevertheless, public or commercial buildings are the sources for the transmission of germs. Concentration the simple idea of a plan and design is shown in Fig. 2 and technology component public buildings follows,

GROUND FLOOR PLAN

FRONT ELEVATION

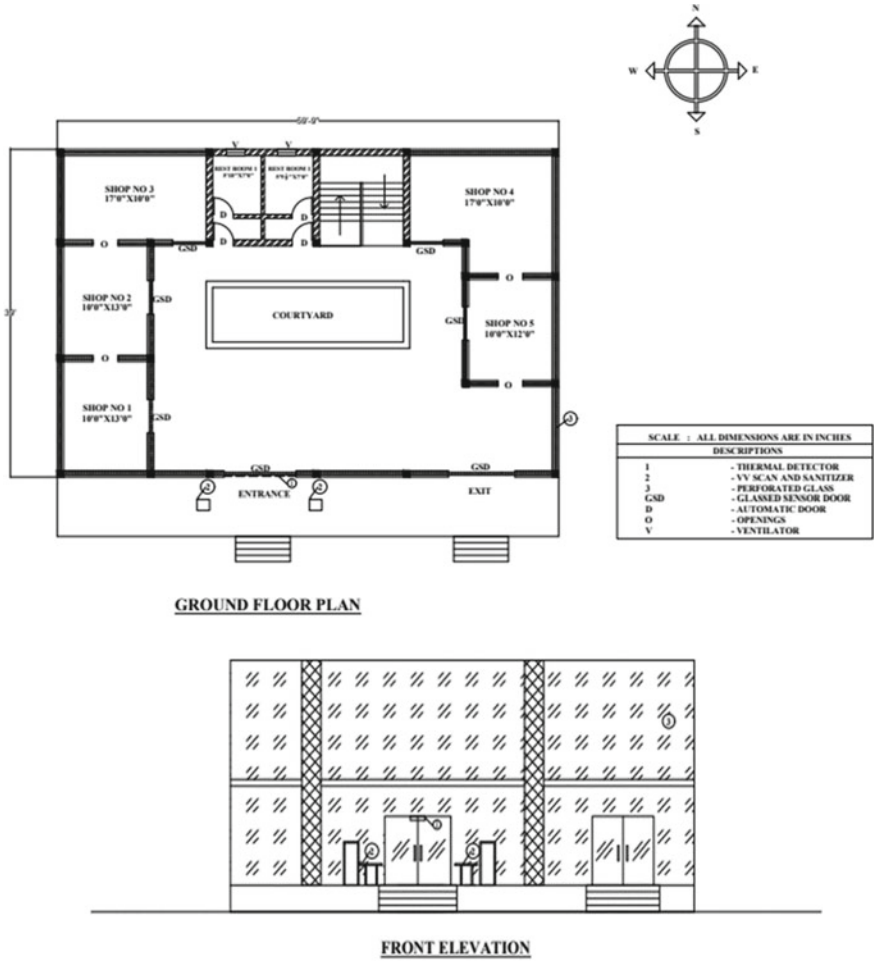**Fig. 2** A simple plan and design of public building

4.1 Plan

The entire building plan is made with decentralized and no point of contact. The entrance pathway and exit pathway exist with spacious, no ways of crowd formation inside the building where it is designed to have two ways system. The mode of people moving inside the building is designed according to their purpose wit touchless facilities [16, 17].

4.2 Entrance

Sensor thermal detector, UV sanitizing, mask-wear checking is over; then, the door is automatically opened, or else alarm is alarmed to give a warning for the affected or suspected people [28]. Even though suspected people can also utilize virtual shopping, which works under the AI system [27], the entrance and exit way be separated and should be placed far from the point of contact of the people moving inside the commercial buildings.

4.3 Walls

The outer walls are constructed using perforated glass panels were allow air and daylight inside the building to act as an energy-saving and germs killing because heat transfer inside the rooms does not allow the virus to grow or spread the inside or partition walls are constructed with virus resisted plywood and painted with germs proof painting.

4.4 Indoors

In indoors, people may cough or sneeze they expel both large droplets and smaller airborne particles named droplet nuclei that can stay and transported around buildings.

Introducing outside air allows increasing air exchange, maintaining 40–60% relative humidity, natural ventilation by opening windows and flush out indoor spaces, mostly increasing daylight access. The final is an implementing targeted disinfection technique, such as mild steam air, UV-C light, and cleaning the surface with machines or robots controlled by smartphones [13].

Medical plants are allowed to grow inside and around the buildings, which purifies contaminated air. This helps even people, while breathing their minds are refreshed [22, 23]. Aesthesis inside the buildings keeps them physiological good and feels better where it improves immunity indirectly [24].

4.5 Floors

Anti-bacterial concrete is used on the surface, finishing on the floor to kill harmful germs. The flooring can be covered with a plywood sheet where it acts as a virus— bacteria proof material. Sanitizing can be done using moving cleaners controlled with mobile.

4.6   Roofs

It is all covered with glass-paneled, and colored sheets were it allows heat and daylight inside. These sheets are provided with a gap where it gives more ventilation and circulates air in and around the building.

4.7   Restroom

The washbasin is controlled with sensor RFID technology where it pours water when hands are showed. An exhaust fan is provided to recirculate the new air indoor, which kills pathogens.

Self-cleaning washrooms are provided to maintain hygienic and safe from spreading of the virus in persons. Sanitizer mild percentage is mixed with water to wash closets frequently controlled with another press in flush. Restroom doors in public spaces were controlled by a spring or pulley connected with leg movement. People can reduce risks at home using similar techniques. House if someone has been infected or is symptomatic, they can be self-isolated in a space where it is next to a bathroom with an exhaust fan that should be operated continuously. This operation helps pull air rest space of the infected home area and out through the bathroom exhaust.

4.8   Doors

The research says that doors made up of natural unfinished wood showing reduction in the abundance of viruses but other surfaces like stainless steel or plastic increases the life time and growth of viruses for long period [3].

These above discussed strategies and techniques are possibilities for the reduction in spreading of virus and this can be applied in every building may exist and newly constructed building for our regional climate.

5   Conclusion

The above study is only a suggestion in this pandemic situation because lockdown periods overs after going out of technology, and design keeps away these pathogen viruses during this epidemic. Introduce far more opportunities for handwashing and sanitizing, as well as RIFD technologies increased technology development. The job opportunities are increased along with safety measures. The cost of the construction may be increased, but as we all know, life is most important, and priority is given

for healthy living. Future research may be extended to bring out more solutions and ideas in the construction field with economics and a sustainable approach.

References

1. Allen JG, Dr. Allen (2020) "Your building can make you sick or keep you well". https://www.nytimes.com/2020/03/04/opinion/coronavirus-buildings.html
2. Van den Wymelenberg K, Dietz L, Fretz M (2020) "How architects can stop COVID-19 from spreading indoors". https://www.fastcompany.com/90493034/how-architects-can-stop-covid-19-from-being-transmitted-indoors
3. Giacobbe A (2020) "How the COVID-19 pandemic will change the built environment". Architecture + Design. https://www.architecturaldigest.com/story/covid-19-design
4. Megaheda NA, Ghoneimb EM (2020) Antivirus-built environment: lessons learned from Covid-19 pandemic. Sustain Cities Soc 61:102350
5. Cirrincione L, Plescia F, Ledda C, Rapisarda V, Martorana D, Moldovan RE, Cannizzaro E (2020) COVID-19 pandemic: prevention and protection measures to be adopted at the workplace. Sustainability 12(9):3603. https://doi.org/10.3390/su12093603
6. Dietz L, Horve P, Coil D, Fretz M, Eisen J, Van Den Wymelenberg K (2000) "2019 novel coronavirus (COVID-19) pandemic: built environment considerations to reduce transmission". mSystems 5(2):e00245–20. https://doi.org/10.1128/mSystems.00245-20
7. Horve P, Lloyd S, Mhuireach G, Dietz L, Fretz M, MacCrone G, Ishaq S (2020) Building upon current knowledge and techniques of indoor microbiology to construct the next era of theory into microorganisms, health, and the built environment. J Eposure Sci Environ Epidemiol 30:219–235
8. Honey-Roses J, Anguelovski I, Bohigas J, Chireh V, Daher C, Konijnendijk C, Nieuwenhuijsen M (2020) "The impact of COVID-19 on public space: a review of the emerging questions". https://doi.org/10.31219/osf.io/rf7xa
9. Budds D (2020) "Design in the age of pandemics". https://www.curbed.com/2020/3/17/21178962/design-pandemics-coronavirus-quarantine
10. Chang V (2020) "The post-pandemic style". https://slate.com/business/2020/04/coronavirus-architecture-1918-flu-cholera-modernism.html
11. Goniewicz K, Khorram-Manesh A, Hertelendy A, Goniewicz M, Naylor K, Burkle F (2020) Current response and management decisions of the European Union to the COVID-19 outbreak: a review. Sustainability 12(9):3838. https://doi.org/10.3390/su12093838
12. Hishan S, Ramakrishnan S, Qureshi M, Khan N, Al-Kumaim N (2020) Pandemic thoughts, civil infrastructure and sustainable development: five insights from COVID-19 across travel lenses. Talent Develop Excellence 12(2s):1690–1696
13. Papu S, Pal S (2020) "Braced for impact: architectural praxis in a post-pandemic society (Version 1)". Sage Submissions. https://doi.org/10.31124/advance.12196959.v1
14. Schellenberg G, Fonberg J (2020) "Housing characteristics and staying at home during the COVID-19 pandemic". https://www150.statcan.gc.ca/n1/pub/45-28-0001/2020001/article/00009-eng.htm
15. Dejtiar F (2020) "Is coronavirus pandemic accelerating the digitalization and automation of cities?". https://www.archdaily.com/936064/is-coronavirus-pandemicaccelerating-the-digitalization-and-automation-of-cities
16. Kashdan R (2020) "Six ways urban spaces may change because of coronavirus". https://www.bostonmagazine.com/property/2020/04/30/urban-spacescoronavirus/
17. Priday C (2020) "Architecture after coronavirus". https://exepose.com/2020/05/05/architecture-after-coronavirus/
18. Alter L (2020) "Architecture after the coronavirus". https://www.treehugger.com/green-architecture/architecture-after-coronavirus.html

19. Muggah R, Ermacora T (2020) "Opinion: redesigning the COVID-19 city". https://www.npr.org/2020/04/20/839418905/opinion-redesigning-the-covid-19-city
20. Beggs C, Kerr K, Donnelly J, Sleigh P, Mara D, Cairns G (2020) An engineering approach to the control of Mycobacterium tuberculosis and other airborne pathogens: a UK hospital based pilot study. Trans R Soc Trop Med Hyg 94(2):141–146
21. Liu L (2020) "Emerging study on the transmission of the novel coronavirus (COVID-19) from urban perspective: evidence from China", Cities, 103, Article 102759
22. Constable H (2020) "How do you build a city for a pandemic?", BBC. https://www.bbc.com/future/article/20200424-how-do-you-build-a-city-for-a-pandemic
23. Hui S (2011) "Green roof urban farming for buildings in high-density urban cities". Paper presented at world green roof conference. China, Hainan, 18–21
24. Makhno S (2020) "Life after coronavirus: how will the pandemic affect our homes?" Dezeen. https://www.dezeen.com/2020/03/25/life-after-coronavirus-impacthomes-design-architecture/
25. Guy S, Farmer G (2001) Reinterpreting sustainable architecture: the place of technology. J Architec Educ 54(3):140–148
26. Hatcher J (2020) "Modular buildings in the time of Covid-19, smart buildings magazine". https://smartbuildingsmagazine.com/features/modular-buildings-inthe-time-of-covid-19
27. Gracy B (2020) "Digital transformation: 4 ways to plan for the post-pandemic normal". Enterprisers Project. https://enterprisersproject.com/article/2020/4/digital-transformation-how-plan-post-pandemic
28. Wainwright O (2020) "Smart lifts, lonely workers, no towers or tourists: architecture after coronavirus". The Guardian. https://www.theguardian.com/artanddesign/2020/apr/13/smart-lifts-lonely-workers-no-towers-architecture-after-covid-19-coronavirus
29. World Health Organization (1988) Regional office for Europe & Ranson Ray P. "Guidelines for healthy housing", WHO Regional Office for Europe. https://apps.who.int/iris/handle/10665/191555le

Risk Reduction and Structural Measures

Role of Cold Form Steel in Covid-19 Infra Structure

R. T. Anitha Ranee and V. G. Srisanthi

Abstract The COVID-19 pandemic requires large scale infrastructure facilities within a short span of time for quarantining the people by introducing partition in the existing building or to construct light weight structures which can be dismantled or altered in future. Medical facilities like covid triage center need to set up in many areas. Also most of hospital facilities like emergency, obstetric services, toilet facilities need to be duplicated for both covid and non covid patients. All the above requirements can be easily fabricated by using cold form steel sections which is known for its ease of construction, light weight, low cost, high strength properties and speedy construction. The speed of construction can be increased tremendously since no skilled man power will be required for the erection of cold form steel structure. It can be assembled by semi-skilled man power as do it yourself (DIY) kit. Minimum tools like screw gun and cutter will only be required for the erection. A prototype CFS-based covid infrastructure with its components will be discussed in detail. Connections which play a key role in cold form steel construction are also covered. Further, in this paper, the sequence and methodology adopted in the installation of the above said services required during COVID-19 has been discussed in detail.

Keywords Triage · Quarantine · Wall panel · Roof panel · Roof joist cladding

1 Covid 19

World is facing one of the deadliest pandemic in recent times in the form of COVID-19. Pandemic caused by a new corona virus called SARS-CoV-2 in the year 2019 has caused COVID-19. The first case of COVID-19 was reported in China, in December 2019. COVID-19 turns out to be dangerous because of its nature of transmission.

R. T. A. Ranee (✉) · V. G. Srisanthi
Department of Civil Engineering, Coimbatore Institute of Technology, Coimbatore, India
e-mail: anitha.rt@cit.edu.in

V. G. Srisanthi
e-mail: srisanthi@cit.edu.in

According to World Health Organization (WHO) studies, this virus spreads mainly when an infected person comes in close contact with other person through the respiratory route after an infected person coughs sneezes or breathes [9]. As a result persons close contact need to be avoided to prevent the transmission of this pandemic and also it was later suggested that all individuals suspected to have symptoms of COVID-19 and COVID-19 infection confirmed persons have to undergo isolation either in hospital or home.

To break the chain of transmission and also for the well-being of the patient to recover soon from the pandemic depending upon the severity of the case, patients need to be isolated. WHO suggested 14 days quarantine to stop the transmission of the disease.

2   Cold Form Steel (CFS)

Cold-formed steel is the steel products shaped by cold working processes carried out near room temperature. The manufacturing process of cold form steel sections involves either press-braking or cold roll forming to achieve the desired shape. These cold-formed steel is used in the construction industry for both structural and non-structural components. Application of cold form steel in construction industry has its origin in United States and Great Britain. Initially, due to lack of cold form steel code availability, its usage was very minimal and used in combination with hot rolled steel. As the codal provisions for cold form steel start emerged with its AISI standards, JIS standards, its application in construction industry also got a boon.

Moreover, cold form steel has many added advantages where new profiles as per our own requirement can be produced due to its feasible nature. Cold form steel components can be obtained from a single supplier source which further minimizes the complication involved in the construction process. Cold form steel structures being light in weight, handling and transportation turns to be efficient. Unlike concrete, steel being recyclable material will behave as an environmental friendly construction material. Cold form steel panels and decks can be provided with enclosed cells for conduit, which makes plumbing and electrical work easy and quick making it convenient for the workers. Construction time at site can be rapidly reduced if building components were fabricated with high accuracy in plant unlike concrete structures.

2.1   *Necessity of Cold Form Steel in Covid Infrastructure*

COVID-19 is a time when infrastructures for health care and quarantining are required in large scale and in a short period of time, especially in remote and under developed places. Hospital facilities along with emergency, obstetric services, toilet facilities need to be set up for both covid and non-covid migrant people for 14 days quarantine.

Also in many areas in India, schools and colleges which are converted as temporary covid isolation center need to be partitioned. All these activities need to be completed in limited time. Keeping the need of hour in mind, cold form steel construction is the best practice that can be adopted to handle the infrastructure necessity. Some of the important advantages of cold-formed steel structures are good thermal insulation, good acoustic insulation, very good fire resistance and excellent earth quake resistance.

2.2 Ease of Construction

Independent time studies suggest that six pairs of experienced erectors could erect CFS structure up to roof level for a size of 8 m × 12 m in under five hours, beginning with spreading and leveling of gravel, laying out footing C section, its anchoring and erection of wall panels. If 1 m wide wall panel rather than 0.5 m wide panels were used, the elapsed time would be reduced by 30 minutes. Compared to this, about 70 man hours are required to erect a concrete basement using prefabricated form work. Conventional wet constructions due to setting of cement, form work striping operations for both footings and column will take three to four days even in good weather to reach finished floor level.

The CFS COVID prototype requires no mechanical handling, heavy equipment, or special tools. Due to its lightness, it gives the advantage of easy portability to any site. It is particularly beneficial in remote areas and scattered lots.

3 Typical Covid Infrastucture Using CFS

For ease of understanding, a COVID prototype 8 m x 12 m module is considered. The module will be able to accommodate 24 patients. Depending on the requirement, the same can be up scaled. Various aspects involved in construction of above prototype of 8 m × 12 m module are:

3.1 Structural Design and Analysis

First phase after conceptualization is design phase. There are number of off the shelf commercially available softwares used for design, vertex BD is one such example. In this software, all load conditions like dead load, live load, wind loads and other site specific details like dimensions are applied. Software will do instant engineering analysis and will provide various design options. Vertex BD software uses finite element analysis for design [8]. Design output can also be checked from conventional design software, and also, individual CFS structural components can be numerically
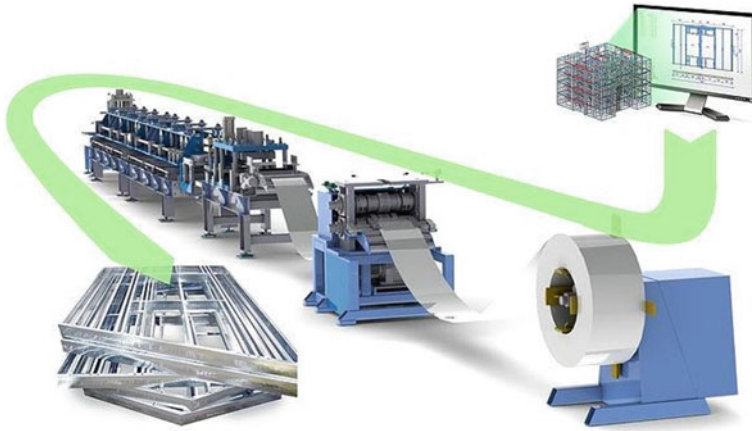
Fig. 1 Process involved in fabrication of cold form steel components. (Photo courtesy vertexcad.com)

validated [1]. Researchers like Chen et al and Young et al has used conventional numerical FEA to design various components of CFS built up section [3, 4]. Ideal design as per steel utilization is selected.

3.2 Production of Components

Once, a specific design is selected vertex BD software feeds the details to components fabrication machine. Machine fabricates various components like C section, joists, wall panel, roof panel from cold-formed steel rolls. During fabrication machine provides even minute details like dimple punch for screw heads, web notches, service holes, etc. Figure 1 gives the board view of the process involved.

3.3 Assembly of Components

Depending upon the site conditions in terms of accessibility, individual components can be assembled at factory or at the site. Transportation of individual panels can give more tonnage transportation per truck.

3.4 Gravel Filling

Once the CFS individual components or semi-build up components reaches the site, erection process starts. The activity in construction site commences with site clearance followed by marking and necessary excavation. The traditional foundation construction begins with sand filling and plain cement concrete (PCC) which serves as a construction leveler and final load distributor, and the above activities are of wet type of construction. Wet construction reduces speed of progress mainly due to setting time of cement. To greatly increase speed of construction, dry construction was considered.

In dry type of construction use of cement has to be totally eliminated or its use reduced to bare minimum quantity. The all dry approach must rely only on dry materials otherwise it loses the advantages of one day construction and all weather construction. Dry gravel filling fits the requirement of dry material in lieu of PCC. The gravel filling facilitates leveling of minor undulations in excavated ground, and it also acts as load distributor from CFS structure to ground (Fig. 2).

3.5 Footings

Footings used in connection with a gravel filling are made from CFS of size between 2 mm and 2.5 mm thick steel in a form of a C, or modified C section. CFS sections are made from Nippon steel SPCD-SD confirming to JIS G 3141 standards. Footings are placed on top of the gravel pad along the whole periphery of the structure to act as load bearing structure. C sections are suitably anchored on gravel filling by fasteners. C sections have slots/connectors for receiving wall panels. In the next stage of erection, the walls in the form of CFS panels are placed on the top of the footings.
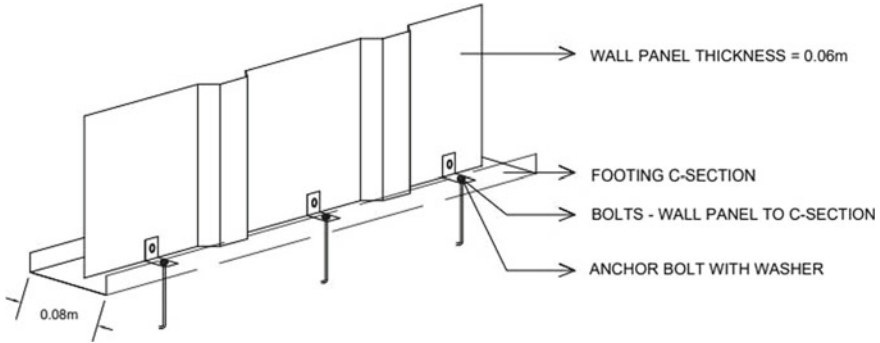
Fig. 3 Anchorage of C section and connection of wall panel with C section

Without the massive concrete in the foundation in the form of PCC, reinforced cement concrete (RCC) footing, RCC column, etc., the total weight that the soil must support is considerably reduced. Even this is suitable for sites with less safe bearing capacity. Additionally, the width of the footing can also be reduced. Just 10 cm wide footings are more than sufficient in most cases. Figure 3 shows anchoring of C section in gravel and connection of wall panel with C section.
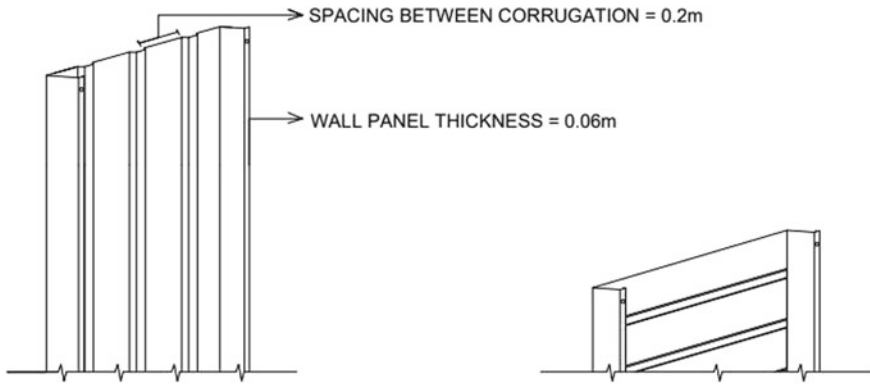
3.6 Wall Panels

The wall panels are basically stressed by the dead loads, live loads and wind load. Figure 4 shows the assumed load distribution in a proto type CFS structure. Wall panels finally distributes superstructure load to gravel filling, which intern distributes to the ground below.

Floor joist and floor deck have to be designed to take live load and dead loads of the floor; in addition, it may be subjected to upward bending moment due to
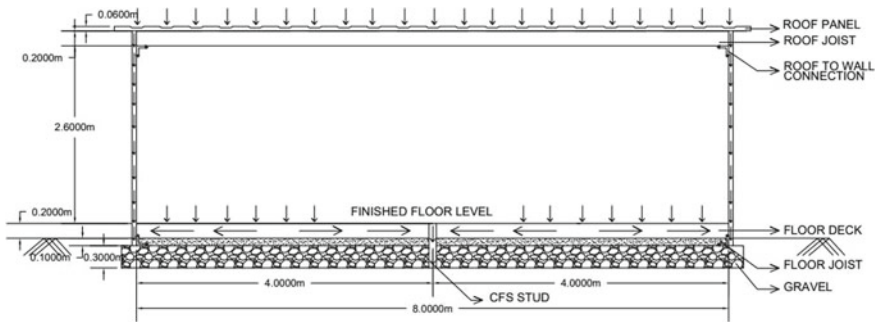
Fig. 4 Cut section of prototype CFS

Fig. 5 A typical wall panel with vertical and horizontal stiffener

bulking of soil. The maximum bending moment due to soil pressure depends upon the amount of soil pressure, its distribution and the depth of the gravel filling below the ground level. The soil pressure depends upon the type of soil and changes in its content of moisture. The soil pressure is lowest in a very permeable soil, heaviest in active soils like clay which swell in winter by accepting moisture and may exert pressures several times larger than those of normal soils. Upward bending moment can be arrested by providing intermediate column studs below floor joist [2]. Figure 5 depicts CFS wall panels used for COVID-19 structure. The wall panels are made from Nippon steel SPCD-SD confirming to JIS G 3141 [6] of sheet thickness 1.5 mm thick with galvanized finish. The wall panels were of height 2.5 m and width 0.5 m with 0.07 m deep ribs at either end of the panel. Generally dimensions of wall panels are calculated by software and fabricated by built-in sheet bending machine.

Buckling of wall panels can be reduced by stiffening the panel by means of either horizontal or vertical ribs (see Figure 5). As the panel is relatively narrow, the horizontal ribs have a greater stiffening effect. Another method to reduce buckling is to split the wall panels into specially designed load bearing studs and very simple panels. Edges of these wall panels would wedge into the corresponding crevices in load bearing studs during the erection. Such design might prove beneficial for a number of reasons:

The walls would be even easier to install, particularly in high wind.

The studs could be perforated creating better thermal insulation thus further reducing the heat transfer. Panels could be easily exchanged in case of damage.

To improve the esthetics and acoustics, wall panel can be clad both on inside and outside or only inside [5]. Thickness of cladding is generally 10 mm. There are wide varieties of cladding materials in the market, some of which are fiber cement board, magnesium oxide boards, ferron boards, etc. In case of constructing covid infrastructure in extreme weather conditions, to minimize effect of outside temperature, insulation has to be provided between wall cladding and wall panel. Various options

for insulations are rock wool, glass wool, thermocol, light weight concrete. Glass wool is the cheapest and widely used insulating material.

3.7   Roof Panels

There are wide variety of roof panels used in CFS structures both in terms of shape and material. Roof shapes are dictated by architecture plan and material by cost, climate, etc. Roof panel used for our covid prototype is corrugated type supported on roof joist. Other than providing roof covering, CFS roof panels also functions as structural components by resisting wind uplift and maintaining the integrity of the building under lateral wind and seismic loads. They also fulfill appealing architectural requirements. The roof panels can be fastened to joist with concealed sliding clips. In high ambient temperature areas, standing seam roof system is used. The standing seam roof system is a special type of roof which can accommodate roof panel movement due to temperature changes.

In covid prototype, top of wall panels needs to be connected with CFS roof joist of 30 cm deep. This joist act as base for placing CFS roof panels. Covid prototype requires joist at 1 m c/c. Roof panels are corrugated sheets made from 1.5 mm thick CFS sheets. Figure 6 shows CFS joist and roof panel assembly. Similarly for roof insulation, wall insulation materials as discussed earlier can also be used.

Final finishing. There are number of site specific requirement that needs to be executed in a structure. Covid proto type needs to be provided with approaches from nearby road/ pavement. Internal and external electrification has to be executed. CFS structure has built-in slots to run electric conduit pipes, this greatly saves wall chiseling work. Similarly plumbing pipes can be run along predefined slots.
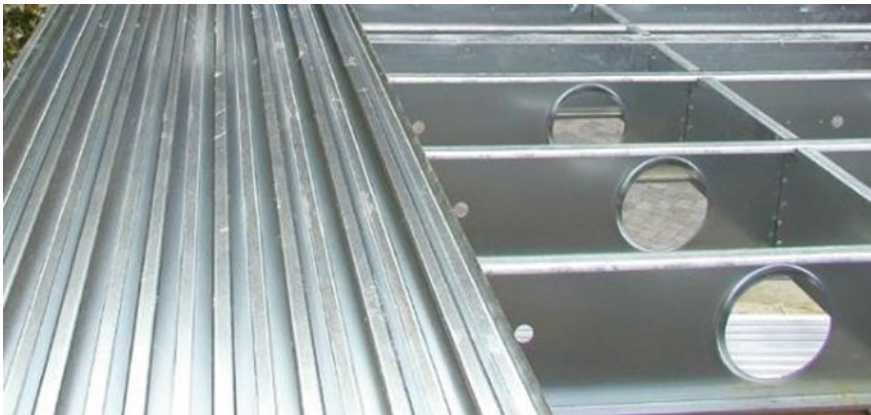
Fig. 6   Placement of roof panel over roof joist. (Photo courtesy rondo.com)

Fig.7 Frame work of CFS partion wall (Photo courtesy rondo.com)

Hospital specific requirements like oxygen supply pipes, medical monitor's needs to be incorporated. Finally, painting and hospital furnishing is done.

Wall Partitions. Another widely used application of CFS in buildings, especially COVID infrastructure is for wall partitions. Advantages of using CFS wall partitions for covid are many, these are helpful to provide temporary partition in existing buildings like marriage halls, convention centers, and additional advantages are as under:

Very convenient. It's lighter than wood or brick wall and takes up half the space because of its hollowed shape. A typical wall panel with one side insulation increases carpet area by 8% and wall with two side insulation increases carpet area by 6%, compared to brick wall. It is easy to transport and storage. Skeleton work of CFS partition and semi-finished partition are shown in Fig. 7 [7].

Ease of installation: CFS partition walls easier to handle because it weighs very less compared to other conventional building materials.

Stability: In case of CFS partition, there is no problems like twisting and warping of wood. Wood also wicks moisture, which can lead to mold growth and rot. A vapor barrier or a gasket between the bottom plate and the concrete floor gives better air tightness and insulation.

Strength: The strength and ductility of CFS walls, along with the holding power of CFS connections, make it ideal for construction in high wind and seismic zones such as cyclone prone eastern coasts.

Insects and Fire: Carpenter ants and termites can severely damage wood construction, but steer clear of metal. Likewise, wood burns and metal does not. A wall built with metal studs is virtually fireproof.
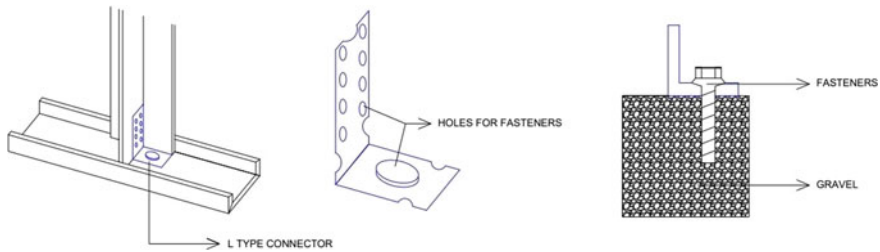
Fig. 8 A typical connection of wall panel with footing C section

3.8 Connections

A connection plays a major part in load transfer. There are number of connections required in fabricating a CFS structure. Even though there are wide varieties of readymade connections available, however, as per requirements connections can be fabricated. One such connection for connecting wall panel to gravel footing is given in Fig. 8.

4 Conclusions

An ideal infrastructure for covid not only requires economy in terms of time, effort, resources but also ease of construction and portability. Structures made of CFS fits ideally for the above requirement. Compared to traditional building materials, economics weighs in favor of CFS. Compared to cement prices, steel has not increased steeply over the last decade. Cement prices have increased by over 60 % in last decade whereas steel prices has only risen by less than 10 %. Also per capita consumption of steel is only 75 kg, compared to global average of 224 kg. Per capita consumption of cement in India is 235 kg which is more than global average. By adopting CFS in large scale, the situation can be reversed. Steps have already been taken in right direction. CFS is also ideal for other infrastructures like low-cost housing, ware houses, etc. Government of India's plan to provide housing for all under Pradhan Mantri Awas Yojana (PMAY) uses CFS in large scale.

References

1. Young BM, Chen J (2008) Design of cold-formed steel built-up closed sections with intermediate stiffeners. J Struct Eng 134(5):727–737
2. Georgievaa I, Schueremansa L, Vandewallea L, Pyla L (2012) Design of built-up cold-formed steel columns according to the direct strength method, Steel Structures and Bridges. Procedia Eng 40:119–124

3. Li L-Y, Chen J-K (2008) An analytical model for analysing distortional buckling of cold-formed steel sections. Thin-Walled Struct 46:1430–1436
4. Zhang J-H, Young B (2018) Finite element analysis and design of cold-formed steel built-up closed section columns with web stiffeners. Thin-Walled Struct 131:223–237
5. Selvaraj S, Madhavan M (2019) Bracing effect of sheathing in point symmetric cold formed steel flexural members. J Construct Steel Res 450–462
6. Japan Industrial Standards (JIS) G (2005) 3141:2–7
7. http://www.rondo.com.au. Last accessed 2020/12/15
8. http://www.vertexcad.com. Last accessed 15 Dec 2020
9. http://www.who.int. Last accessed 15 Dec 2020

Fragility Analysis for Frame with RC and Steel-composite Shear Wall

P. P. Phadnis

Abstract Shear walls are structural members that are widely used in medium and high-rise buildings to increase the overall rigidity and resistance against lateral loads. In multi-storeyed buildings, provision of the reinforced concrete shear wall (RC SW) is restricted due to the overcrowded reinforcement provided at both extremities of the wall. To conquer this condition, a huge amount of reinforcement is replaced by vertical steel profiles encased in the steel–concrete composite shear wall (CM SW). This paper aims to compare the behaviour of the frame with conventional RC SW and frame with CM SW using the capacity spectrum method. The capacity spectrum method captures the randomness and ambiguity associated with capacity spectrum characteristics, damage states, and characteristics of ground motion. The fragility curves based on spectral displacement are developed from the capacity spectrum. Damage probability matrices are generated from fragility curves. It is concluded that the performance behaviour of a frame with the CM SW system is superior in terms of damage probability than a frame with RC SW.

Keywords Reinforced concrete shear wall · Steel–concrete composite shear wall · Capacity spectrum method · Fragility curves · Damage probability matrices

Abbreviations

ϕ_y	Curvature at yield state
L_v	Shear length constant for symmetrical elements (1/2 of the total element length L)
H	Height of total section
d_b	Mean diameter of the longitudinal bars in the affected section (e.g. ø10 = 10 mm)
f_y	Yield strength of the longitudinal reinforcement steel [MPa]

P. P. Phadnis (✉)

Assistant Professor, Department of Technology, Shivaji University, Kolhapur, Maharashtra, India

e-mail: ppp_tech@unishivaji.ac.in

| f_c	Concrete compression strength [MPa]
a_v	$a_v = 1$ If shear cracking is expected to precede flexural yielding at the end section; otherwise, $a_v = 0$.
z	Internal lever arm length, considered equal to d-d' in beams, columns, or walls with barbelled or T-section, or to $0.8\,h$ in walls with rectangular section [mm]
d	Depth to the tension reinforcement [mm]
d'	Depth to the compression reinforcement [mm]
ϕ_y	Yield curvature
ϕ_u	Ultimate curvature
L	Shear length [mm]
L_p	Plastic hinge length [mm], where, $L_p = 0.08L_v + 0.022f_yd_b$
V_{cm}	Shear capacity of steel shape in the composite member
V_s	Shear capacity of reinforcement
V_{rc}	Shear capacity of the RC portion in the composite member
b_s	Section width
d_s	Effective depth
f_c'	Unconfined compressive strength
N_u	Axial load on the section
A_g	Concrete area
A_s	Area of transverse reinforcement
f_s	Yield strength of transverse reinforcement
S	The spacing of transverse reinforcement
ds	Damage state
S_a	Spectral acceleration
$S_{a,ds}$	At given median acceleration
β_{ds}	Standard deviation for particular damage state
$\emptyset$	Standard normal distribution function
$P()$	Probability of being in or exceeding a particular damage state
F	Base shear
Δ	Top displacement
A-B	Details of hinges falling in operational range
B-IO	Details of hinges falling in operational and immediate occupancy range
IO-LS	Details of hinges falling immediate occupancy and life safety range
LS-CP	Details of hinges falling in life safety and collapse prevention range
CP-C	Details of hinges falling in collapse prevention and ultimate strength range
C-D	Details of hinges falling in ultimate strength and residual strength range
D-E	Details of hinge falling in residual strength and failure range

1   Introduction

In multi-storeyed buildings, reinforced concrete shear walls (RC SWs) have been used for several years. The main function of shear wall is to resist lateral shear forces caused due to transverse wind and earthquakes. RC SWs when imposed to huge cyclic loadings cause major disadvantages like spreading of cracks in the tension zones and crushing in the confined compression regions. These may result in deterioration in lateral strength and stiffness, splitting and, finally, result in shear wall failure. The use of steel plate shear walls in mid-rise and high-rise buildings as lateral load withstanding systems is recommended by Zhao Q. and Astanesh-Asl [1]. But, the provision of steel plate shear walls in mid-rise and high-rise buildings consequences in the shortcomings like reduction in stiffness, shear strength, and energy dissipation capability because of the buckling of the compression region. To overcome such adverse conditions, the design codes of many countries suggested provision of boundary elements concentrated with vertical reinforcement and closely spaced ties, at both extremities of RC SW. On the other hand, even with such provision, when the thickness of the wall is less than 300 mm, these boundary elements consequences in congested reinforcement. To upgrade the seismic response of the multi-storeyed frame and to circumvent congested reinforcement at the boundary elements of the shear wall, a novel CM SW system with embedded vertical steel profiles at both extremities is proposed in this study as an alternative of conventional RC SW. The reinforced concrete shear walls (RC SW) are replaced by steel–concrete composite shear walls (CM SW) because of the significant increase in strength, stiffness, and ductility [2, 3]. In practice, these shear walls are always accompanied by moment-resisting frames. Therefore, in this study, performance behaviour of the frame-CM SW dual system has been studied.

Seismic performance and vulnerability analysis of building with their probabilistic nature are the main concern of structural designers. These curves account for the unpredictability and ambiguity linked with capacity spectrum properties, damage levels, and ground shaking. Many researchers proposed empirical and analytical methods to generate fragility curves for potential risk management. In FEMA, P-58–1:2012 [4] report illustrated the development of fundamental building information, response magnitudes, and resulting data utilized as inputs to the fragility analysis. Astriana L. et al. [5] developed spectral acceleration-based fragility curves for frame-RC SW dual system as per HAZUS-MH 2.1 [6] and ATC 40:1996 [7] capacity spectrum method and illustrated that frame-RC SW dual system can resist more lateral force and had enhanced seismic performance with lower probability of damage.

2   Structural Model

Two dual systems, i.e. frame-RC SW and frame-CM SW have been analysed using the capacity spectrum method. The system has two bays of 5 m in X and Y directions,

Fig. 1 Plan of building
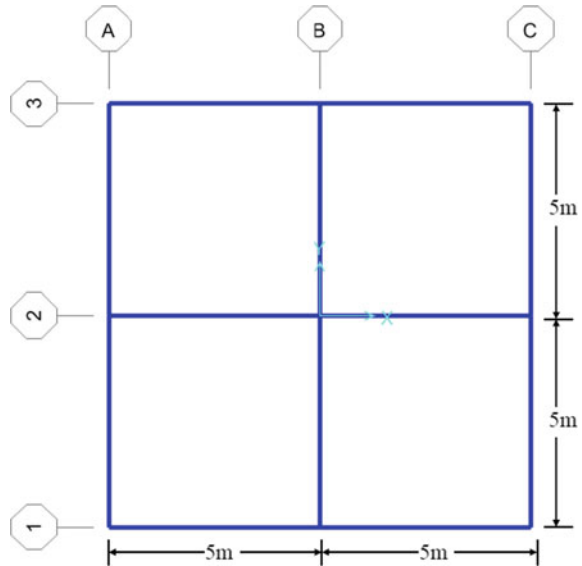
respectively, and storey height of 3.5 m as depicted in Figs. 1 and 2. Shear walls are designed as ductile walls as per provisions of EC2 [8], EC4 [9], and EC8 [10] to avoid brittle failure during the action of lateral forces. The details of the beam, column, RC SW, and CM SW are shown in Figs. 3a–d, respectively.

Materials used in present work are M20 grade concrete, Fe415 grade rebar, and Fe410 grade structural steel. The thickness of slab is 120 mm. A dead load of terrace waterproofing is $1.5kN/m^2$ and floor finish is $0.5kN/m^2$. The imposed load is $2kN/m^2$ at the roof and $4kN/m^2$ at floors. The structure is presumed to be sited in seismic zone V in India.

3 Nonlinear Modelling

A two-dimensional frame-shear wall model is generated for the nonlinear analysis. Beams and columns are simulated as two node beam elements. RC SW and CM SW are modelled as mid-pier element [11] by means of section designer provision existing in SAP2000. In frame-shear wall configuration, junctions of beam and shear wall are rigid. These rigid junctions consist of infinite stiffness. They are implemented in software by offset utility command.
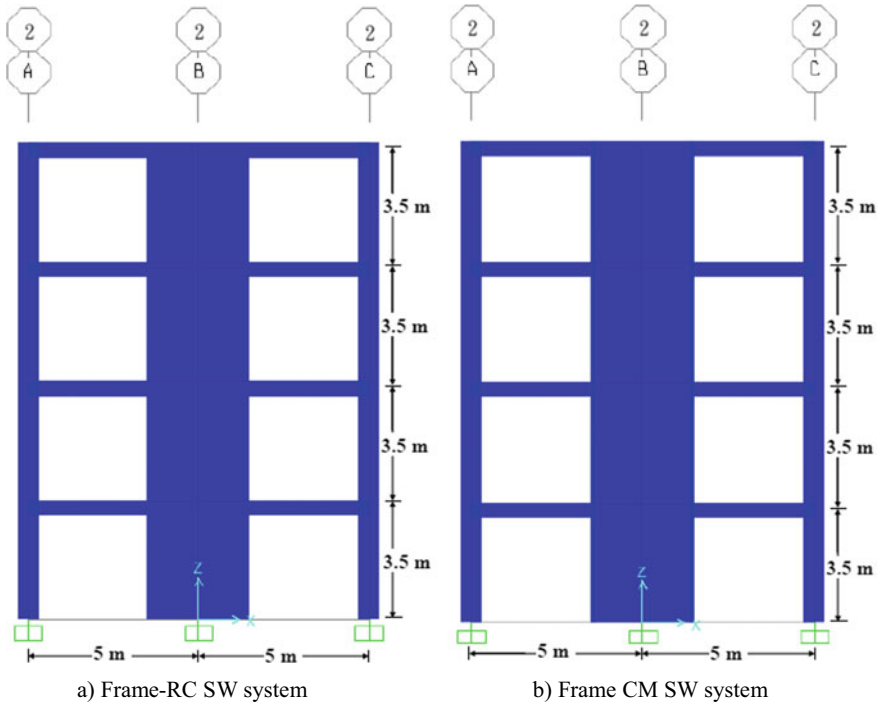
a) Frame-RC SW system   b) Frame CM SW system

Fig. 2 Sectional elevation of middle frame

3.1 Effective Stiffness

The influence of material nonlinearity because of concrete cracking on pushover response of the frame elements has been incorporated. The elements of frame-shear wall system are assigned with the effective moment of inertia to incorporate the influence of concrete cracking. The different design codes of various countries prescribed different values for effective moment of inertia. EC-8 [10] prescribed 0.50 times gross moment of inertia for beams and columns for any extent of axial loading, IS 1893 [12] and ACI 318 [13] assumed 0.70 and 0.35 times for the columns and beams, FEMA 356 [14] (0.50 for beams and 0.70 for columns), and ASCE 41 [15] (0.30 for beams and 0.70 for columns) suggested effective moment of inertia based on the intensity of axial loading. Here, 0.5 times gross moment of inertia is prescribed by Eurocode-8 [10] to be considered as effective for all sections.
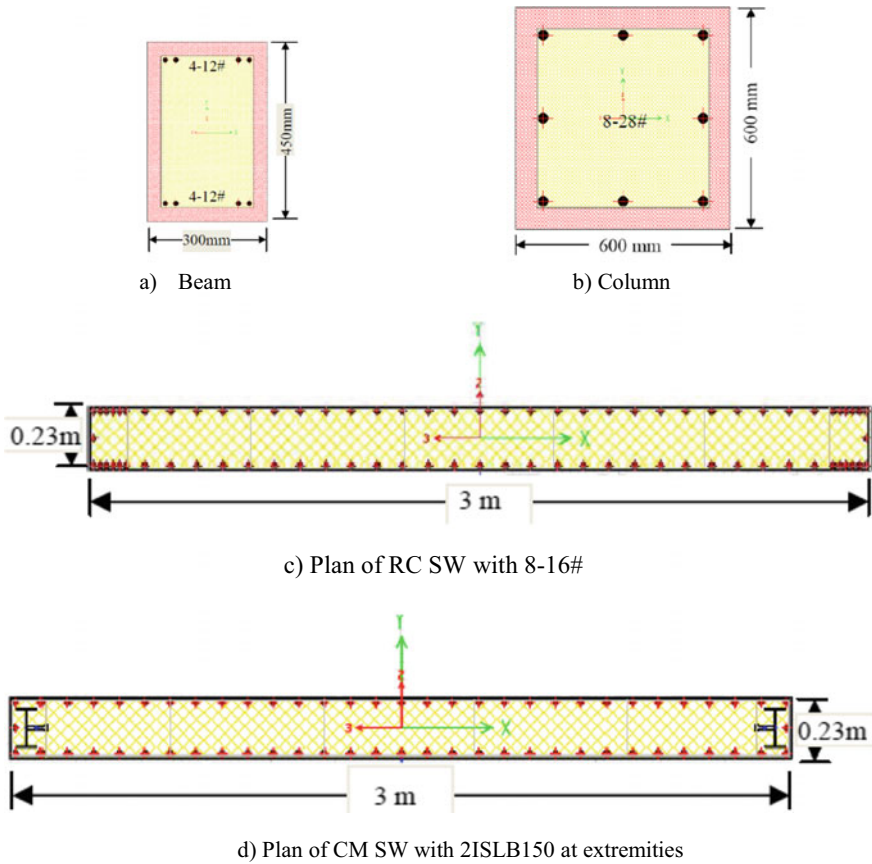
a) Beam

b) Column

c) Plan of RC SW with 8-16#

d) Plan of CM SW with 2ISLB150 at extremities

Fig. 3 Details of frame elements

4 Material Nonlinearity

Material nonlinearity is considered by Mander's confined curve for concrete [16], Park's model [17] for reinforcement and Simple model for structural steel.

Flexural Hinges

For all frame-shear wall dual systems, moment–curvature (M-ϕ) analyses have been fundamental necessity as input for software. Hence, moment-rotation (M-θ) values have been determined from moment–curvature (M-ϕ) values by utilizing formulae specified in Eurocode-8 Part 3 (CEN 2004) [10].

Yield rotation θ_y is estimated as per Eurocode-8 Part 3 (CEN 2004) [10] as specified in Eq. (1).

$$\theta_y = \varnothing_y \frac{L_v + a_v z}{3} + 0.00135\left(1 + 1.5\frac{H}{L_v}\right) + 0.13\varnothing_y \frac{d_b f_y}{\sqrt{f_c}} \tag{1}$$

The rotation at ultimate state θ_u is estimated as per Eurocode-8 Part 3 (CEN 2004) [10] as specified in Eq. (2).

$$\theta_u = \theta_y + \left(\emptyset_u - \emptyset_y\right) L_p \left(1 - \frac{0.5 L_p}{L_v}\right) \tag{2}$$

Sample curve of *M3* hinge (*M-θ* relation) for the beam is depicted in Fig. 4a. The sample curves for *P-M* hinge (*M-θ* behaviour) for column and for RC SW and CM SW are indicated in Fig. 4b, c, respectively.
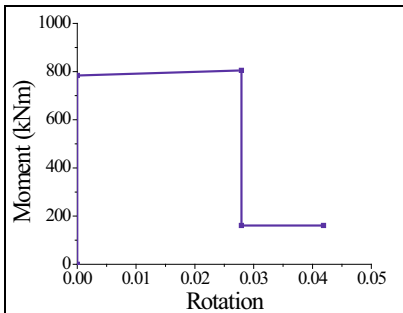
Shear hinges

The shear failure has been modelled for elements of frame-shear wall dual system as force-controlled action (brittle) according to ASCE/SEI 41–06: 2007 [15].

The shear potential of the composite element with embedded steel profile in concrete can be obtained according to Weng C.C. et al. [18] specified Eqs. (3–7)
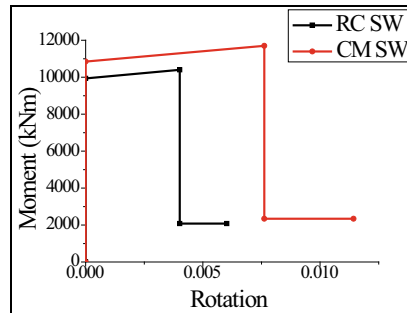
$$\text{Total shear strength} = V_{\text{cm}} + V_s + V_{\text{rc}} \tag{3}$$
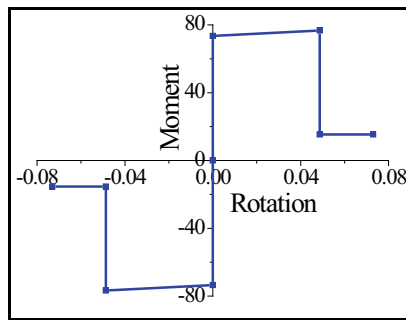
a) *M3* hinge (*M-θ* relation) for beam

b) *P-M* hinge for column

c) *P-M* hinge for RC SW and CM SW

Fig. 4 Hinges for frame elements

Table 1 Shear hinge values for elements of frame-shear wall dual system

Element	Shear strength V (kN)
Beam	162.77
Column	350.72
RC SW	1163.91
CM SW	1360.33

$$V_{\mathrm{cm}} = 0.6 f_{\mathrm{ys}} A_{\mathrm{ws}} \tag{4}$$

A_{ws}—area of steel web of encased steel section.

f_{ys}—yield strength of steel section.

Axial compressive force, bending, and shear are applied to sections as per ACI 318–08 (2008) [13], and diagonal shear capacity of the concrete is determined using Eq. (5),

$$V_{\mathrm{rc}} = V_c + V_{\mathrm{rs}} \tag{5}$$

V_c—shear capacity of concrete.

V_{rs}—shear capacity of reinforcement.

Shear capacity of the concrete is evaluated by using Eq. (6),

$$V_c = 0.166 \left(1 + 0.073 \frac{N_u}{A_g} \right) \sqrt{f'_c} b_s d_s \tag{6}$$

Shear capacity of reinforcement is obtained by using Eq. (7),

$$V_{\mathrm{rs}} = \frac{A_s f_s d_s}{S} \tag{7}$$

Shear hinge values for frame elements are presented in Table 1.

In the present study, beams have been assigned with the only moment (*M3*) and shear hinges (*V*) as they can subject to bending and shear. The columns and shear walls have been allocated with axial force-moment interaction hinges (*P-M*) and shear hinges.

5   Geometric Nonlinearity

During the analysis, geometric nonlinearity is also considered. It is associated with alteration in element shape subjected to lateral loading; the relation between strain–displacement becomes nonlinear. The utility exists in SAP2000 library, and it is just chosen in nonlinear analysis. *P-Δ* effect accounts for the additional moment induced in the column due to gravity loading.

6 Nonlinear Analysis

6.1 Nonlinear Static Analysis (NSA)

Here, NSA is performed to access the seismic response of frame-shear wall systems. An inelastic analysis approach demonstrates how a building responds by identifying damage modes and the dynamic collapse probability. During the NSA, a frame-shear wall system is forced to gravity loads (DL + 0.5LL) and at the simultaneously imposed to predefine gradually increasing lateral load pattern till roof-top displacement achieves a target displacement. Here, the modal pushover analysis is carried out.

6.2 Capacity Spectrum Method (CSM)

The capacity curve determined from NSA can be reconstructed into the capacity spectrum to exploit CSM prescribed by ATC 40:1996 [7]. The storey displacement and the total base shear are transformed to the spectral displacement S_d and spectral acceleration S_a by the application of modal participation factor and effective modal mass for the first fundamental mode. The performance of a building to an earthquake can be obtained by superimposing the capacity curve and seismic demand curve. Capacity spectrum (CS) intersects a reduced demand spectrum (DS) to obtain the performance point (inelastic seismic demand). The performance of the frame-shear wall system is evaluated depending on the performance point, considering immediate occupancy (IO), life safety (LS), and collapse prevention (CP). If the damage condition at this performance point is satisfactory, then the system is considered to be protected for the design basis earthquake.

7 Fragility Analysis

Building seismic performance and vulnerability analysis with its probabilistic nature is presently an interest of the structural designer. Precise building vulnerability may be obtained by developing fragility curves. Fragility curves express the probability of damage to the building. Building fragility curves are lognormal functions that express the probability of reaching or exceeding damage states at given median estimates of spectral response for example spectral displacement.

These curves account the variability and uncertainty related to capacity spectrum properties, damage levels, and ground shaking.

7.1 Fragility Function

Due to the indiscriminate properties of earthquakes, the structural response at certain seismic loading is best determined by the probabilistic approach rather than deterministic. Hence, in performance-based earthquake engineering (PBEE) design approach, the distribution of structural response (engineering demand parameter, EDP, i.e. maximum inter-storey drift ratio) is related probabilistically with intensity measure (IM), i.e. spectral displacement, spectral acceleration, and peak ground acceleration).

This distribution is formulated by relating probability function of engineering demand parameter for given intensity measure (IM), i.e. *P(EDP|IM)*. The damage function is assumed to be lognormal function. To define a probability distribution, median and standard deviation values are required. The conditional probability of being in or exceeding a particular damage state, *ds,* is defined by the fragility function as

$$P\left[\frac{ds}{S_a}\right] = \emptyset\left[\frac{1}{\beta_{ds}}\ln\left(\frac{S_a'}{S_{a,ds}}\right)\right] \tag{8}$$

Discrete damage probabilities can be determined as follows:
Probability of complete damage,

$$P[C] = P[C|S_a]$$

Probability of extensive damage,

$$P[E] = P[E|S_a] - P[C|S_a]$$

Probability of moderate damage,

$$P[M] = P[M|S_a] - P[E|S_a]$$

Probability of slight damage,

$$P[S] = P[S|S_a] - P[M|S_a]$$

Probability of no damage,

$$P[N] = 1 - \{P[S|S_a] + P[M|S_a] + P[E|S_a] + P[C|S_a]\} \tag{9}$$

Table 2 Damage state thresholds as per Barbat [19]

Damage states	Median spectral displacement ($S_{d,ds}$)
Slight	$S_{d,S} = 0.7\, S_{d,y}$
Moderate	$S_{d,M} = S_{d,y}$
Extensive	$S_{d,E} = S_{d,y} + 0.25\,(S_{d,u} - S_{d,y})$
Complete	$S_{d,C} = S_{d,u}$

7.2 Damage States and Variability

The major outcome of pushover analysis is in the form of a load–displacement curve, called a capacity curve. Capacity spectra are determined according to the ATC 40 method from modal pushover analysis. Median spectral displacements are determined as per Barbat, et al. [19] criteria as shown in Table 2.

The stepwise procedure utilized is as follows:

i.   Select the group of buildings as per the classification prescribed in HAZUS technical manual [6].

ii.   Choose the value of standard deviation (SD) related to seismic design levels for respective damage states.

iii.   Choose damage state criteria.

iv.   Determine the values of fragility parameters derived from properties of CSM.

v.   Note the values of standard deviation for the chosen classification of building according to HAZUS technical manual [6].

vi.   Develop fragility curves using Eq. (8).

vii.   Determine damage probabilities using Eq. (9).

8 Result

8.1 Fundamental Time Periods

The modal analysis is carried out, and the results of the fundamental time periods for the frame-RC SW and frame-CM SW are as presented in Table 3.

The fundamental time period of the frame-CM SW is reduced by 6% with respect to the frame-RC SW. This indicates an increase in stiffness of the system due to the provision of CM SW.

Table 3 Fundamental time period

Configuration	Fundamental time period (sec)
Frame-RC SW	0.53
Frame-CM SW	0.49

Table 4 Displacements at first two mode shapes

Configuration	Mode 1		Mode 2	
	Translational displacement (m)	Rotational displacement (rad)	Translational displacement (m)	Rotational displacement (rad)
Frame-RC SW	0.0983	0.00782	0.056	0.0142
Frame-CM SW	0.0980	0.00779	0.053	0.0139

In general, building is considered as torsionally susceptible if any of the first two mode shapes is predominated by rotational displacement with respect to a perpendicular reference axis. A building is considered as torsionally non-susceptible in which first two mode shapes are predominated by translational displacements [20].

Table 4 represents displacements at first two mode shapes for both dual systems considered in the study.

From Table 4, it is observed that frame-RC SW and frame-CM SW systems are not torsion sensitive, and first mode is predominant in both systems. Hence, NSA is sufficient to analyse progressive collapse of the systems.

8.2 Capacity Spectrum

From NSA, capacity curves are obtained. Capacity spectrums (CS) and demand spectrums (DS) are intersected in ADRS format as discussed by ATC 40: 1996 [7] to evaluate performance points. The properties of the capacity spectrum are presented in Table 5.

The base shear capacity of frame-CM SW is 5% more than the base shear capacity frame-RC SW. Lateral strength of frame-CM SW is observed to be enhanced due to the provision of concentrated structural steel profile encased at boundary elements of CM SW. A deformation capacity of frame-CM SW is also improved by 36%. The hinge pattern of frame-CM SW shows that three more hinges are produced at inferior damage level, i.e. operational and immediate occupancy range (B-IO), and one lesser hinge is produced at upper damage level, i.e. immediate occupancy and life safety (IO-LS) range as compared to frame-RC SW system at ultimate state. Hence, CM SW is suggested to enhance the lateral stiffness of the frames situated in earthquake zones.

Salient features of the capacity spectrum are represented in Fig. 5.

From Fig. 5, it is seen that performance point of the frame-CM SW system is shifted towards LS-CP range due to the influence CM SW which increases the strength and stiffness.

Table 5 Damage states and variability

Systems	S_a (g)	S_d (mm)	F (kN)	Δ (mm)	A-B	B-IO	IO-LS	LS-CP	CP-C	C-D	D-E	> E	Total
Frame-RC SW	0.50	74	1192.03	106	63	8	8	0	0	1	0	0	80
Frame-CM SW	0.54	71	1251.35	144	61	11	7	0	0	1	0	0	80

Fig. 5 Capacity spectrum
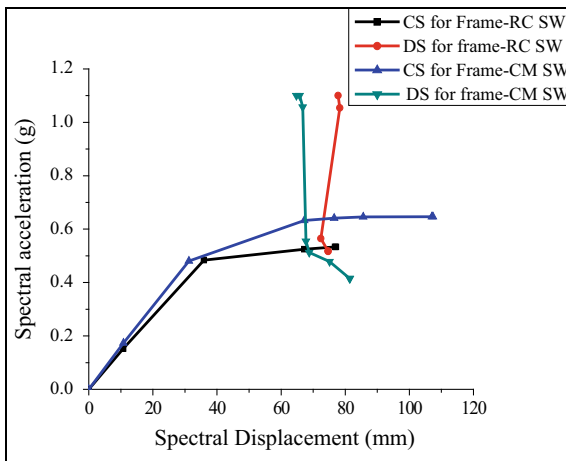
8.3 Fragility Curves

In this case study, four-storeyed, frame-RC SW and frame-CM SW systems are classified as C2M, i.e. mid-rise concrete shear wall building. This classification is as specified in HAZUS document. For future-planned construction, spectral displacement is used as the main variable. The damage thresholds $S_{d,ds}$ and standard deviation β_{ds} for models under consideration are stated in Table 6.

Fragility curves obtained for frame-RC SW and frame-CM SW are presented in Fig. 6.

Damage probabilities for four damage states are determined for spectral displacement equal to 50 mm using Eq. (9) presented in Table 7.

Figure 7 represents discrete damage probabilities in graphical format.

Damage probabilities of slight and moderate damage state of frame-CM SW system are lowered by 2.77% and 22.38% as compared to frame-RC SW system. This reveals that frame-CM SW system offers very least seismic vulnerability for slight and moderate damage states.

Table 6 Damage states and variability

| System	Fragility parameters	Slight	Moderate	Extensive	Complete
Frame-RC SW	Barbat, $S_{d,ds}$ (mm)	44.34	66.51	123.07	201.80
	βds	0.68	0.67	0.68	0.81
Frame-CM SW	Barbat,, $S_{d,ds}$ (mm)	24.57	36.86	41.05	57.52
	βds	0.68	0.67	0.68	0.81

Fig. 6 Fragility curves
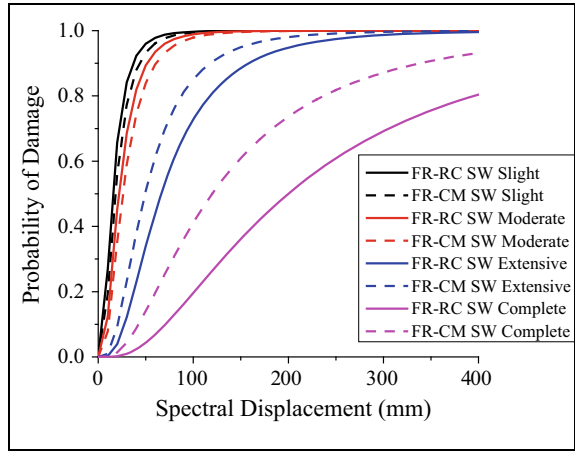
Table 7 Damage probability (%) at $S_d = 150$ mm

System	No damage (%)	Slight (%)	Moderate (%)	Extensive (%)	Complete (%)
Frame-RC SW	3.9837	9.4178	55.419	29.5958	4.3541
Frame-CM SW	6.6705	6.6474	33.0435	36.8412	14.027

Fig. 7 Discrete damage probabilities at $S_d = 150$ mm
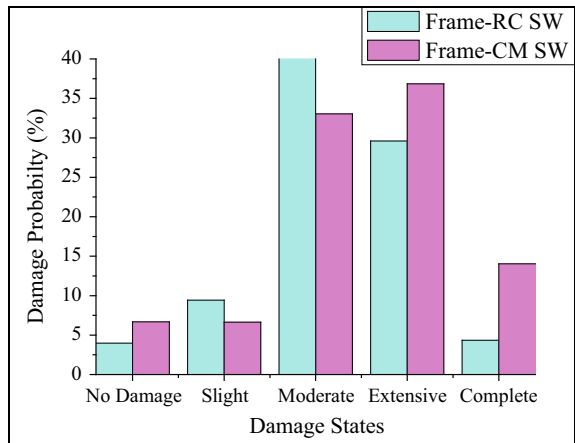
9 Conclusion

The performance of frames with RC SW and CM SW was evaluated through fragility analysis by assigning user-defined hinges. On the basis of outcomes and observations, the subsequent conclusions are presented.

i. .The fundamental time period of the frame-CM SW is reduced by 6% with respect to the frame-RC SW system. This indicates an increase in stiffness of the system due to the provision of CM SW.

ii. The lateral stiffness is noticed to be increased by 6% due to concentrated steel profiles encased for CM SW.

iii. Deformation capacity of the frame-CM SW system is also improved by 36% as compared to the frame-RC SW system due to provision of steel embedded profiles at both extremes of CM SW.

iv The hinging pattern of the frame-CM SW reveals that the development of hinges is at inferior damage levels as compared to the frame-RC SW system. Therefore, the CM SW is suggested to enhance the lateral stiffness of the frames located in seismic zones.

v. At the initial two stages, probabilities of damage are very a smaller. This indicates enhanced initial resistance for the collapse state because of increased stiffness is due to the presence of CM SW in a frame system. The structure has more probable chances of developing extensive and complete damage state. This means that this frame-CM SW system performs better than frame-RC SW system when imposed to earthquakes.

References

1. Zhao Q, Asl A (2007) Seismic behaviour of composite shear wall systems and its application of smart structures technology. Steel Struct 7:69–75

2. Dan D, Fabin A, Stoian V (2011) Theoretical and experimental study on composite steel-concrete shear wall with vertical steel encased profiles. J Constructional Steel Research, Elsevier, 800–813. https://doi.org/10.1016/j.jcsr.2010.12.013

3. Phadnis PP, Kulkarni DK, Kulkarni AB, Karjinni VV (2018) Performance of composite steel-concrete shear walls with encased vertical steel sections. The Indian Concrete J 92(7):74–81

4. FEMA P-58–1 (2012) Seismic performance assessment of building. volume 1–Methodology. Applied Technology Council. California. 94065

5. Astriana L, Sangadji S, Purwanto E, Kristiawan SA (2017) Assessing seismic performance of moment resisting frame and frame-shear wall system using seismic fragility curve. Sustainable Civil Engineering Structures and Construction Materials, SCESCM-2016, Procedia Engineering 171, Elsevier, pp 1069–1076

6. HAZUS®MH 2.1 (2003) Technical manual: Multi-hazard Loss Estimation Methodology Earthquake Model. Federal Emergency Management Agency, Washington, DC, USA

7. ATC 40 (1996) Seismic evaluation and retrofit of concrete buildings (Vol-1). Applied Technology Council, Redwood City, California, USA

8. Eurocode 2 (EC 2) (1992) Design of concrete structures—Part 1–1: General rules and rules for buildings, EN1992–1–1

9. Eurocode 4 (EC4) (1994) Part 1–1: Design of composite steel and concrete structures, general rules and rules for buildings, EN 1994–1–1

10. Eurocode 8 (2004) Part 1: European Committee for Standardization. Design of Structures for Earthquake Resistance: General rules, Seismic action and Rules for Buildings. Brussels

11. Fahjan YM, Doran B, Akbs B, Kubin J (2012) Analysis for performance based-seismic design of RC frames with shear walls. 15th World Conference on Earthquake Engineering, Lisboa

12. IS:1893 Indian Standard (2016) Criteria for earthquake resistant design of structures (Part 1), General Provisions and Buildings. (Sixth Revision), Bureau of Indian Standards, New Dehli, India
13. ACI 318 (2008) Building code requirements for structural concrete and commentary. American Concrete Institute, Detroit
14. FEMA 356 (2000) Federal emergency management agency prestandard and commentary for the seismic rehabilitation of buildings. Building Seismic Safety Council, Washington, DC, USA
15. ASCE/SEI 41–06 (20087) Seismic rehabilitation of existing buildings. American Society of Civil Engineers
16. Mander JB, Priestley MJ, Park R (1988) Observed stress-strain behaviour of confined concrete. ASCE J Structural Engineering 114(8):1827–1849
17. Pauley T, Priestley MJN (1992) Seismic design of reinforced and masonry buildings. Wiley Inter science Inc., USA
18. Weng CC, Yen SI, Chen CC (2001) Shear strength of concrete-encased composite structural members. J Structural Engineering 127(10):1190–1197
19. Barbat AH, Pujaades LG, Lantada N (2008) Seismic damage evaluation in urban areas using capacity spectrum method: Application to Barcelona. Soil Dynamics and Earthquake Engineering, 851–865
20. Avramidis I (2016) Eurocode-compliant seismic analysis and design of R/C buildings. Geotechnical, Geological and Earthquake Engineering. Springer International Publishing, Switzerland. https://doi.org/10.1007/978-3-319-25270-4

Development of VC++ Wrapper for Structural Modeling in OpenSEES

Vijay Kumar Polimeru and Arghadeep Laskar

Abstract Robust finite element frameworks, which support and allow the users to implement state-of-the-art nonlinear finite element and material models are essential to analyze and design seismically resilient structures and for making better decisions (retrofitting or demolition) during seismic assessments of existing structures. OpenSEEs is an object-oriented software framework for developing applications to simulate the behavior of structures under seismic loading conditions. It supports a TCL-based interpreter for finite element modeling of structures to be analyzed (recently a Python-based interpreter has also been added to the source code). The commands written in TCL/Python automatically call the functions implemented in C++ and provide the required output. Majority of the material models and elements implemented in OpenSEEs do not have proper documentation (examples include *hysteretic steel, fiber based nonlinear beam column element, quad element* etc.). Hence, it is often difficult to understand and debug the existing implementations to overcome convergence errors encountered in nonlinear finite element analysis (NLFEA). In the present study, a simple yet elegant VC++ wrapper (vcppwrapper) has been developed to efficiently debug the convergence errors encountered in complex NLFEA problems. The nonlinear finite element model can be directly developed and debugged in the C++ language by using the developed wrapper. The advantages and disadvantages of the nonlinear finite element model of an RC panel tested under pure shear loading developed using the newly developed wrapper and the standard TCL-based interpreter has been demonstrated. Few new libraries have also been added to the OpenSEES source code in Visual Studio for various purposes such as data visualization, unit testing, and matrix operations. Their usefulness in the debugging process has also been presented.

Keywords Seismic resilience · OpenSEEs · Nonlinear finite element model · Convergence issues · Debugging · Wrapper

V. K. Polimeru (✉) · A. Laskar
Department of Civil Engineering, IIT Bombay, Mumbai 400076, India
e-mail: vijaykumarpolimeru@iitb.ac.in

A. Laskar
e-mail: laskar@civil.iitb.ac.in

1 Introduction

Reinforced concrete (RC) wall-type members such as hollow bridge piers, shear walls, deep girders, and nuclear containment vessels are widely used in many large-scale civil engineering structures across the world. These structures exhibit several failure modes when subjected to extensive time-varying loads during their service lives. Shear failure is a very critical failure mode [1] as it is brittle in nature involving rapid deterioration of strength with increasing widths of the shear cracks, low ductility, and low energy dissipation capacities. Hence, this type of failure is not desirable in the earthquake-prone areas. Robust finite element frameworks, which supports and allows the users to implement state-of-the-art nonlinear finite element and material models in order to accurately predict the complete nonlinear behavior (elastic, inelastic, and post-peak failure range) of these structures are essential to study their performance under seismic loads [2]. With the development of accurate simulation models, better decisions (retrofitting or demolition) can be made during seismic assessments of existing structures. Several researchers developed finite element tools and implemented them in frameworks such as Vector [3, 4], FEAP [5], ABAQUS [6], and OpenSEES [7]. OpenSEES is an open-source software developed for earthquake engineering simulations. The source code of the software is accessible to users and developers for implementation of new tools or modification of existing ones. It is designed as an object-oriented framework and is therefore very simple to understand, modify, and implement new material models, elements, and solvers. It contains an extensive library of material models, elements, and solvers for performing quasi-static and dynamic analyses. It is very fast and suitable for performing statistical studies through large number of quasi-static and seismic simulations. One of the major challenges with OpenSEES is to understand the existing implementations of existing material models and elements. Majority of the material models and elements implemented in OpenSEES do not have proper documentation (examples include *hysteretic steel, fiber based nonlinear beam column element, quad element* etc.). Convergence errors are very common in nonlinear finite element analysis and cannot be always resolved by optimizing tolerance limits, number of steps, and displacement/time increment. In such cases, studying the implementations in the source code is the only way to understand and overcome the errors.

In OpenSEES, a TCL-based interpreter is provided for finite element modeling of systems to be analyzed (recently a Python-based interpreter has also added to the source code). The commands written in TCL/Python automatically call the functions implemented in C++ and provides the required output. A typical output message which is printed in the console when an OpenSEES model fails to converge is shown in Fig. 1. The console output does not give any information about the location of the bug.

The convergence issues can be often resolved by following various techniques such as reducing the displacement increment size, reducing the tolerance limit, increasing the number of iterations, changing the analysis algorithm, and changing the test criteria. However, the above-mentioned techniques may not work in complex

```
WARNING: CTestNormDispIncrVaryIter::test() - failed to converge
after : 100 iterations
AcceleratedNewton::solveCurrentStep() - The ConvergenceTest object failed in
test()
StaticAnalysis::analyze() - the Algorithm failed at iteration : 100 with
domain at load factor - 9424.67
OpenSees > analyze failed, returned: -3 error flag
```

Fig. 1 OpenSEES error view in failed analysis step

nonlinear finite element models. It is a challenging task to find and resolve the bug in such cases. The complexity is further increased because the finite element model of the system is in TCL/Python languages, and its source code implementation is in C++. Hence, a simple yet elegant C++ wrapper has been developed in the present study to overcome this difficulty. The nonlinear finite element model can be directly developed in the C++ language by using the developed C++ wrapper, and standard software testing procedures [8, 9] can be used to easily debug the source code. Few new libraries have also been added to the OpenSEES source code in Visual Studio for various purposes such as data visualization, unit testing, and matrix operations. Their usefulness in the debugging process has been briefly presented in Sect. 3 along with few samples of VC++ codes developed in the present study. The term VC++ refers to C++ in Visual Studio, which is slightly different from the standard C++ program in terms of additional proprietary libraries it supports. VC++ is not portable.

2   VC++ Wrapper Implementation

VC++ wrapper is a class of special member functions such as *node, element, and uniaxialMaterial.* which can be used to develop finite element models in VC++ source code. Implementation of VC++ wrapper involves two steps. The first is the identification of all the classes and associated member functions which get activated when the TCL/Python command is invoked in the command prompt. The second step involves encapsulating all the identified member functions that are associated with a TCL/Python command in a single member function of VC++ wrapper class. OpenSEES source code has a plethora of member functions. Hence, it is essential to identify all the member functions that are involved with each command for efficient debugging of the source code. A simple Visual Studio inbuilt feature has been used, to take the TCL input file (say *runc.tcl*) as input to the source code as shown in Fig. 2. Thereafter, identify the member functions behind each TCL command and their calling sequence by using breakpoints. Once all the classes and associated member functions behind a command are identified, they are encapsulated in a member function of *VC++ wrapper* class.

For example, when command *node* is invoked, two functions *Node *temp_node = new Node (tag, ndf, xcrd, ycrd)* and *model_domain >addNode(temp_node)* get invoked. Hence, both these functions are encapsulated in a *node (int tag, double*
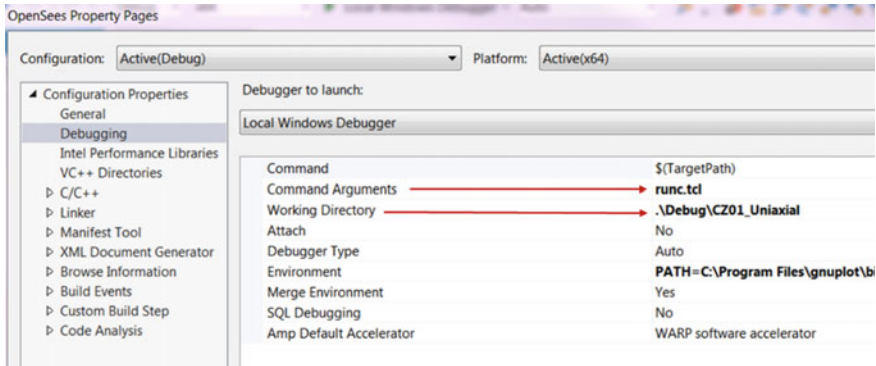
Fig. 2 TCL input file initiation from VC++

xcrd, double ycrd) member function of a *VC++ wrapper* class as shown in Fig. 3. Similarly, definition of a *uniaxialMaterial* member function of a *VC++ wrapper* class is shown in Fig. 4. Few examples of TCL commands and their equivalent VC++ commands are presented in Table 1.

Even though it is difficult to initially create the equivalent VC++ program, it is easier and more convenient to debug the VC++ program compared to the TCL

```
int vcppwrapper::node(int tag, double xcrd, double ycrd)
{
    Node *temp_node = new Node(tag, ndf, xcrd, ycrd);
    model_domain->addNode(temp_node);
    int ndmm = ndm;
    return 0;
}
```

Fig. 3 Node member function definition in VC++

```
  int vcppwrapper::uniaxialMaterial(string material_name, dvec materi-
al_props)
{
  UniaxialMaterial *theMaterial = 0;
  if (material_name.compare("SteelZ01_V1") == 0)
  {
    ... ... ...
    theMaterial = new SteelZ01_V1(tag, fy, E0, fc, rho);
  }
  if (OPS_addUniaxialMaterial(theMaterial) == false) {
            ... ... ...
  }
  return 0;
}
```

Fig. 4 UniaxialMaterial member function definition in VC++

Table 1 Examples of TCL commands and equivalent VC++ commands

Command name	TCL command	VC++ equivalent
Node command	node tag xcrd ycrd	node(tag, xcrd, ycrd);
Fix command	fix tag xres yres	fix({ tag, xres, yres})
UniaxialMaterial command	uniaxialMaterial ConcreteZ01 15 [expr -$wfc] [expr -$epsc]	uniaxialMaterial("ConcreteZ01", { 14, fc, eps_c0});
nDMaterial command	nDMaterial FAReinforcedConcretePlaneStress 21 0.0 11 12 14 15 [expr 0.25*$pi] [expr 0.75*$pi] $rouh $rouv $wfc $wfyv $wE $epsc	nDMaterial("VFARCPlaneStress_1", { 21, Density, 11, 12, 14, 15, Theta_L, Theta_T, rho_L, rho_T, fc, fy_L, E0, eps_c0});
Element command	element quad 1 1 2 3 4 $TPanel PlaneStress 21	element("VFourNodeQuad", { 1, 1, 2, 3,4, TPanel, 21}, "PlaneStress");
Recorder command	recorder Node -file [concat Outputs/Panel_Disp_Node_3.out] -time -node 3 -dof 1 disp;	node_recorder(DispFilename, "disp", 4, 0);

input file and also reduces the effort to switch between TCL and VC++ programming languages. New libraries added to OpenSEES source code in Visual Studio for various purposes such as data visualization, unit testing, and matrix operations are discussed in the following Sect. 3, and the comparison of the input files containing the finite element models developed using the existing TCL interpreter and the newly developed VC++ wrapper is presented in Sect. 4.

3 Additional Libraries Added to OpenSEES in VC++

Two libraries have been primarily used in the present study in conjunction with VC++, namely Armadillo for linear algebra (matrix and vector operations) and MATLAB engine library for plotting and monitoring variables while debugging. Other miscellaneous libraries including Google Test framework and GNU Plot have also been explored. Brief summaries of the libraries are presented in Sects. 3.1 through 3.3.

3.1 Armadillo Library

Armadillo is an open-source linear algebra library for C++ language for mathematical and computational applications [10, 11]. The source code of the library can be downloaded from http://arma.sourceforge.net/. This library has been preferred over vector and matrix classes in existing OpenSEES framework because of its extended functionality in doing matrix and vector operations, simple syntax similar to MATLAB, well written documentation, and open access.

3.2 MATLAB Engine Library

MATLAB engine is a commercial toolbox available in the MATLAB software [12]. MATLAB engine allows data exchange between VC++ and MATLAB. While debugging or implementing some new member functions in the OpenSEES framework, plotting and workspace to view variables are very much essential. Since VC++ does not have any inbuilt plotting library, users must depend on external plotting libraries (such as MATLAB, GNU Plot, Python, and OpenGL). Variables can be plotted and viewed in Visual Studio by either printing them on the console using basic input/output commands (such as *cout*) or by using inbuilt variable viewer. Printing of variables on the console is self-explanatory and supports every data type. However, the inbuilt variable viewer supports only basic C++ data types and Standard Template Library (STL) data types. It does not support Armadillo data types and objects of vector and matrix classes in existing OpenSEES Framework. A special graphical tool for viewing Armadillo data types in Visual Studio have been developed to overcome this difficulty [13]. Both these methods are useful for visualizing variables with scalar values and vectors. However, they are not convenient for visualizing matrices. A view of the Visual Studio inbuilt data viewer and armadillo data viewer showing a matrix is presented in Fig. 5. It can be observed from Fig. 5 that each column of the matrix is shown as a vector. Hence, it is not possible to compare two or more columns of a matrix side by side in the inbuilt VC++ variable viewer. The MATLAB engine has been used in the present study to overcome these two challenges (plotting data and viewing data). Using the MATLAB engine, all functions of MATLAB (including workspace) can be called from VC++ and vice versa. A simple example code to call plot function from VC++ is presented in Table 2.
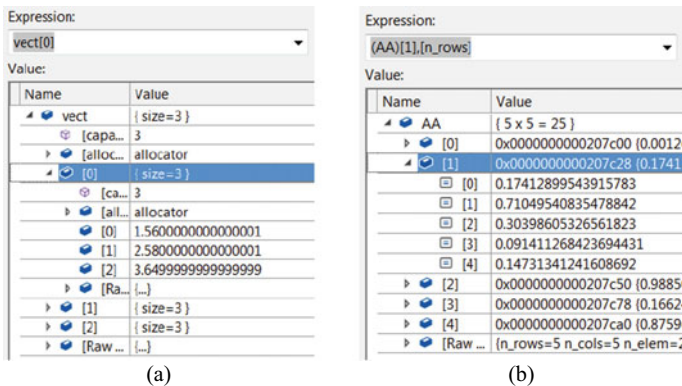
Fig. 5 Visual studio variable viewer **a** Default variable viewer for STL type variable **b** Variable viewer for Armadillo type variable

Table 2 Example code to utilize MATLAB plot function from VC++

```cpp
int Matlab_Plots::Multiple_Line_Plots(dmat PlotData)
{
    Engine *m_pEngine;
    m_pEngine = engOpen(NULL);
    if (m_pEngine == NULL)
    {
        std::cout << "Error" << std::endl;
        exit(1);
    }
    engSetVisible(m_pEngine, 1);
    engEvalString(m_pEngine, "clc;");
    engEvalString(m_pEngine, "close all;");
    engEvalString(m_pEngine, "clear all;");
    Create_2DArray_in_Matlab(*m_pEngine, PlotData);
    string engEvalString_Commands;
    engEvalString_Commands.append("figure;");
    engEvalString_Commands.append("set(0,'defaultaxesfontsize', 14);");
    engEvalString_Commands.append("set(0,'defaultaxesfontname', 'Palatino Li-
notype');");
    engEvalString_Commands.append("for i = 1:(size(PlotData, 2)/2); ");
    engEvalString_Commands.append(" PlotVar = 2*i - 1;");
    engEvalString_Commands.append(" plot(PlotData(:, PlotVar), PlotData(:,
PlotVar + 1));");
    engEvalString_Commands.append(" hold on; ");
    engEvalString_Commands.append(" end;");
    engEvalString_Commands.append(" hold off;");
    char Char_engEvalString_Commands[1000];
    strcpy(Char_engEvalString_Commands, engEvalString_Commands.c_str());
    engEvalString(m_pEngine, Char_engEvalString_Commands);
    return 0;
}
```

3.3 Other Miscellaneous Libraries

Apart from Armadillo and MATLAB Engine, Google Test framework for testing of member and non-member functions and an open-source plotting tool named GNU Plot have also been integrated into OpenSEES in Visual Studio. GNU Plot is an open-source alternative to the MATLAB plotting library, using which real-time plots can be viewed in VC++. Google Test framework is an open-source alternative to Microsoft native unit testing framework, which is simple to use for testing member and non-member functions.

4 Illustrative Examples

In this section, two RC Panels (namely CE2 and CA2) under pure cyclic shear loading and a bridge pier (namely PS1) under seismic loading have been analyzed to demonstrate the effectiveness of the developed wrapper. The material and geometric

properties along with the finite element modeling details of the RC panel and bridge piers using cyclic softened membrane model (CSMM)-based plane stress elements have been previously reported [14]. The CSMM-based plane stress elements have been previously implemented in OpenSEES and used to analyze framed RC shear walls under seismic loads [15] and post-tensioned bridge columns under reversed cyclic loads [16]. The detailed finite element model definition of Panel CE2 developed using existing TCL interpreter and the newly developed VC++ wrapper is presented in Tables 3 and 4, respectively. The cyclic shear strain and stress plots as obtained from the TCL interpreter and VC++ wrapper are presented in Fig. 6. It can be observed from Fig. 6 that in the absence of convergence issues, both the finite element models are equally capable of completely analyzing the cyclic shear stress strain response of RC Panel CE2. However, in some simulations such as the analysis of RC bridge pier PS1 under high PGA earthquake loads, convergence issues are very predominant and cannot be easily resolved by optimizing tolerance limits, number of steps and time increment. In such cases, studying the implementations in the source code is the only way to understand and overcome the convergence issues. It is not directly possible to monitor the value of every variable involved in the analysis in every iteration with TCL interpreter. However, the VC++ wrapper allows the monitoring of variables in every iteration of the analysis. Upon understanding the source of the convergence error, the users can apply appropriate techniques to resolve the bug. A detailed parametric study has been carried out on RC panels under cyclic pure shear loads by using the VC++ wrapper in order to resolve the convergence issues observed in the simulation of RC bridge pier PS1 under high PGA earthquakes. The results of the study show that the inability of the CSMM model to predict the response of bridge pier under high PGA ground motions can be attributed to two main causes. The first cause of complexity is associated with the difficulty in obtaining the orientation angle of applied principal stress plane (θ_1) at every Gauss point in the CSMM-based RC plane stress elements. The second cause of the complexity is the interaction between shear modulus of concrete (G_{12}^c) and the applied principal stress orientation angle as shown in Fig. 7a. Two improvements in the CSMM-based analysis algorithm have been proposed in the present study to overcome the convergence issues of CSMM-based RC plane stress elements. Firstly, a non-iterative approach developed for CSMM-based shell elements [17] has been adopted and implemented in the CSMM-based RC plane stress elements to overcome the difficulty in determining the principal stress orientation angle. Secondly, the value of G_{12}^c is updated using a procedure similar to principal stress orientation angle (i.e., the value of G_{12}^c at every step is calculated based on the concrete stresses and strains obtained in the previous converged step) to overcome the interaction between the shear modulus of concrete and the principal stress orientation angle. The values of concrete shear modulus corresponding to the first step of analysis are calculated assuming the linear elastic constitutive relationships for concrete and reinforcing steel. A new material model named "*ICSMM*" has been developed by implementing the proposed modifications in the shear modulus of concrete and the principal stress orientation angle in the CSMM-based RC plane stress elements and added to the OpenSEES source code. More details on the implementation of the modifications in CSMM can be found

Table 3 Model definition using TCL interpreter

```
wipe;
model basic -ndm 2 -ndf 2
file mkdir Outputs;
logFile [concat Outputs/OpenSees_log.log];
set LPanel 1398;
set HPanel 1398;
set TPanel 178;
node 1 0 0;
node 2 $LPanel 0;
node 3 $LPanel $HPanel;
node 4 0 $HPanel;
fix 1  1 1
fix 2  0 1
set wfc 49.0;
set wfyv 424.1;
set wfyh 424.1;
set wE  200000.0;
set rouv 0.0054;
set rouh 0.0054;
set epsc 0.0023;
uniaxialMaterial    SteelZ01  11   $wfyv    $wE $wfc  $rouv
uniaxialMaterial    SteelZ01  12   $wfyh    $wE $wfc  $rouh
uniaxialMaterial ConcreteZ01  14 [expr -$wfc] [expr -$epsc]
uniaxialMaterial ConcreteZ01  15 [expr -$wfc] [expr -$epsc]
set pi 3.14
nDMaterial FAReinforcedConcretePlaneStress  21  0.0 11 12 14 15 [expr
0.25*$pi] [expr 0.75*$pi]  $rouh $rouv $wfc $wfyv $wE $epsc
element quad 1 1 2 3 4 $TPanel PlaneStress 21
recorder Node -file [concat Outputs/Disp.out] -time -node 4 -dof 1
disp;
recorder Node -file [concat Outputs/Reaction.out] -time -node 1 -dof
1 reaction;
set P 500.0;
pattern Plain 1 "Linear" {
   load 2 [expr  -$P] 0
   load 3 [expr   $P] [expr  $P]
   load 4 [expr   $P] [expr  -$P]
}
system BandGeneral
constraints Plain
numberer Plain
test NormDispIncrVaryIter 1e-3 83 0 numStep   12  60  60  60  12  12
12  12  12  12  12  12  12  … 12  12  12  12  12  12  12  12  12  12
12  12 numIter  10  10  10  … 10  10  10  10  10
algorithm KrylovNewton
integrator DisplacementPath 4 1 83 numStep   12  60  60  60  12  12
12  12  … 12  12  12  12  12  12  12  12  12  12 incre-
ment   0.50     -0.10     -0.10     0.10     0.50     0.50     -
0.50    …     0.50     0.50     0.50     0.50     0.50
0.50
analysis Static
initialize
analyze 1204
```

Table 4 Model definition using VC++ wrapper

```
#include "vcppwrapper.h"
int main(void)
{
  RCPanel_Wrapper panel;
  mkdir("wrapper_test");
  double LPanel = 1398.0;
  double HPanel = 1398.0;
  double TPanel = 178.0;
  double pi = 3.14;
  double fc = 49.0;
  double eps_c0 = 0.0023;
  double fy_L = 424.1;
  double fy_T = 424.1;
  double E0 = 200000;
  double rho_L = 0.0054;
  double rho_T = 0.0054;
  double Density = 0.0;
  double Theta_L = 0.25*pi;
  double Theta_T = 0.75*pi;
  dvec DispPeaks = { 0, 0, 0, 1, -1, 0, 1, 0, -1, … , -5, 0, 3 };
  DispPeaks = DispPeaks * 6;
  double DefaultStepSize = 0.5;
  string ReactionFilename = "wrapper_test\\Reaction_Panel_CE2.out";
  string DispFilename = "wrapper_test\\Disp_Panel_CE2.out";
  dvec IncrementVectorCyclic = panel.Simple_IncrementVecGenera-
tor(DispPeaks, DefaultStepSize);
  panel.domain(2, 2);
  panel.node(1, 0.0, 0.0);
  panel.node(2, LPanel, 0.0);
  panel.node(3, LPanel, HPanel);
  panel.node(4, 0.0, HPanel);
  panel.uniaxialMaterial("SteelZ01_V1", { 11, fy_L, E0, fc, rho_L });
  panel.uniaxialMaterial("SteelZ01_V1", { 12, fy_T, E0, fc, rho_T });
  panel.uniaxialMaterial("ConcreteZ01", { 14, fc, eps_c0 });
  panel.uniaxialMaterial("ConcreteZ01", { 15, fc, eps_c0 });
  panel.nDMaterial("VFARCPlaneStress_1", { 21, Density, 11, 12, 14,
15, Theta_L, Theta_T, rho_L, rho_T, fc, fy_L, E0, eps_c0 });
  panel.element("VFourNodeQuad", { 1, 1, 2, 3 ,4, TPanel, 21 },
"PlaneStress");
  panel.fix({ 1, 1, 1 });
  panel.fix({ 2, 0, 1 });
  panel.time_series("Linear", 1);
  panel.pattern("Plain", 1);
  double P = 500;
  panel.load({ 1, 2, -P, 0.0 });
  panel.load({ 2, 3, P, P });
  panel.load({ 3, 4, P, -P });
  int Dim = size(IncrementVectorCyclic);
  Vector IncrementVector(Dim);
  for (int i = 0; i < Dim; i++) {
    IncrementVector(i) = IncrementVectorCyclic(i);
  };
  Vector IterationVector(Dim);
  for (int i = 0; i < Dim; i++) {
```

(continued)

Table 4 (continued)

```
     IterationVector(i) = 100;
   };
   panel.test("NormDispIncrVaryIter", 1, 1e-7, 5, IterationVector);
   panel.integrator("DisplacementPath", { 1, 4, 0 }, IncrementVector);
   panel.solution_algo("KrylovNewton", { 1 });
   panel.analysis_model();
   panel.constrain_handler("Plain", { 1 });
   panel.dof_numberer("Plain", { 1 });
   panel.system("BandGeneral", { 1 });
   panel.analysis("Static");
   panel.node_recorder(DispFilename, "disp", 4, 0);
   panel.node_recorder(ReactionFilename, "reaction", 1, 0);
   int numSteps = Dim + 10;
   double flag;
   for (int i = 1; i <= numSteps; i++) // numSteps
   {
      flag = panel.analyze(1);
   }
   opserr << flag << endln;
   return 0;
}
```
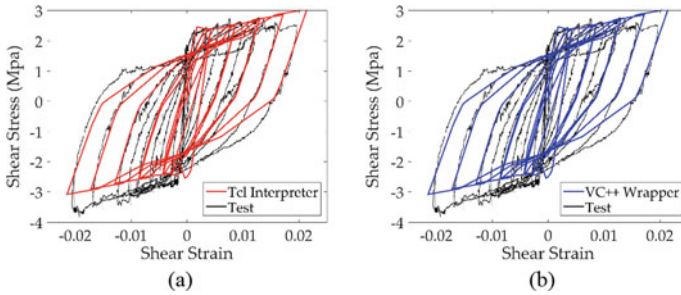

Fig. 6 Comparison of numerical and experimental shear stress–strain plots of panel CE2 **a** TCL interpreter **b** VC++ wrapper
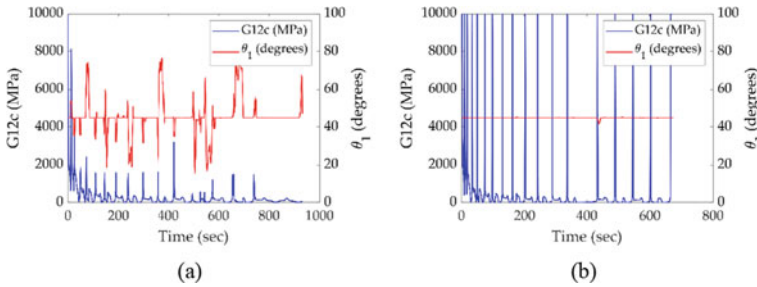
Fig. 7 Comparison of shear modulus of concrete (G_{12}^c) and applied principal stress orientation angle (θ_1) of panel CA2 as obtained from **a** CSMM-based plane stress elements **b** ICSMM-based plane stress elements
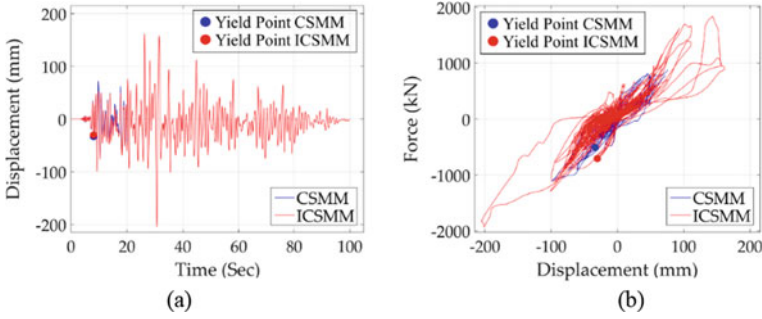
Fig. 8 Seismic response of bridge pier PS1 under scaled imperial valley ground motion [14] **a** Time versus displacement response **b** Load deflection curve

in [14]. The variation of G_{12}^c and θ_1 as obtained from the ICSMM model has been presented in Fig. 7b. The complete load deflection and displacement time history response of bridge pier PS1 as obtained from CSMM and ICSMM-based models are presented in Fig. 8. It can be observed from Fig. 8, that ICSMM-based model is able to capture the complete response of bridge pier PS1.

5 Summary and Conclusions

In the present study, development and implementation details of a simple yet elegant VC++ wrapper (vcppwrapper) has been presented. This wrapper can be used to efficiently debug the convergence errors encountered in complex NLFEA problems. Also, this wrapper helps in understanding the implementations and working mechanisms of materials, elements, solvers etc., which is very essential in debugging the complex nonlinear finite element models built in OpenSEES. Few new libraries (such as Armadillo, MATLAB Engine and Google Test Framework) have also been added to the OpenSEES source code in Visual Studio for various purposes such as data visualization, unit testing, and matrix operations. Examples showing the comparison of TCL implementation and VC++ implementation of an RC panel is also presented. The usefulness of the wrapper in terms of debugging issues that are causing non-convergence problems in RC bridge pier PS1 under high PGA earthquake loads have also been presented. From the study, it is thus concluded that VC++ wrapper can serve as potential and handy tool for OpenSEES users to develop finite element models directly in VC++, which gives more insights into the actual subroutines (such as elements and material models) involved in the simulation and helps debug non-convergence problems.

References

1. Cassese P, Ricci P, Verderame GM (2017) Experimental study on the seismic performance of existing reinforced concrete bridge piers with hollow rectangular section. Eng Struct 144:88–106
2. Li Z, Chen Y, Shi Y (2017) Numerical failure analysis of a continuous reinforced concrete bridge under strong earthquakes using multi-scale models. Earthq Eng Vib 16(2):397–413
3. Polak MA, Vecchio FJ (1993) Nonlinear analysis of reinforced-concrete shells. J Struct Eng ASCE 119(12):3439–3462
4. Hrynyk T (2013) Behaviour and modelling of reinforced concrete slabs and shells under static and dynamic loads, PhD Thesis, University of Toronto
5. Taylor RL (2014) FEAP-A finite element analysis program. UC Berkeley
6. Abaqus G (2011) Abaqus 6.11. Dassault systemes simulia Corp Providence, RI, USA
7. McKenna F, Scott MH, Fenves GL (2015) Nonlinear finite-element analysis software architecture using object composition. J Comput Civ Eng 24(1):95–107
8. Michael F (2004) Working effectively with legacy code. Robert C. Martin Series, Pearson Education. ISBN 9780132931755
9. Zeller A (2009) Why programs fail: a guide to systematic debugging. Elsevier
10. Sanderson C, Curtin R (2016) Armadillo: a template-based C++ library for linear algebra. J Open-Source Software 1(2):26
11. Sanderson C, Curtin R (2019) Practical sparse matrices in C++ with hybrid storage and template-based expression optimisation. Mathematical and Computational Appl 24(3):70
12. MathWorks Inc (2015) TM. MATLAB (R2015a) Version 8.5.0, Natick, Massachusetts
13. Saeed (2017), Is there a way to print an Armadillo matrix or vector in Visual Studio Debug? (https://stackoverflow.com/users/1606402/saeed. Last accessed 30 August 2019
14. Polimeru VK (2021) Finite element analysis of shear critical thin walled RC structures, Ph. D. Thesis, Department of Civil Engineering, IIT Bombay, Maharashtra, India
15. Laskar A, Zhong J, Mo YL, Hsu TTC (2009) Multiscale modeling of reinforced/prestressed concrete thin-walled structures. Interaction and Multiscale Mechanics: An International J 2(1):61–89
16. Laskar A, Mo YL, Hsu TTC (2016) Simulation of post-tensioned bridge columns under reversed-cyclic loads. Mater Struct 49(6):2237–2256
17. Luu CH (2017) Development of CSMM-based shell element for reinforced concrete structures, Ph. D. Dissertation, Department of Civil and Environmental Engineering, University of Houston, Houston, TX

A State-of-the-Art Review on Methods of Retrofitting in Building Structural Members—A Comprehensive Review

M. Kaarthik and **R. Mandurachalam**

Abstract Development on civil engineering is indispensable in the present day; hence, it is essential to maintain structure more reliable and effective from cracks, deterioration and other environmental effects. Strengthening of existing structural members is necessary to achieve more service life to the building structure; hence, retrofitting is a process to enhance the structural capacity to withstand more load that increases the prospect of the building structure to continue survival for more years. Retrofitting can be done in existing structural members such as beams, columns and slabs to enhance the strength. This article presented various advanced techniques adopted to practice retrofitting such as external plate bonding, section enlargement of structural elements, external post-tensioning, epoxy injections, grouting strategies and FRC bars in retrofitting and fiber-reinforced polymer composites. The proposed article provides detailed insight on the retrofitting in structural members with operational evaluation and in situ practicing; furthermore, application of retrofitting techniques in concrete, steel and rebars has been discussed in detail. Future scope and recommendations of the retrofitting practices have been identified in this proposed review article.

Keywords Retrofitting · Structural elements · Beams · Columns · Slabs · Walls

1 Introduction

In the present scenario, retrofitting of structural members plays a significant role in the construction industry to make use of existing structure by strengthening structural members using various techniques which help to enhance the bearing capacity of the structure along with long service life. Ahmed Hassan et al. [1] demonstrated

M. Kaarthik (✉)
Coimbatore Institute of Technology, Coimbatore, India
e-mail: kaarthik@cit.edu.in

R. Mandurachalam
Sri Krishna College of Engineering and Technology, Kuniamuthur, Coimbatore 641008, India

various kinds of reinforced concrete (RC) beams after increased temperature exposure. A numerical event was adopted with some specimens based on temperatures and cast utilizing high strength concrete (HSC), normal concrete (NC) and self-compacting concrete (SCC) to calculate the restoring capacity of RC beams with various retrofitting strategies. Here, for the retrofitting beam capacity, concrete jacketing bonded steel plates and CFRP laminates were used. These strategies had not generated optimum impact at 6000c on normal concrete, while on HSC and SCC beams, the all-retrofitting strategies had a good impact in the desperately worsened beams [1].

Daiyu et al. [2] presented that the practical inquiry on both carbon fiber-reinforced polymer (CFRP) retrofitted and un-retrofitted rectangular strengthened concrete columns with emphasis on the impact of the directions of the lateral loading on the seismic performance of the column. A total of ten massive cantilever rectangular columns are made; among those, five of them retrofitted with CFRP wraps at the plastic hinge areas. It is shown that the direction of lateral loading establishes a beneficial impact on both the columns' seismic performance. The ellipse equation shows that the shear strength of the rectangular reinforced concrete (RC) columns in a non-principal way could be forecasting based on the lateral strength in the principal directions [2]. Figure 1 shows various techniques of retrofitting process by adopting threaded bars and welded steel plates.

Khalid et al. [3] investigated the impact of carbon fiber-reinforced polymer retrofit on defilement accumulation and loading duration along with various specifications for nonlinear transient; the computational models were utilized two-way reinforced concrete slabs exposed to retrofitted and blast loading including CFRP compounds by using finite element (FE) method. The application of retrofitting in both sides of the slab is more convenient to improve the CFRP system by 200% in creating the load-bearing capacity of both the retrofitted and as-built slabs; the displacement is decreased up to 40–70% (maximum) [3].

Fig. 1 Various techniques for retrofitting beams employing threaded bars and welded steel plates [1]

Mingke et al. [4] said the purpose of enhancing the seismic efficiency by using technology for the application of high ductile fiber-reinforced steel (HFFB) walls made of autoclaved aerated cement (AAC) (HDC). There have been five half-scaled AAC walls with a confined wall and 1 URM walls under an in-plane cyclical reverse charge inspection. The test results indicate that the retrofitting techniques used could increase the shear strength and power extravagance of the URM wall, where there is a negligible improvement in the versatility of the retrofitting HDC strips. The formulas introduced were used to measure the lateral obstruction to the test walls that corresponds to different modes of failure [4].

2 Retrofitting of Building Structural Members

The retrofitting of RCC members can be carried out when the building attains damage state like cracks, corrosion, deformation and many more. These cracks occur due to defective designs, improper maintenance and lack of inspections; hence, the damaged structure can be retrofitted by adopting procedures like recasting, patch repair, sprayed overlays and concrete replacement. Structural members such as beams, columns, slabs and walls are essential to practice retrofitting techniques when subjected to any damages.

2.1 Beams

Reinforced concrete beam is a significant structural member which resists lateral load and also plays crucial role in load distribution. Pagadala et al. [5] surveyed the ultra-high molecular weight (UHMW) polyethene on reinforced concrete (RC) beams as geosynthetic retrofitting substance. Two sets of control samples and retrofitting samples were tested, consisting of with and without flexural reinforcement. In this investigation, the UHMW polyethylene is jacketed by epoxy hardener and resin, and also the crack pattern, failure mode and ultimate load-carrying capacity of beam are monitored. The outcome shows that the control specimens had less capacity than the retrofitting specimens through the wrapping strategies [5]. Abolfazl et al. [6] studied the shear's performance of strengthened retrofitted RC beams by utilizing fiber-reinforced polymer (FRP), U-wraps and the impact of FRP anchorage strategies. The used FRP anchorage includes FRP stitching anchor in drilled holes at the terminal position of a U-wrap FRP retrofit with the shear span of the RC beam. Six RC beams were used to monitor the ductility factor, displacement capacity ultimate strength and load–displacement behavior. The proposed strategy is used to transform the failure mode to ductile flexure shear. Furthermore, the productivity of end anchors in increasing ductility of shear retrofitted reinforced concrete beam is described [6].

Archana et al. [7] described the identification of acoustic emission (AE) design in carbon fiber-reinforced polymer retrofitted reinforced concrete beams for degraded

mode recognition to acknowledge the long-term performance and the durability. Six observed along with the AE sensor and examined along with flexural load by developing an identification analysis. In the failure mechanism observation, the AE data executed along with support vector machine (SVM), multilayer perceptron (MLP) and principal component analysis (PCA) methodologies [7]. Gang et al. [8] developed an experiment on the retrofitted beam's rotational performance to column joints along the weak panel zones of welded unreinforced flange-bolted (WUF-B) web haunches and brackets after applied axial load. The result observed that the maximum story drift angle was more than 0.07 rad of every sample along good ductility plump hysteresis loop and high resistance, and 22.3%–31.1% according augments the yield moment to Chinese code. The effectiveness of welding haunches has optimum seismic performance with special moment frame (SMF), where the three joints encounter ductility [8].

Faisal et al. [9] analyzed various kinds of steel covering strategies for retrofitted RC beams after increased temperature submission on SS, HSC and NC beams. Various beams were monitored at the temperature 6000 °C and 4000 °C for 120 min after sted jacketing to improve regular concrete beams and self-compacting concrete of four angles. Here, the significant specifications were the size of steel jacket angle and positions of angles with proper orientation. The excellent beam capacity restore is lower than 10% in the external orientation of angels [9].

2.2 Columns

Column is a vertical member which carries compression and it helps to transfer load from slab to foundation. Xe Hu et al. [10] expressed that to proficiently enhance the anti-blast performance of present reinforced concrete (RC) structures, and three various retrofitting systems using carbon fiber reinforced polymer (CFRP) sheets were introduced. The field trials were carried out on the FRP retrofitted columns subjected to double-end initiation and close in the blast. Brittle failure was detected at both ends of the columns, which proved to be a vulnerable part to the axial bearing ability and where CFRP was uncomfortable to wrap. There is a finite element (FE) model of the RC column installed on the LS-DYNA platform. That is certified by both axial bearing and blast trial data [10].

A systematic model for testing the axial compression strength and stability of retrofitted spliced columns using a steel jacket was introduced and researched by Hongmin et al. [11]. This model will estimate the carrying capacity of retrofitted split columns with a high precision steel jacket. A prescribed splice length will determine a reliable splice joint relationship while preventing negative effects because of incompatible column sections rigidity. This model is used in the retrofit of the wood columns configuration in the historic wood frames and is also used to build a modern, comprehensive wood frame with splice columns [11].

Raju et al. [12] presented that beam–column joint (BCJ) performance considerably made an impression on the dealing of reinforced concrete framed structures during the

temblor. For that, a new process for retrofitting the BCJ using ultra-high-performance hybrid fiber reinforced concrete (UHP-HFRC) is proudly brought into operation. UHP-HFRC enhanced the performance of retrofitted starting damage levels of BCJ. The starting loss level of BCJ remarkably makes an impression on the post-peak dealing of the retrofitted pattern [12].

Dong et al. [13] studied complete cyclical analysis of five square RC columns, not seismically constructed, with hybrid FRP sheets and not packaged to investigate their impacts on cyclic behavior. This work also builds organizational models capable of capturing critical building skills. The results of the test show that wrapping hybrid FRP sheets results in an insignificant increase in start rigidity and maximum power in the initial direction of loading. The analytical model used to measure the deformation potential of the patterns CHF1LD and CHF2LD that cannot be captured during the experiments. The deformation capacity of the RC columns, which wraps two stacks of HFRP, is strengthened to 2.1 times that of the RC column anon-seismically bare [13]. Figure 2 represents failure mode of column subjected to blast test.

Hyunsu et al. [14] stated that the best derivative number and the replaced location of the RC columns are related by a 3D nonlinear time-history description to the command interpreter technology. The use of ant colony optimization technology (ACO) results are accurate. In order to fulfill the current eligibility for seismic architecture, seismic material presented in this work should be mounted in more than 50 percent of the complete columns. The explaining optimization has shown that retrofitting only 60.2% of the columns can tolerate a top acceleration of 0.2 g in both ends of the columns on the important shear areas [14].

2.3 Slabs

Slab is a structural member which is supported by walls and reinforced concrete beams, and it plays a vital role in building element. Ryotaro et al. [15] reported about the two magnetic retardation etiquette of PC-MPJ (precast pre-stressed concrete) frames with reinforced concrete (RC) frames along with cast-in-situ RC slabs for relationship. The compressive strength of the RC slab was lesser than JO MPa in between one sample. The inter-story drift increased when the shear stiffness decreased. The deformation connection is preponderance at the slab to beam alliances of the existing beam by the empirical equation following the Japanese standard for outer seismic retrofitting. Moreover, the in-plane and out of plane bending was tested off the connection slab [15]. Hamed [16] represented the utilization of pre-stressed vertical bolts for damaged retrofitted flat slabs because of punching shear. Some experiments were conducted to evaluate the cracking behavior; deformation characteristics load-carrying capacity, central column size and slab thickness by various codes formula, the differentiation of retrofitting flat slab experiment and evaluated punching shear failure load were presented as an equitable agreement [16]. Figure 3 displays application of GFRP technique in slab.

(a) C2A3

(b) A-type column

(c) B-type column

(d) C-type column
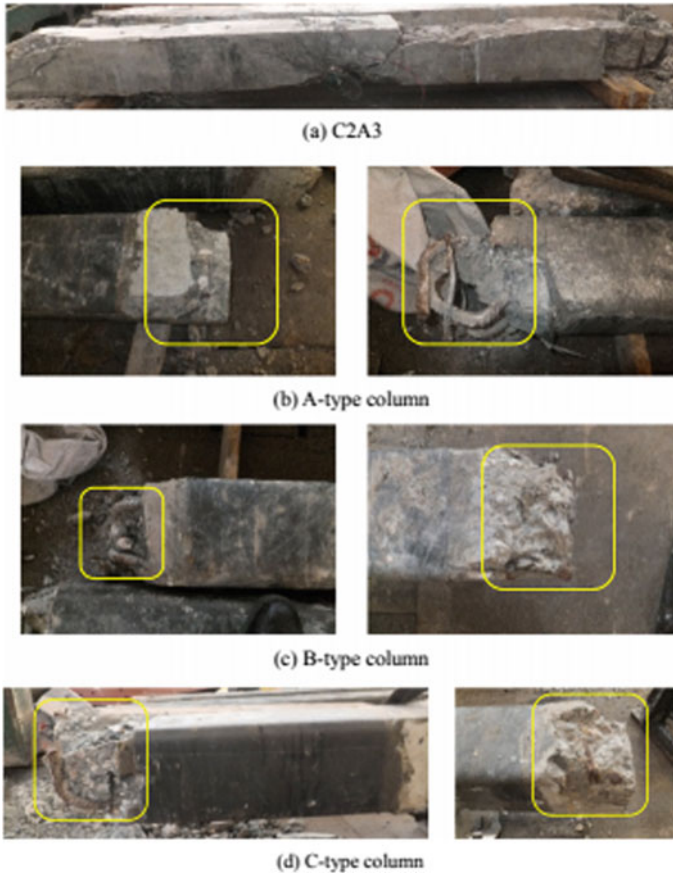
Fig. 2 Mode of failure under blast loading condition [10]

Fig. 3 Retrofitted slab using GFRP [17]

Jin-Won et al. [17] experimented with an analytical analysis of blast pressure of glass fiber reinforced polymer (GFRP) retrofitted RC slabs by using fiber-reinforced polymer (FRP) composites. The finite element modeling (FEM) interpretation was evaluated for FRP retrofitting RC slab's effectiveness with debonding failure dummy and high strain esteem contingent material model. Moreover, the usage of FRR plates or sheets were more convenient and cost-effective in structural members [17]. Azer et al. [18] monitored the blast response of three reinforced concrete hollow core slabs (RCHCS) through a closed explosion about 0.5 m with subjected to 1.5 kg of C4. FE software LS-DYNA conducted an analytical algorithm to enhance the blast resistance of the RC slabs, and also the capacity of CFRP strips as externally bonded reinforcement (EBR) was investigated to control the damage levels and mid-span deviation of the slab due to the explosion. During the explosion, the occurrence of cracks was observed, and the maximum deviation was forecasted [18].

Cailong Ma et al. [19] emphasized the effectiveness of quasi-static tests over RC frames' seismic performance and the failure mode of retrofitting CFRP wraps. With various CFRP retrofitting strategies, four full-scale interior beam–column slab subassemblies were compared to their beam deformation, shear deformation, energy dissipation efficiency, stiffness degradation, ductility displacement, hysteretic performance and failure modes, which occurs due to the existing transverse beams and slabs. For enhancing the seismic efficiency of the weak column beam, the CFRP wraps were used after the column-wage failure mode occurred [19].

2.4 Load-Bearing Walls

The load-bearing wall is a structural structure with beams and plates. Turkmen et al. [20] found that the present exploratory campaign had a primary objective to investigate carbon fiber-reinforced polymer (CFRP) retrofitted mural walls from the plane output of full-scale, flexibly installed deep (FDM). Nine complete masonry walls were retrofitted with CFRP FDM technology during the functional testing process. The experimental results confirmed that the FDM CFRP's retrofitted URM patterns (unreinforced masonry) increased significantly for the lateral resistance and displacement potential of the aircraft. The creation of several sheets and the cyclical decay of masonry [20]. Emadoddin et al. [21] provided the seismic detail of the retrofitted maceration walls of the center of the technology with a calibrated modeling and clarification of the finite element. In a parametric analysis, there are 450 finite element models. The effects of considered parameters on wall weight, ductility and rigidity have been studied. The systemic equations of these walls were based on the measurement of the ultimate force. The effects of the retrofitted walls were evaluated by a simplified equation [21]. Figure 4 depicts failure mode in walls.

Mingke et al. [22] have researched the area of functional and numerical studies on the in-plane treatment of retrofitted cementitious composites (ECC) coatings of unreinforced confined masonry walls. The material model for the morter has been implemented in a sub-routine linked to finite-element software for use with the
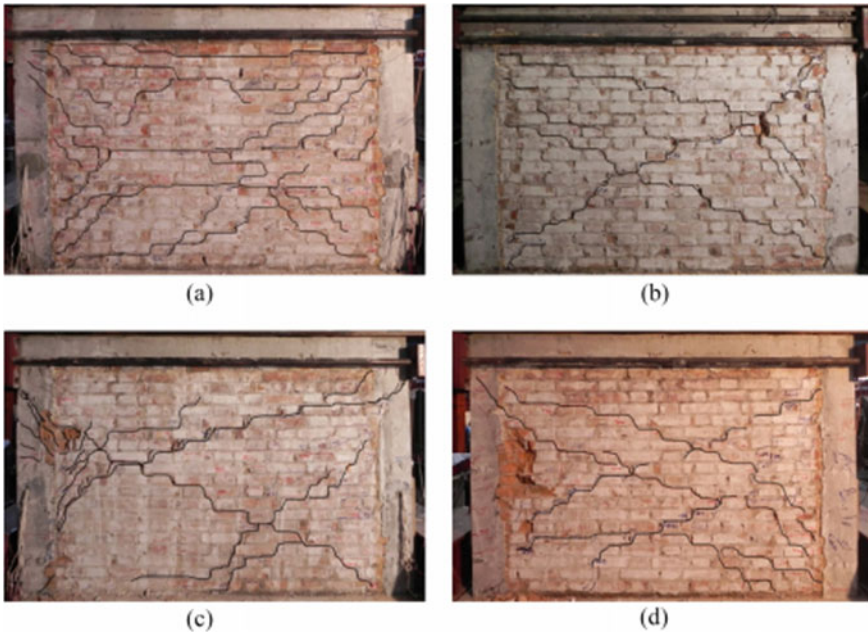
Fig. 4 Mode of failure in walls

VUMAT GUI. There are no thickness-consistency objects to reflect the mortar joints. The ECC was simulated with the mechanical treatment using the damaged concrete plasticity model. The outcome of the in-plan handling of the renovated walls was especially affected by the tensile properties of the ECC and by the effect of the morter power on all walls, mainly in terms of cracking rigidity and loading [22].

The unreinforced masonry (URM) walls were retrofits with regular type 3 coordinated boards (OSB/3), presented in Ornella et al. [23]. Form 3 of OSB has improved URM wall blockage out of plane and ferocity. For 1 and 2 lateral applications, the starting failure load is increased by 40 and 80 percent. The potential for decay of 2 sides of 1 sided application is 50 percent higher. The cost evaluated is 30% more costly than retrofit applications based on fiber [23]. Alireza et al. [24] reported that the effect on the plane display of a wall bearing unreinforced composite engineered composite (ECC) has been virtually investigated. Three damaged and undamaged URM walls have been checked for quasi-static loading. The damaged and undamaged walls were arbitrarily retrofitted to the ECC layer and attached by steel bar dowels to the URM wall base. The reworked URM wall shear strength has been extended remarkably [24, 25].

3 Future Studies and Recommendations

Future scope and ideas help to improve the overall planning of the research in particular research areas to achieve rapid growth. Some of the predicted progress which needs to be enhanced for future research are listed below.

- An advanced monitoring system should be adopted like drones, sensors and many more to predict the behavior of the structure to repair or check it.
- Design flaws should be checked both on-site and office before executing a project to prevent the structure from damage.
- Advanced equipment is necessary to anticipate microcracks and other deterioration in the structure.
- The structure should be observed according to the variation in temperature and environmental effects.
- Non-destructive testing will be highly recommended for future problems occurs in structures.
- IS codes should be revised according to advanced research to make the job easy for engineers.

4 Conclusion

This paper provides detailed information regarding maintenance and retrofitting of the structure by adopting few advanced methods and approaches. Based on the detailed discussion, a few points have been enumerated.

- This presented article overview of strengthening of structural members using various retrofitting techniques.
- The article discussed the importance and purpose of retrofitting which contributes to the sustainability of existing buildings to enhance bearing capacity without demolishing or rebuilding.
- Based on the detailed discussion six significant techniques such as and fiber-reinforced polymer composite (FRC), FRC bars in retrofitting, grouting strategies, section enlargement and external post-tensioning which serves the benefit of strengthening structural members.
- The review also discussed benefits and future research ideas to enhance the overall efficiency.
- The article also discussed ductility, strength and durability of structural members which practiced retrofitting.

References

1. Hassan A, Aldhafairi F, Abd-EL-Hafez LM, Abouelezz AEY (2018) Retrofitting of different types of reinforced concrete beams after exposed to elevated temperature. Eng Struct 194(December):420–430. https://doi.org/10.1016/j.engstruct.2019.05.084
2. Wang D, Wang Z, Yu T, Li H (2018) Seismic performance of CFRP-retrofitted large-scale rectangular RC columns under lateral loading in different directions. Compos Struct 192:475–488. https://doi.org/10.1016/j.compstruct.2018.03.029
3. Mosalam KM, Mosallam AS (2001) Nonlinear transient analysis of reinforced concrete slabs subjected to blast loading and retrofitted with CFRP composites. Compos. Part B Engineering 32(8):623–636. https://doi.org/10.1016/S1359-8368(01)00044-0
4. Deng M, Zhang W, Yang S (2019) In-plane seismic behavior of autoclaved aerated concrete block masonry walls retrofitted with high ductile fiber-reinforced concrete. Eng. Struct 219:110854. https://doi.org/10.1016/j.engstruct.2020.110854.
5. Hazarath P, Vijaya Kumar P (2019) Experimental investigation on flexural deficient RC beams retrofitting with UHMW polyethylene. Mater Today Proc 33:147–155. https://doi.org/10.1016/j.matpr.2020.03.567
6. Eslami A, Moghavem A, Shayegh HR, Ronagh HR (2019) Effect of FRP stitching anchors on ductile performance of shear-deficient RC beams retrofitted using FRP U-wraps. Structures 23:407–414. https://doi.org/10.1016/j.istruc.2019.11.007.
7. Nair A, Cai CS, Kong X (2019) Acoustic emission pattern recognition in CFRP retrofitted RC beams for failure mode identification. Compos Part B Eng 161:691–701. https://doi.org/10.1016/j.compositesb.2018.12.120
8. Shi G, Zhao H, Chen X, Xiao T (2020) Experimental study of cyclic behavior of retrofitted beam-to-column joints with welded haunches. J Constr Steel Res 171:106146. https://doi.org/10.1016/j.jcsr.2020.106146
9. Aldhafairi F, Hassan A, Abd-EL-Hafez LM, Abouelezz AEY (2020) Different techniques of steel jacketing for retrofitting of different types of concrete beams after elevated temperature exposure. Structures 28:713–725.https://doi.org/10.1016/j.istruc.2020.09.017
10. Hu Y, Chen L, Fang Q, Kong X, Shi Y, Cui J (2020) Study of CFRP retrofitted RC column under close-in explosion. Eng Struct 227(October):2021. https://doi.org/10.1016/j.engstruct.2020.111431
11. Li H, Qiu H, Lu Y (2020) An analytical model for the loading capacity of splice-retrofitted slender timber columns. Eng. Struct 225:111274. doi: https://doi.org/10.1016/j.engstruct.2020.111274
12. Sharma R, Bansal PP (2019) Behavior of RC exterior beam column joint retrofitted using UHP-HFRC. Constr Build Mater 195:376–389. https://doi.org/10.1016/j.conbuildmat.2018.11.052
13. Shin DH, Kim HJ (2020) Cyclic response of rectangular RC columns retrofitted by hybrid FRP sheets. Structures 28(May):697–712. https://doi.org/10.1016/j.istruc.2020.09.016
14. Seo H, Kim J, Kwon M (2018) Optimal seismic retrofitted RC column distribution for an existing school building. Eng Struct 168(May):399–404. https://doi.org/10.1016/j.engstruct.2018.04.098
15. Kurosawa R, Sakata H, Qu Z, Suyama T (2019) Cyclic loading tests on RC moment frames retrofitted by PC frames with mild press joints through RC slabs for connection. Eng Struct 197:109440. https://doi.org/10.1016/j.engstruct.2019.109440
16. Askar HS (2015) Usage of prestressed vertical bolts for retrofitting flat slabs damaged due to punching shear. Alexandria Eng. J. 54(3):509–518. https://doi.org/10.1016/j.aej.2015.05.013
17. Nam JW, Kim HJ, Kim SB, Yi NH, Kim JHJ (2010) Numerical evaluation of the retrofit effectiveness for GFRP retrofitted concrete slab subjected to blast pressure. Compos Struct 92(5):1212–1222. https://doi.org/10.1016/j.compstruct.2009.10.031
18. Maazoun A, Matthys S, Belkassem B, Lecompte D, Vantomme J (2019) Blast response of retrofitted reinforced concrete hollow core slabs under a close distance explosion. Eng Struct 191(April):447–459. https://doi.org/10.1016/j.engstruct.2019.04.068

19. Ma C, Wang D, Wang Z (2017) Seismic retrofitting of full-scale RC interior beam-column-slab subassemblies with CFRP wraps. Compos Struct 159:397–409. https://doi.org/10.1016/j.compstruct.2016.09.094

20. Türkmen OS, Wijte SNM, De Vries BT, Ingham JM (2021) Out-of-plane behaviour of clay brick masonry walls retrofitted with flexible deep mounted CFRP strips. Eng Struct 228:111448. https://doi.org/10.1016/j.engstruct.2020.111448

21. Farahani EM, Yekrangnia M, Rezaie M, Bento R (2020) Seismic behavior of masonry walls retrofitted by centercore technique: A numerical study. Constr Build Mater 267:120382. https://doi.org/10.1016/j.conbuildmat.2020.120382

22. Deng M, Yang S (2020) Experimental and numerical evaluation of confined masonry walls retrofitted with engineered cementitious composites. Eng Struct 207:110249. https://doi.org/10.1016/j.engstruct.2020.110249

23. Iuorio O, Dauda JA, Lourenço PB (2020) Experimental evaluation of out-of-plane strength of masonry walls retrofitted with oriented strand board. Constr Build Mater 269:121358. https://doi.org/10.1016/j.conbuildmat.2020.121358

24. Niasar AN, Alaee FJ, Zamani SM (2020) Experimental investigation on the performance of unreinforced masonry wall, retrofitted using engineered cementitious composites. Constr Build Mater 239:117788. https://doi.org/10.1016/j.conbuildmat.2019.117788

25. Vijayan DS, Arvindan DS, Janarthanan TS (2020) Evaluation of ferrock: A greener substitute to cement. Mater Today Proc 22(xxxx):781–787. https://doi.org/10.1016/j.matpr.2019.10.147

Rehabilitation and Retrofitting of Structural Elements Using Various Fibers

N. Varun, **G. Sudarshan**, **A. Shivaraj**, and **G. Sridevi**

Abstract Fiber-reinforced polymers (FRP) are very attractive to use in civil engineering applications due to their high durability, corrosion resistance, potentially high elasticity, and high tensile strength criteria. This study presents analytical study of different parameters on concrete column wrapped with fiber-reinforced polymer (FRP). Parameters like wrap thickness (layers) and type of fiber of them were altered and studied. The enhancement in the compressive strength and stiffness is anticipated by the application of FRP. An analytical model for ultimate stress and strain of confined concrete has been proposed. Finite element method is being used to study the analytical model. Behavior of FRP-wrapped column and beam is studied under loading by considering stress developed deformation and propagation of stresses. Conventional beam and column are analyzed in Ansys workbench, and results are recorded. Later, three beams and three columns are modeled for each fiber like CFRP, GFRP, and AFRP, then they are also modeled in AUTO CAD 3D and analyzed in Ansys and compared.

Keywords FEM · GFRP · CFRP · AFRP · Ansys

1 Introduction

Many structures in due course time develop different distresses leading to deterioration of the structure which make the structure functionally obsolete or structurally

N. Varun
B V Raju Institute of Technology, Narsapur, India

G. Sudarshan (✉) · A. Shivaraj
Assistant Professor, B V Raju Institute of Technology, Narsapur, India

A. Shivaraj
e-mail: shivaraj.a@bvrit.ac.in

G. Sridevi
Professor, B V Raju Institute of Technology, Narsapur, India
e-mail: sridevi.g@bvrit.ac.in

inadequate. Predicting the causes for deterioration in terms of applied loads, environmental factors is vital for the proposed retrofit measures. Generally, the structural elements like columns and beams are more deteriorated, and there is a need to strengthen these elements as to increase the life of the structure and also to increase the strength of the structure. In recent years, use of fiberglass-reinforced panels (FRP) is gaining importance owing to its properties such as lightweight, easy installation, improved chemical resistance, flexibility, corrosion resistance. These are effective in protecting walls from impact and moisture damage.

In order to enhance the stress-carrying capacity and to reduce the deformation, these structural elements are wrapped with FRPs. FEM is an appropriate and reliable means to understand the variation of stress-carrying capacity and deformation in various FRP-wrapped elements.

G. Sridevi et al. [1] studied comparative study on dynamic behavior of RC building with conventional and flat slab. It concludes that RC frame with flat slab system is more vulnerable to seismic loads analyzed by response spectrum analysis as compared to RC building with conventional slab. Further in continuation of their study analyzed multi-story buildings subjected to dynamic seismic load for evaluation of separation gap.

G. Sridevi et al. [2] studied behavior of geocell-reinforced pavements finite element method.

Anju Mary Martin and Mariamol Kuriakose [3]; Bhagya Lakshmi et al. [4]; M. A. Shahawy et al. [5]; Muhammad N. S. and Ida Bagus Rai [6] concluded that FRP wrapping has improved the performance of structural elements in terms of stress-carrying capacity and the deformations. Properties like modulus of elasticity and Poisson's ratio influence the performance of structural elements.

1.1   *Objectives of the Study*

- Comparative study on behavior of wrapped and unwrapped structural elements.
- To understand the suitability of fibers for structural elements.

2   Model Description

Structural elements with and without wrapping are modeled in sophisticated finite element analysis tool Ansys. Total ten columns are modeled; out of those, one is conventional and nine are CFRP, GFRP, and AFRP-wrapped; each FRP having three columns with various thicknesses like 1, 2, and 3 mm.

Likewise, ten beams are also modeled. Column elements are wrapped for four sides, and for beams, it is for soffit only. The assigned material properties of the model are given in Tables. The material properties of the column are given in Table 1. Material properties of beam are presented in Table 2. The material properties

Table 1 Properties of column

Column geometry	Dimensions
Height of the column	1.00 m
Width of the column	0.30 m
Depth of the column	0.30 m

Table 2 Properties of beam

| Beam geometry	Dimensions
Length of the beam	1.00 m
Width of the beam	0.23 m
Depth of the beam	0.3 m

Table 3 Material properties of concrete (M30)

Young's modulus, Ec	27,386.127 (MPa)
Poisson's Ratio, μ	0.25

Table 4 Properties of FRPs used in the study

Material	Modulus of elasticity (MPa)	Density (kg/m3)	Poisson's ratio
CFRP	142,000	1580	0.27
GFRP	44,000	1950	0.24
AFRP	80,000	1380	0.34

of M30 grade concrete and CFRP, GFRP, AFRP fibres are given in Table 3 and 4 respectively. Figure 1 shows Geometry of the column and beam the model created in ANSYS is shown in Fig. 2.

For element, key parameter is the connection between the concrete and FRP. Fixed support constraints are taken for analysis; for column bottom end and for beam, two sides of beam fixed support is assigned. Gradual loading in the form of pressure is applied using loading arrangements.
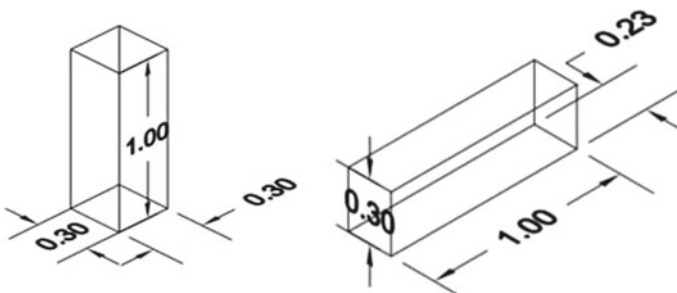
Fig. 1 Geometry of the column and beam
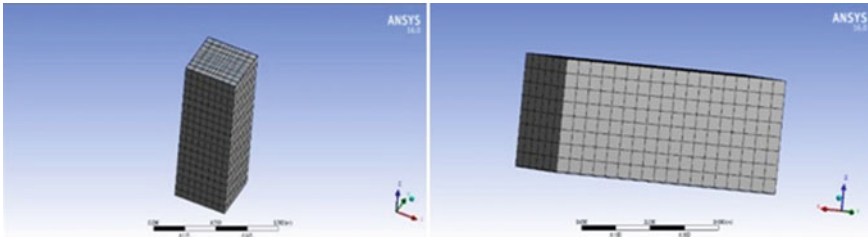
Fig. 2 Ansys model

3 Results and Discussions

Analysis of all four models have been done in Ansys software and compared for principal stress and deformation results with different fiber polymers. The analysis design of them is performed by using Ansys WB 16.0. The results include the variation in stress-carrying capacity, total deformation in column, and total deformation in beam (Table 5).

Column = column without any fiber wrapping.

Column 1 = column with 1 mm thick fiber wrapping.

Column 2 = column with 2 mm thick fiber wrapping.

Column 3 = column with 3 mm thick fiber wrapping.

From Fig. 3, it can be observed that in CFRP, stress-carrying capacity has increased by 69.51, 69.57, and 69.63% for 1, 2, and 3 mm wrapping, respectively, when compared to a normal column. For GFRP, it is increased by 39.77, 39.88, and 39.97% for 1, 2, and 3 mm wrapping, respectively, when compared to normal column. For AFRP, it is increased by 51.43, 51.52, 51.60% for 1, 2, and 3 mm wrapping, respectively, when compared to normal column. It shows that for increasing stress-carrying capacity of column, it should be wrapped with 3 mm CFRP which increases strength by 69.63% (Table 6).

From Fig. 4, it was observed that in CFRP, deformation has reduced by 68, 67.79, and 67.58% for 1, 2, and 3 mm wrapping, respectively, when compared to a normal column. For GFRP, it is reduced by 8.32, 7.71, and 7.11% for 1, 2, and 3 mm wrapping, respectively, when compared to normal column. For AFRP, it is reduced by 28.32, 27.85, and 27.37% for 1, 2, and 3 mm wrapping, respectively, when compared to

Table 5 Stress-carrying capacity of columns

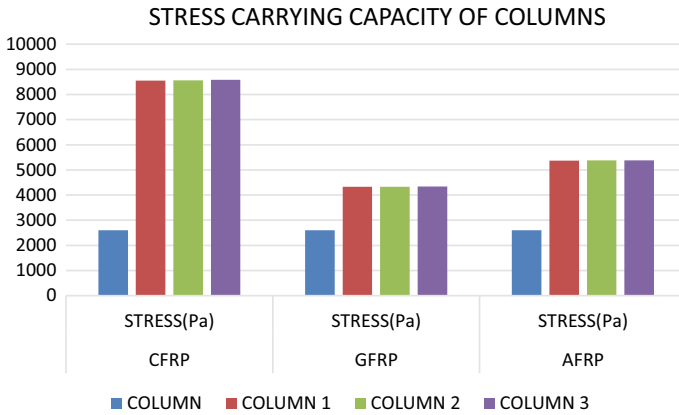| Stress-carrying capacity			
	CFRP stress (Pa)	GFRP stress (Pa)	AFRP stress (Pa)
Column	26.05×10^6	26.05×10^6	26.05×10^6
Column 1	85.46×10^6	43.26×10^6	53.65×10^6
Column 2	85.63×10^6	43.33×10^6	53.75×10^6
Column 3	85.79×10^6	43.40×10^6	53.84×10^6

Fig. 3 Stress-carrying capacity of columns

Table 6 Total deformation of columns

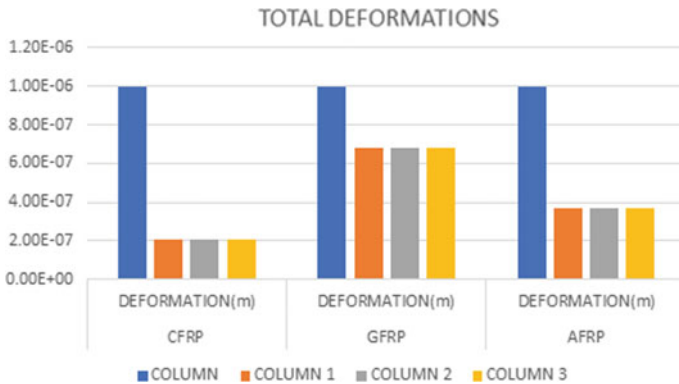|	CFRP deformation (m)	GFRP deformation(m)	AFRP deformation (m)
Column	9.97×10^{-7}	9.97×10^{-7}	9.97×10^{-7}
Column 1	2.10×10^{-7}	6.78×10^{-7}	3.71×10^{-7}
Column 2	2.10×10^{-7}	6.78×10^{-7}	3.71×10^{-7}
Column 3	2.10×10^{-7}	6.78×10^{-7}	3.71×10^{-7}

Fig. 4 Total deformation in columns

normal column. It shows that for reducing deformation of column, it should be wrapped with 1 mm CFRP which reduces deformation by 68% (Table 7).

Beam = beam without any fiber wrapping.

Beam 1 = beam with 1 mm thick fiber wrapping.

Table 7 Total deformations of beams

	CFRP deformation (m)	GFRP deformation (m)	AFRP deformation (m)
Beam	1.47E-06	1.47E-06	1.47E-06
Beam 1	1.44E-06	1.46E-06	1.45E-06
Beam 2	1.42E-06	1.45E-06	1.43E-06
Beam 3	1.40E-06	1.44E-06	1.42E-06
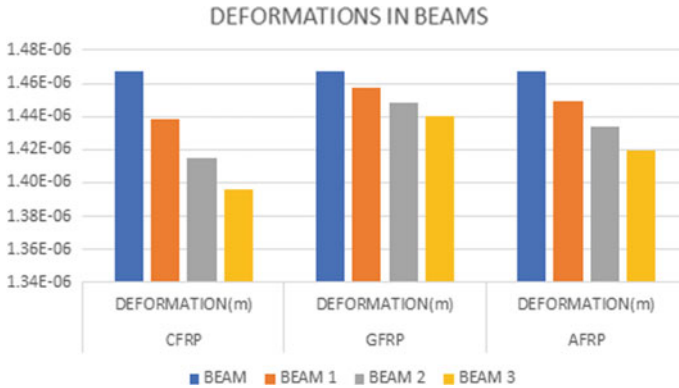
Fig. 5 Graph showing total deformation in beams

Beam 2 = beam with 2 mm thick fiber wrapping.

Beam 3 = beam with 3 mm thick fiber wrapping.

Figure 5 shows that for CFRP, deformation has reduced by 1.94, 3.54, and 4.88% for 1, 2, and 3 mm wrapping, respectively, when compared to a normal beam. For GFRP, it is reduced by 0.66, 1.28, and 1.86% for 1, 2, and 3 mm wrapping, respectively, when compared to normal beam. For AFRP, it is reduced by 1.22, 2.29, and 3.23% for 1, 2, and 3 mm wrapping, respectively, when compared to normal beam. It shows that for reducing deformation in beam, it should be wrapped with 3 mm CFRP which reduces deformation by 4.88%.

4 Conclusion

- In general observation, adoption of FRP's can enhance strength of structural elements considerably.
- Stress carrying capacity of CFRP, GFRP, and AFRP-wrapped elements has been increased by 69.63%, 39.97%, and 51.67%, respectively.
- Deformation of CFRP, GFRP, and AFRP-wrapped column elements has been reduced by 68%, 7.71%, and 28.32%, respectively.

- Deformation of CFRP, GFRP, and AFRP-wrapped beam elements has been reduced by 4.88%, 1.86%, and 3.23%, respectively.
- By looking at the trend of output, it can be concluded that CFRP could be the best among all FRP used for study in order to enhance overall strength of structural elements.

References

1. Sridevi G, Shivaraj A, Sudarshan G, Umesh B (2019) Comparative study on dynamic behavior of RC building with conventional and flat slab. Adv Structural Engineering Rehabilitation. https://doi.org/10.1007/978-981-13-7615-3
2. Sridevi G. Shivaraj A, Sudarshan G (2019) Bridge and structural engineering Indian National Group of the International Association for Bridge and Structural Engineering 48(2)
3. Martin AM, Kuriakose M, Finite element modeling and analysis of reinforced concrete beam retrofitted with fiber reinforced polymer composite
4. Lakshmi B, Mohammed Risal E, Sabees F, Nadeera CA, Ramesh Kumar D (2019) Strengthening of Columns Using CFRP. Published for International Research Journal of Engineering and Technology (IRJET), 6(5)
5. Shahawy MA, Arockiasamy M, Beitelman T, Sowrirajan R (1996) Reinforced concrete rectangular beams strengthened with CFRP laminates. Composites: Part B 27B (1996), 225–233
6. Muhammad NS, Rai IB (2013) Axial and flexural performance of square RC columns wrapped with CFRP under eccentric loading. ASCE J 16(6)

Evaluation of Failure Criteria in RC Structural Elements Due to Additional Internal Stresses Developed in Structural Elements Due to Temperature Exposure

Y. K. Guruprasad and Nisarga Ravi

Abstract Reinforced concrete structural elements such as beams, columns, slabs and shear walls, present in multi-storeyed buildings, undergo damage in the form of stiffness and strength degradation when exposed to high temperature in the event of a fire breakout in such buildings. The physical properties of concrete such as the elastic modulus, compressive and tensile strengths reduce with increase in temperature and time of exposure when compared to the corresponding properties of reinforcing steel. Constrained structural elements in framed structures when exposed to temperature are restricted from expanding. This constraint towards expansion in structural elements causes additional compressive stresses to be induced in them when exposed to temperature. This additional compressive stress that is induced in structural elements adds upon the internal stresses developed due to gravity loads causing an additional stress condition in the structural elements. When the total stress in concrete and reinforcing steel in compression or tension exceeds the maximum material strength values, the structural elements tend to fail. In this work, two temperatures of 300 °C and 450 °C are separately considered and applied on a 3D RC frame model along with the dead and live loads. The behaviour and additional internal stress increase in the structural elements such as the RC beams and RC columns are studied based on the internal stresses induced in these elements due to temperature exposure. Computations are carried out to ascertain the total internal stresses developed in the structural elements due to gravity loads and temperature and are compared with the maximum material strength values. Through this analytical approach, based on the values of the total internal stresses developed in the structural elements, comparative evaluation is carried out to identify structural members that have failed when the total internal stress exceeds the maximum material strength.

Keywords Reinforced concrete · Stiffness degradation · Strength degradation · High-temperature fire exposure · Induced internal stresses

Y. K. Guruprasad (✉) · N. Ravi
Department of Civil Engineering, Ramaiah Institute of Technology, Bangalore, India

195

1 Introduction

Fires cause catastrophic failures of buildings when the temperatures developed inside the building due to a fire temperature reaching very large magnitudes. A series of physio-chemical changes will take place when the concrete structures will be exposed to high temperature. The reduction in the mechanical properties such as strength and stiffness of the concrete structure will takes place due to physio-chemical changes such as loss of the free water, cement paste dehydration which lead to cracking, spalling of concrete and loss of bond between concrete and rebar. When structures are exposed to fire, there is a reduction in the strength, stiffness and overall load carrying capacity of the structural members present in the structure. Due to high temperature exposure, the reduction in strength, stiffness and load carrying capacity of RC structural members take place due accumulation of damage as a result of cracking and reduction of Young's modulus of concrete and steel. When there is reduction in the stiffness of the RC structural members exposed to high temperature, there is an increase in the deflection (transverse and rotational deformation) in the structural members. Whenever the structure get exposed to high temperature apart from reduction in stiffness, there is variation in the internal forces such as axial forces, bending moment and shear force developed in the structural members [1]. When structural members are exposed to elevated temperature that have their ends restrained, compressive stresses and strains are induced in such members. In framed structures with ends of members that are constrained and restricted from expanding [2], tends to induce additional stresses (compressive) in such structural elements. This additional stress induced causes additional internal forces that add up to the gravity loads (dead load and live load). Thus, the net internal forces developed in the structural members due to temperature and gravity loads exceeds the material strength and such structural members undergo failure. Ahmed [3] has carried out multi-storey analysis by the SAP program for a temperature fall of 20 °C and linear gradient temperature. The author has articulated that the linear temperature gradient on roof beams and slabs resulted in significant bending moments, in the internal panel and in specific bays that are the most affected structural elements under temperature loading. Wang and Moore [4] have studied the behaviour of structures subjected to fire conditions using FEM. Work has been carried out to by the authors to assess the behaviour of a column that has been restrained at its ends. Simple method and the computer analysis have been correlated to ascertain the additional axial forces in column. The authors remarked that the program developed was capable of predicting behaviour of steel frames in fire and the additional axial forces depends on the column stiffness. Alberto and Paulo [5] have carried out experimental and numerical study using the FEM program SAFIR, to ascertain fire behaviour of RC columns with restrained thermal elongation. During the tests, it is observed that the restraining forces increased up to a maximum value and then decreased. The application of 500 °C in the FEM program led to small values of fire resistance that was in comparison with the experimental results. Mustafa and Mansour [6] have worked on the changing member-temperature loading case and the section temperature gradient loading case for concrete frame structures. 2-D and

3-D frame buildings were analysed in a finite element structural analysis software package. The authors remarked that beams and columns on the lowest two storeys are affected to greater extent. Wen-Chen and Huang [7] have worked on the behaviour of corner columns under axial loading, biaxial bending and asymmetric fire loading. The test was conducted for column specimens by considering fire duration, steel and cover thickness and 1500 mm centre-portion of the column was subjected to fire. The authors remarked that thicker the cover, the earlier the cover tends to fall off, and the longer the fire, the less the residual strength ratio. Kadhum [8] studied the behaviour and load carrying capacity of rectangular reinforced concrete (RC) rigid beams exposed to fire. Five RC rigid beams were fabricated for the experimental investigations and temperature exposure was about 400 °C and 750 °C for 1.5 h and tested. The results showed that the deleterious responses from load deflection curves, and maximum crack width increases with increasing fire temperature was noticed. Al-janabi and Shakimon [9] have analysed a RC column exposed to fire on non-linear finite element modelling (FEM) in Abaqus 3D model. Vertical displacement and stress distribution have been investigated. From the analysis, it was found that the column ultimate axial displacement increases while the column ultimate failure loads decrease after exposed to fire. It was remarked that the stress distribution varies after fire emphasizing the higher stress on the surface of the column. Cherif Guergah et al. [10] have studied the concrete spalling of the RC beams subjected to fire and the structural stability. Numerical modelling of RC beam subjected to fire, for different boundary conditions has been performed. Here, numerical analysis has been performed by SAFIR code. The results obtained showed that the major influence of spalling on the mechanical stability of structural elements in a fire situation, and that this is by reducing the failure time.

Zhaohui huang et al. [11] have analysed reinforced concrete structure subjected to a standard fire and interactions between the cool and hot zones of the structure. Analysis was carried out using the computer program Vulcan. The authors remarked that an adjacent cooled structure provides restraint and continuity, thereby increasing the fire resistance of the structure within the compartment. Džolev et al. [12] made use of FE method to evaluate the behaviour of reinforced concrete frame structure subjected to fire. Thermal and structural response are obtained using ANSYS. Analysis is performed and critical regions are identified in the frames. A three-story two-bay reinforced concrete structure was analysed, subjected to standard ISO 834 fire curve [13]. It is found that at elevated temperatures in RC, structural members lead to development of thermal strains along with degradation of material strength, reduction in stiffness and reduced load-bearing capacity. **Significance and objective of the present work**: is to study the effect of internal stresses/forces that are induced in structural members (beams, columns…) that are exposed to high temperature. High temperature exposure causes the structural members to fail, when the net internal stresses developed due to thermal expansion taking place in structural members, that are restrained at their ends tend to exceed the material strength or load-carrying capacity of the structural members. This study helps in understanding from the point of view of assessment of stresses that are induced due to high temperature exposure due to end restrains in the structural members. This helps in better

assessment of the damage that has taken place in the structural members, so as to arrive at the existing residual load carrying capacity of the structural members after fire damage, and to decide on a suitable retrofit scheme (if the damage is within repairable limits).

2 Assessment of Additional Internal Forces Developed in Structural Members Exposed to High Temperature

In the present work structural analysis of a seven-storey RC structure considering temperature as a load due to fire exposure [14] has been carried out in ETABS [15]. The standard heating conditions that is adopted for fire resistance of structures is addressed by IS 3809 [16]. The typical plan of the seven-storey RC building has been shown in Fig. 1.

The outer-to-outer dimension of the typical plan considered in the structural analysis is 70×40 m. The details of grade of steel and concrete adopted has been shown in Table 1.

The size of the primary beams provided in the structure are 230×750 mm, and size of the secondary beams provided are 230×650 mm. The column size provided in the structure are 300×600 mm based on the maximum axial load due to gravity
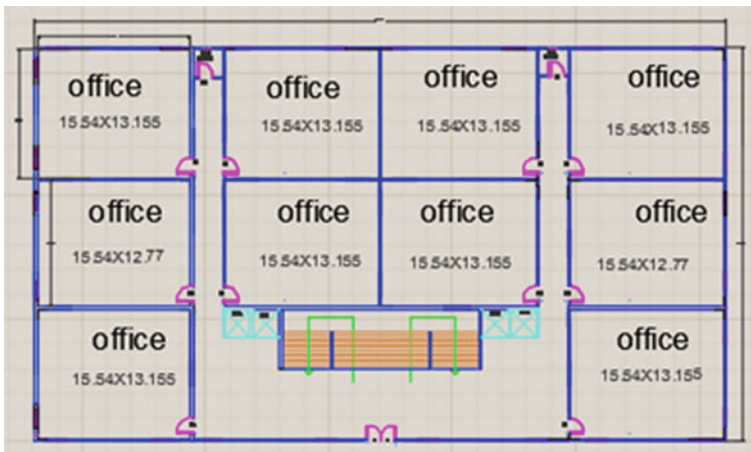
Fig. 1 Typical floor plan of the RC building for office purpose for one to seven storeys

Table 1 Grade of concrete and steel adopted in the analysis

Material	Grade
Concrete	M30
Rebar	Fe415

S. No.	Load type	Load values
1.0	Dead load	1 kN/m^2
2.0	Live load	3 kN/m^2
3.0	Temperature	(a) 300 °C (b) 450 °C
4.0	Load combinations	(a) 1.5 (DL + LL) (b) 1.5 (DL + LL + TL)

Table 2 Dead load, live load and temperature load adopted in the analysis

loads in the columns. The thickness of the RC slab provided in the structure is 150 mm. The supports that are provided at the base of the structure is fixed. The dead load, live load and the temperature (300 °C and 450 ˚C–temperatures in medium to high range fire) that is considered in the analysis is shown in Table 2.

The typical floor plan of the structure exposed to a temperature of 450 ˚C applied on the slab is shown in Fig. 2.

On defining the load cases, the loads were assigned to the structure modelled in the ETABS. Temperatures of 300 ˚C and 450 ˚C were applied separately on the ground, fourth and sixth floors, respectively, onto the slabs and the frame members. Temperatures of 300 ˚C and 450 °C were applied separately at different floor levels as mentioned above to assess the variation in the internal forces developed in the structural members present at different floor levels and the corresponding effects of temperature on the adjacent floors in terms of deflections. The analysis was carried out for all the load cases and load combinations corresponding to above-mentioned temperatures separately. The corresponding results were recorded for
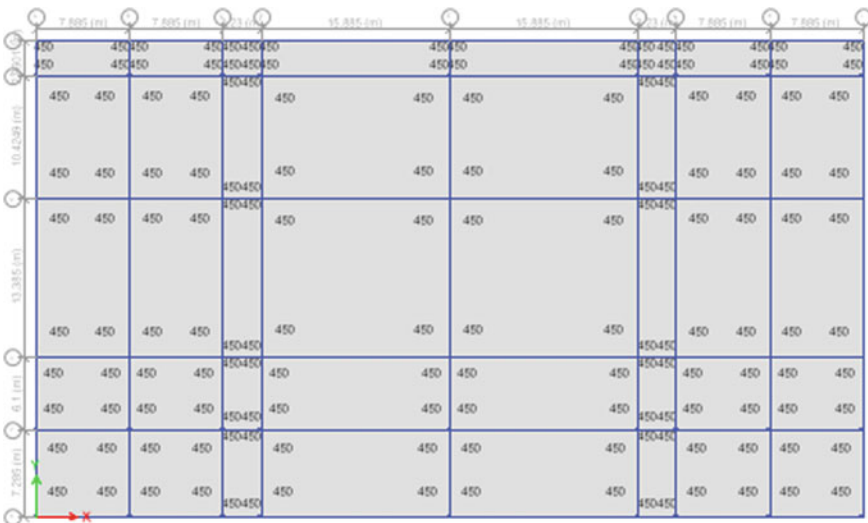
Fig. 2 Typical floor plan exposed to a temperature of 450 ˚C applied on the slab

temperature exposures of 300 ˚C and 450 °C applied separately. Axial forces, bending moments and shear forces were obtained as the analysis results, corresponding to each temperature exposure (300 ˚C and 450 ˚C) separately.

3   Results and Discussion

The deflected shape of the structure when a temperature of 450 °C is applied at the fourth floor is shown in Fig. 3.

Axial forces developed in the columns present in the structure when a temperature of 450 °C is applied at the fourth floor is shown in Fig. 4.

Bending moment in structural members (beams and columns) when a temperature of 450 ˚C is applied at the fourth floor is shown in Fig. 5.

The maximum values of axial forces, bending moment and shear forces that have been recorded in beams and columns present in the entire structure exposed to the following temperatures: 25 ˚C, 300 ˚C and 450 °C at different floors (ground, fourth and sixth floors) are shown in Tables 3 and 4, respectively.

In case of columns, it is observed that the floor exposed to a particular value of high temperature developed axial forces in columns when compared to the same columns present in the structure at ambient temperature. It may be noted from Table 3 that the percentage increase in the axial force, bending moment and shear force in columns due to high temperature exposure are 15.34%, 97.93% and 100% for a temperature exposure of 300 °C; and 22.92%, 149.433% and 100% for a temperature exposure of 450 °C, respectively, when compared to the corresponding values at ambient temperature (25 °C). It is observed from Table 4 that the percentage increase in the axial force, bending moment and shear force in beams due to high temperature exposure are 541.18%, 78.32% and 228.24% for a temperature exposure of 300 ˚C; and 920.03%, 134.86% and 500.76% for a temperature exposure of 450 °C,
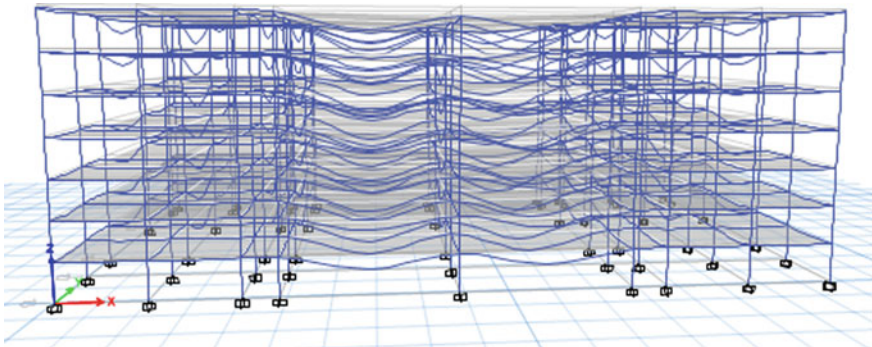
Fig. 3 The deflected shape of the structure when a temperature of 450 °C is applied at the fourth floor
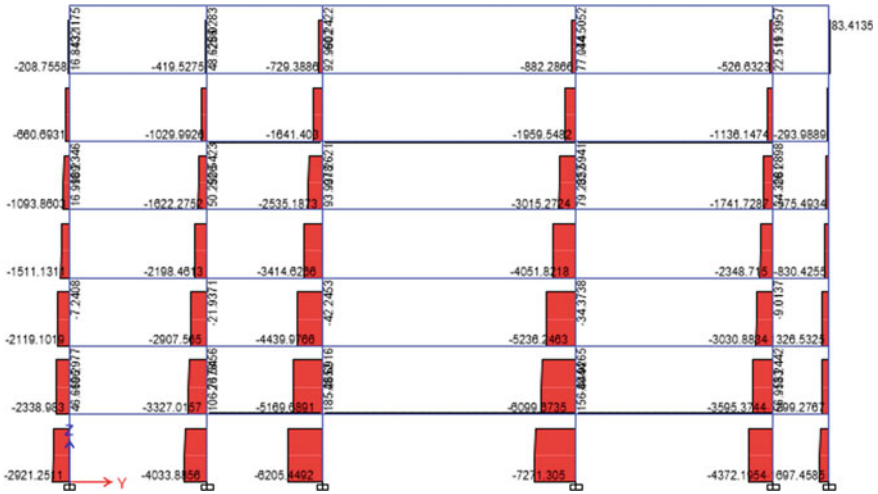
Fig. 4 Axial forces developed in the columns exposed to a temperature of 450 °C applied at the fourth floor
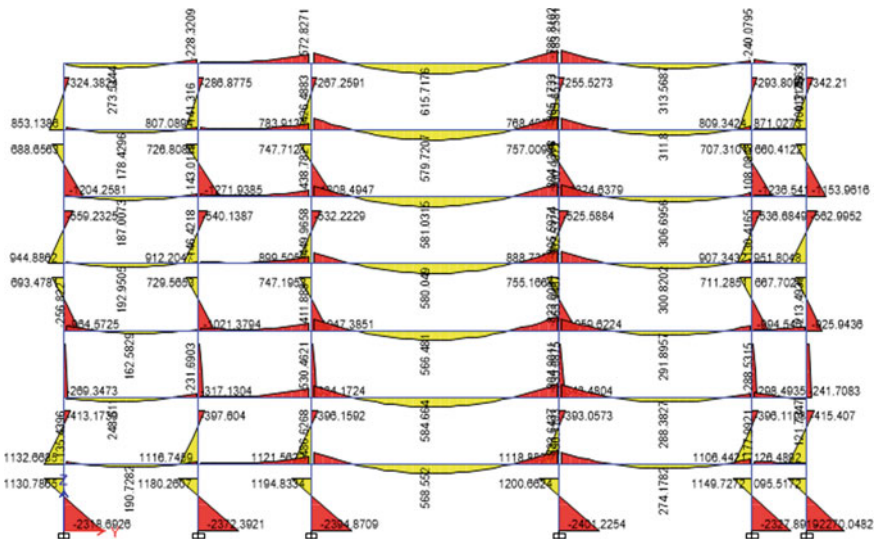
Fig. 5 Bending moment in structural members (beams and columns) when a temperature of 450 °C is applied at the fourth floor

respectively, when compared to the corresponding values at ambient temperature (25 °C).

It is observed from the analysis results that there is a large increase in the magnitude of the axial force, bending moment and shear force in the structural members present

Table 3 Maximum values of axial forces, bending moment and shear forces recorded in columns present in the entire structure exposed to different temperatures: 25 ˚C, 300 ˚C and 450 °C at different floors (ground, fourth and sixth floors)

Temperature exposure	25 °C (ambient temperature)	300 °C	450 °C
Axial force (kN)	4325.30	4989.20	5316.98
Bending moment (kN-m)	296.12	584.54	738.63
Shear force (kN) (lateral)	–	537.02	689.87

Table 4 Maximum values of axial forces, bending moment and shear forces recorded in beams present in the entire structure exposed to different temperatures: 25 ˚C, 300 ˚C and 450 °C at different floors (ground, fourth and sixth floors)

Temperature exposure	25 °C (ambient temperature)	300 ˚C	450 ˚C
Axial force (kN)	36.19	232.30	369.56
Bending moment (kN-m)	375.75	670.06	882.52
Shear force (kN) (lateral)	87.035	285.69	522.88

in the structure when exposed to high temperature (300 ˚C and 450 °C). A large increase in the values of axial forces and bending moment in the beams and columns that are mentioned above resulted in bulking of the beams and columns (observed in Fig. 3), leading to lateral instability of the structure. A large increase in shear force resulted in sudden shear failure of the structural members. It has to be noted that at a temperature of 300 ˚C, the concrete present in the structural members has a drop in compressive strength around 20–30% [17]. At a temperature exposure of 450 °C, there is a reduction in compressive strength of concrete around 35–40%. The strength of steel reduces by about 15–30% [18] for temperature exposures of 300 ˚C and 450˚C, respectively. The reduction in compressive strength of concrete results in reduced load-carrying capacity of structural members. The beams and columns when exposed to elevated temperatures, there is a development of additional internal stresses (compressive) in them on account of temperature exposure when the structural members are restrained due to fixity condition. The additional internal stresses induced cause additional internal forces to sum up with the dead and live loads (gravity loads). When the total internal forces develop in the structural members due to temperature and gravity loads, the stresses in the material present in the structural members tends to exceed the material strength and load carrying capacity leading to failure of the structural members. Therefore, from the damage assessment point of view, the additional internal forces developed due to temperature requires to be addressed, while assessing the damage taken place in the structural members other than the damage induced due to material degradation (reduction in strength) due to high temperature. This assessment of damage helps to further assess the residual load carrying capacity of the structural members so that a suitable retrofit strategy may be applied onto the damaged structural members if the damage is within repairable limits.

4 Conclusion

1. It is observed from the results that when the structure is exposed to high temperature, an increase in the magnitude of the axial forces in the structural members are observed when compared to the corresponding values of axial forces in the same structural members present in the structure at ambient temperature.

2. When structural members are exposed to elevated temperatures, the magnitude of the bending moment and the shear forces in the structural members are observed to increase in magnitude for temperature exposures of 300 ˚C and 450 °C.

3. The results from this study indicate that the percentage increase in the axial force, bending moment and shear force in columns for temperature exposure of 300 ˚C and 450 °C are 15.34%, 97.93%, 100% and 22.92%, 149.433% and 100%, respectively, when compared to the corresponding values at ambient temperature(25 °C).

4. The results from this study show that the percentage increase in the axial force, bending moment and shear force in beams for temperature exposure of 300 ˚C and 450 ˚C are 541.18%, 78.32%, 228.24% and 920.03%, 134.86% and 500.76%, respectively, when compared to the corresponding values at ambient temperature(25 °C).

5. When structural members (beams and columns) are exposed to elevated temperatures in the event of a fire, additional stresses (compressive) develop in such structural elements on account of temperature exposure when the structural members are restrained from expanding due to support and fixity conditions. These additional stresses induced cause additional internal forces to add up to the gravity loads (dead load and live load). When the net internal forces developed in the structural members due to temperature and gravity loads tends to exceed the material strength and load carrying capacity, the structural elements undergo failure due to buckling, shearing or due to crushing of concrete. Therefore, the damage due to additional internal forces induced due to temperature have to be considered while assessing the damage that has taken place in the structural members other than the damage taken place due to material degradation (reduction is compressive strength of concrete and reduction in yield strength of steel) due to temperature exposure. The damage assessment considering the effect of the additional internal forces developed due to temperature helps in designing a retrofit having a better load carrying capacity.

References

1. Martins A, Rodrigues J (2011) Fire behaviour of concrete columns with restrained thermal elongation. J Structural Fire Eng 2(4):319–332
2. Usmani AS, Rotter JM, Lamont S, Sanad AM, Gillie M (2001) Fundamental principles of structural behaviour under thermal effects. Fire Saf J 36(8):721–744

3. Ahmed K (2011) Temperature effects in multi-story buildings. J Engineering Sciences 39(2):249–267
4. Wang YC, Moore DB (1994) Effect of thermal restraint on column behaviour in a frame. Fire Safety Sci 4:1055–1066
5. Miguel A (2011) Joao Paulo CR: Fire behaviour of concrete columns with restrained thermal elongation. J Structural Fire Eng 2(4):319–332
6. Badrah MK, Jadid MN (2013) Investigation of developed thermal forces in long concrete frame structures. Open Civil Engineering J 7:210–217
7. Jau WC, Huang KL (2008) A study of reinforced concrete corner columns after fire. Cement and concrete Composites 30(7):622–638
8. Kadhum MM (2014) Fire resistance of reinforced concrete rigid beams. J Civil Engineering Construction Technology 5(5):35–48
9. Al-janabi ARI, Shakimon, MNF (2017) Finite element modeling of reinforced concrete column after exposure to fire. 3rd International Engineering Conference on Developments in Civil & Computer Engineering Applications
10. Guergah C (2017) Numerical modelling of the fire behaviour of reinforced concrete beam integrating the concrete cover lost by spalling. J Mat Environ Sci 8(10):3690–3705
11. Huang Z, Burgess IW, Plank RJ (2006) Behaviour of reinforced concrete structures in fire. Proc Int Workshop Struct in Fire
12. Džolev I, Cvetkovska M, Lađinović Đ, Radonjanin V (2018) Numerical analysis on the behavior of reinforced concrete frame structures in fire. Computers Concrete 21(6):637–647
13. Szumigała M, Polus L (2015) A comparison of the rise of the temperature of an unprotected steel column subjected to the standard fire curve ISO 834 and to a natural fire model in the office. Eng Trans 63(2):157–170
14. IS 1642 (1989) Fire safety of buildings: Details of construction code of practice. Bureau of Indian Standards
15. CSI Analysis Reference Manual, Computers and Structures (2019)
16. IS 3809 (1979–Reaffirmed 2002) Fire resistance test of structures. Bureau of Indian Standards
17. Kodur V (2014) Properties of concrete at elevated temperatures, ISRN Civil Engineering Article ID 468510, 15 p. https://doi.org/10.1155/2014/468510.
18. Elghazouli AY, Katherine C, Bassam AI, Experimental evaluation of the mechanical properties of steel reinforcement at elevated temperature. Fire Safety J 44(6):909–919. https://doi.org/10.1016/j.firesaf.2009.05.004

Retrofitting of Distressed RC Structures Using Near Surface Mounted Reinforcement

Y. K. Guruprasad, Aditya Poudel, Y. V. Gautam Sandesh, Hage Rabin, and Acintya Upmanyu

Abstract Damage takes place in reinforced concrete structures due to, earthquakes, erroneous design, overloading, corrosion of reinforcement and due to ageing. Damaged reinforced concrete (RC) structural elements (beams, columns, slabs, etc.) can be retrofitted to enhance their load carrying capacity. Non-destructive testing methods are adopted for assessing the extent and degree of damage that has taken place in distressed RC structural elements. Retrofitting of damaged structural elements can be carried out only when the damage that has taken place is within repairable limits. The different types of retrofitting that can be adopted to restore damaged RC structural elements are: reinforced concrete jacketing, FRP wrapping (CFRP/GFRP), epoxy injection to seal cracks, near surface mounted reinforcement and external prestressing. In this particular work, a numerical study is carried out on retrofitting of structural elements, adopting near surface mounted reinforcement using CFRP rods to restore structural elements (beams/columns) that is present in a distressed RC structure that has undergone degradation at the material level on account of ageing. With the application of near surface mounted reinforcement the performance of the distressed structural elements present in the structure is assessed in terms of, increased stiffness and improved resistance towards deflection when such the structure is subjected to any future loading such as an earthquake. A numerical analysis is carried out on the retrofitted structure subjected to earthquake loading to study its performance and assess the efficacy of the retrofit using near surface mounted reinforcement. It was observed by carrying out the analysis of the retrofitted structure, the stiffness of the RC structural elements was observed to have improved that resulted in lower values of displacements.

Keywords Reinforced concrete structures · Distress due to ageing · Retrofitting using near surface mounted reinforcement · CFRP rods · Earthquake loads

Y. K. Guruprasad (✉) · A. Poudel · Y. V. Gautam Sandesh · H. Rabin · A. Upmanyu
Department of Civil Engineering, Ramaiah Institute of Technology, Bengaluru, India

1 Introduction

An earthquake is a natural phenomenon that originates at the focal point that is located a certain depth from the surface of the earth due to release of stored strain energy due to rupture of rocks or movement of a fault plane due to plate boundary movement. The vertical projection of the same focal point is identified on the surface of the earth as the epicentre. Shallow focal points lead to strong earthquake shaking and higher magnitudes of the earthquake. The magnitude and intensity of the earthquake around the epicentre governs the extent of damage the buildings undergo that exists around the epicentre. The damage that has taken place in the structural members present in the buildings due to earthquake is assessed adopting non-destructive testing techniques. Most buildings that undergo damage in the event of an earthquake can be restored adopting suitable retrofitting techniques when the damage is within repairable limits. Okiemute and John [1] worked on non-destructive testing (NDT) methods of concrete that were comparatively advanced when compared to the conventional NDT methods of testing concrete. The NDT methods in their work were adopted to increase the accuracy of NDT measurements and it was also insisted how various NDT methods coupled with artificial intelligence (AI) and Internet of things (IoT) can be used to safeguard national assets in Nigeria. Malek and Kaouther [2] investigated on the variation in compressive strength of aged concretes measured using rebound hammer and ultrasonic pulse velocity which are non-destructive testing method and compared it with destructive testing results. In their work, cylindrical specimens (160 mm × 320 mm) were cast having different w/c ratio and cement content. The authors also studied the effect of w/c ratio and concrete age on the modulus of elasticity of concrete. Their results showed that, as the concrete aged, the values of resistance when obtained through NDT tests and the value of the concrete strength obtained by destructive method after 28 days decreased with increase in the age of concrete. Lorenzis and Nanni [3] have worked on shear strengthening of RC beams adopting near surface mounted (NSM) fibre reinforced polymer rods. The authors have carried out tests on a RC beam with no steel stirrups and retrofitted by application of NSM using CFRP rods as stirrups. The testing and evaluation was done with respect to ultimate load, cracking, failure modes and deflection. The load was applied on the beams with the help of a hydraulic jack connected through an electric pump and a load cell. The failure modes, crack patterns and load–deflection characteristics were obtained from experimental studies. The test results of their study described the enhanced shear capacity of RC beams retrofitted with NSM CFRP rod. An increase in the shear capacity of 106% with respect to the control beam was observed. Belal [4] investigated strengthening of corroded reinforced concrete beams with near surface mounted technique using carbon fibre polymer rods. The author carried out the study that shows the performance of RC beams that have undergone damage due to corrosion of the tension steel reinforcements. The predictions of the mechanical behaviour of the repaired corroded RC beams were out by non-linear models based on FE numerical modelling. The study reviewed the stiffness, ultimate load carrying capacity, ductility and failure modes of the damaged and the NSM CFRP retrofitted

RC beams. Numerical modelling of 2D finite element model was carried out by FEMIX and the 3D modelling was carried out by ABAQUS. It was observed from the results of this study that the NSM technique has enhanced the ultimate load carrying capacity of the RC beam post-retrofit. It was observed that there was a marginal increase in the stiffness of the damaged RC beam after the application of NSM using CFRP rods as retrofit. There was an increase of 10% in the load carrying capacity of the RC beam post-retrofit. On the whole, the retrofit adopting NSM using CFRP rods restored the damaged RC beam by enhancing its ductility that was lost due to steel corrosion.

Nanni and Ludovico [5] used CFRP rebars that were earlier precured to enhance the shear and flexural capacity of a pre-stressed concrete bridge girder that is located at Kansas. A bridge girder as a test specimen was taken out from the bridge when it was fully overloaded. The test specimen was then subjected to testing at various conditions of loading. Their test results showed that there was an increase in both flexural and shear capacity of the girder. It was observed that, the moment carrying capacity increased by about 18% and it was also noted that the shear capacity increased by about 53.1% when two-point loads were applied on the overhanging portion on either side of the girder. Catalin et al. [6] have done seismic evaluations on a single-storey industrial hall after carrying out non-destructive testing of the structure. After the authors analysed the structure, it was learnt that the deformation capacity in the structure required to resist earthquakes was less. Retrofitting by application of a metal jacketing with welded bands and steel angles was applied as well as reinforced concrete jacketing on all four sides of the column cross-section was added. After retrofitting of the structure and thereafter carrying out the analysis of the retrofitted structure, it was found that there was a reduction in the lateral displacements in the structure. It was observed from the authors work that the RC jacketing retrofitting method offers highest values for safety factor (2.41) but imposes a long period of work interruptions with high costs. Reddy et al. [7] have analysed and designed beams for different loading conditions. The beams that showed signs of distress were identified and strengthened using a suitable jacketing technique (CFRP wrap) in ANSYS to enhance their load carrying capacities. After the application of CFRP wrapping as a retrofit, the total deformation was reduced by 45.66%, 46.82% and 46.28% for beam 1, beam 2 and beam 3 respectively.

Aravind et al. [8] have carried out experimental work by applying two-point loadings on beams that were retrofitted with GFRP laminates. It was observed that the failure of the beams occurred due to de-bonding of the laminates. Failure due to de-bonding of laminates occurred in retrofitted beams only at the soffit. To overcome this problem, GFRP laminates were provided along the full length of the beam to take into account shear and bending. Epoxy was applied to adhere the GFRP laminates to the concrete surface. To avoid premature failure, GFRP laminates were provided at the bottom and were extended at the ends. Failure loads of the control beam and beams with corrugated and plain GFRP laminates were 39.2 kN, 45.25 kN and 54.95 kN respectively, and it is observed there was an enhancement in the load carrying capacities of the beam at failure after application of GFRP laminate as a

retrofit measure. Yao [9] analysed RC beams and columns and their seismic performance having near surface-mounted (NSM) basalt fibre-reinforced polymer (BFRP) bars and confinement by BFRP sheet. Axial stress, elastic elongation and bond slip effects, were considered in this study that influenced the displacement model of the loaded end of NSM FRP bars. The authors studied the slip taking place in the FRP bars present in the plastic region (deformed region) of the columns. Fixed end rotations and the moment were determined and these values were assigned to the spring in the model. The method proposed in their work was in close correlation to the experimental results. This method was useful in ascertaining the hysteretic response and pushover curves of strengthened column as well as effective utilization of reinforcement to provide the necessary ductility.

The **objective of the present work** is to assess the efficacy of near surface mounted (NSM) reinforcement adopting CFRP rods applied as a retrofit strategy to reduce the storey displacements in the lateral direction in a structure whose structural members (RC beams and columns) have undergone distress due to material degradation due to ageing, when the same structure is subjected to seismic loading that is priorly designed for earthquake resistance.

Note: The structure that has been adopted in this study is a practical work that has been carried out on an old commercial existing RC building that is about 27 years old. Due to confidentiality reasons of the project, the details of the structure and location have not been disclosed.

2   Application of Near Surface Mounted Reinforcement Adopting CFRP Rods Applied as Seismic Retrofit on the Distressed RC Structure

This section explains the details of the seismic analysis that has been carried out in ETABS on a reinforced concrete (RC) structure that houses distressed RC beams and columns (distressed due to reduced compressive strength of concrete due to ageing) that were priorly not designed for earthquake resistance. The same distressed RC beams and columns have been retrofitted using near surface mounted reinforcement adopting CFRP rods applied on them to assess the percentage reduction in the storey displacements. Retrofitting of the model of the same RC structure is carried out adopting RC jacket [10] applied on the same distressed RC beams and columns to study the extent of reduction in the storey displacements, so that the efficacy and performance of the near surface mounted reinforcement is compared in terms of structural performance with respect to the RC jacket retrofit.

The distressed structure considered in this study is an RC structure having 5 bays along Y-direction and 6 bays along X-direction in plan. Each bay span along X and Y-directions are 5 m and 6 m respectively. There are 6 storeys in the structure, with each storey having a height of 3 m and the building is located in earthquake zone

IV. The structure is a frame structure and has a central RC wall as a lift core and is shown in Fig. 1 ((a) plan and (b) 3D-isoview).

The frame members of the structure have not been priorly designed for earthquake resistance (response reduction factor $R = 3$). The structure is a commercial complex (importance factor $= 1.5$) and is constructed on medium soil. The cross-sectional dimensions of beams present in the existing structure that is parallel to X and Y axes in plan are $b_b \times D_b$: 230 mm $\times$ 500 mm and $b_b \times D_b$: 230 mm $\times$ 600 mm respectively. The beams measuring 230 mm $\times$ 500 mm were provided with, 2Nos-12 mm diameter Fe415 steel at the top face and 3Nos-16 mm diameter Fe415 steel at the bottom face and 8 mm diameter two legged stirrups spaced at 200 mm centre to centre. The beams measuring 230 mm $\times$ 600 mm were provided with, 2Nos-12 mm diameter Fe415 steel at the top face and 3Nos-20 mm diameter Fe415 steel at the bottom face and 8 mm diameter two legged stirrups spaced at 175 mm centre to centre. The cross-sectional dimensions of the columns present in the structure are $b_c \times D_c$: 230 mm $\times$ 600 mm provided with 12Nos-16 mm (8Nos) & 20 mm (4Nos) diameter Fe415 longitudinal compression steel and 8 mm diameter lateral ties spaced at 300 mm centre to centre. The RC slab present in the structure has a thickness of 150 mm and provided with two-way reinforcement (Fe415) of 8 mm diameter spaced at 150 mm centre to centre. The RC wall (lift core) is 200 mm thick and provided with vertical and horizontal reinforcement (Fe415) of 8 mm diameter spaced at 150 mm centre to centre. The RC wall provided is without boundary elements. The details of reinforcement was assessed with the help of profometer for other structural members present, along with confirming the same by chipping off the cover especially only in all distressed RC beams and distressed RC columns at several locations.

M30 grade concrete (compressive strength of 30 MPa) has been adopted for constructing the beams, slabs, RC wall (lift core) and M45 grade concrete (compressive strength of 45 MPa) was used to construct columns. Fe415 grade steel has been used for all the reinforcing steel used in the structure.

The peripheral beams and columns and the next line of internal columns and beams in the structure were identified as distressed due to reduction in the compressive strength based on NDT evaluation (shown in Fig. 1a: in Fig. 1a distressed RC columns identified along grids A, B, G, 1, 2, 5 and 6. In Fig. 1a: Distressed beams identified along grids 1, 6, A, G, 1-AB, 1-FG, 2-AB, 2-FG, 3-AB, 3-FG, 4-AB, 4-FG, 5-AB and 5-FG).

The reduced compressive strength in the above-mentioned distressed beams and columns were found to be 25 MPa and 40 MPa respectively. The reduced compressive strength in the distressed beams and columns was determined adopting non-destructive testing modalities [11, 12] (ultrasonic pulse velocity tests, rebound hammer and core test-semi destructive test).

Response spectrum method [13] of seismic analysis has been carried out in this study on the distressed structural model, to assess the displacements the structure undergoes with the existing distressed material properties present in the structural members in the event of a future earthquake.

In all distressed RC beams 4 Nos of CFRP bars having a diameter of 16 mm were provided as near surface mounted (NSM) reinforcement in the cover region.
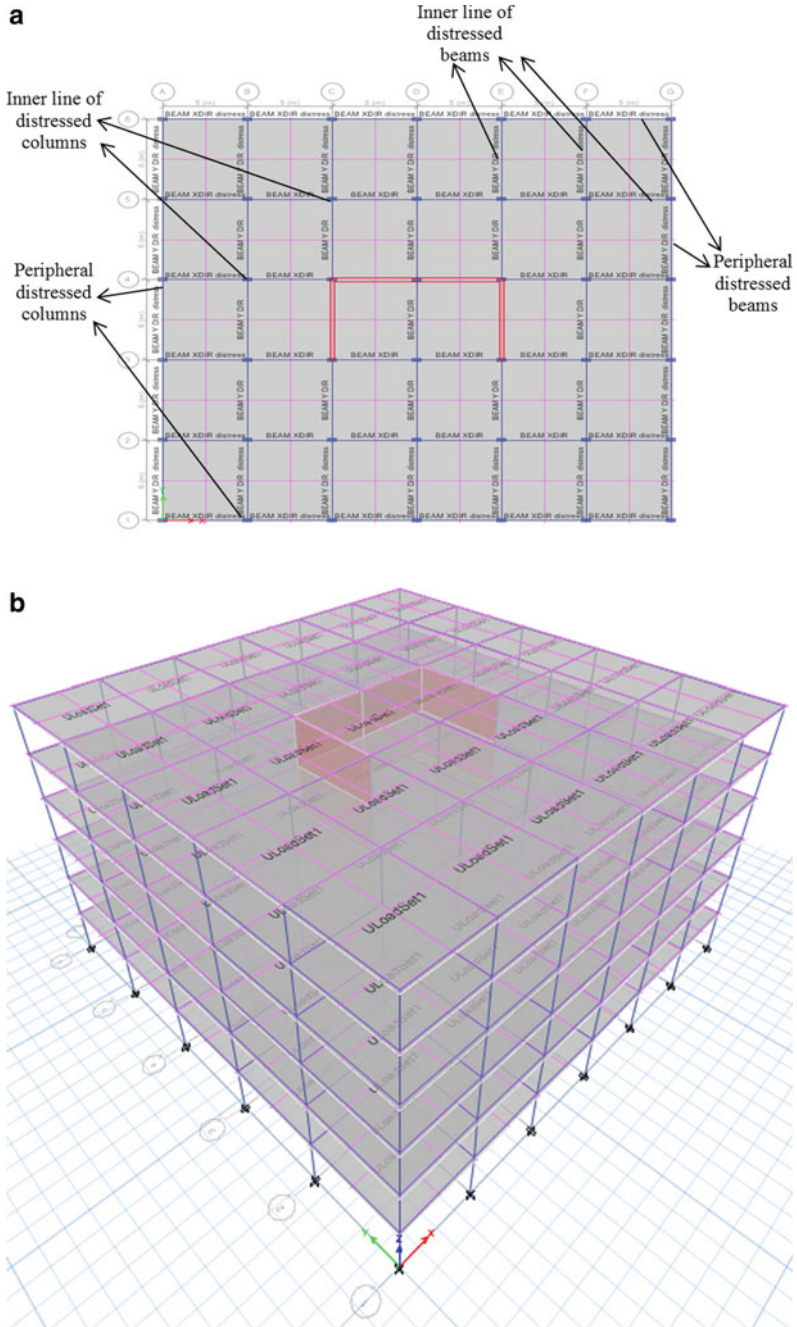
Fig. 1 a Plan of the distressed RC structure: distressed RC columns along grids A, B, G, 1, 2, 5 and 6.; distressed RC beams along grids 1, 6, A, G, 1-AB, 1-FG, 2-AB, 2-FG, 3-AB, 3-FG, 4-AB, 4-FG, 5-AB, 5-FG. **b** 3-D isoview of the distressed RC structure

In all distressed RC columns 8 Nos of CFRP bars having a diameter of 20 mm were provided as near surface mounted (NSM) reinforcement in the cover region distributed on all the faces of the column as shown in Fig. 2a (typical details). The CFRP rods used as near surface mounted (NSM) reinforcement to retrofit distressed RC beams and RC columns have an elastic modulus of 230 MPa and tensile strength of 600 MPa [14] were embedded in the cover region as shown in Fig. 2 (Note: Fig. 2a, b are typical details showing NSM retrofit applied for all the distressed RC beams and distressed RC columns in the structure) to assess the extent of reduction in the storey displacement. The embedded CFRP rods in the cover region are installed with the help of epoxy in actual site conditions. CFRP strip wraps that had an elastic modulus of 220GPa [15] density 1800 kg/m^3 with 0–90 fibre orientation and having a width of 50 mm were provided around distressed RC columns at a spacing of 300 mm. The CFRP strips are provided as an external confining reinforcement, to provide confinement to the near surface reinforcement (CFRP rods) provided in the distressed columns only (shown in Fig. 2b—typical details). Near surface mounted reinforcement (CFRP rods) is provided to the distressed peripheral columns and beams and the next line of columns and beams as shown in Fig. 1a (distressed RC columns identified along grids A, B, G, 1, 2, 5 and 6; distressed beams identified along grids 1, 6, A, G, 1-AB, 1-FG, 2-AB, 2-FG, 3-AB, 3-FG, 4-AB, 4-FG, 5-AB and 5-FG).

RC jacket having a thickness of 100 mm and made up of M30 grade and M45 grade concretes are provided for beams and columns respectively as retrofit to a companion model of the structure as shown in Figs. 3a, b to assess the extent of reduction in
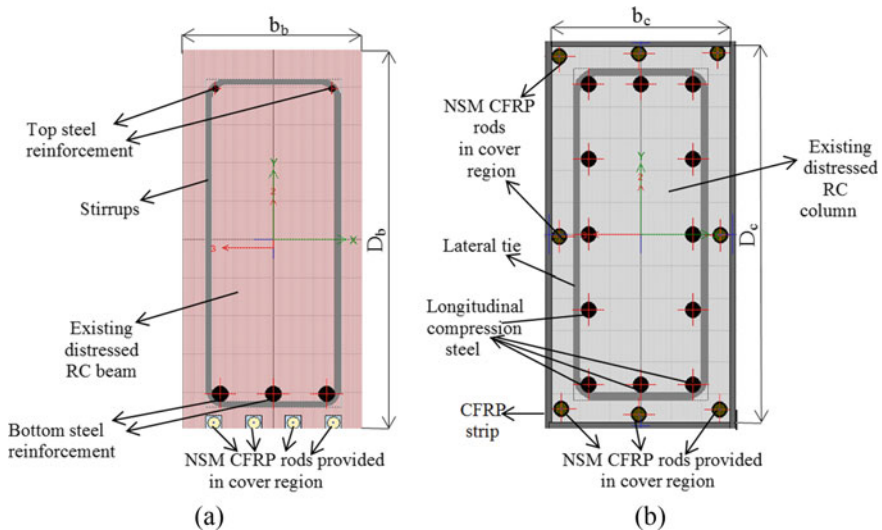
Fig. 2 Typical details of retrofitted cross-sections of **a** distressed RC beams ($b_b \times D_b$), **b** distressed RC columns ($b_c \times D_c$): that are retrofitted adopting CFRP rods as near surface mounted reinforcement
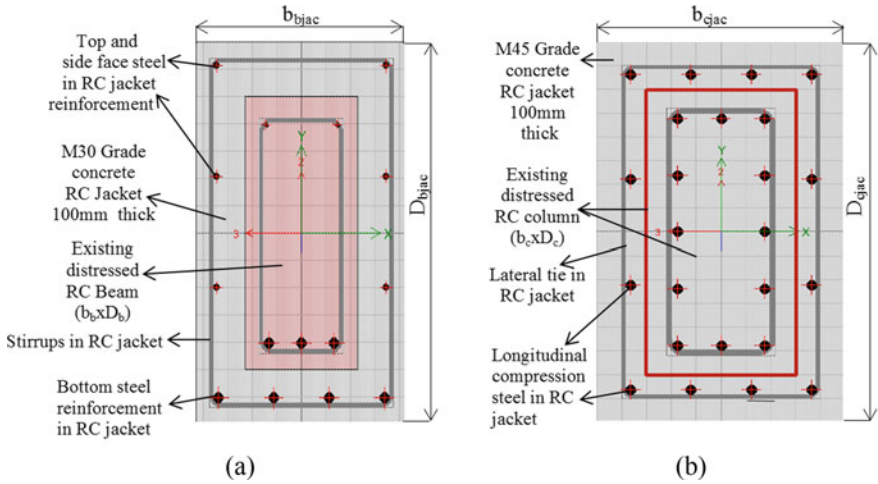
Fig. 3 Typical details of retrofitted cross-sections of **a** jacketed distressed RC beams ($b_{bjac} \times D_{bjac}$), **b** jacketed distressed RC columns ($b_{cjac} \times D_{cjac}$): that are retrofitted adopting RC jacket

the storey displacement after application of the RC jacket. Fe500 steel rebar's are provided as reinforcement in the RC jacket. The provided reinforcement in the RC jacket for beams are 8 mm diameter 2 legged stirrups, 2 numbers of 12 mm diameter rebar's on the top face, 3 numbers of 20 mm diameter rebar's at the bottom face and 12 mm diameter rebar's on the side face as shown in Fig. 3a. The reinforcement provided in the RC jacket provided for the column are 8 mm diameter lateral ties spaced at 200 mm centre to centre, 20 mm diameter rebar's on the faces of the RC jacket as shown in Fig. 3b (Note: Fig. 3a, b are typical details showing RC jacket retrofit applied for all the distressed RC beams and distressed RC columns in the structure). The application of RC jacket retrofit is adopted as a comparative study in this work.

The Loads applied on the structure considered for analysis are: floor finishes, self-weight of structural members, wall load, live load and earthquake loads. The floor finishes considered are: 0.75 kN/m^2. Wall load (brick masonry) was calculated and considered for load bearing walls (225 mm) and partition walls (115 mm) by height × thickness × unit weight of masonry. The unit weight of brick masonry [16] considered for calculation is 19.0 kN/m^3 (burnt clay bricks) [16].

Dead load (DL) = self-weight + floor finishes (as area load on slabs kN/m^2) and wall load as line load (kN/m).

Live load (LL) [17] for commercial occupancy: 4kN/m^2 (as area load applied on slabs) and roof having accessibility.

The earthquake load (EQ) that was considered in response spectrum method of analysis [13] was along X and Y directions $-$ EQ_x and EQ_y respectively. The load combinations considered for the analysis are:

(i)   1.5(DL + LL) [18],
(ii)   1.2[DL + LL ± (EL$_x$ ± 0.3EL$_y$)] [13],
(iii)   1.2[DL + LL ± (EL$_y$ ± 0.3EL$_x$)] [13],
(iv)   1.5[DL + LL ± (EL$_x$ ± 0.3EL$_y$)] [13],
(v)   1.5[DL + LL ± (EL$_y$ ± 0.3EL$_x$)] [13],
(vi)   0.9DL ± 1.5(EL$_x$ ± 0.3EL$_y$)] [13],
(vii)   0.9DL ± 1.5(EL$_y$ ± 0.3EL$_x$)] [13].

3   Results and Discussions

This section presents the results and discussions of the analysis that has been carried out on the distressed RC structure that has been subjected to earthquake loads with and without application of retrofit adopting near surface mounted reinforcement and RC jacket. The load combinations 1.2[DL + LL + (EL$_y$ − 0.3EL$_x$)] [13] and 1.5[DL + LL − (EL$_x$ − 0.3EL$_y$)] [13], are the governing or critical load combinations that was identified while carrying out the earthquake analysis, that resulted in maximum lateral storey displacements in the distressed RC structure with and without applications of retrofit adopting near surface mounted (NSM) reinforcement and RC jacket.

3.1   Results of the Distressed RC Structure Subjected to Earthquake Loads Retrofitted with Near Surface Mounted Reinforcement and RC Jacket

The lateral storey displacements in the distressed RC structure that has not been designed for earthquake resistance and has been subjected to earthquake loads without application of any form of retrofit has been shown in Fig. 4. The lateral storey displacements in the distressed RC structure that has been subjected to earthquake loads and retrofitted with near surface mounted reinforcement and RC jacket applied to beams and columns is shown in Figs. 5 and 6 respectively.

Fig. 4 Lateral storey displacements in the distressed RC structure that has been subjected to earthquake loads without application of any form of retrofit
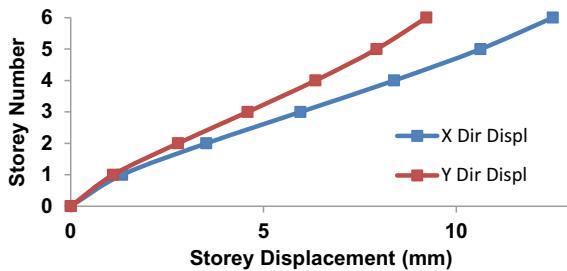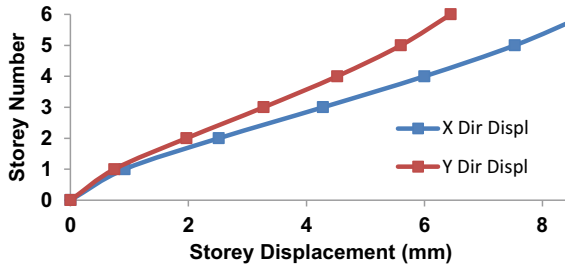
Fig. 5 Lateral storey displacements in the distressed RC structure that has been subjected to earthquake loads and retrofitted with near surface mounted reinforcement adopting CFRP rods applied to beams and columns
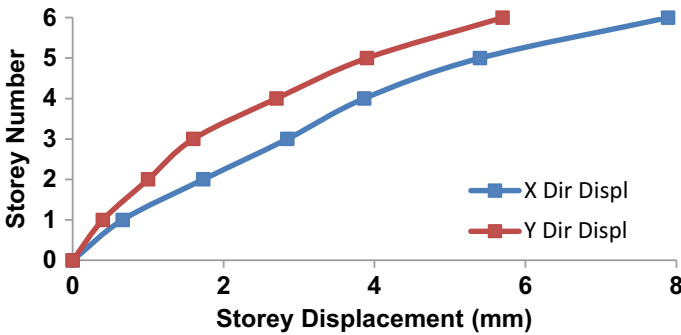
Fig. 6 Lateral storey displacements in the distressed RC structure that has been subjected to earthquake loads and retrofitted RC jacket applied to beams and columns

The variation in the maximum top storey (6 storey) lateral displacements in the distressed RC structure subjected to earthquake loads after application of retrofitting adopting near surface mounted reinforcement and RC jacketing has been tabulated in Table 1

It is observed from the results that the near surface mounted reinforcement adopting CFRP rebars has reduced the storey displacements (in reference to top

Table 1 Maximum top storey (storey 6) lateral displacements in the distressed RC structure subjected to earthquake loads after application of retrofitting adopting near surface mounted reinforcement and RC jacketing

Details of retrofit	Maximum top storey (storey 6) lateral displacement (mm)	Percentage reduction in maximum top storey (storey 6) lateral displacement (mm)
Without any retrofit	12.50	–
NSM retrofit	8.40	32.80
RC jacket retrofit	7.89	36.88

storey displacement) by 32.8%. Whereas, the reduction in the storey displacements (in reference to top storey displacement) when RC jacket retrofit is applied is observed to be 36.88%.

It can be observed from the results that, the difference in reduction in the lateral storey displacements (in reference to top storey displacement) is low (4.02%), for near surface mounted reinforcement using CFRP rebars when compared to RC jacket applied as retrofit, as the distress in structural members due to the reduced compressive strength of concrete is about 5 MPa.

Therefore, these results show that the near surface mounted reinforcement is effective as a retrofit measure applied to control or reduce the lateral displacement in a structure that is subjected to earthquake loads that has not been designed for earthquake resistance priorly.

The near surface mounted reinforcement retrofit can applied as a retrofit measure when the degree of distress in the structure is about 20–30%, as it would result in restoring the structure with lower installation and retrofit costs.

Although the RC jacket retrofit is applied when the distress in the RC structural elements is greater than about 25–30% being in the form of reduced compressive strength or less ductility in the structural elements.

When the distress/damage present in the structural elements present in the structure is less than 25–30%, near surface mounted reinforcement would be preferable from structural performance and from the point of view of economy.

As the unit cost of near surface mounted reinforcement for installation as a retrofit measure is less when compared to, the unit cost of RC jacket retrofit. The unit cost of the RC jacket retrofitting involves the cost of shuttering, bar bending, labour for applying bonding epoxy between old and new concrete along with installation of shear keys at the interface, cost for concrete materials and labour to place the concrete in the RC jacket and thereafter removal of the RC jacket shuttering. Apart from the cost the application of RC jacket retrofit takes a longer time.

4 Conclusion

- It is observed from the results that, from a stability point of the structure subjected to seismic loads, the reduction in the storey drifts (lateral storey displacements) when CFRP rods were applied as near surface mounted reinforcement is 32.8%, and when RC jacket retrofit was applied is 36.88%.
- It can be observed from the results that, the difference in reduction in the lateral storey displacements (in reference to top storey displacement) is lower by about 4.02%, for near surface mounted reinforcement using CFRP rebar's when compared to the lateral storey displacements when RC jacket is applied as retrofit.
- The results from this study indicate that, the near surface mounted reinforcement is effective to restore distressed structures that house distressed structural members (beams and columns) having distress in the range of 20–30%.

- From the point of structural performance in terms of restoring distressed structural members, the near surface mounted-reinforcement retrofit is effective, earlier to install and comparatively lesser in the overall cost of the retrofit when compared to RC jacketing, when the range of distress or damage is within 30%.

References

1. Okiemute, EG, John A (2019) Recent advances in non-destructive testing of concretes and structures: an outlook. J Civ Eng Construction Technol 10(3):20–31
2. Malek J, Kaouther M (2014) Destructive and non-destructive testing of concrete structures. Jordan J Civ Eng 8(4):432
3. Lorenzis L, Nanni A (2001) Shear strenghtening of reinforced concrete beams with near surface mounted fibre reinforced polymer rods. ACI Struct J 98(1)
4. Belal A (2015) Strengthening of corroded reinforced concrete (rc) beams with near surface mounted (NSM) technique using carbon fibre polymer (CFRP) rods; an experimental and finite element (FE) Modelling Study, Ph.D. thesis at I'institute national des sciences appliquees de Toulouse
5. Nanni A, Ludovico M (2004) Shear strengthening of a PC bridge girder with NSM CFRP rectangular bars. Adv Struct Eng 7(4):297–309
6. Catalin B, Patricia MV (2015) The retrofitting of RC columns. In: International conference knowledge based organisation 21(3), international, vol XXI, conference no 3 (2015)
7. Reddy L, Sai Akhil AVS, Shree Harsha G (2019) Retrofitting of RC beams using CFRP jacketing. Int J Recent Technol Eng 7(6C2)
8. Aravind A, Amiya KS, Singha Roy DK, Joseph VT (2013) Retrofitting of reinforced concrete beams using fibre reinforced polymer (FRP) composites. J Urban Environ Eng 7(1):164–175
9. Yao L-Z (2016) Fiber-element modelling for seismic performance of square RC bridge columns retrofitted with NSM BFRP bars and/or BFRP sheet confinement. J Compos Constr 20(4)
10. IS 15988 (2013): Seismic evaluation and strengthening of existing reinforced concrete buildings—guidelines, Bureau of Indian Standards
11. IS13311 (Part1) (1992) Non-destructive testing of concrete—methods of test part 1 ultrasonic pulse velocity. Bureau of Indian Standards
12. IS13311 (Part2) (1992) Non-destructive testing of concrete—methods of test part 2 Rebound hammer , Bureau of Indian Standards
13. IS 1893 (Part1) (2016) Criteria for earthquake resistant design of structures. Bureau of Indian Standards
14. Imad SA, Sief AO, Kamalaldin FH, Mohammed AJ (2020) Properties evaluation of fiber reinforced polymers and their constituent materials used in structures—a review, Mater Today: Proc.https://doi.org/10.1016/j.matpr.2020.07.636
15. György LB, Zsombor KS (2008) Experimental strength analysis of CFRP strips. Concr Struct, pp 61–68
16. IS 875 (Part 1): Code of practice for design loads (other than earthquake) for building and structures-dead loads-unit weights of building materials and stored materials. Bureau of Indian Standards (1987-Reaffirmed 1997)
17. IS 875 (Part 2): Code of practice for design loads (other than earthquake) for building and structures-imposed loads. Bureau of Indian Standards (1987-Reaffirmed 2008)
18. IS456, Plain and reinforced concrete—code of practice. Bureau of Indian Standards (2000-Reaffirmed 2005)

Evidence Based Approach for DRR Case Studies

Analytical Investigation of Infilled Frames with Openings Under Static Loading

M. Vishali, K. S. Satyanarayanan, and V. Thirumurugan

Abstract The structural Reinforced Concrete (RC) Frames with brick masonry infill are extensively utilized in numerous structures. The infill walls interact with the surrounding frames, absorb energy, modify the internal force distribution and contribute to the globe load resistance and increase the structural performance. Besides, openings in infill panels such as windows and doors play an essential role in infill frames and change the behavior of the panel which depends on several criteria known as size and position of the opening. In this study, five numbers of single-bay, single-story reinforced concrete frames prototype frames were analyzed under static loading. The behavior of the RC bare frame, RC infill frame and RC infill frame with different opening such as doors and windows were used for analysis. The objective of this research work is to study the behavior of the infilled frame with different openings when cement mortar interface material is used under static loading through numerical analysis. It is found that the infills with openings improve the performance of RC frames. A comparative study with infilled frames with openings under interface material and bare frame under static loading with varying parameters based on the obtained results such as displacement, stiffness, bending moment, lateral load was observed and to study the critical infill opening is also found.

Keywords Infilled frames · Finite element method · Cement mortar · Openings · Stiffness

1 Introduction

High-rise building is turning out to be more common these days. Such buildings require the specialized system to carry lateral loads such as wind and earthquake. Infilled frame is one of the most typical lateral loads resisting system. The reinforced concrete infilled frame with brick masonry is extensive, and it is utilized in various structural systems. Generally, the frames are intended for gravity loads only and the

M. Vishali (✉) · K. S. Satyanarayanan · V. Thirumurugan
Department of Civil Engineering, College of Engineering and Technology, SRM Institute of Science and Technology, SRM Nagar, Kattankulathur, Tamil Nadu 603203, India
e-mail: vm4814@srmist.edu.in
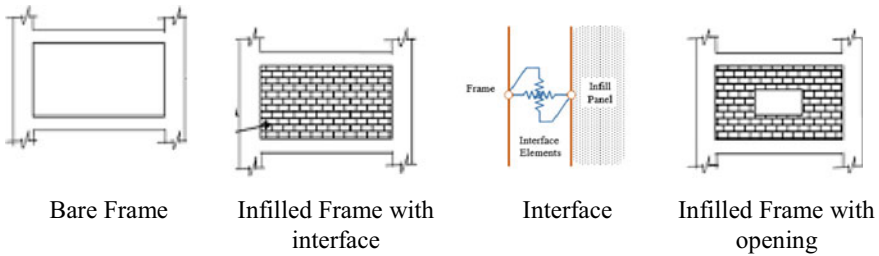
Fig. 1 Infill frames with opening

infill is expected to contribute adequately to the lateral strength of the structure. The gap between the frame and infill is where the interface material is produced which is to enhance privacy via sound insulation and also aids in thermal insulation [1], as shown in Fig. 1. Whereas, the openings in the infill such as doors and windows influence the behavior of the frames and the failure of infill with openings under the activity of lateral loads is basically due to the concentration of stresses near the openings [2].

It has been seen that even infill with openings gives significant lateral stiffness and strength to frames [3]. In order to access and to fundamentally assess the research work done on the infilled frames, infilled frames with the interface and infilled frame with openings, a detailed survey of literature have been undertaken. From the literature survey, it is evident that the infilled frame improves the strength and decreases the ductility behavior of the structure [4]. The influence of the initial gap on the infilled frame behavior was studied; such gaps are used to avoid the loads which are carrying vertical from beams to masonry [5]. The analytical study was carried out between bare frame and infilled frame and comparison study was made. Whereas, it concludes the infilled frame exhibits more lateral stiffness when compared to a Bare Frame (BF) and Infilled Frame with Cement Mortar interface (IFCM) have maximum lateral strength and stiffness of the frame [6, 7], whereas the displacement and ductility ratio decrease [8]. It has been studied from the various literature that the infill with openings provides significant lateral stiffness along with the strength of the frames [9]. The present study unfortunately doesn't have satisfactory guidance for the investigation of masonry infilled frame with openings. The analytical approach in introducing openings in infill has to be made. Linear analysis was performed in bare frame, infilled frame and infilled frame with different configurations of opening frames and then the modeled results are compared.

In this study, a two-dimensional single-bay single-story reinforced concrete infill frame with different configuration of openings (door and window) was modeled and analyzed under static lateral load. Comparative study was carried out between RC bare frame, RC infill frame and three different configurations of openings are compared and to identify the critical case among the configurations of opening.

Table 1 Description and specification of models

S. No.	Model specification	Model description
1	BF	Bare frame
2	IFCM	Infilled frame with cement mortar interface
3	Configuration-I, IFCMO1	Infilled frame with opening (door opening at left with window opening at right)
4	Configuration-II, IFCMO2	Infilled frame with opening (door opening at right with window opening at left)
5	Configuration-III, IFCMO3	Infilled frame with opening (door opening at middle with two window opening on both the sides)

2 Modeling and Analysis

2.1 Details of Models Used

In this study, the analysis was carried out for infilled frame with different positions of openings. The specifications of models were given in Table 1.

2.2 Details of Frame Model

Numerical investigation is a major part to identify critical case. Static analysis has been performed on bare frame as well as on infilled frame [10]. Here, a 2-D single-bay single-story infilled frame with opening under static lateral load was considered for analysis. The concrete elements, infill walls and interface are modeled as solid deformable elements and reinforcements are modeled as wire elements. In the FEM analysis, the structural element model was discretized according to the predefined properties of elements. The mesh convergence study was carried out and mesh size is assigned as 50×50 mm. M30 grade of concrete and Fe415 grade of steel was used as reinforcements, whereas the cross-sectional and reinforcement details of the frame are listed in Tables 2 and 3.

Table 2 Dimensions of the frame and members

Descriptions	Dimensions (mm)
Story height	3500 C/C
Bay width	3000 C/C
Beam	300×300
Column	400×300
Interface thickness	10

Table 3 Reinforcement details of the members

Elements	Main reinforcements	Shear reinforcements
Beams	4 nos of 12 mm dia	8 mm dia @ 200 mm spacing
Columns	4 nos of 16 mm dia	8 mm dia @ 200 mm spacing

2.3   Modeling of Frame

A lateral load of 10 kN is converted as pressure applied over topmost left beam-column joint. The support condition for frame is assigned as pinned. The infill frame was modeled next and discretization is performed in the FEM software package by meshing. In infilled frame, the conventional cement mortar was used as interface which is designated as IFCM is considered. The thickness of the interface was taken as 10 mm throughout the analysis (Figs. 2 and 3).

Fig. 2 Bare frame (BF)
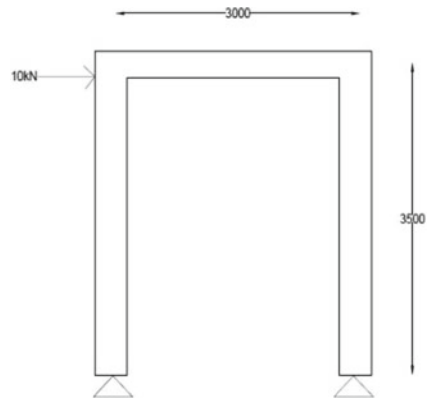
Fig. 3 Infilled frame with cement mortar (IFCM)
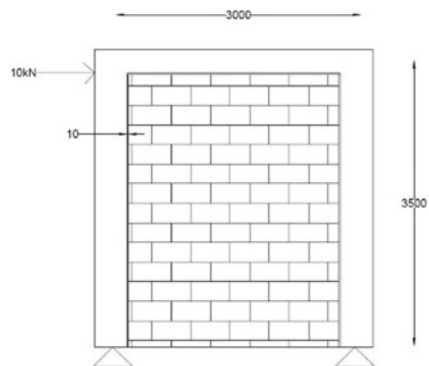
Fig. 4 Configuration-I,
IFCMO1
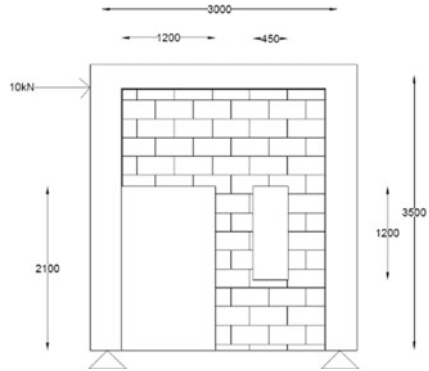
Considering under the design manual on doors and window details in building code [11], the configuration-I designated as IFCMO1 which is of door opening at left side and window opening at right side in the infill (Fig. 4). The dimension of the door opening and window opening are under the reference of National Building Code book [12]. The dimension of door is 1200 × 2100 mm and the window of 450 × 1200 mm along with sill height of 900 mm which is same in the case of configuration-II designated as IFCMO2, where door opening is at the right side and window opening at left side shown in Fig. 5. Whereas in configuration -III which is designated as IFCMO3 has the door opening at the center and two window openings on both the sides. The dimension of the window opening is unaltered, but the depth and width of the door are 900 × 2100 mm (Fig. 6).

Fig. 5 Configuration-II,
IFCMO2
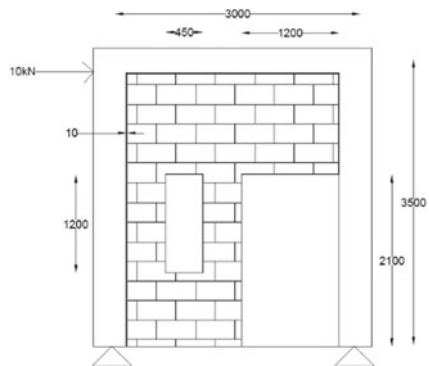
Fig. 6 Configuration-III, IFCMO3
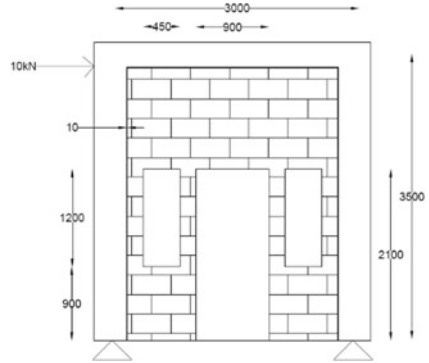
3 Comparison of Results

After performing the analysis on five frame configurations, the results such as lateral displacement, lateral stiffness and lateral load were observed. The bending moment near the beam-column joint is noted.

3.1 Lateral Displacement

The comparison for lateral displacement is carried for all the frame configuration which is shown in Fig. 7. While comparing the all-frame configurations, the maximum lateral displacement occurs in BF. The displacement of BF appears to be 0.65 mm which is 96% higher than the IFCM. In Infilled frame with different
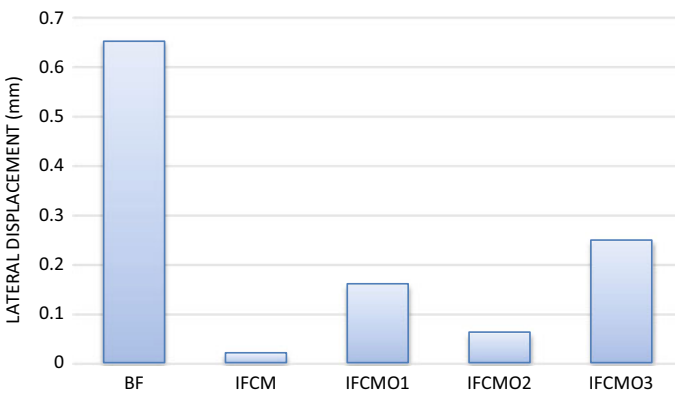
Fig. 7 Comparison of lateral displacement

Table 4 Stiffness comparison

Types of frames	Stiffness (kN/mm)
BF	15
IFCM	500
IFCMO1	62
IFCMO2	161
IFCMO3	40

configurations of opening, the maximum displacement appears in IFCMO3 which is of 35% and 75% more when compared to IFCMO1 and IFCMO2, respectively.

3.2 Stiffness

Stiffness is calculated based on the lateral load and lateral displacement. The calculated stiffness was shown in Table 4. The maximum stiffness occurred in IFCM of 500 kN/mm and the minimum stiffness develops in BF of 15 kN/mm. When compared with the three different configurations of openings in infill the IFCMO3 has minimum stiffness of 40 kN/mm which is 35% and 75% lesser when compared to other two configurations that is IFCMO1 and IFCMO3, respectively.

From the results of Stiffness for three different frame configurations IFCMO1, IFCMO2 and IFCMO3, it was found that the frame configuration IFCMO2 has more stiffness than other two configurations. The reason behind this was the door opening which is located on the right side of the frame and lateral load is applied from the left corner. So, an optimum amount of infill wall reign is located on the left side of the frame which can resist the lateral load applied from the left side of the frame.

3.3 Lateral Load

For the lateral load calculation, the force from the support reaction was considered. While comparing the different frame configurations, the maximum lateral load of 4.49 kN was occurred in BF. The BF attracts more lateral load than IFCM due to the presence of infill wall. The infill acts as an energy dissipating element and absorbs the applied lateral load and behaves as a rigid structure. The absence of infill wall allows the structure to take more lateral load and undergoes more lateral displacement.

On the other hand, while comparing configurations of opening in infill wall, the IFCMO3 consumes more lateral load as the infill wall opening area was more than other two configurations. IFCMO3 has the maximum lateral load when compared with all five frames and which is almost two times greater than bare frame (Fig. 8).
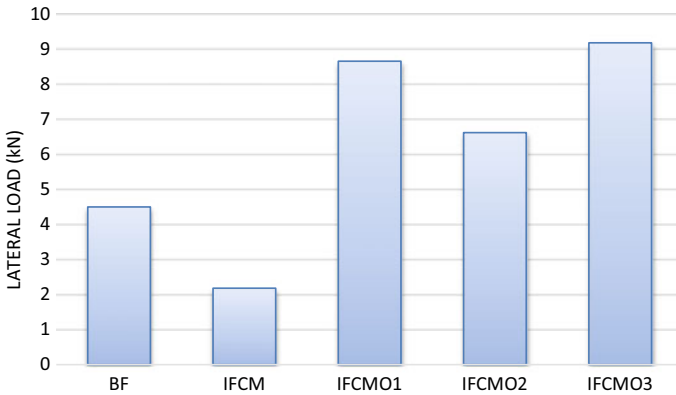
Fig. 8 Lateral load comparison

3.4 Bending Moment

Bending moment of the frame was absorbed near the beam-column joint and the results are compared between different frame configurations. The BF seems to exhibit more moment when compared with IFCM. The bending moment for BF seems to be higher when compared to other frames due to the absence of infill wall. When the size of the opening increases in the infill wall, the frames behave like bare frame. The infill wall act has an additional restrain and provides more rigidity to the IF than BF. The bending moment for BF is 0.8 kN/m, which is 85% more than IFCM. The comparison between bending moment was shown in Fig. 9.

While comparing the bending moment results of three different configurations of opening, it was found that the IFCMO3 has more moment than the other two frame configuration, which is 10% and 56% more when compared to IFCMO1 and
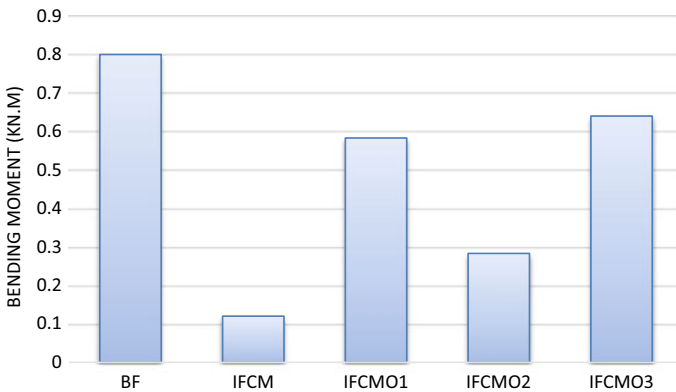
Fig. 9 Bending moment comparison

IFCMO2, respectively. The bending moment for the three different frame configurations was quite higher than infill frame. The presence of openings in the infill wall will lose some rigidity against the lateral load. The IFCMO3 has more opening reign in the infill wall than the other two configuration and this let to increase the moment. The bending moment for BF is 20% more when compared to IFCMO3.

4 Conclusion

A single-bay single-story reinforced concrete bare frame, infilled frame with cement mortar and reinforced concrete infilled frame with different configurations of opening are modeled and analyzed using FEM-based software. From the above comparison of results for five frames, it can be concluded that:

1. The bare frame is more critical as it takes more lateral load and results in greater lateral displacement and exhibits less amount of stiffness then the other frames.
2. In the case of frame with infill wall opening, the configuration-III is found to be critical as it consumes more opening reign and results in higher lateral displacement and lesser stiffness compared with other two configurations of openings.
3. When the stiffness is compared with infill with opening, the configuration-I and configuration-II was found to be 35% and 75% higher than the critical frame, respectively
4. The bare frame exhibits more bending moment when compare with infill frame which is 7 times higher than the infilled frame. Whereas, in case of infill frame with opening the configuration-III have more bending moment when compared with other two configurations.
5. The presents of infill wall in the frame structure performance well enough in terms of lateral stiffness better structural performance and prevents the frame structure from the collapse.

So, to improve the structure performance against lateral loads like wind and seismic forces, reinforced concrete structures should have lateral rigidity to resist them. The inclusion of infill wall in high-rise buildings can perform well against wind and seismic forces. But provision of unnecessary openings in buildings for aesthetical purpose can result in reduction in their structural performance.

References

1. Teguh M (2017) Experimental evaluation of masonry infill walls of RC frame buildings subjected to cyclic loads. Procedia Eng 171:191–200. https://doi.org/10.1016/j.proeng.2017.01.326
2. Sukrawa M, Budiwati IAM (2019) Analysis and design methods for infilled frames with confined openings. Int J Technol 10(2):394–404. https://doi.org/10.14716/ijtech.v10i2.2467

3. Penava D, Sarhosis V, Kožar I, Guljaš I (2018) Contribution of RC columns and masonry wall to the shear resistance of masonry infilled RC frames containing different in size window and door openings. Eng Struct 172(June):105–130. https://doi.org/10.1016/j.engstruct.2018.06.007

4. Jiang H, Liu X, Mao J (2015) Full-scale experimental study on masonry infilled RC moment-resisting frames under cyclic loads. Eng Struct 91:70–84. https://doi.org/10.1016/j.engstruct.2015.02.008

5. Hammoudah SMW, Chaudhary MTA, Essawy AS (2018) Experimental investigation of interface stiffness between concrete masonry infill and reinforced concrete frames. Eng Struct 171(June):779–793. https://doi.org/10.1016/j.engstruct.2018.06.035

6. Muthu Kumar S, Satyanarayanan KS (2018) Study the effect of elastic materials as interface medium used in infilled frames. Mater Today Proc 5(2):8986–8995 https://doi.org/10.1016/j.matpr.2017.12.343

7. Thirumurugan V, Anjali S, Muthu Kumar S, Satyanarayanan KS, Ganesan TP (2016) Parametric study on behaviour of seven storey single bay infilled frame with pneumatic interface. Indian J Sci Technol, 9(23). https://doi.org/10.17485/ijst/2016/v9i23/95969

8. J. J. W. and K. S. S. S. Muthu Kumar, Analytical study on nonlinear performance of Rc two bay three storey frames with infill, Asian J Civ Eng, 18(January):133–149

9. Asteris PG (2012) Modeling of infilled frames with openings. Open Constr Build Technol J 6(1):81–91. https://doi.org/10.2174/1874836801206010081

10. Waghide A, Bhardwaj A, Gupta SC Rev Behav Infilled Walls, pp 134–140

11. "doors_windows_manual.pdf."

12. Kisan M, Sangathan S, Nehru J, Pitroda SG (2005) SP 7 (2005)_ National Building Code Of India 2005(GROUP 1 TO 5).pdf. 2005

Behaviour of Doubly Symmetric Built-Up Cold-Formed Steel Beams

P. Gajalakshmi [ID]**, J. Revathy** [ID]**, S. Anusha, and D. S. Vijayan** [ID]

Abstract This article presents the study on the behaviour of doubly built-up cold-formed beams under flexure. The built-up sections are made by connecting two channel sections back to back which are attached by welding. A series of experiment tests were carried out on beam specimens having with lip and without lip sections, each with 200 mm depth and 240 mm depth respectively. The adopted thickness of beam section is 1.6 mm and 2 mm. The parameters involved in this study are effective width to thickness ratio and sections with and without lip. All the beams failed at local buckling at top flange due to lateral instability of the cold-formed steel structural members and then followed by lateral torsional buckling. The theoretical calculations are made as per IS: 801-1975 code, which is based on the working stress method. The analytical investigation of the built-up section is also carried out using FEM modelling software. All the specimens indicate nearly closer values to each other in theoretical, analytical and experimental study. From this study, it is concluded that doubly symmetric built-up cold-formed sections are preferred for higher load carrying capacity with less complicated buckling modes.

Keywords Cold-formed steel beams · Built-up sections · Doubly symmetric · Local buckling · Torsional buckling

1 Introduction

Cold-formed structural steel members are widely used in transmission towers, bridges, roof trusses and multi-storeyed buildings, etc., because of its high strength to weight ratio, resulting in the reduction of dead weight. Structural steel has become the best alternative for concrete in present days.

P. Gajalakshmi (✉) · J. Revathy · S. Anusha
Department of Civil Engineering, B. S. Abdur Rahman Crescent Institute of Science and Technology, Chennai, Tamil Nadu, India
e-mail: gajalakshmi@crescent.education

D. S. Vijayan
Department of Civil Engineering, Aarupadai Veedu Institute of Technology, Chennai, Tamil Nadu, India

The cold-formed single and built-up sections have been developed and revised over past decades however as yet, few studies have been conducted in the area of built-up sections, in which more complexity exists in terms of the shear-induced relative deformations between the combined components. Various research papers are still under progress to know the exact behaviour of doubly symmetric built-up cold-formed sections. Cold-formed latticed built-up section under flexure with lipped angle by providing various types of stiffeners like L, Channel and Tee sections examined by Anbarasu and Sukumar [1] and Reza and Senthil Selvan [2]. Karthikeyan and Jaisankar [3] studied the buckling strength of cold-formed steel built-up beam. Mohammad [4] evaluated the flexural behaviour of stiffened modified cold-formed steel sections. Wang and Young [5] conducted an experimental investigation of simply supported built-up section beams with different sectional configurations. Basaglia and Camotim [6] investigated the buckling, post buckling, strength and design of cold-formed steel continuous lipped channel beam. From the literature review, cold-formed steel sections are usually slender and not doubly symmetric and hence susceptible to a range of complicated buckling modes and their interactions. To overcome these problems doubly symmetric built-up cold-formed sections are preferred for higher load carrying capacity with less complicated buckling modes. Hence in this study an attempt is made to analyse the behaviour of cold-formed steel doubly symmetric sections.

1.1 Objectives of the Study

The objectives of this study are

1. To investigate the flexural behaviour of doubly symmetric built-up cold form steel beams with and without lip.
2. To assess the load carrying capacity and deflection of built-up cold form sections.
3. To examine various modes of buckling occur in a cold-formed steel members when subjected to flexural loading.

2 Theoretical Study

Cold-formed steel built-up section dimensions are fabricated and assembled through welding to a span of 1000 mm and one end is considered as hinged and other end is free. The end plates and load bearing plates are fabricated using cold-formed steel. The parameters involved in this study are effective width to thickness ratio and sections with and without lip. With reference to the direct strength method as per IS 801: 1975 [7], the dimensions of the specimens are chosen and calculated various parameters as shown in Table 1.

Table 1 Theoretical results

Specimen and label	Sectional properties	Effective width to thickness ratio (w/t)	Bending moment	Load carrying capacity (kN)	Deflection (mm)
S1	Depth = 24 cm Moment of inertia: 1432 cm^4 Width = 9 cm Thickness t = 0.2 cm Section modulus = 119.34 cm^3 Area A = 98.548 cm^2 Yield stress = 2400 kg/cm^2	42	656	19.29	2.3
S2	Depth = 24 cm Width = 9 cm Thickness = 0.2 cm Area = 65.382 cm^2 Moment of inertia = 943.84 cm^4 Section modulus = 63.24 cm^3 Yield stress = 2400 kg/cm^2	42	1086	42.335	0.51
S3	Depth = 20 cm Width = 7 cm Thickness = 0.16 cm Area = 65.382 cm^2 Moment of inertia = 632 cm^4 Section modulus = 63.24 cm^3 Yield stress = 2400 kg/cm^2	40.56	366	10.769	2.84

(continued)

Table 1 (continued)

Specimen and label	Sectional properties	Effective width to thickness ratio (w/t)	Bending moment	Load carrying capacity (kN)	Deflection (mm)
S4	Depth = 20 cm Width = 7 cm Thickness = 0.16 cm Area = 65.382 cm² Moment of inertia = 385 cm⁴ Yield stress = 2400 kg/cm² Lip = 2.5 cm	40.56	547	21.89 kN	0.58

From the theoretical study, the section S2 has more load carrying capacity with 74.56% when compared to all other specimens and also the specimen S2 has very less deflection when compared to all other specimens.

3   Analytical Study

Finite element modelling technique (ANSYS workbench 15.0) [8] is used to study the behaviour of doubly symmetric built-up cold-formed sections. Finite element (FE) analysis in structure is normally used to find the structural behaviour by considering the loading conditions applied on it. Static Analysis is used to model the sections, meshing of the sections into finite elements, solving and reviewing results. The FE model was developed and thin–walled structures are sensitive to initial geometric imperfections, especially at the ultimate load level. In this study, first eigenvalue bucking analysis was performed on the model with no initial perfections to establish the probable collapse mode using ANSYS. For modelling steel, tension coupon tests were conducted by using specimens as shown in Fig. 1a, b and properties of steel are tabulated in Table 2.

Loads are applied on the specimen at L/3 of the specimen to find the ultimate load. And readings are taken by clicking at any point of the specimen and the buckling is noted and also the maximum deflection at specific point is also noted. Figure 2a–d shows the buckling of the cold-formed built-up sections is found to be local buckling of the compression flange at the L/3 location and then followed by lateral torsional buckling. Table 3 shows the ultimate load and deflection of built-up cold-formed sections.

From this analytical study it is clearly observed that that all the specimens have local buckling at the l/3 location and also followed by lateral torsional buckling as
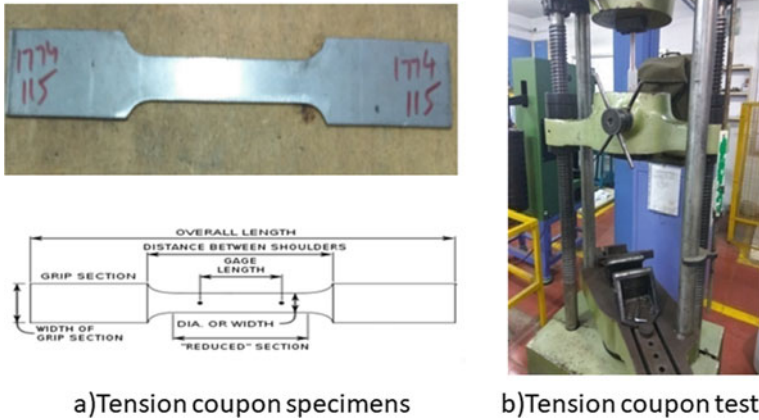
Fig. 1 Tension coupon specimens and test

Table 2 Properties of steel

Yield stress	235 MPa
Ultimate stress	330 MPa
Elongation	36.250%
Yield stress	235 MPa
Ultimate stress	330 Mpa
Breaking load	13,500 N

shown in Fig. 2. In the analytical study, specimen S2 has more load carrying capacity with a 72.72% when compared to all other specimens and also the specimen S2 has very less deflection with a 41.89% when compared to all other specimens.

Finally it is observed from analytical study, the depth of the member increases with decrease in deflection and also the lip section has less deflection when compared to the specimens without lip section.

4 Experimental Study

Experimental study was carried out by conducting flexural test on the cold-formed built-up sections with lip and without lip sections by varying w/t ratios and also the specimen are provided with end bearing stiffeners and one load bearing stiffeners at the mid span.

a) Buckling of S1

b) Buckling of S2

c) Buckling of S3

d) Buckling of S4
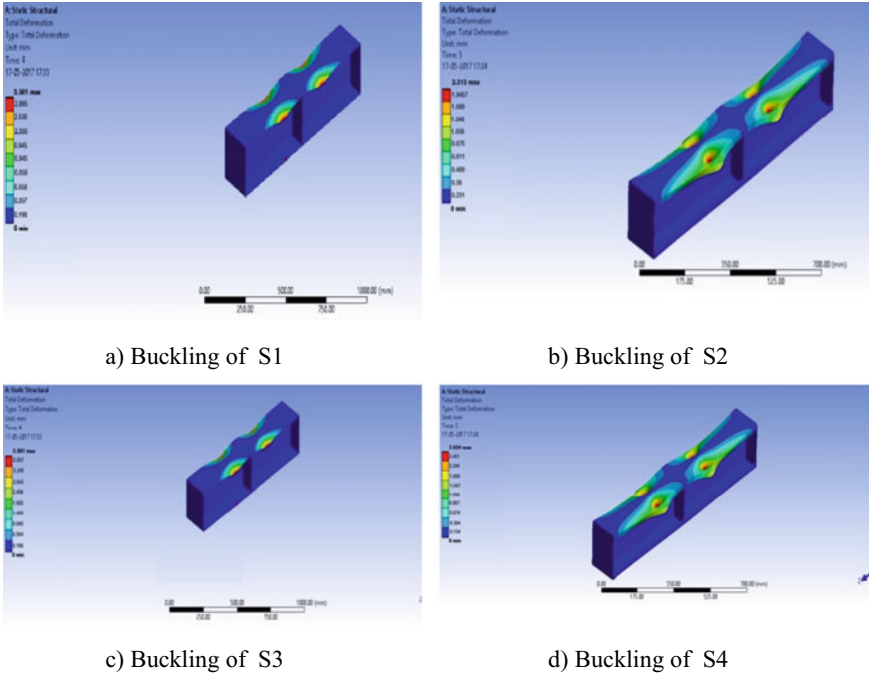
Fig. 2 Buckling modes of specimens from analytical study

Table 3 Results of analytical study

Specimens	Maximum load (kN)	Maximum deflection (mm)
S1	22	3.561
S2	44	2.313
S3	12	3.981
S4	24	2.634

4.1 Experimental Test Setup

All sections are connected back to back through welded connection. The specimen was tested in loading frame of 1000 kN capacity as shown in Fig. 3. Beam is simply supported at both ends two-point loading is placed with L/3 condition at both ends. Deflectometers are provided to find the deflections for each specimens. All the data will be collected by using Data Acquisition System. The end stiffener and one load bearing stiffener is attached to the specimen for grip and prevent twisting of specimen.

Fig. 3 Experimental setup

4.2 Modes of Failure

By varying w/t ratio and depth in the beam, the specimen was loaded gradually up to the failure of the beam and the beam is finally failed between 11 and 46 kN. The specimen having lip has more load carrying capacity when compared to the specimen without lip. The major failure expected in the built-up cold form sections is the connection failure between two channels but it does not happen because of spot welding at the regular intervals between the web and flanges. The indication of failure is only due to the buckling of specimen. All the specimens were failed due to local buckling at the compression flanges and then followed by lateral torsional buckling.

4.3 Experimental Test Results

Table 4 shows the maximum load carrying capacity and deflection of built-up cold-formed sections. In the experimental study, the section S2 has more load carrying capacity with 66.88% when compared to all other specimens and also the specimen S2 has very less deflection with 27.82% when compared to all other specimens.

Table 4 Experimental test results

Specimens	Maximum load (kN)	Maximum deflection (mm)
S1	23	2.96
S2	45	2.62
S3	15	3.26
S4	26	2.83

5 Interpretation of Theoretical, Analytical and Experiment Results

The load carrying capacity of all the specimens obtained from analytical, theoretical and experimental study were compared and is shown in Figs. 4 and 5.

From theoretical, analytical and experimental study, it is concluded that the specimen S2 has more load carrying capacity when compared to all other specimens. All the specimens indicates nearly closer values to each other in theoretical, analytical
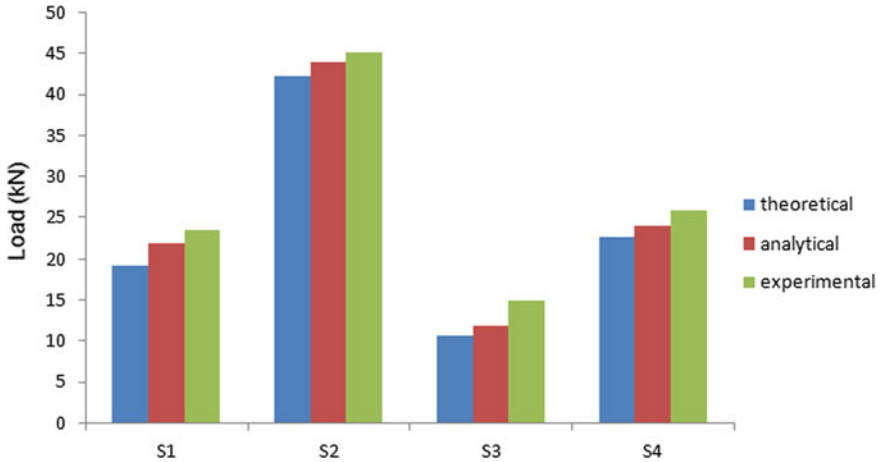
Fig. 4 Comparison of load carrying capacity
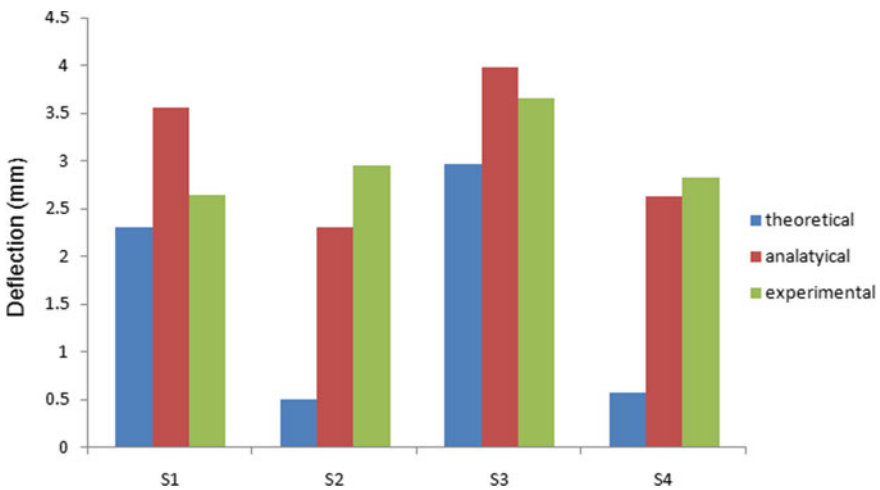
Fig. 5 Comparison of deflection

and experimental study. In this study, specimen S2 has more load carrying capacity of 74.56% when compared to all other specimens and also the specimen S2 has very less deflection of 41.89% when compared to all other specimens as shown in Figs. 3 and 4. By increasing depth, flange width and thickness of the section, load carrying capacity and moment of inertia is also increased.

6 Conclusion

This study analysed the behaviour of doubly symmetric built-up cold-formed steel section under flexure. Theoretical study is carried out as per IS 801-1975. Analytical investigation is done by using ANSYS Workbench15. Experimental study is carried out by testing the specimens in loading frame where deflection and strain values are obtained from deflectometers. The following conclusions are made from this study.

- Load carrying capacity and moment of inertia can be increased, by increasing depth of section, flange width and thickness.
- As the specimen are built-up sections and joint failure between the top flange and bottom flange with the vertical web is prevented because of the spot welding at regular intervals between the flange and web plates provides efficient joint between the assembled plates.
- In the theoretical study, specimen S2 has more load carrying capacity with a 74.56% when compared to all other specimens and also the specimen S2 has very less deflection when compared to all other specimens.
- In the analytical study, specimen S2 has more load carrying capacity with a 72.72% when compared to all other specimens and also the specimen S2 has very less deflection with a 41.89% when compared to all other specimens.
- In the experimental study, specimen S2 has more load carrying capacity with a 66.88% when compared to all other specimens and also the specimen S2 has very less deflection with a 27.82% when compared to all other specimens.
- The lip sections exhibited higher load carrying capacity compared with without lip sections.
- All the specimens fails at local buckling at the L/ 3 location of top compression flange and also leads to lateral torsional buckling.
- Generally, lip sections increased 50% load carrying capacity when compared with without lip sections.
- Doubly symmetric built-up cold-formed sections are preferred for higher load carrying capacity with less complicated buckling modes.

References

1. Anbarasu M, Sukumar S (2014) Local/distortional/global buckling mode interaction on thin walled lipped channel. Latin Am J Solids Struct 11(8):1363–1375
2. Reza W, Senthil Selvan S. (2016) Experimental study on flexural behavior of cold formed steel channel and I sections providing angle stiffener on the web. Indian J Sci Technol 9(35):114–121
3. Karthikeyan KA, Jaisankar G (2016) Numerical and experimental investigation of buckling strength of cold formed steel built-up beams. Int J Eng Sci Comput 6(5):240–248
4. Mohammad S, Dar AR (2015) Flexural behavior of stiffened modified cold-formed steel sections-experimental study. Int J Civ Eng Technol 6(9):109–115
5. Wang L, Young B (2016) Behavior of cold-formed steel built-up sections with intermediate stiffeners under bending. J Struct Eng 142(3):110–124
6. Basaglia C, Camotim D (2013) Buckling, post buckling, strength and DSM design of cold-formed steel continuous lipped channel beams. J Struct Eng ASCE 132(4):515–524
7. IS 801-1975 (2010) Indian Standard Code of Practice for Use of Cold-formed Light Gauge Steel Structural Members in General Building Construction. Bureau of Indian Standards, New Delhi
8. "Ansys Software" (2017) Associated Press, California, May 16. Retrieved June 10 (2017)

Behavior of Ordinary Load-Bearing Masonry Structure Under Distant Large Explosion, Beirut Scenario

Qurat ul Ain , **Mehtab Alam** , **and S. M. Anas**

Abstract Recent explosion of the stored ammonium nitrate at Beirut port was of devastating nature caused serious damage to the structures to the extent of the collapse of even single-story dwelling houses. This disastrous explosion led to a large number of deaths (≈ 200) in addition to grievous injuries, and many more. To replicate the effect of devastating explosion on ordinary unreinforced masonry load-bearing residential structure, single-story finite element (FE) dwelling unit model, with the conventional reinforced concrete slab with M20 concrete and Fe500 steel designed to carry the gravity loads, have been developed using the ABAQUS/Explicit program. With the objective to correlate the damage that occurred to similar structures in Beirut, the model is subjected to an explosive load of 2750 tons of Ammonium Nitrate (≈ 2300 tons of TNT) at standoff distances of 300 and 500 m. The effect of the air-blast pressure has been studied on the load-bearing masonry wall and the supported singly RCC slab of the model under the considered high explosive charge. Concrete-damaged plasticity (CDP) model for concrete and brick masonry available in employed software has been utilized. Damage has been simulated to evaluate the damage dissipation energy and geometric damage parameters of cracks such as average spacing of cracks and their average depth. Macro-modeling has been considered to model the masonry wall and the slab. Stresses have been found out and are compared with those available in the *Indian Standard Code of Practice for Structural Use of Unreinforced Masonry,* IS 1905: 1987. This research work provides insight into damage to ordinary dwelling structures subjected to explosions produced by a high explosive charge.

Keywords Beirut explosion · Explosive-induced disaster; brick masonry · RC slab · Air-blast · Concrete-damaged plasticity (CDP) model · Cracks · Stresses

Q. ul Ain (✉) · M. Alam · S. M. Anas
Department of Civil Engineering, Faculty of Engineering and Technology, Jamia Millia Islamia, New Delhi, Delhi 110025, India

M. Alam
e-mail: malam1@jmi.ac.in

1 Introduction

The accidental detonation of ammonium nitrate at Beirut port on 4th August 2020 is one of the most dreadful non-nuclear explosions in history. Experts declared it to be one-twentieth of the size of the atomic bomb dropped in Hiroshima (Japan) [1]. The shock waves of the Beirut explosion were equivalent to a 3.50 Richter magnitude earthquake as recorded by 16 seismic stations in the vicinity of the port. According to the International Monitoring System (IMS) of the Comprehensive Nuclear-Test-Ban Treaty (CTBT), the signals related to shock waves were received 9000 km away from the port [2]. The explosion was so devastating that significant damage to the buildings (about 13,000 buildings) was reported within a 4 km radius from the explosion site [1]. Allegedly illicit and unsafe storage of the 2750 tons of ammonium nitrate (equivalent to 2300 tons of TNT) in warehouses caused the explosion which led to the 6000 plus casualties and death of about 200 people [3]. Beirut Government Officials confirmed as many as 300,000 people had been made temporarily homeless and that collective losses might reach $10–15 bn [3]. The intensity of the blast was so immense that the masonry walls were smashed to the ground and glass panes shattered up to 2 km from the explosion site. In the past, Ammonium nitrate disasters (total of 37 since 1916) and other such blast inducing disasters had created havoc to the human lives and nearby building structures [4]. Considering such impulsive loading due to explosion (manmade and natural both) on the structures for which they are not designed there is now ever-increasing urgency of exclusive and dedicated research on the behavior of the structures, especially masonry buildings, that are prone to such extreme loading. This paper aims to replicate the damage caused by the recent Beirut explosion to the unreinforced load-bearing masonry buildings.

Dynamic response of the unreinforced load-bearing structures subjected to the air-blast loading has been examined experimentally and through numerical simulations by a number of researchers (Rose et al. [5]; Luccioni et al. [6]; Wu and Hao [7]; Wu et al. [8]; Wei and Stewart [9]; Ahmad et al. [10]; Pereira et al. [11]; Zapata and Weggel [12]; Li et al. [13]; Chácara et al. [14]; Anas et al. [15]). Rose et al. [5] experimentally observed the effect of blast walls in the protection of structures. The results showed that there was a significant decrease in blast pressure (about 30–60%) and impulse (about 70%) in the presence of the blast wall. Wu and Hao [7] performed the numerical simulation of simultaneous ground shock and air-blast pressure on nearby structures of the surface explosion in AUTODYN 2D software. Luccioni et al. [6] performed the analytical analysis of the AMIA (Israel Mutual Society of Argentina) building which collapsed by the terrorist attack in 1994 using the AUTODYN software. The results of the analysis very much matched with those observed from the collapsed actual building. Wu et al. [8] conducted a set of experiments on eight slabs, of which four were constructed with the NSC, two were strengthened with externally bonded carbon fiber strips, and two were cast with the UHPC, one with reinforcement and another without reinforcement. The results inferred that the reinforced-UHPC slab had the highest capacity of bearing the blast loading followed by the plain-UHPC slab which showed better performance than the strengthened slab with carbon fiber

strips. The normal concrete slab showed the least resistance against blast loading. Wei and Stewart [9] performed the numerical simulation to investigate the effects of material strengths, boundary conditions, and wall thickness on the damage and response of unreinforced brick masonry walls exposed to blast loading on the explicit finite element using LS-DYNA software. Goel and Matsagar [16] assessed the response of the structures under blast loading mainly by deflection criteria. Emphasis was laid on the distribution of mass, ductility ratio, and support rotation for the blast-resistant design of structures. The authors discussed briefly the design of the blast-resistant protection wall under blast mitigation strategy. Ahmad et al. [10] conducted experiments on brick masonry walls exposed to varying blast load at different scaled distances. The parameters to be measured are pressure–time history, acceleration time history, and strain at a specific location, which were compared with ConWep and past research. Pereira et al. [11] carried out experiments to investigate the response of the masonry infill wall subjected to the blast loading using the underwater blast wave generators. The numerical model of the wall was designed in the ABAQUS software taking the experimental data with varying properties like elastic modulus, the thickness of the wall, reinforcement, compressive and tensile strengths of infill. On investigating the results of the experiment, it has been inferred that increasing the elastic modulus of masonry and wall thickness proved to increase the blast resistance of the wall to a considerable level. Whereas, other parameters didn't reflect any measurable difference in improving the blast resistance of the wall. Zapata and Weggel [12] at the University of North Carolina tested a two-story unreinforced brick load-bearing building which was scheduled to be demolished. The deflection criteria indicated that the infill wall was near collapse and could not take any further, whereas the load-bearing walls were still able to bear additional load without getting collapsed. The other criteria being the flexural resistance criteria which determined the out-of-plane resistance of the walls acknowledged that the walls attained nearly 80% of their collapse state. Li et al. [13] conducted similar tests as Wu et al. [8] and determined the behavior of the slab under the TNT explosion. The cases for the study were seven slabs, out of which two were cast with the normal strength concrete and five were constructed with the ultra-high-performance concrete (UHPC) with variations in reinforcing ratio, slab thickness, and charge weight. It was reported that the UHPC slab had a much higher blast resistance capacity than the NRC slab and the slab with higher depth also increased the blast resistance of the slabs, whereas the higher reinforcement ratio reduced the damage but its effect was not significant. Anas et al. [15] examined the performance of the masonry heritage building under air-blast pressure without and with ground shock using the ABAQUS/Explicit. On investigating the results of the analysis, it has been established that upon applying air-blast pressure only maximum compressive stress in the central dome, masonry columns, minarets, and piers of the central hall were found to be within permissible limits as given in IS 1905:1987 [17], whereas the tensile stresses were exceeding limits. Upon the application of ground shock and blast pressure simultaneously compressive stress increased by about 133% in masonry columns and by 11% in the minaret, whereas tensile stress rose by 33%, 33%, and 8% in the central dome, piers of the central

prayer hall, and masonry columns of side halls respectively. Shear stresses at many locations were found higher than that given in IS 1905:1987 in both cases.

The aforementioned literature shows that most of the studies were focused on studying the blast response of unreinforced masonry buildings subjected to charge of low magnitude with a close-range of standoff distance. Deflection and stresses were investigated and evaluated. However, no research has been focused to study the effect of high explosive charge on the response of ordinary load-bearing masonry buildings, such as occurred in Beirut. In this study, the air-blast response of the single-story finite element (FE) dwelling unit model, with the conventional reinforced concrete slab with M20 concrete and Fe500 steel designed to carry the gravity loads, has been investigated using ABAQUS/CAE software.

2 Numerical Modeling

In the present work, a high-fidelity program, ABAQUS/CAE 2017 has been used for the finite element simulations of the considered load-bearing structure, consisting of 230 mm thick load-bearing brick unreinforced masonry (URM) walls and a singly reinforced concrete slab. To make the model of the dwelling unit practical, an opening of size 1000 mm width and 2400 mm height to have a form of the door has been provided in the front wall of the FE model (Fig. 1a). The dimensions of the dwelling unit considered are 4000 mm × 4000 mm × 3500 mm (Fig. 1c). FE model has been developed and subjected to the high explosive load of 2300 tons of the TNT at standoff distances of 300 m and 500 m. The effect of the air-blast pressure on the blast response of the developed FE model has been investigated. There are three types of techniques used for modeling of the masonry walls based on the extent of accuracy: (1) Macro-modeling, where masonry units (brick/blocks), mortar joints, and the mortar-unit interface, all are considered as a homogenous continuum; (2) Simplified micro-modeling, where masonry units are modeled by continuum elements,
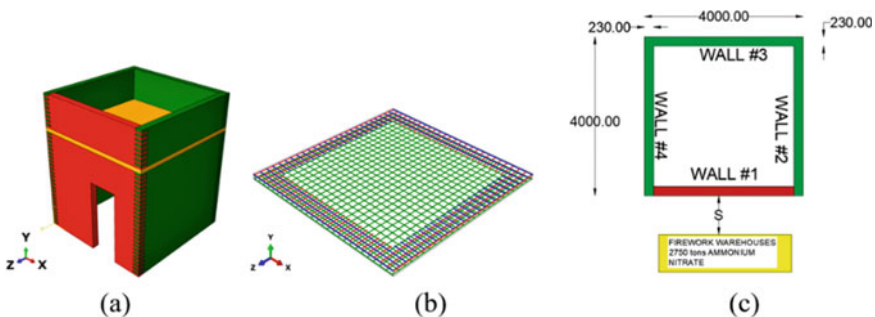
Fig. 1 FE model of the considered load-bearing structure (**a**), rendered view of slab reinforcement (**b**), and dimensions of the dwelling unit and location of explosive (**c**)

and mortar in the joints and unit-mortar interface are represented by dis-continuum elements using contact interaction models available in ABAQUS; (3) Detailed micro-modeling, where the units and mortar in the joints are represented by continuum elements and unit-mortar interface by dis-continuum elements described by contact models [11]. To optimize the computational time, the walls have been modeled using the macro-modeling strategy in the current study.

The masonry walls are discretized with 8-node linear brick explicit solid elements (C3D8R) with reduced integration and hourglass control (ABAQUS User Assistance Guide 2017) with a mesh size of 46 mm for target walls (Wall #1, load-bearing + parapet) and 230 mm for the other walls. The thickness of the slab is 140 mm. The slab is singly reinforced with 8 mm diameter Fe500 steel rebar mesh on the bottom tension side and with the edge reinforcement on the top face as shown in Fig. 1b. The spacing of the reinforcement is 150 mm c/c in both directions (ρ = 0.24%). The thickness of the concrete cover is 20 mm. The compressive strength, elastic modulus, and Poisson's ratio of the concrete are 20 MPa, 21.20 GPa, and 0.20 respectively [18]. The ultimate tensile strength, yield strength, elastic modulus, and Poisson's ratio of the steel are 545 MPa, 500 MPa, 210 GPa, and 0.30, respectively. The slab model is also discretized with 8-node explicit solid elements (C3D8R) but with a mesh size of 20 mm. The re-bars are discretized with 2-node explicit linear 3-D truss elements (T3D2). The re-bars are embedded in the slab model using the EMBEDDED_REGION command [19]. The walls are resting on an arbitrary surface which is assumed fixed. The arbitrary surface in the ABAQUS software has been described using the REFERENCE_POINTS command [19]. A surface-to-surface interaction, with "friction", "hard", and "cohesion" contact models and with penalty contact method as mechanical constraint formulation, has been used to describe the interaction between the slab and the walls and between the walls and the arbitrary surface [19]. FE model has 351,848 nodes and 296,891 elements.

2.1 Air-Blast Loading

An explosion can be enlightened as an event instigated by a small source releasing a tremendous amount of blast energy [20]. It causes an intense oxidized reaction leading to the extrusion of high-pressure hot gas outwards at a faster rate. High air-pressure resulting from blast-induced load trigger destruction to the structures, which becomes the obstruction of these waves. Idealized shock wave comprises of initial positive phase which consists of a sudden linear rise from initial ambient pressure (P_O) to a maximum followed by a quasi-exponential decline in air-pressure for a relatively long duration forming a suction phase [7, 20]. Figure 2a shows the idealized blast pressure–time history proposed by Wu and Hao [7], where t_A is the arrival time of the blast (sec); t_1 is the rising time (s); t_2 is the decreasing time (s); t^- is the negative phase duration (s); t_d is the positive phase duration (s); P_{OP} is the
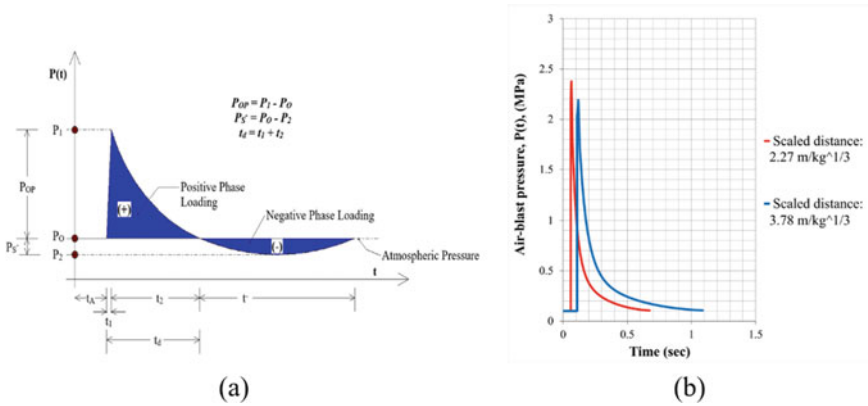
Fig. 2 **a** Idealized blast pressure time history [7] and **b** calculated blast pressure time histories

peak overpressure (MPa); P_O is the ambient pressure (0.1 MPa); and P_S^- is the peak pressure in the negative phase (MPa).

Guidelines given in the current design standards including TM 5-1330 [20], TM 5-855-1 [21], and IS 4991:1968 [22] suggested implying only a positive phase in the analysis by presuming that the negative pressure is considerably weak and does not affect the structural response [23]. Thus, the influence of the negative phase of the blast has been neglected in the present work [24–32]. Following are the empirical equations used for the calculation of blast parameters, proposed by Siddiqui and Ahmad [18, 33] and Wu and Hao [7]:

$$P_{OP} = 1.017Z^{-1.91} \tag{1}$$

$$t_A = 0.40\frac{S^{1.2}W^{-0.2}}{C_a} \tag{2}$$

$$t_d = t_1 + t_2 \tag{3}$$

$$t_1 = 0.0026Z^{0.98} \tag{4}$$

$$t_2 = 0.0003Z^{0.89}W^{0.47} \tag{5}$$

$$P(t) = \begin{cases} P_O, & 0 \le t \le t_A \\ P_O + P_{OP}\left(\frac{t}{t_1}\right), & t_A \le t \le t_1 \\ P_O + P_{OP}\left(1 - \frac{t-t_1}{t_2}\right), \exp\left(-\frac{\beta(t-t_1)}{t_2}\right), & t_1 \le t \end{cases} \tag{6}$$

Table 1 Calculated values of blast wave parameters for $W = 2300$ tons TNT

S (m)	Z (m/kg$^{1/3}$)	P_{OP} (MPa)	t_A (s)	t_1 (ms)	t_d (s)	$t = t_A + t_d$ (s)
300	2.27	2.07	0.06	5.80	0.61	0.67
500	3.78	1.92	0.11	9.50	0.97	1.08

where Z is the scaled distance (m/kg$^{1/3}$), S is the standoff distance (m), W is the weight of TNT (kg), C_a is the speed of sound in air (340 m/s), and β is the decay coefficient and can be calculated from Wu and Hao [7]. The air-blast pressure, $P(t)$ has been applied as pressure versus time application on the target walls (facing the explosive) using the explicit solver available in the ABAQUS/CAE software. Table 1 lists the calculated values of blast parameters, where t is the total duration of the blast. The calculated blast pressure time histories are shown in Fig. 2b.

2.2 Concrete-Damaged Plasticity (CDP) Model

In ABAQUS/CAE, a plasticity-based damage model, i.e., concrete-damaged plasticity model is used for assessing the non-linear behavior of the concrete and other types of quasi-brittle materials subjected to extreme dynamic loadings. The failure mechanism of the material is based on tensile cracking and compressive crushing due to its inelastic behavior [18, 19]. Two hardening variables determine the yield surface under tension and compression and these variables are referred to as tensile equivalent plastic strain $\left(\tilde{\varepsilon}_t^{pl}\right)$ and compressive equivalent plastic strain $\left(\tilde{\varepsilon}_c^{pl}\right)$ [18]. The uniaxial stress–strain curve is assumed to be converted into stress versus inelastic-strain curve [19]. This conversion is executed by ABAQUS software from the user-provided stress versus inelastic-stain data. Upon unloading of the concrete specimen at any point after loading, its response is weakened due to degradation of elastic stiffness, and this degradation of the elastic stiffness is characterized by two damage variables (d_c and d_t) which can take values from zero (no damage) to one (fully damaged) [19]. The uniaxial compressive and tensile responses of the material with respect to the CDP model under compression and tension loadings are given by [19]:

$$\sigma_c = (1 - d_c) E_O \left(\varepsilon_c - \varepsilon_c^{pl,h}\right) \tag{7}$$

$$\sigma_t = (1 - d_t) E_O \left(\varepsilon_t - \varepsilon_t^{pl,h}\right) \tag{8}$$

where σ_c is the nominal compressive stress (MPa), σ_t is the nominal tensile stress (MPa), ε_c is the compressive strain ($\varepsilon_c^{pl,h} + \varepsilon_c^{el}$), ε_t is the tensile strain ($\varepsilon_t^{pl,h} + \varepsilon_t^{el}$), $\varepsilon_c^{pl,h}$ is the plastic hardening compressive strain, $\varepsilon_t^{pl,h}$ is the plastic hardening tensile strain, ε_c^{el} is the elastic hardening compressive strain, ε_t^{el} is the elastic tensile strain,

and E_O is the initial Young's modulus of material. The reduced modulus of elasticity (E_u) of the material is expressed in terms of a scaler degradation variable (d), given as in Eq. (9).

$$E_u = (1 - d_{i=c,t}) E_O \tag{9}$$

Previous research has depicted that the CDP model can accurately predict damage in the RC slabs and brick masonry walls under explosive-induced blast loading [11, 15, 18]. Therefore, the CDP model available in the ABAQUS/CAE software has been employed in the present study for the considered FE model. The input parameters of the CDP model for masonry have been obtained from the study conducted by Valente and Milani [34, 35] and for concrete, these are taken from Hafezolghorani et al. [18].

3   Results and Discussions

IS 1905:1987, Indian Standard Code of Practice for Structural Use of Unreinforced Masonry restricts the maximum allowable compressive, tensile, and shear stresses to 1.10, 0.07, and 0.50 MPa, respectively [17]. From the non-linear explicit blast analysis performed, the following observations are worth mentioning:

- For the considered weight of TNT, increasing the standoff distance by a factor of 1.70 leads to a decrease of damage dissipation energy of the considered load-bearing structure by a factor of 6.00 (Table 2). The decrease in the damage dissipation energy indicates that the considered structure suffers less damage and cracking. However, the maximum displacement and shear stress in the target load-bearing and parapet walls (Wall #1) decrease by a factor of 2.00 (Tables 3, 4, 5 and 6; Figs. 3, 4 and 5).
- The target walls (i.e., load-bearing and parapet walls) first behave like a restraining wall at supports (i.e., Wall #2 & #4). This restraint is mobilized at a very early stage of loading and subsequently, they respond like as simply supported walls (Fig. 3).
- The junction of target walls and transverse walls (Walls #2 & #4), the junction of slab and wall, junction of Wall #3 and transverse walls, and mid-height of the target load-bearing wall near the top portion of the door experience maximum shear stress (>0.50 MPa) (Tables 5 and 6; Fig. 4).
- Damage in the form of diagonal cracks on the rear face of the target load-bearing wall, bulging of transverse walls, vertical cracks at mid-height of Wall #3 and the

Table 2   Summary of damage dissipation energy

Z (m/kg$^{1/3}$)	P_{OP} (MPa)	Damage dissipation energy (J)
2.27	2.07	553,352.90
3.78	1.92	92,225.48

Table 3 Summary of displacements of the target load-bearing wall

Z (m/kg$^{1/3}$)	Max. displacement (mm) of walls and slab			
	Wall #1 (−Z direct.)	Wall #2 & #4 (+X & −X direct.)	Wall #3 (−Z direct.)	Slab (−Y direct.)
2.27	[a] >>> 230	[b] (+2875.20 & −2749)	[a]2305.88	[d]1006.25
3.78	[a] >> 230	[b] (+226.10 & −359.50)	[f]72.06	[d]28.84

[*a] At mid-height of the wall
[*b]Near junction of Wall #1 and Wall #2/#4
[*f]Near junction of Wall #3 and Wall #2/#4
[*d]Near support (i.e., target wall, Wall #1)

Table 4 Summary of displacements of the target parapet wall

Z (m/kg$^{1/3}$)	Max. displacement (mm) in walls			
	Wall #1 (−Z direct.)	Wall #2 (−X direct.)	Wall #4 (−X direct.)	Wall #3 (−Z direct.)
2.27	[a]>>>230	[b]1414	[b]1300	[f]1444
3.78	[a]>>230	[b]83.00	[b]83.89	[f]97.13

[* a] At mid-height of the wall
[*b]Near junction of Wall #1 and Wall #2/#4
[*f]At the junction of wall #3 and parapet wall, near the bottom edge

Table 5 Summary of stresses of the target load-bearing wall

Z (m/kg$^{1/3}$)	Max. Von Mises stress (MPa)			Max. principal stresses (MPa)		
	Wall #1	Wall #2 & #4	Wall #3	Wall #1	Wall #2 & #4	Wall #3
2.27	[g]1.20	[h]0.93	[j]0.99	[c]3.05/[t]0.03	[c]2.14/[t]0.03	[c]1.18/[t]0.03
3.78	[g]1.02	[h]0.60	[j]0.52	[c]1.85/[t]0.03	[c]0.67/[t]0.03	[c]0.46/[t]0.03

[*g] At mid-height of the masonry above the door
[*h]Near junction of Wall #1 and Wall #2/#4
[*j]Near junction of Wall #3 and Wall #2/#4
[*c]Compressive
[*t]Tensile

Table 6 Summary of stresses of the target parapet wall

Z (m/kg$^{1/3}$)	Max. Von Mises stress (MPa)			Max. principal stresses (MPa)		
	Wall #1	Wall #2 & #4	Wall #3	Wall #1	Wall #2 & #4	Wall #3
2.27	[g]1.61	[h]0.60	[j]1.21	[c]2.11 / [t]0.03	[c]0.60 / [t]0.03	[c]1.38 / [t]0.03
3.78	[g]1.12	[h]0.32	[j]0.86	[c]0.90 / [t]0.03	[c]0.28 / [t]0.03	[c]1.18 / [t]0.03

[*g] At mid-height of the masonry above the door
[*h]Near junction of Wall #1 and Wall #2/#4
[*j]Near junction of Wall #3 and Wall #2/#4
[*c]Compressive
[*t]Tensile
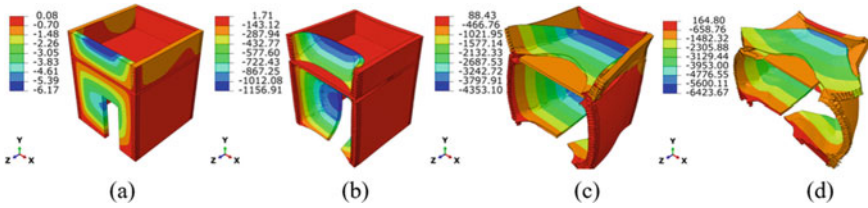
Fig. 3 Distribution of Z-displacement for standoff distance of 300 m at different time steps: **a** 0.034 s, **b** 0.1684 s, **c** 0.4041 s, and **d** 0.6736 s
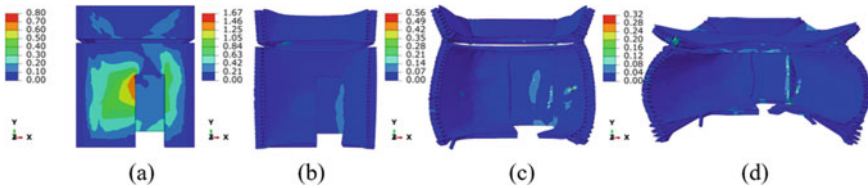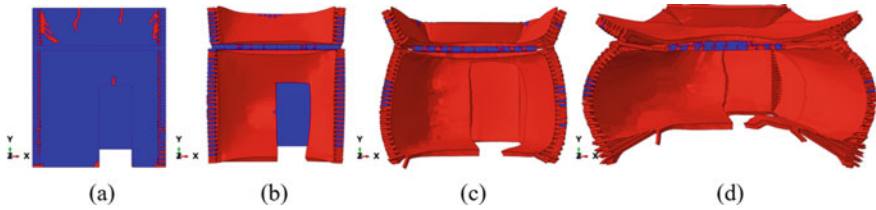

Fig. 4 Distribution of shear stress for standoff distance of 300 m at different time steps: **a** 0.034 s, **b** 0.1684 s, **c** 0.4041 s, and **d** 0.6736 s
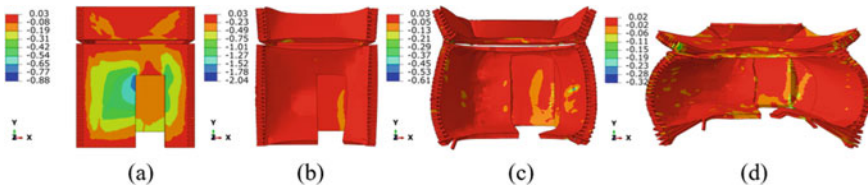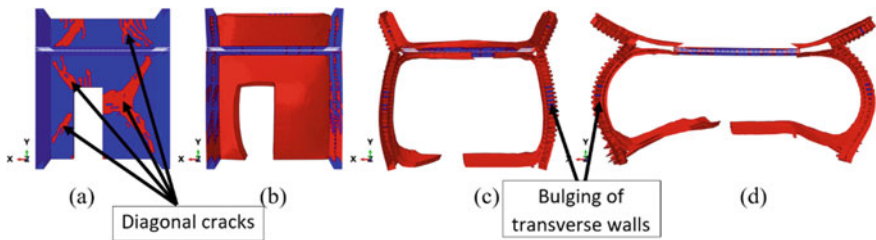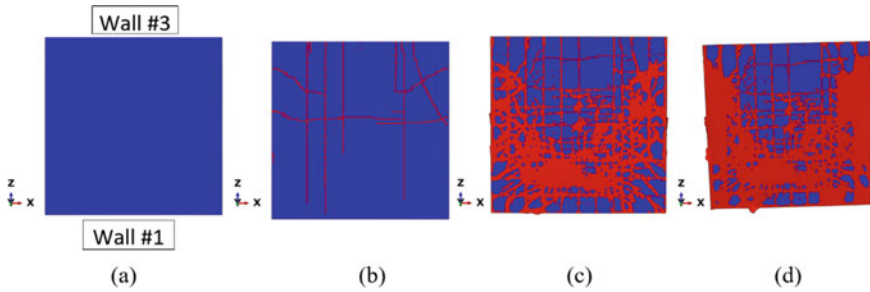

Fig. 5 Distribution of principal stresses for standoff distance of 300 m at different time steps: **a** 0.034 s, **b** 0.1684 s, **c** 0.4041 s, and **d** 0.6736 s

junctions of target walls and transverse walls has been observed under the applied blast loading (Figs. 6 and 7).

- At the earlier stage of loading, the slab remains rested on walls and therefore undergoes negligible displacement in the vertical direction (−Y). Subsequently with increasing displacements in the walls, particularly in the front wall, the slab undergoes large displacement near the target wall under the parapet (Fig. 8).
- A significant number of flexural cracks with an average spacing of 390 mm and depth of 120 mm have been observed on the bottom tension face of the slab subjected to maximum considered blast pressure of 2.07 MPa (Fig. 9).
- The first crack in the slab appears at 0.10 s and 0.16 s under the explosive load of 2300 tons TNT at standoff distances of 300 m and 500 m, respectively. However,

Fig. 6 Distribution of damage (front face) for standoff distance of 300 m at different time steps: **a** 0.034 s, **b** 0.1684 s, **c** 0.4041 s, and **d** 0.6736 s. ("red color": damaged material and "blue color": undamaged material)

Fig. 7 Distribution of damage (rear face) for standoff distance of 300 m at different time steps: **a** 0.034 s, **b** 0.1684 s, **c** 0.4041 s, and **d** 0.6736 s
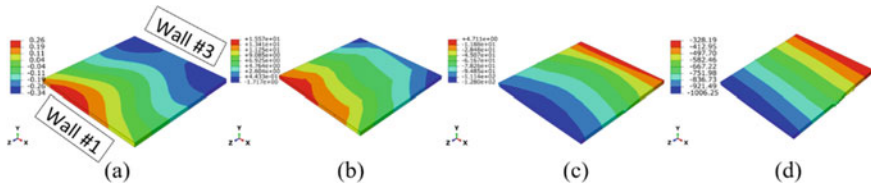
Fig. 8 Distribution of *Y*-displacement of the slab for standoff distance of 300 m at different time steps: **a** 0.034 s, **b** 0.1684 s, **c** 0.4041 s, and **d** 0.6736 s

the first crack in the target walls appears at 0.034 s and 0.054 s at standoff distances of 300 m and 500 m, respectively.

- The maximum displacements of the target walls are found considerably greater than the thickness of the target walls under the explosive loads considered (Tables 3 and 4).

Fig. 9 Formation of cracks on bottom tension face of the slab for standoff distance of 300 m at different time steps: **a** 0.034 s, **b** 0.1684 s, **c** 0.4041 s, and **d** 0.6736 s

- The considered load-bearing structure is enormously damaged under the applied peak overpressures (Figs. 6 and 7).

4 Conclusion

This paper presents non-linear analyses of a load-bearing masonry structure subjected to a high explosive charge of 2300 tons of TNT at large standoff distances of 300 m and 500 m using the ABAQUS/CAE software. Concrete-damaged plasticity (CDP) model for concrete and brick masonry available in the employed software has been utilized. For the considered weight of TNT, increasing the standoff distance from 300 to 500 m makes to decrease the damage dissipation energy of the structure by a factor of 6.00. However, the shear stresses in the target load-bearing and parapet walls (Wall #1) decrease by a factor of 2.00. Damage in the form of diagonal cracks on the rear face of the target load-bearing wall, bulging of transverse walls, vertical cracks at mid-height of rear wall (Wall #3), and damage along the vertical joints of the target walls with transverse walls have been observed under the considered blast pressures. The stresses in general are found exceeding the allowable limit given in IS 1905:1987 at the junction of the target walls and transverse walls (Walls #2 & #4), the junction of slab and wall, junction of rear wall (Wall #3) and transverse walls, and at mid-height of the masonry above the door.

From the results of analyses performed, it can be inferred that load-bearing structures cannot survive under the pressure generated by blast of such magnitude. Therefore, instead of strengthening the unreinforced masonry structure: (1) warehouses for storage of high explosives should be located at far distances from residential area or residential townships should not be allowed to develop in the vicinity of structures for storage of explosives, and (2) high walls with crash worthy claddings should be designed and erected enclosing the explosive storage structures. But nevertheless,

investigation presented may be extended to reinforce the masonry load-bearing structures to estimate enhanced damage dissipation energy by the reinforcement under such high explosive loads.

References

1. Cheaito AM, Al-Hajj S (2020) A brief report on the Beirut port explosion. Mediterr J Emerg Med Acute Care 1(4)
2. Pilger C (2020) Beirut explosion causes strong shock waves—Infrasonic, hydroacoustic and seismic signals registered and investigated by BGR. Federal Institute for Geosciences and Natural Resource. https://www.seismologie.bgr.de/sdac/erdbeben/big_quakes/beirut_200804_eng.html
3. Technical Report (2020) Beirut explosion impact assessment. Ministry of Culture–Directorate General of Antiquities, UNESCO Statement of Solidarity, Strategy& analysis, pp 1–45
4. Sleiti KA (2020) Beirut explosion 2020—ammonium nitrate disasters graphical data. Qatar University Press
5. Rose TA, Smith PD, Mays GC (1995) The effectiveness of walls designed for the protection of structures against air blast from high explosives. Structural and Building Board Structural Panel Paper I0635. 110, pp 78–85
6. Luccioni MB, Ambrosini DR, Danesi FR (2004) Analysis of building collapse under blast loads. Eng Struct 26:63–71
7. Wu C, Hao H (2005) Modelling of simultaneous ground shock and air blast pressure on nearby structures from surface explosions. Int J Impact Eng 31(6):699–717
8. Wu C, Oehlers JD, Rebentrost M, Leach J, Whittaker SA (2009) Blast testing of ultra-high-performance fibre and FRP-retrofitted concrete slabs. Eng Struct 31:2060–2069
9. Wei X, Stewart GM (2010) Model validation and parametric study on the blast response of un reinforced masonry walls. Int J Impact Eng 37(11):1150–1159
10. Ahmad S, Elahi A, Pervaiz H, Rahman GA, Barbhuiya S (2014) Experimental study of masonry wall exposed to blast loading. Materiales de Construccion 64(313):1–11
11. Pereira MJ, Campos J, Lourenco PB (2015) Masonry infill walls under blast loading using confined underwater blast wave generators (WBWG). In: 8th international conference ASCM 2014, Wroclaw, Poland, 92, pp 69–83
12. Zapata JB, Weggel CD (2019) Collapse study of an unreinforced masonry infill walls on progressive collapse performance of reinforced concrete infilled frames. Eng Struct 191:179–193
13. Li J, Wu C, Hao H, Wang Z, Su Y (2016) Experimental investigation of ultra-high-performance concrete slabs under contact explosions. Int J Impact Eng 93:62–75
14. Chácara C, Cannizzaro F, Pantò B, Caliò I, Lourenço BP (2018) Assessment of the dynamic response of unreinforced masonry structures using a macroelement modelling approach. Earthq Eng Struct Dyn 47:2426–2446
15. Anas MS, Ansari MdI, Alam M (2020) Performance of masonry heritage building under air-blast pressure without and with ground shock. Aust J Struct Eng 21(4):329–544

16. Goel DM, Matsagar VA (2014) Blast-resistant design of structures. Pract Periodical Struct Des Constr, ASCE, 19(2)
17. IS 1905:1987 (1987). Indian Standard Code of practice for structural use of unreinforced masonry. Bureau of Indian Standard, New Delhi, India
18. Hafezolghorani M, Hejazi F, Vaghei R, Jaafar MSB, Karimzade K (2017) Simplied design plasticity model for concrete. Struct Eng Int 27(1):68–78
19. ABAQUS/CAE FEA Program (2017) Concrete-damaged plasticity model, explicit solver, three-dimensional solid element library. ABAQUS DS-SIMULIA User Assistance Manual
20. TM 5-1330 (1990) Structures to resist the effects of accidental explosions. Technical Manual, Joint Department of the Army, the Navy and the Air Force
21. TM 5-855-1 (1986) Design & analysis of hardened structures to conventional weapons effects. Department of the Army, Washington DC
22. IS 4991:1968 (1968) Criteria for blast resistant design of structures for explosions above ground. Bureau of Indian Standards, New Delhi, India
23. Hao H, Hao Y, Li J, Chen W (2016) Review of the current practices in blast-resistant analysis and design of concrete structures. Adv Struct Eng 19(8):1193–1223
24. Anas SM, Ansari Md I, Alam M (2021) A study on existing masonry heritage building to explosive-induced blast loading and its response. Int J Struct Eng (Article in press)
25. Anas SM, Alam M (2021) Performance of simply supported concrete beams reinforced with high-strength polymer re-bars under blast-induced impulsive loading. Int J Struct Eng (Article in press)
26. Anas SM, Alam M, Umair M (2021) Experimental and numerical investigations on performance of reinforced concrete slabs under explosive-induced air-blast loading: a state-of-the-art review. Structures, vol 31. Elsevier, pp 428–461
27. Anas SM, Alam M (2021) Air-blast response of free-standing: (1) Unreinforced brick masonry wall, (2) Cavity RC wall, (3) RC walls with (i) Bricks, (ii) Sand, in the cavity: a macro-modeling approach. In: Marano GC, Ray Chaudhuri S, Unni Kartha G, Kavitha PE, Prasad R, Achison RJ (eds) Proceedings of SECON'21. SECON 2021. Lecture Notes in Civil Engineering, vol 171. Springer, Cham, pp 921–930. https://doi.org/10.1007/978-981-33-6389-2_18
28. Anas SM, Alam M (2021) Comparison of existing empirical equations for blast peak positive overpressure from spherical free air and hemispherical surface bursts. Iran J Sci Technol Trans Civil Eng. https://doi.org/10.1007/s40996-021-00718-4
29. Anas SM, Alam M, Umair M (2021) Performance of on-ground double-roof RCC shelter with energy absorption layers under close-in air-blast loading. Asian J Civil Eng. https://doi.org/10.1007/s42107-021-00395-8
30. Anas SM, Alam M, Umair M (2021) Air-blast and ground shockwave parameters, shallow underground blasting, on the ground and buried shallow underground blast-resistant shelters: a review. Int J Protective Struct. https://doi.org/10.1177/20414196211048910
31. Anas SM, Alam M, Umair M (2021) Performance of one-way concrete slabs reinforced with Conventional and Polymer Re-bars Under Air-Blast Loading. In: Chandrasekaran S., Kumar S., Madhuri S. (eds) Recent Advances in Structural Engineering. Lecture Notes in Civil Engineering, vol 135. Springer, Singapore. https://doi.org/10.1007/978-981-33-6389-2_18
32. Anas SM, Alam M, Umair M (2020) Performance of one-way composite reinforced concrete slabs under explosive-induced blast loading. In: 1st International Conference on Energetics, Civil and Agricultural Engineering 2020, ICECAE 2020, vol. 614. Tashkent, Uzbekistan. https://doi.org/10.1088/1755-1315/614/1/012094
33. Siddiqui JI, Ahmad S (2007) Impulsive loading on a concrete structure. Proc Inst Civ Eng Struct Build 160(4):231–241

34. Valente M, Milani G (2016) Non-linear dynamic and static analyses on eight historical Masonry Towers in the North-East of Italy. Eng Struct 114(1):241–270
35. Valente M, Milani G (2016) Seismic assessment of historical Masonry Towers by means of simplified approaches and standard FEM. Constr Build Mater 108(1):74–104

Determination Method of the Structural Strength of Deep Reinforced Concrete Beams Using ANSYS Software

Phan Van-Phuc

Abstract This study presents the numerical method in determining the structural strength of reinforced concrete (RC) deep beams using ANSYS, a commercial finite element analysis software. An investigated RC deep beam with a cross-section of 10×30 cm and a standard length according to the IS 456-2000 was employed to analyze the structural behavior. The nonlinear stress–strain relationship of concrete and reinforcement was considered in the numerical models. In this study, concrete and reinforcing bars elements were modeled using the SOLID65 and LINK180 models, respectively. The results of finite element models were then compared with those of experimental results. A trivial difference between those results highlighted the capability of the numerical model in analyzing the structural behavior as well as damage patterns of the RC deep beams. A parametric study was also performed to quantify the effects of different parameters including geometry and material on the variation of the strength of the deep beam. The results of this study showed quite accurately the strength of RC deep beams. The simulation method by ANSYS software helps in predicting the structural strength faster, and saving money compared to testing methods.

Keywords Deep reinforced concrete beam · Deformation · Reinforced concrete · Stress

1 Introduction

Reinforced concrete (RC) is multiple-use over the world thanks to its advantages such as cheap price, good bearing capacity, easy fabrication, good resistance to an external environment, and good fire … The determination of RC properties and behaviors of a structure is necessary for the design of a building, and the experimental method has good reliability. However, this method is costly and takes a long time to implement.

P. Van-Phuc (✉)
Department of Civil Engineering, Vinh University, 182-Le Duan Street, Vinh 461010, Vietnam
e-mail: vanphuckxd@vinhuni.edu.vn

To solve these problems of the experimental method, then the stimulation method is used to analyze the behavior of a structure, which is based on the finite element.

There is many commercial finite element analysis software such as ANSYS, ABAQUS, SAP2000, ETABS, which are used to analyze construction structure. The numerical simulation method gives accurate results. This study presents the determination method of the critical load of RC deep beam by using ANSYS Workbench 2019 R3 software. This simulation method is based on the theoretical of concrete with Newton–Raphson's nonlinear stress–strain relationship [1], and reinforcements are taken bilinear stress–strain relationship.

A method of analysis and design of deep RC beam has been discovered in the form of truss bar, the RC deep beam structure calculation model can be converted through the truss model as in the study of [2, 3]. Besides, the finite element method with the ABAQUS software has also proceeded to predict the behavior of reinforced concrete deep beams with web openings using the finite element method, and given good results [4].

There were a lot of researches, which were carried out with numerical simulation method based on the finite element as was shown in [5]. A structural system of RC beams and columns is used widely, and scientists have performed experimental as well as simulation studies [6–9]. The study [10] shows that the SOLID65 element of the ANSYS software, which has given quite good results for an RC structure with the nonlinear stress–strain relationship. In that, it allowed to predict crack, crush forms of the RC structure.

According to ACI 318-14 standard [11] and ECP 203-2007 [12], the RC deep beam defines two conditions as follow: beam with a shear span-to-depth ratio less than or equal to 2 or beam with clear span less than or equal to four times its height. According to IS 456-2000 standard, the deep beam was one whose ratio between effective span to deep was less than 2 for simple beam, and less than 2.5 for continuous beam [13]. In the RC beam, usually, the damage is caused by bending moment, and flat strain assumption is used to calculate bearing capacity for the structures. However, for the RC deep beams, the failure kid of type due to shear force is more than bending moment, and the flat cross-section assumption does not give accurate results. If applying the simulation method is the same as a normal RC beam, then the result will be inaccurate, and the behavior of concrete is not reflected in the structure. Because, when consider the normal RC beam model by ANSYS software, we ignore the effect of horizontal strain, and only consider the longitudinal strain of the RC beam. But for the structure is the RC deep beam, the failure kid of type is according to a shear force as in the experiment [14], in the compressive zone of the elements can easily determine that 2 components of compressive stress, which are in a horizontal and vertical direction. Besides, in the past, the simulation method with ANSYS software had been performed on the **Ansys Mechanical (APDL)** software under the form of codes, but implementation on Ansys Mechanical (APDL) was difficult and complicated. This study presents the simulation method of the RC deep beams by ANSYS Workbench 2019 R3 software, to find the critical load, the stress–strain state as well as the location of the tensile cracks, crushes. This method is simple and easy to implement to create the model as well as to solve and review results.

2 Methods

The simulation method has performed with ANSYS Workbench 2019 R3 software on the computer parameters as follows:

- WINDOWS × 64
- Operating System: Windows 10 (Build: 18362)
- Processor Model: Intel(R) Core (TM) i9-9900 K CPU @ 3.60 GHz
- Compiler: Intel(R) FORTRAN Compiler Version 17.0.6 (Build: 20171215)
- Intel(R) C/C++ Compiler Version 17.0.6 (Build: 20171215)
- Intel(R) Math Kernel Library Version 2017.0.3 Product Build 20170413.

2.1 A theory basic of the Concrete

The stress–strain relationship of the concrete is determined according to the study of **Vecchio** and **Collins** [15]. In there, the concrete strength is $f = 37.2$ MPa, and its curve is shown in Fig. 1. The maximum relative strain value of concrete is $\varepsilon_{max} = 0.003$, which is taken according to European standard [16]. A relative elasticity modulus is determined according to **Vecchio** and **Collins** [15], which is $E_c = 36.270$ MPa. The strain at a top of the stress–strain relationship curve is $\varepsilon_0 = 0.002$. In this study, concrete is selected SOLID65 model [17], its properties are shown in the type of kid the command as in Table 1.
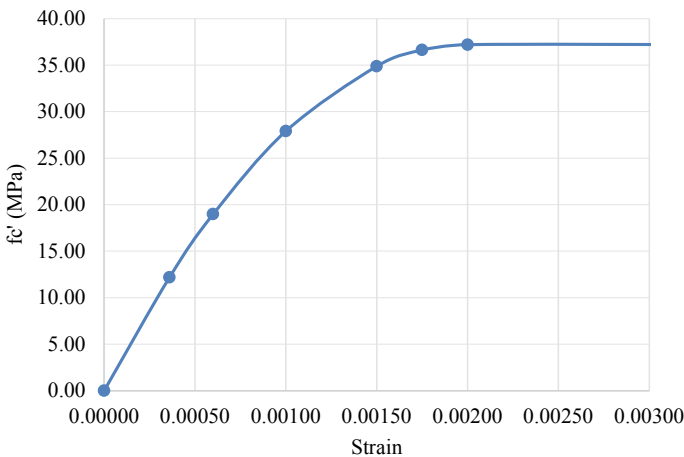
Fig. 1 Stress–strain relationship of concrete

**Table 1** Codes of concrete in ANSYS Workbench 2019 R3 software

Ordinal number	The code
1	ET, MATID, SOLID65
2	R, MATID, 0, 0, 0, 0, 0, 0
3	RMORE, 0, 0, 0, 0, 0
4	MP, EX, MATID, 36, 270
5	MP, PRXY, MATID, 0.2
6	TB, CONCR, MATID, 1, 9
7	TBTEMP, 22
8	TBDATA, 1, 0.3, 1, 3, -1
9	TB, MELAS, MATID, 1, 7
10	TBPT,, 0.00010, 3.62700
11	TBPT,, 0.00050, 16.27500
12	TBPT,, 0.00100, 27.90000
13	TBPT,, 0.00150, 34.87500
14	TBPT,, 0.00200, 37.20000
15	TBPT,, 0.00250, 37.20000
16	TBPT,, 0.00300, 37.20000

2.2 A Theory Basic of Reinforcement

The stress–strain relationship of reinforcement is proposed by the authors, and is used in the form of bilinear relation as in Ref. [1] and is shown in Fig. 2. To create the stress–strain relationship of reinforcement, two necessary parameters are elastic modulus (E_s) and yield strength (f_s). Reinforcement is added into the software under the form of commands as in Table 2.

Fig. 2 Stress–strain relationship of reinforcement
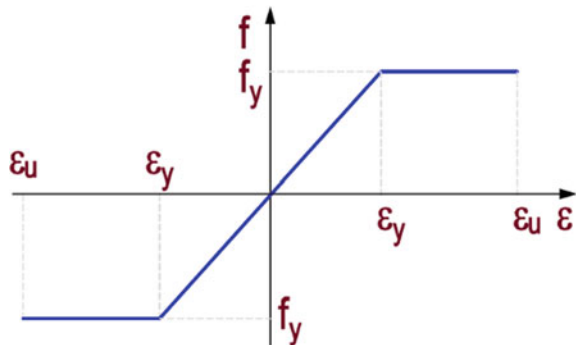
Table 2 Codes of reinforcement in ANSYS Workbench 2019 R3 software

Ordinal number	The code
1	ET, MATID, LINK180
2	MPDATA, EX, MATID,, 2e5
3	MPDATA, PRXY, MATID,, 0.3
4	TB, BISO, MATID, 1, 2
5	TBDATA,, 374, 0

2.3 A Geometrical Model of the Structure

In this study, the deep RC beam is selected for analysis, its parameters are the same in the first experiment of Lu et al. in the study [14]. The RC deep beam model is shown in Fig. 3. In there, support and load positions consider stiff enough during for test. There are 2 reinforcing bars at the bottom of a cross-section of the deep RC beam.
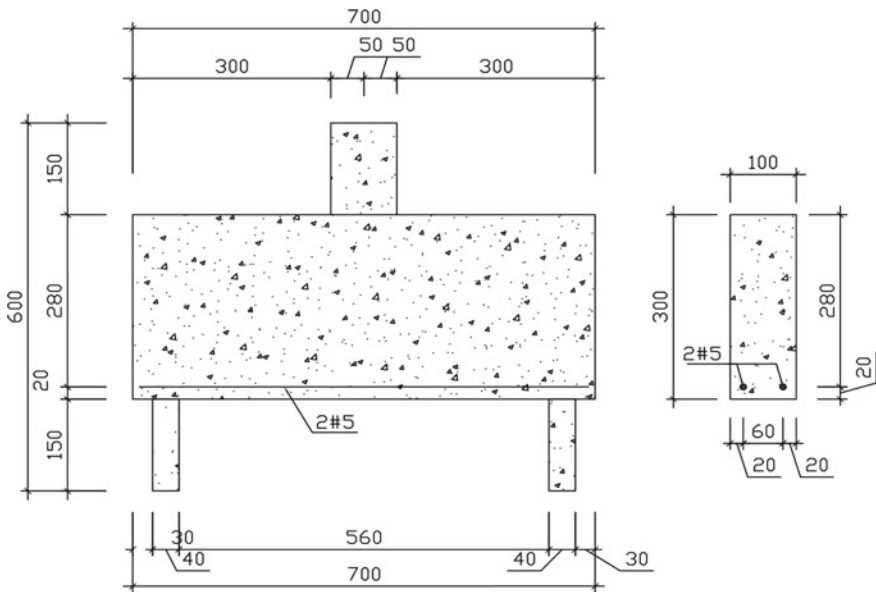
Fig. 3 Geometrical parameters of the deep RC beam [11]
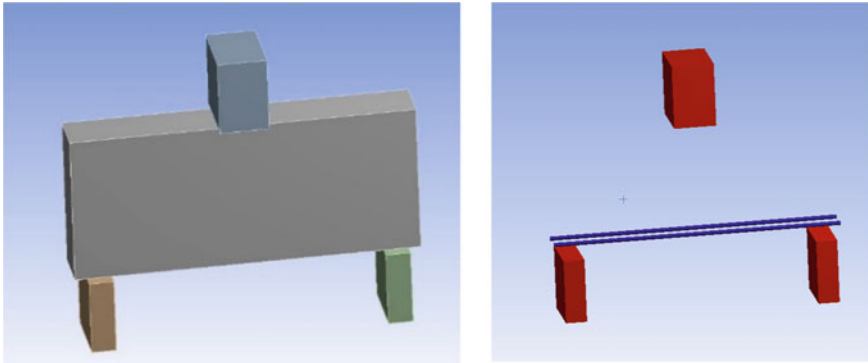
Fig. 4 Models of the deep RC beam and reinforcements in simulation analysis

2.4 A Process of Structural Simulation Method by ANSYS Workbench 2019 R3 Software

Model and meshing

The analysis model is created with the help of graphics software **DesignModeler**, the results of an RC deep beam model are shown in Fig. 4. After that, it is passed through a Mechanical (ANSYS Static) assistance to solve. In which, properties of the concrete and reinforcements are added into forms of the code (Tables 1 and 2) corresponding to their models. To create the simultaneous working between concrete and reinforcing model, the ANSYS software allows simulation of the displacement between SOLID65 and LINK180 model, which is shown types under the form of CEINTF code and using this code as in Table 3 (Figs. 5 and 6).

where: "NM_LongRebars": a name of the reinforcement, "NM_Concrete": the name of the concrete.

The meshing of concrete and reinforcements is quite important in the simulation method. It will affect the calculation results, and a lot of authors found out that the smaller a meshing size, the more accurate the analysis results. But there had a disadvantage in that their analysis time is long, the configuration of the computer must have enough strength to perform. The size of the meshing is large, it will allow

Table 3 Relative displacement code between concrete and reinforcement elements

Ordinal number	Code
1	/PERP7
2	CMSEL, S, NM_LongRebars, ELEM
3	CMSEL, A, NM_Concrete, ELEM
4	CEINTF, 0.0001
5	ALLSEL, ALL
6	/SOLU
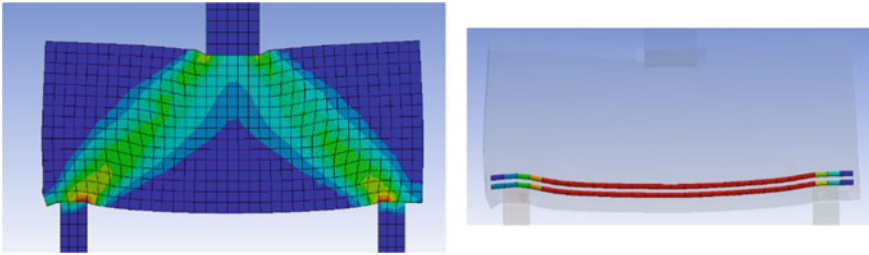
Fig. 5 Equivalent stress in the concrete and longitudinal force in reinforcements
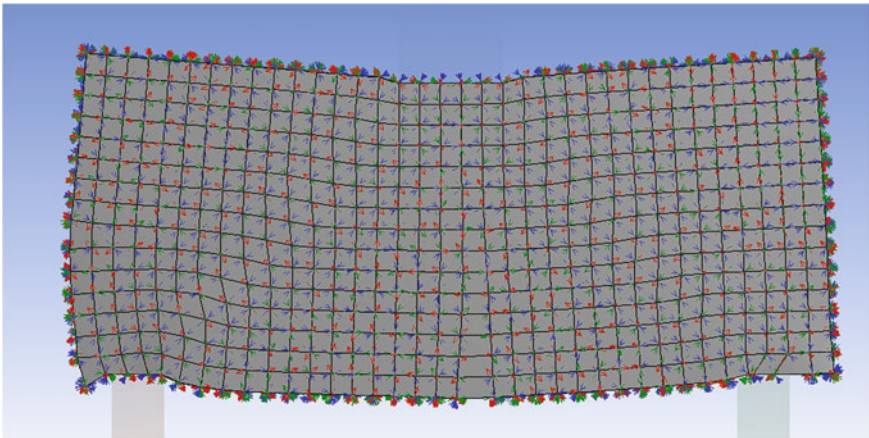
Fig. 6 Vector directions of major stresses in the deep RC beam

the computer to solve faster, but the results are less accurate [18]. Therefore, in this study, the authors have done many different cases by the method of performing case turn. Concrete meshing sizes of cases are shown in Table 4, and the reinforcement meshing sizes are allowed automatically to select by ANSYS software.

Table 4 Sizes of the meshing

Case	Size of elements (mm)	
	Concrete	Reinforcement
1	15 × 15 × 15	15
2	15 × 15 × 15	20
3	20 × 20 × 20	25
4	25 × 25 × 25	30
5	30 × 30 × 30	35
6	50 × 50 × 50	50

Boundary conditions and load

Supporting positions are not allowed displacement in 3 directions, i.e., displacements according to axes of a coordinate system are zero. Based on the test results, the displacement of an impact was less than 2 mm then the structure was damaged. So that, in this study, the load–displacement is given in the z-axis as -2 or -3 mm (the "$-$" is signed represents the positive opposite displacement of the z-axis) and is not displaced on the x and y axes. Values of displacement were chosen for analysis depends on conditions of the meshing size and the number of steps of the load to converge simulation problems.

The analysis process is selected by the authors in the form of "Steps" and "Subteps", whether the analysis problem will converge or not, that is depended much on the choosing of analysis settings and dividing the number of load steps (nonlinear controls).

3   Results

Analysis results of the deep RC beam by finite element software ANSYS Workbench 2019 R3 are shown in Figs. 7, 8, 9, 10, 11 and 12, which are absolute values of loads and displacements. Table 4 shows 6 cases of meshing. Results of the stress in the concrete and reinforcement are shown in Fig. 5. Through Fig. 6, we can easily determine the location of cracks and crushes, which are appeared through the direction of main vectors. Positions at least one of three main vectors pointed out of the element node then cracks may appear. Crack directions are perpendicular to the direction of the main tensile vector. However, whether the crack is appeared or no, they are depended on the magnitude of the main tensile vector. If the value of the main tensile vector is less than the tensile strength of the concrete, then the crack will not appear. Thus, based on Fig. 6, we will preliminarily determine the position and direction of cracks.
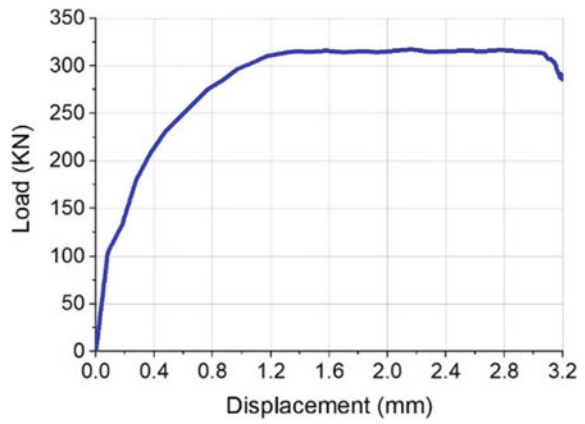

Fig. 7 Load–displacement relationship in the Z-axis corresponding to case 1
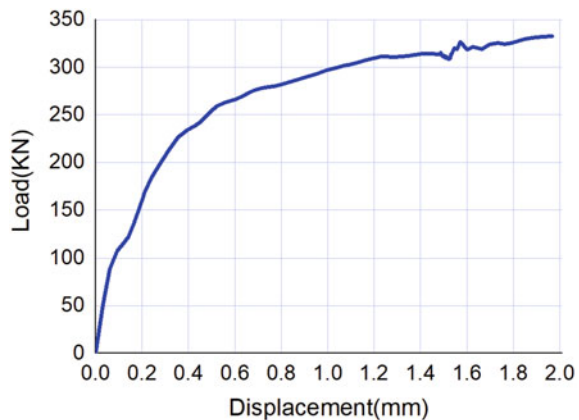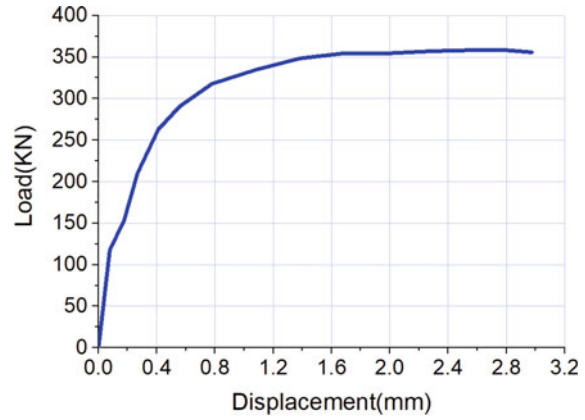
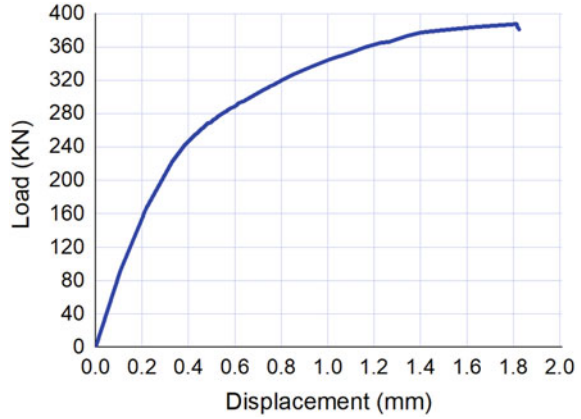**Fig. 8** Load–displacement relationship in the Z-axis corresponding to case 2
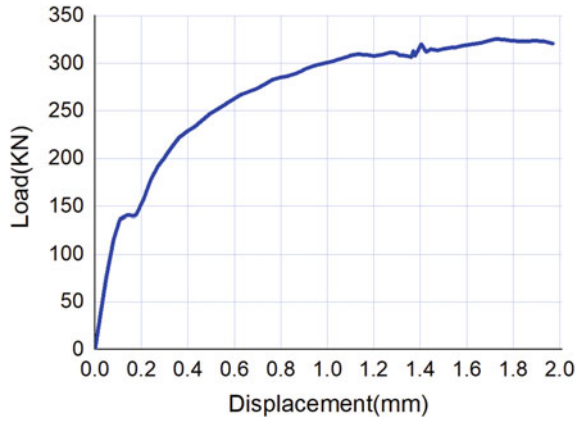
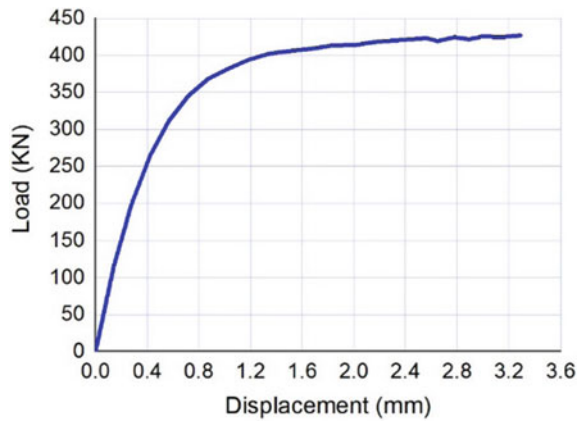**Fig. 9** Load–displacement relationship in the Z-axis corresponding to case 3

Fig. 10 Load–displacement relationship in the Z-axis corresponding to case 4

Fig. 11 Load–displacement
relationship in the Z-axis
corresponding to case 5

Fig. 12 Load–displacement
relationship in the Z-axis
corresponding to case 6

Comparing results between different meshing of cases was shown in Table 4, we had the following results table (Table 5), in which the analytical results were

Table 5 Results of the structural strength of the deep RC beam

Case	Structural strength (KN)		Error (%)
	ANSYS	Experiments	
1	332.87	301.8	10.29
2	325.47		7.84
3	317.05		5.05
4	358.83		18.90
5	387.84		28.51
6	427.07		41.51
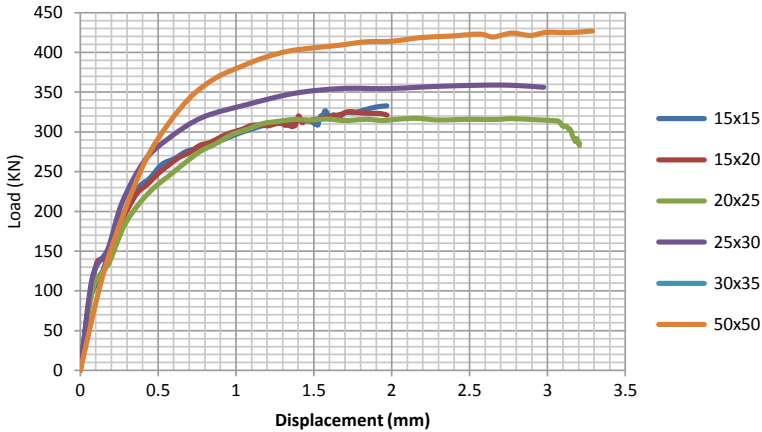
Fig. 13 Load–displacement relationship of the meshing cases

obtained from ANSYS software, and the experimental results were taken from the team's experiments in [14].

From Fig. 13, we have seen the analysis results by finite element software ANSYS with cases 4, 5, and 6 (Table 4), which were given much deviation when these were compared to the other cases, for the case had been the mall element size, such as case 1 and case 2 (Table 4), then the problem of analysis by finite element software ANSYS was difficult to converge.

4 Conclusion

Observing Table 5 and Fig. 13 we have seen that the simulation results of deep RC beams are depended much on the meshing size of concrete elements and reinforcements. The analytical result for case 3 (i.e., the concrete element size is 20 × 20 × 20 mm, and the reinforcement size is 25 mm) is given the small error (5.05%) when is compared to the experimental result. Thus, previous research has made identifies that the smaller the meshing size, the more accurate the simulation for RC deep beams is not right. The authors have recommended the following:

- When simulating the structure of deep RC beams, the concrete element size should be 20 × 20 × 220 mm and the reinforcement element size should be 25 mm.
- The stress–strain relationship of the concrete has been obtained from F.J. Vecchio and M.P. Collins, which is reasonable, while reinforcement should take in a bilinear relationship.
- In structural simulation by ANSYS finite element software, SOLID65 model should use for concrete and LINK180 model for reinforcement.

– Should use ANSYS Workbench software to analyze, which instead of before using ANSYS APDL (Ansys Parametric Design Language), because the simulation process will be more convenient and easier to perform, it has many outstanding advantages.
– Scientists, designers can use ANSYS Workbench to determine structural strength and instead for experiments or mechanical analysis methods.
– Using simulation software to calculate the strength of the structural, load–displacement relationship, which was determined quite accurately (error 5.05%), will be shortened the time as well as be save economic fees for the experiment.

References

1. James KW, Macgregor JG (2009) Reinforced concrete. Mech Des 1
2. Park JW, Kuchma D (2007) Strut-and-tie model analysis for strength prediction of deep beams. ACI Struct J. https://doi.org/10.14359/18947
3. Ismail KS, Guadagnini M, Pilakoutas K (2018) Strut-and-Tie modeling of reinforced concrete deep beams. J Struct Eng. https://doi.org/10.1061/(asce)st.1943-541x.0001974
4. Mohamed AR, Shoukry MS, Saeed JM (2014) Prediction of the behavior of reinforced concrete deep beams with web openings using the finite element method. Alexandria Eng J. https://doi.org/10.1016/j.aej.2014.03.001
5. Deaton JB (2013) Nonlinear finite element analysis of reinforced concrete exterior beam-column joints with nonseismic detailing
6. Santhakumar R, Dhanaraj R, Chandrasekaran E (2007) Behaviour of retrofitted reinforced concrete beams under combined bending and torsion: a numerical study. Electron J Struct Eng 7:1–7
7. Kottb HA, El-Shafey NF, Torkey AA (2015) Behavior of high strength concrete columns under eccentric loads. HBRC J 11(1):22–34. https://doi.org/10.1016/j.hbrcj.2014.02.006
8. Dahmani L, Khennane A, Kaci S (2010) Crack identification in reinforced concrete beams using ANSYS software. Strength Mater 42(2):232–240. https://doi.org/10.1007/s11223-010-9212-6
9. Ziara MM (2009) Behavior of beams strengthened with steel fiber RC overlays. J Adv Concr Technol 7(1):111–121. https://doi.org/10.3151/jact.7.111
10. Yigit A, Al-Ansary M, Khalid M (1996) Finite element modeling of drillstrings. Math Comput Appl 1(2):158–163. https://doi.org/10.3390/mca1020158
11. ACI 318-14 (2014) Building code requirements for structural concrete (ACI 318-14) commentary on building code requirements for structural concrete (ACI 318R-14)
12. Ibrahim MA, El Thakeb A, Mostfa AA, Kottb HA (2018) Proposed formula for design of deep beams with shear openings. HBRC J 14(3):450–465
13. IS 456, IS 456: 2000—Plain and reinforced concrete—code and practice. Bur. Indian Stand., 2000, 624.1834 TAY
14. Lu W-Y, Hsiao H-T, Chen C-L, Huang S-M, Lin M-C (2015) Tests of reinforced concrete deep beams. Comput Concr 15(3):357–372. https://doi.org/10.12989/cac.2015.15.3.357
15. Vecchio FJ, Collins MP (1986) The modified compression-field theory for reinforced concrete elements subjected to shear. ACI J Proc 83(2):219–231. https://doi.org/10.14359/10416
16. BS EN 1992-1-1 (2004) Eurocode 2: design of concrete structures—Part 1-1: general rules and rules for buildings," Br. Stand. Inst., [Authority: The European Union Per Regulation 305/2011, Directive 98/34/EC, Directive 2004/18/EC]

17. Kohnke P (1999) ANSYS theory reference—Release 5.6. p 1286. [Online]. Available: http://research.me.udel.edu/~lwang/teaching/MEx81/ansys56manual.pdf
18. Tavio T, Tata A (2009) Predicting nonlinear behavior and stress-strain relationship of rectangular confined reinforced concrete columns with ANSYS. Civ Eng

Analytical Investigation on Progressive Collapse of 3-D Reinforced Concrete Frames Under High Temperature

M. Vishal and K. S. Satyanarayanan

Abstract Progressive collapse is one of the major concerns in high-rise buildings. Collapse of a single element will trigger complete failure of the building. The study under fire conditions helps to understand the structural behavior of a building in critical fire scenarios. Here the progressive collapse of structures was studied under high-temperature condition and working load. For the progressive collapse analysis, a finite element software called ABAQUS (FEA) was used. A three-dimensional single-bay single-storey reinforced concrete prototype frame was adopted for the analysis. A steady-state analysis was done by applying the service load and temperature simultaneously to the elements of the frame. A comparative study was done by considering the behavior of reinforced concrete key elements like beam, column and slab under high temperature. The major scope such as deflection, stiffness of the frame, bending moment and shear force were observed.

Keywords Progressive collapse · Reinforced concrete frame · High temperature · Prototype frame

1   Introduction

In recent years, developed countries have emerged as centers for high-rise buildings due to land scarcity and high cost of land for construction particularly in developed cities. One of the most undesirable risk in high-rise building witnessed in recent times is progressive collapse especially when fire breaks out. The word "Progressive Collapse" in buildings is defined as the initial or local failure of the segment which propagates a series of events and gives on to the fragmentary or complete failure of the building. Fire accidents are one of the common occurrences in structures that can trigger progressive collapse. The progressive collapse occurs due to fire scenarios are called as fire-induced progressive collapse. The most common example for disaster occurrence due to fire are World Trade Center and Ronan Point Apartment. Many

M. Vishal (✉) · K. S. Satyanarayanan
Department of Civil Engineering, College of Engineering and Technology, SRM Institute of Science and Technology, SRM Nagar, Kattankulathur, Tamil Nadu 603203, India
e-mail: vm8064@srmist.edu.in

guidelines and codes had been generated following these disasters to prevent collapse
of structures from a fire accident. The most recent fire accident in a multi-storey
building was occurred in Abbco Tower (see Fig. 1). It was a 48-storey residential
complex situated in Sharjah.

Concrete elements face more physical and chemical change when it undergoes
high-temperature conditions. Temperature influences both mechanical and thermal
properties of concrete in large scale [1]. The simultaneous action of stresses from
temperature and service load gives a great impact on reinforced concrete elements.
The load-carrying capacity of the concrete reduces as the temperature gets elevated.
The knowledge is limited in understanding the fire resistance of the individual struc-
tural members and how it is being affected by its surrounding members. In general,
microcracks are formed as a result of dehydration due to high temperature and results
in spalling of concrete. The spalling effect leads a way for the fire to reach to the
reinforcements. Once the temperature reaches the reinforcements, the structure may
easily collapse due the load which is already present. This is the process which occurs
in reinforced concrete elements and this process must be studied and analyzed in
different structural configurations to understand the structural performance against
fire in better way.

2 Previous Works on Progressive Collapse

Most of the previous research on progressive collapse were carried out by numerical analysis as the experimental work requires more test arrangement which is practically not possible. Jia-liang Le et al. processed a numerical model of the reinforced concrete frame to show the potential damage zones in the structure against progressive collapse [2]. Anil Agarwal et al. studied the role of interior gravity columns of steel buildings under fire conditions [3]. Mengzhu Diao et al. performed numerical analysis for the fire-induced progressive collapse of a reinforced concrete frame structure [4]. A typical 8-storey frame structure was analyzed to check the performance of the proposed model for performing the fire-induced progressive collapse of entire structures. Xinzheng Lu et al. performed progressive collapse analysis of a high-rise reinforced concrete frame-core tube building under extreme fire condition [5]. The results exposed that, when it is subjected to multiple storey fire, the internal forces in the components are redistributed in the horizontal and vertical directions by way of the vierendeel truss mechanism, leading to a maximum increase of the axial forces in the columns. Jian Jiang et al. performed progressive collapse analysis of 3-D steel frames with concrete slabs exhibited to region fire [6]. It is found that when a single column is heated the frame does not collapse until the load ratio is increased. While heating the four columns, the corner edges of the slab gets cracked and leads to collapse. Eren et al. performed the analysis on impact of masonry infills on the progressive collapse resistance of reinforced concrete framed buildings [7]. They discussed the disadvantages in the mechanical properties of the masonry infills were modeled and developed through fiber modeling and pushdown analysis techniques.

3 Modeling and Analysis

The progressive collapse analysis in frames was performed using finite element software ABAQUS (FEA). Here, a 3-D reinforced concrete single-bay single-storey prototype frame was used for the progressive collapse analysis. Thermo-mechanical analysis was performed to find the effect of stress formed due to loads and stresses formed due to temperature on reinforced concrete frames in steady-state condition. The reinforced concrete frame was modeled as a 3-D deformable model and reinforcements are modeled as wire elements.

M30 grade of concrete and Fe 415 grade of steel was used as reinforcements and basic properties like young's modulus, Poisson's ratio, specific heat, conductivity, thermal expansion and density were adopted for various temperatures. Two frame configurations were performed in this analysis and they are reinforced concrete Bare Frame [BF] and reinforced concrete Bare Frame with Slab [BFS]. For each frame, nine temperature cases were performed from 29 to 800 °C at the interval 100 °C (29 °C, 100 °C, 200 °C…800 °C).

a) Bare Frame (BF) **b)** Bare Frame with Slab (BFS)
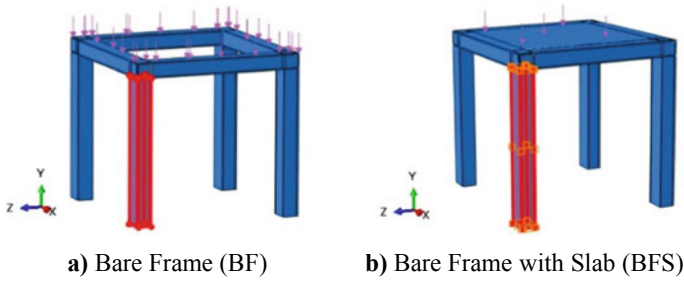
Fig. 2 Frame configurations

Table 1 Dimensions of the frame and members

Elements	Dimensions (mm)
Beam	300×300
Column	400×300
Slab thickness	150
Height of frame	3000 C/C
Length of frame (*X*-direction)	3000 C/C
Width of frame (*Z*-direction)	3000 C/C

Figure 2 shows the frame configurations used for analysis. In both the frames, one of the corner column was heated and the behavior for the rest of the whole frame was observed. The red color portion in Fig. 2 shows the heating region where the temperature was applied.

The structural loads like self-weight, imposed load, floor finishes, wall loads were assigned as per codal provisions [8, 9]. The load was converted as pressure and applied over the beam for bare frame and over beam and slab for bare frame with slab. Since it was an analytical model, the base conditions for both the frames were assigned as pinned support. Based on the mesh convergence study, the mesh size adopted for the frame elements is 50×50 mm and 100×100 mm for slab. The interaction between reinforcement and concrete was assigned as embedded and tie connection was assigned for slab. The cover thickness for the elements was assigned as per IS code [10]. The cross-sectional details and reinforcement details of the frame is listed in Tables 1 and 2.

4 Comparison of Results

After the steady-state analysis performed on various temperature conditions on both the frames, the results such as axial force, deformation and stiffness of the heated column is observed. The bending moment and shear force near the beam-column joint of the heated column is also noted.

Table 2 Reinforcement details of the members

Elements	Specifications
Beam	4 nos. of 12 mm diameter bars as main reinforcement and 8 mm diameter bars @ 200 mm C/C as stirrups
Column	4 nos. of 16 mm diameter bars as main reinforcement and 8 mm diameter bars @ 200 mm C/C as ties
Slab	12 mm diameter bars @ 200 mm C/C as main reinforcement and 12 mm diameter bars @ 200 mm C/C as secondary reinforcement

4.1 Axial Force on Heated Column

From the interpretation of results, the axial load on the heated column show some minor difference on both the frames BF and BFS. But the frame BFS takes some additional load than the frame BF. The load-carrying capacity of the frame BFS is more than the frame BF. Both the frames start to fail from 300 °C, so the load on the heated column starts to decrease. The inclusion of slab in the frame configuration increases the load-carrying capacity and it also increases the stiffness of the frame. This helps to delay the collapse of the system during progressive collapse.

The axial load reaches a maximum at 100 °C for both the frames BF and BFS. The axial load found to be 104 kN for BF and 111 kN for BFS which was 6.73% higher than that of BF. This percentage increase is due to the inclusion of slab, as slab takes some additional load. The axial load for the heated column is displayed in Table 3.

The pictorial representation of the axial load on heated column for various temperatures for both the frames are shown in Fig. 3.

Table 3 Axial load on heated column for various temperatures

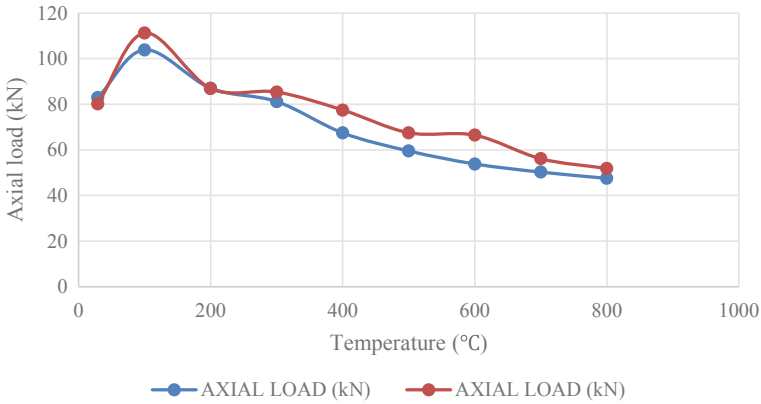| Temperature (°C)	Axial load (kN)	
	BF	BFS
29	83	80
100	104	111
200	87	87
300	81	85
400	67	77
500	60	68
600	54	66
700	50	56
800	48	52

Fig. 3 Axial load comparison between frames BF and BFS

4.2 Column Deformation

The frames undergo thermal deformation due to the temperature effect. The deformation of the heated column on both frames BF and BFS show that the bare frame undergoes more deformation than bare frame with slab. The deformation formed here is upward deformation as a result of expansion of concrete element due to temperature and it is shown in Fig. 5. Even though the load on the heated column of BF was less when compared to BFS, the deformation is more in some cases. This mainly due to the lack of restrain in the bare frame. The frame is more restrained due to the presence of slab and offers some additional stiffness to the frame. The comparison between two frames with respect to deformation of column is shown in Fig. 4.
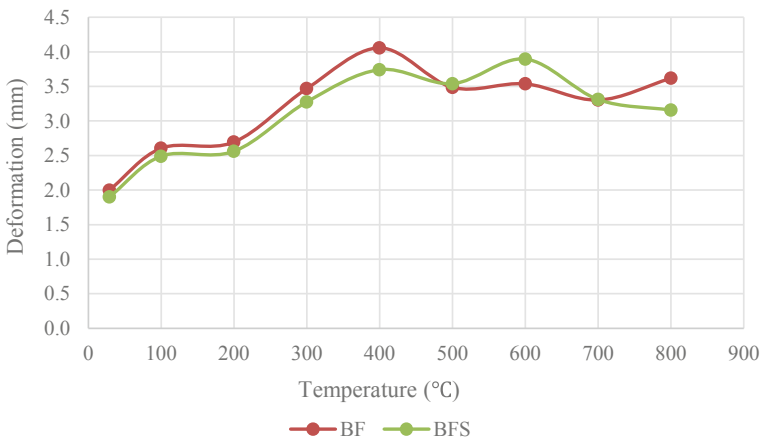
Fig. 4 Deformation of heated column for both the frames under various temperatures
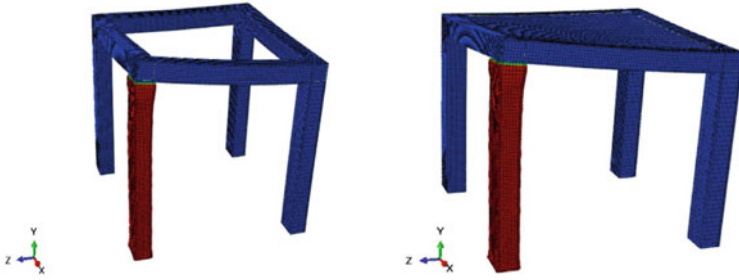
Fig. 5 Thermal expansion of frames due to high temperature

The deformation of the column reaches its peak in 400 and 600 °C. As the frames starts to fail from 300 °C, so the deformation formed near 400 °C is quite high. The deformation occurred in 400 °C is 4.1 mm for BF and 3.7 mm for BFS which is 10.81% higher than that of BFS. The percentage increase is due to the absence of slab in bare frame.

The next peak deformation occurs at 600 °C for BF is 3.5 mm and for BFS is 3.9 mm and it is due to the result of failure of slab at 600 °C. The slab tries to resist the thermal expansion for some limit but after its yield point, the slab reaches its maximum expansion limit and fails. Here the deformation of BFS is 11.42% higher than BF.

4.3 Stiffness of the Heated Column

The stiffness of the heated column is calculated based on the axial load and deformation obtained on that column. From Table 4, it is clear that the stiffness of the

Table 4 Comparison of stiffness of heated column

Temperature (°C)	Stiffness (kN/mm)	
	BF	BFS
29	41	42
100	40	41
200	32	30
300	23	26
400	17	21
500	17	19
600	15	17
700	15	17
800	12	16
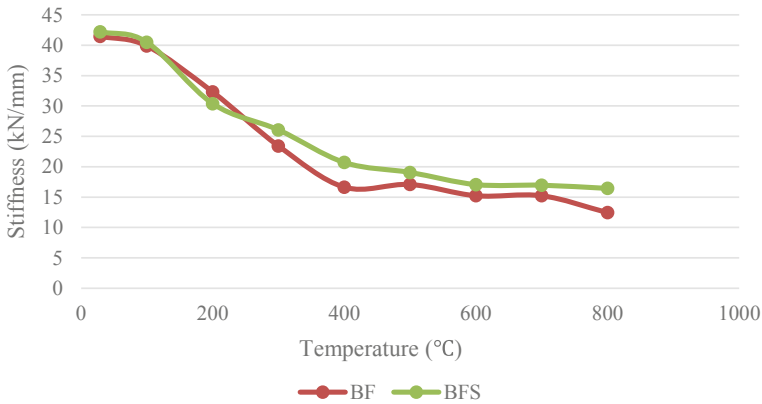
Fig. 6 Comparison between stiffness of the heated column for BF and BFS

column gets reduced as the temperature gets increased. The depletion in stiffness is owing to the change in physical properties of concrete as the temperature increases.

When comparing the frames, the stiffness of bare frame with slab is slightly higher than the bare frame. The reason behind this increase in stiffness was due to the presence of slab. The overall stability of the frame is increased due to the presence of slab. The stiffness between two frames was almost same till 200 °C. Right after the failure of the frames at 300 °C, the stiffness of the BFS is slightly higher than BF. The inclusion slab offers some internal resistance to the frame system and increases the overall structural performance.

The pictorial representation of stiffness of the heated column for the frames is shown in Fig. 6.

4.4 Bending Moment

The bending moment of frame is observed near the beam-column joint of heated column. As the temperature increases the bending moment gets increased. From Fig. 7 we can clearly see that the bending moment of the BF is more than the BFS. The reason behind the reduction in bending moment of BFS than BF is due to the effect of slab. The provision of slab acts as an additional restrain to the frame. But in BF there is no restrain in the form of slab. The comparison bending moment of BF and BFS is shown in Fig. 7.
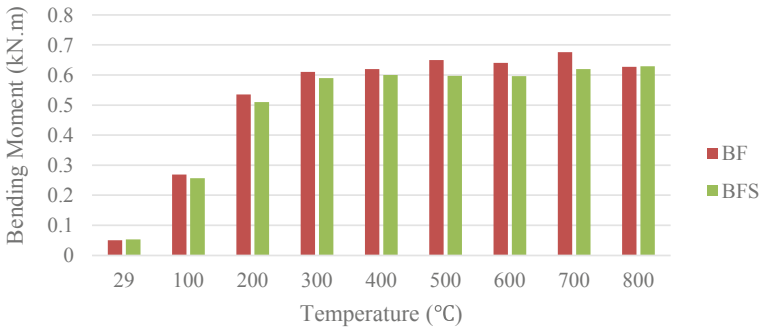
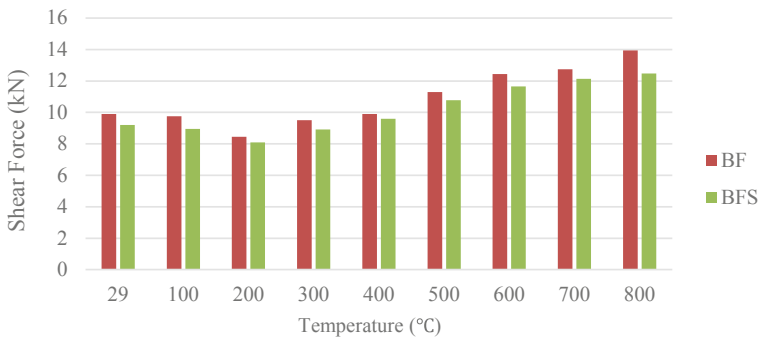**Fig. 7** Bending moment for BF and BFS

Fig. 8 Shear force for BF and BFS

4.5 Shear Force

The shear force for the frame is observed near the beam-column joint of the heated column. The shear force of the bare frame is slightly higher than the bare frame with slab. The shear force drops near the failure of frame at 300 °C and start to increase after that. After the time of failure, the shear force starts to increase as the temperature increases. The comparison shear force of BF and BFS is shown in Fig. 8.

4.6 Slab Deflection

The central deflection of the slab is measured in the frame. The inclusion of slab increases the overall stability of the frame by providing additional stiffness to the frame system. The slab fails near 600 °C and fluctuation in the deflection at the initial temperatures is due to thermal expansion column as the whole system tries to move
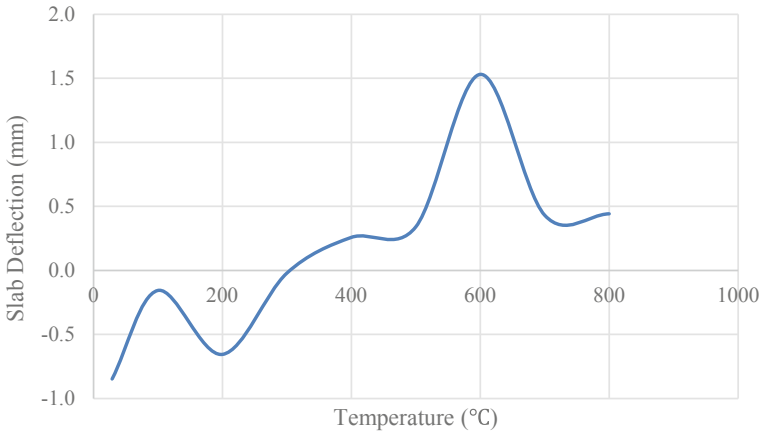
Fig. 9 Deflection of slab

upwards due to temperature effect (see Fig. 9). The peak deflection of the slab was found to be 1.53 mm.

5   Conclusion

From the above analytical results under the various temperatures of the frames BF and BFS, the following observations were made:

1. The load-carrying capacity of the frame BFS was more than frame BF.
2. The stiffness of the frame BFS was more than the frame BF and thus it increases the overall structural performance of the frame.
3. The bending moment of the frame BFS is less than the frame BF due to the presence of slab.
4. The shear force of the frame BFS was also less than the frame BF.
5. The presence of slab in BFS gives some additional rigidity to the frame even after the failure of the column and acts as an alternate load path in the frame.

So, it is clear that the inclusion slab increases the structural performance of frame and also acts as an alternate load path and helps in redistributing the load during the collapse. This might help the structures from preventing the progressive collapse to some extent. So, to improve the structural performance of the frame structures by providing some alternate load path to the frame structure to prevent the progressive collapse.

References

1. Le J, Desharnais M, Xue B, Dai S, Du H (2015) A two-scale computational model for thermo-mechanical analysis of reinforced concrete frames. Eng Struct 105:137–151. https://doi.org/10.1016/j.engstruct.2015.09.041
2. Le J, Xue B (2014) Probabilistic analysis of reinforced concrete frame structures against progressive collapse. Eng Struct 76:313–323. https://doi.org/10.1016/j.engstruct.2014.07.016
3. Agarwal A, Varma AH (2014) Fire induced progressive collapse of steel building structures: the role of interior gravity columns. Eng Struct 58:129–140. https://doi.org/10.1016/j.engstruct.2013.09.020
4. Qian L, Li Y, Diao M, Guan H, Lu X (2020) Experimental and computational assessments of progressive collapse resistance of reinforced concrete planar frames subjected to penultimate column removal scenario. J Perform Constr Facil 34(3):1–10. https://doi.org/10.1061/(ASCE)CF.1943-5509.0001420
5. Li Y, Lu X, Guan H, Ying M, Yan W (2016) A case study on a fire-induced collapse accident of a reinforced concrete frame-supported masonry structure. Fire Technol 52(3):707–729. https://doi.org/10.1007/s10694-015-0491-0
6. Jiang J, Li G (2016) Progressive collapse analysis of 3D steel frames with concrete slabs exposed to localized fire. Eng Struct. https://doi.org/10.1016/j.engstruct.2016.07.041
7. Eren N, Brunesi E, Nascimbene R (2019) Influence of masonry infills on the progressive collapse resistance of reinforced concrete framed buildings. Eng Struct 178(March 2018):375–394. https://doi.org/10.1016/j.engstruct.2018.10.056
8. IS 875:1983 Code of practice for design loads (other than earthquake) for building and structure—Part-1, Dead load. Bureau of Indian Standards, New Delhi
9. IS 875:1983 Code of practice for design loads (other than earthquake) for building and structure—Part-2, Imposed load. Bureau of Indian Standards, New Delhi
10. IS 456:2000 Plain and reinforcement concrete code of practice. Bureau of Indian Standards, New Delhi

Study on Fatigue Response of Concrete and Its Effect on Life-Cycle Behavior of Concrete Structures

Nikul Vadher, Vimal Panara, Vivek Trivedi, Mahesh Mungule, and Kannan K. R. Iyer

Abstract   The life-cycle performance of concrete structures is significantly affected by fatigue response of concrete under cyclic or repetitive loading conditions. Different structures such as bridges, buildings and industrial structures, are subjected to cyclic loading, at different stress levels. The deterioration of the structure and its maintenance requirements would depend on the fatigue effects induced in the material under cyclic loading. In this context, the present study evaluates the fatigue response of M40 concrete at different stress levels under cyclic loading. Efforts are also made to compare the performance of conventional concrete (M40) with high strength concrete (M70). Low frequency cyclic loading has been performed on cylindrical specimen of M40 concrete at three different stress levels, viz., 60, 75 and 90% of σ_c, where σ_c is the compressive strength of cylindrical specimen. The response of M40 and M70 concrete has also been compared at 75% stress levels. From the study, it can be inferred that the fatigue life of concrete is inversely proportional to the stress level for cyclic loading. As stress level reduces, the failure is observed to be more brittle in nature. For the same stress level, high strength concrete (M70) survives lower number of cycles and exhibits relatively brittle failure as compared to M40 concrete. It can be concluded from the study that based on fatigue response of concrete, degradation in its properties and residual strength for further life can be evaluated.

Keywords Fatigue · Concrete structures · Stiffness degradation · Life cycle · Stress–strain response · Cyclic loading

N. Vadher · V. Panara · V. Trivedi · M. Mungule · K. K. R. Iyer (✉)
Department of Civil Engineering, Institute of Infrastructure, Technology, Research and Management, Ahmedabad, India
e-mail: kannaniyer@iitram.ac.in

M. Mungule
e-mail: maheshmungule@iitram.ac.in

1   Introduction

Numerous internal flaws exist in concrete which trigger the formation of cracks during fatigue loading [11] and may lead to its failure. Assessment of fatigue behavior of concrete is important for flyovers, tall structures, machine foundations and airport pavement, where loads are repetitively applied [7]. Failure of such structures may happen under loads that are much lower than the static capacity of the material. Failure of concrete under fatigue is distinctively different from that under static loading. Fatigue failure is generally brittle with little visible signs to reflect the accumulated damage. Depending on the load applied, the fatigue behavior is identified as low cycle fatigue and high cycle fatigue. Low cycle fatigue represents fatigue under repetitive loading at low stress amplitude and is commonly encountered for road, railway bridges and industrial buildings [1]. Under low cycle fatigue, the process of damage accumulation is slow allowing the material to withstand large number of load cycles; however, formation of cracks may be observed in structures subjected to low cycle fatigue [1], and failure would occur as the cracking propagates under fatigue loading. On the other hand, high cycle fatigue represents repetitive loading with high stress amplitude, wherein with each cycle of loading, the accumulated damage increases resulting in failure at lower number of cycles. Airport pavements are typical examples of high cycle fatigue induced due to landing and takeoff of aircrafts.

Under the action of fatigue loads, concrete experiences microstructural changes that results in damage [8]. Isojeh et al. [6] reported that there are mainly 3 stages of fatigue failure: (i) initiation, (ii) propagation; (iii) final rupture. The damage evolves in concrete with each loading cycle and can be measured through deformation parameters namely accumulated strain, residual strain, stiffness degradation, dissipated energy per cycle, crack initiation and propagation [2]. An experimental investigation is often required to understand evolution of these parameters and study their dependence on number of cycles or the stress ratio.

Murdock [9] reported that the fatigue limit for loading would be approximately 50% of the static strength of concrete. Further, the number of fatigue cycles prior to failure is inversely proportional to the frequency of loading and intermittent loading is noted to increase the fatigue life of concrete. Another study evaluated the effect of fatigue response of plain and fiber reinforced concrete [10]. At lower stress levels, fibers are observed to contribute to higher dissipation of energy than at higher stress levels. Higher beneficial effect of polypropylene fibers was observed at lower stress levels, and the steel fibers were observed to be more effective than polypropylene fibers for fiber volume up to 1%. Studies on fatigue response of concrete with recycled aggregates indicates that the stiffness degrades more rapidly with increase in the recycled aggregate content at constant water to cement ratio [4]. Choo et al. [3] proposed a general analytical approach for simulation of low cycle fatigue behavior of reinforced concrete beams and for prediction of number of cycles of loading to failure. It was suggested that the proposed approach can be improved by relating

the post yielding fatigue strain of the reinforcement bar with the number of fatigue cycles.

Earlier studies have noted that the fatigue strain of high strength concrete would be smaller than that of low strength concrete [12], however, the rate of fatigue strain increment of high strength concrete is greater than that of low strength concrete [7]. Nowadays, high strength concrete is being utilized in structures such as bridges, machine foundations, airport pavements, etc. and it would be necessary to understand the response of high strength concrete under fatigue loading. In this direction, the present study attempts to understand the effect of low cycle fatigue loading on response of conventional and high strength concrete.

2 Experimental Details

In the present study, low cycle fatigue studies have been carried out on two different grades of concrete, viz., M40 and M70 grades. The proportion of cement: sand: coarse aggregate was finalized as 1:1.32:2.3 and 1:0.63:1.74 for M40 and M70 concrete respectively. The water to cement ratio was 0.4 and 0.26 for M40 and M70 concrete respectively. 0.5% plasticizer was utilized for M40 concrete, and the slump value was observed as 93 mm. For M70 concrete, 2% plasticizer was required along with 15% metakaolin to achieve the desired workability and strength, while the aggregates between 10 and 20 mm were restricted to 60%, and 40% aggregates were less than 10 mm size, and the slump value was noted at 75 mm. 53 grade OPC cement and zone I sand were used for both grades of concrete. The average compressive strength (cube) for M40 and M70 concrete were 49.21 MPa and 86.33 MPa, respectively. It may be noted that although the average cube compressive strength for high strength concrete was somewhat higher than 80 MPa, considering the observed standard deviation and the requirements stated in IS 456 [5], the concrete has been treated at M70 for computing the 75% peak stress level value (42 MPa). The stress levels for M40 concrete are considered as 60% (19.2 MPa), 75% (24 MPa) and 90% (28.8 MPa) of cylindrical compressive strength (32 MPa), where the cylindrical compressive strength is taken as 80% of designed cube strength (40 MPa). For comparison of high strength concrete with M40 concrete, the M70 concrete has been studied under low frequency cyclic loading at 75% stress level of the cylindrical compressive strength. It may be noted that to represent discontinuous cyclic loading on structures (viz., repeated loading during peak hours and low repetitions during off peak hours), the loading was applied in sets of 50/100 cycles with some waiting period.

3 Results and Discussion

The typical compressive strength-displacement response of M40 concrete at 90% stress level is shown in Fig. 1. It has been observed that the average number of
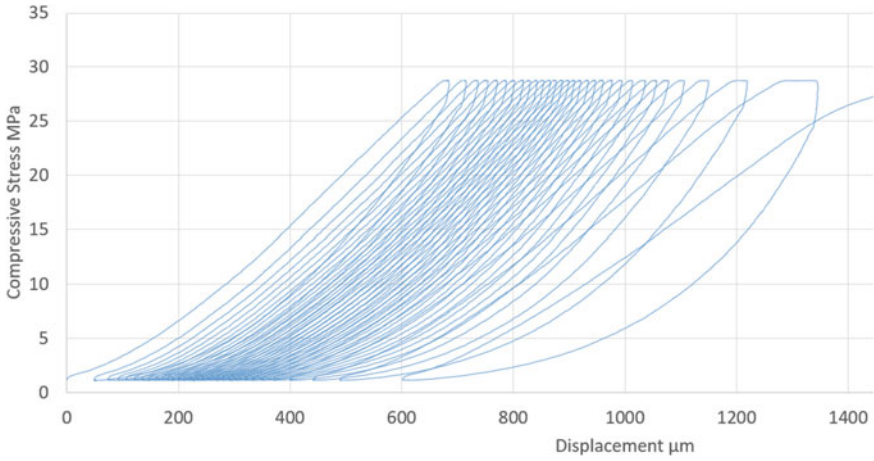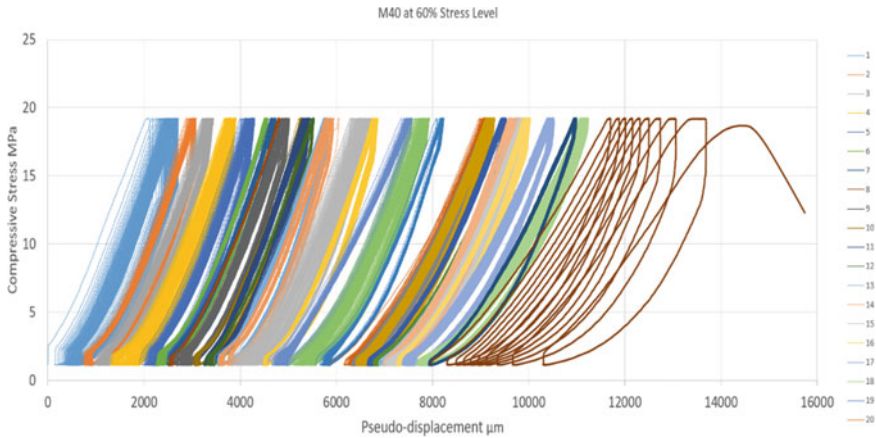
Fig. 1 Typical compressive stress-displacement response at 90% stress level for M40 concrete

cycles before failure for three specimens was about 29 cycles, while the specimen survived failure for almost twice the number of cycles at which the crack initiation was observed. Figure 2 depicts the typical compressive strength-displacement response of M40 concrete at 75% stress level. The specimen survived an average of 526 cycles before fatigue failure. In Fig. 2 (and also in Figs. 3 and 7), the numbers in the legend represents each set of load cycles (50/100 cycles). After each load cycle, the specimen was allowed to relax for a period ranging from 12 to 24 h. This allows the specimen to undergo elastic rebound, a behavior similar to that experienced by concrete in bridge structures. In order to clearly understand the strain accumulation, the deformation is represented by pseudo displacement (which is the combined
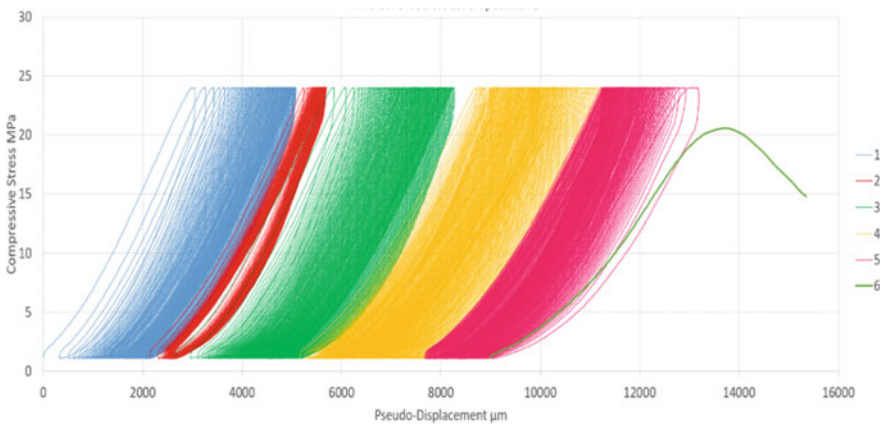
Fig. 2 Compressive stress versus pseudo displacement response at 75% stress level for M40 concrete

Fig. 3 Compressive stress versus pseudo displacement response at 60% stress level for M40 concrete

displacement of all previous cycles at a given point of time). The displacement values for each set of cycles (50/100 cycles) have been positioned at the end of displacement values of previous set of load cycles, so as to clearly depict the change in response of the material over large number of load cycles. The response for M40 concrete studied at 60% stress level under cyclic loading is presented in Fig. 3. The specimen survived 3059 cycles (only one specimen could be tested due to long time duration of low frequency cyclic loading). It can be noted that number of cycles before failure increases significantly at lower stress levels. This indicates that the accumulation of fatigue strain is slower at low stress levels and significantly higher at high stress levels (close to capacity of member). Further, from Figs. 1, 2 and 3, it is noted that prior to failure, the displacement increases significantly, for all stress levels.

Figures 4, 5 and 6, depicts the degradation in loading and unloading modulus with number of cycles of loading. Loading and unloading modulus are computed as slope of the linear portion of loading and unloading curves, respectively. It can be clearly noted that at high stress levels (90%), the reduction in stiffness is not significant, while at lower stress levels (60%), the reduction in stiffness is gradual and significant. The rate of stiffness reduction for 75% stress level lies between 90 and 60% stress levels, as expected.

It has been also observed in the study that the rate of accumulation of displacement is gradual for most part of cyclic loading, however close to failure, there is sudden increase in the displacement.

In order to compare the response of high strength concrete with M40 concrete, the loading/unloading response versus number of cycles for high strength concrete has been plotted in Fig. 7. The typical specimen for high strength concrete at 75% stress level survived for 85 cycles, as against 526 cycles for M40 concrete. This clearly indicates that the response of high strength concrete is brittle in nature and the strain accumulation is much higher in high strength concrete. From Fig. 8, it can
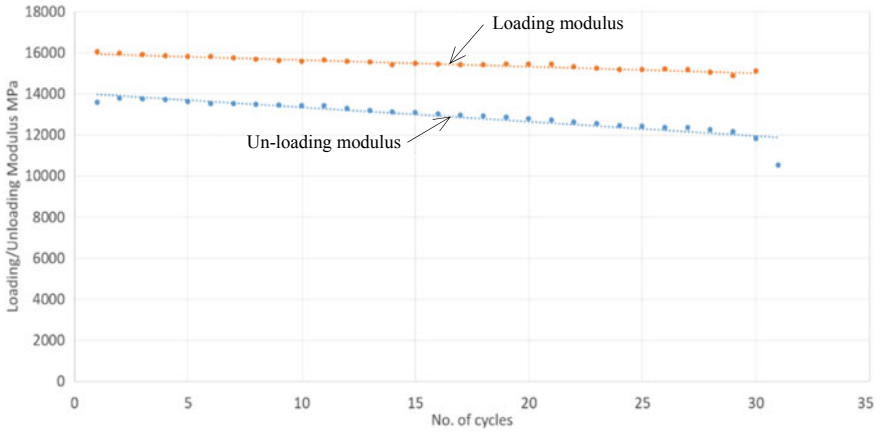
Fig. 4 Loading/unloading modulus versus number of cycles at 90% stress level for M40 concrete
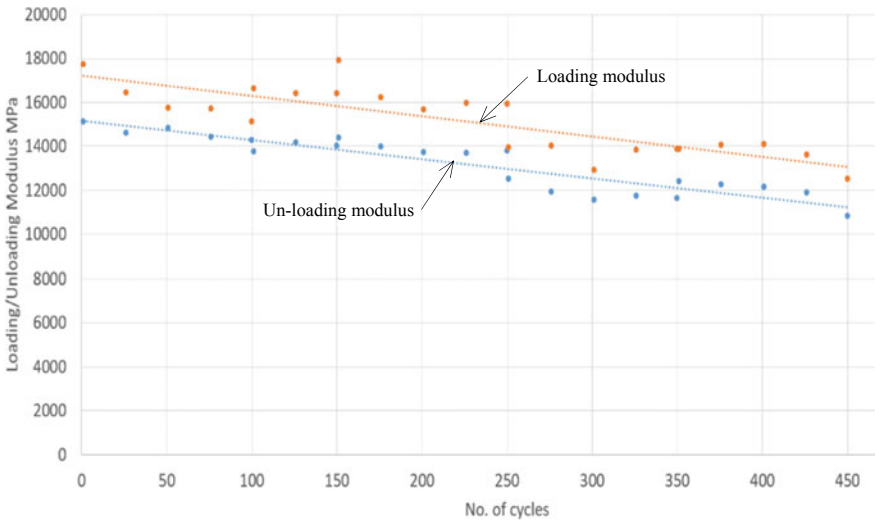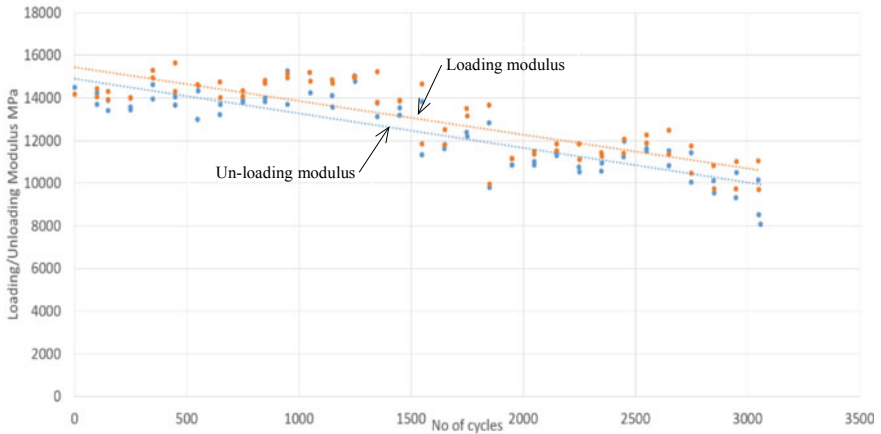

Fig. 5 Loading/unloading modulus versus number of cycles at 75% stress level for M40 concrete

be noted that the degradation in loading/unloading modulus for high strength concrete is less as compared to M40 concrete (refer Fig. 5). This indicates stiffer response of high strength concrete under cyclic loading. It has also been observed that the total accumulated displacement is lower for high strength concrete than conventional concrete, however, after few cycles, the rate of accumulation of displacement is increased. Further studies are required to understand the performance of high strength concrete at different stress levels. Moreover, the present study indicates the need to
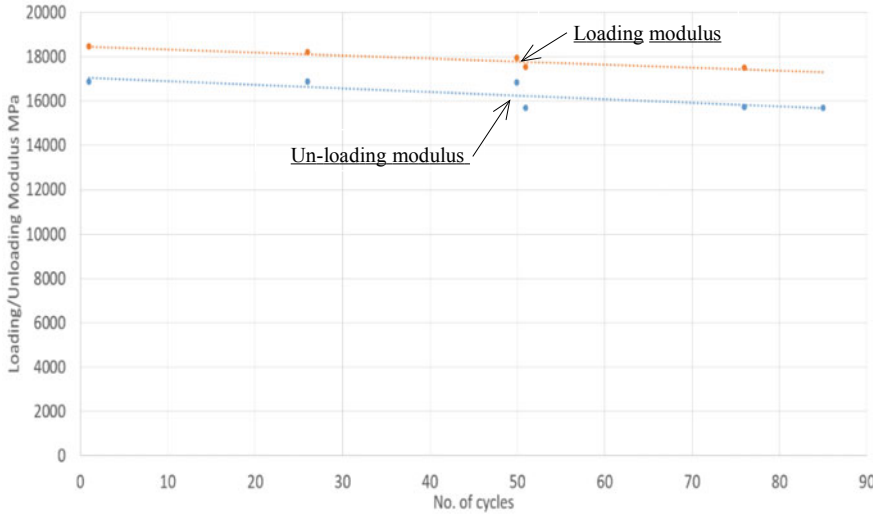
Fig. 6 Loading/unloading modulus versus number of cycles at 60% stress level for M40 concrete
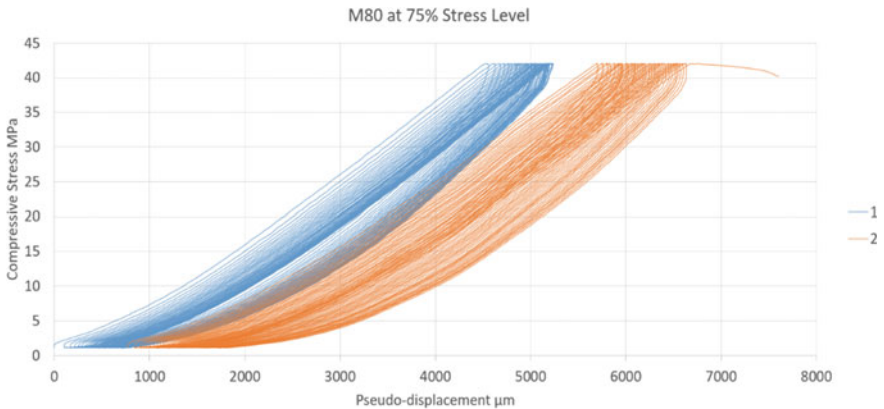

Fig. 7 Compressive stress-pseudo displacement response at 75% stress level for M70 concrete

focus on enhancing the ductility of high strength concrete for their better performance over the life cycle.

Figure 9 shows the typical failure for different specimen. From the figure, it may be noted that for M40 concrete, the extent of damage in specimen is less at lower stress levels (60%) as compared to 75 and 90% stress levels. This indicates that the damage accumulation is less when concrete is loaded at low stress levels. However, the failure has been observed to be more brittle in nature as compared to high stress levels. Further, the extent of damage for M70 grade concrete is lower than M40 concrete at 75% stress levels. The failure for M70 concrete is sudden in nature. Widespread distribution of damage in the material indicates higher energy absorption and gradual release of energy, thereby contributing to ductile response of the

Fig. 8 Loading/unloading modulus versus number of cycles at 75% stress level for M70 concrete

(a)	(b)	(c)	(d)
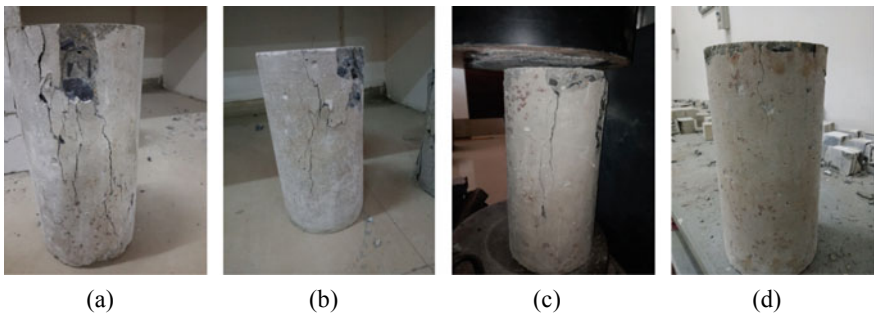
Fig. 9 Typical failure of specimen **a** 90% stress level for M40 concrete **b** 75% stress level for M40 concrete, **c** 60% stress level for M40 concrete and **d** 75% stress level for M70 concrete

material. Localization of damage on the other hand represents limited energy absorption and crack propagation occurs due to rapid energy release, thereby contributing to brittle failure of the material. In the study, it has been noted from the accumulated displacement plots and failure observations that in general that there are three stages of damages in specimen: low or internal damage during 1st stage, constant surface damage during 2nd stage and higher damage accumulation finally leading to failure.

4 Conclusions

The fatigue properties of concrete such as fatigue life and stiffness degradation have been obtaining by testing M40 grade concrete at three different stress levels (60, 75 and 90% of cylindrical strength) and M70 grade concrete at 75% stress level of cylinder strength under cyclic loading. The following conclusion can be drawn from the study:

- The stress level at cyclic loading is inversely proportional to the number of cycles prior to fatigue failure
- As stress level reduces, the failure is observed to be more sudden (brittle) in nature
- For the same stress level, higher strength concrete survives less number of cycles as compared to lower strength concrete. One possible reason could be higher stiffness and brittle nature of high strength concrete. However, this is confirmed at only 75% stress level and needs to be verified at other stress levels also
- M70 concrete fails suddenly without giving any prior warning, in contrast to M40 concrete which shows initiation of damage prior to failure
- The observed damage of specimen in this study can be divided into three segments. The first segment represents slow and gradual increment in damage. The second stage damage propagation is stable propagation and varies linearly with the number of loading cycles. The final stage of damage propagation represents sudden increment in rate of damage propagation, creating instability in the material, leading to its failure.

References

1. Ahsan R (2013) Fatigue in concrete structures. BSRM seminar on fatigue properties of constructional steel
2. Antrim JD (1967) The mechanism of fatigue in cement paste and plain concrete, symposium on concrete strength. DC, USA, Washington
3. Choo FJ, Choi Y, Kwon S, Park K, Yoo S (2018) Low-cycle flexural fatigue behavior of concrete beam reinforced with hybrid FRP-steel rebar. Adv Civ Eng
4. Gordon PM (2011) Low cycle fatigue behavior of concrete with recycled concrete aggregates. Master's thesis presented to the Faculty of California Polytechnic State University, San Luis Obispo
5. IS 456 (2000) Plain and reinforced concrete—code of practice. Bureau of Indian Standards, New Delhi, India
6. Isojeh B, El-Zeghayar M, Vecchio FJ (2017) Concrete damage under fatigue loading in uniaxial compression. Mater J Am Concr J 114(2):225–235
7. Kim JK, Kim YY (1996) Experimental study of the fatigue behaviour of high strength concrete. Cem Concr Res 26(10):1513–1523
8. Mu B, Subramaniam KV, Shah SP (2004) Failure mechanism of concrete under fatigue compressive load. J Mater Civ Eng ASCE 16(6)
9. Murdock J (2007) A critical review of research on fatigue of plain concrete. University of Illinois at Urbana-Champaign Library Large-scale Digitization Project

10. Paskova T, Meyer C (1997) Low-cycle fatigue of plain and fiber-reinforced concrete. Mater J 94(4)
11. Renju D, Keerthy M (2020) A review on fatigue life prediction of plain concrete. IOP Conf Ser Mater Sci Eng 936
12. Vicente MA, Mínguez J, Martínez JA, González DC (2016) High-performance concrete and fiber-reinforced high-performance concrete under fatigue efforts

Study on Behaviour of Diagrid System on a G+36 High Raised Building

V. S. Nagendra and A. Sofi

Abstract Diagrid structures are extensively used in tall buildings for their innovative architectural view and achievably efficient mechanism to limit displacements due to lateral loads. The present study is based on study on the behaviour of a diagrid structural system on G+36 high raised building, using CSI-ETABS software. The diagrid modelling with varying angles are adopted to understand the optimum inclination of diagrid elements. The study deals with the performance characteristics of the building under seismic activity evaluated by response spectrum analysis and nonlinear static pushover analysis. Seismic response of the models was studied in terms of storey displacement, base shear and performance points of the models. The nonlinearity was achieved using plastic hinges. A comparative study based on response spectrum analysis and nonlinear static pushover analysis was deduced.

Keywords ETABS · Diagrid structure · Optimum angle · Pushover analysis · Performance point

1   Introduction

The rapid growths of urban lifestyle and limited space have considerably affected the development of city. Increase in metropolitan type lifestyle and rapid increase of land cost, the buildings have emerged tall into the sky. In fact, as building height increases, the lateral forces have a predominant effect on the structure [1]. Lateral resisting such as shear walls, braced frames, outrigged truss systems is very popular. Diagrid system is widely adopted for innovative architectural aspect in high raised building, improving the aesthetic view. They also provide a high lateral stiffness achieving lesser deflection in structural aspects. The modularity of the diagrids made development is the complex-shaped structures in varying forms [2]. Diagrid is a system

V. S. Nagendra (✉)
Tech Structural Engineering, Vellore Institute of Technology, Vellore 632014, India
e-mail: nagendrav.s2019@vitstudent.ac.in

A. Sofi
Vellore Institute of Technology, Vellore 632014, India

of grid-work or framework composed of diagonally intersected beams. Some of the famous outstanding buildings constructed on diagrid system (see Fig. 1) are Hearst Tower in New York, Swiss Re Tower in London and Tornado Tower in Qatar [3]. The diagrid is generally composed of two diagonal brace members and horizontally aligned rings, together make up a triangular geometrical pattern, which makes up efficient structural system for a high raised building. The distribution of loads in a diagrid is similar to that of a truss system, where loads applied at the nodes are transferred by each member through axial forces. But unlike trusses, in the analysis of diagrid systems, even non-nodal loads are included which include shear forces. The loads acting on structured are taken by the diagrid framework and distributed to earth (see Fig. 2) [4]. This paper study is on understanding the structural behaviour of the high raised building where the vertical columns are removed and mega-diagrid framework adopted to carry the gravity and lateral loads such as winds load and seismic loads.

(a)   (b)   (c)

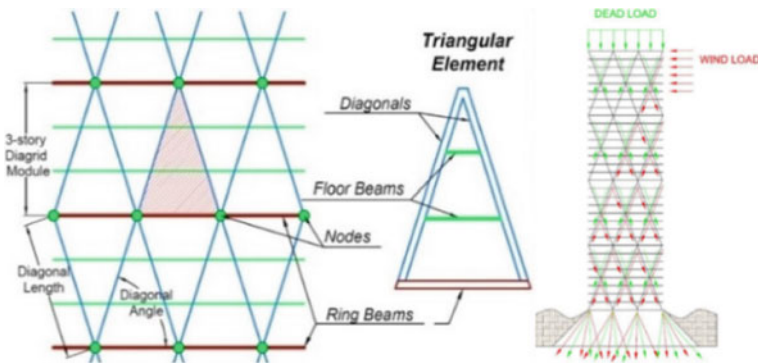**Fig. 1** **a** Hearst Tower, **b** Swiss Re Tower, **c** Tornado Tower [3]

Fig. 2 Diagrid system nomenclature and load distribution in diagrid framework [5]

Table 1 Model description

S. no.	Model	Diagrid module	Diagrid angle	Diagrid member
1	T1	Two storey module	56.30°	Floor G to 24
2	T2	Three storey module	66.03°	CHS 508*16 and floor 24–36
3	T3	Four storey module	71.56°	CHS 508*10
4	T4	Six storey module	77.47°	

Table 2 Model specification

S. no.	Specifications/materials	Dimensions
1	Ht. of basement and floors	3000 mm
2	Beams	ISMB 500, ISWB 500, ISWB 550
3	Thickness of slab	150 mm
4	Thickness of shear wall	350 mm
5	Grade of concrete	M30
6	Grade of steel	Fe500
7	Support condition	Fixed

2 Model Specifications

The present study is done on G+36 high raised building, modelled using CSI-ETABS software. Four towers of varying diagrid angles are modelled, naming T1, T2, T3 and T4, using software. The dead load, live load and wind are considered as per IS 875-Part I, II, III codal standards [6]. The seismic lateral forces are considered as per IS 1893:2016 code [7]. Table 1 gives description of modelled building with their respective diagrid angle, and Table 2 refers to the specifications of the modelled building (Figs. 3, 4 and 5).

3 Seismic Evaluation

For seismic performance evaluation of the models in ETABS, nonlinear pushover analysis and response spectrum method are adopted. The seismic parameters considered are described in Table 3, as per IS 1893:2016 code. The response reduction factor is considered to be five for all structural steel members, including the diagrid framework [8].
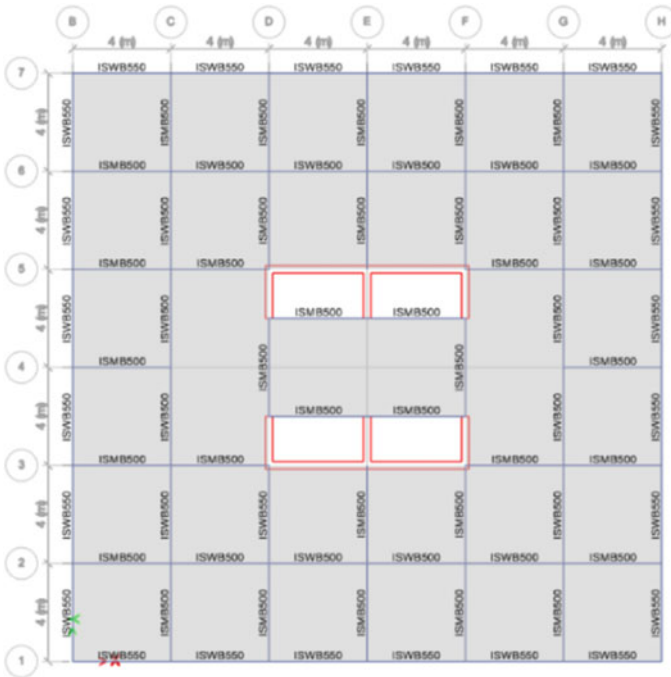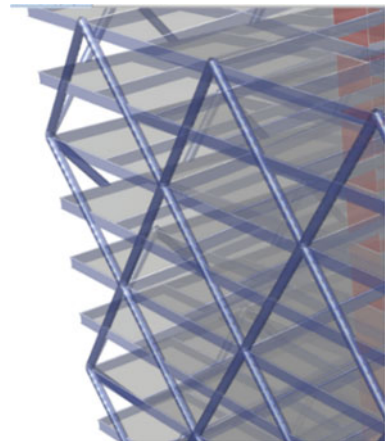
Fig. 3 Plan view of the building

Fig. 4. 3D-rendered view of
T1 building

3.1 Pushover Method

It is a nonlinear static method to evaluate the seismic deformations in structure, when
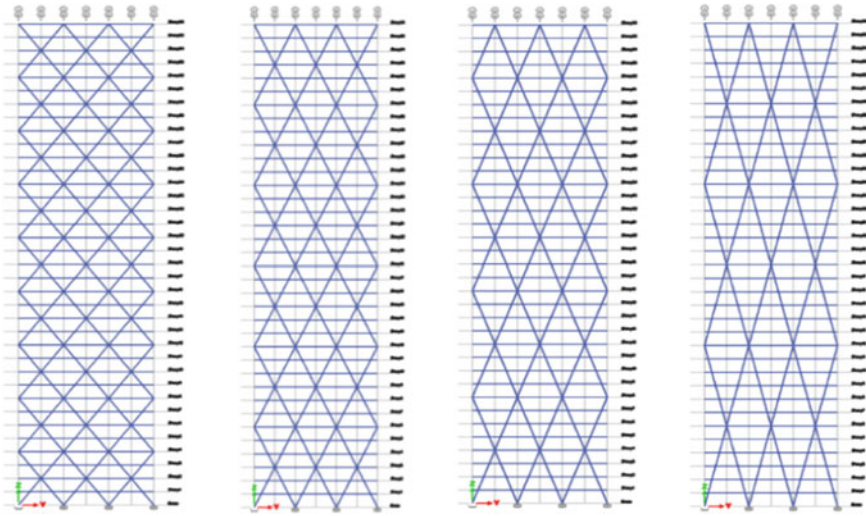subjected to simultaneous action of gravity loads and displacement-controlled lateral

Fig. 5 Elevation view of G+36, naming T1, T2, T3, T4 (from left to right)

Table 3 Seismic parameters

S. no.	Parameters	Magnitude/value
1	Zone factor	0.16 (III)
2	Soil type	II
3	Importance factor	1.2
4	Response factor	5

loads. For nonlinearity in structural members, plastic hinges are provided as per ATC 40 to understand the inelastic behaviour until members undergo ultimate failure [9]. Pushover analysis develops a pushover curve or the capacity curve and represents the relationship between base shear and roof displacement in the structure (see Fig. 6). A graph can be plotted with base shear versus the deformation at the roof top of the structure. The displacement approximate expected to be the maximum response of the structure due to the earthquake ground motion. The various performance levels in the range of immediate occupancy (IO) to life safety (LS) to collapse prevention (CP), and when a hinge reaches point C, hinge being no longer capable to withstand the load, drops off the load, reaching to a point D [10].

3.2 Response Spectrum Method

This is method adopted to evaluate the response of the structure to the earthquake. It can be referred as a plot of peak/steady-state response of displacement or velocity

Fig. 6 Idealized
force-deformation curve [10]
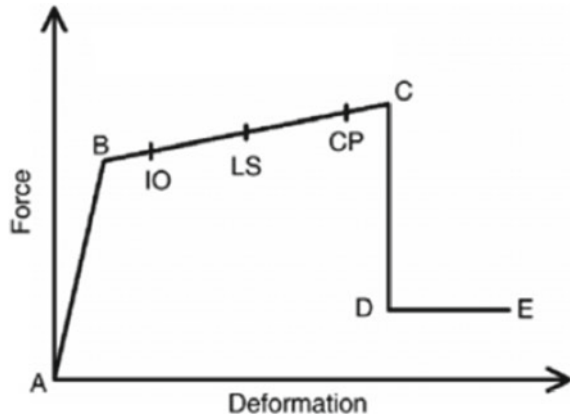
or accelerations, of varying frequencies against the ground motion at the base of the structure. The resulting plotted curves are used to understand the maximum response of structure to that specified earthquake ground motion with its time period [11]. Using these curves, a concept of acceleration displacement response spectra can be adopted, which allow to merge the capacity curve and the response spectrum curves, under Cartesian transformation to evaluate the performance of structure using performance point.

3.3 Performance Point

The load is incremented at each stage and checked at the time until the condition called the 'performance point' is reached. From the results of pushover analysis and response spectrum method analysis, by implementing acceleration displacement response spectrum, which is obtained by the superimposition of base shear (V_b) versus top roof displacement ($\Delta_{\text{roof top}}$) with the spectral acceleration (Sa) versus spectral displacement (Sd), the point of intersection where the capacity curve and demand spectrum curve is found out. This intersection will result in the performance point of the structure (see Fig. 7).

4   Results and Discussion

The four models are analysed with ETABS software, and the behaviour of the structure is observed by evaluating the parameters such as storey displacement, pushover curve and performance point of structure.
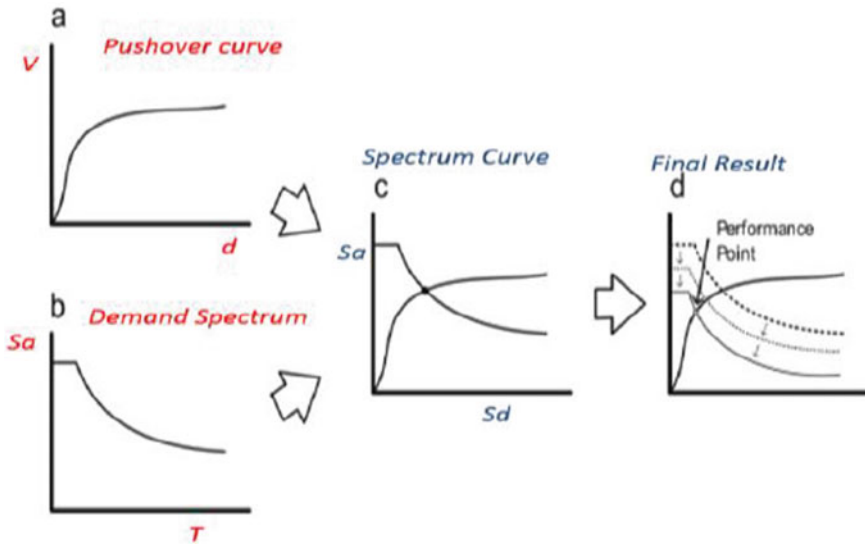
Fig. 7 Performance point obtained by capacity spectrum method [12]

4.1 Storey Displacement

The variation of storey displacement for T1, T2, T3 and T4 is plotted as shown in Fig. 8. It is been observed that the building T4 has maximum storey displacement
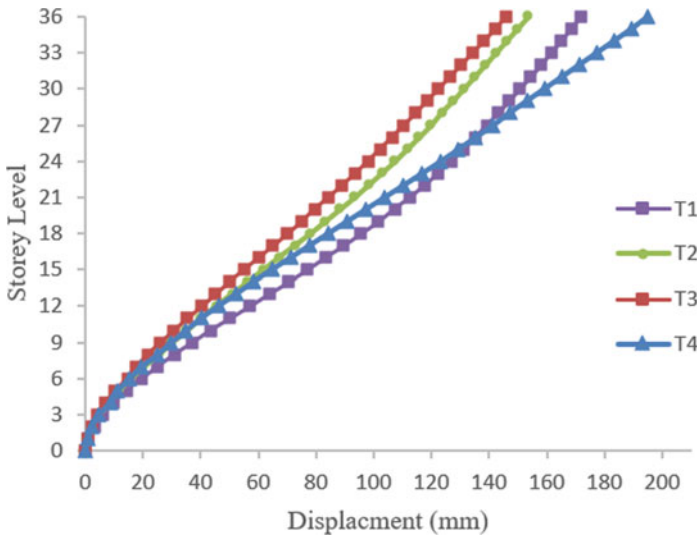

Fig. 8 Variation of storey displacement of buildings T1, T2, T3 and T4

with 195.17 mm, and T3 has least topmost storey displacement with 145.94 mm. Based on this considering buildings T2 and T3 displacement profiles, the optimum angle for a diagrid can be decided to be around 66°–72°.

4.2 Pushover Curve

Pushover analysis is represented in terms of pushover curve for buildings T1, T2, T3 and T4 as in Fig. 9. This curve is obtained by plot between base shear (V_b) versus displacement at roof top ($\Delta_{\text{roof top}}$).

- The maximum base shear in T1 pushover curve was observed to be 64,338.87 kN at displacement of 691.12 mm
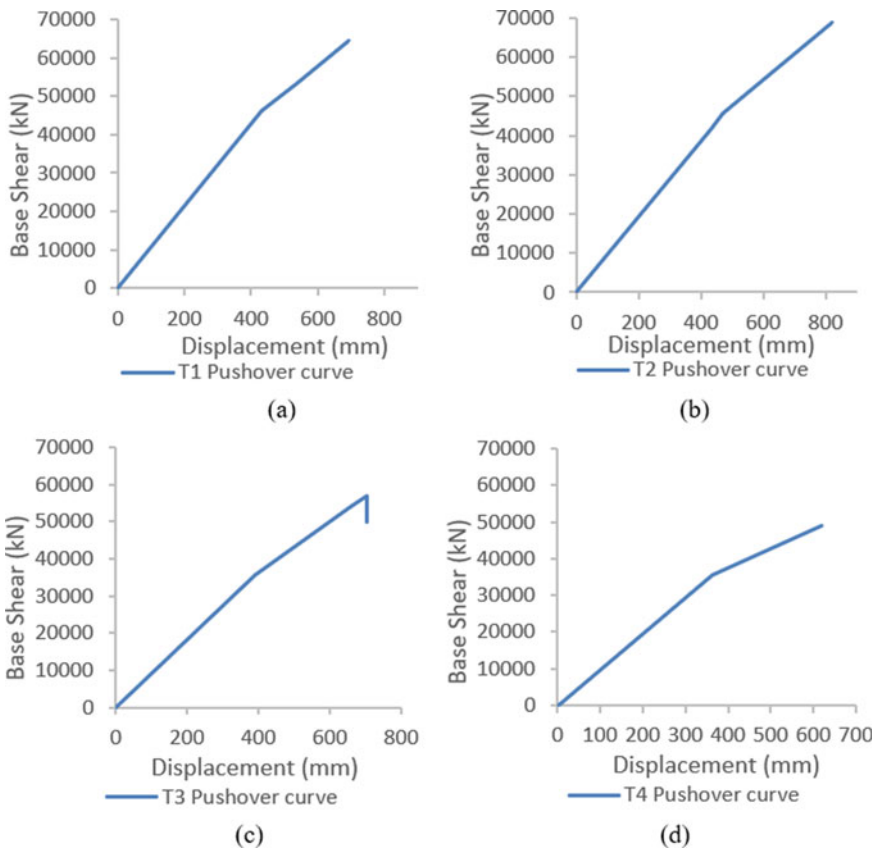
Fig. 9 **a** Pushover curve for building T1, **b** Pushover curve for building T2, **c** Pushover curve for building T3 and **d** Pushover curve for building T4

- The maximum base shear in T2 pushover curve was observed to be 68,713.26 kN at displacement of 821.42 mm
- The maximum base shear in T3 pushover curve was observed to be 57,012.14 kN at displacement of 702.72 mm
- The maximum base shear in T4 pushover curve was observed to be 49,213.13 kN at displacement of 617.57 mm.
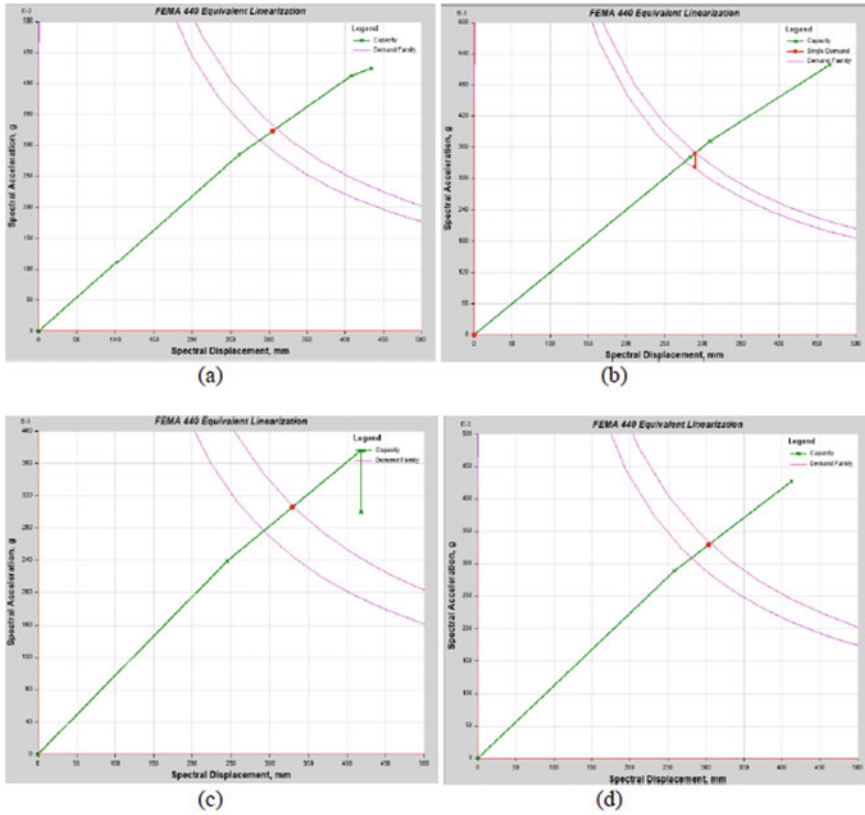
4.3 Performance Point

- For building T1, plot in which the Sa and Sd at performance point are 0.3236 g and 305.493 mm, and the corresponding V_b and $\Delta_{\text{roof top}}$ are 41,108.903 kN and 459.67 mm.
- For building T2, plot in which the Sa and Sd at performance point are 0.3535 g and 336.36 mm, and the corresponding V_b and $\Delta_{\text{roof top}}$ are 46,321.012 kN and 462.71 mm.
- For building T3, plot in which the Sa and Sd at performance point are 0.305 g and 329.44 mm, and the corresponding V_b and $\Delta_{\text{roof top}}$ are 39,096.054 kN and 487.44 mm.
- For building T4, plot in which the Sa and Sd at performance point are 0.328 g and 302.95 mm, and the corresponding V_b and $\Delta_{\text{roof top}}$ are 40,725.854 kN and 455.86 mm (Fig. 10).

5 Conclusions

Based on the structural performance of the G+36 storey tall building with a varying angle of triangular diagrid framework system, the following conclusions were drawn:

1. Building T3 having diagrid framework angle 71.56° has the least storey displacement. Buildings T2, T1 and T4 have 5.29, 17.85 and 33.75% more displacement with respect to building T3.
2. Observing the storey displacement profile, the optimum angle of diagrid framework is approximately between 66° and 72° for a building can be adopted, such that lateral displacements of structure are minimized.
3. From the pushover curve, we can deduce that T2 building can withstand up to a base shear of 68,713.26 kN which is 5.3%, 17.85% and 39.62% more than the buildings T1, T3 and T4, respectively.
4. Based on the performance point obtained by the seismic analysis, the building T2 has shown the best seismic performance followed with T3 having a better seismic performance compared to T1 and T4 buildings.

Fig. 10 **a** Performance point for building T1, **b** Performance point for building T2, **c** Performance point for building T3 and **d** Performance point for building T4

References

1. Moon KS (2011) Diagrid structures for Complex-Shaped Tall Buildings. In: The Twelfth East Asia-Pacific conference on structural engineering and construction. Procedia Eng 14:1343–1350
2. Rujhan A et al (2019) Analysis and design of high-rise building using diagrid structural system. In: International conference on emerging trends in engineering, pp 195–205
3. Lacidogna G et al (2019) A matrix-based method for the structural analysis of diagrid systems. Eng Struct 193:340–352
4. Li ZH, Teng J et al (2015) Analysis and verification on the effect of bending X-shaped joints on the internal force distribution of diagrid tube structures. China Build Sci 31:86–93
5. Asadi E et al (2018) Seismic performance assessment and loss estimation of steel diagrid structures. J Struct Eng 144(10)
6. IS 875: Part I, II, III-Code of practice of Design loads (Dead load, Live load, Wind Load)
7. IS 1893: 2016—Indian Standard Criteria for Earthquake Resistant Design of Structures
8. Adeli H et al (2018) Seismic performance factors for low- to mid-rise steel diagrid structural systems. Struct Des Tall Spec Build 27(15)
9. ATC 40-Seismic evaluation and retrofitting of concrete buildings

10. Kim J, Lee Y-H (2019) Seismic performance evaluation of diagrid system buildings. Struct Des Tall Spec Build 21:736–749
11. Ashour SA et al (2014) Application of pushover analysis for evaluating seismic performance of RC building. Int J Eng Res Technol (IJERT) 3(1):1657–1662
12. Hakim RA, Alama MS (2013) Seismic assessment of an RC building using pushover analysis. Int J Eng Technol Dev 1(3):72–77

A Comparative Study of Flat Slab, Waffle Slab and Post-tensioned Slab Under the Action of Dynamic Loads

C. L. Mahesh Kumar and **K. G. Shwetha**

Abstract   In this modern growing twenty-first century era, we have seen a tremendous increase in construction activities which is taking place in and around and everywhere; hence, there is a demand and obvious shortage of land space for development activity to progress. So, the construction of tall tubular structures has been triggered up time and vertical development to overcome the demand for space over the year. In this paper, a study on the check of stability of the flat slab, post-tensioned slab and waffle slab has been carried out by considering the shear parameters and deflection parameters and their behaviour under the seismic static and dynamic loads. Effects on the lateral displacement, storey shear, storey stiffness, punching shear, short-term and long-term deflection have been studied through the finite element analysis softwares ETABS and SAFE.

Keywords   Flat slabs · Waffle slabs · Storey stiffness · Post-tensioned slabs

1   Introduction

In this modern fast-growing twenty-first century era, we have seen tremendous increase in construction activities which is taking place in and around and everywhere; hence, there is a demand and obvious shortage of land space for the development activity to progress, so construction of tall tubular structures has been triggered up time and over again for vertical development to overcome the demand for space over the year. To tackle this problem, there are several elements which are tried to make cost of construction work least for accommodating manpower and economical by the virtue of introducing the technique of flat slab construction which reduces dead weight of the structure. In this paper, structure with six storey 25×25 m dimension

C. L. Mahesh Kumar (✉) · K. G. Shwetha
Department of Civil Engineering, Nitte Meenakshi Institute of Technology, Yelahanka, Bangalore 560064, India
e-mail: Maheshkumar.cl@nmit.ac.in

K. G. Shwetha
e-mail: Shwetha.kg@nmit.ac.in

plan is considered. The structural models have the identical storey height of 3 m and have a uniform mass distribution over their top. The post-tensioning method is now a days increasing widely, due to its application [1]. About 60% of the land area of our country is susceptible to damaging levels of seismic hazard [2].

In the present study, the performance of flat slab, conventional slab, post-tensioned (Pt) and ribbed slab system structure subjected to various loads [3] and conditions is studied, and the behaviour of structures for the parameters like storey shear, storey displacement and drift ratio is evaluated. The performance of the various systems with respect to the shear behaviour is carried out. Also, long-term and short-term performances of the various systems for shrinkage and creep based on the deflection check can be done.

2 Methodology

2.1 Structural Parameters

In the present study, the performance and durability of flat slab, post-tensioned slab and waffle slab system for various structural loads are studied. In this paper, E-Tabs 2016 tool is used for modelling the buildings and ETABS is an analysis and designing software used in the industry. It stands for "extended three-dimensional analysis of building system". ETABS is a powerful program that can greatly enhance an engineer's analysis and design capabilities for structures. The Structural elements and parameters are shown in Tables 1 and 2.

Table 1 Structural elements properties

Structural elements	Concrete grades for all models
Column	M30
Beam	M30
Slab	M30

Table 2 Structural model parameters

Models	Column	Beam	Slab
Flat slab	C-400 × 400	B-230 × 450 (Peripheral)	Slab 150 mm Drop 250 mm
Waffle slab	C-400 × 400	B-230 × 450 with adjacent spacing of 1000 mm between two ribs	Slab 125 mm Drop 150 mm
Post-tensioned slab	C-400 × 400	B-230 × 450	Slab 100 mm Drop 150 mm

2.2 Seismic Parameters

The seismic parameters considered for the study are

Soil type $=$ II
$I =$ Importance factor $= 1.0$
$R =$ Response reduction factor $= 3.0$
$Z =$ Zone II $= 0.1$ [4].

2.3 Material Properties

Density of concrete: 25 kN/m^3
Density of brick masonry: 20 kN/m^3
Wall thickness: 200 mm.

3 Results and Discussions

3.1 Check for Punching Shear

The depth of the drop is provided by the check on behaviour of the drop to the punching shear.

The critical section for punching shear is assumed to be at a distance of depth/2 for rectangular drops (Fig. 1).

For the flat slabs, the punching shear ratio is expressed as a ratio of punching shear capacity to the shear reinforcement. The maximum ratio is estimated to be 0.868 in case of the flat slabs. The ratio of the punching shear ratio to the shear reinforcement can be increased up to a value of 1 where we get the optimum drop thickness safe in shear. The punching shear plays a major role in design of flat slabs. The Flat slab punching shear is as shown in Fig. 1. Punching shear strength of slab column connection is of importance which depends on the gravity shear ratio [5].

In waffle slabs, the beams in the either direction take up the shear forces and then transfer forces into the column [6], which is different in case of the flat slabs where the loads coming on the slab are directly transferred onto the columns through the drop [7]. In case of the ribbed slab system, some amounts of the shear forces are taken by the beams so the effect of shear on the drop is minimized, and one can expect the drop depth to reduce. A Waffle Slab is a type of building material that has two directional reinforcement on the outside of the material, giving it the shape of the pockets on a waffle [8] waffle slab punching shear is as shown in Fig. 2.

In the present work, the drop thickness is assumed to be 500 mm compared to that of the flat slab system and it is found that the maximum ratio of punching shear
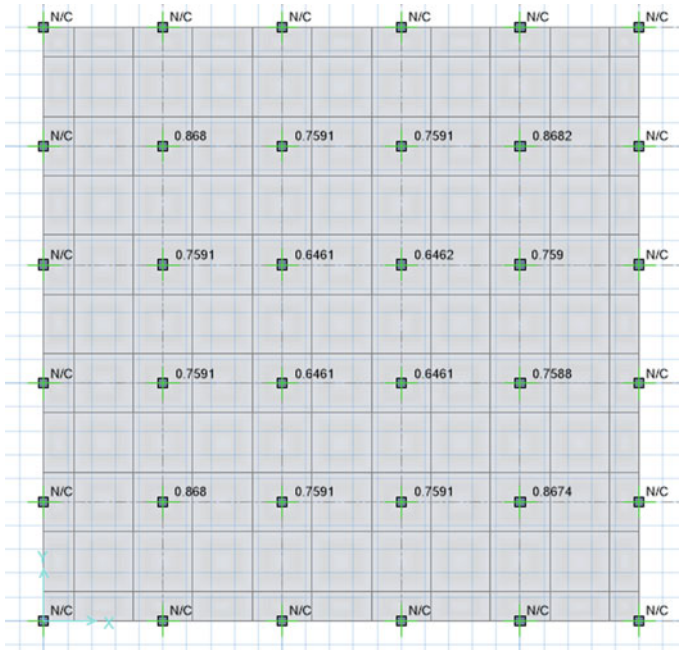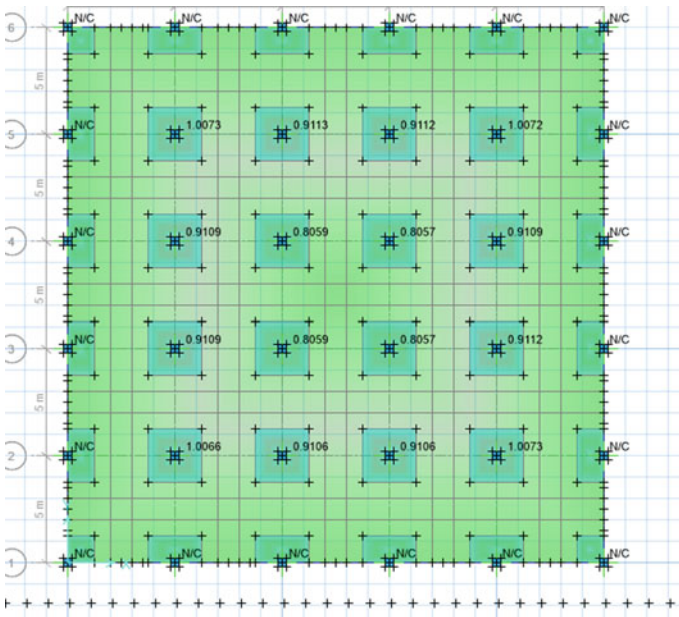
Fig. 1 Flat slab punching shear

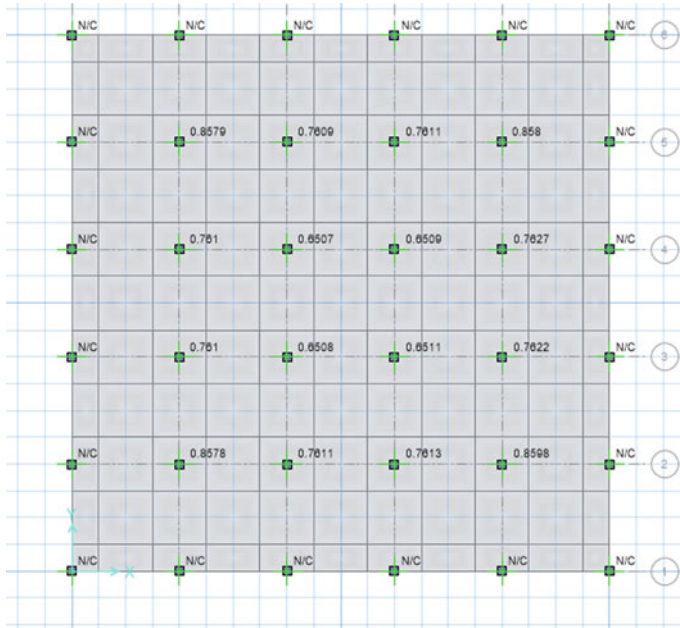**Fig. 2** Waffle slab punching shear

Fig. 3 Post-tensioned flat slab punching shear ratio

to the shear reinforcement provided is 0.5879. The Post tensioned flat slab punching shear is shown in Fig. 3.

3.2 Long-Term and Short-Term Defections of Flat Slab

Short-term deflection in the slab which is expected to occur is 4.81 mm, and the long-term deflection is 14.28 mm is as shown in Figs. 4 and 5.

3.3 Long-Term and Short-Term Defections of Waffle Slab

The short-term deflection is 2.64 mm and long-term 8.52 mm which is less compared to the flat slab system which are shown in Figs. 6, 7 and 8 and Table 3.
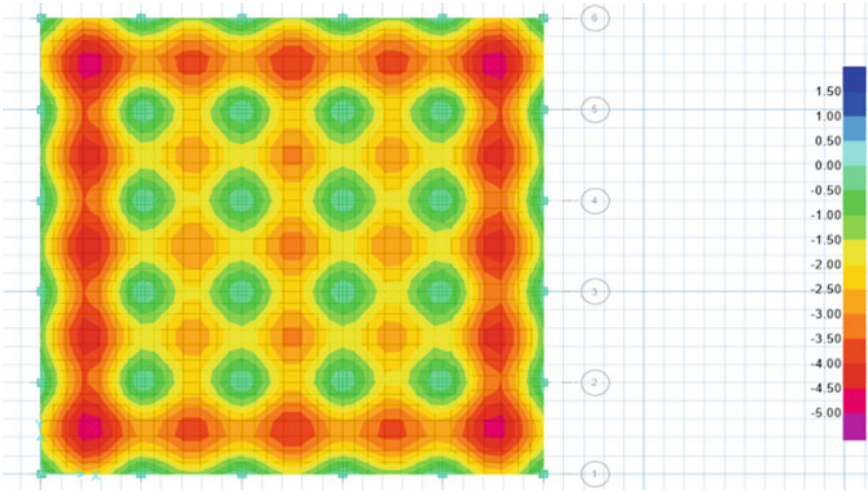
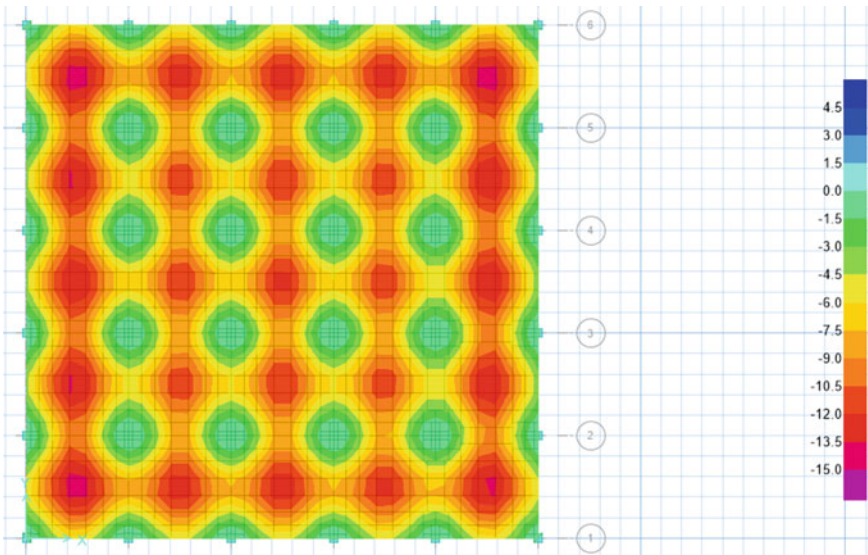**Fig. 4** Short-term deflection of flat slab

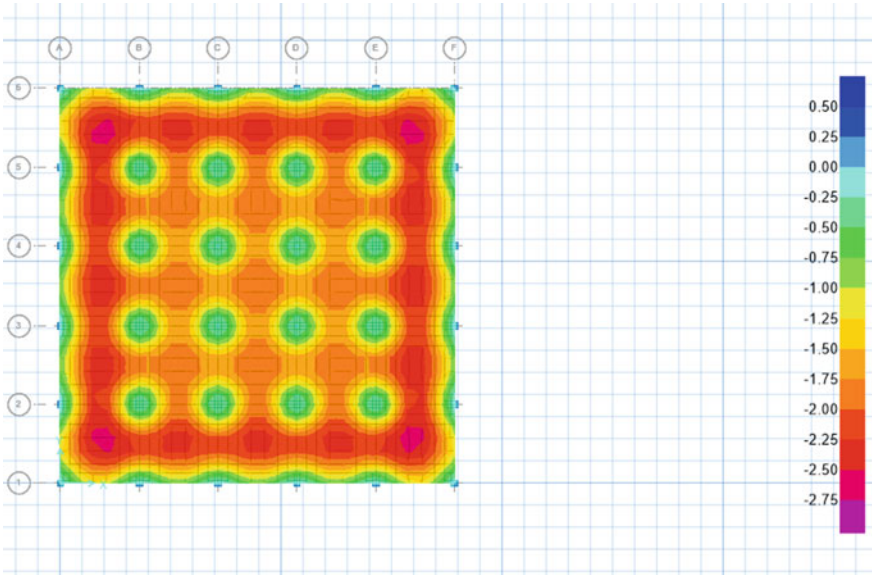
Fig. 5 Long-term deflection of flat slab

Fig. 6 Short-term deflection of waffle slab
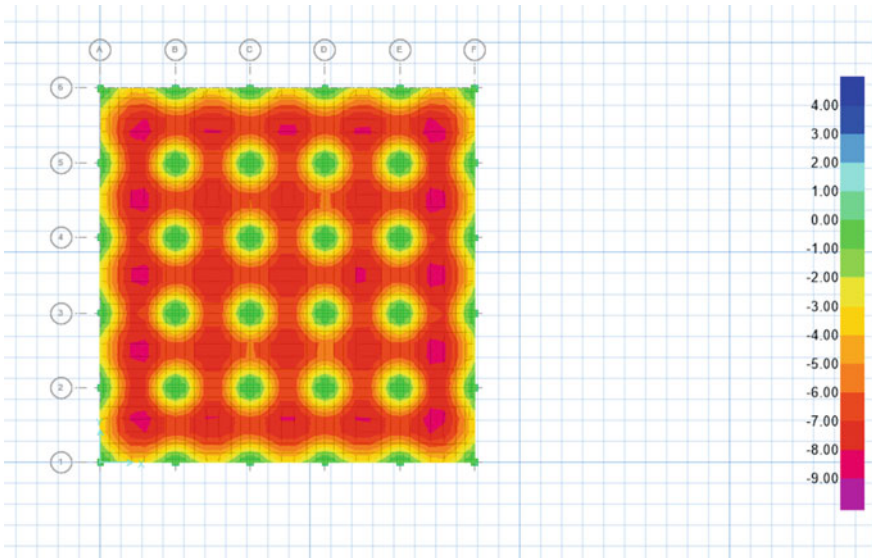
Fig. 7 Long-term deflection of waffle slab
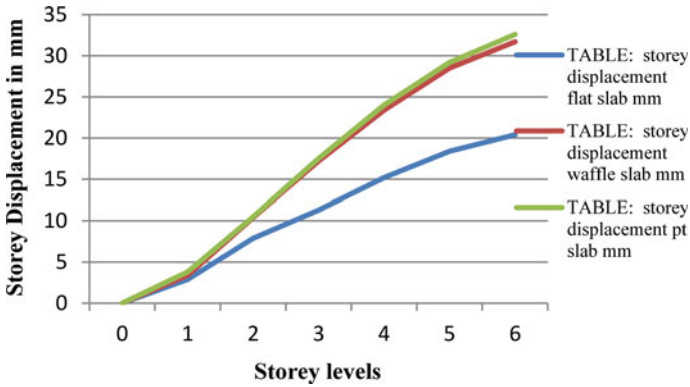
Fig. 8 Displacement versus storey levels for earthquake case

Table 3 Storey displacement in EQ Case for different types of slab system

Storey displacement					
Storey	Elevation	Location	Flat slab	Waffle slab	Pt slab
	m		mm	mm	mm
0	0	Top	0	0	0
1	3	Top	2.9	3.4	3.8
2	6	Top	7.9	10.4	10.5
3	9	Top	11.3	17.2	17.5
4	12	Top	15.2	23.4	24
5	15	Top	18.4	28.5	29.2
6	18	Top	20.4	31.7	32.6

Table 4 Storey displacement in response spectrum for different types of slab system

Storey displacement					
Storey	Elevation	Location	Flat slab	Waffle slab	Pt slab
	m		mm	Mm	mm
0	0	Top	0	0	0
1	3	Top	1.6	1.7	1.6
2	6	Top	3.8	4.3	4.3
3	9	Top	5.8	6.8	6.8
4	12	Top	7.4	8.8	8.9
5	15	Top	8.6	10.3	10.4
6	18	Top	9.3	11.2	11.4
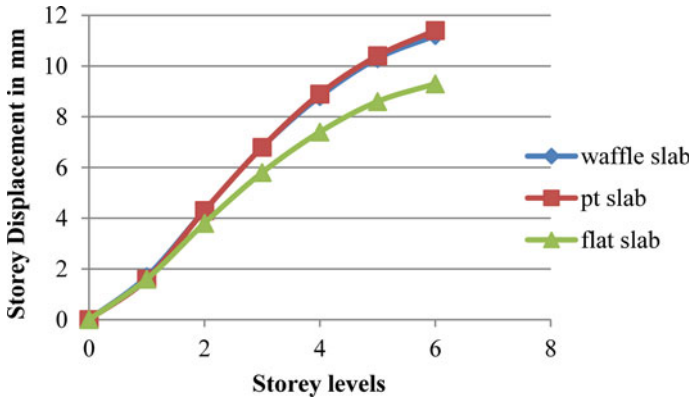
Fig. 9   Displacement versus storey levels for response spectrum

3.4   *Response Spectrum*

3.4.1   Storey Displacements

Storey displacements for different types of slab system are discussed in Table 4 and Displacement v/s storey levels is shown in Fig. 9.

3.5   *Storey Forces*

Storey forces in EQX direction for different types of slab system are discussed Table 5 and Storey shear v/s Storey levels for Shear forces graph is shown in Fig. 10.

Table 5   Storey forces in EQX direction for different types of slab system

Storey	Elevation	Location	Flat slab	Waffle slab	Pt slab
	m		kN	kN	kN
1	3	Top	1418	1457	1273
2	6	Top	1411.6	1446	1264
3	9	Top	1376	1407	1229
4	12	Top	1266	1291	1127
5	15	Top	1030	1047.18	914
6	18	Top	619	628	547
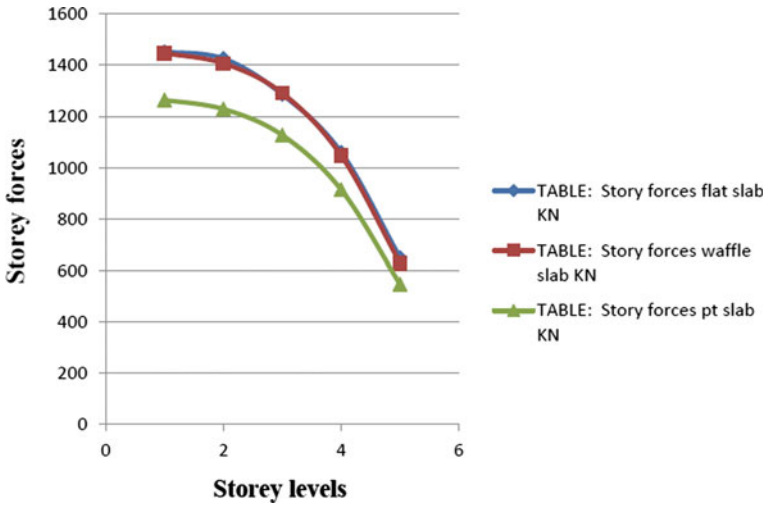
Fig. 10 Storey shear versus storey levels for shear forces

Table 6 Storey forces in spectrum X for different types of slab system

Storey	Elevation	Location	Flat slab	Waffle slab	Pt slab
	m		kN	kN	kN
1	3	Top	791	659	568
2	6	Top	735	606	523
3	9	Top	647	531	457
4	12	Top	542	452	390
5	15	Top	414	360	312
6	18	Top	242	224	196

3.6 Spectrum X

Storey Stiffness forces in spectrum X for different types of slab system is discussed in Table 6 and storey shear plots are shown in Fig. 11.

3.7 Storey Stiffness

Storey Stiffness for different types of slab system is discussed in Table 7 and storey stiffness plots are shown in Fig. 12.
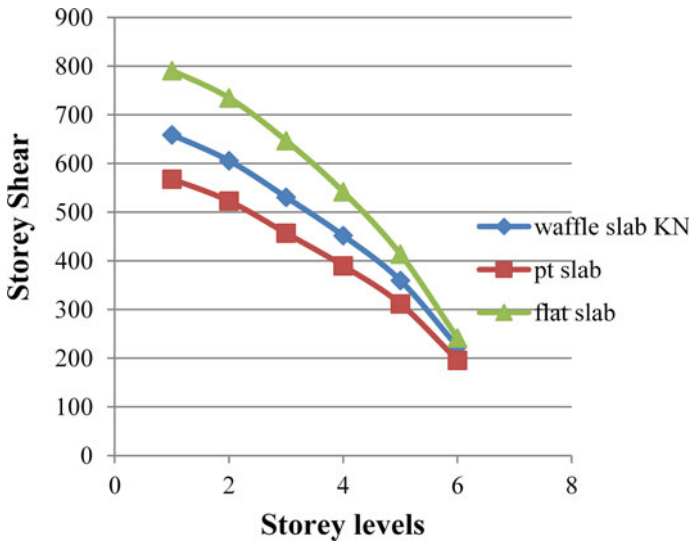
Fig. 11 Storey shear versus storey levels for Spec X

Table 7 Storey stiffness for different types of slab system

Storey	Elevation	Location	Flat slab	Waffle slab	Pt slab
	m		kN/m	kN/m	kN/m
0	0	Top	0	0	0
1	3	Top	501,674	373,437	160,106.7
2	6	Top	337,933	221,544.5	175,622.2
3	9	Top	327,213	207,560	174,616.7
4	12	Top	327,962.5	207,275.2	175,437.2
5	15	Top	330,542.8	208,969.2	189,854.8
6	18	Top	320,543.9	19,175.7	189,552.5

3.8 Response Spectrum Case

Storey Stiffness of Response Spectrum Case for different types of slab system is discussed in Table 8 and storey stiffness plots are shown in Fig. 13.

4 Conclusions

The following conclusion can be drawn out from study of flat slabs, waffle slabs and the post-tensioned flat slabs.
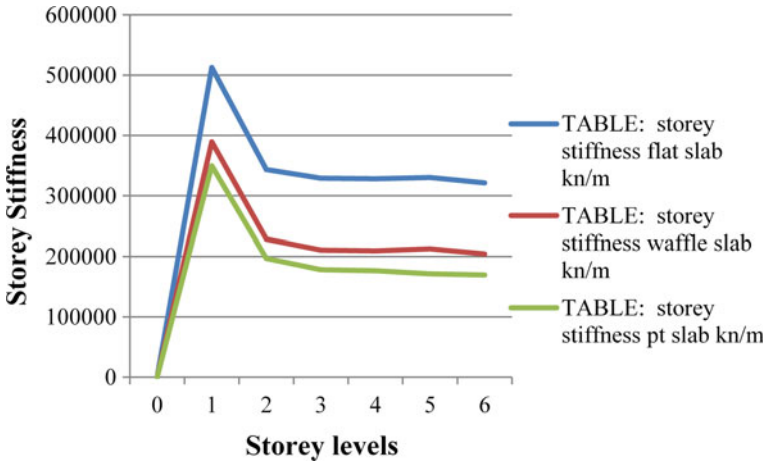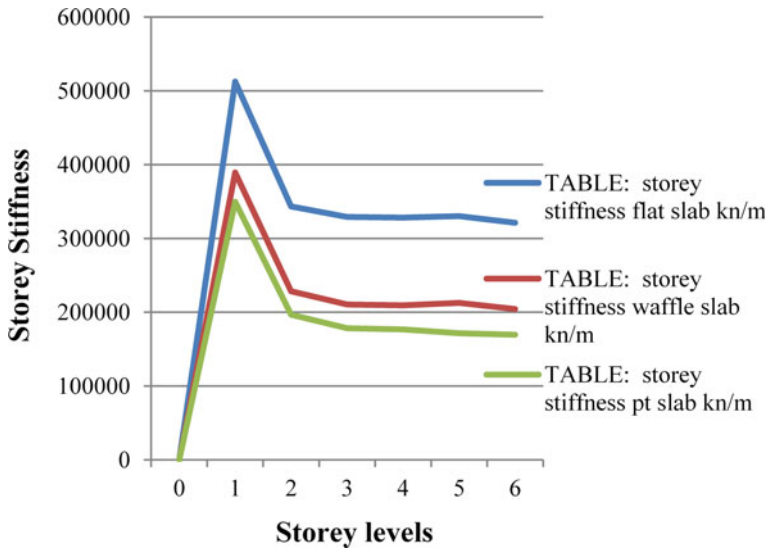
Fig. 12 Storey stiffness versus storey levels for different types of slab system

Table 8 Storey stiffness of response spectrum case for different types of slab system

Storey	Elevation	Location	Flat slab	Waffle slab	Pt slab
	m		kN/m	kN/m	kN/m
0	0	Top	0	0	0
1	3	Top	1418	1457	1273
2	6	Top	1411	1446	1264
3	9	Top	1376	1407	1229
4	12	Top	1266	1291	1127
5	15	Top	1030	1047	914
6	18	Top	619	628	547

1. The drop size required in the case of the flat slab and post-tensioned flat slab is more than the ribbed slab.
2. The deflection of the beam for the short-term and long-term loads waffle slab has lower values compared to the flat slab.
3. The slab reinforcement in the case of the flat slab is more, and waffle slab is less compared to the flat slab. The reinforcement required for the beam too will compensate the difference of the two slabs. Post-tensioned slabs reinforcement is in the form of the tendons.
4. The displacement is more in the case of the post-tensioned slab and is less for ribbed slab compared to the flat slab.
5. Storey shear is high in the case of the flat slab, and in the case of the ribbed slab and the post-tensioned slab, it is more due to high seismic weight mass.
6. Storey stiffness is high in the case of the flat slab, and it is less than the waffle and the post-tensioned slab.

Fig. 13 Storey stiffness versus storey levels for response spectrum case

On behalf of all authors, the corresponding author states that there is no conflict of interest.

References

1. Bahoria BV, Parbat DK (2013) Analysis and design of RCC and post-tensioned flat slabs considering seismic effect. Int J Eng Technol 5(1)
2. Joshi DD, Murnal PB (2013) Performance of flat slab structure using pushover analysis. J Mech Civ Eng 8(3)
3. Indian Standard Code of Practice for Design Loads (other than earthquake) For Buildings and Structures, Part—3 Wind Loads, IS: 875 (Part 3)—1987 (Second Revision), Bureau of Indian Standards, New Delhi, India
4. Indian Standard Criteria for Earthquake Resistant Design of Structures, IS: 1893 (Part 1) 2002
5. Manu KV, Naveen Kumar BM, Priyanka S (2015) Comparative study of flat slabs and conventional RC slabs in high seismic zone. Int Res J Eng Technol 2(6)
6. Sharma A, Claudia Jeya Pushpa D (2015) Analysis of flat slab and waffle slab in multistorey buildings using ETABS. Int J Sci Res Dev 3(2)
7. Mutalik Desai VG, Shaikh MJ (2012) Static and dynamic analysis of a reinforced concrete flat slab frame building for progressive collapse. Eng Struct 40: 205–217. https://doi.org/10.1016/j.engstruct.2012.02.026
8. Szydlowski R, Labuzek B (2017) Post-tensioned concrete long-span slabs in projects of modern building construction. IOP Conf Ser Mater Sci Eng 245. https://doi.org/10.1088/1757-899X/245/2/022065

Numerical Studies on Construction Methods

Numerical Study of GFRP Strengthened Brick Masonry Wallette

Hasim Ali Khan

Abstract The structure of unreinforced masonry (URM) is highly susceptible to seismic activity. Their propensity to collapse has required the concussion to develop procedures for strengthening URM structures to strengthen. To address questions about the seismic vulnerability of buildings with unreinforced masonry (URM), a research programme was explored to examine the efficacy of glass fibre reinforced polymer (GFRP) schemes as a seismic retrofit involvement for out-of-plane loaded URM walls susceptible to shear mode failure during earthquakes. The numerical analysis using a 3D macro nonlinear model of the in-plane shear performance of unreinforced and GFRP reinforced brick masonry specimens is discussed in this paper. Four-point bending experiments are carried out on all specimens. Two different trends emphasize the diagonal and the cross. Numerical tests are conducted in order to check the efficacy of GFRP reinforcement. From the investigation, it is noted that GFRP reinforcement significantly enhances the load-bearing capacity, diagonal shear strength, and rigidity. Flexural intensity is expected to rise from 22 to 37%.

Keywords Strengthening · Masonry · Four-point bending

1 Introduction

Unreinforced brick masonry wall simultaneously exposed to both in-plane shear and out-of-plane bending throughout earthquake [1, 2]. In in-plane, the walls tend to progress a diagonal crack whereas the loads act on the walls within the direction of perpendicular, causes the out-of-plane flexural bending of the walls. When pushed horizontally, the wall appears to overturn or bend just [3]. Various researchers aimed the determination of this result on an individual basis. Out-of-plane bending is significant when being collapsed by in-plane force of masonry walls. Masonry built with dry joints provide considerably develops both in-plane and out-of-plane performance throughout an earthquake [4, 5]. Structural performance of unreinforced masonry improves by strengthening with polymer textile reinforced mortar (TRM).

H. A. Khan (✉)
National Institute of Technology Durgapur, Durgapur, India

The in-plane shear strength is accrued from 128 to 136% whereas the out-of-plane flexural strength is accrued from 466 to 687% [6]. The confined walls of masonry with or without toothing strengthened the relationship between masonry and RC confining interactions [3]. Masonry walls will have larger strength once tested for in-plane shear and out-of-plane flexural under dry and wet conditions [7]. However, the higher than experimental works, numerous numerical examinations [8, 9] are carried recently to predict the characteristics of masonry walls to in-plane shear and out-of-plane bending. A 3D nonlinear finite element (FE) model established by Dolatshahi et al. [10] to determine the curves of interaction of unreinforced masonry walls by bidirectional loadings and it absolutely was valid with experimental findings. To avoid the collapse of such walls, strengthening ways investigated by different researchers [11]. Fibre Reinforced Polymer (FRP) offers considerably will increase the in-plane strength in in-plane loaded also as flexural strength for out-of-plane loaded masonry walls [12]. In various civil construction projects [13, 14], GFRPs are used as reinforcement elements [15–18]. GFRP enhances the in-plane strength of masonry panels effectively [19–21].

The purpose of this investigation is to compute the out-of-plane performance of un-strengthened and reinforced wallettes using geotextile with unique geometric arrangement numerically. To find a flexural collapse mode of wallettes, incremental load can be connected four-point bending test as per ASTM E-518 severally.

2 Numerical Approach

2.1 Introduction

Numerical models of unreinforced and reinforced masonry [16, 18, 22–24] (Majumder et al. 2020) were composed with finite element analysis in ANSYS. A macro nonlinear 3D model displayed to examine the in-plane shear and out-of-plane bending overall performance of controlled and geotextile strengthened brick masonry sample. Material characterization within the paper is taken by Khan et al. [20], Khan et al. [25], Khan et al. [26], Khan et al. (2021).

2.2 Model Description

In the four-point bending test, a 3D macro model is performed to examine the out-of-plane flexural efficiency of masonry wallettes. Wallette size is 600 mm × 600 mm × 125 mm. The element clarification is demonstrated in Fig. 1. Loads are implemented concurrently along one diagonal.

Figure 2a showed the SOLID 187 tetrahedron components using in wallettes.

Fig. 1 Schematics loading diagram of masonry sample
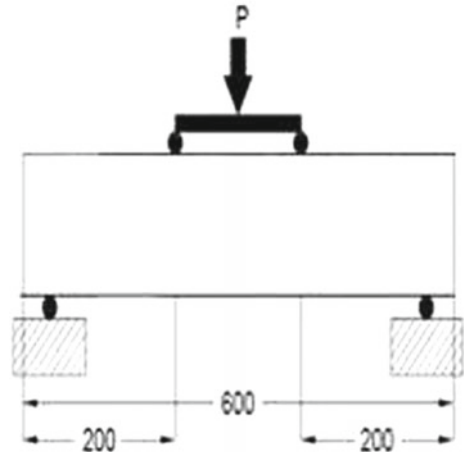
(a) Four-point bending test
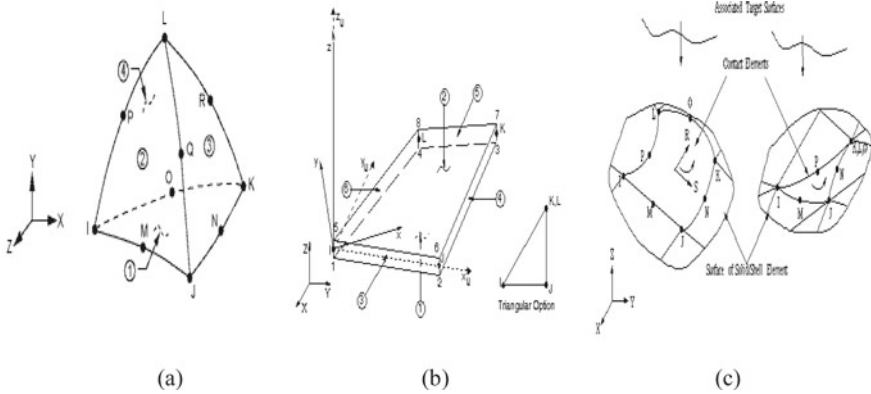
Fig. 2 Components of model

Geotextile is applied with SHELL 63 component and therefore the clarification is appeared in Fig. 2b. The edge among wallettes and geotextile are displayed with CONTA174 component Fig. 2c [20, 27–29]. Nonlinear behaviour is investigated.

Newton–Raphson iteration procedure is applied for obtaining nonlinearity. Figure 3a, b indicates the finite element mesh utilized for the URM panels and for RM panels severally.

(a)UR   (b)RHSS   (c)RXSS
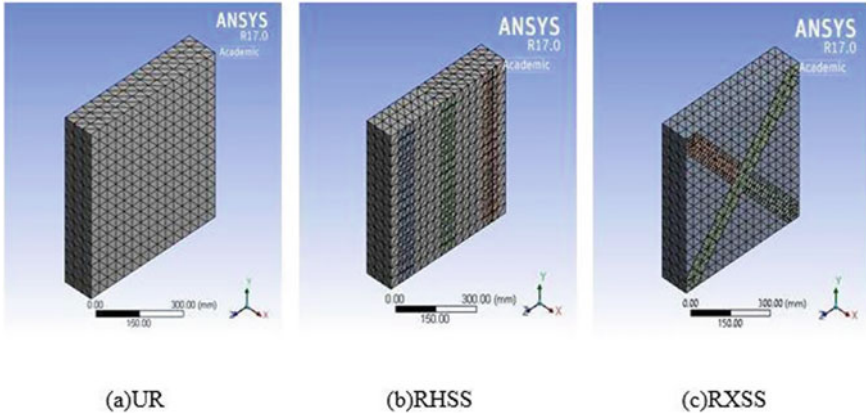
Fig. 3 Details of taking mesh

3 Results and Discussions

The reinforced of masonry sample changed into predictable. The stress distribution is displayed in Figs. 4 and 5. Shear capability is improved from unreinforced to reinforced severally.

Load-deformation diagrams are noticed. Figure 5 displays the graph for wallettes. The comparison the most matches before and after strengthening.

As per ASTM E518, diagonal shear strength and flexural strength for masonry sample are assessed and demonstrated in Table 1.

From Table 1, it had been noticed that the in-plane strength and therefore the flexural strength enhanced from 71.74 to 115.22 kN (60.61%), 3.35 to 5.24 MPa (56.42%)

(a) UR$_{\text{Out-of-plane}}$ (b) RHSS$_{\text{out-of-plane}}$ (c) RXSS$_{\text{Out-of-plane}}$
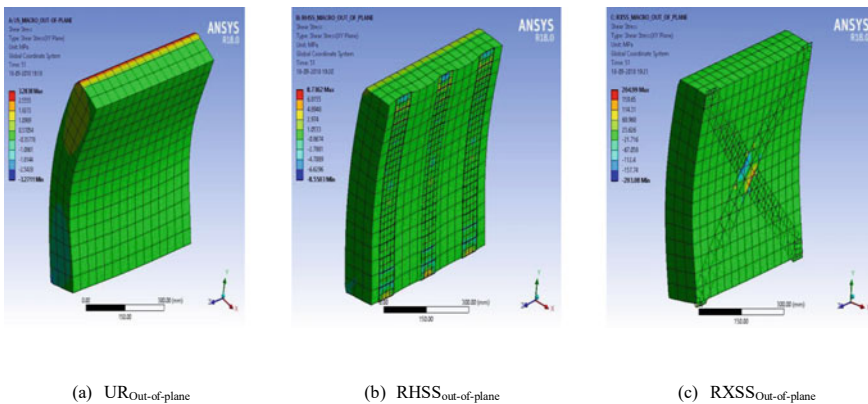
Fig. 4 Stress ordination for **a** UR, **b** RHSS, **c** RXSS at collapse for Out-of-plane loaded wallettes

Fig. 5 Load-deformation performance of masonry panels

Out-of-plane loaded
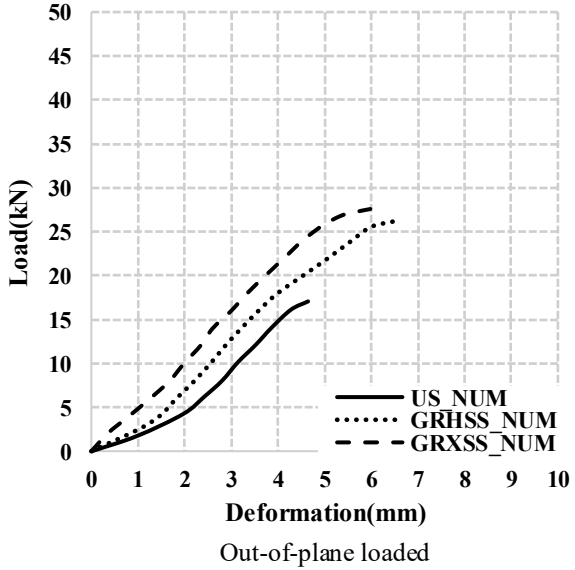
Table 1 Determination of in-plane strength and flexural strength

Strengthening arrangement	Out-of-Plane	
	Bending moment M (kN-m)	Flexural strength f_t' (MPa)
UR	5.24	3.35
RHSS	7.02	4.49
RXSS	7.29	5.24

for the diagonal pattern with respect to un-strengthened panel severally. Furthermore, diagonal patterns were observed to offer better output in terms of intensity over the remaining patterns.

4 Conclusions

With four-point bending checks, the flexural strength of masonry wallets with various reinforcing types, using geotextile, were tested numerically. The comments are listed below:

- The strengthened samples improved the collapse load and deformation from UR to RHSS, RHSS to RXSS severally.

- In the numerical investigation, flexural strength improved from 3.35 to 5.24 MPa (56.42%) with different strengthening patterns as related to un-strengthened samples.
- Furthermore, it turned into additionally noticed that the diagonal strengthening sample gave better stiffness.
- The crack patterns had been noticed closely. The unreinforced wallette indicated brittle collapse.
- The performance constraints are expressively increased parallel and diagonal severally.

References

1. Dolatshahi KM, Aref AJ, Yekrangnia M (2014) Bidirectional behaviour of unreinforced masonry walls. Earthq Eng Struct Dynam 43:2377–2397
2. Khan HA, Nanda RP (2020) Out-of-plane bending of masonry wallette strengthened with geosynthetic. Constr Build Mater 231:117198. https://doi.org/10.1016/j.conbuildmat.2019.117198
3. Singhal V, Rai DC (2014) Role of toothing on in-plane and out-of-plane behavior of confined masonry walls. J Struct Eng 140:1–14
4. Agnihotri P, Singhal V, Rai DC (2013) Effect of in-plane damage on out-of-plane strength of unreinforced masonry walls. Eng Struct 57:1–11
5. Bui TT, Limam A, Sarhosis V, Hjiaj M (2017) Discrete element modelling of the in-plane and out-of-plane behaviour of dry-joint masonry wall constructions. Eng Struct 136:277–294
6. Ismail N, Ingham JM (2016) In-plane and out-of-plane testing of unreinforced masonry walls strengthened using polymer textile reinforced mortar. Eng Struct 118:167–177
7. Memari AM, Grossenbacher SV, Iulo LD (2008) In-plane and out-of-plane load testing and evaluation of sustainable masonry walls. AEI 2008: Building Integration Solutions
8. Milani G (2011) Simple-lower-bound-limit-analysis-homogenization-model-for-in-and-out-of-plane-loaded-masonry-walls. Constr Build Mater 25:4426–4443
9. Milani G, Pizzolato M, Tralli A (2013) Simple-numerical-model-with-second-order-effects-for-out-of-plane-loaded-masonry-walls. Eng Struct 48:98–120
10. Dolatshahi KM, Aref AJ, Whittaker AS (2015) Interaction curves for in-plane and out-of-plane behaviours of unreinforced masonry walls. J Earthq Eng 19:60–84
11. Smith A, Redman T (2009) A critical review of retrofitting methods for unreinforced masonry structures. In: Proceedings of EWB-UK research conference. University of Bristol
12. Umair SM, Numada M, Amin MN, Meguro K (2015) Fiber reinforced polymer and polypropylene composite retrofitting technique for masonry structures. Polymers 7:963–984
13. Nanda RP, Dutta S, Khan HA, Majumder S (2018) Seismic protection of buildings by rubber-soil mixture as foundation isolation. Int J Geotech Earthq Eng 9(1):99–109. https://doi.org/10.4018/IJGEE.2018010106
14. Nanda RP, Dutta S, Das A, Khan HA (2018) Geosynthetic liner as foundation isolation for seismic protection. Int J Geosyn Ground Eng 3(21):1–7. https://doi.org/10.1007/s40891-017-0098-2
15. Maxwell S, Kim W, Edil TB, Benson CH (2005) Effectiveness of GFRPs in stabilizing soft subgrades. Final Rep. No. 0092-45-15, 2005, Department of Civil and Environmental Engineering, University of Wisconsin-Madison, Madison, WI
16. Majumder S, Saha S (2020) Behaviour of reinforced concrete beam strengthened in shear with geosynthetic. Adv Struct Eng 23(9):136943322090182. https://doi.org/10.1177/1369433220901820

17. Majumder S, Saha S (2020) Experimental and numerical investigation on cyclic behaviour of RC beam column joints reinforced with geogrid material. Mater Today Proc 38(5):2316–2324. https://doi.org/10.1016/j.matpr.2020.06.415
18. Khan HA, Nanda RP, Das D (2021) Numerical analysis of geosynthetic strengthened brick masonry panels. In: Proceedings of 13th international conference on vibration problems, Indian Institute of Technology Guwahati, Advances in Structural Vibration, Lecture Notes in Mechanical Engineering, Springer. https://doi.org/10.1007/978-981-15-5862-7_4
19. Khan HA, Nanda RP, Roy P (2016) Retrofitting of brick masonry panels with glass fibre reinforced polymers. IOSR J Mech Civ Eng 1:11–18
20. Khan HA, Nanda RP, Das D (2017) In-plane strength of masonry panel strengthened with GFRP. Constr Build Mater 156:351–361
21. Nanda RP, Khan HA, Pal A (2017) Seismic-retrofitting-of-unreinforced-brick-masonry-panels-with-glass-fibre-reinforced-polymers. Int J Geotech Earthq Eng 8(1):28–37
22. Majumder S, Khan HA, Nanda RP (2017) Pushover analysis of multi-storied RC buildings with and without openings in infill walls. J Civ Eng Environ Technol 4(1):68–72
23. Majumder S, Khan HA, Nanda RP (2017) Effect of masonry infills and openings on earthquake performance of RC buildings. In: Proceedings of 13th international conference on vibration problems. Indian Institute of Technology Guwahati
24. Majumder S, Saha S (2021) Quasi-static cyclic performance of RC exterior beam-column joint assemblages strengthened with geosynthetic materials. Structures 29:1210–1228. https://doi.org/10.1016/j.istruc.2020.12.010
25. Khan HA, Nanda RP, Das D (2018) Numerical analysis of geosynthetic strengthened brick masonry wallettes subject to in-plane and out-of-plane loading. In: Proceedings of the 16th symposium on earthquake engineering. Indian Institute of Technology Roorkee, pp 252–257
26. Khan HA, Nanda RP, Das D (2019) Numerical analysis of capacity interaction of brick masonry wallettes strengthened with geosynthetic. In: Proceedings of 13th North American Masonry conference, Salt Lake City, Utah, Paper No- 178. The Masonry Society Journal, pp 1554–1564
27. Khan HA, Nanda RP, Das D (2018) Review of retrofitting technique of un-reinforced masonry structure. In: Proceeding of the second international conference on advances in concrete, structural, and geotechnical engineering- ACSGE. Birla Institute of Technology and Science, Pilani, Jaipur, pp 252–257
28. ASTM E 519 (2001) American Society for Testing and Materials (ASTM), Standard test method for diagonal tension (shear) in masonry assemblages
29. Zucchini A, Lourenç o PB (2004) A coupled homogenisation-damage model for masonry cracking. Eng Struct 82:917–992
30. ASTM E 518 (2002) American Society for Testing and Materials (ASTM), Standard Test Method for determination of the flexural bond strength of unreinforced masonry panels in Masonry Assemblages
31. ANSYS (2017) Release 17.0. ANSYS Inc.

Numerical Analysis of Geotextile-Strengthened Shear Critical RC Beam

Subhrasmita Majumder and **Showmen Saha**

Abstract It was found that existing reinforced concrete (RC) beams are deficient in shear on many occasions. Shear-deficiencies are occurred by different causes, due to insufficient shear strengthening or reduction of corrosion-induced steel—bar, increased duty load and defects. The present study is investigated the shear behaviour of geotextile-strengthened RC beam by nonlinear finite element simulations. Shear critical RC beam specimens strengthened with outer bonded geo-textile material. The 3D macro-nonlinear model of all the RC beams was carried out using ANSYS-18 FE software. The numerical study observed that load-carrying capacity was increased in geotextile reinforced concrete beam by 34.6% compared to the control beam. Similarly, a significant improvement was observed in ultimate failure displacement, energy dissipation capacities of the strengthened beam by 98.2% and 72.8%, sequentially, with respect to the control beam. Hence, it was observed that geotextile could be effective as a strengthening material in the RC beam.

Keywords Geotextile · Shear deficiency · Finite element analysis · Ductility · Energy dissipation

1 Introduction

The lifespan of reinforced concrete (RC) structures depends on lots of factors, including material properties and weather conditions. It may be reduced due to many reasons such as failure of concrete structure improper design, chemical reaction, natural disasters, etc., [1, 2]. Earthquakes are one of the dangerous natural hazards with the sudden violent movement of the earth's surface with the release of energy. Earthquakes inflict massive destruction in terms of human lives, property, and structural collapse. The destruction and human loss that were experienced during earthquakes all around the world are reminders of that. Even though earthquake engineering technology has made considerable strides, earthquakes continue to pose significant threats to human lives. Earthquake tolerant architecture is also important

S. Majumder (✉) · S. Saha
National Institute of Technology Durgapur, Durgapur, India

and should be given priority [3–5]. Many old structures that are not designed to resist seismic forces have now become outdated due to more advanced design codes and specifications. Therefore, these existing structures need to repair and retrofit to reduce damage and destruction. Strengthening and retrofitting of existing structural members have become very important in recent years.

In recent years, strengthening of RC beams has acknowledged extensive consideration among scientists and engineers. The RC buildings should possess a ductile behaviour to give better performance under the impact of earthquake forces. Various efforts have been made by the researchers to find the best materials and methods for improving the load-carrying capability of seismically deficient structures. For strengthening of the poor RC beam structure to increase their service-life, numerous techniques are available. These techniques are the application of steel plates [6], different types of fibre reinforced polymer (FRP) [7] aluminium Alloy plates [8], ferrocement [9], steel wire mesh [10], etc. However,nowadays, many studies have been carried out on new materials for enhancing the load-bearing capacity of RC structures. Still, there is an expansion in the propensity to grow new items and applications on a standard premise to take care of various structural designing issues.

The geosynthetic material can stabilise as a reinforcement of soil and protect environmental works enhances the load-bearing capacity of pavements and masonry walls [11–13]. Majumder and Saha [14] studied the efficiency of geosynthetic material in strengthening the RC structures by external and internal confinement. The results show that this new strengthening or reinforcing technique is very effective for RC structure. Sadek and lissel [15] investigated the seismic performance of GFRP and geogrid reinforced masonry wall where geogrid reinforced wall showed better performance when compared to the GFRP reinforced masonry wall. Itani et al. [16] investigated Uniaxial geogrid's efficiency as a longitudinal bar in RC slab. Another experiment was performed by Chidambaram and Agarwal [17, 18], where geogrid material used as the shear reinforcement in the shear deficit RC beam with and without steel fibre. Meski and Chehab [19] conducted an experiment using three distinct types of geogrid materials as a longitudinal bar small RC beam: uniaxial, biaxial, and triaxial. Majumder and Saha [20] investigated the effectiveness of geogrid material as shear reinforcement in RC beam-column joints through an experimental and numerical analysis. All the test results confirmed that the application of geogrid composite as longitudinal and transverse reinforcement in RC structures upgrade the flexural strength, ductility and load-carrying capacity. Majumder and Saha [21] investigated geosynthetic material's efficiency in strengthening the shear deficit RC beams. Another experiment is conducted by Majumder and Saha [22], where RC beam-column-joint confined with geosynthetic material. The test results showed that geosynthetic material significantly improved the seismic performance of RC beam-column joints.

The present study investigates the effectiveness of externally bonded geotextile material in strengthening shear deficit RC beam specimens by numerical investigation.

2   Material Properties

In this programme, RC beam specimen's dimension kept as follows: 1050 mm × 150 mm × 100 mm. The concrete-mixed proportion was used as cement: sand: aggregate in the proportion of 1: 1.83: 3.19. The details of the concrete properties have given in Table 1.

One kind of geosynthetic, i.e., non-woven geotextile, was used for strengthening of the beams by external confinement for shear strengthening. Here, the control beam is represented as 'CB', and the geotextile bonded beam represents 'GT'. Hence, 'CB' signifies the 'Control Beam' and the 'GT' refers to the 'Geotextile' bonded RC beam. The properties of the geotextile material presented in Table 2.

3   Finite Element Modelling

The numerical 3D macro-models in ANSYS-18 [23] of the strengthening beam including control are developed to study RC beam's flexural strength under the three-point bending test. In this review, the primary assisted beam boundary state is used for analysis and a central load is steadily applied. The precise configuration of the RC beam is assumed in the model as a homogeneous factor. For this analysis, a concrete body modelled as SOLID187 is made up of ten nodded tetrahedron components with three degrees of freedom at each node, quadratic displacement activity and plasticity, large deflection, and large strain capabilities. The geotextile materials are modelled using shell 63, which is a four-node element with bending and membrane capability and six degrees of freedom at each node. The interface between the concrete body and the geo-synthetic substance is modelled as a bonded action using CONTA174.

As per their geometrical configurations, mesh size is kept distinct for RC beam and geotextile. 25 mm is maintained for concrete body mesh size; 10 mm is preferred for geotextile mesh size (Fig. 1).

4   Results and Discussion

4.1   Failure Patterns

Finite element analysis (FEA) for all types of beams is developed with enough accuracy in lesser time and cost. Figure 2 represents the equivalent stress contour of all the beam patterns, including the control beam. From this Fig. 2, it can be demonstrated that in the control beam, the equivalent stress is maximum on the tension zone of concrete, but in the case of the geotextile bonded beam, the stress is maximum on the geotextile strips, respectively.

Table 1 Concrete properties [22]

28-days compressive-strength (MPa)	Tensile-strength (MPa)	w/c (%)	Cement (kg/m³)	Water (kg/m3)	Fine-aggregate (kg/m3)	Coarse—aggregate (kg/m3)	
						12.5 mm	20 mm
27.5	3.1	0.45	393	177	672	491	736

Table 2 Mechanical properties of strengthening material

Material	Tensile-Strength @ 5% strain (MPa)	Poison's Ratio	Thickness (mm)	Mass-per-unit-area (g/m2)	Elongation At yield point (%)
Non-woven geotextile	52	0.26	0.18	255	42

(i) SOLID 187   (ii) SHELL 63   (iii) CONTA174
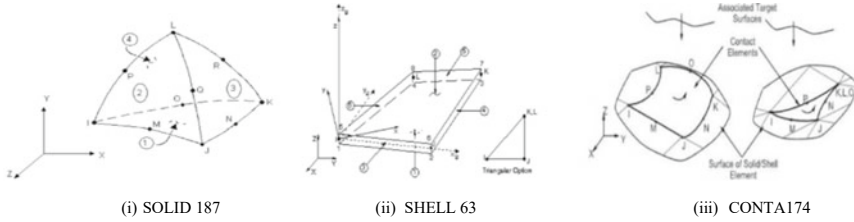
**Fig. 1** Elements of the proposed model [24]

Figure 3 displays the load-displacement responses from the finite element (FE) analysis. The load-bearing capacity of the geotextile bonded RC beam is considerably higher than the control beam, as seen in Fig. 3. The percentages of increment in load-carrying capability are 34.6. The geotextile-strengthened beam's ultimate failure displacement was also enhanced by 92.8 %.
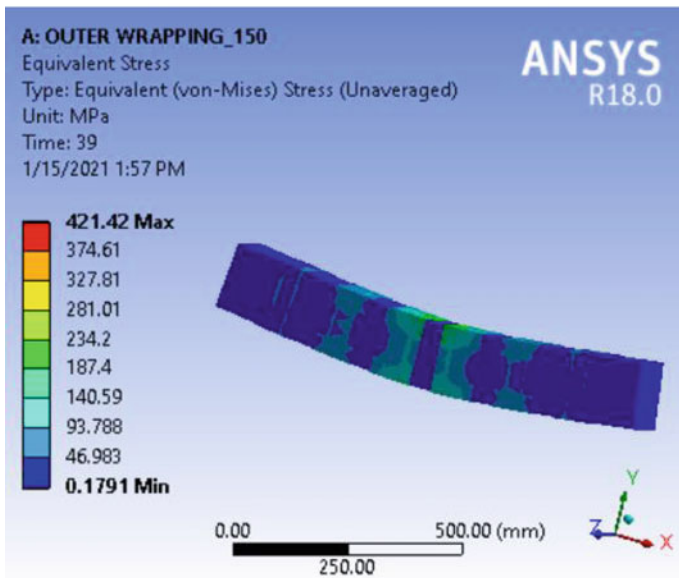
4.2 Energy Dissipation Capacity

The energy dissipation capacity (ED) is obtained by the load-displacement graph region (Fig. 4). The geotextile bonded beam's ED capacity is significantly increased by 78.2 %, which shows better ductility behaviour than the control beam.

5 Conclusions

An analytical study was carried out to investigate the performance of geotextile bonded RC beam specimen on load-deformation capacity, energy absorption capacity. Shear deficit RC beam specimens strengthened with geotextile material modelled in finite element software, ANSYS. From the numerical results, the equivalent stress con-tour mode of the geotextile bonded beam is improved compared to the control beam. The load-carrying capacity of GT is increased by 34.6% as compared to the CB. The energy dissipation capacity of the geotextile bonded beam is significantly increased by 78.2%, which shows better ductility behaviour than
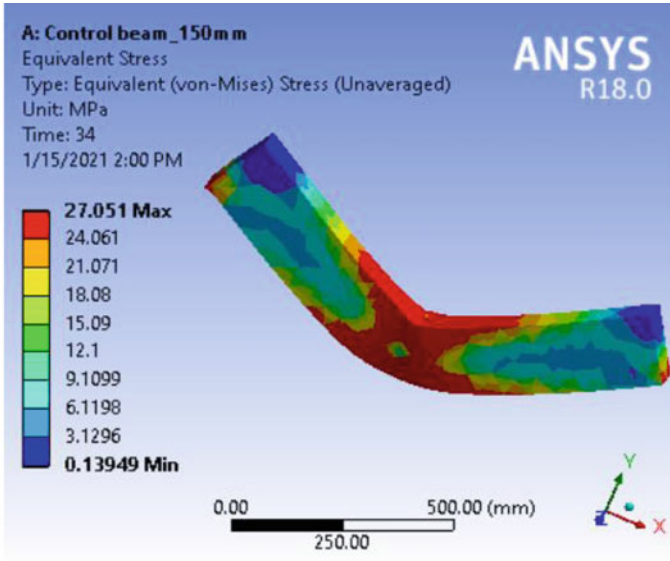
(i)   Control Beam

(ii)   Geotextile-strengthened beam

Fig. 2 Equivalent stress contour of RC beam
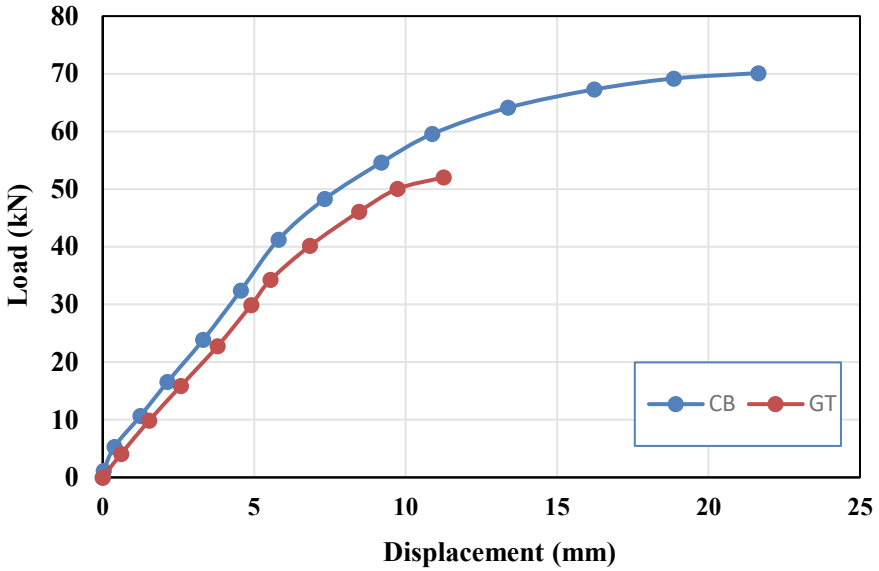
Fig. 3 Load–displacement graph of RC beam specimens

Fig. 4 Energy dissipation capacity of the GT bonded beam in comparison with CB
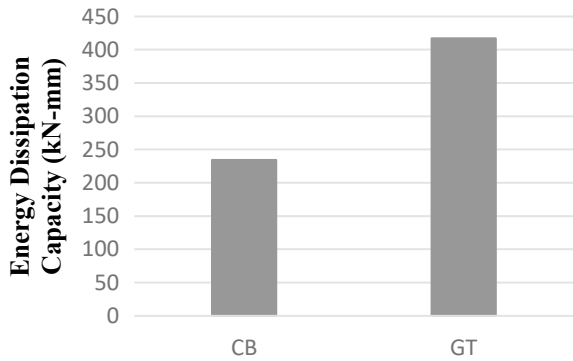
the control beam. Hence, geogrid seems to be an alternative material with excellent ductile behaviour to strengthen the RC beam.

References

1. Nanda RP, Behera B, Majumder S, Khan HA (2018) RC beam strengthening by glass fiber reinforced polymer. Int J Eng Technol Sci Res 5:21–26
2. Majumder S, Nanda RP, Saha S (2018) Review on strengthening of structural and non-structural members using fibre reinforced polymer". Conference proceedings on advances in concrete, structural and geotechnical engineering (ACSGE), Bits Pilani, Jaipur, India

3. Nanda RP, Majumder S (2019) Pushover analysis of base isolated rc frame buildings with masonry infills. Int J Geotech Earthquake Eng 10(2):18–31

4. Majumder S, Khan HA, Nanda RP (2017) Pushover analysisof Multi-storied RC Buildings with and without Openings in Infill Walls. J CivilEng Environ 4(1):68–72

5. Nanda RP, Sayantan D, Khan HA, Majumder S (2018) Seismic protection of buildings byrubber-soil mixture as foundation isolation. Int J Geotech Earthquake Eng 9(1):99–109

6. Rahman MM, Jumaat MZ, Rahman MA, Qeshta IM (2015) Innovative hybrid bonding method for strengthening reinforced concrete beam in flexure. Constr Build Mater 79:370–378

7. Meier U (1995) Strengthening of structures using carbon fibre/ epoxy composites. Constr Build Mater 9(6):341–351

8. Rasheed HA, Abdalla J, Hawileh R, Al-Tamimi AK (2017) Flexural behavior of reinforced concrete beams strengthened with externally bonded Aluminum Alloy plates. Eng Struct 147:473–485

9. Jayasree S, Ganesan N, Abraham R (2016) Effect of ferrocement jacketing on the flexural behaviour of beams with corroded reinforcements. Constr Build Mater 121:92–99

10. Qeshta IM, Shafigh P, Jumaat MZ (2015) Flexural behaviour of RC beams strengthened with wire mesh-epoxy Composite. Constr Build Mater 79:104–114

11. Palmeira EM, Tatsuoka F, Bathurst RJ, Stevenson PE, Zornberg JG (2008) Advances in geosynthetics materials and applications for soil reinforcement and environmental protection works. Electron J Geotech Eng

12. Khan HA, Nanda RP, Das D (2017) In-plane strength of masonry panel strengthened with geosynthetic. Constr Build Mater 156:351–361

13. Khan HA, Nanda RP (2020) Out-of-plane bending of masonry wallette strengthened with geosynthetic. Constr Build Mater 231:117198

14. Majumder S, Saha S (2021) Shear behaviour of RC beams strengthened using geosynthetic materials by external and internal confinement. Structures 32:1665–1678

15. Sadek H and Lissel S (2013) Seismic performance of masonry walls with GFRP and geogrid bed joint reinforcement. Constr Build Mater 41:977–989

16. Itani H, Saad G, Chehab G (2016) The use of geogrid reinforcement for enhancing the performance of concrete overlays: an experimental and numerical assessment. Constr Build Mater 124:826–837

17. Chidambaram RS, Agarwal P (2014) The confining effect of geo-grid on the mechanical properties of concrete specimens under compression and flexure. Constr Build Mater 71:628–637

18. Chidambaram RS, Agarwal P (2015) Flexural and shear behavior of geo-grid confined RC beams with steel fiber reinforced concrete. Constr Build Mater 78:271–280

19. Meski EF, Chehab G (2014) Flexural behavior of concrete beams reinforced with different types of geogrids. J Mater Civ Eng 26(8):04014038

20. Majumder S, Saha S (2020) Experimental and numerical investigation on cyclic behaviour of RC beam column joints reinforced with geogrid material. Mater Today Proc

21. Majumder S, Saha S (2020) Behaviour of reinforced concrete beam strengthened in shear with geosynthetic. Adv Struct Eng 23(9):1851–1864. https://doi.org/10.1177/1369433220901820

22. Majumder S, Saha S (2021) Quasi-static cyclic performance of RC exterior beam-column joint assemblages strengthened with geosynthetic materials. Structures 29:1210–1228

23. ANSYS (2017) Release 18.0. ANSYS Inc

24. Majumder S, Nanda RP, Saha S (2018) Experimental and numerical investigation of RC beam strengthened with geogrid confinement. Conference proceedings on 16th symposium on earthquake engineering (16SEE), IIT Roorkee, India

Prevention Methods and Safety Engineering

Vulnerability of Railway Switches and Crossings Exposed to Flooding Conditions

Mehmet Hamarat, Mayorkinos Papaelias, and Sakdirat Kaewunruen

Abstract Turnouts are a part of modern railway tracks to divert railway traffic from one route to another route. Their complex geometry and structure impose significant dynamic track loads. Particularly, common crossings laid on ballasted tracks are well-known among the infrastructure managers for their drawbacks. Numerous studies have been devoted to analyze a railway turnout with a common crossing. Nevertheless, almost all of them considers that turnouts are working in a dry environment. In reality, railway tracks are exposed to extreme conditions such as flooding, which could damage the power supply, signaling systems, rolling stocks and the infrastructure. The so-called phenomenon 'washed out' or 'washed away' ballast affects directly the dynamic behavior of rolling stock and can cause derailments with fatalities. In 2018, for instance, 25 people were killed in an accident in Turkey as a result of 'washed away ballast.' Few studies analyze unprecedented events in railway tracks in terms of vehicle-track interaction. However, no studies on turnouts was encountered in the literature. Hence, it is a significant contribution to analyze a railway turnout in case flooding occurs. In this study, the beam oriented finite element model, validated previously, is manipulated to analyze the dynamic behavior of a turnout under dry and wet conditions as well as washed away ballast scenarios. The outcomes of the study show that considering the effects of flooding on dynamic forces during operation and design phases could be a key to prevent undesired events.

Keywords Turnout · Railway · Flooding · Dynamic · Finite element method analysis

M. Hamarat (✉) · S. Kaewunruen
Department of Civil Engineering, School of Engineering, The University of Birmingham, Birmingham B152TT, UK
e-mail: mzh670@bham.ac.uk

M. Papaelias
School of Metallurgy and Materials, The University of Birmingham, Birmingham B152TT, UK

1 Introduction

Railways is a safe, secure and rapid transportation mode to convey a large amount of cargo and passengers. The technology behind it has been evolving over the centuries and has no boundaries to reach [1–6]. However, a large portion of the current network is established on ballasted track technology, relatively old technology in which support structure is a ballast bed that is composed of crushed rocks. The ballasted tracks are inexpensive to construct and have superior properties in terms of noise and vibration mitigation [7]. Furthermore, their porous structure exhibit natural drainage. The problem in ballasted tracks is resilience or insufficiency to provide long-term track stability due to the structure of ballast bed that is highly susceptible to dynamic forces and environmental factors, causing uneven track stiffness and requiring frequent maintenance to restore even track stiffness. Furthermore, providing an evenly distributed track stiffness becomes more challenging at transition points on the track, such as turnouts owing to their asymmetrical and stiff structure that require special maintenance technology.

Turnouts are imperative for railway tracks as they enable diversions of traffic flow from one track to another track. Their asymmetrical structure and complex geometry induce high-frequency impact forces and cause asymmetrical loading conditions, which frequently leads to ballast deterioration and rail damages [8]. Numerous studies have been conducted to analyze and develop a better understanding of the behavior of railway turnouts [8–23]. Nevertheless, most of the studies consider an ideal mid-temperature dry weather condition and neglect the extreme events. Neglecting a few recent studies [24–31], a similar approach is also valid for normal track sections. The reason might be the low frequency of occurrence and the general tendency to stop any rail operations under extreme events [32]. Such an operation contains large uncertainties in terms of operational status and could be very dangerous and fatal. Nonetheless, in some cases, the extreme events are inevitable owing to their unforeseen nature. In 2018, it was reported that a deadly accident in Turkey was due to washed away ballast after an unexpected sudden downpour of rain [33]. Hence, it is crucial to investigate such unprecedented events such as flooding to prevent financial and more importantly, human losses. Despite several studies on railway tracks exposed to flooding, to the authors' knowledge, no study has been encountered in the literature, which assesses the topic in terms of the dynamic behavior of railway tracks as well as turnouts. Consequently, this paper is the first to present the outcomes of the analysis on the dynamic behavior of a turnout system that is exposed to different flooding conditions.

A validated finite element model that was used previously to analyze turnout behavior under dry conditions [34] is modified to represent flood conditions. Two different flood scenarios are tested in the simulation environment. In the first scenario, the relative surface water level is considered, where it is assumed that the porous structure of ballast allows water flow, and therefore, there is no washed away ballast. In the second scenario, the assumption is that the ballast bed lose its draining ability and become impermeable structure. Then, the water flow occurs from the weakest

Fig. 1 A flooded turnout. The picture courtesy of East Midlands Railways

point on the ballast bed where water flow is strong enough to drag the ballast particles, leading to the loss of structural integrity. In that case, several bearers have no ground support (Fig. 1).

2 Numerical Model

The finite element model in [34] is based on a 48 m standard turnout with 1:9 crossing angle, including a small section of normal track. The model uses an equivalent profile for rails to downgrade the complexity of 3D model due to computational limitations. A descriptive figure is presented in Fig. 2.

The model is a composition of the beam and spring-dashboard elements. 77 bearers ranging from 2.4 m to 4.7 m length are modeled with an average spacing of 0.71 m. Fastening systems are simplified as a rubber rail pad and implemented
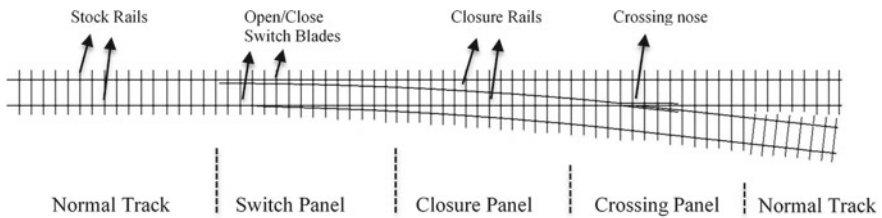
Fig. 2 The used layout of a standard turnout

Table 1 Dynamic material properties used in the numerical model

Element	No elements	Properties	Value
Rail	1980	ρ [1] E [2] PR [3]	7800 210 0.3
Bearer	3070	ρ [1] E [2] PR [3]	2500 38 0.2
Rail Pad	245	k [4]	1300
Ballast (0%, 29%, 57%, 100%, 114%)	5900	k [4] c [5]	14.6, 13.7, 13.4, 11.3,6.5 1.16, 1.77, 1.82, 2.37, 3.3
Primary Suspension	8	k [4] c [5]	1.15 2.5

into the model as spring elements. Additionally, damping properties of rail pads are neglected due to the insignificant contribution of pad stiffness into total track damping in comparison with ballast bed. A common concept of 'beam on an elastic foundation' is adopted in the model. Therefore, the ballast bed is represented by spring-dashboard couples. The number of the spring elements is adjusted against the length of the bearers. The ground below the elastic foundation is assumed rigid to be able to define boundary conditions. Boundary conditions allow components to move in their vertical planes. Material properties are inherited from the previous model with an exemption for ballast properties. The ballast properties have been selected with reference to [24], where the effects of different water levels are investigated. Selected water levels and ballast properties are presented in Table 1 as well as other fundamental parameters. For the second scenario, in the case of washed away ballast, the spring elements representing ballast bed was removed for two critical sections (i.e., switch and crossing panels).

The vehicle in the model, consisting of a bogie and two wheelsets, is represented by rigid bodies and springs. The geometry of the car body is neglected owing to the negligible influence on dynamic forces but the weight of the car body is distributed over the bogie. The mass per wheel is 10 tons. The boundary conditions for the vehicle enable longitudinal and vertical movements as well as pitch and roll motion. The travel direction of the vehicle is the facing direction on through route of the turnout and traveling speed is 25 kph. The vehicle speed is selected based on the experience of the second author. Last but not least, the contact between track and vehicle is defined by Hertzian contact theory in which the contact forces are calculated based on the virtual penetration and contact stiffness in FEM environment.

The solver settings are also obtained from the previous model, where an explicit time integration, well-known for its stability, used to solve equations of motions. Furthermore, preloading is applied to avoid unrealistic vibrations due to gravitational forces. The model has sufficient detailing to obtain accurate results with high resolution in an acceptable calculation time. The original model was validated by

field measurements. Here, it is assumed that the validity of the model will not change with the manipulation of the ballast bed properties. This assumption has been done due to lack of field measurements that can be used as a reference point.

1 Density (kg/m3). 2 Modulus of elasticity (GPa). 3 Poisson Ratio. 4 Stiffness (MN/m) 5 Damping coefficient (kNs/m).

3 Results and Discussions

Several track parameters are taken into account to assess the performance of a railway track whether a corrective action is necessary or not. These parameters are measured by determining the position of rails. One should bear in mind that the rails could be subjected to a vehicle loading or no loading. Hence, two different measurement concepts are applied in practice. In this study, the concept of measurements under vehicle loadings is assumed to calculate the track parameters. Indeed, only one track parameter, cross-level, is considered due to the aim of the study and boundary conditions applied in the simulation. The basic definition of the cross-level is the height difference between two rails, which must be kept in certain limits. The limits could vary among the countries as they are decided by the experience of the Infrastructure Managers. Here, the maintenance manual [35] is followed to evaluate the degree of the cross-level. In the manual, it is recommended to take measurements at two different intervals to identify short and long twist defects. The twist value is obtained by subtraction of adjacent measurement points, which should be below the maintenance threshold values in the manual. The threshold value of short twists at 25 kph is between 17–18 mm, whereas it is 50–55 mm for long twists. Above threshold values, the maintenance is compulsory. It is noteworthy that there are a few more threshold values above the maintenance thresholds which is applied to determine maintenance priority. The occurrence of long twist is neglected at this point, considering the length of turnout and its rigid structure. Besides, there could be discrepancies in other practices such that only one specific interval, 3 m, is used to measure cross-level [36]. Thus, the cross-level values are obtained in the simulations at every 2 m, in parallel to the manual, to detect short twist defects. However, it should be emphasized that the thresholds defined in [36] are referenced while discussing the results. This is because the thresholds are not only expressed as millimetric values but also as gradient values. For instance, twists with a gradient between 1 in 127 and 1 in 200 must be repaired in 10 days following the detection. Finally yet importantly, the right rail that is aligned with the crossing nose is selected as a reference rail. If the cross-level has a positive value, it means that the left rail is at a higher position from the ground in comparison with the right rail.

### 3.1 The Effect of Surface Water Level on Cross-Level at Turnouts

Surface water levels could show variations in different flood scenarios. As indicated in [24], the level of surface water affects the stiffness and damping properties of ballast structure that have an impact on the dynamic behavior of vehicle and track system. Since the available information on ballast structure under flood condition is limited, similar idea applied in [24] is adopted in this study. Here, it is assumed that the ballast structure is exposed to four different surface water levels. The level representation is normalized where water level that covers all structure is considered as %100 flooding. Similarly, the reference case, the dry condition, is indicated as 0% flooding.

The results of different surface water levels are presented in Fig. 2. As can be seen from the figure, the level of surface water is decisive on the magnitude of cross-level. The higher water level means the higher cross-level. The discrepancy seems to be insignificant from 0 to % 100 flooding, whereas 10% above the reference point doubles the cross-level value. The figure also present the asymmetrical stiffness distribution along the turnout due to its geometry. The turnout structure generally acts stiffer at sections under the rail on the crossing side (Fig. 2 top), which seems to lead to negative cross-level. Similarly, track stiffness increase toward the longest bearer and the upward trend continues in the direction of the longest bearer. The bearer with no.20, laid at switch panel, has a similar length to a standard bearer, whereas the bearer with no.60 is far longer and provide higher track stiffness. Another evidence of the effect of high stiffness on the cross-level is the sudden decrease in the magnitude of the cross-level after no.60 bearer, which results from the transition between turnout structure and normal track section. Lastly, it seems that the cross-level values are in the range of permissible limits and the turnouts could maintain their functions under flooding conditions at low speeds if their structural integrity is protected.

3.2 The Effect of Washed Away Ballast at Switch Panel

As mentioned previously, railway track could be suffered from washed away ballast in the event of flooding. In that case, the bearers lose ground support and hang on the rails. It should be reminded that in this scenario, it is assumed that all ballast particles at washed away section are dragged, and therefore, no partial support is observed for the bearers on the contrary to the reality where partial support at some bearers could be observed. Here, three different scenarios have been considered in the simulation such that the length of the washed away section is 3, 5 and 10 bearers.

As presented in Fig. 3, the number of washed away ballast have negative impacts on the cross-level values significantly at the switch section. Interestingly, the cross-level has a positive value first (Fig. 3 top) and then a negative value. To explain that, the working principles of a turnout should be considered. When a vehicle is directed
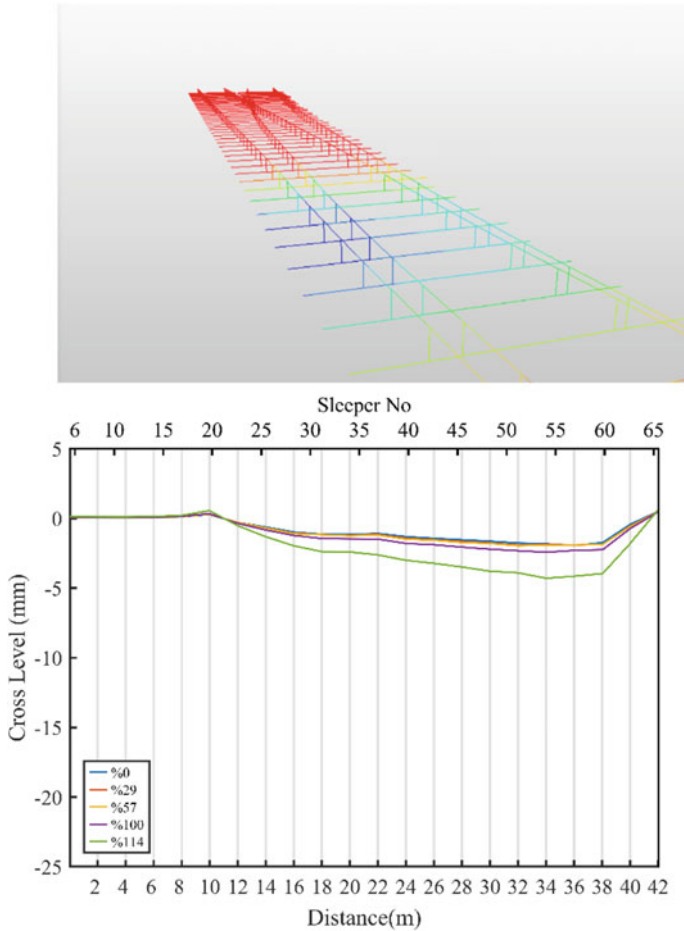
Fig. 3 A graphical demonstration of vertical displacement in the vicinity of the bearer with no.30, where blue color represents the lowest (top). Cross-level values in different surface water levels (bottom)

to a certain route, one switch blade is opened. Simultaneously, the other is closed and stuck to the stock rail. Hence, the support conditions of railway track change with the location of switchblades. The open switchblade is positioned away from the left rail and produce a new support point that affects load distribution. Consequently, the left rail is relatively stiffer first and have positive cross-level. However, the stiffness value becomes higher at the right rail side, later and negative cross-level value becomes significant.

The number of unsupported bearer due to washed away ballast has a direct contribution to the magnitude of cross-level. Maximum cross-level, around 10 mm, is observed when ten bearers are unsupported. It is important that vehicle might become

unstable at that point since the direction cross-level suddenly changes from positive to negative and bearers are unsupported. In other cases, there is a small disturbance between bearers with the numbers of 15 and 25. The rest of turnout have similar behavior to the supported scenario as mentioned previously. In general, the cross-level parameters are still in the permissible range concerning twist calculation in the manual [35].

3.3   *The Effect of Washed Away Ballast at Crossing Panel*

The crossing panel is the point where high-frequency high magnitude impact forces occur at the crossing nose, a position on the right rail. These forces present challenges in term of track and vehicle safety and integrity of the system. As indicated in [34], these forces could be up to 3 times higher than normal static wheel load. Interestingly, in previous sections, the cross-level value in this section exhibits negligible behavior. It seems that the contribution of impact forces into cross-level values seems to be limited. Hence, in Fig. 4 below, the cross-level values, the highest among all scenarios, are believed to result from the stiff structure of the crossing panel (Fig. 4 top). In other words, the loss of ballast support has a less negative impact on the right rail at crossing panel, particularly in comparison with the case of washed away ballast at switch panel. As a consequence, the left rail has a relatively larger displacement which produces more cross-level.

Figure 4 also illustrates that the contribution of the number of unsupported bearers is evident as the highest magnitude is presented in the case of 10 unsupported bearers. In that case, the cross-level values are acceptable in [35]. However, it should be repaired in 10 days according to [36] (Fig. 5).

4   Conclusions

This study provides new insights into the understanding of the dynamic behavior of a turnout system during an unprecedented event of flooding. The outcome of the study could be summarized as follows. First of all, the asymmetric topology of a turnout causes a negative cross-level even in a dry environment, showing that the loading conditions on rails are not balanced. A further investigation is recommended to evaluate whether it is beneficial to increase the ballast stiffness under the left rail/ stock rail or not. Secondly, the effect of unsupported bearers on cross-level due to washed away ballast is obvious. An expansion of washed away section causes the more severe cross-level difference. Hence, based on the current simulation and its limitations, it could be concluded that the risk of a derailment is highly likely with the expansion. Therefore, it is recommended that train operation be terminated instantly with any suspicion of washed away ballast, particularly at crossing panel, for safety concerns. Thirdly, the impact of surface water levels seems to be indistinctive below
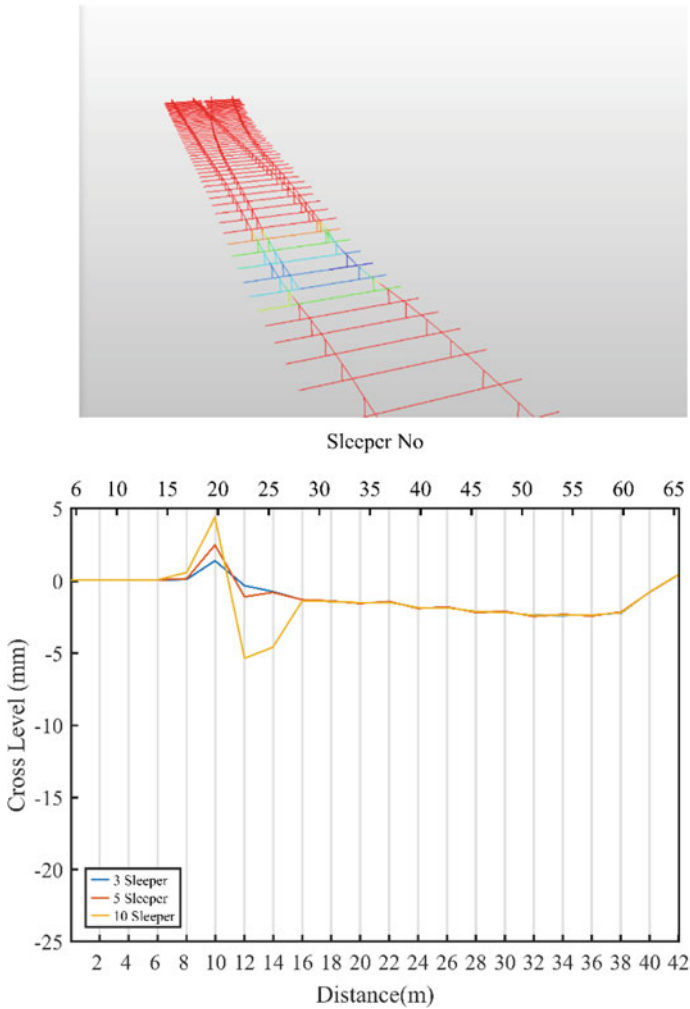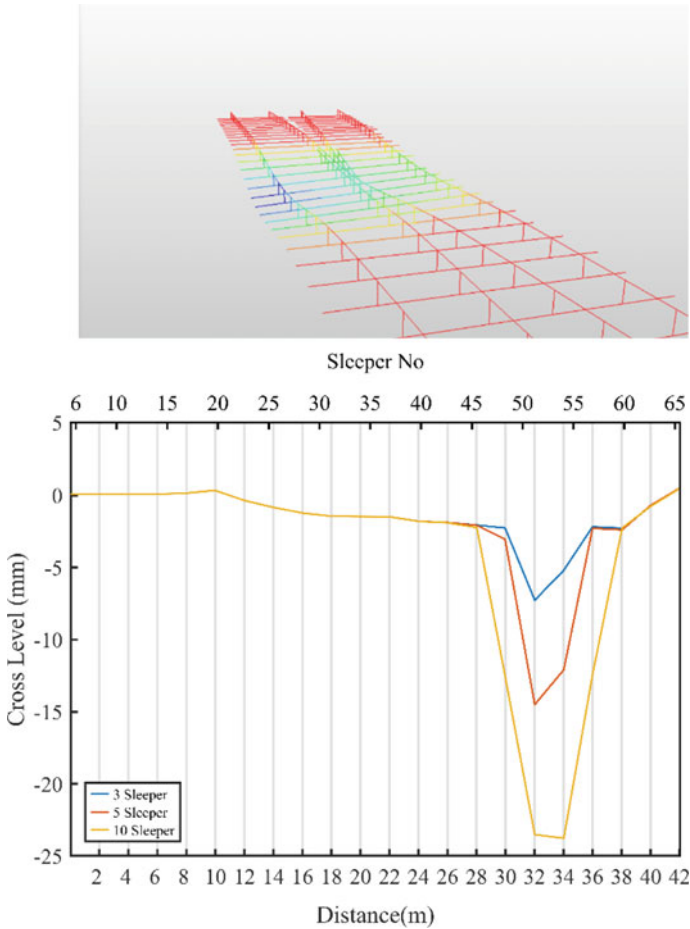
Fig. 4 A graphical demonstration of vertical displacement in the vicinity of the bearer with no.18, where blue color represents the lowest (top). Cross-level values for 3, 5 and 10 bearers at switch panel subjected to washed away ballast (bottom)

the normalized water level. In other words, the ballast structure seems to provide significant support unless the ballast bed is not fully under water. However, the validity of this conclusion is strongly related to the validity of the study from which the ballast parameters were collected.

Finally, outcomes of this study indicate that turnouts could inherently suffer from twist defects under vehicle loading owing to its asymmetrical structure, a potential cause of a derailment. Particularly taking the amplification characteristic of high speeds into account, further studies should be conducted at different vehicle speeds

Fig. 5 A graphical demonstration of vertical displacement in the vicinity of the bearer with no.50, where blue color represents the lowest (top). Cross-level values for 3, 5 and 10 bearers at crossing panel subjected to washed away ballast (bottom)

in different scenarios to improve the understanding of dynamic behavior of a turnout system in the case of flooding.

References

1. Virgin Hyperloop homepage, https://virginhyperloop.com/. Last accessed 28 Nov 2020
2. Kaewunruen S, Rungskunroch P (2019) A through-life evaluation of end-of-life rolling stocks considering asset recycling, energy recovering, and financial benefit. J Clean Prod 212:1008–1024
3. Kaewunruen S, Sussman JM, Einstein HH (2016) Strategic framework to achieve carbon-efficient construction and maintenance of railway infrastructure systems. Front Environ Sci 3:6
4. Krezo S et al (2016) Field investigation and parametric study of greenhouse gas emissions from railway plain-line renewals. Transp Res Part D: Transp Environ 42:77–90
5. Ngamkhanong C, Kaewunruen S, Costa BJA (2018) State-of-the-art review of railway track resilience monitoring. Infrastructures 3(1):3
6. Kaewunruen S, Sussman JM, Matsumoto A (2016) Grand challenges in transportation and transit systems. Frontiers Built Environ 2:4
7. Ngamkhanong C, Nascimento AT, Kaewunruen S (2019) Economics of track resilience. In IOP Conference Series. Materials Science and Engineering
8. Kaewunruen S (2014) Monitoring in-service performance of fibre-reinforced foamed urethane sleepers/bearers in railway urban turnout systems. Struct Monitoring Maintenance 1(1):131
9. Hamarat M et al (2020) The effect of unsupported sleepers/bearers on dynamic phenomena of a railway turnout system under impact loads. Appl Sci 10(7):2320
10. Kaewunruen S, You R, Ishida M (2017) Composites for timber-replacement bearers in railway switches and crossings. Infrastructures 2(4):13
11. Sengsri P et al (2020) Experimental and numerical investigations into dynamic modal parameters of fiber-reinforced foamed urethane composite beams in railway switches and crossings. Vibration 3(3):174–188
12. Dindar S, Kaewunruen S, An M (2020) Bayesian network-based human error reliability assessment of derailments. Reliab Eng Syst Safety 197:106825
13. Andersson C, Dahlberg T (1998) Wheel/rail impacts at a railway turnout crossing. Proc Inst Mech Eng Part F: J Rail Rapid Transit 212(2):123–134
14. Ekberg A, Paulsson B (2010) INNOTRACK: concluding technical report.: International Union of Railways (UIC)
15. Esveld C (2001) Modern railway track, 2nd edn. MRT-productions, Netherlands
16. Grossoni I et al (2015) Dynamics of a vehicle–track coupling system at a rail joint. Proc Inst Mech Eng Part F: J Rail Rapid Transit 229(4):364–374
17. Kassa E, Nielsen JC (2008) Dynamic interaction between train and railway turnout: full-scale field test and validation of simulation models. Veh Syst Dyn 46(S1):521–534
18. Manalo A et al (2010) A review of alternative materials for replacing existing timber sleepers. Compos Struct 92(3):603–611
19. Sae Siew J, Mirza O, Kaewunruen S (2017) Torsional effect on track-support structures of railway turnouts crossing impact. J Transp Eng Part A: Syst 143(2):06016001
20. Wei Z et al (2017) Wheel–rail impact at crossings: relating dynamic frictional contact to degradation. J Comput Nonlinear Dyn 12(4)
21. Kaewunruen S, Lian Q (2019) Digital twin aided sustainability-based lifecycle management for railway turnout systems. J Clean Prod 228:1537–1551
22. Wang P (2015) Design of high-speed railway turnouts: theory and applications. Academic Press, USA
23. Kaewunruen S et al (2017) Asymetrical influences on nonlinear dynamics of railway turnout bearers
24. Kaewunruen S, Tang T (2019) Idealisations of dynamic modelling for railway ballast in flood conditions. Appl Sci 9(9):1785
25. Li D, Kaewunruen S (2019) Effect of extreme climate on topology of railway prestressed concrete sleepers. Climate 7(1):17

26. Ludvigsen J, Klæboe R (2014) Extreme weather impacts on freight railways in Europe. Nat Hazards 70(1):767–787
27. Binti Sa'adin SL, Kaewunruen S, Jaroszweski D. (2016) Operational readiness for climate change of Malaysia high-speed rail. In Proceedings of the Institution of Civil Engineers Transport
28. Binti Sa'adin, S.L., Kaewunruen, S. and Jaroszweski, D.: Risks of Climate Change with Respect to the Singapore-Malaysia High Speed Rail System. Climate, 4(4), 65 (2016).
29. Binti Sa'adin, S.L., Kaewunruen, S. and Jaroszweski, D.: Heavy rainfall and flood vulnerability of Singapore-Malaysia high speed rail system. Australian Journal of Civil Engineering, 14 (2), 123–131 (2016).
30. Kaewunruen S et al (2018) Vulnerability of structural concrete to extreme climate variances. Climate 6(2):40
31. Dindar S et al (2018) Bayesian Network-based probability analysis of train derailments caused by various extreme weather patterns on railway turnouts. Saf Sci 110:20–30
32. Quinn, A., et al.: Rail Adapt: Adapting the Railway for the Future. A Report for the International Union of Railways (UIC), (2017).
33. Daily Mail, https://www.dailymail.co.uk/news/article-5932793/24-die-318-injured-Turkey-train-derails-following-heavy-rain.html. Last accessed 28 Nov 2020
34. Hamarat M et al (2019) New insights from multibody dynamic analyses of a turnout system under impact loads. Appl Sci 9(19):4080
35. RailCorp (2019) TMC 203-track inspection in engineering manual-track. Australia
36. Railtrack Plc (2002) Twist faults. The Permanent Way Institution, Birmingham

Stability Assessment of a Fire-damaged Retrofitted RC Structure Having Vertical Irregularity

Mohammed Mazharuddin and Y. K. Guruprasad

Abstract Reinforced concrete (RC) structural members are susceptible to damage in the event of a fire outbreak in the structure. High-temperature fire causes damage to the concrete and reinforcement present in the structural member. This condition results in reduced load carrying capacity and loss of bond between concrete and steel, causing possible failure of the structural members. In this work, a numerical study is carried out to study the behaviour and stability of a multi-storeyed RC structural building having vertical irregularities that are exposed to high temperature due to fire. The vertical irregularities present in the structure considered in this study are due to the presence of a mezzanine floor and cantilever portions of floors in the building that are supported by floating RC columns. Fire in the form of high temperature is applied in the portion of the structure where the vertical irregularities are more prominent. The vertical irregularities cause lateral deflections of slender RC columns due to local buckling on account of high temperature exposure due to degradation of the material causing instability in the structure. Slender RC column that is damaged due to exposure to high temperature is sub-modelled, and a finite element analysis of the sub-model is carried out to assess the extent of high temperature variation across the volume of the member, to understand the damage taken place in the structural members due to high temperature. The distressed structural members (RC columns) that have developed reduced stiffness and lower load carrying capacities on account of fire damage are retrofitted adopting RC jacket and steel plate bonding applied individually around such members. The efficacy of individual retrofits adopting RC jackets and steel plate bonding is studied. The overall structural stability and improvement in the load carrying capacity of the retrofitted structural members and the structure having vertical irregularity that has undergone damage due to high temperature exposure due to fire are assessed.

Keywords Damage · High-temperature fire · Vertical irregularity · RC jacket and steel bonded plates

M. Mazharuddin (✉) · Y. K. Guruprasad
Department of Civil Engineering, Ramaiah Institute of Technology, Bengaluru, India

1   Introduction

Structural members are susceptible to damage or undergo distress in the event of natural disasters such as fire, earthquake and wind. In the event of a fire that takes place in a structure, huge amount of structural damage is caused before the fire is extinguished. Discontinuity or lack of redundancy in a structure causes local failure that may lead to progressive collapse of the structure [1] when extreme loads act on the structure. Columns are the most critical members when RC structure is subjected to fire [2]. The buckling of columns when subjected to fire results in additional moments on beams [3]. When concrete present in the structural members is subjected to a temperature of about 300°C, the compressive strength of concrete starts to degrade. At a higher temperature beyond 500°C, concrete is considered to have lost 50% of its strength. RC structural members are assumed to have failed when the temperature of reinforcement present in the structural member reaches 593 °C [4].

Behrouz et al. [5] carried out a finite element study on two RC structures that are designed for different performance levels when subjected to post-earthquake fire (PEF). Fire resistance of a RC structure that is designed for immediate occupancy (IO) level is 300% more when it is subjected to only fire as compared to the structure that is subjected to PEF. Similarly, fire resistance of a RC structure that is designed for life safety (LS) level is 400% more when it is subjected to only fire as compared to the structure that is subjected to PEF. It is seen that local collapse of the structure is observed when it is subjected to only fire, while global collapse of the structure is seen in case of PEF. Huang et al. [2] carried out a finite element study on behaviour of RC structures subjected to fire. RC columns initially expand due to high temperature exposure and contract due to reduction in temperature that results in damage of structural members. Corner columns in the plan of structure have more deflection than the inner columns. RC slabs develop small-tension rings in the central portion and compression rings at the peripheral region. At high temperatures, internal bays of the structure are more resistant than the corner bays due to existence of floor continuity and more restraints at the internal bay. Behrouz et al. [3] carried out a finite element study on travelling fires in an irregular steel structure having vertical irregularity that exists due to different setback lengths provided in the plan at each floor level. It is found that an irregular structure collapses at a relatively lesser time as compared to a regular structure in case of travelling fire in the structure. The fire rating resistances (FRR) of structural members in an irregular structure results in different values based on the direction of travelling fire due to non-uniform distribution of gravity loads. It is proposed that FRR should be increased by 16% for a regular structure and 25% for an irregular structure or insulation thickness should be increased for the structural members to reduce the values of FRR. It is observed from the previous works that have been carried out that not much attention has been given towards retrofitting of RC structures having vertical irregularities that have undergone damage due to high-temperature fires.

The **objective of the present study** is to assess the instability in the behaviour of a RC structure having vertical irregularities (mezzanine floor supported by slender

column and floating RC columns supporting cantilever portions of floors at higher levels) when exposed to high-temperature fire and to assess the efficacy of the retrofit adopting RC jacket and steel plates to restore such a distressed structure in the post-fire condition.

2 Analysis of RC Structure Subjected to High-temperature Fire

In this section, the procedure to assess the behaviour of a RC structure that was priorly designed to resist gravity loads when subjected to a high-temperature fire and to understand behaviour of the same structure after application of retrofit adopting RC jacket and steel plate bonding individually to the structural members present in the structure in the post-fire condition has been presented. In this study, an RC structure is considered that has vertical irregularities namely mezzanine floor supported by slender columns and floating RC columns supporting cantilever portions of floors at higher levels to resist gravity loads. The analysis of the structure is carried out by applying temperature due to a fire condition in the portions of the structure that have vertical (mezzanine floor supported by slender columns and floating RC columns supporting cantilever portions of floors at higher levels). In this study, an office building having four bays measuring 4 m per bay in both the X and Y directions has been considered. The top two storeys are provided with a cantilever portion having a cantilever span of 2 m along the X-direction at the right-end corner of the building. A mezzanine floor is provided at storey 1 of the building towards the rear left corner portion of the building. The mezzanine floor has a total height of 6 m. The plan, elevation and three-dimensional model of the RC structure having vertical irregularities considered for this study are shown in Figs. 1a–c, respectively.

The thickness of the RC slab provided is 150 mm for all the floors in entire structure. The beams that are provided below the outer walls or main walls in plan have
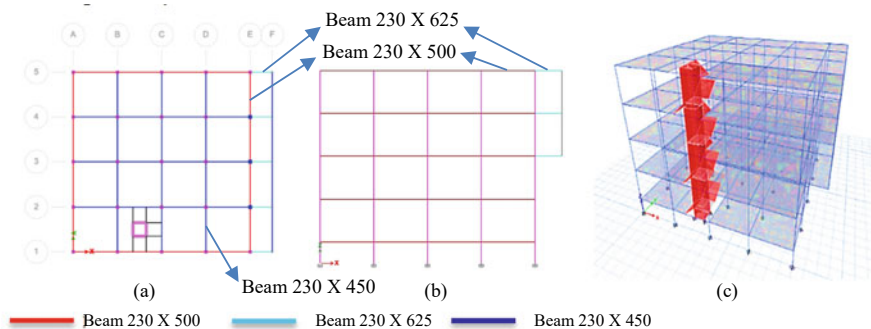
Fig. 1 **a** Plan, **b** Elevation and **c** 3D model of RC building

the cross-sectional dimensions of 230 mm × 500 mm. The edge beams (located at grid F) that are supported by floating RC columns have cross-sectional dimensions of 230 mm X 450 mm. The beams that support the floating RC columns in the cantilever portions have the cross-sectional dimensions of 230 mm × 625 mm (located at grids E–F 1, E–F 2, E–F 3, E–F 4 and E–F 5). All other beams have cross-sectional dimensions of 230 mm × 450 mm. RC columns located at grids E-2, E-3 and E-4 in the plan of the structure have a cross-sectional size of 350 mm × 350 mm. The floating RC columns that support the cantilever portion have a cross-sectional size of 200 mm × 200 mm, and all other RC columns have a cross-sectional size of 300 mm × 300 mm. The corner RC column supporting the mezzanine floor has a cross-sectional size of 300 mm × 300 mm in cross-section and has a length of 6 m. The floor height of each storey in the structure is 3 m other than the mezzanine floor that has a floor height of 6 m. An open-well stair case (having a flight width of 1.4 m) has been provided around a 150 mm thick shear RC wall having end columns of 200 mm × 200 mm cross-sectional size that has been provided as a lift well.

The gravity loads applied on the structure are:

Floor finish = 1.2kN/m^2.
Exterior or outer wall load = 13.8kN/m.
Interior or partition wall load = 6kN/m.
Parapet wall of 1 m height = 2kN/m^2.
Live load for office = 4kN/m^2.
Live load for stairs = 5kN/m^2.
Live load for corridor or passage = 5kN/m^2.
Roof live load (accessible) = 2kN/m^2.

Material properties of M20 grade concrete (Mander's stress–strain curve for unconfined concrete) [6] that has been provided for RC beams, RC columns, and RC slabs and material properties of M25 grade concrete that has been adopted for the RC jacket are shown in Fig. 2. Material properties of steel reinforcement of Fe500 grade (EN 1992–1–2) [7] that has been adopted in this work corresponding to ambient temperature (20$^°$C) are shown in Fig. 3.
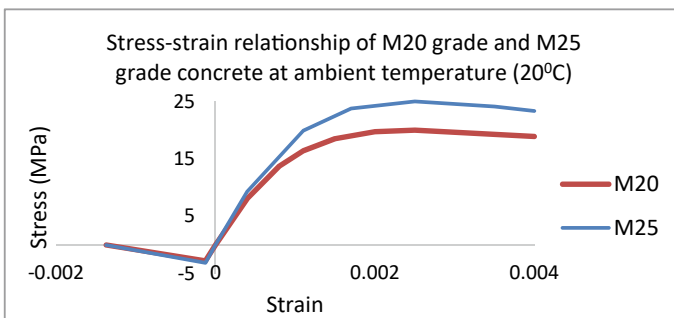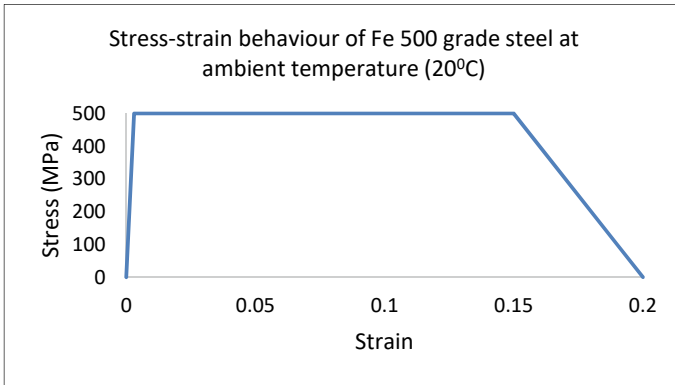

Fig. 2 Stress–strain curve of concrete at ambient temperature (20$^°$C) [6]

**Fig. 3** Stress–strain curve of steel at ambient temperature $(20°C)$ [7]

In this study, temperature due to fire is applied in the portions of the structure that have vertical irregularity (mezzanine floor supported by slender columns and floating RC columns supporting cantilever portions of floors at higher levels) to assess the behaviour of the structure having the vertical irregularities when the temperature due to fire is applied only in the portion where vertical irregularities are present. The structure is analysed for gravity loads at ambient temperature in the first step [8]. Due to the fire that has taken place in the building, temperature of the materials present in the structure increases. Since, RC structures undergo damage at elevated temperatures, maximum temperature that has attained in the structure (exposed surface of structural members) due to fire is considered to be $400°C$ for Case 1 and $600°C$ for Case 2 in this study. To determine the effect of vertical irregularities present in the structure subjected to fire, two different sets of structural models are analysed. The structural models corresponding to Set 1 have been subjected to high temperature due to fire in the portion where mezzanine floor exists (yellow region) as shown in Fig. 4a. While the structural models corresponding to Set 2 have been subjected to high temperature, due to fire in the cantilever portion in the top, top-two storeys (yellow region) are shown in Fig. 4b.

In the second step, temperature exposures of $400°C$ (Case 1) and $600°C$ (Case 2) are applied in the portions where vertical irregularities exist to assess the behaviour of structure due to sudden rise of temperature in both models corresponding to Set 1 and Set 2.

Due to fire, mechanical properties of concrete and steel reinforcement such as strain, modulus of elasticity and material strength tend to change in magnitude at elevated temperatures of exposure. The material properties of concrete and steel at elevated temperatures are obtained by applying reduction factors corresponding to the exposure temperature, in accordance with EN 1992–1-2 (2004) [7] as shown in Figs. 5 and 6, respectively.

In the third step, the strength reduction due to temperature exposure is applied to concrete and steel reinforcement present in the structural members that are exposed

(a)   (b)
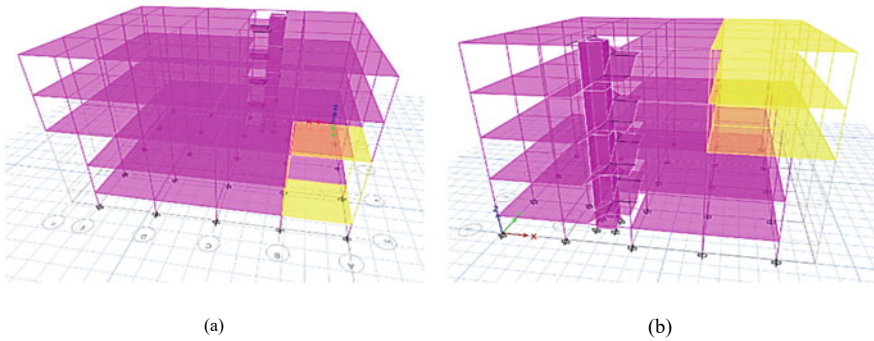
Fig. 4 High temperature applied at **a** Mezzanine floor **b** Last bay and cantilever portion of the building
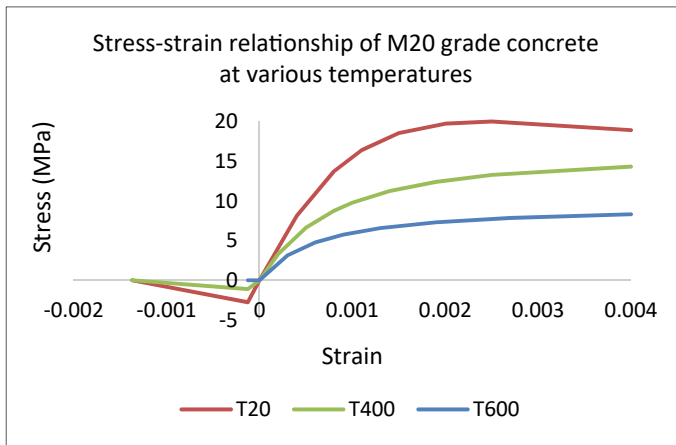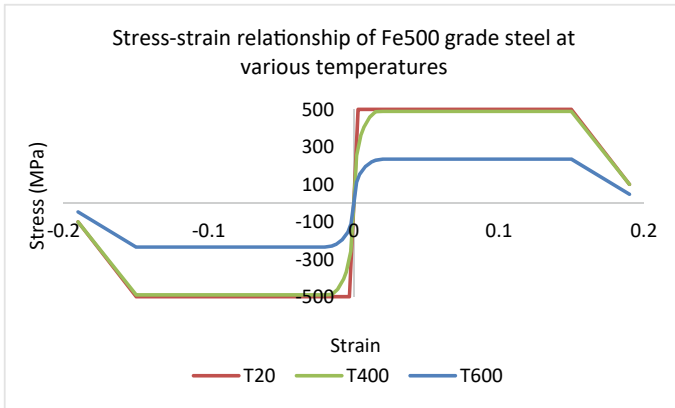

Fig. 5 Stress–strain relationship of M20 concrete at various temperatures [7]

to temperatures (as mentioned in step 2) of 400°C and 600°C in Case 1 and Case 2, respectively.

In the fourth step, only the strength reduction of concrete and steel reinforcement due to temperature exposure (without temperature load) is applied on structural members to assess the behaviour of the structure after the structural members have cooled and attained an ambient temperature.

In the fifth step, the existing RC columns that are damaged due to fire are retrofitted separately with the help of an RC jacket having a thickness of 100 mm [9] and steel bonded plates having a thickness of 10 mm throughout the height of the building, to study the effectiveness of a particular type of retrofit applied to such RC columns. The RC jacket adopted in this study has M25 grade concrete and Fe 500 grade steel reinforcement, while the steel bonded plates adopted are of Fe 345 grade steel. The

Fig. 6 Stress–strain relationship of HYSD 500 steel at various temperatures [7]

typical cross-sections of (a) RC columns retrofitted with the RC jackets and (b) RC columns retrofitted with steel bonded plates are shown in Fig. 7. The typical cross-sections of RC columns retrofitted with RC jackets and RC columns retrofitted with steel bonded plates are shown in Figs. 7a, b, respectively. The retrofitting of RC columns adopted for structural models corresponding to Set 1 and Set 2 in plan is shown in Figs. 8a, b, respectively.

In models corresponding to Set 2, floating RC columns are supported by RC columns that begin from the foundation level and are interconnected by beams from the point of stability. The RC columns that support the floating RC columns have a cross-sectional dimension of 400 mm × 400 mm when the RC jacket retrofit is provided around them. The RC columns that are supporting the floating RC columns when steel bonded plate retrofit is provided have a cross-sectional dimension of 200 mm × 200 mm.

The following nomenclatures are adopted for the different steps in the analysis that has been carried out on the structural models:

Step 1: **D 20**: material properties corresponding to ambient temperature is applied.
Step 2: **T 400 or T 600**: temperature load of $400\degree$C (Case 1) or $600\degree$C (Case 2) is applied.

Fig. 7 Typical cross-section of RC column retrofitted with **a** RC jacket **b** Steel bonded plates

(a)   (b)
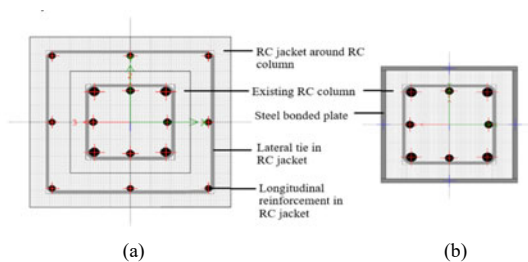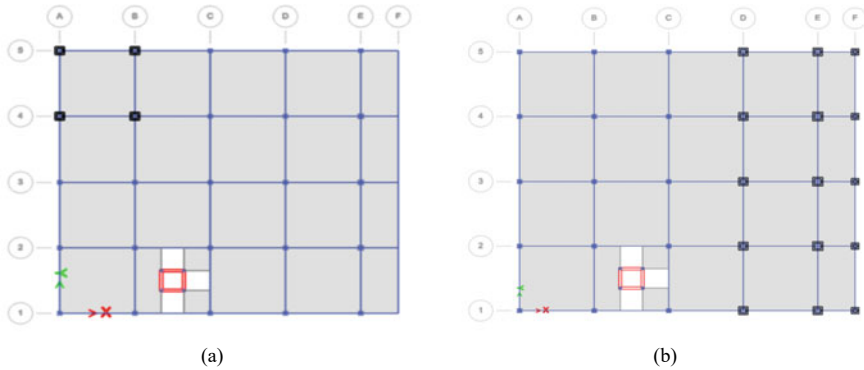
Fig. 8 Retrofitting of RC columns in plan corresponding to **a** Set 1 and **b** Set 2 models

Step 3: **T-D 400 or T-D 600**: temperature load of $400°$C or $600°$C and material properties corresponding to high temperature (as per EN: 1992–1-2) exposures of $400°$C or $600°$C are applied.

Step 4: **D 400 or D600**: material properties corresponding to high temperature exposures of $400°$C or $600°$C are applied without any temperature load.

Step 5: **J-D 400 or J-D 600**: RC jacket retrofit is applied to the damaged RC columns that has reduced strength due to high temperature exposures of $400°$C or $600°$C.

Step 6: **S-D 400 or S-D 600**: steel bonded plate retrofit is applied to the damaged RC columns that has reduced strength due to high temperature exposures of $400°$C or $600°$C.

A slender RC column having a cross-sectional size of 300 mm X 300 mm and height of 6 m is adopted to support the mezzanine floor, and the same column is sub-modelled in Abaqus for different temperature exposures ($400°$C in Case 1 and $600°$C in Case 2). The temperature time histories up to the temperatures of $400°$C and $600°$C in Cases 1 and 2 are applied using the ISO curve [10]. Temperatures of $400°$C and $600°$C are applied on two faces of the slender RC columns in Cases 1 and 2, respectively, as shown in Fig. 9. Material properties of concrete such as thermal conductivity and specific heat are adopted as per EN 1992–1-2 (2004) [7].

Temperature distribution across the volume of the slender RC column is studied when it is subjected to high temperatures ($400°$C and $600°$C) for an exposure time of 1 h.

3 Results and Discussions

In this section, the results and discussions have been reported corresponding to the analysis that has been carried out on the RC structure having vertical irregularities

Fig. 9 Temperature applied
on two faces of a finite
element model of slender RC
column
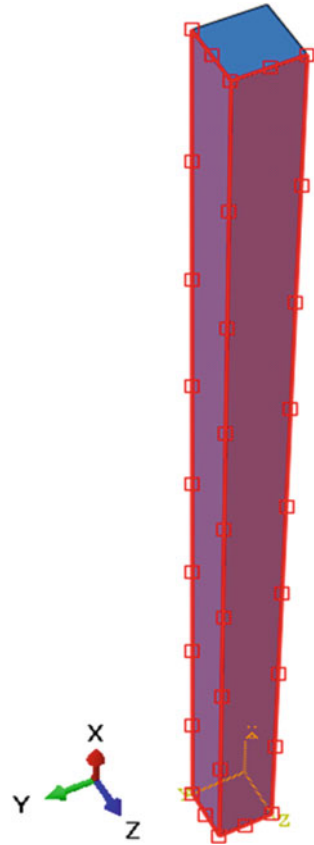
subjected to high temperature exposure on account of fire without retrofit, and the results of same RC structure are reported after application of retrofit.

3.1 Results of Set 1 Models in ETABS

In the models corresponding to Set 1, high temperature due to fire is applied in the portion where mezzanine floor is present in the structure. For comparison, joint displacements at grid A-5 in plan are considered at different steps (Step 1 to Step 5 as mentioned in section 2) for Set 1 models as shown in Tables 1, 2, 3 and 4.

The joint displacements increase with an increase in the value of the applied temperature due to thermal expansion of structural members in the mezzanine floor. Further increase in displacements is observed when material strength of structural members exposed to a high-temperature fire tends to reduce. It is observed that there is an increase in the length of the RC slender column due to thermal expansion when

Table 1 Horizontal joint displacements (mm) at different steps of analysis for Set 1 models for a temperature exposure of 400°C

Storeys	D 20	T 400	T-D 400	D 400	J-D 400	S-D 400
Roof	1.56	0.54	0.56	1.57	0.93	1.10
Storey 4	0.97	0.32	0.34	0.98	0.62	0.72
Storey 3	0.43	7.65	7.66	0.44	0.32	0.34
Storey 2	0.10	10.77	**11.04**	0.10	0.08	0.07
Storey 1	0.01	7.38	7.37	0.00	0.00	0.00
Base	0.00	0.00	0.00	0.00	0.00	0.00

Table 2 Vertical joint displacements (mm) at different steps of analysis of Set 1 models for a temperature exposure of 400°C

Storeys	D 20	T 400	T-D 400	D 400	J-D 400	S-D 400
Roof	−1.24	12.42	12.33	−1.36	−0.50	−0.59
Storey 4	−1.17	12.45	12.36	−1.29	−0.47	−0.56
Storey 3	−0.97	12.57	12.48	−1.09	−0.39	−0.47
Storey2	−0.63	6.15	**6.11**	−0.69	−0.26	−0.31
Storey 1	−0.28	−0.25	−0.25	−0.28	−0.11	−0.14
Base	0.00	0.00	0.00	0.00	0.00	0.00

Table 3 Horizontal joint displacements (mm) at different steps of analysis of Set 1 models for a temperature exposure of 600°C

Storeys	D 20	T 600	T-D 600	D 600	J-D 600	S-D 600
Roof	1.56	0.03	0.11	1.61	0.96	1.14
Storey 4	0.97	−0.01	0.06	1.01	0.65	0.74
Storey 3	0.43	11.26	11.30	0.45	0.33	0.36
Storey 2	0.10	16.10	**17.25**	0.11	0.08	0.07
Storey 1	0.01	11.07	11.03	−0.01	0.00	−0.01
Base	0.00	0.00	0.00	0.00	0.00	0.00

Table 4 Vertical joint displacements (mm) at different steps of analysis of Set 1 models for a temperature exposure of 600°C

Storeys	D 20	T 600	T-D 600	D 600	J-D 600	S-D 600
Roof	−1.24	19.25	18.98	−1.62	−0.54	−0.65
Storey 4	−1.17	19.26	19.00	−1.56	−0.51	−0.62
Storey 3	−0.97	19.34	19.09	−1.35	−0.42	−0.52
Storey 2	−0.63	9.55	**9.42**	−0.82	−0.28	−0.34
Storey 1	−0.28	−0.24	−0.25	−0.29	−0.12	−0.15
Base	0.00	0.00	0.00	0.00	0.00	0.00

exposed to high temperature. The values under T-D 400 and T-D 600 at storey 2 in Tables 1, 2, 3 and 4 represents, the maximum horizontal and vertical displacements due to high-temperature fire exposure and loss of material strength at the top of the slender RC column at temperatures of 400°C and 600°C, respectively. The increase in the length of the RC slender column gives rise to an increase in the tensile axial displacement, whereas the gravity loads tend to cause a compressive axial displacement along with considering the effect of deteriorated material properties, causing a net effect of shortening of the column. Therefore, the resulting net vertical displacement in the RC slender column tends to reduce in magnitude. Retrofitting of distressed RC columns adopting RC jackets or steel bonded plates tends to reduce the displacements due to the already existing gravity loads acting on the structure as it has been observed in the results. This indicates that the event of buckling of the slender RC column that was exposed to high temperature has been averted due to application of RC jacket and steel bonded plate as retrofitting measures and to have restored the stability of the slender RC column. Displacement values that are obtained after application of RC jackets and steel bonded plates as retrofits are found to be more or less close. The above-stated observations are mentioned based on the tabulated results of the displacements shown in Tables 1, 2, 3 and 4.

3.2 Results of Set 2 Models in ETABS

In the models corresponding to Set 2, high temperature is applied in the last bay including the cantilever portion of the structure. For comparison, joint displacements at grid F-5 in plan are considered at different steps (Step 1 to Step 5 as mentioned in Sect. 2) for models corresponding to Set 2 as shown in Tables 5, 6, 7 and 8.

The joint displacements are observed to increase when there is a high temperature exposure due to thermal expansion of structural members. Since in this study, the temperature due to fire has been applied in the cantilever portion, displacements are predominant in this particular portion of the building and presence of vertical irregularity further causes instability in the structure. After application of the retrofit

Table 5 Horizontal joint displacements (mm) at different steps of analysis of Set 2 models for a temperature exposure of 400°C

Storeys	D 20	T 400	T-D 400	D 400	J-D 400	S-D 400
Roof	0.04	18.66	20.11	−0.01	0.46	0.45
Storey 4	0.22	20.46	20.35	0.19	0.38	0.40
Storey 3	0.40	20.79	20.71	0.40	0.27	0.32
Storey 2	–	–	–	–	0.15	0.18
Storey 1	–	–	–	–	0.02	0.02
Base	–	–	–	–	0.00	0.00

Table 6 Vertical joint displacements (mm) at different steps of analysis of Set 2 models for a temperature exposure of 400°C

Storeys	D 20	T 400	T-D 400	D 400	J-D 400	S-D 400
Roof	−4.87	8.22	7.77	−5.31	−0.29	−0.73
Storey 4	−4.86	1.63	1.18	−5.30	−0.27	−0.71
Storey 3	−4.86	−4.98	−5.43	−5.30	−0.22	−0.65
Storey 2	–	–	–	–	−0.14	−0.40
Storey 1	–	–	–	–	−0.05	−0.14
Base	–	–	–	–	0.00	0.00

Table 7 Horizontal joint displacements (mm) at different steps of analysis of Set 2 models for a temperature exposure of 600°C

Storeys	D 20	T 600	T-D 600	D 600	J-D 600	S-D 600
Roof	0.04	30.34	29.81	−0.10	0.51	0.49
Storey 4	0.22	30.59	30.11	0.15	0.42	0.43
Storey 3	0.40	30.99	30.60	0.40	0.29	0.33
Storey 2	–	–	–	–	0.15	0.18
Storey 1	–	–	–	–	0.02	0.02
Base	–	–	–	–	0.00	0.00

Table 8 Vertical joint displacements (mm) at different steps of analysis of Set 2 models for a temperature exposure of 600°C

Storeys	D 20	T 600	T-D 600	D 600	J-D 600	S-D 600
Roof	−4.87	14.83	13.23	−6.25	−0.29	−0.76
Storey 4	−4.86	4.93	3.34	−6.25	−0.27	−0.73
Storey 3	−4.86	−4.98	−6.58	−6.24	−0.22	−0.67
Storey 2	–	–	–	–	−0.14	−0.41
Storey 1	–	–	–	–	−0.05	−0.14
Base	–	–	–	–	0.00	0.00

on the fire-damaged structural members (floating columns supporting the cantilever portion), the displacements are observed to have reduced.

Table 9 Temperature distribution across the cross-section of slender RC column

Distance from exposed face(mm)	Temperature Case 1 ($^{\circ}$C)	Temperature Case 2 ($^{\circ}$C)
0	400	600
37.5	293.202	409.184
75	155.544	202.345
112.5	74.1967	91.8283
150	37.8357	43.4656
187.5	24.9542	26.4751
225	21.1867	21.5386
262.5	20.2568	20.3295
300	20.0931	20.1182

3.3 Finite Element Analysis Results of the Slender RC Column Supporting the Mezzanine Floor Having Vertical Irregularity Exposed to High Temperature

The slender RC column that supports the mezzanine floor present in the structure is exposed to high temperatures of 400°C (Case 1) and 600°C (Case 2) for a duration of 1 h, due to a fire breakout in the mezzanine floor portion. The temperature distribution across the cross-section of the slender RC column in Case 1 and Case 2 is shown in Table 9 and in Fig. 10 for Case 1 and Case 2, respectively.

It is observed from the results in Table 9 and Fig. 10 that the temperature in the region where the reinforcement is provided in the slender RC column attains a value more than 200°C in both Case 1 and Case 2. Hence, the elastic modulus of the reinforcing steel tends to reduce as this may be observed in the stress–strain response of reinforcing steel exposed to high temperature as shown in Fig. 6 [7]. Due to increase in temperature around the core region of slender RC column, there

(a)   (b)
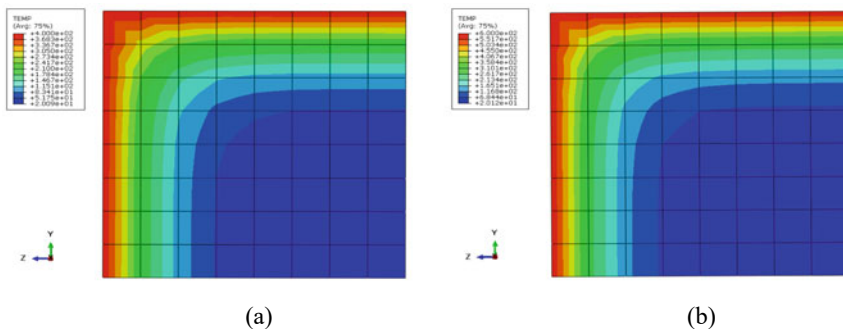
Fig. 10 Temperature distribution across the cross-section of slender RC column in **a** Case 1 (400°C) and **b** Case 2 (600°C)
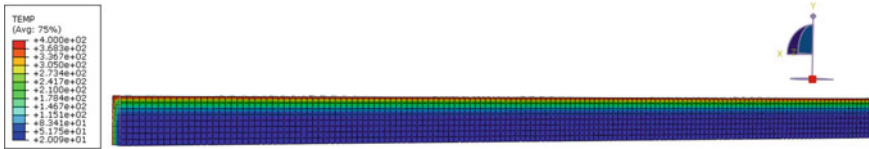
Fig. 11 Temperature distribution across the length of slender RC column in Case 1 (400°C)
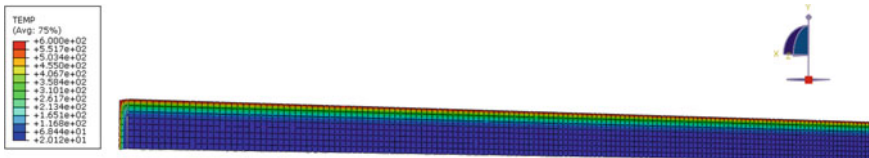
Fig. 12 Temperature distribution across the length of slender RC column in Case 2 (600°C)

is a loss of strength and accumulation of damage due to temperature exposure that causes the slender RC column to buckle. Temperature distribution across the length of RC column for Case 1 and Case 2 is shown in Figs. 11 and 12, respectively.

4 Conclusion

- Vertical irregularities present in the RC structure (slender RC column in mezzanine floor and floating RC columns in the cantilever portions) when exposed to a high-temperature fire develop large displacements (horizontal and vertical) in that portion of the structure leading to instability.
- RC jacket and steel bonded plate retrofits that are individually applied on to slender RC columns that have undergone damage due to temperature exposure are observed to considerably reduce the displacements (horizontal and vertical) and restore the stability and load carrying capacity of such columns that are subjected to gravity loads.
- It is observed from the results of this study that the RC jacket and steel plate bonding applied individually to retrofit slender RC columns that have undergone fire damage and are present in the portions of the building that have vertical irregularity are found to be equally effective in reducing the displacements due to gravity loads and also help in restoring the stability of such columns.
- Degradation at material level takes place around the core portion in the slender RC columns that are exposed to high temperatures due to fire as observed from the results of this study (Table 9 and Fig. 10). This phenomenon causes buckling of the slender RC column. It is also observed from the results (Tables 1, 2, 3 and 4) that RC jacket and steel plate bonding retrofits reduce the displacements and avert

the buckling effectively in the fire-damaged slender RC columns due to gravity loads.

References

1. Vismitha V, Dr. Raghu Prasad BK, Dr. Amarnath K (2016) Response of tall buildings when subjected to fire. Int Res J Eng Technol 03(08):494–500
2. Huang Z, Burgess IW, Plank RJ (2006) Behaviour of reinforced concrete structures in fire
3. Behnam B (2020) Vulnerability assessment of irregular steel structures under traveling fires. Struct Design Tall Spec Build 29:1–13
4. Behnam B (2017) On the interaction between span length and opening ratio of RC frames under natural fires. Struct Build 171:1–15. Institution of civil engineers publishing
5. Behnam B, Ronagh H (2013) Performance of reinforced concrete structures subjected to fire following earthquake. Eur J Environ Civ Eng 17(4):270–292
6. Mander JB, Priestley MJN, Park R (1988) Theoretical stress-strain model for confined concrete. J Struct Eng 114(8):1804–1826
7. EN 1992–1–2 (2004) Eurocode 2: Design of concrete structures—Part 1–2: General rules—Structural fire design
8. IS 456 (2000) Plain and reinforced concrete – Code of practice
9. IS 15988 (2013) Seismic evaluation and strengthening of existing reinforced concrete buildings—guidelines
10. ISO 834 (1975) Fire resistance tests—elements of building construction

Computational Fluid Dynamic Analysis in Dam Spillway Due to Sector Gate Opening

N. H. Hassan, M. H. Zawawi, and M. R. M. Radzi

Abstract This paper analyzes fluid dynamic in dam spillway with 4.9 m of sector gate opening. Hydraulic parameters that were determined in this study are pressure, velocity and streamline. A three-dimensional (3D) computational fluid dynamics (CFD) model of dam spillway structure and boundary condition were developed using ANSYS FLUENT. CFD model results show that the highest velocity value which is 14.8 m/s and the largest hydraulic jump occur is at the middle between two energy dissipators of the dam spillway. Hydraulic jump type that occurred which is oscillating jump is determined by the Froude value of 2.988. The high velocity contributes to the large hydraulic jump that may lead to damaging effects to stilling basin surface at downstream. Structural integrity for sustainability of spillway should be ensured for future mitigation.

1 Introduction

Development of numerical modeling has led to its widespread use as a standard design tool in many engineering disciplines such as hydraulic engineering [1]. Principles of fundamental upon numerical models is alike for all models regardless of the broad range of numerical model applications [2]. Various types of numerical techniques such as finite element method (FEM) or finite volume method (FVM) is used to formulate a set of algebraic equations [3]. It represents partial differential equations [3]. Through some form of either matrix or iterative solution, an approximate solution to algebraic equations can be obtained. Technically, this solution is

---

N. H. Hassan · M. H. Zawawi (✉)
Department of Civil Enginering, Universiti Tenaga Nasional, 43000 Kajang, Malaysia
e-mail: MHafiz@uniten.edu.my

M. R. M. Radzi
Tenaga Nasional Berhad, 59200 Kuala Lumpur, Malaysia

very computationally intensive which makes the use of modern computational power crucial to the use of numerical models [4].

Computational fluid dynamics (CFD) is one of the algorithms and numerical models for solving problems and analyzing fluid flow [5]. Time and cost of experiments for modeling the hydraulic structures can be reduced by using CFD as a relevant technique [6]. Thus, the ability of CFD to analyze or model fluid flow is considerable for the interest on the part of hydraulic engineers. This study is focusing on the use of CFD to model water flow through an ogee spillway of a hydroelectric dam on regard the fact that CFD is utilized for model flow in every hydroelectric station. There are many limitations in order to conduct experiment at real dam scale. Therefore, this study serves the purpose of simulate the real operating condition at the site.

Hydraulic design is important in the early stage of project to ensure structural integrity of a spillway [7]. It is one of the most studied subjects in hydraulic engineering. Spillway is amidst the most appurtenant hydraulic dam structure project process [7, 8]. In all types of dams, design of spillway is essential because water overflow that caused by probable maximum flood (PMF) discharge may eventually assist to crack or destruction of the dam [9]. Sufficient capacity of dam to avoid overtopping is also important for the spillway facilities to be designed [10]. Besides that, the values of pressure and velocity of water flow along the apron is crucial to be measured [11, 12] to ensure the design is safe.

Usually, physical models are developed to conduct an experiment for water flow analysis [13, 14]. Nevertheless, study on water flow analysis or hydraulic characteristics of this structure has been done with advancing in the field of CFD [15]. This is distinctly in initial process of design and analysis where the development of physical models would be proscriptive on the basis of time and cost [16]. A rapid evaluation of the existing conditions can be produced using current CFD techniques [16]. Ansys FLUENT impart to use the technique of CFD as one of the software packages [15]. Numerical method has been used in this paper to analyze the flow dynamics at hydroelectric dam spillway due to section gate opening.

2 Methodology

The methodology appertains to preprocessing, numerical simulation and post-processing. Preprocessing is the early stage of this study before simulation is conducted while numerical simulation is where the simulation is processed. Lastly, post-processing is where all the results were extracted to be analyzed. All materials and methods of numerical modeling will be discussed in this part.

2.1 Pre-Processing

A 3D model drawing was developed on the report to as built drawing spillway that was collected to impart in geometry part. In this study, fluid dynamic is discussed on the sector gate with 4.9 m gap opening. 4.9 m sector gate opening is one of operating conditions of a hydroelectric dam spillway which is the highest gap opening. The process of 3D model drawing development was constructed in SolidWorks software. The 3D model drawing was then uploaded in Ansys FLUENT software. Figure 1 shows the 3D model drawing of the hydroelectric dam spillway while Fig. 2 shows the model and boundary condition in Ansys FLUENT software to be defined. The boundary condition consists structure part and fluid part which is water and air is shown.

Mesh sensitivity assessment is conducted at this part. Size of mesh is analyzed from the largest to the smallest size which contain hexahedron and tetrahedron. Mesh size accuracy of the model is increased because computation cost increased [6]. The computational grid contains 207,926 cells. Another important parameter when it comes to wall functions mesh is y-plus (y +). y + is the non-dimensional distance from the wall to the first node from the wall. It provides reasonably accurate predictions for the majority of high-Reynolds-number, wall-bounded flows. The y + value is be between 30 and 300. Ansys FLUENT numerically solved Navier–Stokes equation by FVM. Continuity equation at 3D Cartesian coordinates as brief reference on the equations that calculated in the software is given as Eq. (1).
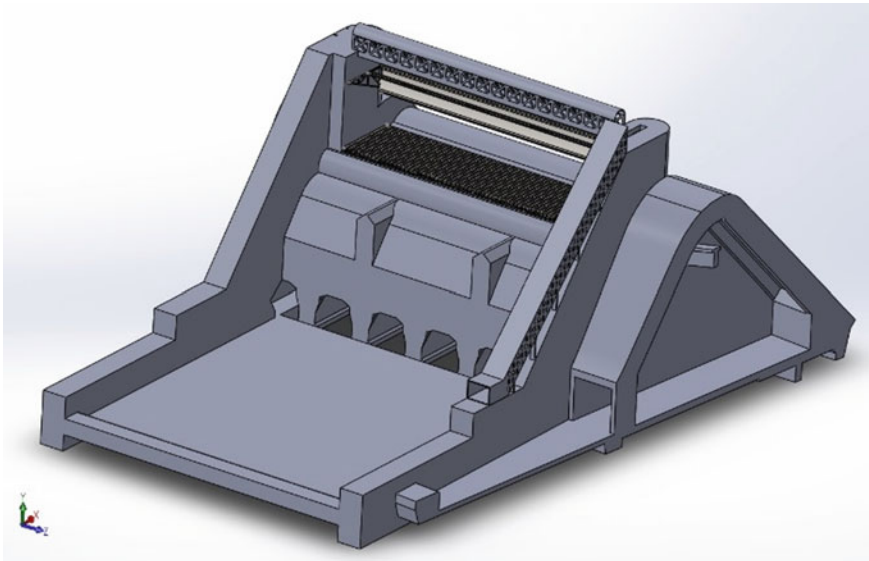
Fig. 1 3D model drawing of spillway structure
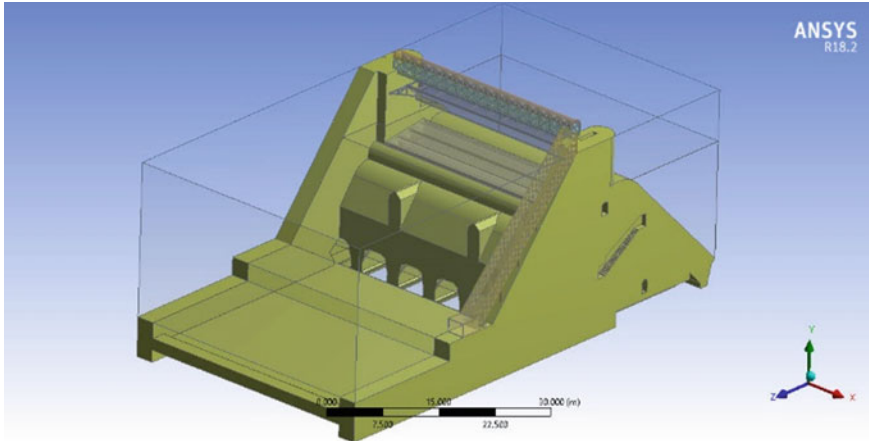
Fig. 2 3D model of spillway in Ansys FLUENT

$$v_f \frac{\partial \rho}{\partial t} + \frac{\partial}{\partial x}(uA_x) + \frac{\partial}{\partial y}(vA_y) + \frac{\partial}{\partial z}(wA_z) = \frac{\text{PSOR}}{\rho} \tag{1}$$

where *vf* is the fluid volume fraction; *u, v, z* is velocities component in the *x, y, z* direction; *Ax, Ay, Az* cross-sectional area of the flow; *PSOR* the source term; ρ fluid density and 3D momentum equations derived as in Eq. (2).

$$\begin{aligned}
\frac{\partial u}{\partial t} + \frac{1}{v_f}(uA_x\frac{\partial u}{\partial x} + vA_y\frac{\partial u}{\partial y} + wA_s\frac{\partial u}{\partial z}) &= -\frac{1}{\rho}\frac{\partial P}{\partial x} + G_x + f_x \\
\frac{\partial v}{\partial t} + \frac{1}{v_f}(uA_x\frac{\partial u}{\partial x} + vA_y\frac{\partial u}{\partial y} + wA_z\frac{\partial u}{\partial z}) &= -\frac{1}{\rho}\frac{\partial P}{\partial y} + G_y + f_y \\
\frac{\partial w}{\partial t} + \frac{1}{v_f}(uA_x\frac{\partial u}{\partial x} + vA_y\frac{\partial u}{\partial y} + wA_z\frac{\partial u}{\partial z}) &= -\frac{1}{\rho}\frac{\partial P}{\partial z} + G_z + f_z
\end{aligned} \tag{2}$$

where *Gx, Gy, Gz* is the acceleration produced by fluids of body; *P* is the fluid pressure; *fx, fy, fz* is acceleration of viscosity in 3D and *vf* is regards to the volume of fluid as define by Eq. (3).

$$\frac{\partial F}{\partial t} + \frac{1}{v_f}[\frac{\partial}{\partial x}(FA_xu) + \frac{\partial}{\partial y}(F_yv) + \frac{\partial}{\partial z}(w)] = 0 \tag{3}$$

Computational cells volume fraction of volume of fluid (VOF) method is used for model the free surface profile. It takes value between 0 and 1 since volume fraction *F* represents fluid amount in each of the mesh cell [6].

A spillway model demands the presence of free surface to represents air–water interface. VOF model is one such method for definitely tracking the interface between
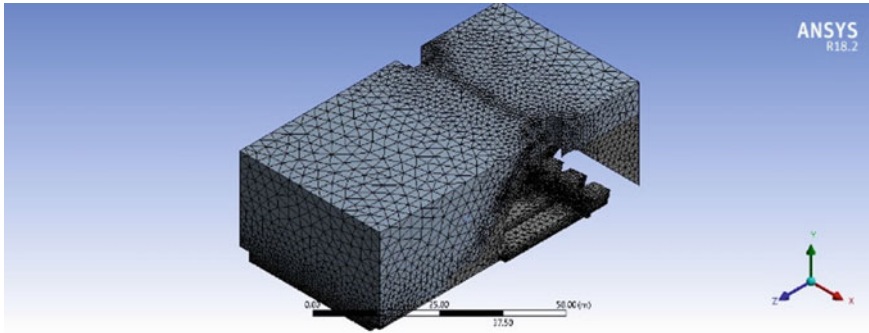
Fig. 3 Fluid meshing process

immiscible liquids [17]. Boundary conditions of structure and fluid were set as shown in Fig. 2. Figure 3 shows the meshing processing for geometry of fluid which is water and air. Using Ansys FLUENT, Reynolds-averaged Navier–Stokes (RANS) equations solve CFD that applied to spillway modeling. The modifications include model the flow past obstacles such as spillways and algorithms to track the free surface. In order to acquire closed form Navier–Stokes equations model of turbulence, realizable k-ε (RKE) has been presented. This approach entails statistical methods to extract out an averaged equation that involve quantity of turbulence. Turbulence model is required to directly capture every scale of motion [18].

k-ε is reasonably accurate for broad type of flows [19–21]. The model contents definite Reynolds stress by mathematical constraints that constant with the turbulent flows physic. It is also probably providing boundary layers under solid adverse pressure gradients, superior performance for flows that involve rotation, recirculation and separation [22]. A new transport equation for dissipation rate has been produced from an exact equation for vorticity fluctuation of mean-square transport [23]. The first one is turbulence kinetic energy and the second one is dissipation rate of turbulence energy. RKE gives a superior ability to determine the mean flow of the complex structures in every measure of comparison virtually [21].

2.2 Numerical Simulation

Water elevation of 49 m which is the height of the spillway crest elevation was initiated. The computational grid contains 207,926 cells. A uniform inflow velocity at upstream part of the model was applied to obtain a target flow rate. Figure 2 summarizes the boundary conditions used in simulation. Velocity at inlet of boundary conditions and velocity of the flow for inlet mixture phase are used to define the scalar properties. Velocity into the inlet is set at 1 m/s while volume fraction under

multiphase section is set at 1 for water phase inlet. Pressure at inlet and outlet are equal to the atmospheric pressure of 0 Pa and time step size is set at 0.1–5 s.

2.3 Post-Processing

Post-processing is the final solution where quantities of interest of pressure, velocity and streamline are extracted. Figures 4, 5, 6, 7 and 8 show visualizations of the simulation.

Figure 4 shows water pressure at the spillway structure. The maximum value for the pressure is 0.08078 Pa. One of two pressure boundary conditions which are stagnation and static analyzed the boundary condition at upstream area. The approach velocity may not be significant, and therefore, it is eliminated in some applications, [11]. However, the approach velocity in this study is considered significant at higher flows. Figure 5 shows the velocity of water at the spillway. The maximum value for the mean velocity is 0.1266 m/s.

The streamline in Fig. 6 shows the flow pattern through the spillway from the upstream to the downstream. Despite this study not including the experiment part, all of the fundamentals and methods used are similar to Sultan Abu Bakar Dam study that has been done by Abas [24]. Simulation result for both studies are then be compared for validation purpose.
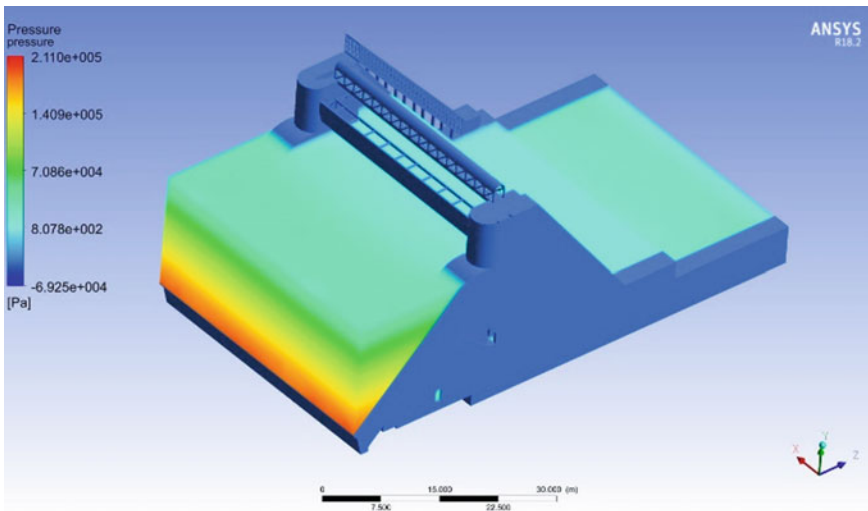
Fig. 4 Pressure of water at spillway
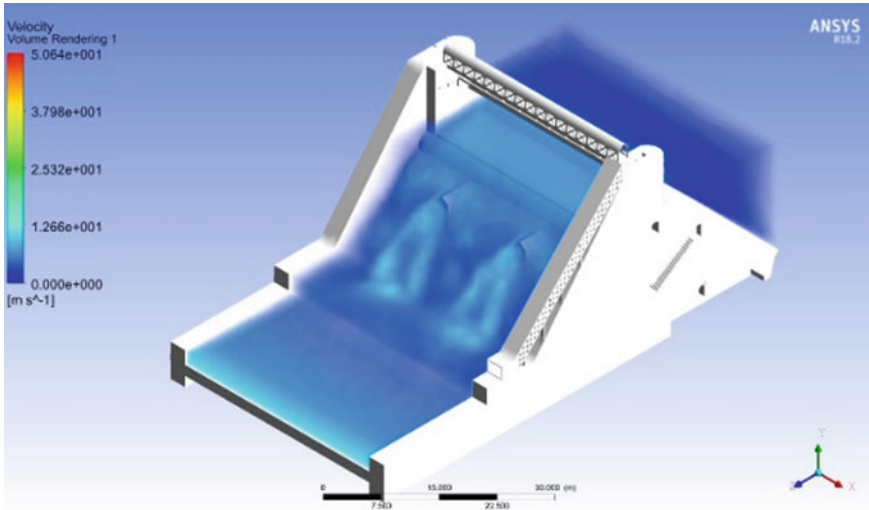
Fig. 5 Velocity of water at spillway
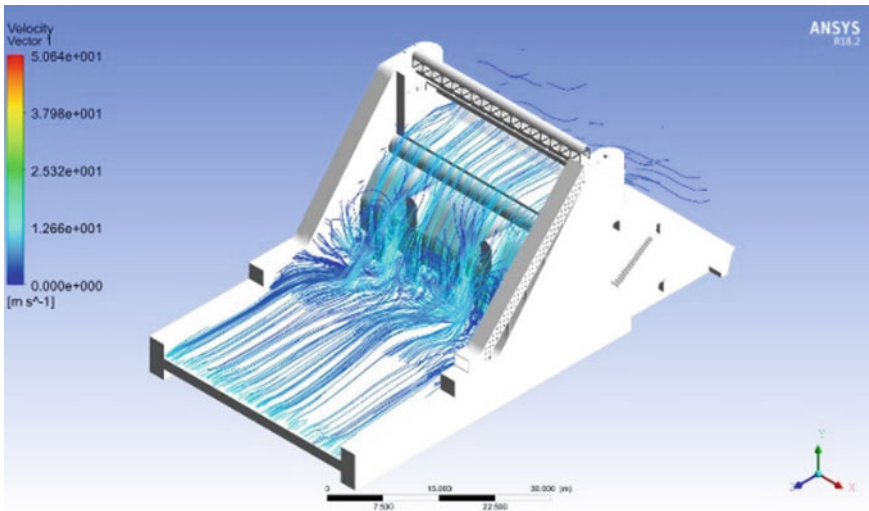
Fig. 6 Flow pattern at spillway

3 Results and Discussion

Fluid dynamics principle can be used to understand various condition and phenomena [21]. The use of CFD to model water flow through spillways is focused in this study. Flow pattern at spillway inlet affects the behavior of water in spillway. It is affected by

operating condition effect on increasing the capability of spillway for PMF passed. Optimizing the sector gate operating can cause flow disturbances on spillway and loss of turbulence [11, 22]. Therefore, discharge spillway coefficient capacity may be reduced by the non-uniformity of flow in the approach channel.

Based on Fig. 4, the minimum value of pressure is extracted from upstream and the pressure then drastically changed approach zero at downstream area. The values of velocity in Fig. 5 determined as spurious and most of the vectors were located close to crest of the spillway. Dam flow rate is dependent on the water level. A hydraulic jump could occur when water in spillway is flowing supercritical and meet subcritical flow by a deepening of the obstruction and channel in spillway as shown in Fig. 6. It causes water to suddenly jump to the other specific energy state. The rise in Froude number of the supercritical flow produce the amount of energy dissipated in a jump increase.

Prediction of flow profile due to downstream flow will allow prediction of such occurrences. Estimation of the super and sub-critical flow will also allow specific control to be applied at the spillway side by using energy dissipator [23]. Diversion and vortex flows in streamline create cross wave and cause non-uniformity through the spillway at the downstream.

Three sections were divided by the energy dissipators as shown in Fig. 7. Based on Fig. 8, three planes were made to capture water flow velocity cross sections. Figure 9 shows the cross sections of the velocity for the all the three planes. Types of the jump as shown in Table 1 is determined by the value of Froud before the jump, Fr_1. Based on the result shown in Table 2, all of the three hydraulic jumps were classified as oscillating jump based on the Froude value obtained. Energy loss, height and length of the jump were also obtained for the all the planes.
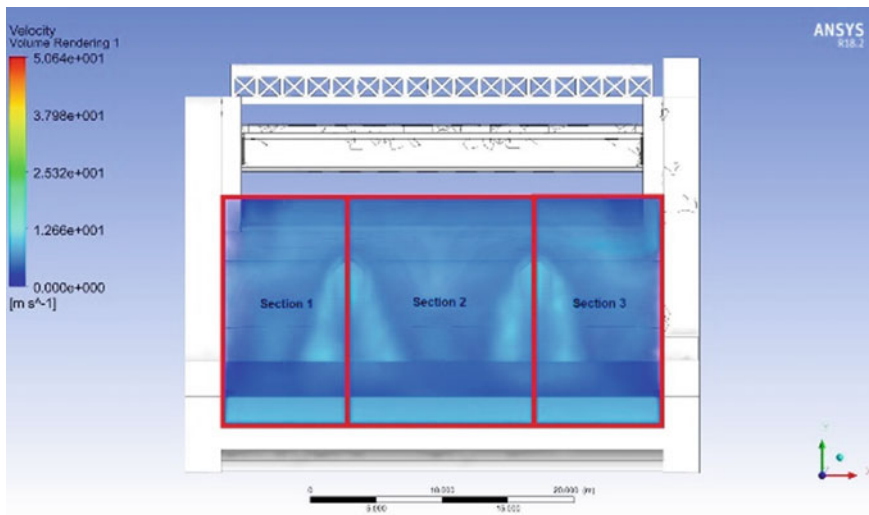

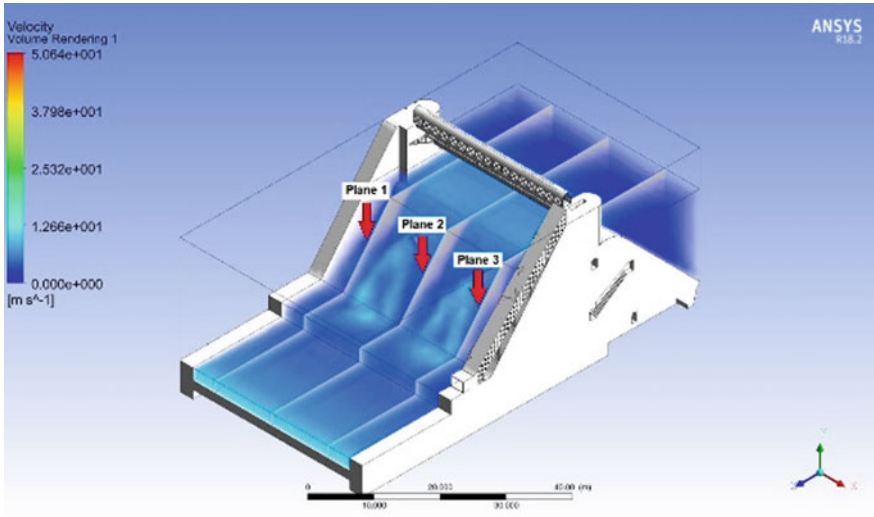**Fig. 7** Sections divided by the energy dissipators
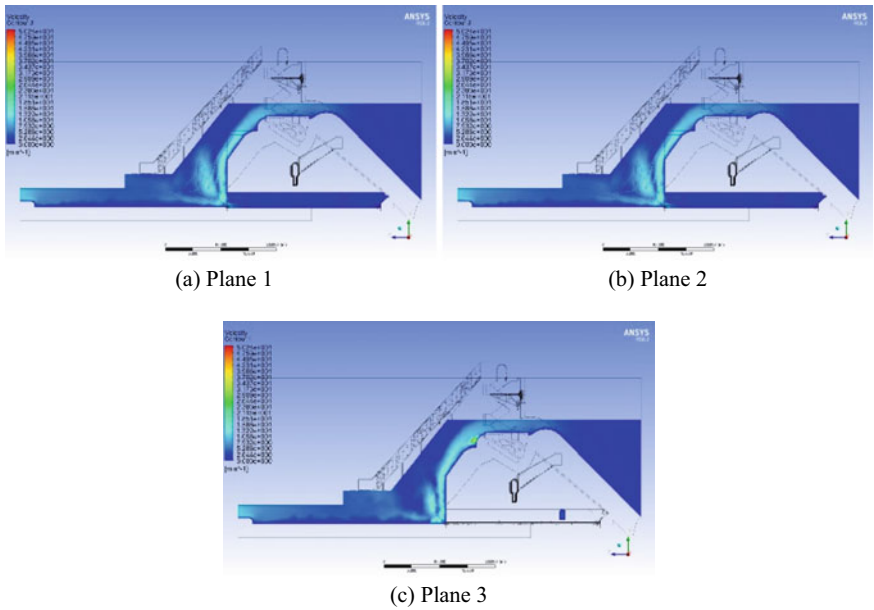
Fig. 8 Planes for the cross sections

(a) Plane 1   (b) Plane 2

(c) Plane 3

Fig. 9 Cross sections of water velocity

Table 1 Type of jumps

Froude value	Jump types
$Fr_1 = 1.0–1.7$	Undular jump
$Fr_1 = 1.7–2.5$	Weak jump
$Fr_1 = 2.5–4.5$	Oscillating jump
$Fr_1 = 4.5–9.0$	Steady jump
$Fr_1 > 9.0$	Strong jump

Table 2 Results for hydraulic jump parameters

Cross section	Plane 1	Plane 2	Plane 3
Froude value, Fr_1	2.523	2.988	2.843
Energy loss, E_L (m)	1.873	3.484	2.923
Height of jump (m)	5.257	6.888	6.379
Length of jump, Lj (m)	36.27	47.53	44.02
Jump type	Oscillating jump	Oscillating jump	Oscillating jump

Experiment using physical models were conducted to analyze water flow behavior and condition for a dam in the past. Meanwhile, recently, it is used for validation process of the simulation. This study uses Sultan Abu Bakar Dam study by Abas (2018) as validation process [24]. Fundamental method that were being used for fluid dynamic analysis for this study comparing to Sultan Abu Bakar fluid dynamic study is similar. A comparison between both numerical simulations has been done in the study. Therefore, up to 90% precision of physical and numerical model results in Sultan Abu Bakar Dam study can be compared to verify the dam numerical simulation result. The study presented experimental and numerical simulation approaches to analyze fluid dynamic through radial gate gap height. It shown that it is in compliance with numerical and physical models in flow characteristics.

4 Conclusion

From this study, it can be concluded that there are three different velocities in the receiving ends at the spillway stilling basin. The largest hydraulic jump occurred is at the Plane 2 which dissipates 3.484 m energy compared to Plane 1 and Plane 3, which are 1.873 m and 2.923 m energy, respectively. It shows that higher the velocity, the more damaging effect to the stilling basin surface. This is due to the high amount of energy dissipate contributes in high stress distribution, through collision of water with

the surface of dam stilling basin. Therefore, it could be a significant information and analysis for dam operators to ensure structural integrity of the spillway for mitigation measure.

References

1. Zawawi MH, Saleha A, Salwa A, Hassan NH, Zahari NM, Ramli MZ, Muda ZC (2018) "A review: fundamentals of computational fluid dynamics (CFD)". In AIP conference proceedings 2030(1):020252. AIP Publishing LLC
2. Chanel PG (2008) An evaluation of computational fluid dynamics for spillways. Thesis (MSC), University of Manitoba, Canada, PhD diss.
3. Hassan NH, Zawawi MH, Abas MA, Radzi MRM, Hassani A, Zahari NM, Ramli MZ, Kamaruddin MA, Sidek LM (2020) "Stress and deformation analysis on dam spillway structure due to water discharge." In AIP conference proceedings 2291(1):020104. AIP Publishing LLC
4. Itou A, Nakanishi T, Mizuguchi T, Yoshida M, Saburi T (2005) High performance parallel computing for computational fluid dynamics (CFD) 51(156), Komatsu Technical Report
5. Rumsey C (2006) Introduction: computational fluid dynamics validation for synthetic jets. AIAA J 44(2):193–193
6. Parsaie A, Haghiabi AH, Moradinejad A (2015) CFD modeling of flow pattern in spillway's approach channel. Sustain Water Resour Manag. 1(3):245–251
7. Coleman HW, Wei CY, Lindell JE (2004) "Chapter 17. Hydraulic design of spillways." Hydraul D . Handb 1–54
8. Zaki SAA, Hassan NH, Zawawi MH, Abas MA, Mazlan AZA, Zainol MRRMA, Radzi MRM. "Numerical and physical model analysis comparison for velocity of water at spillway." In International conference on dam safety management and engineering, pp 408–416. Springer, Singapore, 2019.V. D. M. Oliviera and L. Thompson, "Spillway Design," pp. 1–8
9. Mohamad G et al (2018) "Prediction of the flow-induced vibration response of the chenderoh dam left bank section." MATEC Web of Conference 217 01001:1–6
10. Zawawi MH, Aziz NA, Radzi MRM, Hassan NH, Ramli MZ, Zahari NM, Abbas MA, Saleha A, Salwa A, Muda ZC (2018) "Computational fluid dynamic analysis at dam spillway due to different gate openings." In AIP Conference Proceedings 2030(1):020245. AIP Publishing LLC
11. Ho DKH, Boyes KM, Donohoo SM (2001) "Investigation of spillway behaviour under increased maximum flood by computational fluid dynamics technique." 14th Australas Fluid Mech Conf no December, pp 577–580
12. Moradinejad A, Parssai A, Noriemamzade M (2015) "Numerical modeling of flow pattern in kamal saleh dam spillway approach channel." Appl Sci Reports 10(2)
13. Chanel PG, Doering JC (2008) Assessment of spillway modeling using computational fluid dynamics. Can J Civ Eng 35(12):1481–1485
14. Ewing T, Jonker M, Willey J (2015) "Efficient and cost-effective modelling and analysis of hydraulic structures using CFD." Australian national committee on large dams incorporated (ANCOLD Inc)
15. Serafeim A, Avgeris L, Hrissanthou V, Bellos K (2017) "Experimental and numerical simulation of the flow over a spillway." In Proc 10th World Congress on Water Resour Env (EWRA)
16. Salwa A, Zawawi MH, Ramli MZ, Zahari NM, Saleha A, Hassan NH, Radzi MRM, Sidek LM, Muda ZC (2018) "Condition assessment on hydropower dam based on simulation approach: a review." In AIP conference proceedings 2030(1):020254. AIP Publishing LLC
17. FLUENT (2006) "Modeling turbulent flows," ANSYS. Inc., pp 6–2, 6–49
18. Beg MN, ITN MCA (2017) "Application of CFD modelling in water resources engineering." Early Stage Researcher QUICS

19. Ghazali MHM, Zawawi MH, Hassan NH, Radzi MRM, Mazlan AZA, Abas MA, Zainol MRRMA (2018) Structural dynamic analysis of the chenderoh dam sector gate section. In MATEC Web of Conferences, vol 217, EDP Sciences, p 02002
20. Iaccarino G (2004) "Simulation of turbulent flows," Stanford Lect Notes Course ME469B
21. SStenmark E (2013) "On multiphase flow models in ansys cfd software," 59
22. Olsen NRB (2001) "CFD modeling for hydraulic structures." Department of hydraulic and environmental engineering, The Norwegian University of Science and Technology 37
23. Peltier Y, Dewals B, Archambeau P, Pirotton M, Erpicum S (2018) Pressure and velocity on an ogee spillway crest operating at high head ratio: experimental measurements and validation. J Hydro-Environ Res 19(May):128–136
24. Ng FC et al (2018) "Fluid/structure interaction study on the variation of radial gate's gap height in dam," IOP Conf Ser Mater Sci Eng 370(1)

Integration of Building Information Modeling (BIM) and Artificial Intelligence (AI) to Detect Combined Defects of Infrastructure in the Railway System

Jessada Sresakoolchai⬡ **and Sakdirat Kaewunruen**⬡

Abstract Due to the high demand for the railway system nowadays, the speed and load of rolling stocks tend to increase. At the same time, the effect of extreme climate is also more severe. These result in the deterioration of the railway infrastructure which cause defects to the railway infrastructure. Defects can affect passenger comfort and operating safety of the railway system. Detecting defects of the railway infrastructure in the early stage of defect development can reduce the risk to the railway operation, cost of maintenance and make the asset management more efficient. This study aims to apply building information modeling (BIM) integrated with artificial intelligence (AI) to develop the detection system of defects in railway infrastructure. In this study, dipped joint and settlement are used as examples of combined defects in the railway infrastructure. To detect defects, AI techniques are applied. Deep neural network and convolutional neural network are used to develop predictive models to detect defects in the railway infrastructure and rolling stock. The results of the study show that the developed models have the potential to detect defects with accuracies up to 99% and are beneficial for the asset management of the railway system in terms of risk management, passenger comfort, and cost-efficiency.

Keywords Building information modeling · Artificial intelligence · Railway infrastructure · Railway defects · Dipped joint · Settlement

1 Introduction

The demand for railway transportation is increasing [1]. The speed and load of rolling stock tend to increase. Moreover, the global warming and climate change also result in severe weather conditions [2–5]. As a result, railway infrastructure deteriorates faster and defects occur. Defects can affect passenger comfort, create

J. Sresakoolchai (✉) · S. Kaewunruen
Department of Civil Engineering, University of Birmingham, Birmingham, UK
e-mail: jss814@student.bham.ac.uk

S. Kaewunruen
e-mail: s.kaewunruen@bham.ac.uk

some noise or serious incidents such as derailment [6]. Detecting defects in the early stage can reduce negative effects and maintain passenger comfort, safety, and good asset management [7].

Railway inspection can be conducted in various ways such as visual track inspection [8], ultrasonic inspection [9], magnetic induction sensors [10], and eddy current [11]. Nowadays, the application of artificial intelligence (AI) is interested in being applied to defect railway defects because it is non-destructive testing (NDT), fast and requires a lower cost to inspect railway infrastructure. Different AI techniques can be used to develop models to detect defects such as convolutional neural network (CNN), deep neural network (DNN), regression, decision tree, or random forest.

To apply AI efficiently in railway defect detection, sufficient data is required as well as data management. Building information modeling (BIM) is an approach to manage data throughout the project life. Integration of BIM and AI will maximize their benefits. Information of railway infrastructure components is contained in the BIM model and can be used throughout the project life.

This study aims to integrate BIM and AI to detect combined defects in the railway infrastructure. Dipped joint and settlement are used as case studies. Data is generated by using simulations from a verified software called D-Track. BIM model is developed to contain information. In this study, predictive models are developed by using DNN and CNN.

2 Literature Review

2.1 Building Information Modeling (BIM)

BIM is the information management throughout the project life cycle [12]. The main role of BIM is to allow the full collaboration possible by sharing a model by every party related to the project.

BIM has been used in building construction for a long time. The development of BIM application in a building is extended to 6D [13, 14]. The application of BIM in the railway system tends to be interested; however, the application is relatively low. There are attempts to apply BIM in the railway system. Kaewunruen and Lian [15] applied digital twin or BIM to railway turnout in the sustainability aspect. They demonstrated effective ways to apply BIM to railway turnout in different stages through the project life cycle. Besides railway turnout, BIM was applied in railway station [16] in different aspects such as potential of a renovation of old railway stations and sustainability [17, 18].

2.2 Artificial Intelligence (AI)

Artificial intelligence or AI is "the study and design of intelligent agents" to achieve particular purposes [19]. Examples of AI's advantages are human error reduction, risk reduction in some tasks that need human labor, a continuation of work, good for repetitive jobs, faster operation, routine application, and good for complex questions [20].

AI can be used to optimize the speed profile of rolling stocks. Huang et al. [21] applied random forest regression and support vector machine regression to calculate speed profile and energy consumption. They found that the developed models could calculate energy consumption with an error of less than 0.1 kWh and reduce energy consumption by 2.84%. AI was used to improve railway safety at railway stations. In 2019, Alawad et al. [22] used a decision tree to analyze fatal accidents. Sysyn et al. [23] applied image processing to predict rail contact fatigue on crossings. AI is used to predict other incidents such as broken rail [24], defected insulator surface [25], and railway surface defects [26]. Mandriota et al. [27] applied machine vision to detect corrugation. Image processing was used for detecting railway defects in other studies [28–34]. The more advanced technique to detect rail defects was a 3D laser with an accuracy of 93% [35]. From the literature, it can be seen that a popular technique was image processing which additional devices were required to be installed. An advanced technique such as laser sensors also required the installation. Therefore, an alternative technique which is cost-efficient and reliable such as AI is interesting to apply for railway defect detection.

It can be seen that integration between BIM and AI has never been done in the railway system aspect. In addition, the development of predictive models to detect combined defects is limited. Therefore, this study aims to fill this gap to demonstrate how to integrate BIM and AI together and the potential of AI models to detect combined defects in railway infrastructure.

3 Methodology

3.1 BIM Model Development

The BIM model in this study is developed by using Civil 3D software. The BIM model developed in this study is aimed to be a 6D model to contain design, cost, time, and maintenance information. The development of the BIM model is described as follows.

The development is started from 2D drawings. Horizontal alignment and vertical alignment are shown in 2D drawings. Based on 2D drawings, the BIM model is developed using the software through a corridor which depended on alignment, profile, and assembly. The corridor is created in form of solid 3D. Then, an industry

foundation classes (IFC) are exported from solid 3D. From BIM model development, IFC files are outcomes which can be shown in Fig. 1.

The 4D model is further developed from the 3D model. In this study, the D is defined as the schedule. Navisworks is used in this study to determine the project schedule. The IFC file is appended in Navisworks. Every rail component can be added as a task automatically. The created schedule is exchangeable with other schedule software such as Microsoft Project and Primavera P6. An example of a schedule which created by Navisworks can be shown in Fig. 2.

The 5D model is developed to calculate material quantity and cost. In this step, material quantity is directly affected by the sub-assembly definition. Quantity takeoff can be done and demonstrated in form of a table.
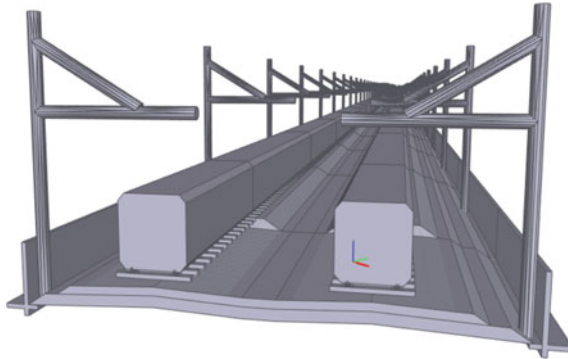
Fig. 1 Examples for BIM models which created by using Civil 3D
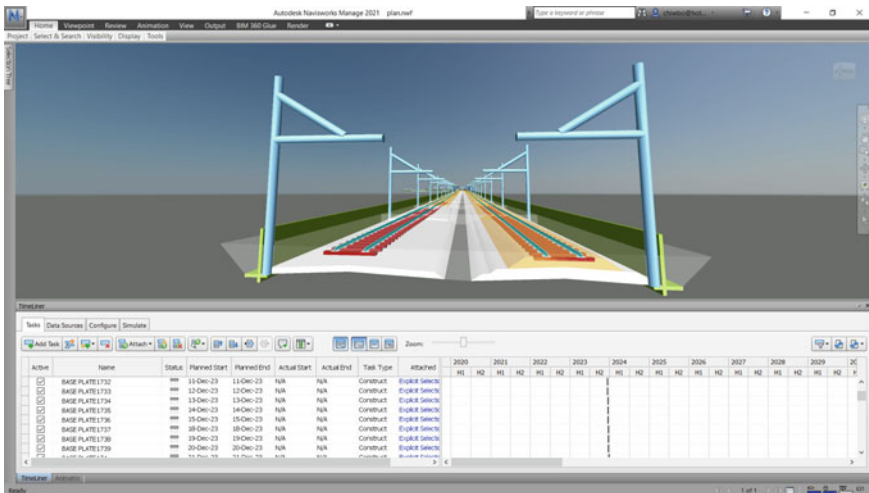
Fig. 2 Example of schedule created by Navisworks from the BIM model

For the 6D model, it is related to information management. In this study, information is used later for developing AI models. Information which contained in the BIM model as the 6D is featured for AI models. To include additional information in the BIM model, information is added through property set definitions. For the ease of information management, dynamo for Civil 3D is used.

Up to this step, the BIM model is created and ready to add information into the model. Every object in the model can contain its own information, and sets of information can be different depending on the demand of use. This can be done via property set definitions. The following section will present data which additionally stored in the BIM model to develop AI models and detect combined defects in the railway infrastructure.

3.2 Data Preparation and Characteristic

Data which used in this study is simulated by using a software called D-Track. D-Track was developed by Cai [36] in 1996 to study railway track dynamic behaviors. In 2005, Steffens [37] developed the dynamic analysis of rail track structure (DARTS) model and its interface based on D-Track. However, Steffens found that there was a significant difference between benchmarks and models. Leong [38] improved D-Track for more accuracy until the error was less than 10% compared to actual field data. It can be concluded that the accuracy of D-Track is satisfied, so it is used in this study to simulate dynamic track behavior data.

Characteristic of the railway system can be set in D-Track such which consists of track properties, vehicle properties, defect properties, and defect locations. The output of the software is various. In this study, accelerations of wheel-rail contact are used.

For simulations, different parameters are added to generate data. Varied parameters consist of sizes of dipped joint, sizes of settlement, speeds of vehicle, and weights of vehicle. A summary of varied parameters for simulation is shown in Table 1.

From Table 1, the total number of simulations is 1650. Examples of output from D-Track are shown in Fig. 3. From the figure, accelerations are simulated by the

Table 1 A summary of varied parameters in D-Track

Parameters	Range	Step	Unit	Remarks
Sizes of dipped joint	0–10	2.5	mm	The length of the dipped joint is 1000 mm
Sizes of settlement	0–100	20	mm	The lengths of the settlement are 3000 and 10,000 mm. for short and long settlement, respectively
Speeds of vehicle	20–200	20	Km/h	
Weights of vehicle	40–80	20	Tons	
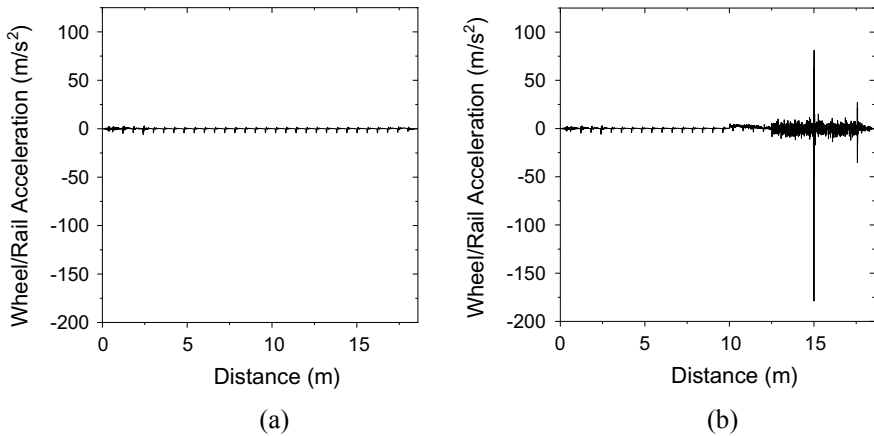
Fig. 3 Examples of D-track output: **a** Wheel/rail acceleration when the rail is defect-free; **b** Wheel/rail acceleration when the rail has dipped joint and settlement

following parameter: Speed of the vehicle is 20 km/h, and weight of the vehicle is 40 tons when Fig. 3a shows a simulation without defect, and Fig. 3b shows a simulation with dipped joint of 2.5 mm and short settlement of 20 mm. It can be seen that when the rail has defects, peak and bottom values are clearly identified. Note that Fig. 3 presents accelerations from a wheel only. There is another set of data from another wheel from simulations.

Generated wheel/rail accelerations are stored in the BIM model for each section of the track to detect combined defects further. This study applies DNN and CNN to develop AI models to detect combined defects. Data is used in two ways depending on AI techniques. For DNN, data is used as simplified data. For CNN, data is used as raw data.

In case of CNN, two sets of raw data are used as features. However, data needs to be processed for DNN. In this study, 14 features are used for training DNN models which consist of speed of vehicle, weight of vehicle, and three peak values and bottom values from two sets of wheel/rail accelerations. To process data and prepare data, Excel Macro is used.

3.3 AI Model Development

In this study, DNN and CNN are applied to develop AI models for detecting combined defects of dipped joint and settlement. This study purposes two approaches to develop predictive models. The first approach is to develop a model to detect combined defects. For the first approach, there are four classes: Class 1 defect-free rail, Class 2 rail with dipped joint, Class 3 rail with settlement, and Class 4 railway with dipped joint and settlement. The second approach is to develop series models to detect dipped

joint and settlement independently. Therefore, there are two predictive models in the second approach, namely a model to detect dipped joint and a model to detect settlement. Each model has two classes which are with and without defect classes.

For DNN, the number of hidden layers and hidden nodes is tunned as other parameters such as learning rate, momentum, and activation function to provide the best performance.

For CNN, two sets of raw data are fed into models. CNN is used for feature extraction without the knowledge of feature engineering which is an important advantage of CNN. A CNN model consists of two parts, namely the feature extraction part and classification part. Hyperparameters are tuned to make the model provide the best outcome.

Both DNN and CNN models are developed with dropout to prevent overfitting and enhance the accuracy of predictive models. About 70% of the dataset is used as the training data, and 30% of the dataset is used as testing data.

4 Result and Discussion

From the BIM model development, required features which used to develop predictive models can be stored in the BIM model. In this study, wheel/rail accelerations are used as features in ANN and CNN models. Speeds and weights of the vehicle are used in ANN models. Information in the BIM model can be manageable by using dynamo for Civil 3D. When information from the BIM model is exported to spreadsheet software, it can be managed by using spreadsheet macro. In this study, Excel Macro is used to manage and process information.

To assess the performance of developed predictive models, accuracy, precision, and recall are used. As mentioned, DNN and CNN are used to develop models. The performance of each technique is shown as follows.

4.1 The First Approach: One Model for Detecting Both Dipped Joint and Settlement

There are four classes when this approach is used as mentioned. The performances of DNN and CNN are shown in Table 2.

From Table 2, the accuracy of CNN is clearly higher than DNN. In terms of precisions, the CNN model has significantly higher precisions than DNN. As well as recalls, the CNN model performs better than the DNN model. Therefore, for the first approach, it can be concluded that the CNN model is better than the DNN model to detect combined defects.

Table 2 Performance of DNN and CNN for detecting combined defects using the first approach

Class	Accuracy		Precision		Recall	
	DNN	CNN	DNN	CNN	DNN	CNN
Class 1 defect-free rail	0.86	0.99	1.00	1.00	0.93	1.00
Class 2 rail with dipped joint			0.00	0.97	0.00	0.88
Class 3 rail with settlement			0.90	1.00	0.68	0.99
Class 4 rail with dipped joint and settlement			0.86	0.98	0.98	0.99

4.2 The Second Approach: Two Individual Models for Detecting Dipped Joint and Settlement Separately

Two models are developed to detect dipped joint and settlement individually. Model 1 is used to detect dipped joints, and Model 2 is used to detect settlements. From Table 3, it can be seen that the CNN model also performs better than the DNN model in every aspect. The recall of Model 2 developed by DNN is 0.26 which is significantly low. Therefore, it can be concluded that the DNN model should not be used to detect the settlement. From Tables 2 and 3, the overall accuracies of both the CNN and DNN models developed by the first approach are slightly higher than the models developed by the second approach.

From Tables 2 and 3, it can be concluded that in this case, using separated models to detect dipped joint and settlement does not provide better performance. Therefore, using a single model is sufficient to detect combined defects. Based on the results in this study, the CNN model performs better than the DNN model. The CNN model can detect combined defects very accurately with an accuracy of 0.99. At the same time, both precisions and recalls are about 0.90 or higher which could be concluded that it is satisfactory and reliable to use in practice.

Table 3 Performance of DNN and CNN for detecting dipped joint and settlement individually using the second approach

Class	Accuracy		Precision		Recall	
	DNN	CNN	DNN	CNN	DNN	CNN
Model 1 dipped joint detection						
Class 1 rail without dipped joint	0.88	0.99	0.62	1.00	0.87	0.99
Class 2 rail with dipped joint			0.97	1.00	0.89	1.00
Model 2 settlement detection						
Class 1 rail without settlement	0.93	0.99	1.00	0.96	0.26	0.94
Class 2 rail with settlement			0.93	0.99	1.00	1.00
Total accuracy	**0.82**	**0.98**				

5   Conclusion

This study applies BIM and AI together to detect combined defects in the railway infrastructure. This study uses dipped joint and settlement as case studies. Data is generated numerically using D-Track. The BIM model in this study is developed using Civil 3D. The developed BIM model can store information which manageable using dynamo for Civil 3D. This information is further used to develop AI models to detect combined defects.

DNN and CNN are used to develop predictive models for detecting combined defects. Information stored in the BIM model is used as features for developing models. The total number of samples is 1650. About 70% of the dataset is used as training data, while another 30% of the dataset is used as testing data. It is found that CNN performs better than DNN in every aspect. The accuracies of the CNN models are almost 100%. At the same time, precisions and recalls of CNN models are about 90% or higher. This shows that CNN has the potential to detect combined defects in the railway infrastructure.

References

1. Ngamkhanong C, Kaewunruen S, Costa BJAJI (2018) State-of-the-art review of railway track resilience monitoring 3(1):3
2. Binti Sa'adin SL, Kaewunruen S, Jaroszweski D (2016) Operational readiness for climate change of Malaysia high-speed rail. in Proceedings of the Institution of Civil Engineers-Transport. Thomas Telford Ltd
3. Binti Sa'adin SL, Kaewunruen S, Jaroszweski D (2016) Risks of climate change with respect to the Singapore–Malaysia high speed rail system 4(4):65
4. Kaewunruen S et al (2018) Vulnerability Struct Concrete Extreme Clim Variances 6(2):40
5. Binti Saadin SL, Kaewunruen S, Jaroszweski D (2016) Heavy rainfall and flood vulnerability of Singapore-Malaysia high speed rail system. Australian J Civil Eng 14(2):123–131
6. Dindar S et al (2018) Bayesian Network-based probability analysis of train derailments caused by various extreme weather patterns on railway turnouts. Saf Sci 110:20–30
7. Kaewunruen S, Sussman JM, Matsumoto A (2016) Grand challenges in transportation and transit systems 2(4)
8. Network Rail (2019) Visual track inspection
9. Network Rail (2019) Ultrasonic rail inspection
10. Bray DE (2000) Historical review of technology development in NDE. In Proceedings of the 15th world conference on NDT, Roma, Italy
11. Rockstroh B et al (2008) Ultrasonic and eddy-current inspection of rail wheels and wheel set axles. in 17th world conference on nondestructive testing

12. Kaewunruen S, Rungskunroch P, Jennings DV (2019) A through-life evaluation of end-of-life rolling stocks considering asset recycling, energy recovering, and financial benefit. J Clean Prod 212:1008–1024
13. Kaewunruen S, Rungskunroch P, Welsh JJS (2019) A digital-twin evaluation of net zero energy building for existing buildings 11(1):159
14. Kaewunruen S, Sresakoolchai J, Kerinnonta LJS (2019) Potential reconstruction design of an existing townhouse in washington dc for approaching net zero energy building goal 11(23):6631
15. Kaewunruen S, Lian QJJOCP (2019) Digital twin aided sustainability-based lifecycle management for railway turnout systems 228:1537–1551
16. Kaewunruen S, Xu NJFIBE (2018) Digital twin for sustainability evaluation of railway station buildings 4:77
17. Krezo S et al (2016) Field investigation and parametric study of greenhouse gas emissions from railway plain-line renewals. Transp Res Part D: Transp Environ 42:77–90
18. Kaewunruen S, Sussman JM, Einstein HH (2015) Strategic framework to achieve carbon-efficient construction and maintenance of railway infrastructure systems 3 (6)
19. ScienceDaily (2020) Artificial intelligence. Available from: https://www.sciencedaily.com/terms/artificial_intelligence.htm
20. Kumar S (2019) Advantages and disadvantages of artificial intelligence
21. Huang K et al (2019) Discrete train speed profile optimization for urban rail transit: a data-driven model and integrated algorithms based on machine learning 2019
22. Alawad H, Kaewunruen S, An MJIA (2019) Learning from accidents: machine learning for safety at railway stations 8:633–648
23. Sysyn M et al (2019) Prediction of rail contact fatigue on crossings using image processing and machine learning methods 5(2):123–132
24. Zhang Z, Zhou K, Liu X (2020) Broken rail prediction with machine learning-based approach. In ASME/IEEE joint rail conference. Am Soc Mech Eng
25. Kang G et al (2018) Deep architecture for high-speed railway insulator surface defect detection: denoising autoencoder with multitask learning 68(8):2679–2690
26. Shang L et al (2018) Detection of rail surface defects based on CNN image recognition and classification. In 2018 20th international conference on advanced communication technology (ICACT) IEEE
27. Mandriota C et al (2004) Filter-based feature selection for rail defect detection 15(4):179–185
28. Deutschl E et al (2004) Defect detection on rail surfaces by a vision based system. In IEEE intelligent vehicles symposium, 2004 IEEE
29. Jie L et al (2009) Real-time rail head surface defect detection: a geometrical approach. In 2009 IEEE international symposium on industrial electronics. IEEE
30. Tan P et al (2019) Multialgorithm fusion image processing for high speed railway dropper failure-defect detection
31. Tastimur C et al (2016) Rail defect detection and classification with real time image processing technique 5(12):283
32. Yu H et al (2018) A coarse-to-fine model for rail surface defect detection 68(3):656–666
33. Taştimur C et al (2016) Rail defect detection with real time image processing technique. In 2016 IEEE 14th international conference on industrial informatics (INDIN). IEEE.
34. Feng H et al (2013) Automatic fastener classification and defect detection in vision-based railway inspection systems 63(4):877–888
35. Xiong Z et al (2017) A 3D laser profiling system for rail surface defect detection 17(8):1791
36. Cai Z (1994) Modelling of rail track dynamics and wheel/rail interaction
37. Steffens DM (2005) Identification and development of a model of railway track dynamic behaviour. Queensland University of Technology
38. Leong J (2007) Development of a limit state design methodology for railway track., Queensland University of Technology

Cross Cutting Issue in DRR and Infrastructure

Blast Performance of RCC Slab and Influence of Its Design Parameters

Emal Ahmadi [ID]**, Mehtab Alam** [ID]**, and S. M. Anas** [ID]

Abstract Catastrophic failure of the RCC slab under explosive-induced blast loading could be disastrous for other elements in the structure. In the present work, a finite element model of one-way-reinforced cement concrete slab tested under blast loading for which experimental results/observations are available in the literature has been developed with respect to concrete cover, thickness, re-bar diameter, spacing, and concrete strength via Abaqus/explicit. The analysis of the slab has been done by applying different peak overpressures produced from the TNT explosive charges at different standoff distances in free air, and the results are validated. Through finite element simulations, the design parameters likely to influence the blast performance of the slabs such as cover to reinforcement, reinforcement ratio, and strength of concrete have been considered in the modeling, and their results have been comprehensively investigated. Three thicknesses of the concrete cover such as 10, 15, and 20 mm have been considered keeping the overall depth of the slab constant. The concrete strength of 30, 40, and 50 MPa following *Indian Standard Criteria for Blast Resistant Design of Structures for Explosions Above Ground* (IS: 4991–1968) and the reinforcing steel with strength 600 MPa have been considered. The longitudinal reinforcement ratio is varied from 0.39 to 2.24% by an increment of 0.37% keeping the concrete cover, concrete/steel strength, and transverse reinforcement ratio constant. Concrete-damaged plasticity (CDP) model has been utilized to simulate the damage and to evaluate geometric parameters of cracks. The effects of the respective parameter on the results obtained from the simulations have been compared and discussed.

Keywords Reinforced cement concrete (RCC) slabs · Air-blast · Explosive-induced disaster · Peak overpressure · Concrete cover · Concrete strength · Steel ratio · CDP model · Damage · Cracks

E. Ahmadi (✉) · M. Alam · S. M. Anas
Department of Civil Engineering, Faculty of Engineering and Technology, Jamia Millia Islamia, New Delhi 110025, India

M. Alam
e-mail: malam1@jmi.ac.in

1 Introduction

In recent decades, frequent occurrence of subversive blasts and accidental explosions has generated concern over a general vulnerability to explosion seen in many conventionally designed concrete structures, with localized damage, causing structural collapse in some cases [2]. In addition to the direct blast wave generated from the explosion, the failure of structural elements can increase the total casualties [2, 10, 11]. Reinforced concrete (RC) is the principal material used for concrete structures. However, during the design of structural elements, such extreme loading has not been taken into consideration [3–9]. Thus, it is significantly important to examine the performance of structural elements under blast loading. In the present work, a finite element model of one-way-reinforced concrete slab tested under blast loading for which experimental results/observations are available in the literature has been developed with respect to concrete cover, thickness, re-bar diameter, spacing, and concrete strength via Abaqus/explicit. Through finite element simulations, the design parameters likely to influence the blast performance of the slabs such as cover to reinforcement, longitudinal reinforcement ratio, and strength of concrete and steel have been considered in the modeling, and their results have been comprehensively investigated.

Several experimental and analytical studies have been conducted to study the behavior of one-way RCC slabs under blast loadings [10, 11, 16–22, 25–27]. Schenker et al. [21] described the full-scale field explosion tests on protected and unprotected concrete slabs. The experimental setup was deployed on four locations, the amplifiers were placed inside the underground shelter, and a blast is generated by the explosion nearly 1000 kg hemispherical TNT charge at a distance of 20 m. Wu et al. [25] conducted field explosion tests to investigate the blast resistance of the slab, and eight concrete slabs were tested. Six slabs were tested to determine the response to blast loading. They were considered TNT explosive charge and the size from 1 to 20 kg of equivalent TNT composition. The result shows that the UHPFC has a very large energy-absorption capacity. The energy-attraction capacity of RUHPFC was larger than the UHPFC and NSC slabs (approximately 15–20 times greater). Silva and Lu [22] estimated the explosive charge weight and standoff distance to impose certain levels of damage on (RC) structures. The blast loads ranged for RC slabs between 1 and 6. The load transformation factor (LTF) for elastic and plastic is in the range of 0.64–0.54. The result showed that structure members are significantly higher charge weights at higher ductility levels. Li et al. [19] investigated ultra-high-performance concrete slab and normal strength concrete slab under contact explosion. The ultra-high-strength concrete was observed which resists a large blast at a small-scale distance. From experimental results due to contribution from ultra-high compressive and steel fiber reinforcement, UHPC has significantly reduced concrete punching. Iannitti et al. [16], the described numerical model was validated by comparison with experimental results for three different explosive charges (2.10, 6.30, and 105 kg) without partition. The main result of the work was the identification of the mechanisms that determine the damage generation and design more effective

structures. Kumar et al. [17], an experimental and numerical study has been carried out to investigate the damage resistance of reinforced concrete (RC) slabs. They have been exposed to blasts developed by three different weights and explosives equivalent to the number of explosives. Experimental and numerical investigated the performance of RC slabs under the close-in explosion of 0.20–0.55 kg TNT. Li et al. [18] conducted field explosion tests to investigate to failure characteristic of RC slabs under combined blast and fragment loading. Totally, in experiments, three shots were conducted, the standoff distance is same 3.50, 3.00, and 1.60 m, the curve reached and the peak were 202.6 kPa at 3.16 ms, and the blast mass and distance affect the damage mode in the range of 0.20–2.00 kg. As a result, there were many types of failure in the RC slabs, such as spall, crack, and also the failure of the reinforcement, and the tensile strength was greater than the concrete tensile strength in the damaged area.

2 Numerical Modeling

2.1 Blast Loading

The idealized time history of air-blast wave pressure proposed by Wu and Hao [24] shown in Fig. 1a consists of negative and positive pressure phases, where P_i (or P_{OP}) is the peak overpressure, t_A is the arrival time of shock wave, t_1 is the rising time, t_2 is the decreasing time, t_d is the duration of positive phase, P_o is the standard atmospheric pressure, and t^- is the negative phase duration. Blast design guidelines available in IS 4991(1968) [15] and TM-5–1300(1990) [23] suggest only considering the positive pressure phase in the design and analysis of concrete structures by assuming the other phase is much weaker and does not affect the structural damage response [12, 14]. Hence, the effect of the negative pressure phase on the behavior of reinforced cement concrete slabs under blast loading has been neglected [3–9]. The values of
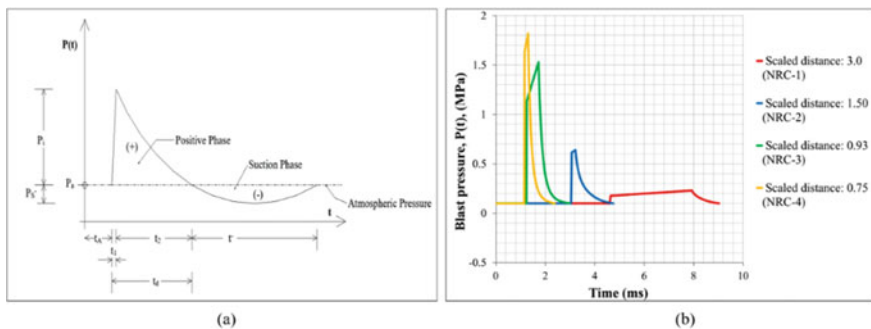
Fig. 1 a Typical blast-time history [24]; and b Calculated blast histories

Table 1 Calculated values of blast parameters

Slab ID	Z (m/kg$^{1/3}$)	P_{OP} (MPa)	t_A ($\times 10^{-2}$ s)	t_1 ($\times 10^{-2}$ s)	t_2 ($\times 10^{-2}$ s)	$t = t_a + t_d$ ($\times 10^{-2}$ s)
R-1	3.00	0.13	0.47	0.33	0.44	0.91
R-2	1.50	0.54	0.31	0.02	0.17	0.48
R-3	0.93	1.43	0.13	0.05	0.18	0.31
R-4	0.75	1.72'	0.12	0.02	0.12	0.24

blast wave parameters such as rising time, the arrival time of blast wave, duration of positive phase have been calculated by using empirical formulas given by Wu and Hao [24] for different scaled distances. The experiment results of peak overpressure (P_{OP}) published by Wu et al. [25] are summarized in Table 1. The values of t_A, t_1, t_2, and total duration (t) are calculated using empirical relations given by [25]. An explicit solver in Abaqus/CAE has been used to simulate the blast [1]. Simply supported conditions are assigned to the short edges of the slabs. The calculated blast-time histories are shown in Fig. 1b.

2.2 Concrete Modeling

Concrete-damaged plasticity (CDP) model has been utilized in the present work to evaluate the damage in the slabs subjected to blast loading. CDP model is a plasticity-based material model that considers the compressive crushing and tensile cracking as two failure mechanisms of concrete [1]. The evolution of the failure surface is controlled by the two variables, i.e., compressive equivalent plastic strain ($\varepsilon_c^{pl,h}$) and tensile equivalent plastic strain ($\varepsilon_t^{pl,h}$) [1]. In this model, the plastic hardening strain in compression plays a key role to describe the relationship between the compressive strength of the concrete and damage parameters. These variables are linked to failure mechanisms under compression and tension loadings [13]. It is assumed that the uniaxial stress–strain curves can be changed into the stress versus plastic strain curves. This alteration is executed automatically by the Abaqus/CAE from the user-provided stress versus inelastic-strain data [1]. The damaged variables can take values from 0 which represents undamaged material to 1 that represents the damaged material [1, 13]. The CDP parameters for M30, M40, and M50 grade concrete have been obtained from Hafezolghorani et al. [13]. A fine mesh size of 6.25 mm has been adopted following the convergence test. Finite element model of the slab has 879,941 nodes and 819,640 elements.

3 Results and Discussions

In this work, experimental data published by Wu et al. [25] on four RCC slabs have been assumed as a benchmark to examine the effect of concrete cover, concrete strength, and reinforcement ratio on the response of the slabs subjected to blast loading. A summary of predicted maximum mid-span displacements and available values is presented in Table 2. There is a close agreement between the analytical and experimental results. The predicted values of maximum displacement in the slabs are within 6% of the measured values (Table 2). Figure 2 shows that the FE model of the slab with a 6.25 mm mesh size successfully captured the formation of cracks along the span of the R-3 and R-4 slabs.

Table 2 Comparison of displacements

Slab ID	Z (m/kg$^{1/3}$)	Maximum mid-span displacement (mm) of slab of 40 MPa concrete strength, 10 mm concrete cover, 1.13% reinforcement ratio, and 600 MPa steel strength		Percentage difference (%)
		Experimental result [25]	FEA result	
R-1	3.00	1.50	1.70	12.50
R-2	1.50	10.50	10.40	1.00
R-3	0.93	13.90	12.95	7.00
R-4	0.75	38.90	38.59	1.00
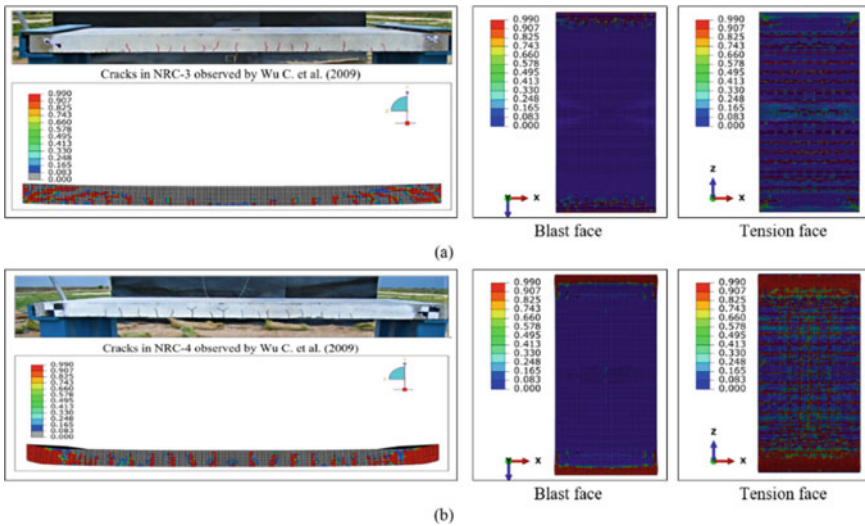
Fig. 2 Formation of cracks along the length of the slabs with 10 mm concrete cover: **a** R-3 ($t = 2.98$ ms) and **b** R-4 ($t = 2.38$ ms)

The following combinations of the design parameters have been made:

1. Combination A (concrete cover—10, 15, and 20 mm; concrete strength—40 MPa; steel strength—600 MPa; reinforcement ratio—1.13%)
2. Combination B (concrete cover—10, 15, and 20 mm; concrete strength—30 MPa; steel strength—600 MPa; reinforcement ratio—1.13%)
3. Combination C (concrete cover—10, 15, and 20 mm; concrete strength—50 MPa; steel strength—600 MPa; reinforcement ratio—1.13%)
4. Combination D (concrete cover—10, 15, and 20 mm; concrete strength—30 MPa; steel strength—600 MPa; reinforcement ratio—0.39, 0.76, 1.13, 1.50, 1.87, and 2.24%)
5. Combination E (concrete cover—10, 15, and 20 mm; concrete strength—40 MPa; steel strength—600 MPa; reinforcement ratio—0.39, 0.76, 1.13, 1.50, 1.87, and 2.24%)
6. Combination F (concrete cover—10, 15, and 20 mm; concrete strength—50 MPa; steel strength—600 MPa; reinforcement ratio—0.39, 0.76, 1.13, 1.50, 1.87, and 2.24%)

3.1 For Combination A

- Increase in cover for a peak overpressure value, the mid-span displacement is not significantly influenced. However, percentage reduction with 15 mm cover is lesser than with 20 mm cover with respect to 10 mm cover for each of the values of blast peak overpressure considered (Table 3).
- For the comparatively lower value of the peak overpressure (0.13 MPa), the reduction in displacement is lower for 15 mm cover as compared to 10 mm cover (2%) than the displacements under moderate peak overpressures ($0.54 \leq P_{OP}(MPa) \leq 1.72$). However, the decrease in the displacement of the slab with a 20 mm cover is the same as in the case of slab subjected to moderate peak overpressures (6%). Thus, a 20 mm cover is found to be more effective to control the displacement as compared to 10 and 15 mm covers of the slabs subjected to a range of peak overpressure considered (Table 3 and Figs. 3 and 4).

Table 3 Summary of maximum displacement (mm) of the slabs of 40 MPa concrete strength with different concrete covers (Combination A)

Slab ID	P_{OP} (MPa)	10 mm	15 mm	20 mm
R-1	0.13	1.70	1.66 ([a]2)	1.60 ([a]6)
R-2	0.54	10.40	10.14 ([a]3)	9.83 ([a]6)
R-3	1.43	12.95	12.52 ([a]3)	12.19 ([a]6)
R-4	1.72'	38.59	37.16 ([a]3)	36.43 ([a]6)

[a]Percentage decrease in displacement with respect to 10 mm
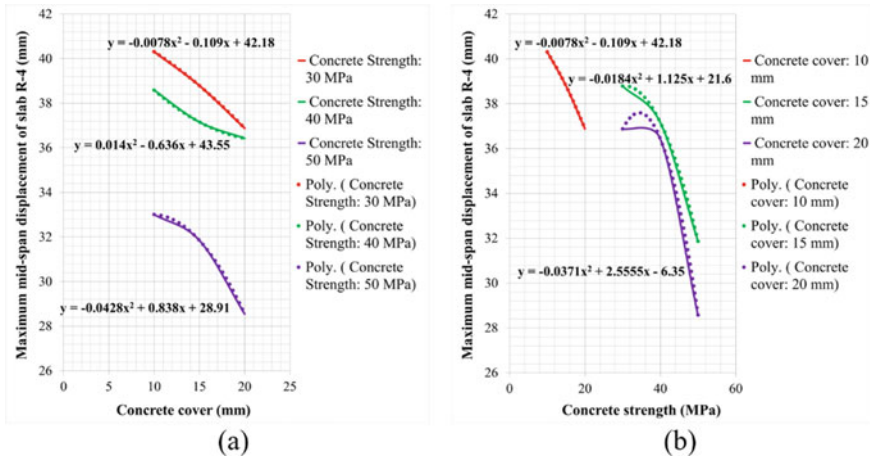
Fig. 3 Best fitted curves for maximum displacement of the R-4 slab for Combinations A–C in terms of concrete cover (a) and concrete strength (b)
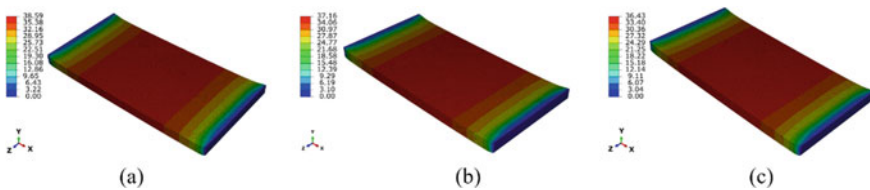
Fig. 4 Distribution of resultant displacement of R-4 slab with different concrete covers: **a** 10 mm, **b** 15 mm, and **c** 20 mm

- The damage resistance of the slabs is found to be increasing with higher concrete cover under the peak overpressure considered in this study (Tables 4 and 5).
- The slab under lower peak overpressure possesses much higher damage resistance with higher concrete cover as compared to the slab subjected to moderate peak overpressure (Tables 4 and 5).

Table 4 Summary of damage dissipation energy (J) of the slabs of 40 MPa concrete strength with different concrete covers (Combination A)

Slab ID	P_{OP} (MPa)	10 mm	15 mm	20 mm
R-1	0.13	36.27	10.11 ([a]72)	6.90 ([a]81)
R-2	0.54	1692.21	1223.26 ([a]28)	957.56 ([a]43)
R-3	1.43	6335.55	5343.68 ([a]16)	4726.46 ([a]25)
R-4	1.72'	77,594.95	71,487.32 ([a]8)	65,236.03 ([a]16)

[a]Percentage decrease in damage dissipation energy with respect to 10 mm

Table 5 Summary of average depth (mm) of flexural cracks developed on the slabs of 40 MPa concrete strength with different concrete covers (Combination A)

Slab ID	P_{OP} (MPa)	10 mm	15 mm	20 mm
R-1	0.13	25	b	b
R-2	0.54	37.50	31.25 ([a]17)	23.86 ([a]36)
R-3	1.43	43.75	36.97 ([a]16)	30.50 ([a]31)
R-4	1.72'	93.75	75.00 ([a]20)	68.75 ([a]27)

[a]Percentage decrease in average depth with respect to 10 mm
[b]No noticeable cracking

- The slab with a 20 mm concrete cover is found to have possessed maximum damage resistance, and the slab with a 10 mm concrete cover has the minimum damage resistance under the peak overpressures considered (Tables 4 and 5).
- More is the concrete cover, less is the depth of flexural cracks produced by peak overpressure (Table 5).

3.2   For Combinations A-C

- Higher concrete strength slab with an appropriate cover is found performing better with regards to maximum displacement, damage dissipation energy, and depth of flexural cracks as compared to normal strength concrete slab with a smaller concrete cover (Tables 6, 7, 8 and Figs. 5, 6, 7).

Table 6 Summary of maximum displacement (mm) of R-4 slab of different concrete strengths (Combinations A-C)

Concrete cover (mm)	30 MPa	40 MPa	50 MPa
10	40.31	38.59	33.01
15	38.79 ([a]4)	37.16 ([a]3)	31.85 ([a]4)
20	36.88 ([a]9)	36.43 ([a]6)	28.55 ([a]14)

[a]Percentage decrease in displacement with respect to 10 mm

Table 7 Summary of damage dissipation energy (J) of R-4 slab of different concrete strengths (Combinations A-C)

Concrete cover (mm)	30 MPa	40 MPa	50 MPa
10	80,105.80	77,594.95	57,283.85
15	74,665.60 ([a]7)	71,487.32 ([a]8)	52,532.36 ([a]8)
20	72,085.05 ([a]10)	65,236.03 ([a]16)	43,960.63 ([a]23)

[a]Percentage decrease in damage dissipation energy with respect to 10 mm

Table 8 Summary of average depth of flexural cracks developed on R-4 slab of different concrete strengths (Combinations A-C)

Concrete cover (mm)	30 MPa	40 MPa	50 MPa
10	98.25	93.75	80.50
15	87.50 ([a]11)	75.00 ([a]20)	65.60 ([a]18)
20	81.25 ([a]17)	68.75 ([a]27)	58.50 ([a]27)

[a]Percentage decrease in average depth with respect to 10 mm

(a)　　　　　(b)　　　　　(c)
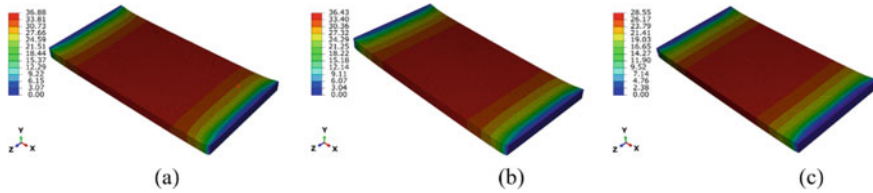
Fig. 5 Distribution of resultant displacement of R-4 slab of different concrete strengths with 20 mm concrete cover: **a** 30 MPa, **b** 40 MPa, and **c** 50 MPa

(a)　　　　　(b)　　　　　(c)

(d)　　　　　(e)　　　　　(f)
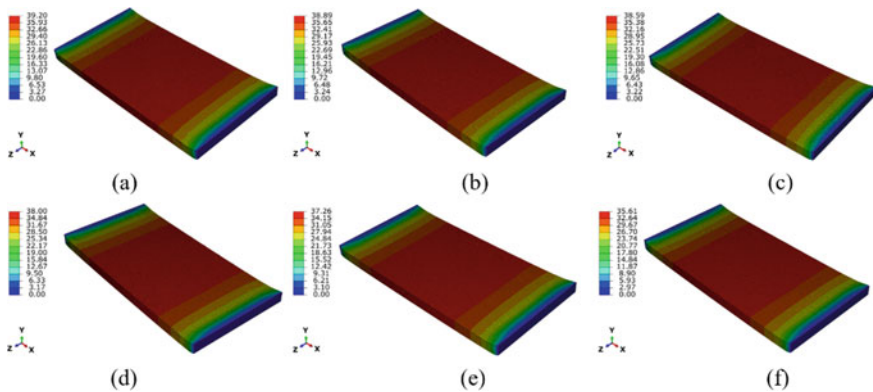
Fig. 6 Distribution of resultant displacement of R-4 slab with different reinforcement ratios (Combination E): **a** 0.39%, **b** 0.76%, **c** 1.13%, **d** 1.50%, **e** 1.87%, and **f** 2.24%

3.3　For Combinations D-F

- The variation in the reinforcement ratio of the slabs does not influence the maximum displacement of the slab R-4 subjected to peak overpressure of 1.72 MPa (Tables 9, 10, 11 and Fig. 6). However, the reinforcement ratio influences the damage resistance of the slab; i.e., damage resistance of the slab increases with the increase of the reinforcement ratio (Tables 12, 13, 14, 15, 16, 17).
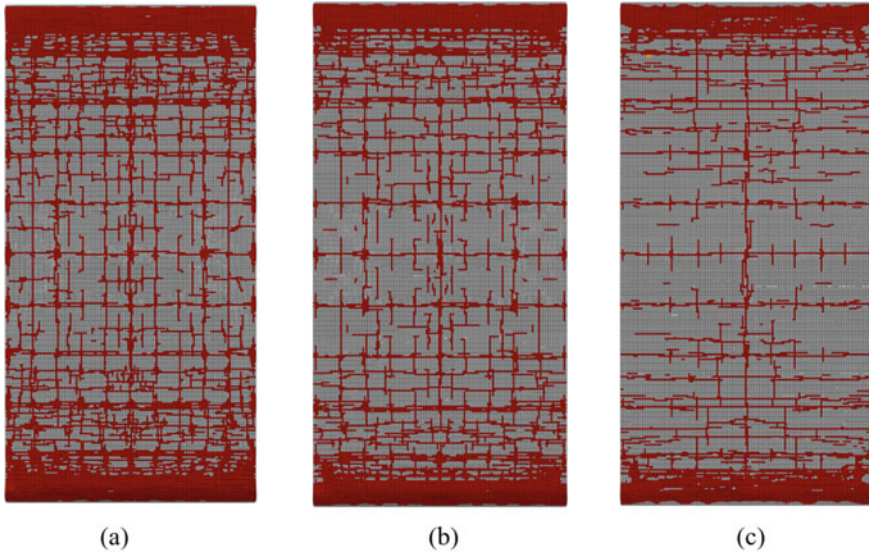
Fig. 7 Formation of cracks on bottom tension face of the slab R-4 of different concrete strengths and with 20 mm cover and 1.13% reinforcement ratio (Combinations A-C): **a** 30 MPa, **b** 40 MPa, and **c** 50 MPa

Table 9 Summary of maximum mid-span displacement (mm) of R-4 slab of 30 MPa concrete strength with different reinforcement ratios (Combination D)

Concrete cover (mm)	0.39%	0.76%	1.13%	1.50%	1.87%	2.24%
10	41.02	40.64	40.31	39.84	38.68	37.24
15	39.55 ([a]4)	39.26 ([a]3)	38.79 ([a]4)	38.66 ([a]3)	37.67 ([a]3)	36.14 ([a]3)
20	37.47 ([a]9)	37.19 ([a]8)	36.88 ([a]9)	36.29 ([a]9)	35.13 ([a]9)	34.05 ([a]9)

[a]Percentage decrease in displacement with respect to 10 mm

Table 10 Summary of maximum displacement (mm) of R-4 slab of 40 MPa concrete strength with different reinforcement ratios (Combination E)

Concrete cover (mm)	0.39%	0.76%	1.13%	1.50%	1.87%	2.24%
10	39.20	38.89	38.59	38.00	37.26	35.61
15	37.76 ([a]4)	37.45 ([a]4)	37.16 ([a]4)	36.57 ([a]4)	35.45 ([a]5)	34.14 ([a]4)
20	37.04 ([a]6)	36.72 ([a]6)	36.43 ([a]6)	35.82 ([a]6)	35.10 ([a]6)	33.61 ([a]6)

[a]Percentage decrease in displacement with respect to 10 mm

Table 11 Summary of maximum displacement (mm) of R-4 slab of 50 MPa concrete strength with different reinforcement ratios (Combination F)

Concrete cover (mm)	0.39%	0.76%	1.13%	1.50%	1.87%	2.24%
10	33.90	33.46	33.01	32.58	31.54	30.50
15	32.72 ([a]4)	32.45 ([a]3)	31.85 ([a]4)	31.22 ([a]4)	30.04 ([a]5)	29.15 ([a]4)
20	29.30 ([a]14)	28.99 ([a]13)	28.55 ([a]14)	27.94 ([a]14)	26.73 ([a]15)	25.53 ([a]16)

[a]Percentage decrease in displacement with respect to 10 mm

Table 12 Summary of damage dissipation energy of R-4 slab of 30 MPa concrete strength with different reinforcement ratios (Combination D)

Concrete cover (mm)	0.39%	0.76%	1.13%	1.50%	1.87%	2.24%
10	83,749.90	81,391.70	80,105.80	78,928.20	76,829.10	70,503.30
15	80,131.70 ([a]4)	77,633.48 ([a]5)	74,665.60 ([a]7)	73,111.01 ([a]7)	70,003.30 ([a]9)	67,628.35 ([a]4)
20	75,516.42 ([a]10)	73,877.11 ([a]9)	72,085.05 ([a]10)	69,952.25 ([a]11)	67,222.10 ([a]13)	65,356.14 ([a]7)

[a]Percentage decrease in damage dissipation energy with respect to 10 mm

Table 13 Summary of average depth of flexural cracks developed on R-4 slab of 30 MPa concrete strength with different reinforcement ratios (Combination D)

Concrete cover (mm)	0.39%	0.76%	1.13%	1.50%	1.87%	2.24%
10	100	99.25	98.25	96.50	92.59	83.75
15	94	92.30	87.50	85.88	82.40	77.05
20	88	84.36	81.25	80.05	78.00	72.86

Table 14 Summary of damage dissipation energy of R-4 slab of 40 MPa concrete strength with different reinforcement ratios (Combination E)

Concrete cover (mm)	0.39%	0.76%	1.13%	1.50%	1.87%	2.24%
10	79,720.19	78,611.39	77,594.95	74,945.49	72,376.92	67,322.17
15	77,532.58 ([a]3)	76,189.85 ([a]3)	71,487.32 ([a]8)	70,044.63 ([a]7)	68,509.03 ([a]5)	65,679.51 ([a]2)
20	72,132.97 ([a]10)	70,811.96 ([a]10)	65,236.03 ([a]16)	62,727.08 ([a]16)	60,811.96 ([a]16)	58,270.61 ([a]13)

[a]Percentage decrease in damage dissipation energy with respect to 10 mm

Table 15 Summary of average depth of flexural cracks developed on R-4 slab of 40 MPa concrete strength with different reinforcement ratios (Combination E)

Concrete cover (mm)	0.39%	0.76%	1.13%	1.50%	1.87%	2.24%
10	96.56	95.15	93.75	90.95	87.18	80.62
15	88.83	85.635	75.00	72.76	66.75	60.46
20	79.17	76.12	68.75	65.48	59.85	54.00

Table 16 Summary of damage dissipation energy of R-4 slab of 50 MPa concrete strength with different reinforcement ratios (Combination F)

Concrete cover (mm)	0.39%	0.76%	1.13%	1.50%	1.87%	2.24%
10	60,844.60	59,026.20	57,283.85	55,735.09	51,434.70	48,133.34
15	55,081.11 (a9)	54,421.05 (a8)	52,532.36 (a8)	50,235.22 (a10)	46,881.64 (a9)	43,177.69 (a10)
20	45,556.10 (a25)	44,984.20 (a24)	43,960.63 (a23)	42,557.20 (a24)	39,013.50 (a24)	34,414.54 (a29)

[a]Percentage decrease in damage dissipation energy with respect to 10 mm

Table 17 Summary of average depth of flexural cracks developed on R-4 slab of 50 MPa concrete strength with different reinforcement ratios (Combination F)

Concrete cover (mm)	0.39%	0.76%	1.13%	1.50%	1.87%	2.24%
10	85.33	83.31	80.50	78.00	72.45	67.62
15	75.94	70.81	65.60	62.40	55.78	50.25
20	66.14	62.48	58.50	54.60	47.81	43.95

4 Conclusions

This paper presents the finite element simulations of an RCC slab subjected to peak overpressures of 0.13, 0.54, 1.43, and 1.72 MPa using the Abaqus/CAE software. Increase in cover for a peak overpressure value, the mid-span displacement is not significantly influenced. However, percentage reduction with 15 mm cover is found lesser than with 20 mm cover with respect to 10 mm cover for each of the values of blast peak overpressure considered. The reduction in displacement with 15 mm cover is 3% with respect to 10 mm cover for each of the peak overpressure considered except 0.13 MPa peak overpressure, and the reduction is 2%. However, the percentage reduction for all the peak overpressure considered with 20 mm cover remains the same (6%) with respect to 10 mm cover. Thus, a 20 mm cover is found to be more effective to control the displacement as compared to 10 and 15 mm covers of the slabs subjected to a range of peak overpressure considered. The damage resistance of the slabs is found to be increasing with higher concrete cover under the applied blast loading. A higher concrete strength slab with 15 and 20 mm concrete covers performs better

with regards to maximum displacement as compared to normal strength concrete slab with a smaller concrete cover. Not the reinforcement ratio but the strength of concrete with moderate cover contributes to control the maximum mid-span displacement of the slab R-4 subjected to maximum peak overpressure of 1.72 MPa considered in this study. However, the reinforcement ratio influences the damage resistance of the slab; i.e., damage resistance of the slab increases with the increase of the reinforcement ratio. A higher reinforcement ratio improves the damage resistance of the slab but does not influence the mid-span displacement.

References

1. ABAQUS/CAE FEA program. Concrete-damaged plasticity model, explicit solver, three dimensional solid element library. ABAQUS DS-SIMULIA User Manual (2017)
2. Anas SM, Ansari MdI, Alam M (2020) Performance of masonry heritage building under air-blast pressure without and with ground shock. Aust J Struct Eng 21(4):329–344
3. Anas SM, Ansari Md I, Alam M (2021) A study on existing masonry heritage building to explosive-induced blast loading and its response. Int J Struct Eng (Article in press)
4. Anas SM, Alam M (2021) Performance of simply supported concrete beams reinforced with high-strength polymer re-bars under blast-induced impulsive loading. Int J Struct Eng (Article in press)
5. Anas SM, Alam M, Umair M (2021) Experimental and numerical investigations on performance of reinforced concrete slabs under explosive-induced air-blast loading: a state-of-the-art review. In: Structures, vol 31. Elsevier, pp 428–461
6. Anas SM, Alam M (2021) Air-blast response of free-standing: (1) Unreinforced brick masonry wall, (2) Cavity RC wall, (3) RC walls with (i) Bricks, (ii) Sand, in the cavity: a macro-modeling approach. In: Marano GC, Ray Chaudhuri S, Unni Kartha G, Kavitha PE, Prasad R, Achison RJ (eds) Proceedings of SECON'21. SECON 2021. Lecture notes in civil engineering, vol 171. Springer, Cham, pp 921–930. https://doi.org/10.1007/978-981-33-6389-2_18.
7. Anas SM, Alam M (2021) Comparison of existing empirical equations for blast peak positive overpressure from spherical free air and hemispherical surface bursts. Iran J Sci Technol Trans Civil Eng. https://doi.org/10.1007/s40996-021-00718-4
8. Anas SM, Alam M, Umair M (2021) Performance of on-ground double-roof RCC shelter with energy absorption layers under close-in air-blast loading. Asian J Civil Eng. https://doi.org/10.1007/s42107-021-00395-8
9. Anas SM, Alam M, Umair M (2021) Air-blast and ground shockwave parameters, shallow underground blasting, on the ground and buried shallow underground blast-resistant shelters: a review. Int J Protective Struct. https://doi.org/10.1177/20414196211048910
10. Anas SM, Alam M, Umair M (2020) Performance of one-way composite reinforced concrete slabs under explosive-induced blast loading. 1st International Conference on Energetics, Civil and Agricultural Engineering 2020, ICECAE 2020, Tashkent, Uzbekistan, vol 614
11. Anas SM, Alam M, Umair M (2021) Performance of one-way concrete slabs reinforced with conventional and polymer re-bars under air-blast loading. In: Chandrasekaran S, Kumar S, Madhuri S (eds) Recent advances in structural engineering. Lecture notes in civil engineering, vol 135. Springer, Singapore. https://doi.org/10.1007/978-981-33-6389-2_18
12. Goel DM, Matsagar AV (2014) Blast-resistant design of structures. Practice Periodical on Structural Design and Construction, ASCE 19(2):040140071–040140079
13. Hafezolghorani M, Hejazi F, Vaghei R, Jaafar BSM, Karimzade K (2017) Simplified damage plasticity model for concrete. Struct Eng Int 27(1):68–78
14. Hao H, Hao Y, Li J, Chen W (2016) Review of the current practices in blast-resistant analysis and design of concrete structures. Adv Structural Eng 19(8):1193–1223

15. IS 4991. Criteria for blast resistant design of structures for explosions above ground. Bureau of Indian Standards, New Delhi (1968)
16. Iannitti G, Bonora N, Curiale G, Muro DS, Marfia S, Ruggiero A, Sacco E, Scafati S, Testa G (2018) Analysis of reinforced concrete slabs under blast loading. IGF Workshop "Fracture and Structural Integrity", Procedia Structural Integrity, vol 9, pp 272–278
17. Kumar V, Kartik VK, Iqbal AM (2020) Experimental and numerical investigation of reinforced concrete slabs under blast loading. Eng Struct 206:1–13
18. Li Y, Chen Z, Ren X, Tao R, Gao R, Fang D (2020) Experimental and numerical study on damage mode of RC slabs under combined blast and fragment loading. Int J Impact Eng 142:1–11
19. Li J, Wu C, Hao H (2015) Investigation of ultra-high performance concrete slab and normal strength concrete slab under contact explosion. Eng Struct 102:395–408
20. Low YH, Hao H (2002) Reliability analysis of direct shear and flexural failure modes of RC slabs under explosive loading. Eng Struct 24:189–198
21. Schenker A, Anteby I, Gal E, Kivity Y, Nizri E, Sadot O, Michaelis R, Levintant O, Dor BG (2008) Full-scale field tests of concrete slabs subjected to blast loads. Int J Impact Eng 35:184–198
22. Silva FP, Lu B (2009) Blast resistance capacity of reinforced concrete slabs. J Struct Eng 135(6):708–716
23. TM 5–1300. Structures to resist the effects of accidental explosions. Technical Manual, Joint Department of the Army, the Navy, and the Air Force, US (1990)
24. Wu C, Hao H (2005) Modeling of simultaneous ground shock and airblast pressure on nearby structures from surface explosions. Int J Impact Eng 31(6):699–717
25. Wu C, Oehlers JD, Rebentrost M, Leach J, Whittaker SA (2009) Blast testing of ultra-high performance fibre and FRP-retrofitted concrete slabs. Eng Struct 31:2060–2069
26. Zhao FC, Chen YJ (2013) Damage mechanism and mode of square reinforced concrete slab subjected to blast loading. Theoret Appl Fract Mech 63–64:54–62
27. Zhou QX, Kuznetsov AV, Hao H, Waschl J (2008) Numerical prediction of concrete slab response to blast loading. Int J Impact Eng 35(10):1186–1200

Self-Flowable Rich Cementitious Matrices for Ferrocement Jacketed Beam-Column Joint

J. Revathy [ID], P. Gajalakshmi [ID], D. S. Vijayan [ID], and M. Rajalakshmi

Abstract Beam-column joints are considered as the weakest and vulnerable region in the structural system, as they are subjected to high shear forces under seismic action. Hence, the efficacy of the deficient beam-column joint could be retrofitted by various advanced techniques. This study focusses on the efficacy of employing the developed self-flowable cementitious mortar for ferrocement jacketed beam-column joint. A rich self-flowable and high-strength nanosilica-based cementitious mortar is utilized for the ferrocement jacketing techniques. With the intended repair solutions, a series of ten one-fourth scale reinforced concrete exterior beam-column joints that are designed as per IS 456: 2000 was fabricated and tested under simulated cyclic seismic loading. In this study, ferrocement jacketing is employed with two different types of wire mesh confined with durable rich self-flowable cementitious mortar. The performance of the beam-column joint was examined with respect to load-carrying capacity, energy dissipation and ductility. The test results indicated that the developed rich flowable matrices employed for ferrocement jacketed beam-column joint showed an appreciable increase in load-carrying capacity of 40.62% and attained maximum energy-absorption capacity by 14.26%.

Keywords Beam-column joint · Cementitious · Ferrocement · Flowable · Jacketing · Nanosilica

1 Introduction

Beam-column joints have significant importance in any reinforced concrete structure as they play a crucial role in transferring the load from beams to columns. The behaviour of the beam-column joint greatly influences the structural response of

J. Revathy (✉) · P. Gajalakshmi · M. Rajalakshmi
Department of Civil Engineering, B. S. Abdur Rahman Crescent Institute of Science and Technology, Chennai, India
e-mail: revathyj@crescent.education

D. S. Vijayan
Department of Civil Engineering, Aarupadai Veedu Institute of Technology, Chennai, India

the structure. Particularly, under seismic activity, the beam-column junction is more susceptible to failure as it is subjected to high shear forces. For this reason, it is important to maintain the stability and integrity of the structure through the proper and adequate design of beam-column junction. In general, most of the structures are designed and detailed only for gravity loads and lateral loads, which are lower than the loads generated during an earthquake. This results in poor performance of the beam-column joints. Moreover, unsafe beam-column joint increases the chances of the ultimate collapse of the structure, even when the rest of the structural members satisfies the design requirements. Hence, it is essential to rehabilitate the existing beam-column joint for improving the behaviour under seismic activity.

A practical and effective solution, to improve the behaviour of beam-column joint, is to apply jackets of ferrocement [1] in the junctions of beam-column. This could be identified as a successful technique owing to its characteristics such as good tensile strength, lightweight, economy, water tightness, ease in application, long life. It is understood that ferrocement jacketing technique improves the performance of the structural joints. Bo li et al. [2] carried out an experimental study on reinforced concrete interior beam-column joints rehabilitated by ferrocement jackets. The interior beam-column joints were rehabilitated using ferrocement jackets with embedded diagonal reinforcement. Ravichandran et al. [3] investigated eight full-scale beam-column joint specimens, out of which two were treated as control, and the other six specimens were strengthened using ferrocement jacketing technique. The results indicated an increase in energy dissipation, ultimate load, stiffness and ductility in the strengthened specimens than in control specimens. Sheela et al. [4] investigated the performance of reinforced concrete beam-column joints that were strengthened using different composite materials. Singh and Shri [5] performed a study on the effect of the strength and ductility of ferrocement jackets for damaged exterior reinforced concrete beam-column joints. It was also observed that ferrocement jacketing did not suffer any debonding even at failure. Venkatesan et al. [6] worked on the structural behaviour of beam-column joints retrofitted with ferrocement laminates. In this research, strengthening of shear-deficient beam-column joint through retrofitting with ferrocement jacketing was studied. Hence, it was concluded that ferrocement could be efficiently used for seismic retrofitting of reinforced beam-column joint. It is understood that ferrocement jacketing in structural joints improves its behaviour. However, enhancement of the properties of cement mortar used for ferrocement presents a scope for research.

Currently, nanotechnology has shown a significant attention towards the potential use of smaller size particles (1 to 100 nm scale) in concrete. Utilizing of nanoparticles in the cement based materials proves to alter its properties from conventional materials [7]. Many researchers studied on the utilization of nanoparticles in concrete or mortar, including nanosilica, [8], nanoironoxide, [9], nanotitanium oxide [10]. A rich self-flowable and high-strength nanosilica-based cementitious mortar is utilized for the ferrocement jacketing techniques. Hence, this study focusses on the efficacy of employing the developed self-flowable cementitious mortar for ferrocement jacketed beam-column joint.

2   Test Programme for Beam-Column Joint

2.1   Materials

Ordinary portland cement of 53 grade confirming to IS 4031–1988 with a specific gravity of 3.14 and fineness of 5% was used in the present study. River sand with a fineness modulus of 3.11 and the specific gravity of 2.66 was adopted. The crushed granite of less than 20 mm size with a specific gravity of 2.75 was used. The mix proportion was designed as 1:1.88:3.17 with a water-cement ratio of 0.45. The concrete mixture for the beam-column joint was designed as per IS 10262—2009. The average compressive strength of three concrete cube specimens after 28 days was 32 N/mm^2. The reinforcement provided in the structural member was 12 mm diameter and 8 mm diameter with a yield strength of 436 N/mm^2 and 289 N/mm^2, respectively.

Rich and special cementitious mortar mixes were prepared to achieve the high strength and self-flowable mortar [7]. The materials used for the preparation of rich cementitious mortar mixes include ordinary portland cement of ASTM type I with a specific gravity of 3.15 and river sand with a specific gravity of 2.65 and a fineness modulus of 2.80. Superplasticizer of a modified polycarboxylic ether with a specific gravity of 1.08 was added in all the mixes to achieve the workability. Nanosilica (SiO_2) with a particle size of 20 nm, a specific surface area of 200 m^2/g and a density of 50 g/L was used. Nanosilica of 3% dosage was replaced with cement. The rich self-flowable mortar mix has a ratio of 1:2 with water-to-binder ratio was kept as 0.38 and a flow percentage of 50–60%. The rich self-flowable mortar attained the compressive strength and tensile strength of 60 N/mm^2 and 3.98 N/mm^2, respectively. Galvanized iron-welded square mesh of 1 mm thickness with 15 mm size opening and expanded mesh of 1 mm thickness were used for ferrocement retrofitting.

2.2   Preparation of Beam-Column Joint

The test specimens were scaled at one-fourth model of a typical exterior beam-column joints. The cross-section of the column and beam was kept as 250 mm × 150 mm and 150 mm × 200 mm, respectively. The height of the column was 800 mm. The cantilever portion of the beam was kept as 550 mm in length. The reinforcement details of the beam-column joint specimens were prepared and designed as per IS 456: 2000 and are shown in Fig. 1. The shaded zone in Fig. 1 indicated for the provision of ferrocement jacketing. One exterior beam-column joint was proposed as the reference specimen (BC1), and the other four beam-column joint were served as retrofitted specimens (BC2, BC3, BC4 and BC5). Two beam-column joints were retrofitted with two layers of a square (BC2) and expanded wire mesh (BC4) bonded by conventional cement mortar, whereas the other two beam-column joints were retrofitted with two layers of a square (BC3) and expanded wire mesh (BC5) bonded
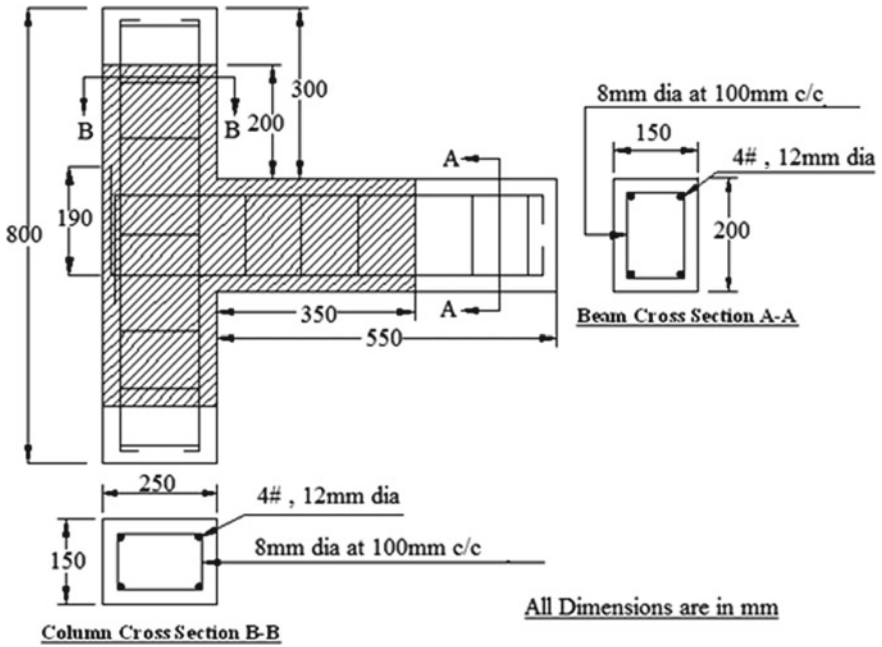
Fig. 1 Schematic reinforcement detailing as per IS 456–2000

by rich flowable nanosilica-based cementitious mortar. Totally, ten specimens were tested with two samples in each category. The fabricated steel cage was placed in the wooden mould, Fig. 2a, and concrete mixture was poured in layers, and compaction

(a) Steel cage in wooden mould   (b) Exterior beam-column joint specimen

Fig. 2 Sample of beam-column joint

was done. The specimens were covered with wet burlap in the laboratory environment. The specimens were demoulded after 2 days cured for 28 days, Fig. 2b. Figure 2 shows a sample of beam-column joint specimen.

2.3 Experimental Testing of Beam-Column Joint

One-fourth modelled exterior beam-column joint specimens were tested under cyclic loading conditions in a loading frame as shown in Fig. 3. The ends of the columns were restrained at its ends. A constant axial load of about 20% of the axial capacity of the column was applied. For the reversal cyclic loading in the beam portion, two hydraulic jacks were used. The load was applied by using a load cell, and the deflection was measured through LVDT at the free end of the beam. The measured readings were acquired through a data logging system. The reference specimen (BC1) was loaded till failure of the specimen, and its ultimate capacity was observed. Other four specimens were loaded up to 80% of the reference specimen to produce the damaging effects. The damaged specimens were then retrofitted with ferrocement jacketing and were tested again for cyclic loading condition.

Fig. 3 Experimental testing of beam-column joint
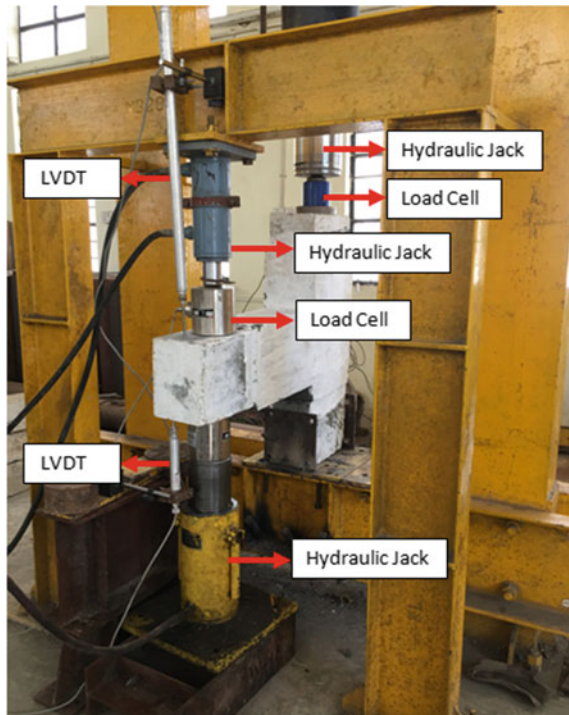
Fig. 4 Process of retrofitting the beam-column joint specimen

2.4 Process of Ferrocement Jacketing

The four exterior beam-column joint specimens (BC2, BC3, BC4 and BC5) were loaded up to 80% of the ultimate load were employed for the ferrocement jacketing techniques. The damaged surfaces of these specimens were first cleaned, and then it was wrapped with two layers of galvanized wire mesh of square opening and expanded mesh. The cement slurry and developed rich flowable nanosilica-based cementitious mortar of 20 mm thick were applied to the surface of beam-column joint. The mix ratio is of 1:2 with a water-binder ratio of 0.38. The retrofitted specimens were cured for a period of 14 days and tested under cyclic loading (Fig. 4).

3 Results and Discussion

3.1 Behaviour of Beam-Column Joint Specimens

The hysteresis behaviour of the reference specimen BC1 and retrofitted specimens BC2, BC3, BC4 and BC5 are shown in Fig. 5. The hysteresis curves of reference specimen BC1, retrofitted specimens BC2 and BC3 specimens are compared, and it can be seen clearly that specimens retrofitted with welded mesh survive more number of load cycles with lesser deflection than the reference specimen. Furthermore, BC3 specimen retrofitted with developed rich flowable nanosilica-based cementitious mortar has superior performance than BC2 specimen. By making the comparison between the hysteresis curve of BC1 and retrofitted specimens BC4 and BC5, it can be observed that BC4 and BC5 have more number of load cycles than the reference specimen.

The first crack load observed for the reference specimen was 24.4 kN. The retrofitted specimens BC2, BC3, BC4 and BC5 had their first crack load, respectively, at 17.9 kN, 20 kN, 10.1 kN, 15.3 kN. The increase in crack resistance of the BC3 and BC5 is due to the pore filling effect of nanoparticles. When compared with reference specimen, the retrofitted specimens BC2, BC3, BC4 and BC5 exhibit an

(a) BC 1

(b) BC2

(c) BC3

(d) BC4

(e) BC5
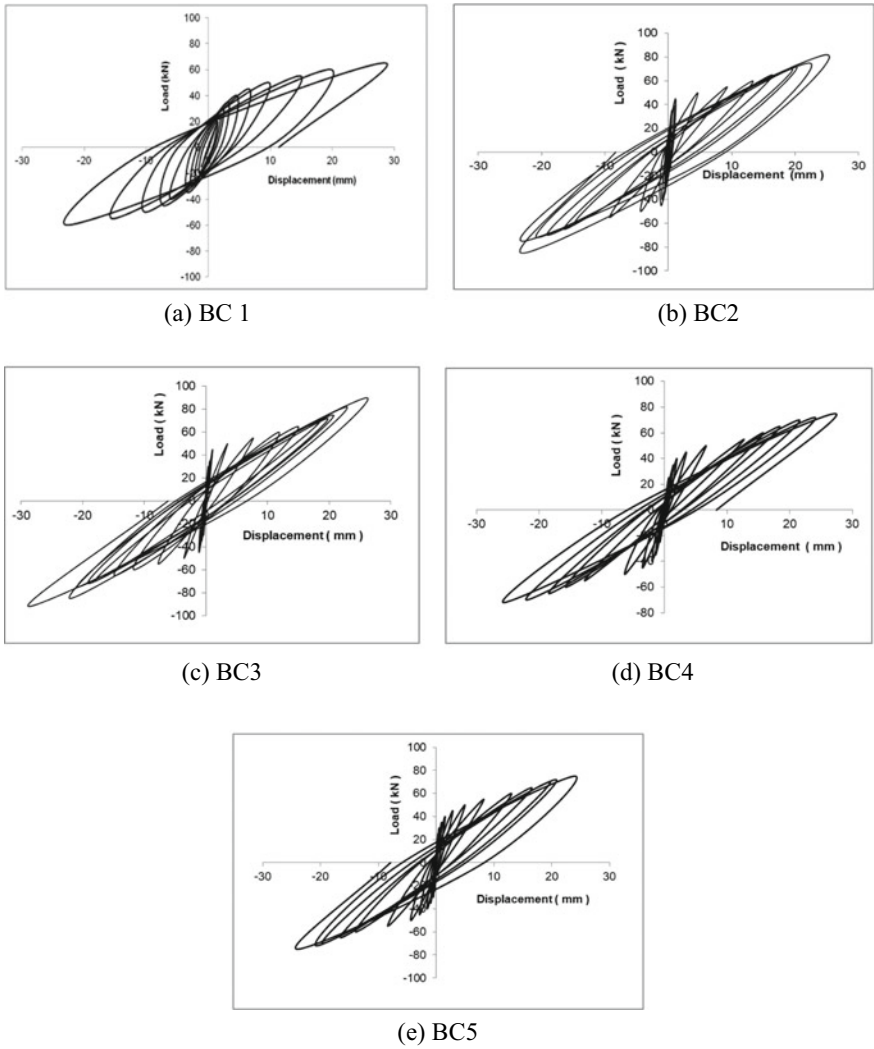
Fig. 5 Hysteresis behaviour of exterior beam-column joint specimens

increase in ultimate load by 32.18%, 40.62%, 9.375% and 18.75%, respectively, in the push and 36.66, 43.33, 10 and 20% in pull. It can also be noted that the deflection at ultimate load of the retrofitted specimens BC2, BC4 and BC5 decreases by 11.9%, 4.05% and 15.43%, respectively, in the push and 13.75, 4.08 and 4.72% in pull.

Table 1 Ductility ratio and energy-absorption capacity of beam-column joint specimens

Specimen	Ultimate load (P_u) (kN)	Yield load (P_y) (kN)	Ductility ratio	Stiffness (kN/mm)	Energy-absorption capacity (kN-mm)
BC1	64	59	1.08	2.25	1443.25
BC2	85	72	1.18	3.4	1494.20
BC3	90	80	1.12	3.2	1649.08
BC4	70	60	1.16	2.79	1547.20
BC5	76	68	1.11	2.91	1396.46

3.2 Stiffness

Stiffness is defined as the load required to cause unit deflection of the beam-column joint. Table 1 presents the stiffness of the beam-column joint specimens. It can be observed that stiffness of retrofitted specimens BC2, BC3, BC4 and BC5 was higher than that of the reference specimen correspondingly by 51.1, 42.2, 24, 29.3. The specimen retrofitted with welded square mesh has more stiffness than the other specimens. In the case of expanded mesh, BC5 has more stiffness than the BC4 specimen.

3.3 Ductility

The ductility ratio is defined as the ratio of deflection at ultimate load and yield load. The ductility ratio for the reference specimen is 1.42, whereas it was considerably increased after ferrocement retrofitting technique, and it is presented in Table 1.

3.4 Energy-Absorption Capacity

The energy-absorption capacity is calculated as the area under the load–deflection curve. The energy-absorption capacities for the reference and retrofitted specimens are shown in Table 1. The retrofitted specimens BC2, BC3, BC4 and BC5 showed an increase in energy-absorption capacity, respectively, by 3.53, 14.26, 7.20 and 3.69% in comparison with reference specimen.

3.5 Crack Pattern and Failure Mode

The crack patterns of all the exterior beam-column joint specimen are shown in Fig. 6. Cracks in the range of 0.5 mm to 2 mm could be observed at the beam portion

(a) BC1 specimen

(b) BC2 specimen

(c) BC3 specimen

(d) BC4 specimen

(e) BC5 specimen

Fig. 6 Crack patterns in exterior beam-column joint specimens

as well as at the junction of specimens. More number of cracks were formed in BC2 and BC4 specimens, whereas cracks were minimal in the case of BC3 and BC5. This is due to the enhanced crack-resisting property of rich flowable nanosilica-based cementitious mortar. When the loads were further increased, the cracks were widened approximately of 2.2 mm and delamination occurred at failure load.

4   Conclusion

The following conclusions were drawn from the experimental study:

1. The exterior beam-column joints retrofitted with ferrocement jacket were found to be very effective in load-carrying capacity, deflection, cracking behaviour and stiffness when compared to the control specimen.
2. The beam-column joint specimens employed with rich flowable nanosilica-based cementitious mortar showed a maximum improvement in the load-carrying capacity.
3. The retrofitted specimen BC3 exhibits an increase in maximum ultimate load by 40.62%, in comparison with the reference specimen.
4. All the retrofitted specimens showed a maximum increase in ductility and energy-absorption capacity when compared to the reference specimen. The maximum energy-absorption capacity of 14.26% was attained by the BC3 specimen.
5. Cracks were minimal in the case of BC3 and BC5. This is due to enhanced crack-resisting property of rich flowable nanosilica-based cementitious mortar. At ultimate load, delamination of the retrofitted layer occurred.

References

1. ACI Committee 549-Thin Reinforced Cementitious Products and Ferrocement, 1980
2. Li B, Sui-shu Lam E, Wu B, Wang Y-Y (2013) Experimental investigation on reinforced concrete interior beam-column joints rehabilitated by ferrocement jackets. Engineering Struc 56:897–909
3. Ravichandran K, Antony Jeyashar C (2012) Seismic retrofitting of an exterior beam column joint using ferrocement. International J Engineering and Applied Science 4(2):35–58
4. Sheela S, Anu Geetha B (2012) Studies on the performance of RC beam-column joints strengthened using different composite materials. J Institution of Engineering, (India): Series A 93(1):63–71
5. Singh, Shri D (2015) Experimental studies on strength and ductility of ferrocement jacketed RC beam-column joints. Int J Civil Struc Eng 5(3):199–205
6. Venkatesan B, Ilangovan R (2016) Structural behaviour of beam column joint retrofitted with ferrocement laminates. International J Adv Engineering Tech 7(2):1272–1280
7. Revathy J, Gajalakshmi P, Aseem Ahmed M (2020) Flowable nano SiO_2 based cementitious mortar for ferrocement jacketed column. Materials Today: Proceed 22(3):836–842

8. Revathy J, Gajalakshmi P, Sanju S (2019) Investigation on the Performance Characteristics of Concrete Incorporating Nanoparticles. Jordan J Civil Engineering 13:351–360
9. Oltulu M, Sahin R (2013) Effect of nano-SiO$_2$, nano-Al$_2$O$_3$ and nano-Fe$_2$O$_3$ powders on compressive strengths and capillary water absorption of cement mortar containing fly ash: a comparative study. Energy Buildings 58:292–301
10. Shen W (2015) Preparation of titanium dioxide nano particle modified photo catalytic self-cleaning concrete. J Clean Prod 87(15):762–776

An Experimental Investigation on Applications of Fiber-Reinforced Composites for Rehabilitation of Concrete Beams

Onkar K. Chothe and Vinay M. Agrawal

Abstract All concrete structures suffer damage and deterioration during their service life. The damage generally observed are cracks, spalling, excessive deflection and also exposure of embedded reinforcements at times. The rehabilitation of such damaged structures is necessary to maintain the serviceability. The present study focuses on rehabilitation of concrete beams with the usage of composite fibers. Composite fibers are been increasingly used in concrete structures due to their high strength-to-weight ratio. In the present study, concrete beams were tested for strength capacities with glass fiber and carbon fiber-reinforced polymer composite. The used composite materials have demonstrated significant improvement in flexural strength as compared to beam without any composite fiber. Six reinforced concrete beams were tested, three each with a wrapping of glass fiber and carbon fiber. Experimental results conclude that load caring capacity has increased for GFRP beams and CFRP beams. The observed increment was of the order of 22% to 43% and 50% to 55%, respectively, for glass and carbon fiber. The paper also demonstrated the step-by-step procedure of applying glass and carbon fiber in beams in different layers.

Keywords Rehabilitation · Composite · Compressive load · Flexural strength · Polymer

1 Introduction

1.1 Fiber-Reinforced Polymer (FRP)

Fiber-reinforced polymer (FRP) composites are being increasingly used for rehabilitation of bridge components. There are many advantages associated with application of FRP due to higher strength-to-weight ratio, non-corrosive nature of FRP material

---
O. K. Chothe · V. M. Agrawal (✉)
National Institute of Construction Management and Research, NICMAR Goa Campus, Goa 403401, India

O. K. Chothe
e-mail: ochothe@nicmar.ac.in

Table 1 Properties of glass, aramid, and carbon fibers [3]

Sl. no	Type of FRP	Percentage of fiber	Density in Kg/m^3	Tensile strength in kg/cm^2
1	G FRP	50–80	1600–2000	4000–18,000
2	C FRP	65–75	1600–1900	12,000–22,500
3	A FRP	60–70	1050–1250	10,000–18,000

and ease in installation and handling. Nowadays, FRP material, preferably glass fiber-reinforced polymer sheet, is used for rehabilitation purpose and re-strengthening of members due to its low cost as compared to other polymers. FRP behavior under loads are similar to reinforced concrete members. The fiber reinforcement can carry load in pre-designed directions as well as the resin used as a medium to transfer stresses and provide physical protection for the fibers. Glass fiber, carbon fiber or aramid fiber materials is the most common types used for rehabilitation of bridge. Depending upon the type of fiber used, product is known as glass fiber-reinforced plastic (GFRP) if glass fiber is used, carbon fiber-reinforced plastic (CFRP) if carbon fiber is used, and aramid fiber-reinforced plastic (AFRP) if aramid fiber is used [1, 2]. Engineering properties of different fibers are shown in Table 1 below.

2 Application of FRP

To improve flexural strength of member, FRP can be applied at the tension face of the member. Strips of FRP are installed using epoxy so that bonding with member is ascertained followed by making shallow grooves. FRP provides confinement to the longitudinal steel bars, and also, the compressive strength of concrete increases by lateral confinement of FRP [4, 5]. There are two methods for rehabilitation of the structure which use FRP:

- Wet lay-up method.
- Pre-fabrication of FRP followed by its application. (dry layup method)

Surface preparation: Proper preparation of concrete element surface is required for perfect bond of FRP sheets with concrete surface. Proper contact between the concrete element surface and the FRP sheets could be achieved by smoothening of concrete surface. The adhesive is used to attach the composites and the concrete surface. The concrete surface is roughened. The concrete element are washed out by using hot water and mild detergent. Dust, grease and other separate particles are removed by using washing. Dust particles or grease will affect on the bond between the cement element surface and FRP sheet. Epoxy grouting is used for fill up the cracks which more than 0.3 mm width.

Wet layup method: Firstly, epoxy coat is applied on concrete element surface with proper quality. Secondly, coat is applied by saturated FRP sheet with proper precautions. Because the skewed alignment of fiber may direct to faulty work, misalignment

of the fiber may lead to unsound work. If any bend or twist is present, fiber could be properly aligned and slightly stretched. The number of layers depend upon the requirement of thickness. Next, the layer of FRP sheets can be applied properly to the surface on which the layer of FRP sheet is applied. Precaution should be taken for no any voids in that layer to achieve strength [6].

Normally, polyester resins are used in wet layup process. However, vinyl ester or epoxy resin can also be used. Fibers may be either glass fiber or carbon fiber. Glass fiber is cheaper than the carbon fiber. In most of the field application, glass fiber is used for wet layup method. Main advantage of wet layup process is that pre-fabrication of FRP product is not required. Each and every surface of concrete element are covered by this process.

Pre-fabrication of FRP (dry layup method): In this method, pre-fabricated FRP component is used. Proper size is made for fixing the FRP sheets layer to the concrete element structure. Surface preparation is the same as is done in case of wet layup process. After that, epoxy is applied on the concrete surface. Next, FRP sheet with proper size and thickness is pasted on that epoxy. Subsequently, the voids from the layers are removed by using roller for good bonding to concrete surface. After curing of the surface applied epoxy, it becomes part of the structure. Dry layup method would provide better results and quality as compared to wet layup process. The only problem is that the surface profile is not regular and corner cannot be properly covered in this method [7, 8].

Surface finish: The final step in the rehabilitative process is the finish coating. Finish coats must be applied between twelve- and seventy-two hours of the FRP installation to allow the coating and the epoxy to cure together. If the coating is applied before this time period, it can crack as the epoxy curing takes place. If it is applied after this time period, a light sanding of the cured epoxy is required to achieve proper bond. All composite surfaces can then paint to match the existing structure. Regarding this, acrylic paint or urethane coating can be applied.

3 FRP Rehabilitation of Various Types

FRP rehabilitation may be of different types, depending on case to case and member to member. The following are the types, which may be choosing either one or combined [9–11].

- Rehabilitation work to enhance the flexural capacity.
- Rehabilitation work to enhance the shear capacity
- Rehabilitation work to enhance the axial force carrying capacity.

Rehabilitation work to enhance the flexural capacity: For FRP sheets, thickness is designed on the tension side. It acts as an external reinforcement, added external FRP reinforcement along with internal steel reinforcement. This internal and external reinforcement provide the desired quantity of reinforcement on the tension zone. Because of that the neutral axis is shifted on the tension side and that increases the total

compressive force on the compression side. As such, the structure is strengthened to the desired extent. Length of FRP reinforcement is also calculated as per the steel reinforcement. As well as, the length of the reinforcement is calculated even away from the zone of requirement to ensure transfer of force through bond length. In addition to the zone of requirement, FRP sheet is extended beyond that in such a manner that adequate anchorage may be available to transfer the force safely.

While pasting the FRP sheets, the direction of the fibers is most important because strength is maximum in the axial direction of fiber which is shown in Fig. 1. In flexural member, steel reinforcement is provided along the span direction and similar to that FRP sheets are provided.

For avoiding de-bonding, FRP in the form of "U" strip is provided at the end to ensure proper end anchorage to the FRP sheet at the end which is shown in Fig. 2. Anchorage must be passing through the bottom of FRP sheet provided for flexural strengthening. If the structure is required for strengthening in shear also, then contribution of "U" strip may be there in transferring the shear force as well.

Slab is also flexural member. The following Fig. 3 shows the direction of FRP strengthening for one-way and two-way slabs. In one-way slab, FRP strips are provided parallel to length of slab. In two-way slab, FRP strips are provided in both directions as shown in Fig. 3.

Rehabilitation work to enhance shear capacity: Flexural failure is designed for ductile failure while the shear failure is brittle one. As such, the structure in case of failure should fail in flexural mode and not in shear mode. For shear strengthening, FRP strips are provided as the shear leg in the form of ring in RCC beam. Spacing,
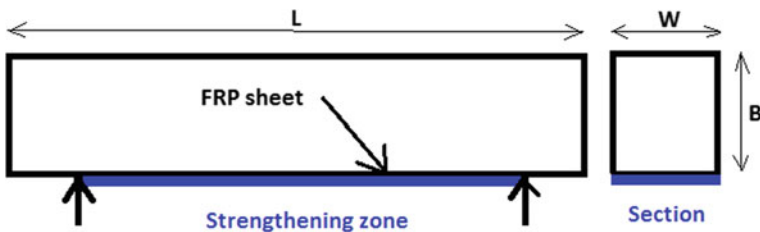
Fig. 1 Strengthening of beam with FRP
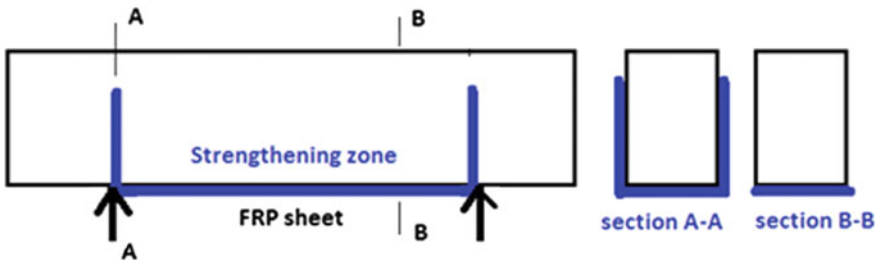
Fig. 2 FRP along with FRP U strips
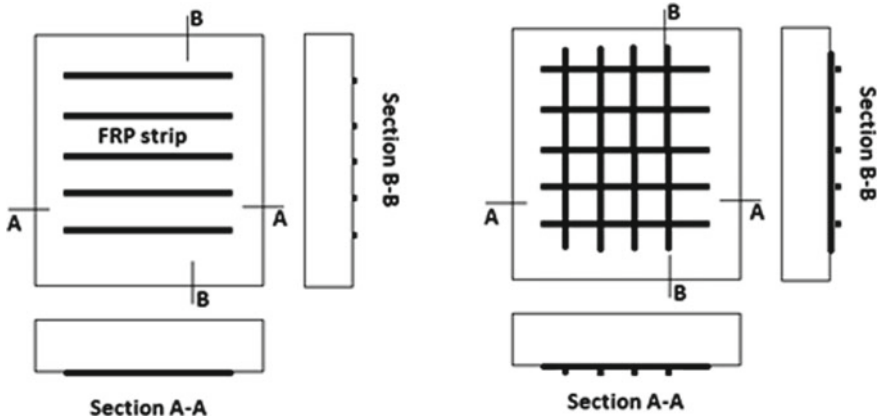
Fig. 3 One-way slab and two-way slab

Fig. 4 FRP strips strengthening of RCC beam in shear zone

width, and the number of the strips can be decided as per design calculation. FRP strips can be wrapped on side of element or in U form or all side wrapping as shown in Fig. 4.

Rehabilitation on account of axial force: Climatic conditions and age factors affect on the strength and load carrying capacity of concrete elements of structure. Load carrying capacity and strength of concrete element can be improved by FRP sheet wrapping with epoxy material. When axial load is considered for failure of element of structure, spiral wrapping or band wrapping should be considered.

4   Experimental Work

The behavior of FRP composite beam is investigated under flexural loading. The beams were cracked prior to loading and tested for flexural strength after appropriate retrofitting. Totally, six beams were tested. Out of these, three beams were retrofitted with GFRP and three beams are retrofitted with CFRP.

Test Objectives: The objective of this investigation is to examine experimentally the benefits of external bonding of glass fiber and carbon fiber to strengthen, rehabilitate the flexural members, and to evaluate its effect on load carrying behavior.

Materials: IS: 10262:2009 is used for mix design of 53 grade concrete. For experimental purpose, the mix proportion is taken as water (0.38): cement (1.0): fine aggregate (1.89): coarse aggregate (2.83). As well as, the quantities per bag cement are water (19 kg): cement (50 kg): fine aggregate (94.5 kg): course aggregate (141.5 kg).

Experimental Program: Mostly, beams are strong in shear strength but weak in flexural strength. Flexural strength of the beams was improved by using GFRP and CFRP material wrapping at all faces. To observe the experimental results, totally six beams were cast for GFRP and CFRP. Testing of specimens before retrofitting is the initial requirement of the project. Analysis of retrofitting will fully deal with the existing performance and after the performance. A single layer of 700 mm x 600 mm of CFRP and GFRP is wrapped on beams to investigate the effect of FRP on flexural strength.

All the beams were tested under simply supported condition. The testing was done under two-point loading using the Universal Testing Machine of 60 ton capacity. All beams tested statically up to failure of the beam in a single load cycle. The experimental work to study the flexural strength of RC beams was carried out on the rectangular beams. Cracks formed on the faces of the beams were marked and identified. Experimental testing setup is shown in Fig. 5, and arrangement for testing of beam is shown in Fig. 6.

Fig. 5 Experimental testing setup
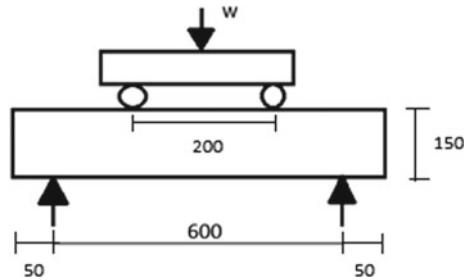
Fig. 6 Arrangement of testing setup

Fig. 7 Beam specimen's geometry and reinforcement details
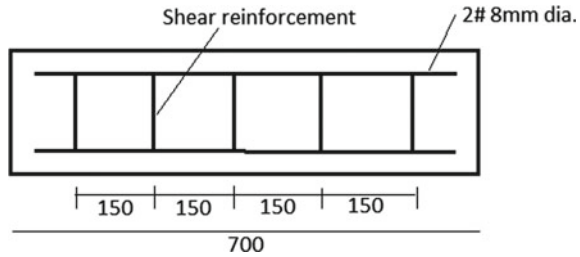
Details of beam specimen: IS 456–2000 is used to calculate minimum steel reinforcement. There are two groups of specimens; reinforced concrete beams are 700 mm long with 600 mm effective span. These beams are constructed in laboratory and tested under two-point loading flexural test. Beams are provided with steel bar stirrups of 8 mm dia. and 150 mm center-to-center distance. Stirrups are provided to prevent shear failure. The beam specimen's geometry and reinforcement details are shown in Fig. 7.

Casting of beams: After theoretical design, the next step is casting of specimens which involves the preparation of casting schedule and planning of the casting to obtain required quantity specimen. In this, we have to prepare the reinforcement cage which finally is placed in mold or formwork to cast the specimen.

The experimental work consists of testing of six simply supported beams. All beams had the same dimensions and reinforcement. The available steel molds in laboratory of cross section 150 mm × 150 mm and length of 750 mm are used for casting of the beams. Flexural reinforcements are provided at bottom of beam (two 8 mm dia.) The required quantity of cement, sand, coarse aggregates, and water as per mix design was taken by using the weighing machine. Then, the mixing is done manually, and after the homogeneous concrete paste is done, concrete was placed in the molds and compaction was done by using the compression machine. The beams were placed in curing tank for 28 days. The molds used for casting of beams are shown in Fig. 8.

Nomenclature of specimens: The test specimens were divided into two groups, one for CFRP and another for GFRP. Beams were identified by a numbering code, for example: C1, C2, C3 for CFRP beams and G1, G2, G3 for GFRP beams.

Fig. 8 Molds used for casting of beams and cubes
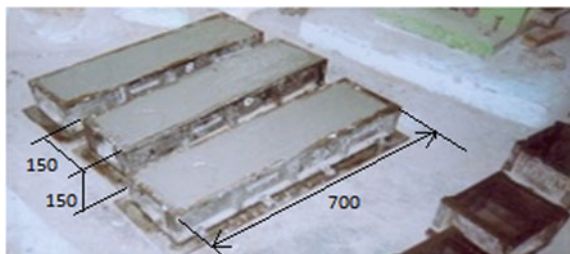
Table 2 Comparison of casted beams and beams with application of fiber (GFRP and CFRP) according to loading

S. no	Normal beams (KN)	Same beams after application of fiber and epoxy resins (KN)	Percent of load increment	Flexural strength of normal beam (N/mm^2)	Flexural strength of strengthen beam (N/mm^2)
G1	91.5	111.3	22	16.47	20.03
G2	92.3	119.9	30	16.61	21.58
G3	90.5	129.5	43	16.29	23.31
C1	92.5	139.2	50	16.65	25.06
C2	91.8	140.9	53	16.52	25.36
C3	93.4	142.7	53	16.81	25.69

Strengthening of Beams: The FRP composite was applied to the surface of the concrete specimen using wet-lay procedure recommended by the manufacturer. Beams were externally bonded with FRP layer at tension face and at moment region; i.e., the direction of the fibers was arranged parallel to the axis of the beam (longitudinal direction or 00) in order to act as flexural reinforcement. During the application, the resin saturates into the glass fiber, carbon fiber and also the adhesive to bond the glass fiber sheet, carbon sheet to the concrete surface.

Application Methodology of GFRP and CFRP on Concrete Surface: The procedure is included with the crack repairing and applying the epoxy material to concrete element surface for FRP sheets. The application methodology consists of the following steps such as surface preparation of concrete element is the first step. The second step is application of primer and putty on the concrete element surface. Mixing of resin was done in accordance with the FRP system manufacturers suggested procedure. The last step is application of GFRP and CFRP on concrete element surface[12–14]. Table 2 provides the information about comparative statement between the casted beams and beams with application of fiber (GFRP and CFRP). Similar data are presented in Figs. 9 and 10.

5 Photographs of Experimental Work

The below photographs are related to the experimental work as well as the step-by-step procedure for FRP wrapping.
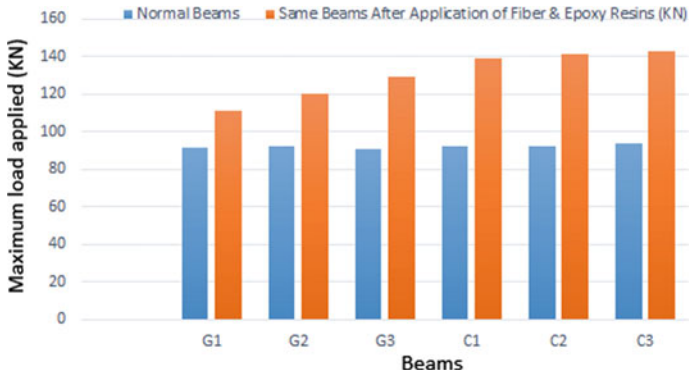
Fig. 9 Comparison of casted beams and beams with application of fiber (GFRP and CFRP) according to loading
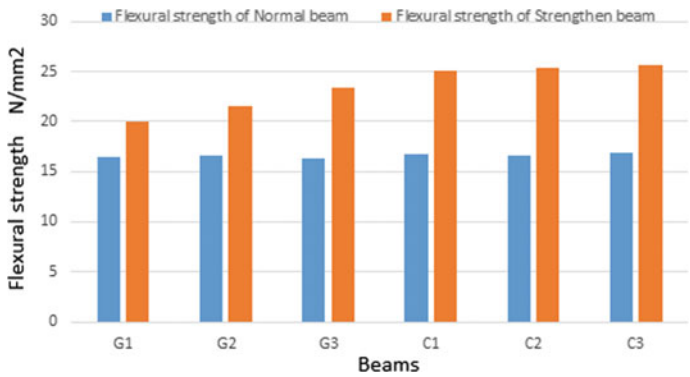
Fig. 10 Comparison of casted beams and beams with application of fiber (GFRP and CFRP) according to flexural strength

Step 1 - Testing a beam

Step 4 - Applying primer on beam

Step 2 - Cracks developed on beam

Step 5 - Wrapping FRP with saturant

Step 3 - Cracks filled with putty

Step 6 - Testing of FRP beams
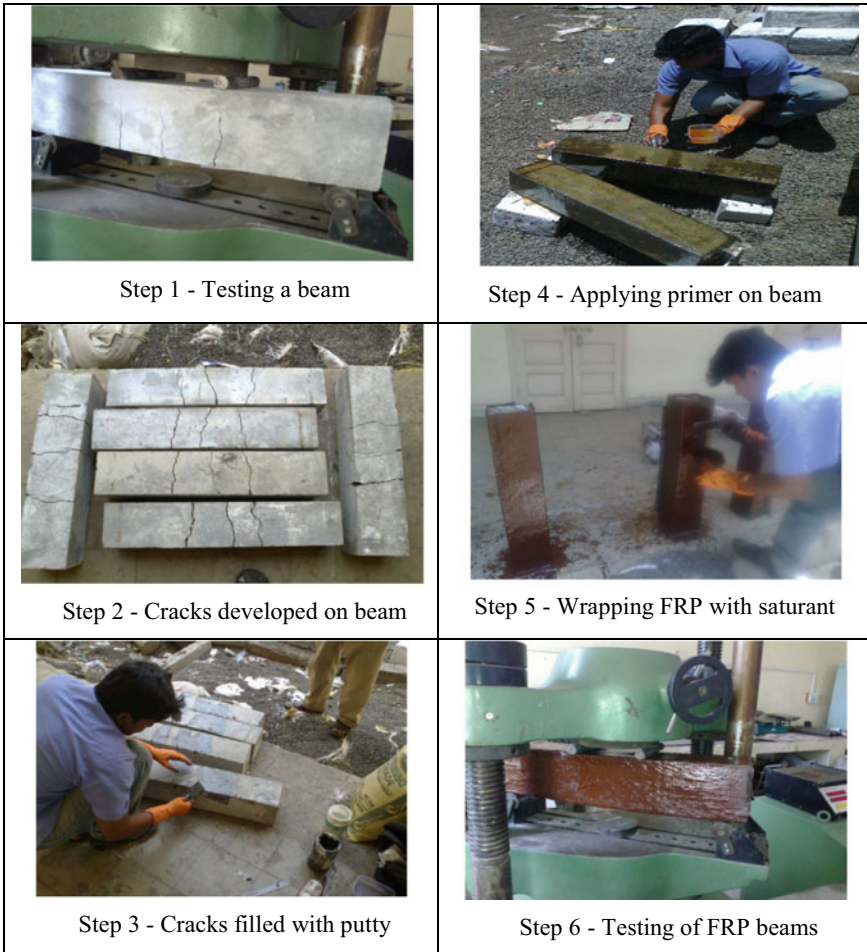
6 Conclusion

The beams failed at an average load of 92 KN in conventional ductile flexural with yielding of the steel followed by crushing of the concrete in the compression zone. After preloading, the beams are retrofitted by using GFRP, CFRP, and epoxy resin and tested after the curing is complete; then, it is observed that the beams were bend at center in the form of sagging manner by minor millimeters of deflection.

- After application of glass fiber with epoxy resins to beams G1, G2, G3, and placing in sunlight for 3 days, GFRP beams flexural strength was increased by 22%, 30%, and 40%, respectively.

- After the application of carbon fiber with epoxy resins to beams C1, C2, C3 and placing in sunlight for 3 days, CFRP beams flexural strength was increased by 50%, 53%, and 53%, respectively.

References

1. Chhabra Y (2004) Bridge rehabilitation techniques: Master builder Article, Singapore, pp 1–9
2. Gupta RK (2005) Use of FRP in strengthening/rehabilitation of concrete structures, pp 1–14
3. Potyrała PB (2011) Use of fiber reinforced polymer composites in bridge construction. State of the Art in Hybrid and All-Composite Structures, Construction Engineering, pp 1–47
4. American Concrete Institute.ACI 230 (2005) 7th International symposium on fiber reinforced polymer (FRP) reinforcement for concrete structure, Farmington Hills
5. Rizkalla SH, Hassan TK (2002) Rehabilitation of concrete structures with Frp, Department of Civil Engineering, North Carolina State University, pp 1–10
6. Tedesco JW (1998) Rehabilitation of a reinforced concrete bridge using FRP laminates, The Alabama Department of Transportation Montgomery, Alabama, pp 13–54
7. Nanni A (2001) Carbon fibers in civil structures: Rehabilitation and new CONSTRUCTION, Center for Infrastructure Engineering Studies ,University of Missouri, pp 1–6
8. Salib S (2012) Fiber reinforced polymers (FRP): A Vital Option for the Structural Rehabilitation of Concrete Bridges, Ryerson University Toronto, Canada, pp1- 10
9. Rizkallai S (2011) Rehabilitation of structures and bridges, university of Manitobai, pp 1–9
10. Tabatabai H, Al Ghorbanpoor, Turnquist-Nass A (2005) Rehabilitation Techniques For Concrete Bridges , Wisconsin Highway Research Program Project No. 0092–01–06, pp 1–88
11. Rai G, R & M International (2011) Rehabilitation and Strengthening of Bridges by using FRP composites, pp 1–18
12. Brühwiler E, Denarié E (2008) Rehabilitation of concrete structures using Ultra-High PerformanceFiber Reinforced Concrete, The Second International Symposium on Ultra High Performance Concrete, pp 1–8.
13. Attari N, Amziane S, Chemrouk M (2012) Flexural strengthening of concrete beams using CFRP. GFRP and hybrid FRP sheets, Construction and Building Materials, Elsevier 37:746–757
14. Moodi Y, Mousavi SR, Ghavidel A, Sohrabi MR, Rashki M (2018) Using response surface methodology and providing a modified model using whale algorithm for estimating the compressive strength of columns confined with FRP sheets, Construction and Building Materials, Elsevier 183:163–170

Two-Layered Steel Fiber Concrete Beam with Concrete Grade Change in Layers

Thi My Dung Do ⓘ**, Thanh Quang Khai Lam** ⓘ**, Van Thuc Ngo** ⓘ**, and Thi Thu Nga Nguyen** ⓘ

Abstract When surveying and designing the structure in multi-layered reinforced concrete beams, the change in the initial input parameters can influence the stress–strain state of beams and influence formation and development of cracks in the laminated concrete beams. In this paper, after testing these two-layered reinforced concrete beams, the authors simulated the two-layered reinforced concrete beams with ANSYS software in which the case of a concrete layer of steel fiber on top and the concrete layer of steel fiber on bottom of the normal concrete layer have been surveyed. The results of research established load–stresses and load–displacement relationships in two-layered concrete beams in the middle of span, formation, and cracks growth with increased load from 0 kN until the beams fail. In these two-layered concrete beams, through the use of a steel fiber concrete layer in the beam and a change in concrete grade in each concrete layer, with a beam size of 15 × 30 × 220 cm, the load at which concrete beams begin to crack is calculated and the load at which they are prepared for damage was also calculated in this analysis, and in numerical simulation using ANSYS, material nonlinearity was considered.

Keywords Material nonlinear · Shear · Double-layered beam · Fiber content · Stress–strain · crack

1 Introduction

Steel fiber concrete materials have been studied in depth; through adding steel fibers to the concrete, it improves the concrete's mechanical properties such as increased construction life, strong impact resistance, reduced cracks, increased bearing ability, and studied by many authors, both experimentation and simulation [1, 2], these studies have established load–stress and load–displacement relationships in which

---

T. M. D. Do · T. Q. K. Lam (✉) · V. T. Ngo
Mien Tay Construction University, 20B Pho Co Dieu Street, Ward 3, Vinh Long, Vietnam

T. T. N. Nguyen
University of Transport Technology, Thanh Xuan, 54 Trieu Khuc Street, Hanoi, Vietnam

steel fiber concrete is used in multi-layered shell, considering the ability to slide between shell layers [3–5].

Steel fibers in high-strength concrete or nano-concrete have improved the bearing capacity of the concrete, enhancing nano-concrete flexibility, considering nano-silica effects to high-performance concrete strength, studying the effects of nano-silica on crack toughness, based on double-K model [6–9]. Steel fiber concrete is used in bending beams, and this study has used experimental and simulation methods to check at the input parameters of steel fiber concrete beams that affect the stress–strain condition and the formation and creation of concrete beam cracks [10, 11].

In the study of laminated beams, consideration should be given to sliding between layers, cracks propagation in beams, buckling analysis, flexural performance in composite beams, and detailed results have been obtained in studies [12–14]. Moreover, the experimental and the finite element methods were both studied on several different aspects, such as finite element study of the moment–curvature of the double-layered concrete beam; design method for beams consisting of normal and fibered high-strength concrete, two-layer beams from normal and fibered high-strength concrete, experimental investigation of full-scale two-layer reinforced concrete beams [15–18], and research in two-layer reinforced continuous concrete beams [19].

In the study of two-layer pre-stressed concrete beams, the authors have experimentally surveyed and the study results on these two-layer beams are compared with those of single-layer pre-stressed concrete beams [20, 21]; in order to do research of double-layered beams by Iskhakov, several other authors have studied the flexure behavior of double-layer beams [22]. Moreover, there are detailed studies on improving the quality of construction of mass concrete, model construction of prefabricated concrete frame, quality of construction works, etc. [23–29].

The authors of this paper used ANSYS to model the working of two-layered concrete beams after considering factors such as the amount of steel fiber in the concrete, the spacing between shear steel stirrups at the beam's ends, the number of tensile steel bars, and so on. After testing these two-layered beams, the steel fiber concrete layer is above and the steel fiber concrete layer is below normal concrete layer. Results of the research that have built the relationships of load–stress, load–displacement, formation, and cracks growth, with increased load from 0 kN until the beams fail. In these beams, with the change of concrete grade in each concrete layer and the use of a steel fiber layer in beam, with a size of $15 \times 30 \times 220$ cm, the load at which concrete beams start to crack, the load at which they are also prepared for damage in this analysis, and in numerical simulation by ANSYS, material nonlinearity is considered.

2 Materials and Methods

2.1 Beam Design Model and Testing

In this study, beams with the percentage of steel fibers in concrete are $\mu = 2\%$ by volum, the spacing between shear steel stirrups at the beam's ends, $\phi6a50$, at the middle of the beam $\phi6a200$, $2\phi22$ tensile steel bars, $2\phi10$ compressed steel bars, two-layered concrete beams with a layer of concrete in steel fiber above and a layer of concrete in steel fiber below the normal concrete layer.

Model of two-layered concrete beams in design is shown in Fig. 1

Concrete beams on the test pedestal, after the installation of deformation, displacement measuring devices, etc., with increased load from 0 kN until the beams fail, are shown in Fig. 2

a) Beam model of concrete layer of steel fiber on top

b) Beam model of concrete layer of steel fiber on bottom
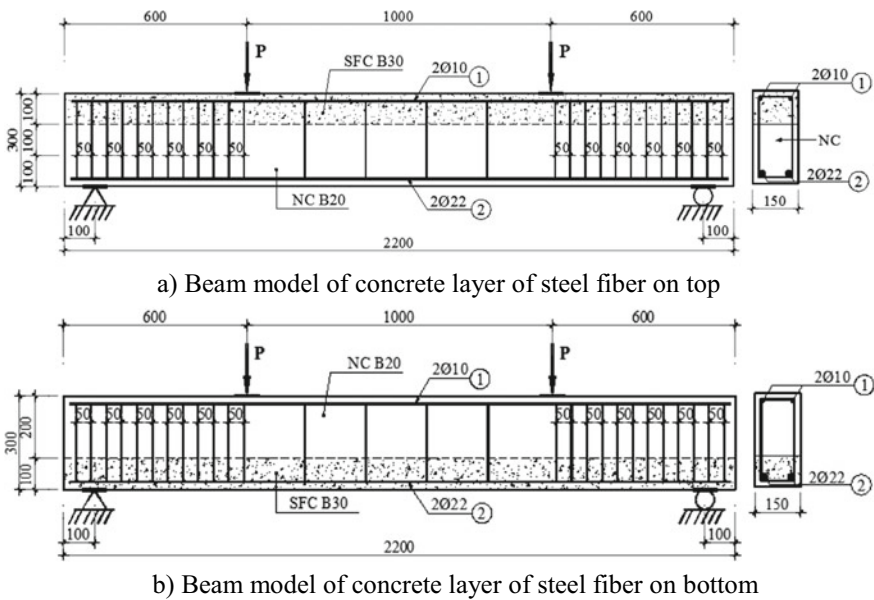
Fig. 1 Concrete beams model in design

Fig. 2 Concrete beams on the test pedestal

2.2 Establish a Finite Element Model for Steel Fiber Reinforced Concrete Beams in ANSYS

2.2.1 Element Types

Concrete: The SOLID65 element was used to simulate concrete, and the steel fibers content in the concrete was simulated through the concrete reinforcement constant as a percentage (Fig. 3a).

Rebar: beam188 element is used in this study (Fig. 3b).

Choose the steel fiber dispersion model in concrete: Three models are used for the concrete steel fiber model: the smeared, the embedded, and the discrete models. In this research, a smeared model should be used for steel fibers that are dispersed in concrete. (Fig. 4).

Choose concrete cracking model: There are two ways to model concrete cracks: discrete and smeared. In this research, we are more interested in the behavior relationship between load and displacement than crack shape or local stress. Choose the smeared model for concrete cracks. (Fig. 5).

a) Solid65 element   b) beam188 element
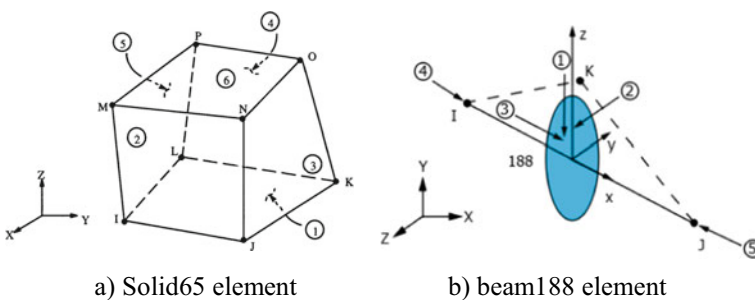
Fig. 3 Element types of beam
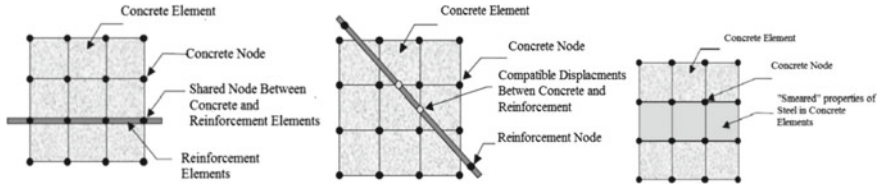
Fig. 4 Steel fiber model in concrete
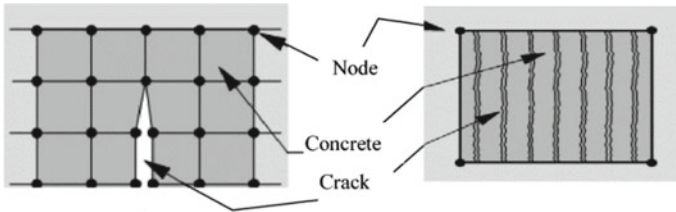
Fig. 5 Concrete cracking model

2.2.2 Material Properties

According to the Kachlakev model, we select the concrete model under compression based on the analysis of stress–strain models of compressive concrete presented above. This model has been predefined in ANSYS by the stress–strain model of concrete under tensile stress. (Fig. 6).

Destructive standards: In this analysis, the destructive standard of Willam and Warnke is used and established in ANSYS. (Fig. 7).

Two-layered beam model, boundary condition, is shown in Fig. 8
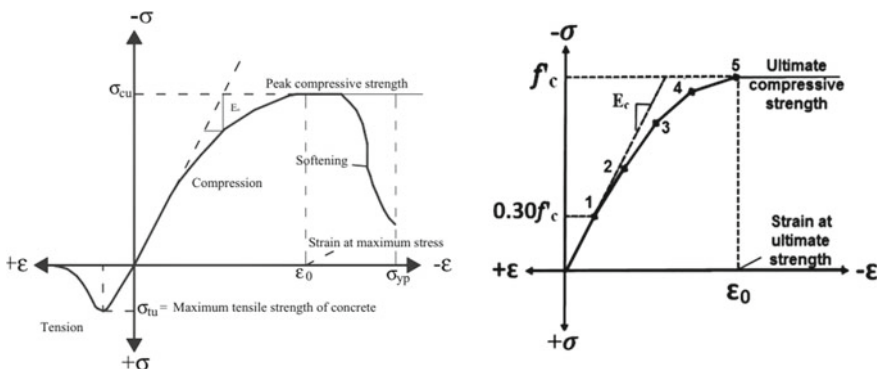
Fig. 6 Typical uniaxial compressive and tensile stress–strain curve for concrete

Fig. 7 Failure surface for
concrete
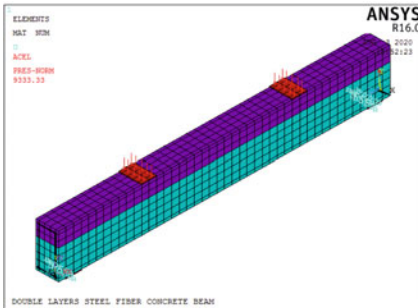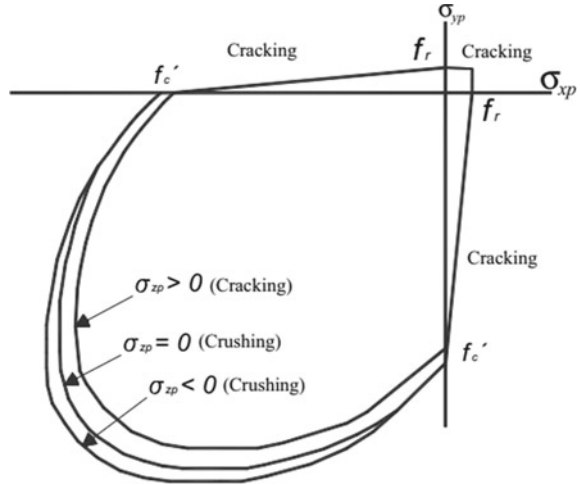
a) Layer of steel fiber concrete above   b) Layer of steel fiber concrete below
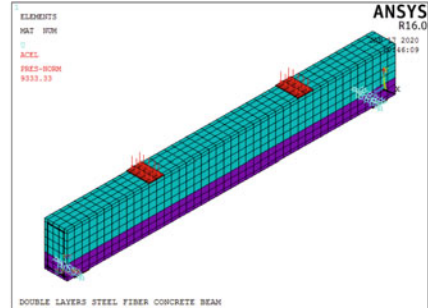
Fig. 8 Two-layered beam model in ANSYS

3   Results and Discussion

3.1   *Experiments (EXP) and ANSYS Simulations*

The shape and development of cracks between the tested beams and ANSYS are
similar. Beams with the layer of steel fiber concrete is above, and the cracks develop
more than the layer of steel fiber concrete which is below. It means, the layer of steel
fiber concrete below has increased beam tensile ability (Fig. 9).

Results of vertical displacement of the beams are shown in Fig. 10.

Comment: Study results between experiment and ANSYS (Fig. 10): Although
there are variations, but the difference in value between the two experimental methods
and simulated ANSYS is really small. It can investigate the effect of the concrete

a) Cracks in experimental beam, with the above layer of steel fiber concrete

b) Cracks in experimental beam, with the below layer of steel fiber concrete

Fig. 9 Cracks in beam by experiment and ANSYS method

a) Layer of steel fibre concrete above

b) Layer of steel fibre concrete below
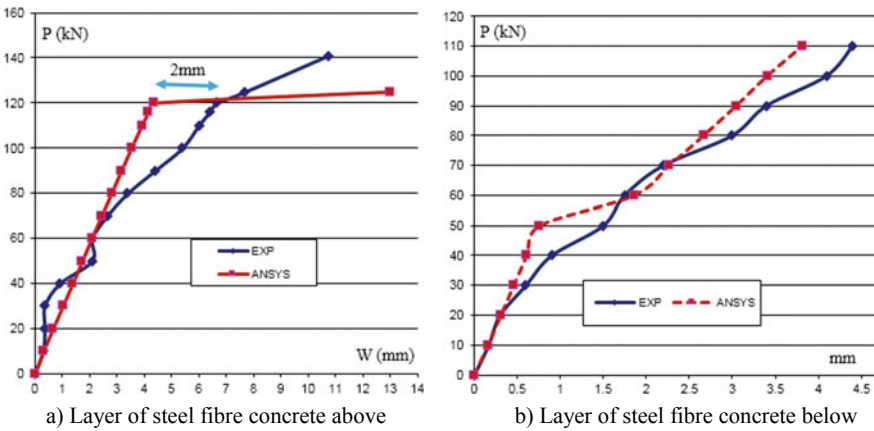
Fig. 10 Experiment and ANSYS were used to determine the vertical displacement of beams

grade change in the layers of two-layered concrete beams developed by the ANSYS program.

3.2 Impact of Concrete Gradation Changes in Layers of Two-Layered Beams

3.2.1 Two-Layered Concrete Beams with Steel Fiber Concrete Layer Above

We have cases of investigating the change in concrete grade in two-layered concrete beams, which is presented by Table 1.

The beams that start to crack with the three cases above in Table 1 are shown in Fig. 11.

Comment: In Fig. 11, when the concrete grade in both layers of concrete beams is of the same grade (both layers of case 2, B30), the crack occurs less than case 1 and case 3. The concrete grade of normal concrete (B40) is greater than that of the above (B30) layer of steel fiber concrete, and the crack occurs later than case 1 and case 2, $P_{crack} = 8$ kN.

Table 1 Concrete grade in all surveyed cases

Case	Concrete grade: B1	Concrete grade: B2
1	B30	B40
2	B30	B30
3	B40	B30

a) Case 1, P_{crack}=7kN

b) Case 2, P_{crack}=7kN

c) Case 3, P_{crack}=8kN

Fig. 11 Beams start to crack in cases

a) Case 1, P_{max}=82kN

b) Case 2, P_{max}=85kN

c) Case 3, P_{max}=80kN
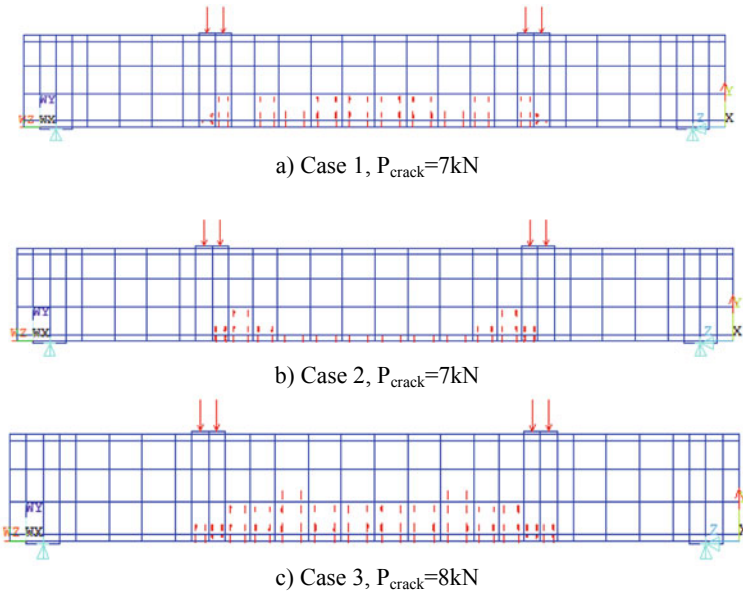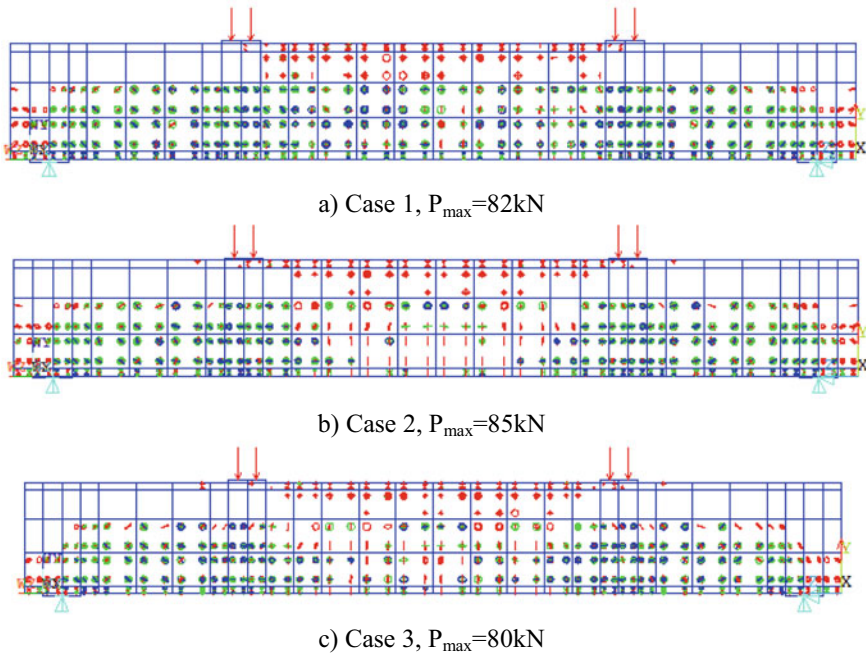
Fig. 12 Beams start to be damaged in cases

Beams that start to be damaged with the three cases above in Table 1 are shown in Fig. 12.

Comment: In Fig. 11, we see that the number of cracks appears very low in case 2, but in Fig. 12, case 2 is damaged at the latest, $P_{max} = 85k$ N, while in case 1 and case 3, it is 82 and 80 kN. Explain, in this beam, layers of the same concrete grade will work better than in other cases with different concrete grades. In all three cases of this analysis, the crack is primarily formed in the normal concrete layer below, but less formed in the steel fiber concrete layer above.

Load–stress and load–vertical displacement relationships of beam are shown in Fig. 13.

Comment: In the beam's compressive stress area, when the load is less than 50 kN, all three cases have the same value, but when the beams begin get damaged, there is a difference in the value and the smallest compressive stress of case 2 (Fig. 13a), but in all three cases, the change value is not high and the maximum difference is 0.8 MPa (Fig. 13b), and in all cases, the vertical displacement value is higher than in other cases where the load is greater than 60 kN in the tensile stress area.

a) Load - compressive stress relationship

b) Load - tensile stress relationship

c) Load - vertical displacement relationship
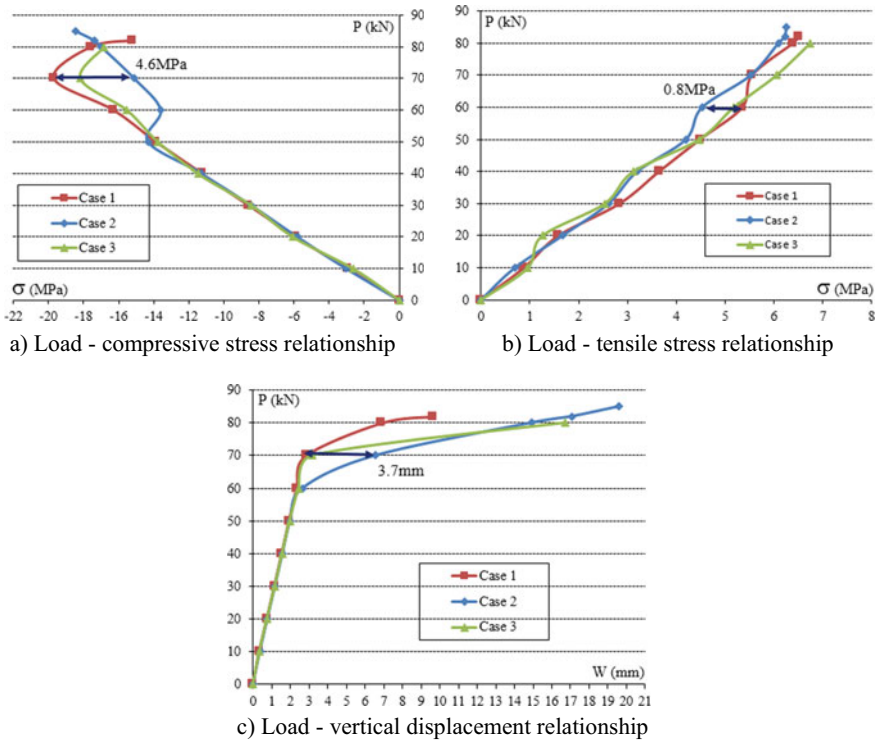
Fig. 13 Relationships between load and stress and load and vertical displacement

3.2.2 Two-Layered Concrete Beams of Concrete Layers in Steel Fiber Below

B1 is concrete grade of normal concrete layer, and B2 is concrete grade of steel fiber concrete layer which is presented in Table 1.

Beams start to crack in cases are shown in Fig. 14.

Comment: When the beams change from the above-mentioned layer of steel fiber concrete to the below layer of steel fiber concrete, the beams start to crack at 27 kN load of case 1 and case 3, 31 kN of case 3 (Fig. 14) compared to the cases in Fig. 11; however, cracks do not occur in the below steel fiber concrete layer; cracks appear in the normal concrete layer at the top, and cracks occur from the supports to the loads location. Show that the below steel fiber concrete layer works better than the above steel fiber concrete layer, and the below concrete layer is the steel fiber concrete layer in case 3 in Fig. 14c and this layer has the strength of B40 which is greater than the above concrete layer so that the beams work better.

Beams start to be damaged in cases are shown in Fig. 15.

Comment: In Fig. 14, the damaged beams in the cases are all greater than 80 kN with the above-mentioned steel fiber layer, while in case 1 and case 2 the below steel

a) Case 1 and case 2, $P_{crack}=27kN$

b) Case 3, $P_{crack}=31kN$

Fig. 14 Beams start to crack in cases

a) Case 1 and case 2, $P_{max}=57kN$

b) Case 3, $P_{max}=72kN$
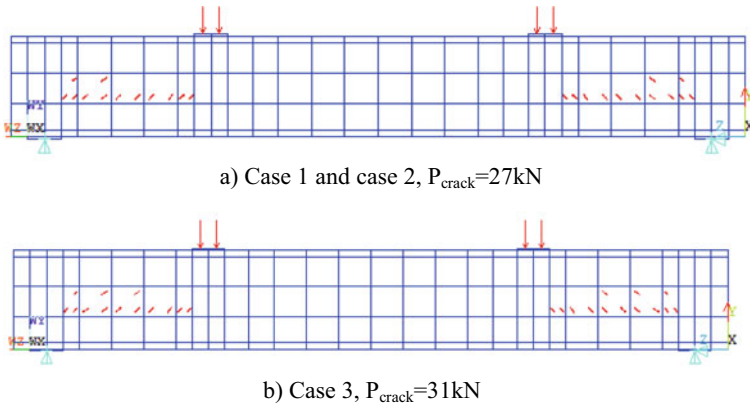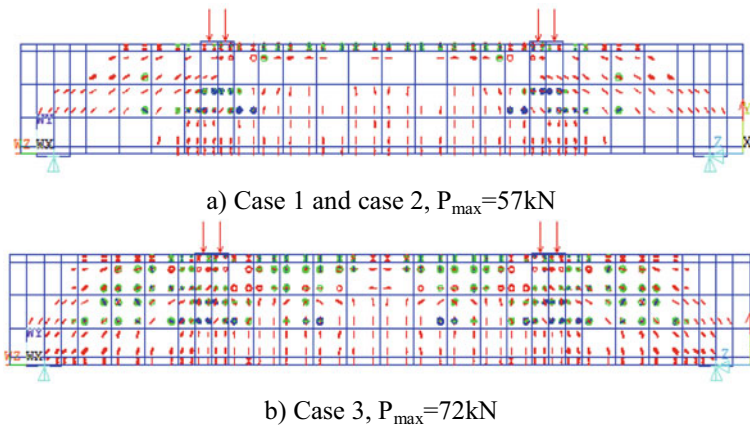
Fig. 15 Beams start to be damaged in cases

fiber layer is 57 and 72 kN for case 3 (Fig. 15), the beams with the above-mentioned steel fiber concrete layer will be broken later than the below fiber concrete layer.

At the midpoint of a concrete beam's span, load–stresses and load–displacement relationships are shown in Fig. 16.

Comment: In Fig. 16, compressive stress, tensile stress zone, and vertical displacement at the middle of the beam span in these cases do not change much value; however, the beam is strengthened in case 3, pushed from 57 to 72 kN.

a) Load - compressive stress relationship

b) Load - tensile stress relationship

c) Load - vertical displacement relationship
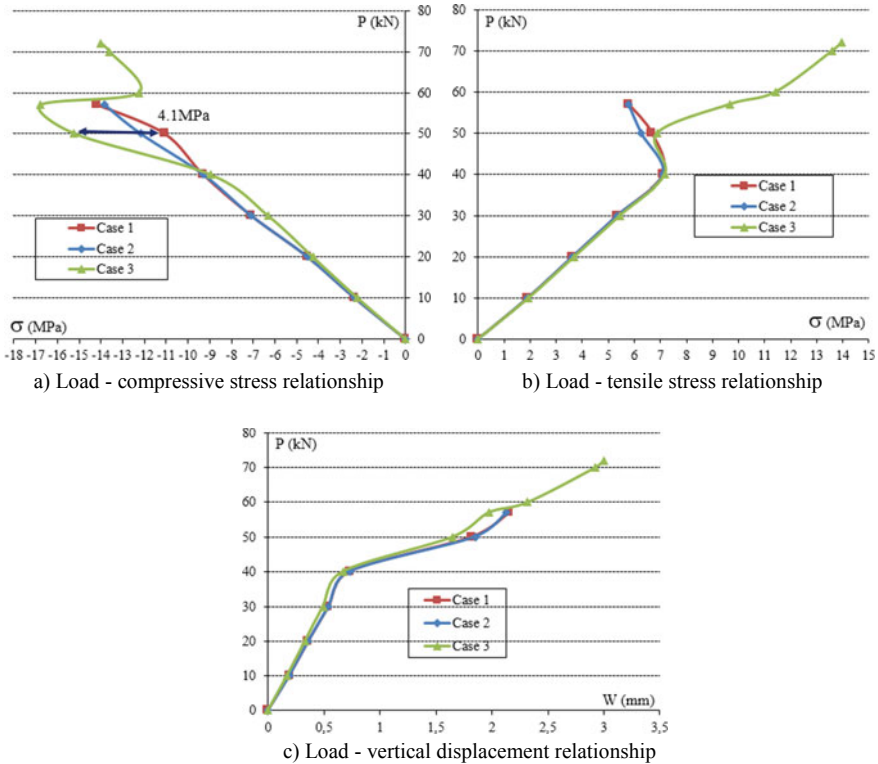
Fig. 16 Relationships between load and stress and load and vertical displacement

3.2.3 Compare the Location Effects of the Concrete Layer of Steel Fiber

Load–stress and load–vertical displacement in case studies where the concrete layer of steel fiber is above what is compared to the below concrete layer of steel fiber.

Case 1: is shown in Fig. 17.

Comment: In the compressive stress zone (Fig. 17a), we see that the difference between the above-mentioned steel fiber concrete layer and the lower steel fiber concrete layer of case 1 is 2.8 MPa at a load of 50 kN, and the lower compressive stress value of the steel fiber concrete layer is less than the other. Similarly, with a load of 40 kN in the region of tensile stress (Fig. 17b), the difference is 3.4 MPa, this value is high, and the lower layer of concrete steel fiber has a greater tensile stress value than the other case. The vertical displacement in the middle of the beam's span is not large, the greatest difference being 0.8 mm at 40 kN load (Fig. 17c).

Case 2: is shown in Fig. 18.

Comment: The compressive stress value (Fig. 18a) in both positions of the concrete layer of steel fiber does not vary significantly, and the difference is 2.3 MPa at a load
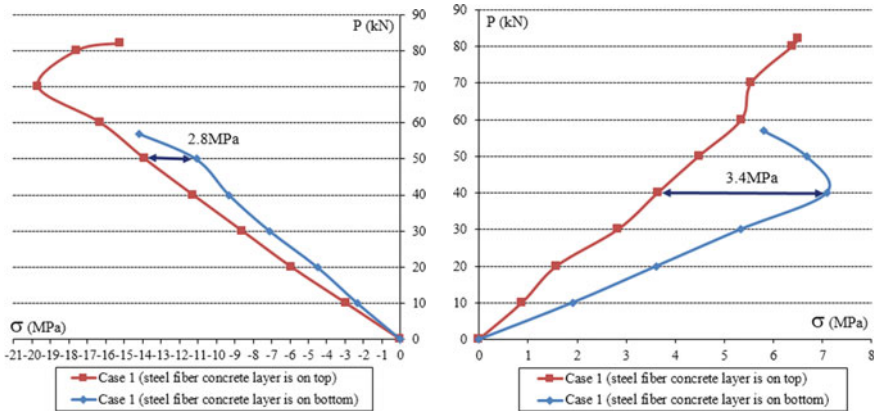
a) Load - compressive stress relationship

b) Load - tensile stress relationship
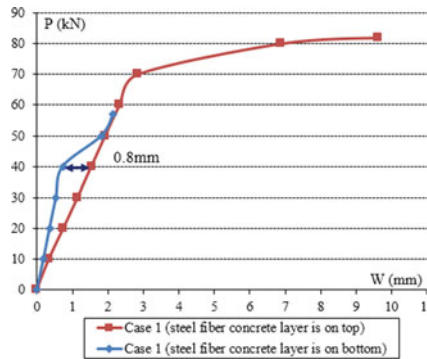
c) Load - vertical displacement relationship

Fig. 17 Relationships between load and stress and load and vertical displacement, case 1

of 50 kN, and the layer of concrete steel fiber below has a lower value than the layer of concrete steel fiber above. Similarly, there is a difference in tensile stress value in the tensile stress zone, and at a load of 40 kN, the difference is 3.8 MPa (Fig. 18b), and other cases have a greater stress value in the lower steel fiber concrete layer. The vertical displacement in the mid-span did not substantially change (Fig. 18c). The survey shows that concrete beams with the above-mentioned layer of steel fiber concrete would increase the bearing capacity of concrete beams from 57 to 85 kN compared to the layer below that of steel fiber concrete.

Case 3: is shown in Fig. 19.

Comment: In Fig. 10a, the maximum difference in compressive stress is 2 MPa when the load is from 0 to 60 kN, and as it reaches this load level, the concrete beams begin to decrease the compressive stress value and the difference is 4.5 MPa. The tensile stress values change quickly and become increasingly different as the

a) Load - compressive stress relationship

b) Load - tensile stress relationship

c) Load - vertical displacement relationship
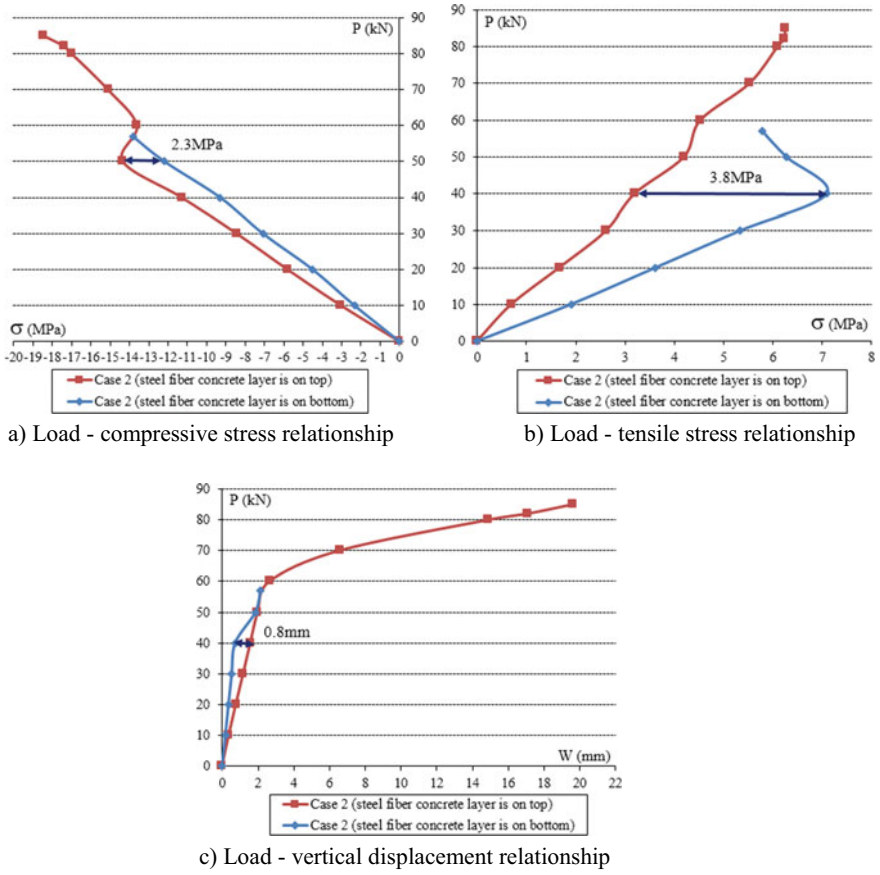
Fig. 18 Relationships between load and stress and load and vertical displacement, case 2

concrete beams fail, and the concrete beams with the below concrete layer are more valuable than beams with an above steel fiber concrete layer (Fig. 19).

4   Conclusion

Based on the study results, the conclusions are as follows:

1.   By adding steel fibers to the concrete, it would significantly improve some of the concrete's mechanical properties such as reducing the number of cracks and increased load capacity in beams.
2.   There are differences in measurement results between the experimental method and the simulation method: the experiment is affected by the measuring devices,

a) Load - compressive stress relationship

b) Load - tensile stress relationship

c) Load - vertical displacement relationship
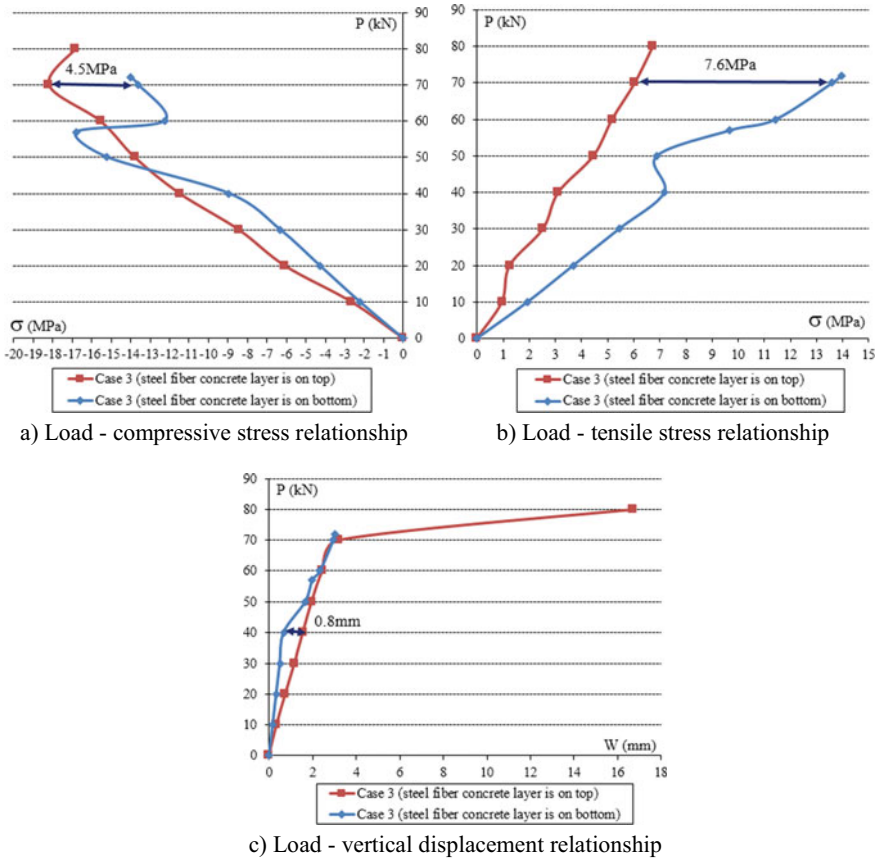
Fig. 19 Relationships between load and stress and load and vertical displacement, case 3

the experimental environment and conditions, etc. However, the difference does not exceed the value in this analysis.

3. In the case of two-layered concrete beams with the above concrete layers of steel fiber concrete, the normal concrete layer, the values of compressive stress, tensile stress, and vertical displacement of concrete beams in the middle span of case studies are no different.

4. Double-layer concrete beam with a layer of steel fiber concrete is below the normal layer of concrete, and the concrete beams tend to show cracks later than when the concrete layer of steel fiber is on top. But when the beams begin to fail, it is broken sooner on the contrary. The stress values and the vertical displacement were not significantly different.

5. In each case study, the effect of the location of the concrete layer of steel fiber in the concrete beams when the layer of concrete of steel fiber is above and the layer of concrete of steel fiber below is different. The below steel fiber concrete

layer has a lower value in the compressive stress area, and the tensile stress region has a higher tensile stress value than the two-layer concrete beams with the above layer of steel fiber concrete. As for the vertical displacement in the middle of the span, the values are less variable.

References

1. Do TMD, Lam TQK, Ngo VT, Nguyen TTN (2020) Analysis of high performance concrete with steel fiber reinforcement. International Journal of Mechanical and Production Engineering Research and Development 10(3):8139–8147. https://doi.org/10.24247/ijmperdjun2020772
2. Do TMD, Lam TQK, Ngo VT (2020) Analysis of textile and steel fibers based reinforced concrete beam. International Journal of Mechanical and Production Engineering Research and Development 10(3):8033–8040. https://doi.org/10.24247/ijmperdjun2020763
3. Khai, L.T.Q., Dung, D.T.M. Stress-strain in multi-layer reinforced concrete doubly curved shell roof. International Journal of Innovative Technology and Exploring Engineering, 8(4S2), 2019. Pp. 419–424
4. Lam, T.Q.K., Do, T.M.D. Effect of each shell thickness on deformation stress and the ability for causing the cracks in the multilayer doubly curved shell roof. International Journal of Innovative Technology and Exploring Engineering, 8(6C2), 2019. Pp. 215–220
5. Lam TQK, Do TMD (2019) Sliding between layers in 2-layer reinforced concrete beams and shell. International Journal of Engineering and Advanced Technology 8(5):1867–1871
6. Ngo, V.T., Khai Lam, T.Q., Dung Do, T.M., Nguyen, T.C. Nano concrete aggregation with steel fibers: A problem to enhance the tensile strength of concrete. E3S Web of Conferences, 135 03001, 2019. DOI: https://doi.org/10.1051/e3sconf/201913503001
7. Ngo VT, Lam TQK, Do TMD, Nguyen TC (2020) Increased plasticity of nano concrete with steel fibers. Magazine of Civil Engineering 93(1):27–34. https://doi.org/10.18720/MCE.93.3
8. Ngo, V.T., Bui, T.T., Lam, T.Q.K., Nguyen, T.T.N., Nguyen, V.H. Experimental evaluation of Nano Silica effects to high performance concrete strength in early age. IOP Conf Series: Materials Science and Engineering, 869 032011, 2020. DOI: https://doi.org/10.1088/1757-899X/869/3/032011
9. Ngo VT, Bui TT, Lam TQK, Do TMD (2020) Study the effects of nano-silica on crack toughness of high performance concrete base on double-K model. International Journal of Mechanical and Production Engineering Research and Development 10(3):8041–8050. https://doi.org/10.24247/ijmperdjun2020764
10. Khai Lam TQ, Thi My DD, Ngo VT, Chuc Nguyen T, Phuoc Huynh T (2020) Numerical simulation and experiment on steel fiber concrete beams. Journal Physics: Conference Series 1425:012007. https://doi.org/10.1088/1742-6596/1425/1/012007
11. Do TMD, Lam TQK (2021) Design parameters of steel fiber concrete beams. Magazine Civil Eng 102(2)
12. Gokmen A (2013) Buckling analysis of delaminated composite beams. Indian journal of engineering & materials sciences 20:276–282
13. Ammapalayam RK, Shanmughasundaram K (2019) Flexural performance of hybrid engineered cementitious composite layered reinforced concrete beams. Periodica Polytechnica Civil Engineering 62(4):921–929. https://doi.org/10.3311/PPci.11748
14. Adam S, Fariborz MT (2019) An investigation of crack propagation in steel fiber-rreinforced composite beams. Periodica Polytechnica Civil Engineering 62(4):956–962. https://doi.org/10.3311/PPci.10910
15. Mirza APM, Rizaldy KS, Poppy P, Fuad IK, Andika BNRP (2019) Finite element analysis of the bending moment-curvature of the double-layered graded concrete beam. IOP Conf Series: Materials Science Eng 494:012064. https://doi.org/10.1088/1757-899X/494/1/012064

16. Iskhakov I, Ribakov Y (2007) A design method for two-layer beams consisting of normal and fibered high strength concrete. Mater Des 28(5):1672–1677. https://doi.org/10.1016/j.matdes.2006.03.017
17. Iskhakov I, Ribakov Y (2011) Two-layer beams from normal and fibered high strength concrete. Conference: Modern Methods and Advances in Structural Engineering and Construction. https://doi.org/10.3850/978-981-08-7920-4_S3-M029-cd
18. Iskhakov I, Ribakov Y, Holschemacher K, Mueller T (2014) Experimental investigation of full scale two-layer reinforced concrete beams. Mech Adv Mater Struct 21:273–283. https://doi.org/10.1080/15376494.2012.680673
19. Iskhakov I, Yuri R, Klaus H (2017) Experimental investigation of continuous two-layer reinforced concrete beams. 18(1):205–215. https://doi.org/10.1002/suco.201600027
20. Iskhakov I, Yuri R, Klaus H, Stefan K (2019) Experimental investigation of prestressed two layer reinforced concrete beams. Structural Concrete, pp 1–12. https://doi.org/10.1002/suco.201900328
21. Iskhakov I, Yuri R, Klaus H, Stefan K (2020) Experimental investigation and comparison of prestressed single-layer and repaired two-layer reinforced concrete beams. Struct Concr. https://doi.org/10.1002/suco.201900556
22. Butean C, Heghes B (2020) Flexure Behavior of a Two Layer Reinforced Concrete Beam. Procedia Manufacturing 46:110–115
23. Do TMD, Lam TQK (2019) Solutions to improve the quality of mass concrete construction in climate conditions of Southern Vietnam. Int J Innovative Technology Exploring Engineering 8(6C2):188–192
24. Tran HQ, Lam TQK, Do TMD (2019) Model of prefabricated concrete frame in the condition of southern Vietnam. E3S Web of Conferences 135:03043. https://doi.org/10.1051/e3sconf/201913503043
25. Do TMD, Lam TQK (2019) Analysis of risk problems in construction by R software. Int J Engineering Adv Technology 8(5):1872–1875
26. Do TMD, Lam TQK (2020) Quality of construction works at the design phase. Lecture Notes in Civil Engineering 70:15–24. https://doi.org/10.1007/978-3-030-42351-3_2
27. Do TMD, Nguyen TC, Lam TQK (2020) Investigating the effectiveness of insulation for walls of buildings in Vietnamese climatic condition. IOP Conf Series: Materials Science Engineering 869:032008. https://doi.org/10.1088/1757-899X/869/3/032008
28. Lam TQK, Do TMD, Ngo VT, Nguyen TTN, Pham DQ (2002) Concrete grade change in the layers of three-layer steel fibre reinforced concrete beams. J Achievements Materials Manufacturing Engineering 102(1). https://doi.org/10.5604/01.3001.0014.6325
29. Do TMD, Lam TQK (2021) Design parameters of double layers steel fiber concrete beams. Lecture Notes in Civil Engineering 130:299–321. https://doi.org/10.1007/978-981-33-6208-6_30

Effective Peripheral Distribution of Base Isolators for Plan Asymmetric Buildings to Minimise Torsion

R. Rithuparna, V. N. Varada, and S. C. Mohan

Abstract The naturally occurring ground motion results in disasters such as the collapse of structure and fatality if the built structures are not adequately designed to take the seismic load. Buildings with irregularities in plan and elevation are more prone to seismic damage due to the torsional effect that comes into play because of the eccentricity created between their centre of mass and centre of stiffness. Base isolation is a very effective way to eliminate the ill-effects of seismic forces and is one of the most widely implemented techniques. The main challenge in using base isolation for asymmetric buildings is to address the associated torsional vibrations. This study focusses on the influence of base isolation techniques in mitigating the torsional effect on plan asymmetric buildings. L-shaped buildings with greater plan eccentricity in *X*-direction was chosen for the study. The response of fixed base and base isolated asymmetric structures was compared and analysed using SAP2000 software. The effectiveness of various distribution of isolators was also explored to obtain the most economical option of isolating a building. Among the distributions studied, peripheral distribution gave a similar performance as that of uniform distribution for almost all the cases. Hence, the provision of isolators under the peripheral columns alone can be an effective way of reducing the total cost incurred in isolating a building.

Keywords Asymmetric building · Base isolation · Peripheral distribution

1 Introduction

The study of past earthquakes has revealed that they have caused massive damage to properties and life loss. Various measures were developed for safeguarding these structures from the adverse effect of earthquakes. The conventional techniques adopted involve strengthening and stiffening the building by providing special structural components such as shear walls and bracings. However, alternate means to

R. Rithuparna (✉) · V. N. Varada · S. C. Mohan
Department of Civil Engineering, Birla Institute of Technology and Science Pilani, Hyderabad Campus, Hyderabad, India

reduce the demand on the structure by providing dampers and base isolators have proved to be more effective. Many researchers have reported a reduction in the seismic response of base isolated buildings owing to the decoupling of the building from the ground. These isolators help shift the fundamental period of building vibration to a higher range outside the predominant period of ground motions. Therefore, isolating a building will eliminate the building's probability of resonating with the seismic force acting on it. Besides, the energy dissipating mechanism of base isolators reduces the seismic demand on the superstructure.

With more and more architectural styles reflecting complex and irregular building plans, torsion becomes inevitable when the structures are dynamically excited. The torsion in the building can be attributed to the eccentricity between the centre of mass (CM) through which the external force acts and the centre of rigidity (CR) through which the resistance is offered. The torsional effect causes differential displacement of the stiff and flexible edges at the same floor level of the building under lateral loads. Asymmetric buildings in seismically active regions are more vulnerable to damage and necessitate careful and well-planned design. One solution for bringing down torsion in the building is to isolate them from the ground motions seismically. Various researchers studied the torsional behaviour of base isolated plan asymmetric buildings, and the seismic response was reported to reduce substantially [1–3]. It was stated by the researchers that eccentricity in the isolation system has a more remarkable effect on the torsion in the building compared to the superstructure's eccentricity [4, 5].

On the contrary, Nagarajaiah et al. reported that the eccentricity of both superstructure and the isolation system plays a crucial role in the behaviour of isolated buildings [6]. Furthermore, a proper design of base isolators will ensure the building's first mode of vibration to be predominantly translational with minimal contribution from the torsional motion. The complete decoupling of the building will result in a uniform distribution of stresses in all the columns [1]. An eccentricity between the centre of the isolation system (CI) and CR of the superstructure was necessary to effectively counteract the torsion created in the superstructure [7]. The most preferred distribution of base isolators is the one in which CI coincides with CM of the superstructure. The displacement at the isolator level was reported to be minimum for this distribution. However, Kilar and Koren observed that this distribution resulted in more significant roof level displacement and caused greater damage to the flexible sides of the superstructure. Location of CI farther away from CM develops torsion due to inertial force (acts through CI), which neutralises the torsion due to external force (acts through CM). CI $= -$CM/2 was suggested to be the most favourable distribution to keep the top displacement and the base displacement well under the tolerance limit [8].

To investigate base isolators' influence on plan asymmetric buildings, L-shaped building models were created and analysed for seven ground motion data in SAP2000 software. Since employing a base isolator is an expensive option, research on bringing down the cost is gaining attention. A comparative study on the seismic responses of the buildings was carried out for various distributions of base isolators to arrive at an effective and economical option. Parametric study of buildings with different

eccentricities located in seismic zone 5 was conducted. The responses in terms of storey drift and difference in roof displacement of flexible and stiff edges of the model are presented. The design procedure, as per UBC 97 recommendations for lead rubber bearings as seismic isolators, is discussed [9].

2 Building Models Description

The numerical modelling technique used is a standard procedure followed for modelling and analysing buildings in SAP 2000 software, which is verified to be in line with the existing study. For details of the model used for validation, refer to the paper published by Mounashree et al. [10].

2.1 Fixed Base Buildings

An asymmetrical six-storey L-shaped building (model 1) of 3 m storey height was modelled in SAP2000. An exterior wall load of 13.11 kN/m and an interior wall load of 8.55 kN/m was applied on the beams. A load of 10 kN/m^2 was provided on the left side bay slabs alone, apart from the 3 kN/m^2 of live load. These loads were uniformly distributed on all the slabs except the roof. The additional UDL of 10 kN/m^2 brought about an eccentricity of 5.8% in X-direction and 1% in Y-direction. Hence, an earthquake in Y-direction is more critical while studying the torsional effect of this building. Figure 1a, b shows the elevation view and plan view of the building, respectively with its CM at (11.05, 6.38) and CR at (12.78, 6.22).

To study the effect of higher eccentricity, a second model with columns of size 300 mm x 500 mm was provided at two frames in the right end of the L-shaped building (L-shaped model 2). This created an eccentricity of 10.4% in X-direction and 2.3% in Y-direction. The actual behaviour of these buildings was studied by performing linear dynamic time history analysis, according to IS1893: 2016 [11].

(a) Elevation   (b) Plan view
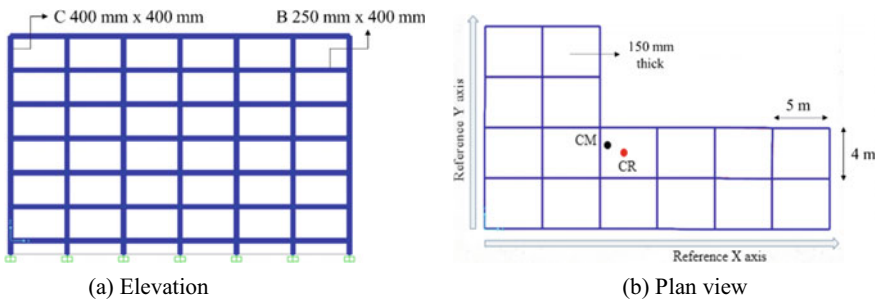
Fig. 1 Model of L-shaped building

They were subjected to seven real-time ground motions, namely El Centro, Loma Prieta, Kobe, Northridge, Chamba, Uttarkashi and Trinidad earthquake data as per NEHRP recommendations [12]. These data were scaled up or down to match the target response spectrum corresponding to the building's location. Buildings of importance factor equal to 1 and a response reduction factor of 3 were chosen. They are located in a site of medium soil type in Rann of Kutch, Gujarat. Since the location is prone to frequent earthquakes of high magnitude, it falls under seismic zone 5 as per IS 1893:2016 classification [11].

2.2   Base Isolated Buildings

The buildings were isolated using lead rubber bearings (LRB), and the design procedure for LRB as per UBC 97 is explained below [9, 13]. The isolated period (T_D) is assumed to be thrice the time period of fixed base building.

Design displacement: It is the minimum lateral displacement of the isolation system in the direction of the seismic force under consideration.

$$D_D = \frac{\left(g/4\pi^2\right)C_{VD}T_D}{B_D} \tag{1}$$

C_{VD} is a seismic coefficient that depends on the seismic zone factor and the soil profile type. The coefficient is chosen from Table 16R of UBC 97. The type of soil profile is assigned based on the average shear wave velocity in the soil. If sufficient details of the soil property are unavailable, then the soil type is taken as S_D.

B_D is the damping coefficient related to the effective damping of isolators at the design displacement. Referring to Table A-16-C of UBC 97, the damping coefficient is obtained corresponding to the required effective damping of the system.

Bearing horizontal stiffness:

$$k_{\text{eff}} = \frac{W}{g}\left(2\pi/T_D\right)^2 \tag{2}$$

W is the maximum load to be sustained by a single isolator which is obtained from the analysis of the fixed base building.

Energy dissipated per cycle: Lead rubber bearings are modelled as bilinear elements with the area under the hysteresis giving the energy dissipated per cycle.

$$W_D = 2\pi k_{\text{eff}} D_D^2 \beta \tag{3}$$

β is the effective damping ratio of the isolator.

Characteristic strength of lead: It is the value at which the hysteresis loop of the lead intercepts the axis representing force applied.

$$Q_D = \frac{W_D}{4D_D} \tag{4}$$

Post-yield stiffness of rubber: Since LRBs are modelled as bilinear elements, they have a pre-yield (k_1) and a post-yield stiffness (k_2).

$$k_2 = k_{\text{eff}} - \frac{Q_D}{D_D} \tag{5}$$

Owing to the difficulties in measuring k_1, it is assumed to be ten times k_2.
Yield displacement (Distance from end-J):

$$D_y = \frac{Q_D}{k_1 - k_2} \tag{6}$$

Recalculating characteristic strength:

$$Q_R = \frac{W_D}{4(D_D - D_y)} \tag{7}$$

Area of lead plug:

$$A_{\text{LRB}} = \frac{Q_R}{\text{yield strength of lead}} \tag{8}$$

Assume yield strength of lead $= 10$ MPa.
Recalculation of rubber stiffness:

$$k_2 = k_{\text{eff}} - \frac{Q_R}{D_D} \tag{9}$$

Total thickness of the rubber:

$$t_r = \frac{D_D}{\gamma} \tag{10}$$

Assume maximum shear strain of rubber, $\gamma = 100\%$
Area of bearing:

$$A_{\text{LRB}} = \frac{k_{\text{eff}} t_r}{G} \tag{11}$$

Single layer rubber thickness:

$$t = \frac{D_{\text{LRB}}}{4S} \tag{12}$$

Shape factor:

$$S = \frac{f_v}{2.4 f_H} \tag{13}$$

f_v and f_H are the vertical and horizontal frequency, respectively.
No. of rubber layers:

$$N = \frac{t_r}{t} \tag{14}$$

Assume the thickness of steel shim plates and endplates. Calculate the total height of bearing.

Yield strength:

$$F_y = Q_R + k_2 D_y \tag{15}$$

Vertical stiffness:

$$k_v = \frac{E_c A}{t_r} \tag{16}$$

E_c—instantaneous compression modulus under vertical load

$$E_c = 6GS^2 \left(1 - \frac{6GS^2}{K} \right) \tag{17}$$

K—bulk modulus of rubber.
Post-yield stiffness ratio:

$$n = \frac{k_2}{k_1} \tag{18}$$

Base isolators of the same lateral stiffness and damping were modelled as two joint link elements (rubber isolator) in SAP2000 v21. Details of linear and nonlinear properties which were assigned to the link element are shown in Table 1. Plinth beams (300 mm × 450 mm) were provided at the ground level of the building to ensure proper transfer of load from the superstructure to the base isolator.

Firstly, base isolators were distributed uniformly with a bearing under each column. The second distribution was associated with a peripheral arrangement of bearings wherein they were placed only under the exterior columns with roller support under the interior columns.

Table 1 Link element properties

Axial direction	
Effective stiffness, k_v	285,442 kN/m
Effective damping	0
Lateral direction	
Linear	
Effective stiffness	765.32 kN/m
Effective damping	0.25 kN-sec/m
Distance from end J, D_y	0.0108 m
Non-linear	
Stiffness	578.602 kN/m
Yield strength, F_y	65.21 kN
Post-yield stiffness ratio	0.1

3 Results and Discussions

3.1 Modal Analysis

Eigenvalue analysis was performed for all the building models. Figure 2a, b depicts the deformed shape for mode 1 of fixed base and base isolated buildings. The mode shape for the isolated building seems very different from the fixed base building. The isolated building showed rigid body motion, and hence, it causes minimal discomfort to the people residing in the building.

Table 2 reveals that the isolated building's time period was lengthened by almost three times that of the fixed base building. The fundamental time period was 10.5% higher for the peripheral distribution than for the uniform distribution of isolators. The increase in the time period can be attributed to the reduction in horizontal stiffness on providing roller support under the interior columns.

(a) Fixed base   (b) Base isolated
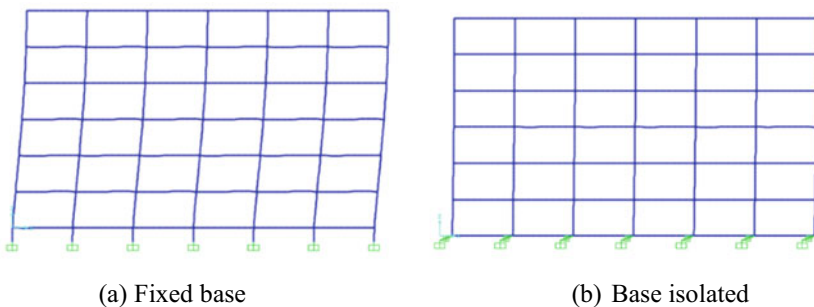
Fig. 2 Deformed shape of building models

Table 2 Fundamental time period in sec

Category	L-shaped model 1	L-shaped model 2
Fixed base	1.43	1.43
Uniform	4.18	4.15
Peripheral	4.62	4.44

3.2 Time History Analysis

The results of the analysis performed on the models are presented in the following sections.

The Difference in Displacement at Roof Level. When asymmetric buildings are subjected to lateral loads, the displacement at one edge will be higher than that at the other edge due to the non-coincidence of CR and CM. The difference in displacement at the two edges can be considered as a measure of torsion in the building. Figure 3 depicts a significant reduction in the torsion for the uniformly distributed model compared to that of the fixed base model. Comparable results were obtained for the peripherally distributed model as well.

Inter-storey Drift. Inter-storey drift is a measure of how much a storey has displaced compared to the storey below it, thereby gives the relative displacement or drift between two successive storeys.

L-Shaped Model 1

Figures 4, 5 and 6 represent a comparison of drift for building model 1. A noticeable reduction in drift for isolated buildings subjected to both *X*- and *Y*-direction earthquakes is visible.

L-Shaped model 2

For the second variant of building with greater eccentricity, similar observations were made. Figures 7, 8 and 9 shows the comparison of drift for the building.
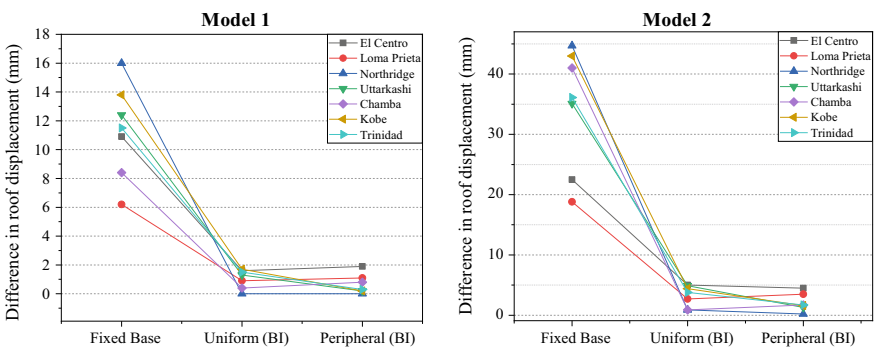
Fig. 3 Difference in roof displacement of flexible and stiff edge of building models
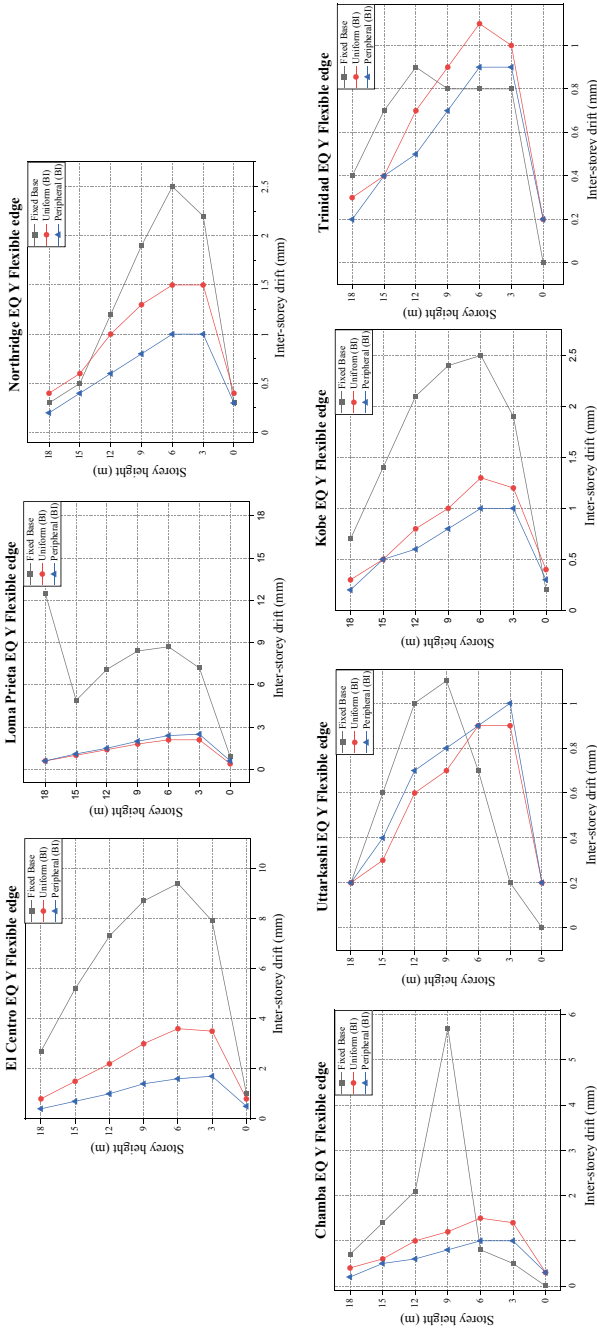
Fig. 4 Comparison of inter-storey drift for the flexible edge of model 1 subjected to EQY
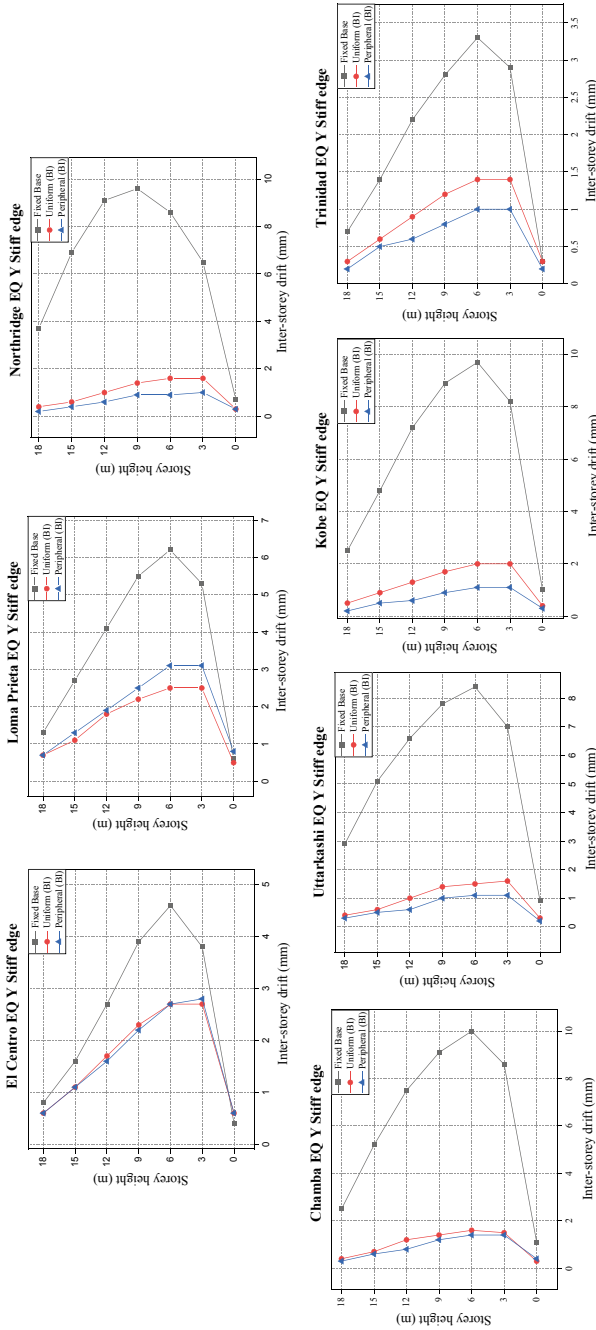
Fig. 5 Comparison of inter-storey drift for the stiff edge of model 1 subjected to EQY
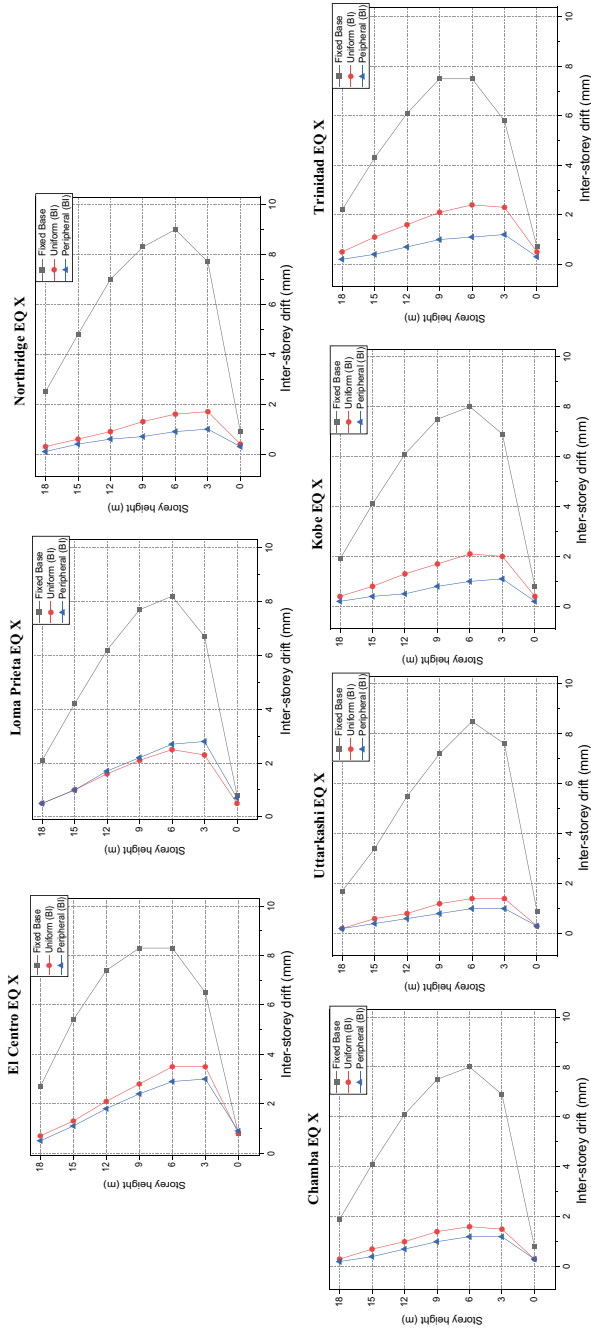
Fig. 6 Comparison of the inter-storey drift of model 1 subjected to EQX
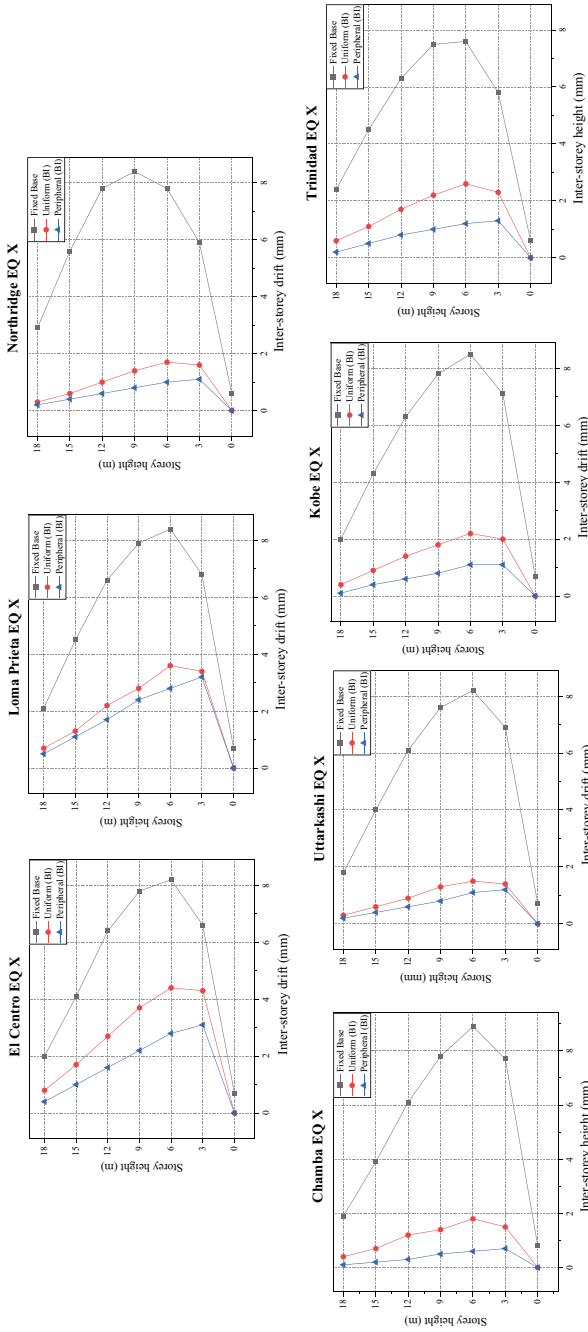
Fig. 7 Comparison of the inter-storey drift of model 2 subjected to EQX
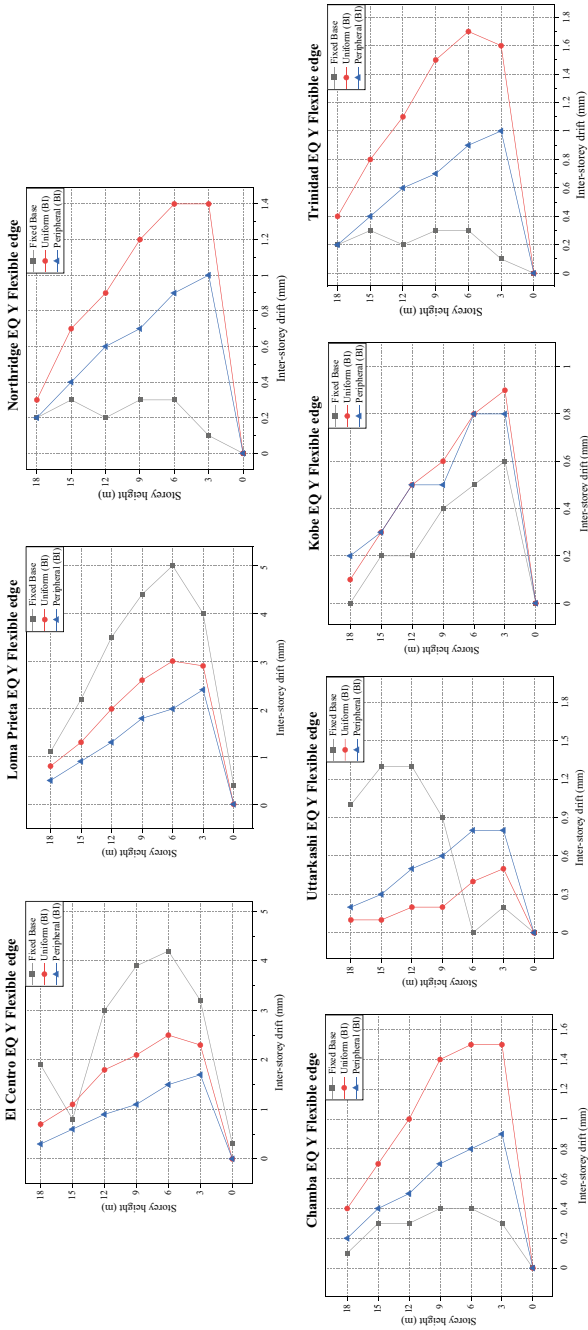
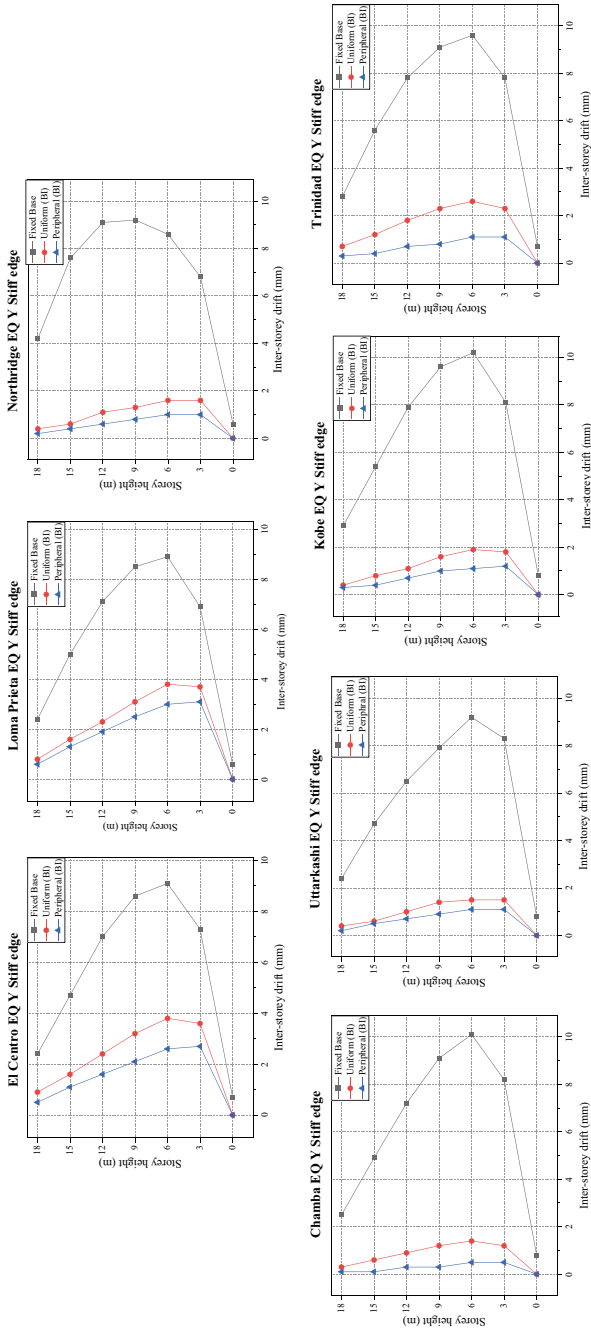**Fig. 8** Comparison of inter-storey drift for the flexible edge of model 2 subjected to EQY

Fig. 9 Comparison of inter-storey drift for the stiff edge of model 2 subjected to EQY

Table 3 Percentage reduction in parameters for building with peripheral distribution

Seismic parameter	Building model	Direction of EQ	% Reduction
Difference in roof displacement for flexible and stiff edge	Model 1	Y	86.4–99.4
	Model 2	Y	78–98
Inter-storey drift	Model 1	X	68.7–88.2
		Y	65.2–82
	Model 2	X	65–93
		Y	71–97

It is evident that isolating the buildings has led to a considerable reduction in the drift. The only exception was the flexible edge of model 2 subjected to the *Y*-direction earthquake. The fixed base model seems to have performed slightly better than the base isolated models in this case. However, the difference is not of much significance since it falls below 0.9 mm. It is further observed that the reduction in drift for buildings with peripheral distribution has outperformed that of uniform distribution for all the cases.

The key findings from the study are discussed below.

- Provision of base isolators lengthened the time period of the building significantly. Moreover, the time period was higher for the peripheral distribution of isolators compared to the uniform distribution.
- Inter-storey drift was reduced by a large margin for base isolated buildings. Additionally, the percentage reduction in the drift was 60 to 90% higher for building with peripheral distribution than fixed base building, as shown in Table 3.
- For a building with 10% eccentricity, the inter-storey drift was found to increase for the flexible edge of base isolated buildings; nevertheless, the difference is not significant. On the contrary, base isolators were fully effective in reducing the drift at all the storey levels for the stiff edge of the building.
- Difference in the displacement of flexible and stiff edges gives a measure of torsion in the building. It was found to reduce considerably with the application of base isolators. The value was comparable and, in some cases, better for peripheral distribution of isolators.

4 Conclusion and Future Scope

The effect of providing base isolators in reducing torsion of plan asymmetric L-shaped buildings with different eccentricities was studied. The seismic response of building models was noted. It can be concluded that base isolators effectively reduced torsion in the buildings considered in this study. Cost effectiveness is one of the major aspects considered while choosing a seismic protection system. Although isolators perform well compared to other systems, their application is limited owing to their high cost. Peripheral distribution acts as an economical option since they produced

similar or better results than the uniform distribution of isolators. Thus, enabling the use of fewer expensive isolators to achieve satisfactory performance of isolated buildings.

This study can be extended to other plan asymmetric buildings. Further research needs to be carried out for buildings with greater eccentricity since the isolators were found to be less effective in reducing the drift at the flexible edge of such buildings. Additionally, behaviour under more varieties of distribution of base isolators could be studied in future. A more economical option of base isolation using other techniques such as friction bearings, fibre reinforced elastomeric bearings can be explored.

References

1. De Angelis F, Cancellara D (2018) Dynamic analysis and vulnerability reduction of asymmetric structures: Fixed base vs base isolated system. Compos Struct 219:203–220
2. Di Sarno L, Chioccarelli E, Cosenza E (2011) Seismic response analysis of an irregular base isolated building. Bulletin Earthquake Eng 9(5):1673–1702
3. Tena-Colunga A, Zambrana-Rojas C (2004) Torsional response of base-isolated structures due to stiffness asymmetries of the isolation system. 13th World Conference on Earthquake Engineering, pp 3–8. Canada
4. Lee DM (1980) Base isolation for torsion reduction in asymmetric structures under earthquake loading. Earthquake Eng Struct Dynam 8:349–359
5. Tena-Colunga A, Zambrana-Rojas C (2006) Dynamic torsional amplifications of base-isolated structures with an eccentric isolation system. Eng Struct 28:72–83
6. Nagarajaiah S, Reinhorn AM, Constantinou MC (1993) Torsion in Base—Isolated Structures with Elastomeric Isolation Systems. J Struct Eng 119:130–149
7. Seguin CE, Almazán JL, De la Llera JC (2013) Torsional balance of seismically isolated asymmetric structures. Eng Struct 46:703–717
8. Kilar V, Koren D (2009) Seismic behaviour of asymmetric base isolated structures with various distributions of isolators. Eng Struct 31(4):910–921
9. Universal Building Code 1997 Volume 2. International Conference of Building Officials, California, USA.
10. Mounashree MS, Hema H, Harisha SM (2019) Comparative Study on Influence of Lead Rubber Bearing on RC Structures with Flat Slab and Conventional Slab System Under Seismic Loading. In: Das B, Neithalath N (eds) Sustainable Construction and Building Materials 2018, LNCE, vol 25. Springer, Singapore, pp 115–126
11. IS:1893 (2016) Criteria for Earthquake Resistant Design of Structures: Part 1 General Provisions and Buildings. Bureau of Indian Standards, New Delhi, India
12. NEHRP Recommended Provisions for Seismic Regulations for New Buildings and Other Structures, FEMA 450. Federal Emergency Management Agency, Washington DC
13. Naeim F, Kelly JM (1999) Design of seismic isolated structures, from theory to practice. 1st edn. Wiley

Highways Upgradation in the Hilly Areas and Its Impact—An Example of Uttarakhand

P. S. Prasad and **Kishor Kumar**

Abstract Uttarakhand is one of the Himalayan states where a visionary scheme of Government of India was launched in 2016 to widen all the highways totalling to about 900 km (with broad design of two lanes with paved shoulders) leading to Chardhams (Gangotri, Yamnotri, Kedarnath, Badrinath and the Kailash Mansarovar in Tibet). During widening of these highways, multiple kinds of problems related to slope instability and drainage were observed. Ground observations indicate towards the inadequate prior assessment of vulnerability of the slopes to the cutting, methods of the cutting as well as the mitigation and management deficiencies. Most of the highway stretches, therefore, widened so far have been affected by the landslide and like slope processes, and the number has increased multifold compared with the already existed landslides. This indicates towards the lack of planning and understanding about the slope vulnerability; as a result, an opportune chance of constructing a wider, disaster resilient and environmentally safe highway network in very important border state has been missed. This present study will try to highlight the issues which had been addressed prior and during the highway upgradation/modernization and will also discuss the possible rectification in future for risk-free management of the highway.

Keywords Highways · Slope instability · Drainage · Landslide · Mitigation measures

1 Introduction

Uttarakhand state was created on 9th November 2000 as a 27th state in the northern part of India carved from the hill districts of Uttar Pradesh. The geographical area of Uttarakhand is 55,673 km^2, of which 83% of the total area covered with hills and remaining area is in plains. Around 62% of the total area of the state covered under dense forest. The altitude of the state varies from 215 to 7816 m above mean sea level (MSL). It borders with Himachal Pradesh in the northwest, Haryana in

P. S. Prasad (✉) · K. Kumar
CSIR Central Road Research Institute, New Delhi, India

461

the west and Uttar Pradesh in the south. This state is also having international boundaries with Tibet, PRC in the north and Nepal in the east [1]. This state is very rich in flora and fauna with dense forests, snow-covered mountains and rich in water with snow-fed rivers. The total population of the state is around 1.12 crores as on May 2020 (http://www.populationu.com/in/uttarakhand-population). The state economy is mainly tourism and agriculture-based. This hill state has immense potential in domestic, international, outbound, adventure, wildlife, wellness, cultural and pilgrimage tourism. Tourism helps in economic growth of country and state. It will also help in local employment opportunities.

Roads are the only mode of transportation within the state and act as a lifeline of the people of Uttarakhand. The road network is, therefore, most significant for economic growth of the state including infrastructural developmental activities. There is a network of nineteen national highways (NH) of 2513 km length extending through the state. Some of the national highways are connecting to the international borders and, hence, are very important from strategic point of view. Government of India has planned and launched a visionary project in the year 2016 to widen the existing Chardham NH roads of around 900 km (Fig. 1) to double lane with paved shoulders (all weathered roads) for improving the safety and facilities to pilgrims, local residents, administration and also to army for their activities in the international borders. The upgradation will also improve the time and safety of commuters during transportation, improve fuel consumption of vehicles and enhance the tourism, employment and economy of people of the state. Presently, widening of these roads is still under progress. Various kinds of problems like slope instability, drainage, muck dumping and their stability, felling of trees are observed during widening of these roads. The present paper addresses the geotechnical issues (slope instability of
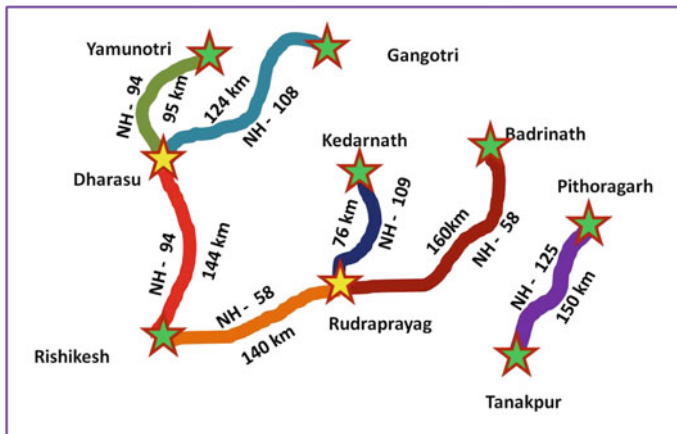
Fig. 1 Government of India's Chardham roads widening programme (under progress)

uphill cut slopes, drainage, muck dumping and their stability) related to prior and during highway upgradation/road widening and possible mitigation measures for safe management of highway.

2   Important Issues to Be Considered Before Upgradation/Widening of Highway

2.1   *Landslide Susceptibility*

Uttarakhand region is one of the multi-hazard-prone states of India, and 93% of its total area (53,566 km^2) is hilly and mountainous. The young mountains are geodynamically active, and therefore, the fragile geological formations, network of tectonic structure like faults and thrusts, folded rocks, combination of harder and softer strata, high and steep slopes, combined with changing climatic extremes and seismic events make a perfect combination for hazardous events like slope failure [2]. National highways in Uttarakhand had suffered from a variety of landslides and other mass movements. For example there are hundreds of landslides along the NH–58 staring from Rishikesh to Badrinath covering a distance of 320 km. There are 61 major number of landslides developed, and many of which are historic, 4–5 decades old and recurring every year during monsoon. Kaliasaur landslide (147 km), Pakhi landslide (250 km), Tangni landslide (254 km), Patalganga landslide (256 km) and Lambagarh landslide (302 km) are a few among the critical ones [3].

The monsoon period is from June to September, and maximum rainfall occurs in the months of July and August (Dehradun.nic.in/climate/). National highways in Uttarakhand had suffered from different types/mixtures of landslides, rock falls and subsidence during an unprecedented rainfall of July 1970. The heavy rain shadowed by the cloudburst at the higher peaks of Patalganga engendered a successions of landslides all along the two tributaries of Patalganga. A colossal quantity of debris discharged by the Patalganga River congested the main river Alaknanda and created a 20 m high artificial dam [4]. With the breaching of artificial dam, the number of villages and many other settlements all along the downstream was washed away within a few hours. The impetus of this flash flood was so high that the entire Srinagar city (which is positioned about 100 km on the downstream side of artificial dam point), was heavily flooded and was bursting with silt and sand [5]. Since 1970, population and related developmental accomplishments in the Uttarakhand state have got augmented multiple without any disaster mitigation and management planning. Vulnerability of the hill slopes to landslide disasters has also amplified comparatively to the developmental activities (Kumar et al. 2005). The number of landslides on NH–58 before 2013 is shown in Fig. 2. Similarly, during 2013 flash floods in Uttarakhand, several national highways had suffered again with many new landslides and reactivation of existing landslides. The condition of the national highways during 2013 flash floods is shown in photographs 1 and 2.
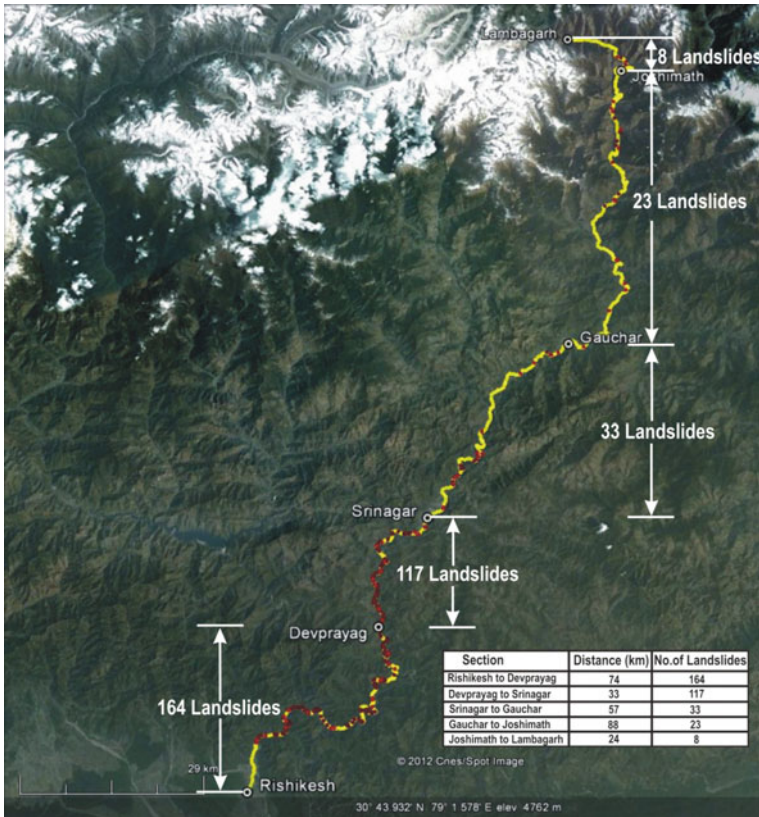
Fig. 2 Number of landslide incidences on NH–58 in Uttarakhand (before 2013)

As the climate change impact has increased the variability on the rainfall intensity, amount and time domain, the number of extreme events of rainfall has also increased. This has developed further challenges for management of the highways in landslide-prone areas. To better manage the highways, it is, therefore, required to consider the inherent fragility of the region into the planning and design of the highway constructions/planning. Failing which we may further complicate the problems on the risk-less functioning of the highways in the region.

2.2 Road Width

The actual road width required for construction of two lane road in mountainous region (hills) is presented in Table 1 [6], and extra road width should be provided on curves [7] as per Table 2. Typical hill road cross-section for an existing single lane is shown in Fig. 3. The two lanes widening portion should be adjusted in such a way that

Photograph 1   The highway filled up with debris due to debris flow in Gaurikund

the excavation towards uphill portion should be minimum. Figure 4 shows the typical cross-section of single lane road to be widened to double lane road towards uphill side. If the road is to be widened towards the uphill slope, it requires proper geological study and stability analysis of rock/soil slope. Depending upon the strength of the rock, the slope of cut will vary, and if it is a soil, then the angle of cut slope should not be more than the angle of shearing resistance of soil. If the widening of the road to be considered towards downhill slope with reinforce soil slope, it avoids the problem of slope instability of existing stabilized uphill slopes. Figure 5 shows the typical cross-section of single lane road to be widened to double lane road towards downhill side. While making the DPR detailed geological, geotechnical investigation is required. The data regarding number of trees to be cut/forest area while widening the road portion are also required. Due to environmental conditions, the widening of the road should be designed in such a way that the number of trees to be cut should be minimum. If the road is to be widened towards uphill slope and due to right of way restriction the steep slope is to be cut, then the slope should be stabilized with steel anchors with rope net/concrete cladding with steel anchors as shown in Photograph 3.

Photograph 2   Highway breached and many new landslides occurred on NH–58

Table 1   Total full-road width for two lane roads in mountainous region

Two lane width	7 m
Shoulders	
Hill side	1.5 m (paved shoulder)
Valley side	1.5 m (paved shoulder) + 1 m (earthen shoulder) = 2.5 m
Width of Parapet	0.6 m
Side drain	0.6 m

Table 2   Extra width of road on curves

Radius of curve (m)	Extra width (m)
Up to 40	1.5
41–60	1.2
61–100	0.9
101–300	0.6
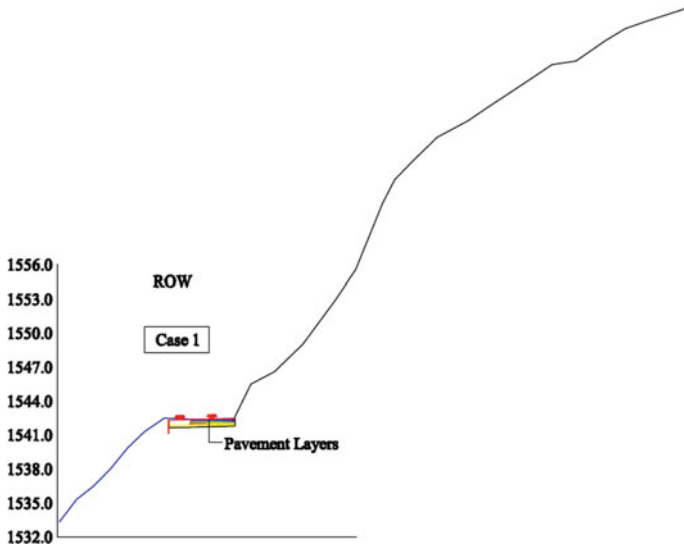
Fig. 3 Typical hill road cross-section for an existing single lane
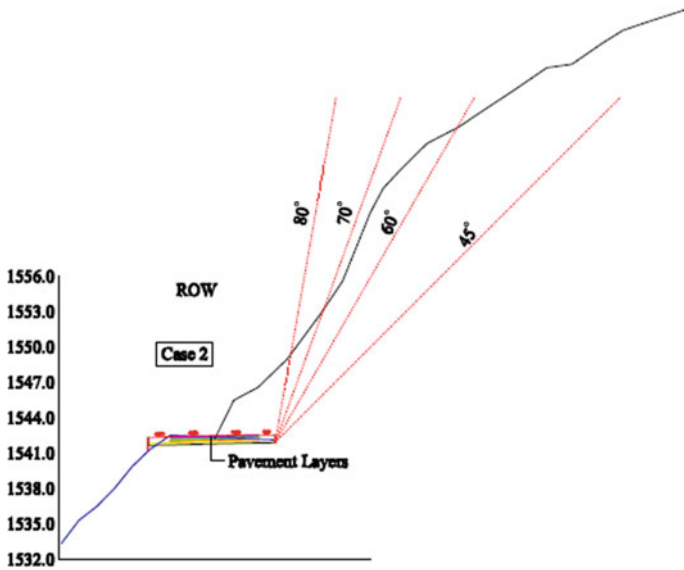
Fig. 4 Typical cross-section of single lane road to be widened to double lane road towards uphill side
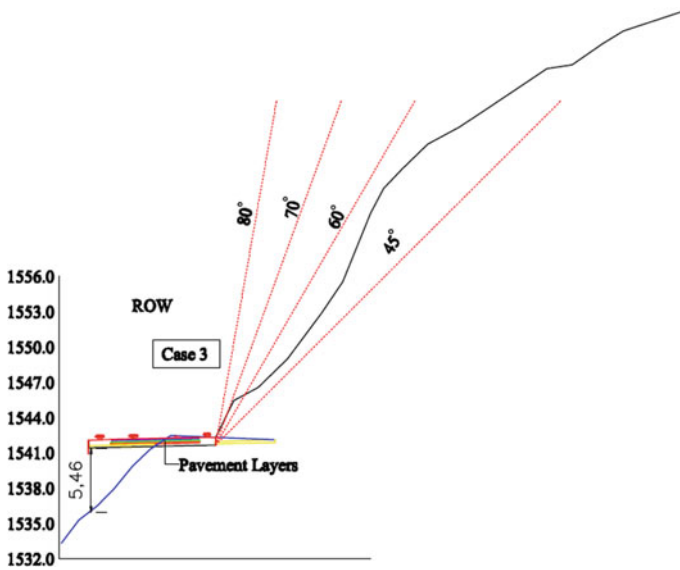
Fig. 5 Typical cross-section of single lane road to be widened to double lane road towards downhill side

3 Man-made Disasters

3.1 Condition of Uphill Slopes Due to Widening of National Highway

During field investigation, it was observed that most of the road widening on national highways (NH) were carried out towards the uphill slope. It was observed that at some locations, the slopes have been stabilized with remedial/protection measures (soil nailing (grouted) coupled with steel rope net and erosion control measures). Irrespective of geological conditions, solution of remedial measures implemented is almost same. That is why, the stabilized slope failed in one location (Photograph 4). But in many locations, the steep cut slopes are protected with breast walls (masonry walls/gabion walls). Most of the steep cut slopes may fail during rainy season or after rainy season. These slopes should be properly investigated and stabilized with suitable remedial measures. The DPR of some packages even not suggested any stabilization measures for both uphill and downhill slopes. During site visit of Chardham Yatra roads (hill roads), it was identified that more than 100 locations are prone to the landslide/rock fall on widening portion of highway. Some landslides are already occurred during monsoon season of 2020. Typical steep uphill cut slopes and failed slopes are shown in Photographs 5 and 6.

Photograph 3 Probable stabilization measures for steep cut slopes

3.2 Dumping Yards

During field visit, it was observed that the excavated material merely dumped on downhill slopes at selected dumping yards with gabion wall (height 1–1.5 m) at the toe. In some areas, the construction agencies have dumped the material downhill slope. This will not only cause additional load on the downhill slope but will also destroy the whole morphology including the drainage on it and may fail in future due

Photograph 4 Slope protection measures are implemented. But, failed due to activation of slide

Photograph 5 Condition of the failed cut slope on widening portion of highway

to slope increasing instability (Photograph 7). At some locations, the excavated material is dumped on downhill side which blocks the river (Photograph 8). Due to inefficient measures, these dumping yards may fail in future due to slope degrading, slope instability and even may block the river/natural streams. If not properly protected, during the rains and subsequent flash floods, which often appear, these dumped debris will also wash away and erode the banks of river/streams and make downhill slopes further unstable. These dumping yards, therefore, should be properly designed, and

Photograph 6 Landslides are created due to steep cut slope

the dumping material should be properly spread on the surface and compacted properly. The stability of the dumping yard should be ensured with or without protection measures. Erosion control measures should be implemented on sloping surface.

3.3 Drainage Measures

Since rainfall in the state is generally high, properly designed drainage all along the highway is important. During site visit, it was observed that drainage measures were

Photograph 7 Dumping of excavated material on downhill slope

not implemented in many locations. The drainage measures in many locations were very poor. The typical Photograph 9 presents the culvert left at downhill side of the slope without stepped chute. Proper cross-drainage works should be provided at a regular intervals. The cross-drainage works with stepped chutes should be designed properly.

3.4 Natural Springs

During the site visit, a few natural springs were observed at some locations along the highway (Photograph 10). During widening, cutting the uphill slope causes changes in geological and hydrological conditions of the slope. Due to this reason, some of these springs may disappear after widening. Hence, while widening the road, proper precautionary measures should be considered and implemented such that these spring live forever after widening the road.

4 Conclusions

Government of India launched a noble project in 2016 to widen the existing national highways with broad design of two lanes with paved shoulders leading to Chardhams to enhance the developmental activities, facilities of local inhabitants, safety to commuters, military, tourism, employment and economy of Uttarakhand state. However, the purposes of widening can be accomplished only if the entire network

Photograph 8   Dumping of excavated material on a downhill slope in river portion

of highways become disaster resilient (from landslides/rock falls and like processes). It was, in that logic, good decision to include in the DPR two tunnels and some bypasses to avoid landslides (e.g. to bypass the Kaliasaur landslide, the authorities proposed a new alignment with three bridges to cross Alknanda River). However, in many other cases, the uphill slopes are cut very steep with a provision of only a breast wall which resulted the occurrence of landslides/rock falls in many places. As mostly quoted, due to right of way (RoW) restrictions, in the already steep terrain, the steep uphill cut slopes are inevitable. In that case, it is must to conduct detailed geological, geomorphological and geotechnical investigations to design the cut slopes as well as the protective measures. The preventive measures implemented were fragmentary

Photograph 9 Culverts left open without stepped chutes on downhill slope

Photograph 10 Natural springs along the highway

in nature. It is required that the whole scheme of required measures is implemented in one go as the fragmentary approach implementing only a few selective does not work and even may do more harm than the good, in many cases. This approach, as observed, has not worked and, instead, created unwanted problems on the slopes, thereby risking the life of the commuter and damage to the highway. In many places, it was also observed that the debris dumped on downhill without any planning. This causes the downhill slopes more denudation and instability. The debris material should also not be in dumped riverside. The selected dumping yards should be properly designed, and the dumping methodology should be properly implemented at the site. As the Uttarakhand state gets high rainfall, appropriate drainage measures should be implemented all along the highways.

References

1. Tolangay D, Moktan S (2020) Trend of studies on carbon sequestration dynamics in the Himalaya hotspot region: a review. J Appl Nat Sci 12(4):647–660
2. Kumar K, Kathait A, Prasad PS, Goyal N, Singh K, Singh I, Gangopadhyay S (2012) Geoenvironmental appraisal of landslide hazards on highways. In: Proceedings of 13th Esri India user conference 2012, December 5–6, 2012, in New Delhi, India
3. Negi IS, Kumar K, Kathait A, Prasad PS (2013) Cost assessment of losses due to recent reactivation of Kaliasaur landslide on National Highway 58 in Garhwal Himalaya. Nat Hazards 68(2):901–914
4. Kumar K, Sati D (2005) Exploring the history of Alaknanda–Patalganga tragedy of 1970 & possibility of its recurrence and impacts on Patalganga Basin—a GIS and remote sensing based study. In: Proceedings of the 8th annual international conference. Map India, New Delhi
5. Kumar K, Devrani R, Mathur S (2010) Landslide hazard potential analysis using GIS, Patalganga valley, Garhwal, Western Himalayan region of India. Eur J Sci Res 45(3):346–366
6. IRC 52 (2019) Guidelines for the alignment survey and geometric design of Hill roads. Indian Roads Congress, Kama Koti Marg, New Delhi
7. IRC: SP 73 (2015) Manual of specifications & standards for two laning of Highways with Paved Shoulder. Indian Roads Congress, Kama Koti Marg, New Delhi

Out-of-plane Response of Clay Brick Unreinforced and Strengthened Masonry Walls Under Explosive-induced Air-blast Loading

S. M. Anas ⬤, Mehtab Alam ⬤, and Mohammad Umair⬤

Abstract In recent years, structural engineers and designers are showing their concern about the increasing occurrence of accidental explosions and subversive blasts. Such events induce impulsive loads of abnormal intensity on adjoining buildings leading to the failure of their load-bearing components which may result even in their progressive collapse. Civilian buildings such as universities, schools, and hospitals have been targeted in recent years. Performance of masonry walls being the primary components of the load-bearing structure is of paramount importance under such extreme loadings. In framed structures, generally, panel walls are of unreinforced masonry (URM) and are capable of resisting low-magnitude out-of-plane loads caused by wind and earthquake; however, they are vulnerable to high air pressure generated by explosive-induced detonation. In this study, the out-of-plane behavior of clay brick unreinforced masonry walls under air-blast loading has been investigated using commercial software, Abaqus/CAE 2017. Finite element (FE) models of a single-story dwelling house, consisting of 230 mm thick load-bearing masonry walls and a conventional singly reinforced concrete slab with M20 concrete grade and Fe500 steel, have been developed for this purpose. FE models are subjected to experimental blast peak overpressures available in the literature. For the accuracy of the results, only the target wall has been modeled using a detailed micro-modeling strategy; however, macro-modeling has been opted for other walls to optimize the computational running time. To improve the blast resistance of the wall, analyzes have been extended by strengthening the walls with the reinforced concrete horizontal bands as per IS 4326 (1993) after every three, four, and five courses in different FE models. Concrete-damaged plasticity (CDP) model for concrete and masonry has been utilized for the damage assessment of the walls. Based on the results

S. M. Anas (✉) · M. Alam · M. Umair
Department of Civil Engineering, Faculty of Engineering and Technology, Jamia Millia Islamia, Delhi, New Delhi 110025, India

M. Alam
e-mail: malam1@jmi.ac.in

M. Umair
e-mail: mumair@jmi.ac.in

obtained, this study recommends the provisions for improving the performance of the load-bearing masonry walls under explosive-induced air-blast loading.

Keywords Air-blast loading · Explosive-induced disaster · Brick masonry walls · Out-of-plane (OOP) loading · Concrete-damaged plasticity (CDP) model · Peak overpressure · Cracks · Damage dissipation energy · Damage · Stresses

1   Introduction

The analysis of the masonry buildings and their response attracts significant scientific research because the overwhelming majority of the heritage buildings and a large portion of modern constructions are made of masonry [1]. Sufficient amount of experimental and numerical investigations have been made by the researchers to assess the dynamic response of the masonry walls under quasi-static and seismic loadings [2–4]. However, their out-of-plane behavior to explosive-induced close-in air-blast loads received less attention, with a focus only on macro-modeling/continuum approaches and not on micro-modeling strategies.

Accidental explosions, bombing attacks, and man-made explosions have increased in frequency over recent years. Some recent examples are the Beirut explosion (August 2020), the explosion at an ammunition warehouse in Ryazan City (October 2020), the bombing on a school building in Peshawar City (November 2020), and the bombing and attack on the Kabul University (November 2020) [5–11]. The motivation of the present investigation lies in the current international context. There is currently a need for the sectional committee and organizations to better examine the threat of explosive-induced blasts meant to destroy civilian buildings. Heritage brick and stone masonry structures are often primary targets. Of particular, concern is clay brick masonry walls which are perceived as a source of explosive-induced hazard to the building occupants when an external blast occurs close to the building [12]. Since most structures are not designed to resist such extreme loadings, the failure consequences can be devastating and irreparable. Therefore, there is an urgent need to upgrade the provisions of the current design standards especially for the masonry buildings likely to take air-blast loading.

Performance of the unreinforced masonry walls under the explosive-induced air-blast loadings has been experimentally and analytically investigated by several researchers in recent decades [1, 12–19]. However, the effect of the reinforcement on the blast resistance of the brick masonry wall using a micro-modeling strategy has not been investigated earlier which is the novelty of the current work. Gabrielsen et al. [14] experimentally investigated the effect of arching on the blast resistance of the full-scale clay brick unreinforced masonry walls. Dennis et al. [13] conducted explosion tests to investigate the performance of the concrete block (CMU) unreinforced masonry walls under blast loading. The results were compared and found to be in reasonable agreement with those obtained from the high-performance computing (HPC) method proposed by U.S. Army Corporations of Engineers (USACE). Zapata

and Weggel [19] conducted explosion tests inside a two-story ordinary unreinforced clay brick masonry wall building which was scheduled to be demolished. Results revealed that the partition wall experienced a maximum displacement of 250 mm at the center. The experimental results were compared and found to be in good agreement with those computed from the single degree-of-freedom blast effects design spreadsheet (SBEDS) method. Wei and Stewart [18] conducted parametric investigations to study the effect of mortal strength, brick strength, wall thickness, and boundary condition on the behavior of the clay brick URM walls under different reflected peak pressures. It was reported that the effect of brick strength and mortar strength on maximum mid-span deflection and damage resistance of the walls was insignificant under higher blast pressures (> 2 MPa). Ahmad et al. [20] conducted free-air-blast tests on 2000 × 2000 × 370 mm free-standing URM wall at different standoff distances (between 3 and 4 m) and proposed several empirical relations to estimate air-blast and ground shock wave parameters. Pereira et al. [17] experimentally investigated the behavior of the clay brick URM wall subjected to a reflected peak blast pressure of 0.149 MPa. Large cracks were observed, mostly concentrated at the mid-height of the wall, and extended to the top and bottom edges as well as corners of the wall. Gagnet et al. [21] experimentally and numerically examined the response of arching and non-arching URM walls under different blast peak overpressures. The test results were compared and found consistent with those obtained from the single-degree-of-freedom (SDOF) approach and Wiehle and Moradi empirical methods.

The goals of the present investigation are:

1. To develop FE models of a single-story dwelling house, consisting of load-bearing masonry walls and a conventional singly reinforced concrete slab.
2. To evaluate central displacement, stresses, crack/damage patterns, and damage dissipation energy under the considered air-blast loading.
3. To enhance the blast resistance of the wall with the horizontal RC bands.

2 Numerical Modeling

A high-fidelity physics-based FE program Abaqus/CAE 2017 has been employed in the present work to simulate the blast response of the considered load-bearing structure. Four FE models have been developed. The first model (#1) is consisting of 230 mm thick load-bearing unreinforced brick masonry walls and a 140 mm thick conventional RC slab (Fig. 1a). The dimensions of each wall are 17 bricks wide (4070 mm) by 41 courses high (3270 mm). In the second (#2), third (#3), and fourth (#4) FE models, the load-bearing walls are strengthened with the RC horizontal band as per IS 4326(1993) [22] after every three, four, and five courses, respectively, (see Fig. 1c). The dimensions of the clay bricks are 230 × 110 × 70 mm (length x width x thickness). The thickness of the mortar joints is 10 mm. The thickness of the RC band is 60 mm. The bricks are laid in an English bond arrangement as shown in Fig. 1a. The accuracy of the employed program and used numerical method to model the

blast has been discussed in the previously published studies by the authors [1, 5–11, 23, 24]. There are three techniques used for the modeling of the masonry walls: (a) Macro-modeling, where units (bricks/blocks), mortar joints, and the interface between the units and mortar are considered as a homogeneous continuum; (b) simplified micro-modeling, where the units are modeled by continuum elements and mortar in the joints and unit-mortar interface are described by dis-continuum elements; (c) detailed micro-modeling, where the units and mortar in the joints are represented by continuum elements and unit-mortar interface by dis-continuum elements described by contact models available in Abaqus/CAE program,. For the accuracy of the results, only the target wall (Wall #1) has been modeled using a detailed micro-modeling strategy; however, macro-modeling has been opted for other walls (Walls #2 to #4) to optimize the computational running time (see Figs. 1a and b). The blast loading is defined as pressure versus time application using the LOAD_SEGMENT command. Air-blast effect on the masonry wall is simulated using the explicit solver solves the equation of motion with increments and modify the stiffness matrix after each increment of load and corresponding displacement considering geometric and material non-linearity [5–11].

Micro- and macro- models of the walls are discretized with 8-node linear brick explicit elements (C3D8R) with reduced integration and hourglass control (Abaqus user assistance guide, 2017). A mesh size of 23 mm has been adopted for the target wall (micro-wall), whereas a mesh size of 28.75 mm has been considered for the macro-walls following the convergence test conducted at scaled distances of 1.17 and 0.93 m/kg$^{1/3}$. The slab is reinforced at the bottom tension side with 8 mm diameter High-yield strength-deformed steel re-bars of grade Fe500 at a fixed spacing of 150 mm c/c ($\rho = 0.24\%$) and with the edge reinforcement at the top side, as shown in Fig. 2a. The reinforcement details of the RC band are shown in Fig. 2b. The compressive strength, Young's modulus, and Poisson's ratio of the concrete are 20 MPa, 21.20 GPa, and 0.20, respectively. The ultimate tensile strength, yield strength, Young's modulus, and Poisson's ratio of the steel are 545 MPa, 500 MPa, 210 GPa, and 0.30,
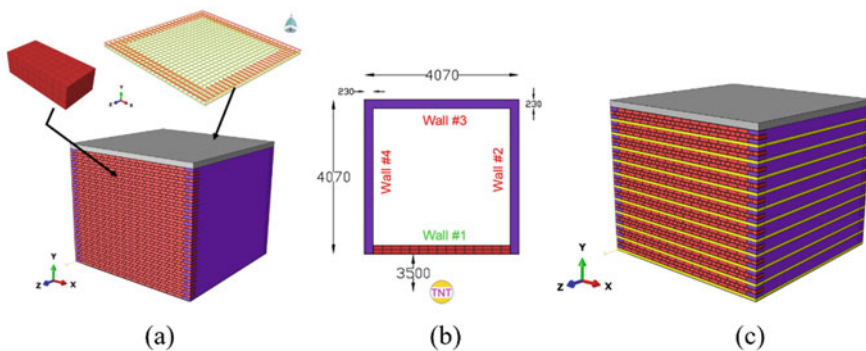
Fig. 1 **a** FE model (#1) of a single-story dwelling house, consisting of load-bearing masonry walls and a conventional RC slab; **b** Dimensions (mm) of the dwelling unit and location of TNT; and **c** FE model (#2) with RC horizontal band after every three courses
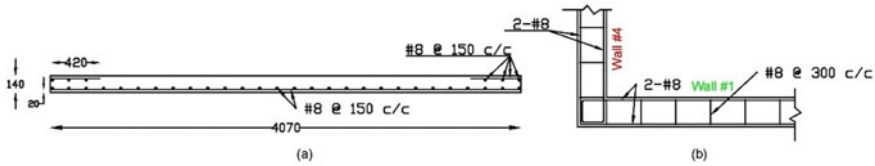
Fig. 2 Dimensions (mm) and reinforcement details of RC slab (**a**) and RC band (**b**)

respectively. The concrete is also discretized with 8-node explicit solid elements (C3D8R) with hourglass control and reduced integration. The re-bars are discretized with 2-node explicit linear 3-D truss elements (T3D2). The re-bars are embedded in the slab FE model using the EMBEDDED_REGION constraint. This approach constrained translational degrees of freedom of the embedded reinforcement element nodes to the degrees of freedom of the surrounding concrete element nodes [25]. Effects associated with the steel reinforcement–concrete interface, such as bond-slip, are modeled approximately by introducing some tension stiffening into the concrete modeling to simulate load transfer across cracks through the steel reinforcement. Mesh sizes of 20 and 23 mm have been adopted for the slab and bands following the convergence test. FE model #1 has 1,150,844 nodes and 824,497 elements. FE model #2 has 1,259,820 nodes and 870,434 elements. FE model #3 has 1,233,182 nodes and 853,857 elements. FE model #4 has 1,229,874 nodes and 860,914 elements. The walls are resting on an arbitrary surface which is assumed fixed. The arbitrary surface in the employed software has been modeled using reference points. A surface-to-surface contact interaction, with "friction," "hard," and "cohesion" contact models and with penalty contact method as mechanical constraint formulation available in the Abaqus program has been used to model the interaction between the slab and the walls and between the walls and arbitrary surface.

2.1 Micro-modeling

The interface between the bricks and mortar has some cohesion prior to failure, and thereafter, the bricks and mortar joints can slide along each other at the interfaces to provide friction [26]. Therefore, an explicit general contact interaction, with "friction," "hard contact," "cohesion," and "damage evolution" models, has been employed to describe the brick–mortar interfaces. The cohesion (or strength) in the interfaces depends on the shear and normal stresses of the masonry joint interfaces [26]. The failure criterion of the unit-mortar interface is expressed as in Eq. (1):

$$\left(\frac{|\sigma_N|}{\sigma_N^{\max}}\right)^2 + \left(\frac{|\sigma_S|}{\sigma_S^{\max}}\right)^2 + \left(\frac{|\sigma_T|}{\sigma_T^{\max}}\right)^2 = 1 \qquad (1)$$

Here, σ_N = normal stress in masonry joints (MPa); $\sigma_N^{\max}$ = tensile strength of masonry joints (MPa); σ_S = tangential shear stress in masonry joints (MPa); $\sigma_S^{\max}$ = shear strength of masonry joints (MPa); σ_T = tangential shear stress in joints; $\sigma_T^{\max}$ = shear strength of masonry joints (MPa). Non-thickness cohesive element is used to describe the brick-mortar interface. The elastic properties of clay bricks, mortar, unit-mortar interfaces, and input parameters for contact interaction models under out-of-plane loading have been taken from the experimental study conducted by Abdulla et al. [2]. The coefficient of friction between the unit-mortar interfaces is taken 0.75.

2.2 Material Model

Concrete-damaged plasticity (CDP) model, a modification of the Drucker-Prager model proposed by [27] and [28], was developed to simulate the nonlinear behavior of the materials such as concrete and masonry under quasi-static and extreme dynamic loadings. The evolution of the failure surface is controlled by two damage variables, i.e., compression damage (D_c) and tension damage (D_t), which are connected to failure mechanisms of the material under compression and tension loadings [29, 30]. It is assumed that the uniaxial stress–strain curves can be converted into stress versus inelastic-strain curves [29]. This conversion is performed automatically by the Abaqus/CAE program from the user-provided stress versus plastic strain data. The uniaxial compressive and tensile responses of the material with respect to the CDP model under compression and tension loadings are given by:

$$\sigma_c = (1 - D_c)E_0\big(\varepsilon_c - \varepsilon_c^{\mathrm{pl},h}\big) \tag{2}$$

$$\sigma_t = (1 - D_t)E_0\Big(\varepsilon_t - \varepsilon_t^{\mathrm{pl},h}\Big) \tag{3}$$

$$E_u = \big(1 - D_{i=c,t}\big)E_0 \tag{4}$$

Here, σ_c = nominal compressive stress; σ_t = nominal tensile stress; ε_c = Compressive strain ($\varepsilon_c^{\mathrm{pl},h} + \varepsilon_c^{\mathrm{el}}$); ε_t = Tensile strain ($\varepsilon_t^{\mathrm{pl},h} + \varepsilon_t^{\mathrm{el}}$); $\varepsilon_c^{\mathrm{pl},h}$ = plastic hardening compressive strain; $\varepsilon_t^{pl,h}$ = plastic hardening tensile strain; $\varepsilon_c^{\mathrm{el}}$ = elastic compressive strain; $\varepsilon_t^{\mathrm{el}}$ = elastic tensile strain; E_0 = initial elasticity modulus of the material; D_c and D_t are compression and tension damage variables; and E_u = reduced elastic modulus. Previous research has indicated that the CDP model can accurately predict damage/crack patterns in the RC slab and brick masonry wall under explosive-induced blast loading [1, 17, 23, 24]. Therefore, the CDP model available in the Abaqus/CAE software has been employed in the current work for concrete and masonry. CDP model parameters for M20 grade concrete have been obtained from
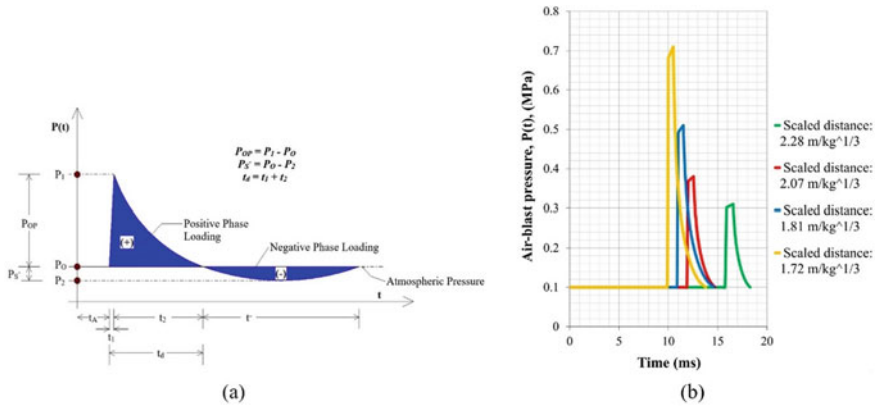
Fig. 3 **a** Idealized air-blast time history [31] and **b** Estimated air-blast time histories

the experimental study conducted by Hafezolghorani et al. [30] and for masonry have been taken from Valente and Milani [3, 4].

2.3 Air-blast Loading

Figure 3a shows the idealized air-blast pressure–time history proposed by Wu and Hao [31], where P_{OP} is the peak overpressure; P_S—is the maximum negative pressure; P_O is the ambient air pressure ($\approx$0.1 MPa); t_A is the arrival time of shock wave; t_1 is the rising time; t_2 is the decreasing time; t^- is the negative blast phase duration; and t_d is the duration of positive blast phase. In general, the blast load is characterized by two phases, namely: the positive phase and the negative blast phase [31–33]. As can be seen from Fig. 3a, the positive blast phase is simplified into three parts: a constant ambient air pressure (PO) followed by a sudden linear rise in air pressure to the peak value at the wavefront and then quasi-exponential decay of the varying pressure, $P(t)$. In the negative blast phase, the pressure falls below the ambient pressure and a partial vacuum is formed (i.e., air is absorbed). Current design guidelines for blast protective structures usually recommend utilizing only the positive blast phase by assuming that the negative phase of the blast is normally much weaker and does not affect typical structures [25, 33, 34]. Thus, the influence of the suction blast phase on the performance of the considered models has been neglected in the study. Table 1 lists the experimental values of air-blast wave parameters at a fixed standoff distance of 3.50 m obtained from Ahmad et al. [20], where W_{TNT} is the weight of TNT; Z is the scaled distance; and t is the total duration of the air-blast (neglecting negative phase). Figure 3b shows the air-blast time histories calculated using the empirical equation proposed by Wu and Hao [31].

Table 1 Experimental values of air-blast parameters obtained from Ahmad et al. [20]

W_{TNT} (kg)	Z (m/kg$^{1/3}$)	P_{OP} (MPa)	t_A (ms)	t_1 (ms)	t_2 (ms)	t_d (ms)	$t = t_A + t_d$ (ms)
3.60	2.28	0.21	15.90	0.67	1.73	2.40	18.30
4.80	2.07	0.28	12.00	0.55	2.20	2.75	14.75
7.20	1.81	0.41	10.99	0.52	3.12	3.64	14.63
8.40	1.72	0.61	10.00	0.49	3.31	3.80	13.80

3 Results and Discussions

From the nonlinear explicit blast analyses conducted, the following observations are worth mentioning:

- Referring to Table 2, increasing the explosive charge by a factor of 2 leads to an increase of the damage dissipation energy of FE model #1 (without bands) by a factor of 5 for the considered standoff distance (3.50 m). The increase in the damage dissipation energy indicates that the considered load-bearing structure suffers more damage and cracking. However, the maximum central displacement and stresses in the target wall (i.e., Wall #1) increase by a factor of 2 (Tables 2 and 3).
- The target wall (Wall #1) first behaves like a restraining wall at supports (i.e., Walls #2 and #4). This restraint is mobilized at a very early stage of loading and then it behaves as a simply supported wall (Fig. 4).
- The slab experiences reflected pressure from the target wall (facing the explosive), and due to lateral displacement of the transverse walls (Walls #2 and #4) at the top junction, the corners of the slab got more exposure to the reflected blast pressure

Table 2 Summary of displacements and damage dissipation energy (DDE) for FE model #1

Z (m/kg$^{1/3}$)	Max. displacement (D_{max}; mm) in walls and slab				Damage dissipation energy (J)
	Wall #1 (−Z direct.)	Walls #2 and #4 (+X and −X directs.)	Wall #3 (−Z direct.)	Slab (+Y direct.)	
2.28	[a]35.56	[b]±8.89	[f]2.24	[d]3.95	2679.06
2.07	[a]41.50 ([P]17)	[b]±10.38 ([P]17)	[f]2.62 ([P]17)	[d]5.21 ([P]17)	4570.85 ([r]71)
1.81	[a]61.90 ([P]74)	[b]±15.48 ([P]74)	[f]4.80 ([P] > 100)	[d]8.23 ([P]74)	13,680 ([r]> 100)
1.72	[a]82.58 ([P]132)	[b]±20.64 ([P]132)	[f]6.89 ([P] > 100)	[d]11.57 ([P]132)	33,790 ([r]> 100)

[a] at mid-height of the wall; [b] near junction of Wall #1 and Wall #2/#4; [f] near junction of Wall #3 and Wall #2/#4; [d] near support (i.e., target wall, Wall #1); [P] percentage increase in displacement (%); [r] percentage increase in damage (%)

Table 3 Summary of stresses of the masonry walls of FE model #1

Z (m/kg$^{1/3}$)	Max. von mises stress (V$_m$; MPa)			Max. principal stresses (P$_m$; MPa)		
	Wall #1	Walls #2 and #4	Wall #3	Wall #1	Walls #2 and #4	Wall #3
2.28	^{g}2.80	^{h}2.34	^{j}0.78	^{t}0.07, ^{c}3.64	^{t}0.07, ^{c}1.42	^{t}0.07, ^{c}0.43
2.07	^{g}4.16	^{h}3.47	^{j}2.77	^{t}0.08, ^{c}4.48	^{t}0.08, ^{c}2.62	^{t}0.08, ^{c}0.76
1.81	^{g}5.13	^{h}4.27	^{j}3.42	^{t}0.08, ^{c}5.66	^{t}0.08, ^{c}3.36	^{t}0.08, ^{c}2.21
1.72	^{g}6.74	^{h}5.40	^{j}4.05	^{t}0.09, ^{c}7.20	^{t}0.09, ^{c}5.37	^{t}0.09, ^{c}3.55

^{g} at brick and mortar interfaces; ^{h} near junction of Wall #1 and Wall #2/#4; ^{j} near junction of Wall #3 and Wall #2/#4; ^{c} compressive; ^{t} tensile
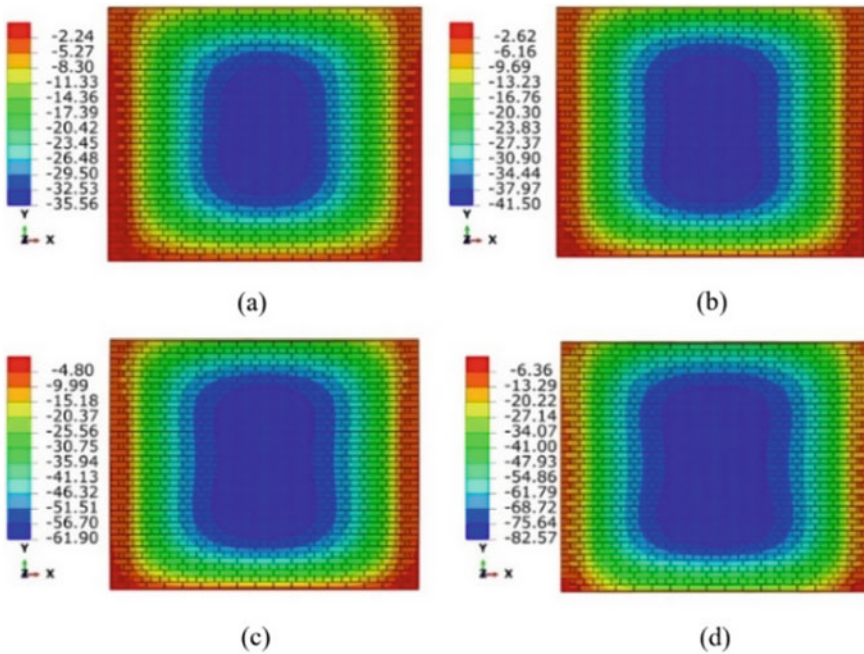
Fig. 4 Distribution of displacement (Z, mm) of the target wall (Wall #1) of FE model #1 at different scaled distances: **a** Z = 2.28, **b** Z = 2.07, **c** Z = 1.81, and **d** Z = 1.72 m/kg$^{1/3}$

and undergo an upward maximum displacement of magnitude more than that at the middle of the edge of the slab (Figs. 5 and 6).

- A good number of flexural cracks with an average spacing of 50 mm and crack depth of 130 mm have been observed on the tension side of the slab of FE model #1 subjected to the maximum explosive load of 8.40 kg TNT (Table 4 and Fig. 7d).
- Shear failure at supports of the slab has been observed (Fig. 7).
- Junction of slab and walls, the junction of Wall #1 and transverse walls (Walls #2 and #4), brick and mortar joint interfaces, and bottom tension side of the
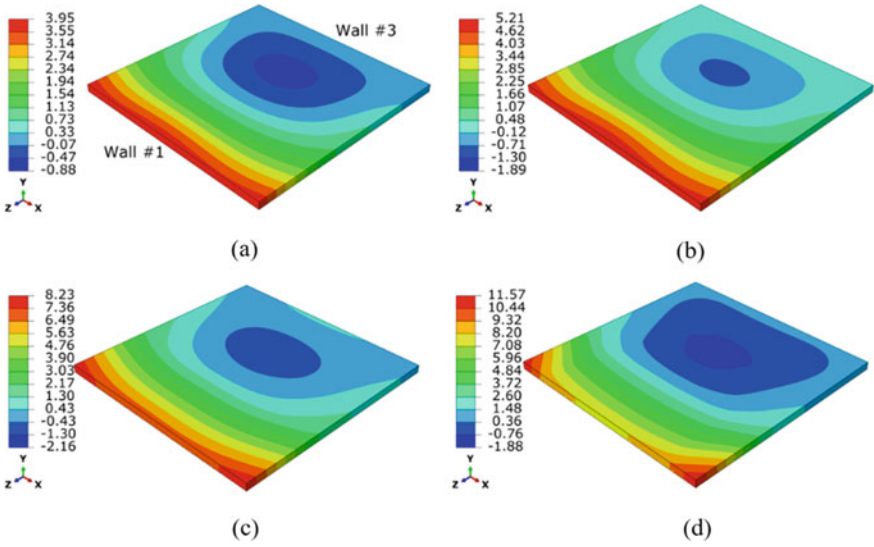
Fig. 5 Distribution of displacement (Y, mm) of RC slab of FE model #1 at different scaled distances: **a** $Z = 2.28$, **b** $Z = 2.07$, **c** $Z = 1.81$, and **d** $Z = 1.72$ m/kg$^{1/3}$
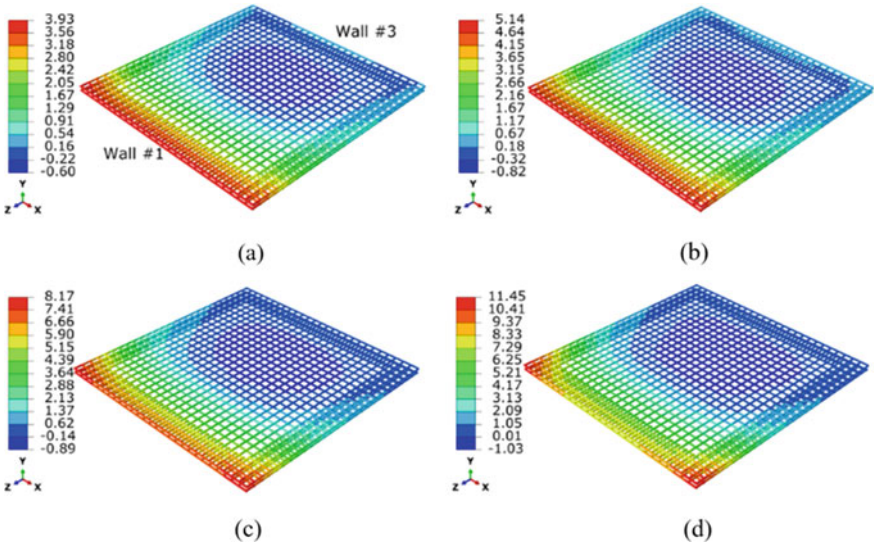
Fig. 6 Distribution of displacement (Y, mm) in the reinforcement of RC slab of FE model #1 at different scaled distances: **a** $Z = 2.28$, **b** $Z = 2.07$, **c** $Z = 1.81$, and **d** $Z = 1.72$ m/kg$^{1/3}$

Table 4 Geometric parameters of cracks of RC slab of FE model #1

Z (m/kg$^{1/3}$)	Average spacing (mm)		Number of cracks		Average depth (mm)	
	Q	M$_{span}$	Q	M$_{span}$	Q	M$_{span}$
2.28	160	–	2	–	40	–
2.07	140	–	2	–	45	–
1.81	140	80	2	10	45	100
1.72	140	50	2	15	45	130

Q near the support (Wall #1); M$_{span}$ mid-span
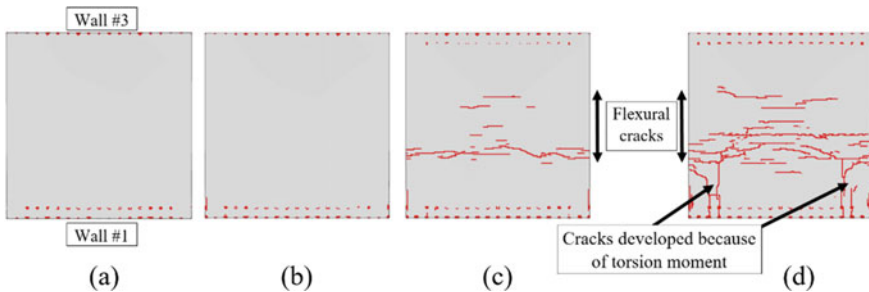
Fig. 7 Pattern of cracks on the bottom tension side of slab of FE model #1 at different scaled distances: **a** $Z = 2.28$, **b** $Z = 2.07$, **c** $Z = 1.81$, and **d** $Z = 1.72$ m/kg$^{1/3}$

slab experience maximum tension damage, whereas the brick and mortar joint interfaces and the junction of the walls suffer maximum compression damage (Fig. 9).

- Damage along the vertical joints of the two adjacent walls (Walls #2 and #4) and horizontal cracks at the junction of the slab and top edge of the target wall have been observed on the front face of the target wall subjected to the max. TNT charge is of 8.40 kg at a standoff distance of 3.50 m (Fig. 9), whereas horizontal cracks at the brick–mortar joint interface have been observed on the rear side of the wall.

- For the considered FE models and explosive loads, the brick–mortar interface near the top and bottom of the target wall (Wall #1) experiences maximum shear stress (see Fig. 8). However, the horizontal RC bands helped all of the walls to remain intact and significantly improved the cracking resistance and other dynamic responses considered (Table 5; Figs. 8 and 9).

4 Conclusion

This study performs finite element simulations of the considered load-bearing structure subjected to the explosive loads of 3.60, 4.80, 7.20, and 8.40 kg TNT at a fixed
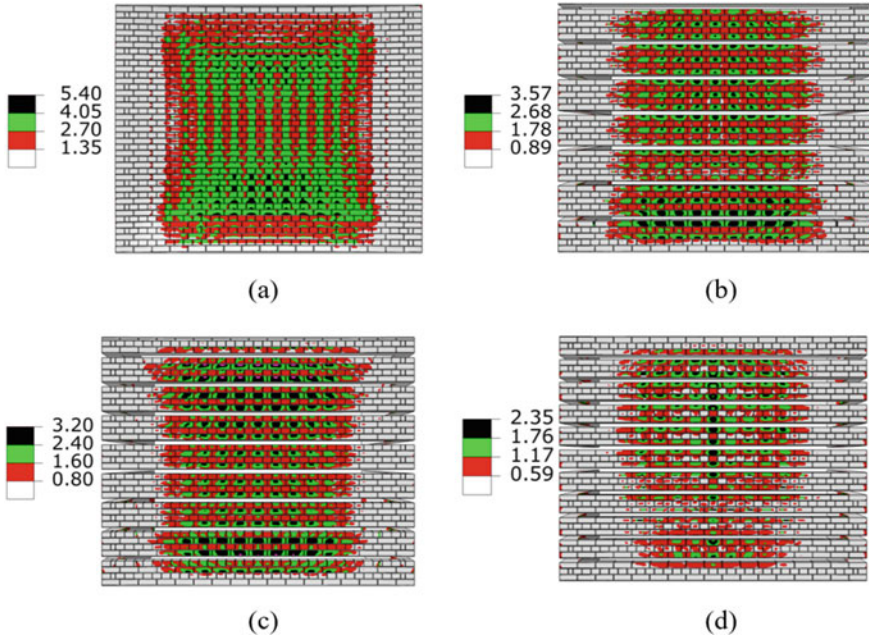
Fig. 8 Distribution of shear stress of the target wall (Wall #1) at a scaled distance of 1.72 m/kg$^{1/3}$ for different FE models at $t = 13.80$ ms: **a** #1 (without bands), **b** #4 (RC band after every 5 courses), **c** #3 (band after every 4 courses), and **d** #2 (band after every 3 courses)

Table 5 Summary of responses of the target wall (Wall #1) without and with RC band at a scaled distance of 1.72 m/kg$^{1/3}$ ($t = 13.80$ ms)

FE model	D_{max} (mm)	V_m (MPa)	P_m (MPa)	DDE (J)
#1 (without RC band)	82.58	5.40	^{t}0.09/^{c}4.77	33,790
#2 (with RC band after every 3 courses)	23.02 (^{w}72)	2.35 (^{w}56)	^{t}0.07/^{c}1.81 (^{w}22/^{w}62)	4134.22 (^{w}88)
#3 (with RC band after every 4 courses)	34.84 (^{w}58)	3.20 (^{w}41)	^{t}0.07/^{c}2.37 (^{w}22/^{w}50)	6404 (^{w}81)
#4 (with RC band after every 5 courses)	44.54 (^{w}46)	3.57 (^{w}34)	^{t}0.08/^{c}3.35 (^{w}11/^{w}30)	9431.33 (^{w}72)

^{c} compressive; ^{t} tensile; ^{w} percentage decrease (%)

standoff distance of 3.50 m in free air. A sophisticated material damage model for concrete and brick masonry has been employed in the study. Obvious variation in the blast performance of the target masonry wall of FE model #1 (without bands) has been observed such as the decrease of the scaled distance increases the central displacement, stresses, damage dissipation energy, and cracks. Strengthening the target wall (Wall #1, facing the explosive) with the horizontal RC band of thickness 60 mm after every three courses (FE model #2) reduces the maximum central displacement
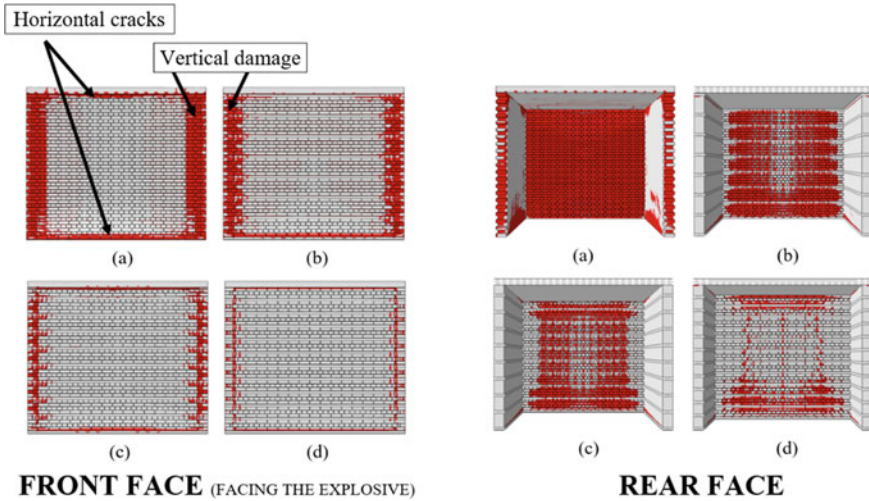
Fig. 9 Tension damage distribution on the front and rear sides of Wall #1 at a scaled distance of 1.72 m/kg$^{1/3}$ for different FE models at $t = 13.80$ ms: **a** #1 (without bands), **b** #4 (RC band after every 5 courses), **c** #3 (band after every 4 courses), and **d** #2 (band after every 3 courses) (red color: "damaged region")

by 72%, shear stress by 56%, and damage dissipation energy (or damage) by 88% in comparison to unreinforced masonry target wall under the maximum explosive load of 8.40 kg TNT considered at a scaled distance of 1.72 m/kg$^{1/3}$. The use of the horizontal band in the target wall after every four courses decreases the central displacement by 58%, shear stress by 41%, and damage by 81% with respect to the unreinforced target wall subjected to the maximum explosive charge of 8.40 kg TNT. The reduction of 46% in central displacement, 34% in shear stress, and 72% in the damage has been observed in the target wall strengthened with the horizontal band after every five courses with respect to the displacement, shear stress, and damage in the unreinforced target wall. The application of the horizontal RC band in the target wall considered in this study improves its performance with regards to central displacement and damage dissipation energy; however, the band after every three courses in the wall is found to be more effectively improving the cracking resistance under the maximum explosive load of 8.40 kg TNT considered. The above conclusions may prove to be useful to not only design engineers but also the sectional committee for developing the codal provisions of the masonry structures likely to take air-blast loads.

References

1. Anas MS, Ansari MdI, Alam M (2020) Performance of masonry heritage building under air-blast pressure without and with ground shock. Aust J Struct Eng 21(4):329–344
2. Abdullah FK, Cunningham SL, Gillie M (2017) Simulating masonry wall behavior using a simplified micro-model approach. Eng Struct 151:349–365
3. Valente M, Milani G (2016) Non-linear dynamic and static analyses on eight historical masonry towers in the north-east of Italy. Eng Struct 114(1):241–270
4. Valente M, Milani G (2016) Seismic assessment of historical masonry towers by means of simplified approaches and standard FEM. Constr Build Mater 108(1):74–104
5. Anas SM, Ansari Md I, Alam M (2021) A study on existing masonry heritage building to explosive-induced blast loading and its response. Int J Struct Eng (Article in press)
6. Anas SM, Alam M (2021) Performance of simply supported concrete beams reinforced with high-strength polymer re-bars under blast-induced impulsive loading. Int J Struct Eng (Article in press)
7. Anas SM, Alam M, Umair M (2021) Experimental and numerical investigations on performance of reinforced concrete slabs under explosive-induced air-blast loading: a state-of-the-art review. In: Structures, vol 31. Elsevier, pp 428–461
8. Anas SM, Alam M (2021) Air-blast response of free-standing: (1) Unreinforced brick masonry wall, (2) Cavity RC wall, (3) RC walls with (i) Bricks, (ii) Sand, in the cavity: a macro-modeling approach. In: Marano GC, Ray Chaudhuri S, Unni Kartha G, Kavitha PE, Prasad R, Achison RJ (eds) Proceedings of SECON'21. SECON 2021. Lecture notes in civil engineering, vol 171. Springer, Cham, pp 921–930. https://doi.org/10.1007/978-981-33-6389-2_18
9. Anas SM, Alam M (2021) Comparison of existing empirical equations for blast peak positive overpressure from spherical free air and hemispherical surface bursts. Iran J Sci Technol Trans Civil Eng. https://doi.org/10.1007/s40996-021-00718-4
10. Anas SM, Alam M, Umair M (2021) Performance of on-ground double-roof RCC shelter with energy absorption layers under close-in air-blast loading. Asian J Civil Eng. https://doi.org/10.1007/s42107-021-00395-8
11. Anas SM, Alam M, Umair M (2021) Air-blast and ground shockwave parameters, shallow underground blasting, on the ground and buried shallow underground blast-resistant shelters: a review. Int J Protective Struct. https://doi.org/10.1177/20414196211048910
12. Carney P, Myers JJ (2016) Out-of-plane static and blast resistance of unreinforced masonry wall connections strengthened with FRP. Am Concr Inst Special Publ ACI 230(4):229–248
13. Dennis TS, Baylot TJ, Woodson CS (2002) Response of ¼-scale concrete masonry unit (CMU) walls to blast. J Eng Mech 128(2):134–142
14. Gabrielson B, Wilton C, Kaplan K (1975) Response of arching walls and debris from interior walls caused by blast loading. Tech Rep URS Research Company, San Mateo, CA
15. Hrynyk DT, Myers JJ (2008) Out-of-plane behavior of URM arching walls with modern blast retrofits: experimental results and analytical model. J Struct Eng 134(10):1589–1597
16. Irshidat M, Al-Ostaz A, Cheng A, Mullen C (2009) Blast resistance of unreinforced masonry (URM) walls retrofitted with Nano-reinforced elastomeric materials. In: Structures congress 2009. Texas, US, pp 2133–2142
17. Pereira MJ, Campos J, Lourenco BP (2015) Masonry infill walls under blast loading using confined underwater blast wave generators (WBWG). Eng Struct 92(1):69–83
18. Wei X, Stewart GM (2010) Model validation and parametric study on the blast response of unreinforced masonry walls. Int J Impact Eng 37(11):1150–1159
19. Zapata JB, Weggel CD (2008) Collapse study of an unreinforced masonry bearing wall building subjected to internal blast loading. J Perform Constr Facil 22(2):92–100
20. Ahmad S, Elahi A, Pervaiz H, Rahman AGA, Barbhuiya S (2014) Experimental study of masonry wall exposed to blast loading. Mater De Constr 64(313):1–11
21. Gagnet ME, Hoemann MJ, Davidson SJ (2017) Assessment of resistance definitions used for blast analysis of unreinforced masonry walls. Int J Protective Struct 8(1):125–151

22. IS 4326 (1993) Indian standard earthquake resistant design and construction of buildings-code of practice. Bureau of Indian Standards, New Delhi
23. Anas SM, Alam M, Umair M (2021) Performance of one-way concrete slabs reinforced with conventional and polymer re-bars under air-blast loading. In: Chandrasekaran S, Kumar S, Madhuri S (eds) Recent advances in structural engineering. Lecture notes in civil engineering, vol 135. Springer, Singapore. https://doi.org/10.1007/978-981-33-6389-2_18
24. Anas SM, Alam M, Umair M (2020) Performance of one-way composite reinforced concrete slabs under explosive-induced blast loading. In: 1st international conference on energetics, civil and agricultural engineering 2020, ICECAE 2020, Tashkent, Uzbekistan, vol 614. https://doi.org/10.1088/1755-1315/614/1/012094
25. Hao H, Hao Y, Li J, Chen W (2016) Review of the current practices in blast-resistant analysis and design of concrete structures. Adv Struct Eng 19(8):1193–1223
26. Yu J, Gan PY, Wu J, Wu H (2019) Effect of concrete masonry infill walls on progressive collapse performance of reinforced concrete infilled frames. Eng Struct 191:179–193
27. Lee J, Fenves LG (1998) Plastic-damage model for cyclic loading of concrete structures. J Eng Mech 124(8):892–900
28. Lubliner J, Oliver J, Oller S, Onate E (1989) A plastic-damage model for concrete. Int J Solids Struct 25(3):299–326
29. ABAQUS/CAE FEA Program (2017) Concrete-damaged plasticity model, explicit solver, three dimensional solid element library. ABAQUS DS-SIMULIA User Manual
30. Hafezolghorani M, Hejazi F, Vaghei R, Jaafar BSM, Karimzade K (2017) Simplified damage plasticity model for concrete. Struct Eng Int 27(1):68–78
31. Wu C, Hao H (2005) Modeling of simultaneous ground shock and airblast pressure on nearby structures from surface explosions. Int J Impact Eng 31(6):699–717
32. Goel DM, Matsagar AV (2014) Blast-resistant design of structures. Pract Periodical Struct Des Constr 19(2):040140071–040140079
33. IS 4991 (1968) Criteria for blast resistant design of structures for explosions above ground. Bureau of Indian Standards, New Delhi
34. TM 5-1300 (1990) Structures to resist the effects of accidental explosions. Technical Manual, Joint Department of the Army, the Navy, and the Air Force, US

Particle Image Velocimetry Dynamic Analysis on the Penstock Vortex Flow for the Dam Reliability Study

N. M. Zahari, M. H. Zawawi, Fei Chong Ng, L. M. Sidek, Aizat Abas, F. Nurhikmah, Nurhanani A. Aziz, Tung Lun Hao, and M. R. M. Radzi

Abstract This paper detailed the particle image velocimetry (PIV) experimental work in the study of vortex flow in the penstock section. The scaled-down physical model for the penstock pipe and turbines was constructed for the PIV analysis. From the study, it was found that there is no visible vortex being observed in the penstock pipe at the present operating configuration. Upon being compared with the numerical simulated penstock flow, a slight discrepancy of 12% is recorded, indicating the findings are acceptable. In conclusion, the PIV approach on the scaled-down model is suitable for the flow visualization work in dam reliability analysis.

Keywords Particle image velocimetry · Penstock · Vortex

1 Introduction

Vortex is defined as a swirling flow region that rotating around an axis, either be straight or be curved. Vortex generally formed during the abrupt transition from open channel flow to pressure flow. In the dam structure, vortex formation may attribute to the operation conditions and is undesirable [1, 2]. Consequently, the power generated by the turbine blades would be decreased due to the vortex formation. Thus, the hydroelectric power generation potentially lowered to 80%. Additionally, both

N. M. Zahari (✉) · M. H. Zawawi · F. Nurhikmah · N. A. Aziz · T. L. Hao
Department of Civil Engineering, College of Engineering, Universiti Tenaga Nasional (UNITEN), 43000 Kajang, Selangor, Malaysia

F. C. Ng · A. Abas
School of Mechanical Engineering, Universiti Sains Malaysia, Engineering Campus, 14300 Nibong Tebal, Pulau Pinang, Malaysia

L. M. Sidek
Institute of Energy Infrastructure (IEI), Universiti Tenaga Nasional (UNITEN), 43000 Kajang, Selangor, Malaysia

M. R. M. Radzi
Hydro Life Extention Program (HELP), Business Development (Asset) Unit, TNB Power Generation Division, PJX HM Shah Tower, Jalan Persiaran Barat, 46050 Petaling Jaya, Selangor, Malaysia

erosion and accretion are likely to occur and further pose a threat to the reliability of dam structure and affect the continuous operation of the dam and hydroelectric power station.

Therefore, dam reliability study was essential to safeguard the structural integrity and performances of dam and hydroelectric generation [3, 4]. In the past works of literature, the structural reliability of the dam was mainly investigated from the perspective on the interaction with fluid flow. The structural stress and deformation were induced by the rapid and continuous water flow throughout the dam operation [5–8]. To scrutinize the vortex flow in the intake section, flow visualization approach can be implemented to study vortex flow dynamics. Accordingly, the particle image velocimetry (PIV) was adopted to analyze the dynamic nature of vortex flow. PIV can be efficiently executed using transparent model and clear working fluid with seeding particles. Previously, PIV had seen various successful applications in the various fluid flows sectors, such as hydraulic engineering [9] and electronic packaging [10, 11]. It was reported that PIV could provide substantial information on the flow dynamics and vectors, thereby PIV would be helpful in the investigation of vortex flow for the current context.

This works detailed the particle image velocimetry (PIV) experimental approach in the study of vortex flow observed in the penstock at bottom section of dam. A scaled-down physical model of the penstock and turbine model was constructed using clear Perspex block, which provided unobstructed view for the flow visualization during PIV analysis. The flow profile was studied to determine the dynamic nature of the penstock flow as subjected to the present operating condition.

2 Methodology

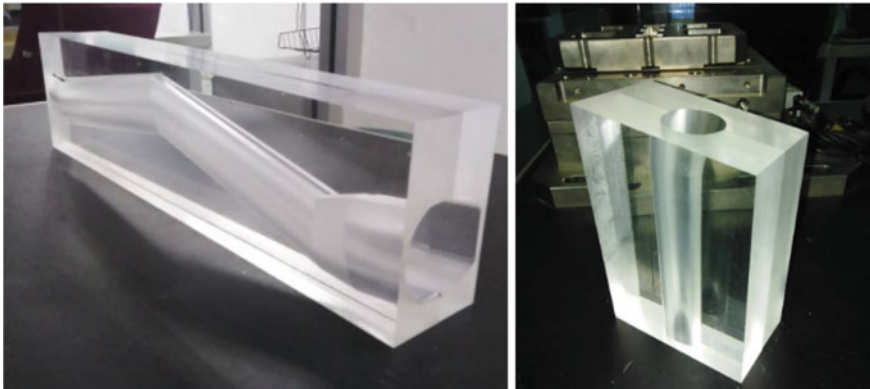### 2.1 Construction of Scaled-Down Penstock Hydraulic Model

The current investigated scaled-down (1:130) penstock pipe as located in the bottom section of investigated dam was detailed in the drawing given in Fig. 1. It generally composed of two main components, the pipe section and turbine housing with blades.

The scaled-down model of penstock pipe was fabricated using the computer numerical control (CNC) cutting machine. Clear Perspex was chosen as the material to provide unobstructed view during the flow visualization. To ease the construction and, thus, to accommodate the huge variation in the inclination angles along three planes, the upper and lower sections of penstock pipe were fabricated separately, as shown in Fig. 2. Subsequently, suitable amount of silicone sealant was applied on all interconnections upon joining both sections together to prevent water leakage.

Due to high complexity of turbine geometry, the 3D printing machine was used for its fabrication. Figures 3 and 4 showed the printed sections of the turbine house and the turbine blade, respectively. Lastly, all the penstock pipe, turbine housing, and turbine blades were assembled as shown in Fig. 5, for the use of subsequent particle image velocimetry experiment.
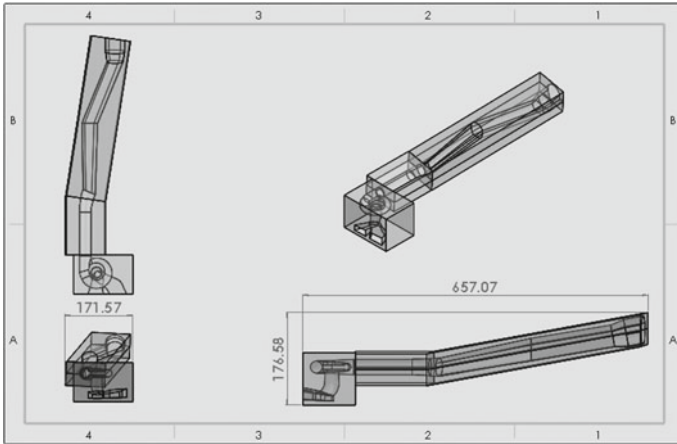
Fig. 1 Detailed view of the scaled-down penstock at the bottom section (mm)

Fig. 2 Upper section (left) and lower section (right) of the penstock pipe model

2.2 Construction of Scaled-Down Penstock Hydraulic Model

Particle image velocimetry (PIV) is a non-invasive optical method used to identify instantaneous vector field in a cross-sectional fluid flow. The velocity field can be determined based on the movement of the tracer particles that are being introduced to the flow. The tracer particles are illuminated at two-time instances that are subsequently being recorded using a camera. Since the time interval between the two light pulses are known, the magnitude and direction of the particles group can be determined. PIV translates the continuum Eulerian flow into particle Langrangian approach to visualize the flow dynamics especially its velocity vector [9–12].

Fig. 3 3D printed turbine housing

Fig. 4 3D printed turbine blades and shaft

Figure 6 illustrated the outline for the PIV experimental procedures, while Fig. 7 showed the actual PIV setup. After the setup was completed, the Dantec 10 μm seeding particles were mixed homogenously with water in the tank. Later, the thin laser sheet was directed on the plane of flow water and illuminating the seeding particles suspended along with the water flow. High-speed camera was placed perpendicularly in front of the illuminated plane to record and track the movement of seeding particles that suspended on the water flow. Finally, the post-processing was conducted

Fig. 5 Assembly of scaled-down penstock model
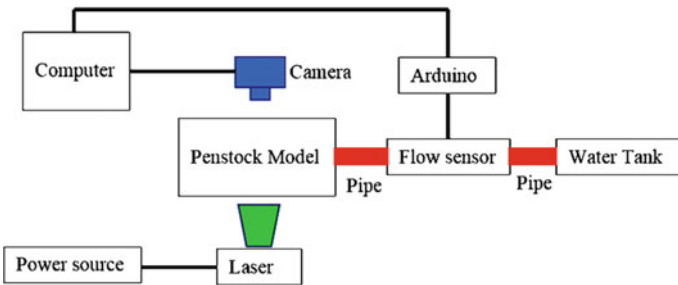
Fig. 6 Schematic of the PIV experiment in the investigation of water flow in scaled-down penstock model
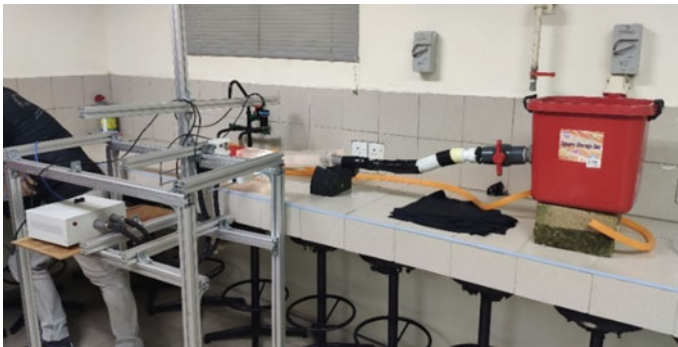
Fig. 7 Actual PIV experiment on the scaled-down penstock model

Fig. 8 Region (highlighted in red box) of the penstock pipe being investigated

to enhance the images quality and remove unwanted noises. The flow velocity distribution of water flow in penstock was analyzed based on the two consecutive images with known time interval, Δt. The flow velocity of water, u, is determined using the relative displacement of a neighboring seeding particle, Δx, related by the relation:

$$u = \frac{\Delta x}{\Delta t} \tag{1}$$

Figure 8 depicted the region of interest in which the flow being analyzed in the PIV experiment, which being identified as one of the critical part in the penstock. The camera was positioned directly above the model, focusing onto the region of interest. To attain dynamic similarity between the actual penstock and scaled-down model, the water flow rate is set at 1.181 l/s by considering the invariant of Froude number.

Figure 9 showed the post-processed of the captured image frames seeded with particles. The average flow field was obtained with frame rate of 240 frame per second (fps). To enhance the accuracy, the PIV experiments were repeated for three times on the same region.

3   Results and Discussion

Figure 10 shows the velocity vectors of the penstock flow as obtained from the PIV analysis, for three iterations. It was found that the flow in the investigated region is unsteady in nature. The flow direction changes because of the shape of the penstock. Nonetheless, there is no visible vortex formed as the flow vectors are in uniform flow despite being unsteady.
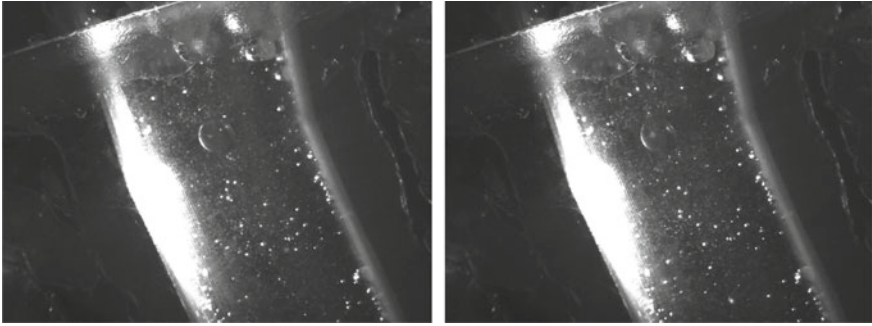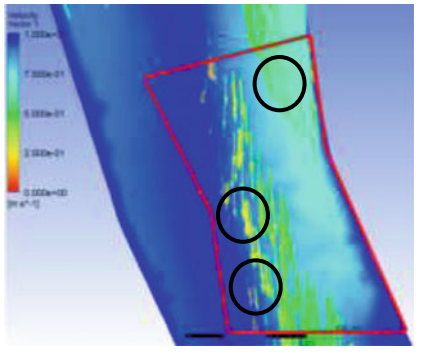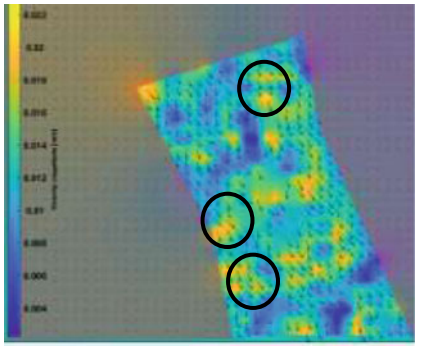
Fig. 9 Post-processed images
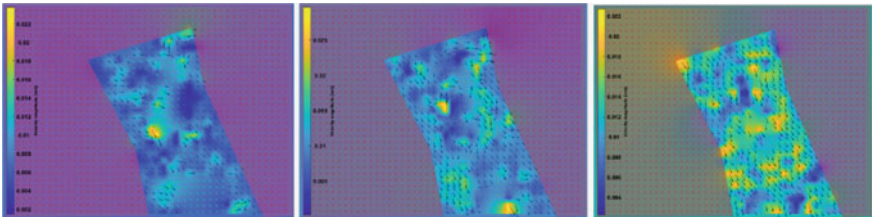
Fig. 10 Velocity vectors of the water flow at the investigated region

The maximum flow velocity as obtained from the PIV experiment is 0.022 m/s. Upon compared to the finite volume method (FVM)-based numerical simulated penstock flow with maximum flow velocity of 0.025 m/s, a slight discrepancy of 12% was recorded. In the engineering field of computational fluid dynamic (CFD) analyses, the acceptance tolerance on the numerical accuracy with respect the validating experiment is generally less than 15% as reported in the past works [13–15]. Nonetheless, this acceptance limit is subjective as it is heavily dependent on both the research requirements and the complexity of models. Qualitatively, both the numerical and experimental flow patterns and velocity contours are comparable. The black circles in Table 1 emphasized the similarity between the numerical simulation and PIV experiment flow patterns and behaviors, in terms of the streamline directions at each location. Both experimental and numerical flow vectors are flowing in unsteady uniform direction. Moreover, both findings revealed the middle section of the investigated plane has faster flow velocity compared to the side sections.

4 Conclusion

Particle image velocimetry (PIV) experimental analysis was applied on the dam reliability problem, to study the vortex flow in the penstock of dam bottom outlet.

Table 1 Comparison of simulated and experimental flow velocity contours

Finite volume method simulation	Particle image velocimetry experiment
Maximal velocity: 0.025 m/s	Maximal velocity: 0.022 m/s

Scaled-down physical model of penstock at the scale of 1:130 was fabricated using clear Perspex block. The experiment showed there is no visible vortex being formed on the region of penstock pipe, despite the flow in the vicinity is unsteady in nature. Further comparison with numerical simulated flow in penstock revealed there is 12% discrepancy existed between the experimental and numerical maximal flow velocities, for which it indicated the findings were acceptable. Using the prescribed PIV setup, the flow visualization in dam structure is made possible and viable for the subsequent dam reliability study.

References

1. Azman A et al (2020) The impact of Vortex formation due to the operational dam condition: a review. IOP Conf Ser: Mater Sci Eng 920(1). https://doi.org/10.1088/1757-899X/920/1/012025
2. Nurhikmah F et al (2020) Review on Vortex simulation using computational fluid dynamic. AIP Conf Proc 2291:020084. https://doi.org/10.1063/5.0024634
3. Siacara AT, Napa-García GF, Beck AT, Futai MM (2020) Reliability analysis of earth dams using direct coupling. J Rock Mech Geotech Eng 12(2):366–380. https://doi.org/10.1016/j.jrmge.2019.07.012
4. Yi P, Liu J, Xu C (2015) Reliability analysis of high rockfill dam stability. Math Probl Eng 2015:512648. https://doi.org/10.1155/2015/512648
5. Ng FC et al (2020) Fluid/structure interaction numerical study on the mechanical integrity of water dam reservoir banks. IOP Conf Ser: Mater Sci Eng 815(1). https://doi.org/10.1088/1757-899X/815/1/012021
6. Zawawi MH et al (2020) Reliability analysis on the reservoir dam spillway structure using fluid-structure interaction. IOP Conf Ser: Mater Sci Eng 920(1). https://doi.org/10.1088/1757-899X/920/1/012030
7. Ng FC et al (2018) Fluid/structure interaction study on the variation of radial gate's gap height in dam. IOP Conf Ser: Mater Sci Eng 370(1). https://doi.org/10.1088/1757-899X/370/1/012063

8. Ng FC et al (2018) Effect of the gap height of radial gate on the volumetric flow rate in dam. IOP Conf Ser: Mater Sci Eng 370(1). https://doi.org/10.1088/1757-899X/370/1/012062

9. Azman A et al (2020) Effect of barrier height on the design of stepped spillway using smoothed particle hydrodynamics and particle image velocimetry. KSCE J Civ Eng 24(2). https://doi.org/10.1007/s12205-020-1605-x

10. Ng FC, Abas A, Abdullah MZ (2018) Effect of solder bump shapes on underfill flow in flip-chip encapsulation using analytical, numerical and PIV experimental approaches. Microelectron Reliab 81. https://doi.org/10.1016/j.microrel.2017.12.025

11. Ng FC et al (2018) Visualization of underfill flow in ball grid array (BGA) using particle image velocimetry (PIV). IOP Conf Ser: Mater Sci Eng 370(1). https://doi.org/10.1088/1757-899X/370/1/012064

12. Zahari NM et al (2020) Simulation on air-fly ash particles using discrete phase method. IOP Conf Ser: Mater Sci Eng 920:012021. https://doi.org/10.1088/1757-899X/920/1/012021

13. Abas A et al (2018) Effect of scale size, orientation type and dispensing method on void formation in the CUF encapsulation of BGA. Sādhanā 43(4):1–14. https://doi.org/10.1007/s12046-018-0849-3

14. Sapian AR (2009) Validation of the computational fluid dynamics (CFD) method for predicting wind flow around a high-rise building (HRB) in an urban boundary layer condition. J Constr Dev Countries 14(2):1–20

15. Ng FC et al (2020) Symmetrical unit-cell numerical approach for flip-chip underfill flow simulation. CFD Lett 12(8):55–63. https://doi.org/10.37934/cfdl.12.8.5563

Performance of Base-Isolated RC Building Under Surface Blast Loading

Sunita Tolani, S. D. Bharti, M. K. Shrimali, and Sourabh Vern

Abstract The effectiveness of the base-isolation technique for the mitigation of structural response under earthquake and wind forces has been widely investigated. The response of a building under surface blast loading is critical, as in that case the structure is subjected to both the high magnitude air pressure and ground shock effect. In the present study, the usefulness of the base-isolation technique in reducing the structural damage caused by the surface explosion is investigated. For this purpose, non-linear time history analysis of the 3D model of a six-storey building under surface explosion loading is performed. Responses of the building under the fixed-base condition and isolated-base condition are compared to investigate the effectiveness of base isolation in mitigating the surface blast effect. Also, the effect of base-isolator parameters on its performance is investigated. Results of the study show that base isolation can be useful in mitigating the surface explosion effect on a building if a proper selection of isolator parameters is made.

Keywords N-Z bearing · Surface blast · Air pressure · Ground shock · Non-linear time history analysis

1 Introduction

Due to increased terrorist attacks on buildings in the past few decades, the concern of structural engineers towards the safety of structures against blast loading is increased. Many uncertainties are involved with the blast loading as its intensity depends upon its distance from the building and the charge weight used for the explosion. Apart from this, the location of the charge weight with respect to the ground surface also influences the nature of the load exerted on the building. An air blast exerts sudden air pressure on the building, while a surface blast causes both the air pressure and ground vibration effect on the building. The effect of air blast effect on buildings is widely researched [1–4], whereas literature on the effect of surface blast considering both

S. Tolani (✉) · S. D. Bharti · M. K. Shrimali · S. Vern
National Center for Disaster Mitigation and Management, Malaviya National Institute of Technology Jaipur, Jaipur, India

the air pressure and ground vibration effect is meagre. Wu and Hao [5] developed empirical equations to obtain air pressure and ground shock time histories generated due to surface explosion with the help of numerical simulation of surface blast on granite rock mass. In another study, Wu and Hao [6] studied the effect of the surface blast on a single storey masonry infilled RC building and found that surface blast-induced air pressure governs the response of the building for small scaled distances, whereas for large scaled distance ground shock effect becomes predominant. In the previous studies [7, 8], it is observed that for multi-storey buildings, relative effects of surface blast-induced ground shock and air pressure depend upon various factors, such as building height, charge weight and standoff distance. For small buildings, the ground shock effect governs the response of the building for large standoff distances only, whereas for medium to high-rise buildings ground shock effect may govern the response for small standoff distance also.

Many studies have been carried out for the mitigation of blast effect on structures. Mondal et al. [9] investigated the usefulness of N-Z bearing for mitigation of the effect underground blast-induced ground motion. Niollet et al. [10] proposed that mild-steel cylindrical solid bars can be used as blast barriers to mitigate the effect of air blast loading. Zhang and Phillips [11] investigated the performance of a base-isolated system under surface blast-induced air pressure loading and proposed that supplemental passive devices such as non-linear bumpers and tuned mass dampers can be used to improve performance of the base-isolated building under blast loading. In the available literature on base-isolated buildings under blast loading, the air blast or underground blast effects are considered. Performance of base-isolated buildings under surface blast conditions considering both the air pressure and ground shock effect is not investigated.

In the present study, the effectiveness of the base-isolation technique in reducing the building response under surface blast condition is investigated. Also, the effect of the isolator parameters on the response of the base-isolated structure is studied, and a combination of isolator parameters is found for which the damage of the structure is minimum. A six-storey building is considered for investigation. Charge weight is considered as 500 kg TNT and standoff distances are taken as 5, 10, 15 and 30 m. Response quantities include peak top floor displacement, inter-storey drift ratio, number of hinges formed in building and isolator displacement.

2 Theory

2.1 Modelling of the Building

The reinforced concrete six-storey building is modelled using SAP 2000 (version 17) software. The columns and beams are modelled as line elements and the slabs are modelled as shell elements. The building is designed for gravity load and earthquake load as per the recommendations of the Indian seismic code [12]. To investigate the
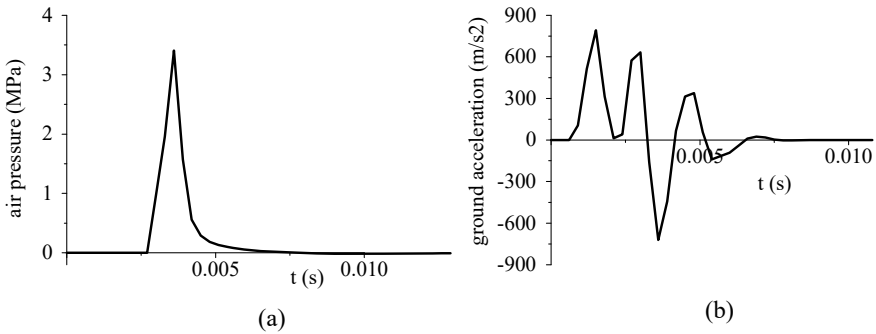
Fig. 1 **a** Simulated air pressure time history at the bottom storey, **b** Simulated ground acceleration time history for 500 kg of TNT at 5 m standoff distance

effectiveness of the base isolation technique to mitigate blast load effect, the response of the building is investigated for two base conditions, i.e. (i) fixed-base condition and (ii) isolated base condition. The non-linear time history analysis of the building is carried out with the help of the Hilber–Hughes–Taylor direct time integration approach ($\beta = 0.25$, $\gamma = 0.5$). The Rayleigh mass and stiffness proportional damping is considered with 5% critical damping for the first two vibration modes. The non-linear deformation of the building is taken into account by providing plastic hinges at the beam and column ends and assigning the default back-bone curve of the SAP 2000 for the hysteretic plastic hinge behaviour.

2.2 Blast Loading

The air pressure time histories and ground acceleration time histories for different blast load conditions are simulated with the help of available literature [5]. Figure 1 shows air pressure time history and ground shock time history for 500 kg TNT and 5 m standoff distance.

The air pressure time histories are applied to the front face of the building exposed to the blast source, and ground acceleration time history is applied at the base of the structure.

2.3 Base-Isolation Technique

For base-isolated building, N-Z bearing is considered as a base isolator. Bouc-Wen's bilinear hysteretic model is considered for force–deformation behaviour of the building. There are mainly three parameters that describe Wen's model namely (i)

**Fig. 2** Bouc-Wen's bilinear force–deformation curve
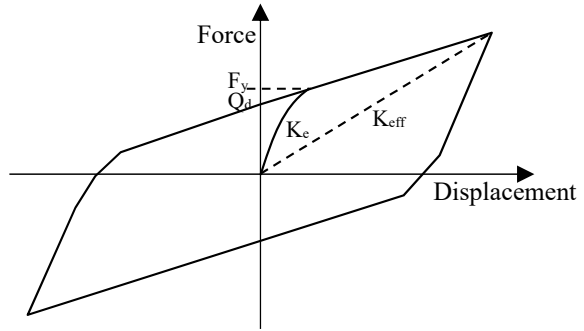
yield strength (F_y), (ii) post-yield stiffness ratio (α) and (iii) characteristic strength (Q_d) as shown in Fig. 2.

3 Numerical Study

A six-storey reinforced concrete building is considered for investigation. Figure 3 shows 3-D view of the building. The building has four equal spans in both directions with each span of 4 m length and each storey height equal to 3 m. The dead load of the building includes self-weight of the structural elements (column, beam and slab), floor finish load and wall load. Live load on each floor is considered as 3 KN/m^2.

Fig. 3 3-D view of building
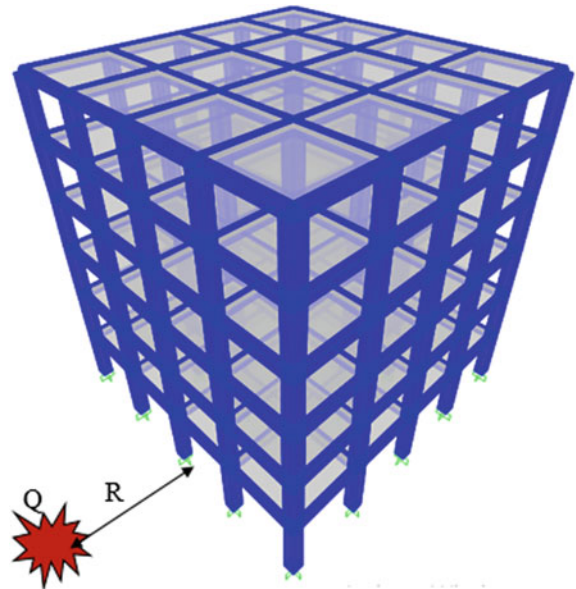
Table 1 Properties of building

Beam size (mm)	Column size (mm)	Beam R/F (%)	Column R/F (%)	Slab Size (mm)	Fundamental period T_1(s)
350 × 450	550 × 550	1.2 (top face) 0.9 (bottom face)	1.9	150	0.63

Table 2 Properties of base-isolator

Effective stiffness 'K_{eff}' (KN/m)	Initial stiffness 'k_1' (KN/m)	Effective damping 'β' (%)	Post-Yield stiffness ratio (α)	Yield force (F_y)	Vertical stiffness 'Kv' (KN/m)
1240	9765	10	0.1	39.1	200,758

The concrete grade is considered as M30 and steel grade as Fe 415. The building is designed for the gravity load and peak ground acceleration 0.36 g (Zone V) as per IS 1893-2002 [12]. Properties of the building are shown in Table 1.

Properties of the N-Z bearing used for the analysis of base-isolated building are shown in Table 2. The fundamental period of the base-isolated structure is 1.8 s.

Effect of the isolator parameters on the response of base-isolated building is studied for different values of effective damping (10%, 15% and 20%) and post-yield stiffness ratio (0.05, 0.1, 0.15, 0.2). For blast load analysis charge weight is considered as 500 kg TNT and standoff distances are considered as 5, 1, 15 and 30 m.

4 Results and Discussions

The response of the building is investigated under four cases of surface blast:

Case 1: 500 kg TNT blast at 5 m standoff distance;
Case 2: 500 kg TNT blast at 10 m standoff distance;
Case 3: 500 kg TNT blast at 15 m standoff distance;
Case 4: 500 kg TNT blast at 30 m standoff distance.

Figure 4 shows top floor displacement of fixed-base building cased due to the four above-mentioned surface blast conditions. Plots show the top floor displacement of the building for air pressure only, ground shock only and for the combined effect of both the forces. It can be seen from the figures that for distances 5–15 m (Case 1, 2, 3), vibrations of the building caused due to air pressure and ground shock are in opposite phase, and for 30 m standoff distance (Case 4), vibrations caused due to both the forces are in the same phase. Thus, the combined effect may be additive of the two effects, or it may be the difference of the two depending upon the phases of vibration.
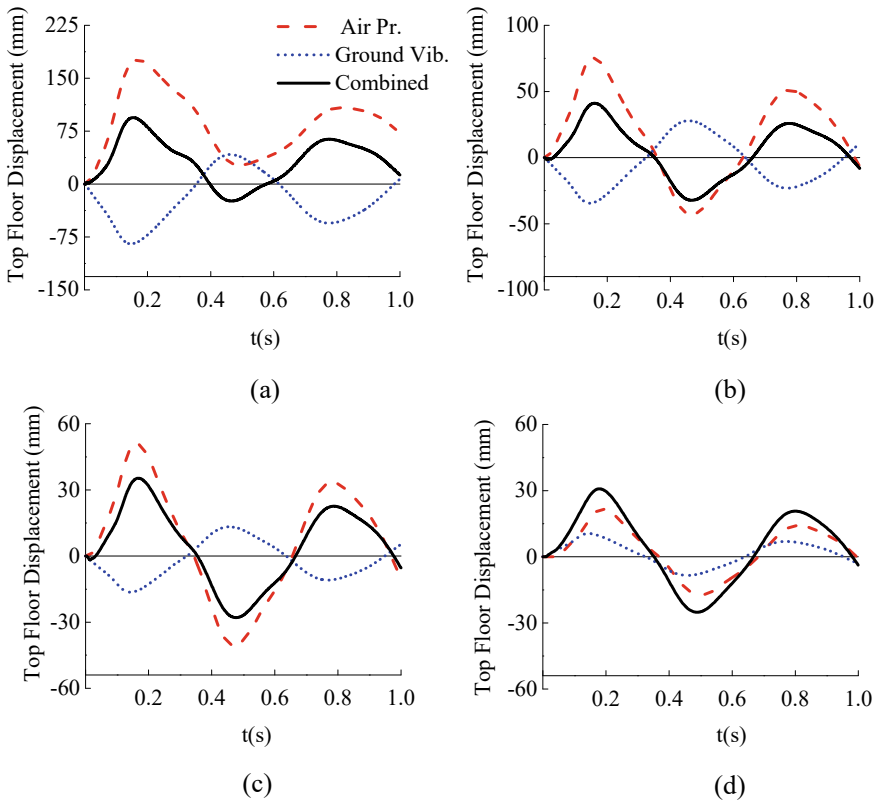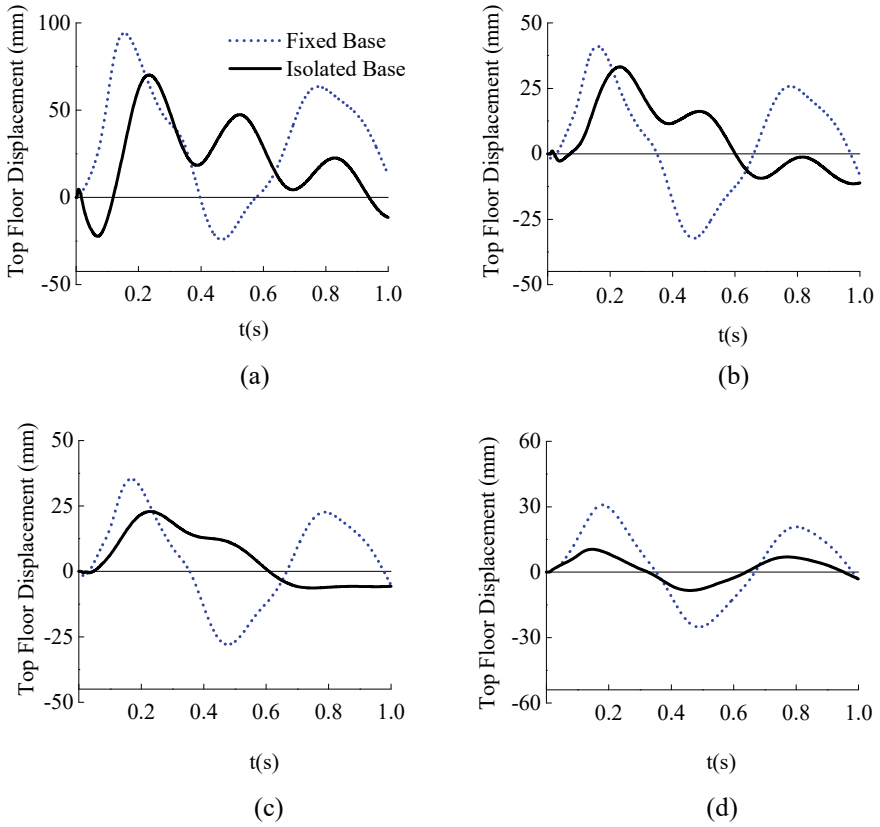
Fig. 4 Top floor displacement of fixed-base building due to surface explosion. **a** Case 1; **b** Case 2; **c** Case 3; **d** Case 4

Figure 5 shows top floor displacement caused due to the combined effect of the air pressure and ground shock generated by the surface blast for fixed-base building and base-isolated building. It can be seen from the figures that for small standoff distances (5–15 m), the reduction in peak top floor displacement is 20–25%, and for large standoff distance, the response is reduced by 35%.

Figures 6 and 7 show peak responses of building under the fixed-base condition and isolated-base condition, respectively. It can be seen that there is almost a 20–30% reduction in top floor displacement by providing base-isolation system. Maximum inter-storey drift is reduced for Case 1, but for Cases 2, 3 and 4, no considerable reduction is observed due to base isolation. The number of hinges formed, which represent damage to the structure is significantly reduced for the base-isolated building. Thus, it can be surmised that with the help of base isolation, damage of the building caused by the surface explosion can be reduced.

Figure 8 shows the variation of the number of hinges formed and isolator displacement against the post-yield stiffness ratio (α) for surface blast Case-1. The variations

Fig. 5 Top floor displacement of building due to surface explosion of 500 kg TNT at standoff distance. **a** Case 1; **b** Case 2; **c** Case 3; **d** Case 4
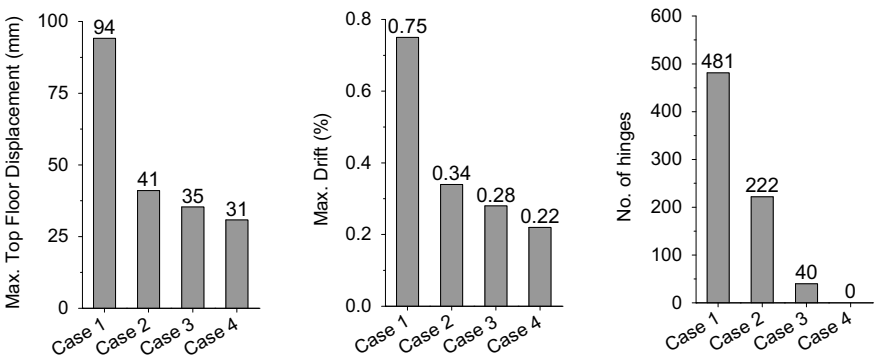
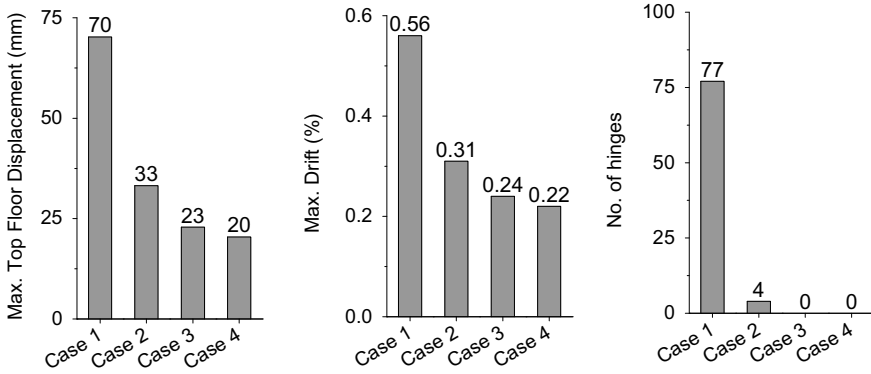**Fig. 6** Peak responses of fixed-base building

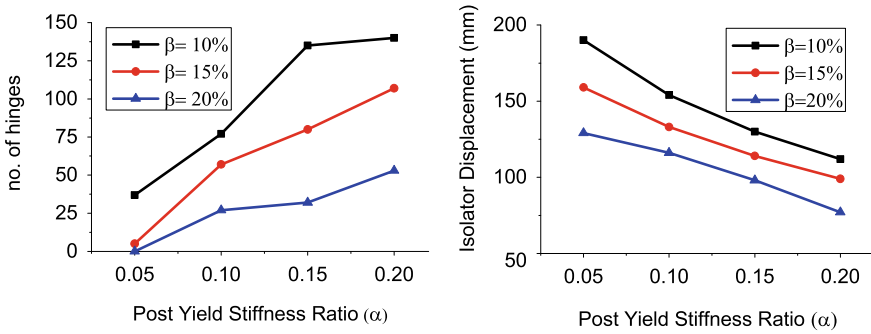**Fig. 7** Peak responses of base-isolated building

Fig. 8 Effect of post-yield stiffness ratio and isolator damping ratio on the response of base-isolated building under surface blast condition (Case-1)

are plotted for different values of isolator damping ($\beta = 10\%$, 15% and 20%). It is observed from the figures that with an increase in the value of α, the isolator displacement decreases, but the number of hinges formed in the building increases. Further, an increase in the isolator damping decreases both the bearing displacement and the number of hinges formed. From the figure, it can be seen that for $\alpha = 0.05$ and $\beta = 20\%$ no hinges are formed in the building.

5 Conclusions

Effectiveness of base-isolation technique in reducing the response of building structure under surface blast loading is investigated, and the influence of isolator properties on the response of base-isolated building is examined. The study yielded the following results:

1. Base-isolation technique is effective in reducing top floor displacement, inter-storey drift and damage (number of hinges) of the building under near blast condition.
2. For distant blast, top floor displacement and the number of hinges formed are reduced due to base isolation, but there is not a considerable reduction in inter-storey drift.
3. For a base-isolated building under surface blast conditions, with the increase in the value of the post-yield stiffness ratio, the isolator displacement decreases, but damage to the structure (number of hinges) increases.
4. With the increase in isolator damping ratio, both the isolator displacement and the number of hinges are reduced. Thus, damage to the structure can be minimized by proper selection of isolator parameters.

References

1. Ngo T, Mendis P, Gupta A, Ramsay J (2007) Blast loading and blast effects on structures—an overview. Electron J Struct Eng 7:76–91
2. Goel MD, Matsagar VA, Gupta AK, Marburg S (2012) An abridged review of blast wave parameters. Def Sci J 62:300–306. https://doi.org/10.14429/dsj.62.1149
3. Jayasooriya R, Thambiratnam DP, Perera NJ, Kosse V (2011) Blast and residual capacity analysis of reinforced concrete framed buildings. Eng Struct 33:3483–3495. https://doi.org/10.1016/j.engstruct.2011.07.011
4. Qian K, Li B (2017) Dynamic and residual behavior of reinforced concrete floors following instantaneous removal of a column. Eng Struct 148:175–184. https://doi.org/10.1016/j.engstruct.2017.06.059
5. Wu C, Hao H (2005) Modeling of simultaneous ground shock and airblast pressure on nearby structures from surface explosions. Int J Impact Eng 31:699–717. https://doi.org/10.1016/j.ijimpeng.2004.03.002
6. Wu C, Hao H (2007) Numerical simulation of structural response and damage to simultaneous ground shock and airblast loads. Int J Impact Eng 34:556–572. https://doi.org/10.1016/j.ijimpeng.2005.11.003
7. Tolani S, Bharti SD, Shrimali MK, Datta TK (2020) Effect of surface blast on multistory buildings. J Perform Constr Facil 34:1–15. https://doi.org/10.1061/(ASCE)CF.1943-5509.0001415
8. Tolani S, Bharti SD, Shrimali MK, Datta TK (2021) Estimation of the effect of surface blast on buildings. Proc Inst Civ Eng Struct Build 55:1–13. https://doi.org/10.1680/jstbu.19.00055
9. Mondal PD, Ghosh AD, Chakraborty S (2014) Performance of N-Z systems in the mitigation of underground blast induced vibration of structures. J Vib Control 20:2019–2031. https://doi.org/10.1177/1077546313481050
10. Niollet JE, Chung Kim Yuen S, Nurick GN (2015) A study to assess the use of cylindrical bars as blast barriers. Int J Protective Struct 6:263–286. https://doi.org/10.1260/2041-4196.6.2.263
11. Zhang R, Phillips BM (2016) Performance and protection of base-isolated structures under blast loading. J Eng Mech 138:683–694. https://doi.org/10.1061/(ASCE)EM.1943-7889
12. Bureau of Indian Standards (2002) Criteria for earthquake resistant design of structures, pp 500

Influence of Charge Locations on Close-in Air-blast Response of Pre-tensioned Concrete U-girder

S. M. Anas , **Mehtab Alam** , **and Mohammad Umair**

Abstract Safety of the public transportation infrastructure, especially bridges, against explosive-induced detonation is of serious concern for the civic life in the megacities, and their failure may cause severe social and economic consequences. The current state-of-the-art of design practices for the bridge structures do not take into consideration the air-blast loading generated by explosions. Explosion-induced loading is generally of impulsive nature. Response of the structure subjected to such extreme loading shall depend upon the magnitude of the loading and stiffness of the structure. The load and the stiffness shall decide the degree of damage to the structure. With small damage, the structure may respond in the form of free vibrations. However, a severely damaged structure of course shall undergo large plastic deformations. Girders being the critical components of most of the bridges are independent of the superstructure types, and thus, their survival is of paramount importance for the integrity of the bridge. Therefore, damage resistance and dynamic response of the girder under air-blast loading are of significant importance. In this study, the influence of the charge locations on the performance of the pre-tensioned simply supported concrete U-girder under close-in air-blast loading has been investigated using the commercial software, Abaqus/CAE 2017. A finite element model of the girder supported on the elastomeric bearings with the rail track and rolling stock has been developed for this purpose. The model is subjected to the blast peak overpressures of 982, 3877, and 7004 MPa. A sophisticated material damage model has been utilized in the study for the damage assessment of the girder. The maximum displacements of the U-girder have been compared with the provisions of the American design standard codes of practice for bridge superstructures.

S. M. Anas (✉) · M. Alam · M. Umair
Department of Civil Engineering, Faculty of Engineering and Technology, Jamia Millia Islamia, Delhi, New Delhi 110025, India

M. Alam
e-mail: malam1@jmi.ac.in

M. Umair
e-mail: mumair@jmi.ac.in

1 Introduction

Public transportation infrastructure is one of the lifelines of the metropolitan cities. The rise in fanaticism and accidental explosions challenge the safety of the public transportation infrastructure, especially bridges, against explosive-induced detonation and is, therefore, receiving attention from structural engineers [24]. Such explosive loadings can affect city life by causing great inconvenience leading to chaos in the city. During warfare, such events may have far-reaching consequences. The bridges are designed for all possible loads other than the explosive-induced loadings [23, 24]. Limited and general provisions for the prevention of progressive collapse of the bridge structures after blasts are discussed in the current bridge design standards [23]. Therefore, it is interesting to study the response of a bridge structure under the air-blast loading. In the present study, a simply supported U-girder of pre-tensioned concrete has been considered to study the effect of the charge locations on the blast performance of the girder.

In recent decades, there has been a remarkable shift in the manner in which bridge construction projects are implemented in urban India. The construction of pre-cast superstructure depends upon the feasibility of the transportation, type of pre-casting facility (longline/short bench), type of pre-stressing (pre-/post-tensioning), the methodology of construction (segmental/full-span), and cross-section of the girder (I-girder/box girder/U-girder for two tracks/segmental two-track U-girder) [36]. The typical pre-stressed girder sections that have been used by the Rail Corporations (RCs) are: (1) pre-/post-tensioned I-girders with a cast in situ slab, (2) segmental box girder, (3) segmental box girder with external pre-stressing, (4) segmental two-track post-tensioned U-girder, and (5) pre-tensioned twin U-girder [36]. The sectional efficiencies of the I-, box-, and U-girders are 0.47, 0.52, and 0.50, respectively [36]. Over the years, the box and I-shaped girders have been used in the construction of the metro-bridges. Recently, RCs have decided to standardize the usage of the U-shaped pre-tensioned girders as it saves both time and cost of construction. Besides, the laying of tracks can be done quickly on U-girders. The approximate span and weight of one U-girder are 28 m and 160 MT, respectively [36].

Studies on the performance of the bridges under air-blast loading are very rare in comparison to studies on the blast response of the buildings. Williamson and Winget [37] discussed the effects of air-blast on the bridge components and outlined a procedure to mitigate explosive-induced threats through risk assessment and risk management strategies. Winget et al. [40] outlined a procedure for the blast-resistant design of bridges. It was reported that the bridge geometry and clearance can greatly affect the below-deck explosion. Williamson et al. [38, 39] experimentally and numerically investigated the effect of pier geometry, standoff distance, and explosive charge on

the blast performance of the reinforced concrete (RC) bridge columns at different standoff distances ranging from 2.40 to 5.80y m, where "*y*" is a standoff parameter. It was concluded that the geometry of the pier significantly affects the blast performance in comparison to other parameters considered. Fujikura et al. [18] and Fujikura and Bruneau [17] conducted small-scale field tests to investigate the performance of the concrete-filled steel tubular (CFST) columns, ductile RC columns, and steel jacketed RC columns under air-blast loading and proposed a moment-direct shear interaction method. The blast performance of the CFST columns was found to be the most superior in comparison to the blast response of the seismically designed RC and steel jacketed RC columns. Ibrahim et al. [30] and Ibrahim and Salim [29] numerically investigated the effect of detonation distance, charge mass, steel strength, and concrete strength on the blast response of the RC deck slab using an artificial neural network (ANN) method and computed the area of damage caused by the blast. The damage in the deck slab was observed primarily in the form of concrete spalling and cratering. Results showed that increasing the strength of the steel did not influence the damage resistance of the deck subjected to blast loading. Pan et al. [35] investigated the response of 24-m single span RC slab-on-girder bridge subjected to explosive loads of 10 and 100 kg TNT (above and below deck) using the multi-Euler domain solver available in the Ansys AUTODYN program. Results indicated that the considered girder was not able to withstand the blast waves resulting from a 100 kg TNT charge. Hu et al. [24] numerically investigated the influence of geometry (circular and square), the arrangement of reinforcement, and standoff distance on the blast response of the RC piers. The maximum displacement of the square pier was found to be much higher (approximately 2 to 3 times more) than that of the circular pier when subjected to similar air-blast loading. It was concluded that the arrangement of longitudinal re-bars affects 74% of shear forces and failure modes of the pier under close-in blast loading. Hu et al. [23] experimentally investigated the performance of old single-span RC slab-on-girder bridge under above-deck air-blast loading. Three failure modes were observed, i.e., shear, flexure-shear, and flexural failures.

The literature review shows that mostly numerical investigations have been conducted by the researchers to study the effect of charge mass, standoff distance, reinforcement arrangement, geometry, steel strength, and concrete strength on the blast performance of the bridge components such as girders, piers, and deck slab. Failure modes and blast mitigation strategies for the bridge components had been discussed and investigated in the past. However, the effect of the charge locations on the blast response of the simply supported U-girder of pre-tensioned concrete was not focused upon.

The goals of this study are:

1. To develop FE model of the pre-tensioned U-girder, with rail track and rolling stock, supported on the elastomeric bearings using the Abaqus/CAE program.
2. To investigate the effect of charge locations on the close-in air-blast response of the girder.
3. To evaluate displacements, damage/crack patterns, and damage dissipation energy.

2   Numerical Modeling

A high-fidelity physics-based commercial software Abaqus/CAE 2017 has been employed in the present work to simulate the blast response of the considered girder. FE model consisting of the pre-tensioned U-girder with a rolling stock has been developed as shown in Fig. 1. The girder is supported on the elastomeric bearings. Two locations of the rolling stock have been considered in the study, one near the end support and the other at the mid-span section of the girder. The rail track is consisting of longitudinal beams, rails, and steel plates. The rolling stock is consisting of tiers (conning wheels and flanges), axles, and a wheelset joining system (Fig. 1b). The two locations of the rolling stock are describing the two charge locations considered in this study. Girder has been provided with the nominal conventional reinforcement in the form of the high-yield strength-deformed (HYSD) steel re-bars in accordance with IS 1786 [28] and also provided with a total 84 number of tendons in two layers in the deck slab in accordance with the IRS concrete bridge code [25]. Each tendon consists of 7-ply strands of 15.20 mm diameter. The rendered views of the pre-stressing and nominal reinforcements are shown in Fig. 2a and b, respectively. The spacing of the strands near the junction of flanges and deck slab is 60 mm c/c and is increased to 105 mm c/c at the mid-span. The thickness of the deck slab is 300 mm near the junction of flanges and deck slab and is reduced to 250 mm at the mid-span. The thickness of the girder flanges is 230 mm. The total weight of one U-girder is 165 tons. The thickness of the concrete cover is 40 mm. The total elongation of strands is about 1050 mm, and the total jacking force (pre-tensioned force) is about 1680 T. The dimensions of the elastomeric bearings are 260 × 480 × 85 mm (Fig. 2c). The thickness of one elastomer layer is 8 mm. The thickness of one steel reinforcement layer is 3 mm. Input parameters, including material properties of end steel plate and elastomer and stiffness properties, used for the FE modeling of the elastomeric bearings have been taken from the studies conducted by Akogul and
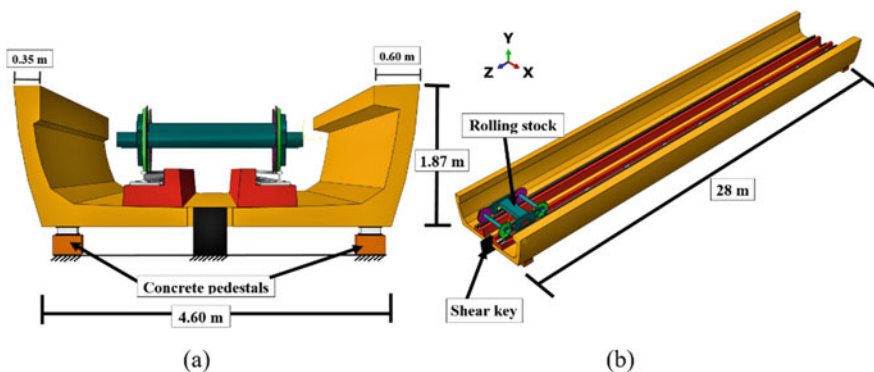
Fig. 1 Rendered views of the pre-tensioned concrete U-girder with the rolling stock near end support: **a** Elevation view and **b** Isometric view
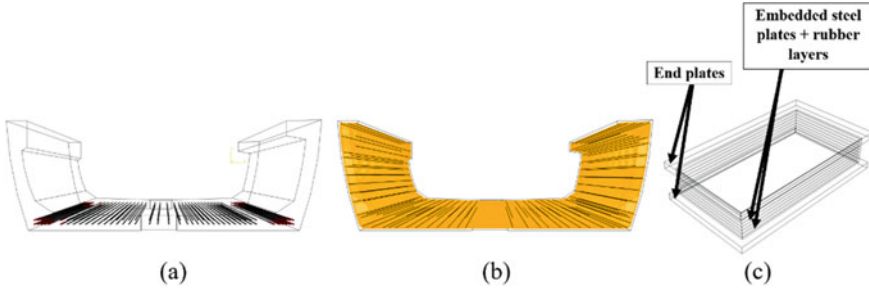
Fig. 2 Rendered view of pre-stressing reinforcement (**a**), Ordinary reinforcement (**b**), and Elastomeric bearing (**c**)

Celik [4] and Gupta et al. [20]. Head-hardened rails of grade 1080 HH have been considered in the present work following the IRS-T-12-2009 design manual [26]. Input parameters for modeling the rails have been obtained from Krishnamoorthy et al. [32]. The maximum distance between the running faces of two rails is 1.44 m (i.e., standard gage line). The ultimate tensile strength, yield strength, and ultimate percentage elongation of the rails are 1080 MPa, 460 MPa, and 10%, respectively [26]. TIE_CONSTRAINT has been used to model the interaction between longitudinal beams and rails. The material properties and dimensions of the rolling stock have been taken from *Engineering Standard Rolling Stock-Wheel and Axles Reference Manual*, ESR 0331 [16]. Shear keys are placed at the ends of the girder to restrain the lateral displacements of the girder (Fig. 1b). COUPLING_CONSTRAINT along with the self-contact interaction model has been utilized to describe the interaction between the girder and shear keys. The compressive strength, Young's modulus, and Poisson's ratio of the concrete are 50 MPa, 33.40 GPa, and 0.20, respectively. The ultimate tensile strength, yield strength, Young's modulus, and Poisson's ratio of the steel are 545 MPa, 500 MPa, 210 GPa, and 0.30, respectively.

The tendons are modeled as linear elastic, whereas the strands are modeled as a bi-linear hardening model. The pre-stressing strands or tendons are discretized with 2-node linear 3D truss elements (T3D2). The concrete is discretized with 10-node explicit continuum 3D modified quadratic tetrahedron elements (C3D10M) [3]. The re-bars or reinforcements are also discretized with 2-node explicit linear 3-D truss elements (T3D2). The HYSD steel re-bars, steel strands, and steel reinforcement layers are embedded in the girder and elastomeric bearings FE model using the EMBEDDED_REGION constraint (Abaqus user assistance guide 2017). This approach constrained translational degrees of freedom of the embedded reinforcement element nodes to the degrees of freedom of the surrounding concrete element nodes [33]. Effects associated with the steel reinforcement–concrete interface, such as bond-slip, are modeled approximately by introducing some tension stiffening into the concrete modeling to simulate load transfer across cracks through the steel reinforcement. A mesh size of 50 mm has been adopted for the girder model following the convergence test conducted under the peak overpressures of 982 and 7004 MPa. FE model has 1,782,495 nodes and 676,207 elements. The elastomeric

bearings are resting on the concrete pedestals which are assumed fixed. A surface-to-surface contact interaction, with "friction" and "hard" contact models and with penalty contact method as mechanical constraint formulation, available in the Abaqus program has been used to model the interaction between end plates and elastomeric bearings, end plates and concrete pedestals, girder and end plates, longitudinal beams and girder, and between rails and wheels of the rolling stock. The specific details of the girder can be revealed after seeking permission from the concerned authority and, therefore, are being kept confidential due to security reasons. The accuracy of the employed program and used numerical method to simulate the air-blast has been discussed in the previously published studies by the authors [3–5, 35–41].

2.1 Concrete-Damaged Plasticity (CDP) Model

In recent decades, several researchers have developed various material damage models to simulate the nonlinear response of the concrete subjected to impulsive and blast loadings. The concrete formulations are classified as the elasticity model, the plasticity model, and the elastoplastic numerical model, depending on the different problems considered. In the present study, a plasticity-based concrete damage model, i.e., the concrete-damaged plasticity (CDP) model has been employed because the CDP model has been proven to be appropriate in simulating the concrete response under both quasi-static and extreme dynamic loadings [21]. The evolution of the failure surface is controlled by two damage scalars, i.e., compressive scalar (D_c) and tensile scalar (D_t), which are connected to failure mechanisms of the concrete under compression and tension loadings [33, 34]. It is assumed that the uniaxial stress–strain curves can be converted into stress versus inelastic-strain curves [3]. This conversion is performed automatically by the Abaqus/CAE software from the user-provided stress versus plastic strain data. The uniaxial compressive and tensile responses of the concrete with respect to the CDP model under compression and tension loadings are given by [3]:

$$\sigma_c = (1 - D_c)E_0\left(\varepsilon_c - \varepsilon_c^{pl,h}\right) \tag{1}$$

$$\sigma_t = (1 - D_t)E_0\left(\varepsilon_t - \varepsilon_t^{pl,h}\right) \tag{2}$$

Here, σ_c = nominal compressive stress (MPa); σ_t = nominal tensile stress (MPa); ε_c = compressive strain ($\varepsilon_c^{pl,h} + \varepsilon_c^{el}$); ε_t = tensile strain ($\varepsilon_t^{pl,h} + \varepsilon_t^{el}$); $\varepsilon_c^{pl,h}$ = plastic hardening compressive strain; $\varepsilon_t^{pl,h}$ = plastic hardening tensile strain; ε_c^{el} = elastic compressive strain; ε_t^{el} = elastic tensile strain; and D_c and D_t = compressive and tensile scalars. In the CDP model, the damaged elastic modulus of the concrete (E_u) can be obtained by

$$E_u = \left(1 - D_{i=c,t}\right)E_0 \tag{3}$$

where E_0 is the undamaged elastic modulus of concrete (MPa) and D is the cumulative damage scalar. CDP model parameters for M50 grade concrete have been obtained from the experimental study conducted by Hafezolghorani et al. [21].

2.2 Air-blast Loading

An explosive-induced detonation is "a phenomenon in which energy is released in a very fast and violent manner" [15]. In general, the duration of the air-blast typically ranges from tens to thousands of milliseconds, in which air pressure of several thousand megapascals is produced. Two blast wave parameters defined a simple explosive-induced event, i.e., the weight of the explosive (W) and the detonation distance (S). To describe the combined effect of charge weight and detonation distance, a scaled distance (Z) was proposed by Kennedy [31] and given as in Eq. (4).

$$Z = \frac{S}{W^{\frac{1}{3}}} \ (\text{m/kg}^{1/3}) \tag{4}$$

When an explosion occurs, a high-energy reaction will produce hot gases with peak overpressures up to 100 MPa, after which the peak overpressure (P_{OP}) falls in a quasi-exponential manner to ambient air pressure (P_O) with time and distance from the target [15, 41]. Eventually, this situation returns to equilibrium, as shown in Fig. 3a, where P_{OP} is the peak overpressure; P_{S^-} is the maximum negative pressure; P_O is the ambient air pressure (≈ 0.1Mpa); t_A is the arrival time of shock wave; t_1 is the rising time; t_2 is the decreasing time; t^- is the negative blast phase duration; and t_d is the duration of positive blast phase. The air-blast pressure profile shown in Fig. 3a is expressed by an exponential equation proposed by Wu and Hao [41]:
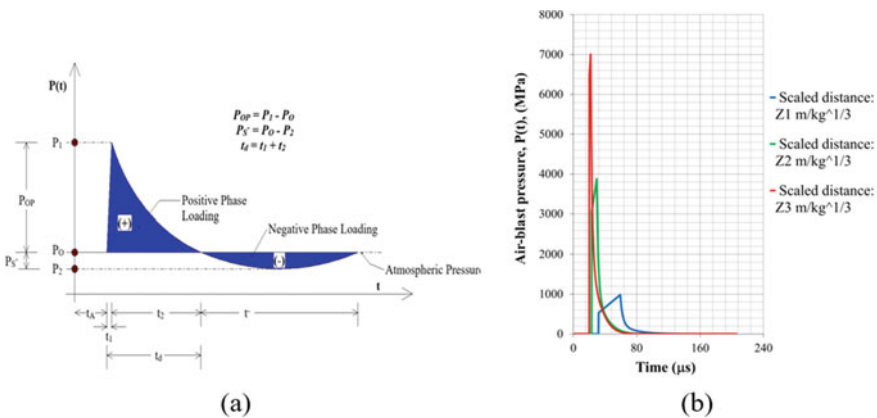
Fig. 3 **a** Idealized air-blast time history [41] and **b** Estimated air-blast time histories

Table 1 Estimated values of air-blast parameters at different scaled distances

Z (m/kg$^{1/3}$)	P_{OP} (Mpa)	t_A (μs)	t_1 (μs)	t_2 (μs)	t_d (μs)	$t_{total} = t_A + t_d$ (μs)
Z1	982.00	31.96	27.20	113.58	140.78	172.74
Z2	3877.00	23.16	6.29	146.94	153.23	176.39
Z3	7004.00	20.16	1.64	164.17	165.81	185.97

$$P(t) = \begin{cases} P_O, & (0 \leq t < t_a) \\ P_O + P_{OP}\left(\frac{t}{t_1}\right), & (t_A \leq t \leq t_1) \\ P_O + P_{OP}\left(1 - \frac{t-t_1}{t_2}\right) \cdot \exp\left(-\frac{(t-t_1)}{t_2}\right), & (t_1 \leq t) \end{cases} \text{(MPa)} \quad (5)$$

where $P(t)$ is the air-blast pressure at time "t" and Ψ is the co-efficient of decay and can be computed from [5, 41]. Current design guidelines for the blast protective structures usually recommend utilizing only the positive blast phase by assuming that the negative phase of the blast is normally much weaker and does not affect typical structures [19, 22, 27]. Thus, the influence of the suction blast phase on the performance of the considered model has been neglected in the study. Table 1 lists the values of the air-blast wave parameters, where *Z1*, *Z2*, and *Z3* are the undisclosed scaled distances and *t* is the total duration of the air-blast (neglecting negative phase). Figure 3b shows the estimated air-blast time histories.

3 Results and Discussions

AASHTO [1] and AASHTO [2] American design standards for bridge structures restrict the maximum allowable displacement in the girders to L/800 for no intended pedestrian traffic and L/1000 for intended pedestrian traffic, where "L" is the span of the girder in "mm." The maximum allowable displacement limit considered in the present study is 28 mm (i.e., L/1000). From the nonlinear explicit blast analyses conducted, the following observations are worth mentioning:

- Increasing the peak blast overpressure by factors of 4 and 7 leads to an increase of the damage dissipation energy of the FE model (for both locations of the rolling stock) by factors of 9 and 12 on account of not longitudinal but transverse bending in the girder due to the flanges (Table 2). The increase in the damage dissipation energy indicates that the girder suffers more damage and cracking.
- Large plastic deformations of 10.71, 15.06, and 25.95 mm have occurred leading to the damage of the top corner concrete under the peak overpressures of 982, 3877, and 7004 MPa, respectively (Figs. 4, 5, and 6b).
- The damage in the girder with the rolling stock at the mid-span section is found much greater (approximately 1.50–2.00 times more) than that with the rolling stock near end support under the considered blast loading because the ends of the girder are restrained by the bearings (Table 2 and Fig. 12).

| P_{OP} (MPa)	Cumulative damage dissipation energy ($\times 10^9$ J)	
	With rolling stock near end support	With rolling stock at mid-span section
982.00	2.32	4.56
3877.00	20.07	45.44
7004.00	27.30	56.90
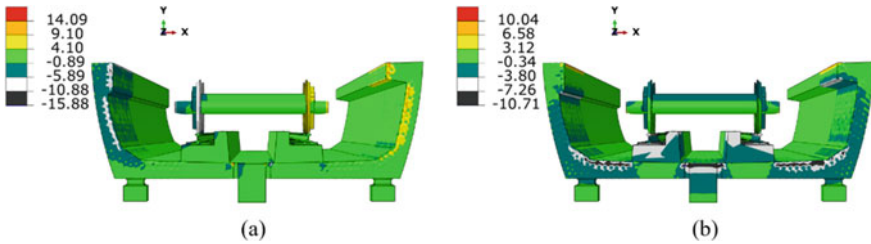
Table 2 Summary of damage dissipation energy

Fig. 4 Distribution of displacements of the girder under peak overpressure of 982 MPa, with the rolling stock near end support: **a** X-displacement and **b** Y-displacement

- Flanges are bending/stretching outward and also bending in the longitudinal direction leading to concrete spalling on the inner top compression face of the flange.
- Longitudinal cracks have been observed on the bottom face of the deck slab of the girder due to transverse bending and transverse stretching (Figs. 8, 9, 10, and 11).
- The lateral displacements of the left flange in the –X-direction are found higher than that of the right flange in the +X-direction. It is because of the difference in thickness of the flanges (or moment of inertia) at their top (Figs. 4, 5, 6, and 7a).
- Damage in the form of concrete spalling led by flexural failure has been observed on the compression side of the deck slab and flanges of the girder under the considered air-blast loading (Figs. 8, 9, 10, and 11).
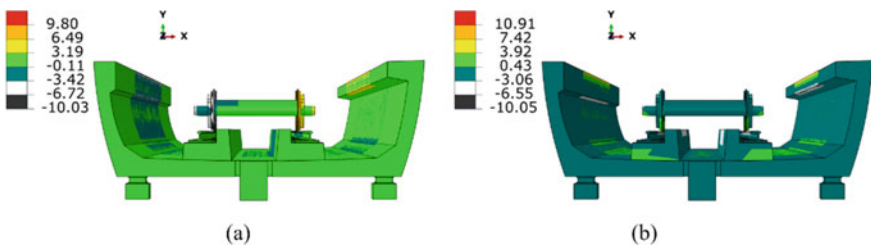

Fig. 5 Distribution of displacements of the girder under peak overpressure of 982 MPa, with the rolling stock at mid-span section: **a** X-displacement and **b** Y-displacement
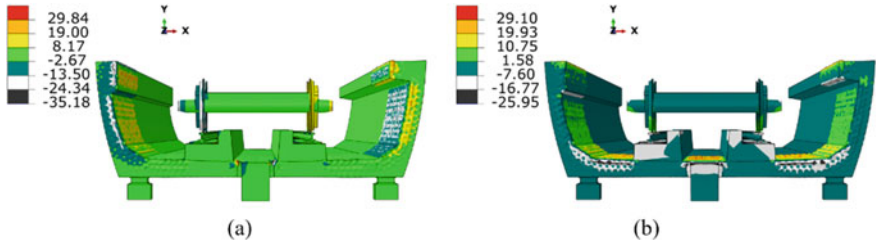
Fig. 6 Distribution of displacements of the girder under peak overpressure of 7004 MPa, with the rolling stock near end support: **a** X-displacement and **b** Y-displacement
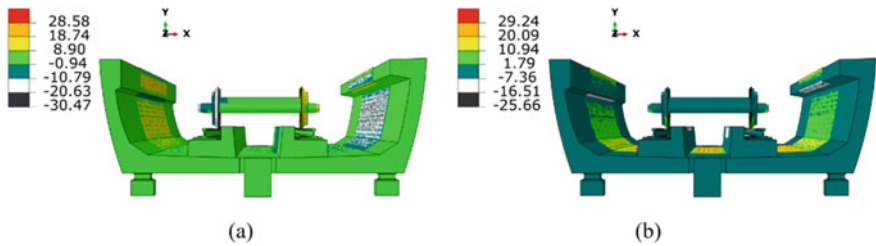
Fig. 7 Distribution of displacements of the girder under peak overpressure of 7004 MPa, with the rolling stock at mid-span section: **a** X-displacement and **b** Y-displacement
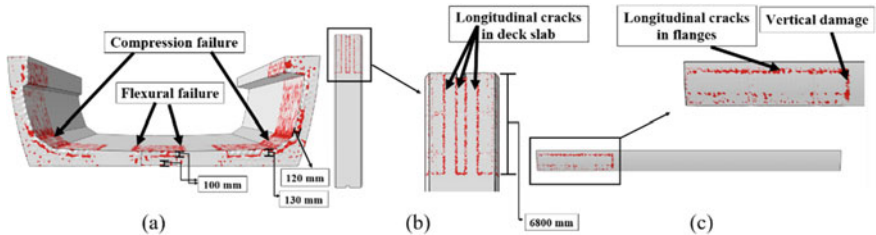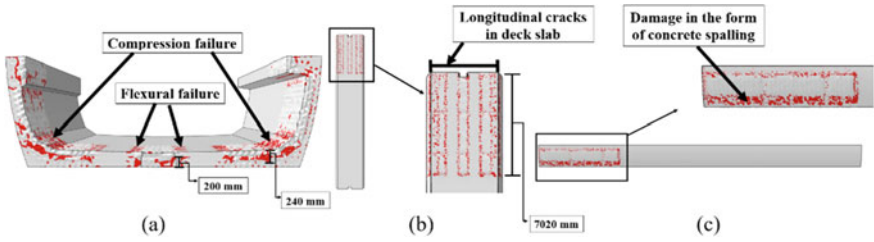

Fig. 8 Pattern of cracks in the girder under peak overpressure of 982 MPa, with the rolling stock near end support: **a** Cross-section view, **b** Bottom side, and **c** Flange along the span
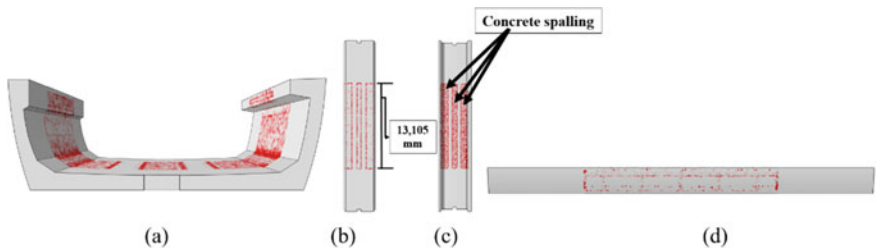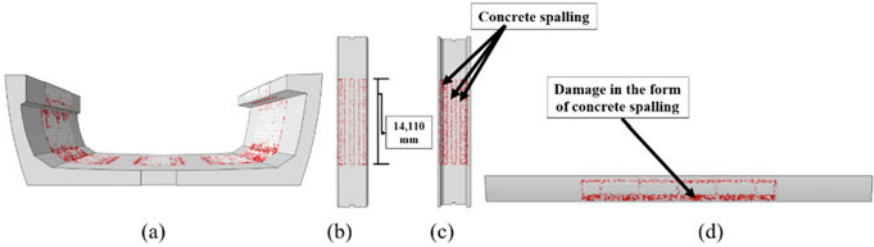

Fig. 9 Pattern of cracks in the girder under peak overpressure of 982 MPa, with the rolling stock at mid-span section: **a** Cross-section, **b** Bottom side, **c** Top side, and **d** Flange along the span
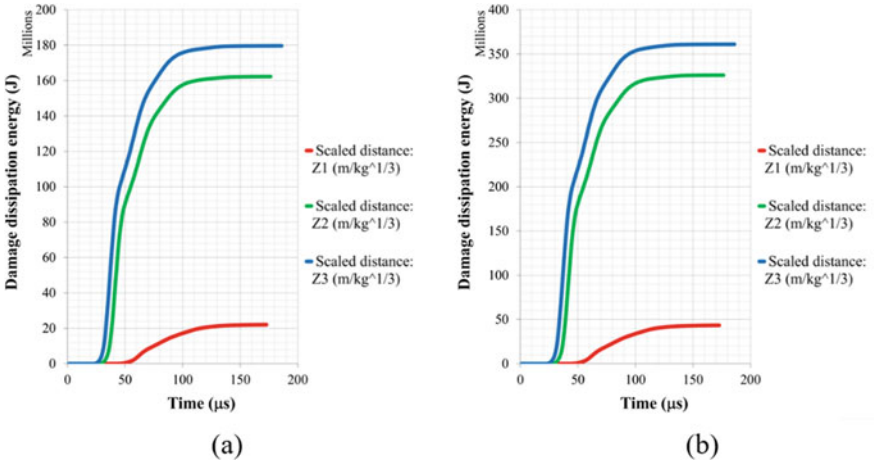
Fig. 10 Pattern of cracks in the girder under peak overpressure of 7004 MPa, with the rolling stock near end support: **a** Cross-section view, **b** Bottom side, and **c** Flange along the span

Fig. 11 Pattern of cracks in the girder under peak overpressure of 7004 MPa, with the rolling stock at mid-span section: **a** Cross-section view, **b** Bottom side, **c** Top side, and **d** Flange along the span

Fig. 12 Damage dissipation energy profiles of the girder: **a** With the rolling stock near end support and **b** With the rolling stock at mid-span section

Table 3 Summary of maximum displacements

P_{OP} (MPa)	Maximum Y-displacement (downward, mm)							
	Girder deck slab		Elastomeric bearings		Longitudinal beams		Rails	
	RS_{end}	RS_{mid}	RS_{end}	RS_{mid}	RS_{end}	RS_{mid}	RS_{end}	RS_{mid}
982.00	3.80	3.06	3.80	3.06	7.26	6.55	10.71	10.05
3877.00	5.88	5.55	5.88	5.55	12.06	11.74	15.06	14.74
7004.00	7.60	7.36	7.60	7.36	16.77	16.51	25.95	25.66

* RS_{end}: with rolling stock near end support; RS_{mid}: with rolling stock at mid-span section

- Flexural cracks with an average spacing of 500 mm, crack length of 7020 mm, and crack depth of 200 mm have been developed on the bottom side at the mid-span of the deck slab of the girder, with the rolling stock near end support, subjected to the maximum considered air-blast pressure of 7004 MPa (Fig. 10).
- The maximum downward displacements of the deck slab, longitudinal beams, elastomeric bearings, and rails of the FE model with the rolling stock near end support are found slightly higher than those with the rolling stock at mid-span section under the considered air-blast pressures (Table 3).
- Longitudinal cracks with an average spacing of 350 mm, crack length of 14,110 mm, and crack depth of 120 mm have been developed on the bottom side at mid-span of the deck slab of the girder, with the rolling stock at mid-span section, subjected to the maximum considered air-blast pressure of 7004 MPa (Fig. 11).
- The maximum displacements of the girder are found within the permissible limit.

4   Conclusion

This paper presents the finite element simulations of the pre-tensioned simply supported concrete U-girder subjected to air-blast pressures of 982, 3877, and 7004 MPa. The location of the detonation has been considered above the deck slab of the girder near the simple support of the girder and at the mid-span section. The simulations are conducted using the nonlinear finite element program, Abaqus/CAE. For the considered locations of the rolling stock, the maximum displacements of the U-girder are found within the permissible limit given in the AASHTO [1] and AASHTO [2] codes of practice for the bridge structures. However, the depth of flexural cracks on the bottom side of the deck slab of the girder is found more than half of the thickness of the deck. The damage dissipation energy in the girder with the rolling stock at the mid-span section is significantly greater (approximately 1.50–2.00 times more) than that with the rolling stock near end support under the considered air-blast loadings. The increase in the damage dissipation energy indicates that the girder suffers more damage and cracking. Damage in the form of concrete spalling led

by flexural failure has been observed on the compression side of the deck slab and flanges. Increasing the peak overpressure by factors of 4 and 7 leads to an increase of the damage dissipation energy of the girder by factors of 9 and 12. However, the displacement of the deck slab increases by factors of 1.50 and 2.00, respectively.

To improve the cracking resistance of the girder, an additional investigation needs to be conducted to study the effect of girder strengthening under close-in air-blast loading.

References

1. AASHTO (2002) Standard specifications for highway bridges. American Association of State Highway and Transportation Officials, Washington, DC
2. AASHTO (2014) Load and resistance factor design (LRFD) for highway bridge superstructures. American Association of State Highway and Transportation Officials, Washington, DC
3. ABAQUS/CAE FEA Program (2017) Concrete-damaged plasticity model, explicit solver, three dimensional solid element library. ABAQUS DS-SIMULIA user manual
4. Akogul C, Celik CO (2008) Effect of elastomeric bearing modeling parameters on the seismic design of RC highway bridges with precast concrete girders. In: The 14th World conference on earthquake engineering. Beijing, China
5. Anas SM, Ansari MdI, Alam M (2020) Performance of masonry heritage building under air-blast pressure without and with ground shock. Aust J Struct Eng 21(4):329–344
6. Anas SM, Ansari Md I, Alam M (2021) A study on existing masonry heritage building to explosive-induced blast loading and its response. Int J Struct Eng (Article in press)
7. Anas SM, Alam M (2021) Performance of simply supported concrete beams reinforced with high-strength polymer re-bars under blast-induced impulsive loading. Int J Struct Eng (Article in press)
8. Anas SM, Alam M, Umair M (2021) Experimental and numerical investigations on performance of reinforced concrete slabs under explosive-induced air-blast loading: a state-of-the-art review. In: Structures, vol 31. Elsevier, pp 428–461
9. Anas SM, Alam M (2021) Air-blast response of free-standing: (1) Unreinforced brick masonry wall, (2) Cavity RC wall, (3) RC walls with (i) Bricks, (ii) Sand, in the cavity: a macro-modeling approach. In: Marano GC, Ray Chaudhuri S, Unni Kartha G, Kavitha PE, Prasad R, Achison RJ (eds) Proceedings of SECON'21. SECON 2021. Lecture notes in civil engineering, vol 171. Springer, Cham, pp 921–930. https://doi.org/10.1007/978-981-33-6389-2_18
10. Anas SM, Alam M (2021) Comparison of existing empirical equations for blast peak positive overpressure from spherical free air and hemispherical surface bursts. Iran J Sci Technol Trans Civil Eng. https://doi.org/10.1007/s40996-021-00718-4
11. Anas SM, Alam M, Umair M (2021) Performance of one-way concrete slabs reinforced with conventional and polymer re-bars under air-blast loading. In: Chandrasekaran S, Kumar S, Madhuri S (eds) Recent advances in structural engineering. Lecture notes in civil engineering, vol 135. Springer, Singapore. https://doi.org/10.1007/978-981-33-6389-2_18
12. Anas SM, Alam M, Umair M (2021) Performance of on-ground double-roof RCC shelter with energy absorption layers under close-in air-blast loading. Asian J Civil Eng. https://doi.org/10.1007/s42107-021-00395-8
13. Anas SM, Alam M, Umair M (2021) Air-blast and ground shockwave parameters, shallow underground blasting, on the ground and buried shallow underground blast-resistant shelters: a review. Int J Protective Struct. https://doi.org/10.1177/20414196211048910
14. Anas SM, Alam M, Umair M (2020) Performance of one-way composite reinforced concrete slabs under explosive-induced blast loading. In: 1st International conference on energetics, civil and agricultural engineering 2020, ICECAE 2020, vol 614. Tashkent, Uzbekistan

15. Baker WE (1973) Explosions in air. University of Texas Press, Austin, TX
16. ESR 0331 (2013) Engineering standard rolling stock: wheel and axles reference manual. Technical Specialist Rolling Stock Performance Standards
17. Fujikara S, Bruneau M (2011) Experimental investigation of seismically resistant bridge piers under blast loading. J Bridge Eng 16(1):63–71
18. Fujikara S, Bruneau M, Garcia LD (2008) Experimental investigation of multihazard resistant bridge piers having concrete-filled steel tube under blast loading. J Bridge Eng 13(6):586–594
19. Goel DM, Matsagar AV (2014) Blast-resistant design of structures. Pract Periodical Struct Des Constr 19(2):040140071–040140079
20. Gupta A, Verma PD, Dasouni SJ, Shanker G (2014) Suitability of POT PTFE bearing in bridges. Int J Current Res Acad Rev 2(5):47–53
21. Hafezolghorani M, Hejazi F, Vaghei R, Jaafar BSM, Karimzade K (2017) Simplified damage plasticity model for concrete. Struct Eng Int 27(1):68–78
22. Hao H, Hao Y, Li J, Chen W (2016) Review of the current practices in blast-resistant analysis and design of concrete structures. Adv Struct Eng 19(8):1193–1223
23. Hu Z, Fang QJ, Sun ZL (2017) Blast effect zones and damage mechanisms of concrete bridges under above-deck car-bomb attacks. Int J Damage Mech 17(1):1–17
24. Hu JZ, Wu L, Zhang FY, Sun ZL (2016) Dynamic responses of concrete piers under close-in blast loading. Int J Damage Mech 20(1):1–20
25. IRS Concrete Bridge Code (1997) Indian Railway standard code of practice for plain, reinforced & prestressed concrete for general bridge construction. Research Designs and Standards Organisation, Lucknow
26. IRST-12–2009 (2009) Indian Railway standard specification for flat bottom rails. Research Designs and Standards Organisation, Lucknow
27. IS 4991 (1968) Criteria for blast resistant design of structures for explosions above ground. Bureau of Indian Standards, New Delhi
28. IS 1786 (2008) Indian Standard high strength deformed steel bars and wires for concrete reinforcement-specification. Bureau of Indian Standards, New Delhi
29. Ibrahim A, Salim H (2013) Finite-element analysis of reinforced-concrete box girder bridges under close-in detonations. J Perform Constr Facil 27(6):774–784
30. Ibrahim A, Salim H, Flood I (2011) Damage prediction for RC slabs under near-field blasts using artificial neural network. Int J Protective Struct 2(3):315–332
31. Kennedy WD (1946) Explosions and explosives in air, effects of impact and explosion. Summary of Technical Report of Division 2, vol 1. NDRC, Washington, DC
32. Krishnamoorthy RR, Saleheen Z, Effendy A, Alisibramulisi A, Awaludin A (2018) The effect of rubber pads on the stress distribution for concrete railway sleepers. In: 14th International conference on concrete engineering and technology, vol 431, pp 1–9
33. Lee J, Fenves LG (1998) Plastic-damage model for cyclic loading of concrete structures. J Eng Mech 124(8):892–900
34. Lubliner J, Oliver J, Oller S, Onate E (1989) A plastic-damage model for concrete. Int J Solids Struct 25(3):299–326
35. Pan Y, Chan BYB, Cheung SM (2013) Blast loading effects on an RC Slab-On-Girder bridge superstructure using the multi-Euler domain method. J Bridge Eng 18(11):1152–1163
36. Tandon M (2019) Precast concrete construction technologies for metro projects in India. NBM&CW Infra Construction & Equipment Magazine
37. Williamson BT, Winget GD (2005) Risk management and design of critical bridges for terrorist attacks. J Bridge Eng 10(1):96–106
38. Williamson BE, Bayrak O, Davis C, Williams DG (2011) Performance of bridge columns subjected to blast loads. I: experimental program. J Bridge Eng 16(6):693–702
39. Williamson BE, Bayrak O, Davis C, Williams DG (2011) Performance of bridge columns subjected to blast loads. I: results and recommendations. J Bridge Eng 16(6):703–710

40. Winget GD, Marchand AK, Williamson BE (2005) Analysis and design of critical bridges subjected to blast loads. J Struct Eng 131(8):1243–1255
41. Wu C, Hao H (2005) Modeling of simultaneous ground shock and airblast pressure on nearby structures from surface explosions. Int J Impact Eng 31(6):699–717